

NASA/CP-1998-206858/VOL1

ANALYTIC  
IN-12



6 p.

**Report**

## **AAS/GSFC 13th International Symposium on Space Flight Dynamics**

### **Volume 1**

*Tom Stengle, Editor*

*Proceedings of a conference held at  
Goddard Space Flight Center, Greenbelt, Maryland  
May 11-15, 1998*

National Aeronautics and  
Space Administration

**Goddard Space Flight Center**  
Greenbelt, Maryland 20771

---

May 1998

## The NASA STI Program Office ... in Profile

Since its founding, NASA has been dedicated to the advancement of aeronautics and space science. The NASA Scientific and Technical Information (STI) Program Office plays a key part in helping NASA maintain this important role.

The NASA STI Program Office is operated by Langley Research Center, the lead center for NASA's scientific and technical information. The NASA STI Program Office provides access to the NASA STI Database, the largest collection of aeronautical and space science STI in the world. The Program Office is also NASA's institutional mechanism for disseminating the results of its research and development activities. These results are published by NASA in the NASA STI Report Series, which includes the following report types:

- **TECHNICAL PUBLICATION.** Reports of completed research or a major significant phase of research that present the results of NASA programs and include extensive data or theoretical analysis. Includes compilations of significant scientific and technical data and information deemed to be of continuing reference value. NASA's counterpart of peer-reviewed formal professional papers but has less stringent limitations on manuscript length and extent of graphic presentations.
- **TECHNICAL MEMORANDUM.** Scientific and technical findings that are preliminary or of specialized interest, e.g., quick release reports, working papers, and bibliographies that contain minimal annotation. Does not contain extensive analysis.
- **CONTRACTOR REPORT.** Scientific and technical findings by NASA-sponsored contractors and grantees.
- **CONFERENCE PUBLICATION.** Collected papers from scientific and technical conferences, symposia, seminars, and other meetings sponsored or cosponsored by NASA.
- **SPECIAL PUBLICATION.** Scientific, technical, or historical information from NASA programs, projects, and mission, often concerned with subjects having substantial public interest.
- **TECHNICAL TRANSLATION.** English-language translations of foreign scientific and technical material pertinent to NASA's mission.

Specialized services that complement the STI Program Office's diverse offerings include creating custom thesauri, building customized databases, organizing and publishing research results . . . even providing videos.

For more information about the NASA STI Program Office, see the following:

- Access the NASA STI Program Home Page at <http://www.sti.nasa.gov/STI-homepage.html>
- E-mail your question via the Internet to [help@sti.nasa.gov](mailto:help@sti.nasa.gov)
- Fax your question to the NASA Access Help Desk at (301) 621-0134
- Telephone the NASA Access Help Desk at (301) 621-0390
- Write to:  
NASA Access Help Desk  
NASA Center for AeroSpace Information  
800 Elkridge Landing Road  
Linthicum Heights, MD 21090-2934



51-18  
169283  
337502  
168

## SKYBRIDGE STATION KEEPING STRATEGY

Pascal BROUSSE<sup>†</sup>, Pierre ROZANES<sup>†</sup>, Erick LANSARD<sup>††</sup>, Vincent MARTINOT<sup>††</sup>

This paper gives the results of a study which was conducted on the SkyBridge constellation station keeping within an Alcatel and CNES partnership framework. The first step consisted in proving the feasibility of the station keeping on the candidate orbits taking into account a relatively new and stringent station keeping criterion. Then, once the mission orbit choice had been made, the study enabled us to detail the perturbations on the real orbit and to define the type of station keeping maneuver to be performed.

The last part consisted in imagining the best possible station keeping strategy for a constellation in terms of robustness and ground workload.

The SkyBridge station keeping definition is not complete; the results presented here are not final and may still change according to choice of system or satellite.

### INTRODUCTION

The SkyBridge project, designed and promoted by Alcatel Telecom is an ambitious satellite Telecommunications program. Its goal is to offer continuous interactive multimedia services to millions of users around the world by means of a constellation of Low Earth Orbit satellites.

The baseline SkyBridge constellation consisted of a nominal 64-satellite constellation. In a partnership framework with Alcatel the CNES flight dynamics division is in charge of studying station keeping strategy.

The major problems raised by constellation station keeping analysis are, first, to assess the feasibility of a strategy in relation with the mission requirements and, then, to define a strategy which limits the operational workload generated by the orbit control of a large number of satellites.

---

<sup>†</sup> Space Mathematics Division, Mission Analysis Department, Toulouse Space Center, CNES, 18 avenue Edouard Belin, F-31401 Toulouse cedex, France. Emails : [Pascal.Brousse@cnes.fr](mailto:Pascal.Brousse@cnes.fr), [Pierre.Rozanes@cnes.fr](mailto:Pierre.Rozanes@cnes.fr)

<sup>††</sup> Alcatel, 26 avenue J.F. Champolion, BP 1187, 31037 Toulouse cedex 1, France. Emails : [erick.lansard.alcatel@e-mail.com](mailto:erick.lansard.alcatel@e-mail.com), [vincent.martinot.alcatel@e-mail.com](mailto:vincent.martinot.alcatel@e-mail.com).

For such a telecommunication service, the mission requirements lead the choice of an altitude which is as high as possible but still compatible with the allowed radiation level. In the range of altitudes selected from service quality criterion, based on geometrical coverage, minimum elevation threshold and link budget constraints, many orbit perturbations have same amplitude. The drag is not anymore the predominant perturbation, the classical station keeping strategy as the ones used at lower orbits has to be adapted to the relative importance of the lunisolar and solar radiation pressure perturbations.

Those perturbations and their effects in terms of orbital behavior must be carefully analyzed, particularly with realistic assumptions on the size, mass and shape of the satellite to precisely determine the long term orbit evolution caused by non-gravitational forces which are the main input data for the station keeping definition.

Moreover, such a telecommunication system requires a station keeping criterion which is not commonly used. The SkyBridge system is designed to provide wide band communication over the entire world to a huge set of identical terminals which have the same pointing capability. This terminal feature determines the maximum deviation allowed between the so-called reference orbit and the actual orbit and then defines the station keeping constraints which must be fulfilled over the complete orbit. As for the reference orbit it must be simple enough to be loaded once for all into the user terminal and to provide all the orbital data needed to keep the terminal in good working order: visibility dates of each of the 64 satellites, antenna pointing data for each visibility, etc..

Another key point of a constellation station keeping strategy design is its efficiency to limit the operational workload with regards to the large number of satellites. Even if the orbit surveillance and control is supposed to be automatic with human intervention only in contingency cases, the number of maneuvers should be reduced to a minimum to increase the reliability of the station keeping operation and, then, to decrease the operational workload. And this reliability should be obtained without adding, as far as possible, constraints on the telecommunication mission such as attitude maneuver before orbit maneuver which could require, in the best case, on board antenna pointing reprogramming and, in the worst case, telecommunication mission interruption.

This paper describes the SkyBridge station keeping strategy analysis and shows the feasibility of the envisaged strategies

## SKYBRIDGE STATION KEEPING REQUIREMENTS

The main requirement of the SkyBridge constellation is to provide a continuous world-wide single coverage in Ku band already used by geostationary satellites. Due to the risk of interference, a frequency sharing constraint has been introduced. The geometric modeling of this constraint is defined as in Figure 1.

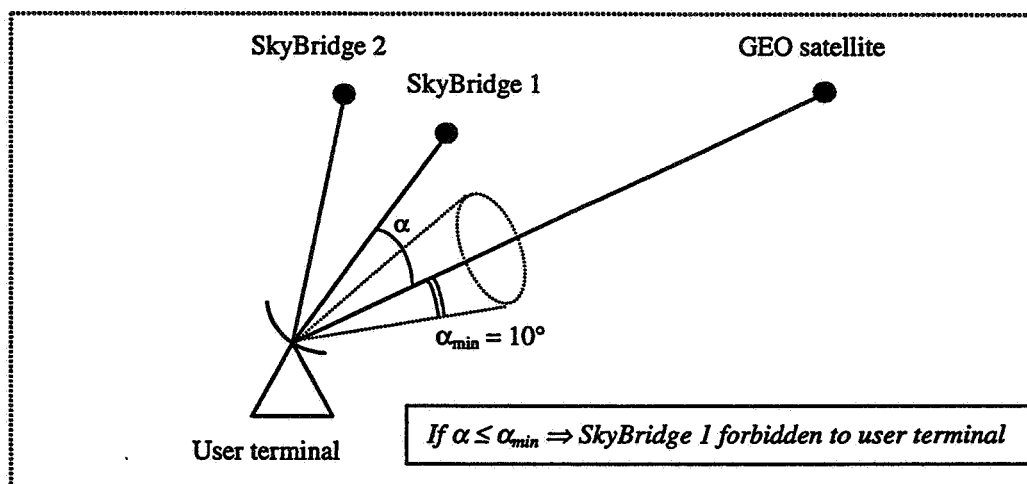


Figure 1 : Frequency Sharing Constraint

Any ground point ( user terminal ) in visibility with a SkyBridge satellite with an elevation angle above 10 degrees, cannot establish a link with this satellite if the angle between the line of sight of the user terminal to the satellite and the line of sight of the user terminal to any point of the geostationary ring is less than 10 degrees.

Despite this constraint, the system is designed to provide to any user terminal located between 70° S and 70°N a continuous single coverage.

It has been decided that the orbital data needed to schedule the terminal antenna pointing will be loaded once for all into the terminal. This solution was supposed to be simpler than a regular broadcast of updated ephemeris of all the satellites to all the terminals.

But, in order to store limited orbital data in the terminals, the reference orbit should be phased in relation to the Earth with a cycle duration of several days, to obtain a repetitive geometry.

The station keeping constraint is given by the maximum authorized deviation between the actual orbit and the reference orbit tracked in open loop by the terminals. For the time being, the system specification defines a maximum deviation of 0.5 degrees between the line of sight of the user terminal to the reference position and the line of sight of the user terminal to the actual position.

The SkyBridge station keeping requirements, phased reference orbit with a maximum angular deviation of 0.5 deg, leads inevitably to absolute station keeping.

Indeed, the purpose of the relative station keeping is to keep the relative geometry of the constellation constant while allowing the altitude to decrease. The major interest of this kind of strategy is to decrease the total number of station keeping maneuvers but, unfortunately, relative station keeping is not applicable if the orbit is to remain phased in relation to the Earth.

At the early stages of the project, two altitudes were envisaged : one 24 hour resonant orbit at an altitude of 1630 km and a non resonant orbit at an altitude of 1457 km.

### **STATION KEEPING FEASIBILITY AT AN ALTITUDE OF 1630 KM**

The nominal SkyBridge station keeping orbit is a phased circular orbit and the first step of the station keeping definition was to choose the cycle duration and the nominal altitude. The inclination of the orbit was already fixed at 55 deg.

Taking into account the J2 term of the Earth potential, the parameters of the phased orbit at these altitude and inclination were as follows:

semi major axis : 8008.000 km

number of node periods during the cycle : 12

cycle duration : 0.9902 days

eccentricity : 0

inclination : 55 deg.

With this orbit, the geometry of the constellation is periodical with a period duration of 1 day; this notably limits the amount of data corresponding to the visibility schedule and pointing data stored in terminals.

But this very short cycle duration raised the problem of the strong resonance of the orbit in relation with the Earth potential perturbation. The aim of the preliminary study was to assess the feasibility of the station keeping taking into account this strong resonance and the stringent constraint of 0.5 deg maximum deviation.

This resonance due to the earth potential causes a disturbance whose amplitude is much higher than the amplitude of the other perturbations; the station keeping feasibility study must therefore identify the maximum effect of this disturbance.

The resonant earth potential terms can be easily identified by using the Kaula development of the disturbing potential.

$$R = \frac{\mu}{a} \sum_{l=2}^{\infty} \sum_{m=0}^l \sum_{p=0}^l \sum_{q=-\infty}^{+\infty} \left( \frac{ae}{a} \right)^l F_{lmp}(i) G_{lpq}(e) S_{lmpq}$$

$$S_{lmpq} = \cos \Psi_{lmp} \times \begin{cases} Clm & \text{if } l-m \text{ is even} \\ -Slm & \text{if } l-m \text{ is odd} \end{cases} + \sin \Psi_{lmp} \times \begin{cases} Slm & \text{if } l-m \text{ is even} \\ Clm & \text{if } l-m \text{ is odd} \end{cases}$$

$$\Psi_{lmp} = (l-2p+q)M + (l-2p)\omega + m(\Omega - \theta) \quad \text{where } \theta \text{ is the sidereal time and } ae \text{ the Earth radius.}$$

As the orbit is circular, we only consider term  $q = 0$  as functions  $G_{lpq}(e)$  are null for  $e=0$  and  $q \neq 0$ .

The perturbations occur for  $\dot{\Psi}_{lmpq} = 0$

which occurs for  $l-2p=1$   $m=12$  and  $l-2p=2$  and  $m=24$ .

The quadruplets  $(l,m,p,q)$  corresponding to the main resonant terms are therefore:

$(13,12,6,0), (15,12,7,0), (17,12,8,0), \dots, (23,12,11,0), (24,24,11,0)$

The effect of these resonant terms on the semi-major axis and the inclination is a periodic effect with a very long period equivalent over a shorter time horizon to a secular effect. An analytical development allows the maximum amplitude of the phenomena to be calculated on the semi-major axis and on the inclination.

For this orbit at an altitude of 1630 km, we obtain the following values:

1.29 m/day on  $a$

and 0.0237 deg/year on  $i$ .

This effect is the maximum effect on this orbit but the actual value, in fact, depends on the initial phase and longitude of the ascending node of the orbit.

A station keeping simulation by converting the maximum angular deviation of 0.5 deg into a maximum phase deviation and a maximum node longitude deviation leads to following station keeping costs:

Total  $\Delta v$ : 20.5 m/s for a life of 8 years

inter-maneuver time: 39.5 days

with combined semi-major axis and inclination maneuvers.

The station keeping cost, although high, is not necessarily very design-critical in relation to the one generated by the positioning. This result demonstrated that the use of this orbit was feasible from a station keeping point of view.

Yet, additional radiation and space debris considerations led the constellation designers to envisage a lower altitude in order to improve the life time of the satellite. An altitude of 1457 km was then selected as the nominal station keeping altitude.

## NOMINAL ORBIT PERTURBATIONS AT AN ALTITUDE OF 1457 KM

### Nominal parameters of the reference orbit

The first step of the new altitude analysis was to define the corresponding nominal parameters :

the inclination was still fixed at 55 deg,

the number of nodal periods per day was chosen equal to  $12+11/28$  which gives a semi major axis equal to 7834.983 km and a cycle duration of 27.709970 days

Because the purpose of the reference orbit is to have constant parameters, it was decided to choose a frozen eccentricity. Indeed it is unthinkable to have a reference orbit with an eccentricity vector which is time variable, it is simpler to have a constant eccentricity vector which is achieved by freezing the eccentricity  $\begin{pmatrix} \dot{e} = 0 \\ \dot{\omega} = 0 \end{pmatrix}$ .

Taking into account the zonal terms of the earth potential from J2 to J16 and the nominal values of the semi major axis and the inclination, the components of the reference eccentricity vector are as follows :

$$e = 0.94064 \cdot 10^{-3}$$

$$\omega = 90 \text{ deg}$$

The initial values of the other orbital parameters  $\Omega$  and  $\alpha = \omega + M$  are not specified because they could range from 0 deg to 360 deg depending on date and on satellite considered in the constellation.

In fact, all the right ascension of the ascending node and phase values will be deduced, at a given date, from the constellation architecture and the actual values reached by the first 4 satellites launched in the plan which will become the first plan of the constellation. Today there is no requirement on the initial value of the ascending node longitude of this first plan.

The nominal mean parameters of the reference orbit are summarized below :

$$a = 7834.983 \text{ km}$$

$$i = 55 \text{ deg}$$

$$e = 0.94064 \cdot 10^{-3}$$

$$w = 90 \text{ deg}$$

The SkyBridge constellation architecture is given by the Figure 2.

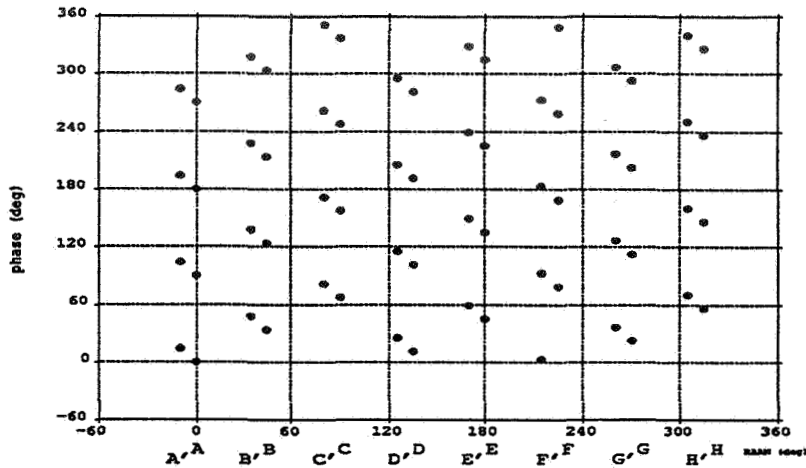


**Figure 2 : SkyBridge Constellation Architecture**

### **Orbit perturbations**

The hypotheses on the satellite surface and mass taken into account to compute the orbit perturbations are the following :

solar panel surface :  $47 \text{ m}^2$

average satellite body surface :  $4 \text{ m}^2$

satellite mass :  $1000 \text{ kg}$

The perturbations to be analyzed are the perturbations leading to deviation of the actual orbit with respect to the reference orbit. The long term deviation between the two orbits will be controlled by the station keeping strategy to fulfill the maximum deviation constraint.

The relative perturbations between two different orbital planes of the constellation due to the relative geometry of each plane with respect to the sun, the moon and the earth are not analyzed because they have no impact on the station keeping strategy definition, they just produce a natural shift between the maneuver calendar of each satellite.

The main results of our perturbation analysis are presented below.

### Atmospheric drag perturbation

The atmospheric drag leads to a decrease of the semi-major axis at different rates depending on the solar activity (Figure 3).

Solar activity	$da/dt$ (m/j)
<i>high</i>	<i>0.44</i>
<i>medium</i>	<i>0.17</i>
<i>low</i>	<i>0.10</i>

### SkyBridge Station Keeping: Drag

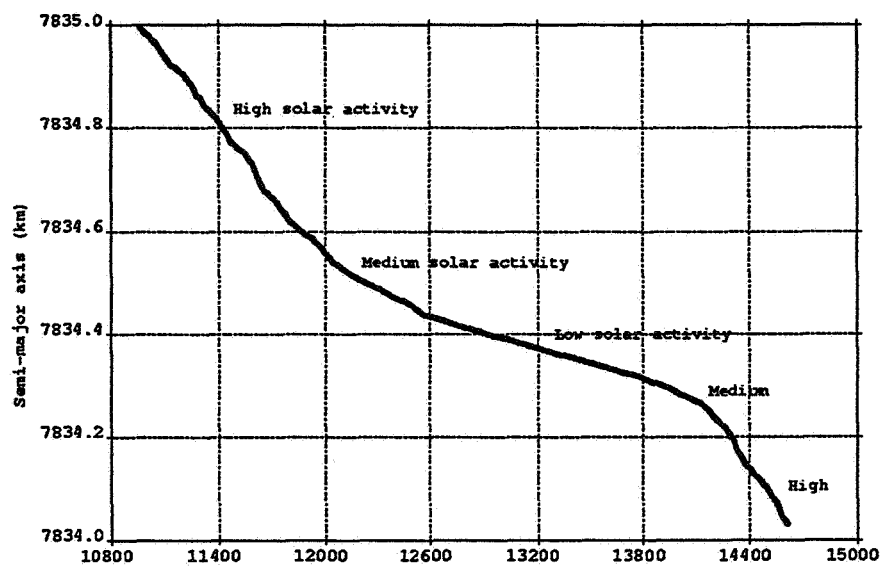


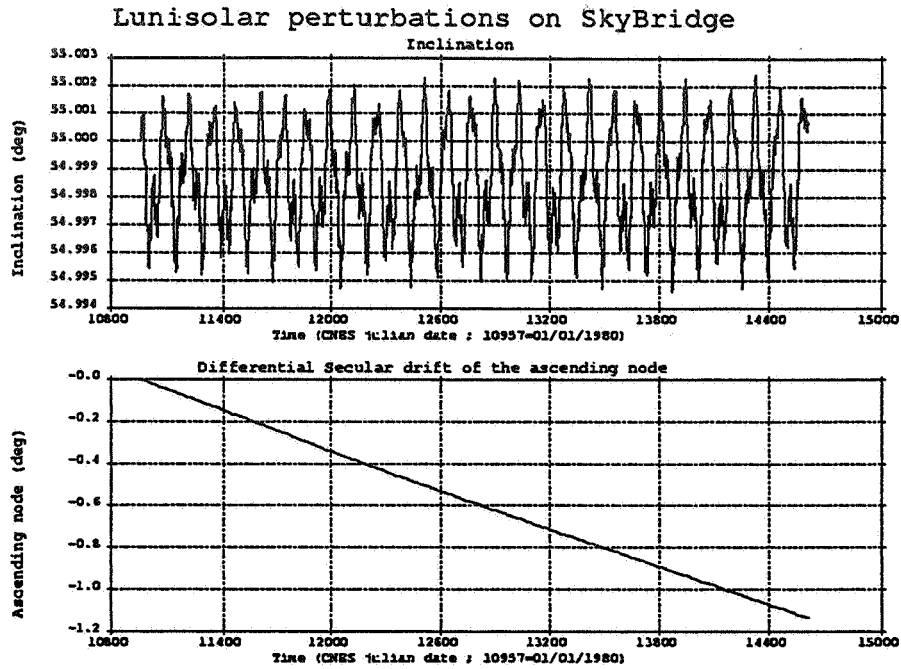
Figure 3 : Drag Perturbation Between 1980 And 1990

### Perturbations due to the luni-solar potential

As shown in Figure 4, the luni solar potential leads to a periodical evolution of the inclination but generates a secular drift on  $\Omega$  which has to be controlled .

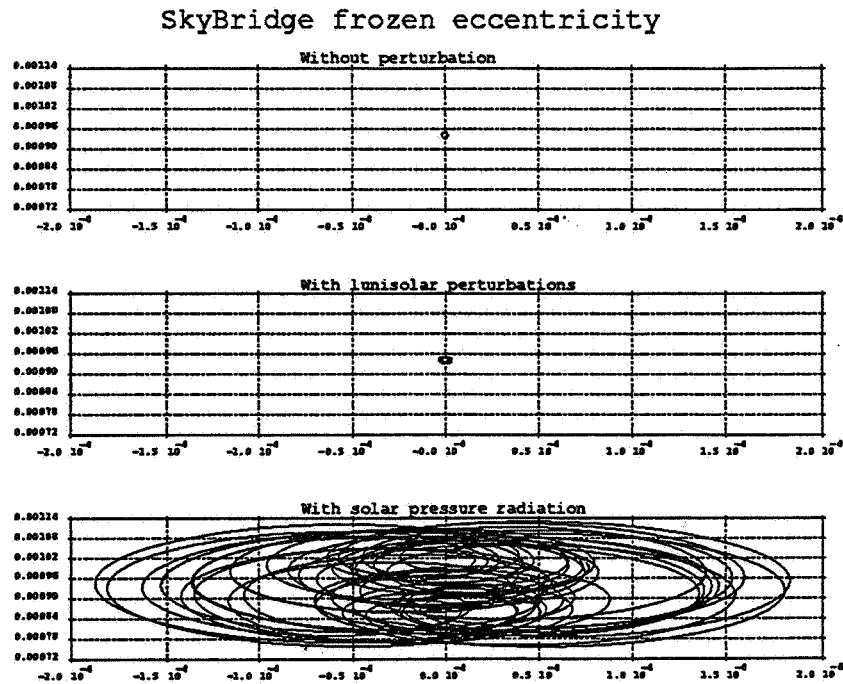
$\Omega$	<i>0.12 deg/year</i>
$i$	<i>Two periods :</i> <i>130 days due to the moon</i> <i>48 days due to the sun</i>





### Perturbation due to the solar radiation pressure

The main effect of the solar radiation pressure is a periodic evolution of the eccentricity around the frozen eccentricity



## STATION KEEPING STRATEGIES

### Station keeping criterion

The SkyBridge station keeping requirement is based on the maximum angular deviation seen from a ground station between the actual satellite and its reference position. The user terminal tracks the satellite in open loop following the reference orbit and the allowed angular deviation,  $\delta$ , compatible with the terminal link budget is fixed to 0.5 deg whatever the relative geometry between the user and the satellite.

To define the station keeping strategy, the maximum value of  $\delta$  reached over a complete orbit has to be written as a function of the orbital parameter deviation between the reference orbit and the actual orbit.

To obtain this equation, the first step is to write the maximum angular deviation,  $\delta_c$ , seen from the earth center between two orbits :

$$\delta_c^2 = (\delta\alpha + \cos i \delta\Omega)^2 + \delta i^2 + (\sin i \delta\Omega)^2$$

where :

- $\delta\alpha$  is the phase deviation
- $\delta\Omega$  is the RAAN deviation
- $\delta i$  is the inclination deviation

and considering small angles.

Then  $\delta_c$  can be easily linked to  $\delta$  by the following formula :

$$\tan \delta = \frac{a \sin \delta_c}{a \cos \delta_c - ae}$$

The following drawing (Figure 6) shows the optimal evolution over time of  $\delta$  considering only an initial phase deviation and the atmospheric drag as disturbance.

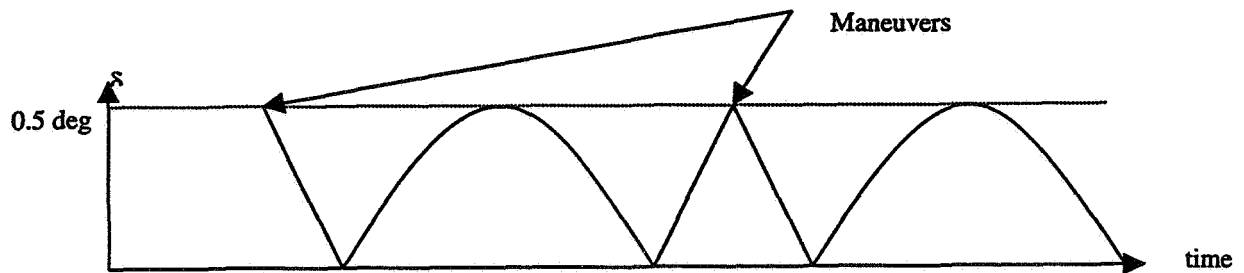
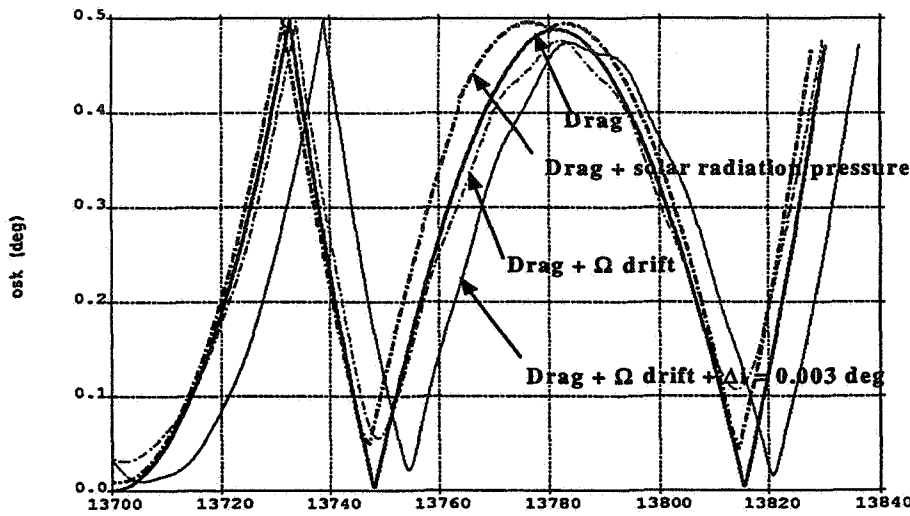


Figure 6 : Sketch Of The Station Keeping Criterion Evolution

And the Figure 7 shows the effects of the different perturbations on the actual evolution of  $\delta$ .



**Figure 7 : Effects Of Perturbations On The Station Keeping Criterion Evolution**

It appears that :

- the atmospheric drag is still the main perturbation for the station keeping criterion,
- an initial inclination offset of 0.003 deg on the actual orbit allows the secular drift on  $\delta\Omega$  to be decreased. As there is no secular evolution on the inclination deviation, this enables us to write roughly  $\delta$  as the sum of a term which is a function of  $\delta\alpha$  and a quasi constant term

$$\delta^2 = \delta\alpha^2 + 2 \delta\alpha \delta\Omega \cos i + \delta\Omega^2 + \delta i^2$$

So the main purpose of the SkyBridge strategy is to maintain the semi-major axis around its reference value taking into account the satellite attitude law used to maintain the solar panels pointed towards the sun for power optimization.

### Satellite attitude law

To permanently orient the solar panels towards the sun two degrees of freedom are used :

- a rotation around the Z axis which is the nadir axis,
- and a rotation around the Y axis which is the rotation axis of the solar panels.

The optimal combination of these two rotations leads to a continuous yaw steering of the spacecraft over its orbit. The theoretical law is given with the notation of Figure 8 by the following formula

$$\operatorname{tg} \phi = -\frac{\operatorname{tg} \beta}{\sin(\alpha - \alpha_0)}$$

where  $\beta$  is the angle between the sun line and the orbital plane,

$\phi$  is the spacecraft yaw axis.

and  $\alpha$  is the in orbit position in reference with  $\alpha_0$  which is the canonical position.

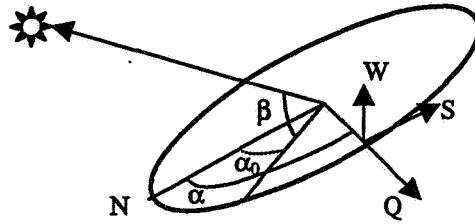


Figure 8 : Angle Definition

Even if a simplified law is loaded into the satellite, the yaw angle follows a periodic evolution whose amplitude is a function of  $\beta$ .

The yaw steering strategy is used continuously except when  $\beta < \beta_0$ . When  $\beta$  is near this angular limit a fixed yaw attitude is utilized to avoid excessive yaw rates. In this case, the satellite is positioned at a yaw angle of 0 or 180 deg.

According to this attitude law, three orbit control strategies are possible which adapt differently to attitude control.

#### **Strategy 1:**

With this strategy, we only correct the semi-major axis when yaw steering is disable. In this mode, the yaw angle is equal to 0 deg or 180 deg, the nozzle is then oriented according to the speed of the satellite or opposing the speed of the satellite. This configuration enables the semi-major axis to be increased or decreased.

The yaw steering mode is disable periodically every 47 days during a period lasting several days.

This strategy does not allow correction of  $\Omega$  or correction of  $i$ .

#### **Strategy 2:**

In this strategy, whatever the attitude of the satellite, an attitude manoeuvre is performed before the orbit maneuver to obtain optimum maneuver attitude. This strategy enables all optimum orbit corrections but leads to strong coupling between the attitude and the orbital maneuvers.

This strategy leads to a depointing of the solar panels during orbital corrections and can lead to an interruption in the telecommunication service.

#### **Strategy 3:**

In this strategy, we will make semi-major axis maneuvers whatever the yaw angle value ensuring that the off-plane thrusts induced do not lead to evolutions of  $\delta\Omega$  and  $\delta i$  incompatible with the station keeping strategy. To avoid the off-plane component from being too high, the manoeuvre are only performed when the yaw angle is lower than 60 deg.

This strategy enables semi major axis corrections to be made practically at all times. It also enables  $\Omega$  and  $i$  corrections to be made if required.

#### **Station keeping strategy trade-off**

The station keeping of a constellation must be as flexible as possible to, on the one hand, generate minimum possible constraints on the mission and, on the other hand, to limit the operational constraints.

A strategy which is not robust may lead to extra operational work in case of unexpected dispersion. Although this extra work maybe possible for a single satellite system, it is certainly very difficult to absorb when controlling a constellation.

This is why, at this stage in the study, strategy 3 seems the most suitable. Indeed, it enables maneuvers to be made practically at all times without generating additional attitude maneuvers.

Strategy 1 is highly constraining concerning possible maneuver slots; it is therefore not very robust in case of dispersion and generates a higher number of maneuvers.

Strategy 2, although optimum for orbit control, generates too high a constraint on the payload which must take into account the scheduled maneuvers to repoint its onboard antennas.

Strategy 3 leads to negligible extra costs in terms of consumption while offering all the possibility of types of maneuvers which makes the strategy robust to dispersion. Also, it generates a number of maneuvers near to the optimum number of maneuvers.

The table below summarizes the performances of each of the strategies over a life time of 8 years and taking into account a medium solar activity.

Strategy	total $\Delta v$ (m/s)	total $\Delta vt$ (m/s)	average $\Delta v$ (mm/s)	Number of maneuvers	Average time interval between (days)
1	0.25	0.25	5	46	62
2	0.24	0.24	7	35	80
3	0.38	0.24	11	36	78

## CONCLUSION

This study conducted by CNES in partnership with Alcatel has enabled us to prove the feasibility of the SkyBridge station keeping on two different orbits, one being highly resonant.

As, finally, a non-resonant orbit was chosen, the perturbations were analyzed to evidence the perturbations of the real orbit in relation to the reference orbit.

Lastly, a strategy robust to dispersions and without additional constraints was proposed. It seems today the most suitable for controlling this 64-satellite constellation.

Of course, the Skybridge station keeping is not yet frozen and still subject to refinements. Bu the current paper shows that there exists efficient feasible solutions and the trade-offs between the possible options are well understood.

## **ACKNOWLEDGEMENTS**

The authors would like to thank Luc Lefebvre and Laurent Lagarde from CNES for their contribution to this work.

## **REFERENCES**

1. JL Palmade "The SkyBridge constellation design" International Workshop on Mission Design & Implementation of Satellite Constellations, November 1997.
2. RB Frauenholz " The Role of Anomalous Satellite-Fixed Accelerations in Topex/Poseidon Orbit Maintenance" AAS/AIAA Astrodynamics Specialist Conference, August 1993.
3. L. Lefebvre. "Relative Station Keeping Optimization For The Starsys Constellation" 12<sup>th</sup> International Symposium on Space Flight Dynamics. June 1997.





337506  
121.

AAS 98-301

52-43

169284

## MULTI-SUNSYNCHRONOUS CONSTELLATIONS FOR CONTINUOUS SURVEILLANCE IN TROPICAL REGIONS

Marco M. Castronuovo<sup>†</sup>, Carlo Olivieri<sup>\*</sup> and Giovanni Laneve<sup>‡</sup>

Uniform Homogeneous Constellations (UHC) of small satellites on multi-sun-synchronous (MSS) orbits, which allow to revisit any given location every  $m$  nodal days with an integer number  $n/m$  of different illumination geometries repeated every  $n$  days, have been considered. These constellations could offer a good means of continuous surveillance for the tropical regions where natural disasters, such as floodings and droughts, are most common.

A study has been carried out to ascertain how they allow to obtain efficient revisit coverages and repeat cycles, deploying satellites on one or more orbital planes whose inclination has been chosen equal to tropical latitudes. The dynamical behaviour of a satellite constellation has been simulated, so to analyze the configuration and coverage evolution under the effects of the major perturbations.

### INTRODUCTION

Satellite remote sensing offers the only means of obtaining synoptic coverage of large geographical regions; sunsynchronous quasi-polar orbits allow to observe from low altitudes a wide latitudinal range, excluding the polar caps.

However longitudinal coverage is strictly related to the swath width of the onboard instrument and to the required revisit frequency of observation; the spatial gaps occurring between two consecutive satellite ground traces is uniformly reduced if a suitable value  $m$  of nodal days is accepted. The gap is so much wider how lower is the latitude; for this reason the observation of low latitude areas is critical since here a high spatial resolution and fast response to the detection of natural and human-caused catastrophes is particularly required. The best solution is obtained when the gap (either temporal or spatial) is reduced by using a constellation with satellites located on circular Multi-SunSynchronous (MSS) orbits<sup>1</sup>. A study has been carried out to obtain efficient

---

<sup>†</sup> Post Doc Fellow of the Università degli Studi di Roma "La Sapienza", Scuola d'Ingegneria Aerospaziale, Via Eudossiana 16, Rome, Italy. Phone: ++39 6 812-0529, FAX: ++39 6 810-6351. e-mail: castronu@crasan.psm.uniroma1.it

<sup>\*</sup> Full Professor of the Università degli Studi di Roma "La Sapienza", affiliated with the Centro di Ricerca Progetto San Marco, Via Salaria 851, 00138 Rome, Italy.

<sup>‡</sup> Assistant Professor of the Università degli Studi di Roma "La Sapienza", Scuola d'Ingegneria Aerospaziale, Via Eudossiana 16, Rome, Italy.

revisit coverages and repeat cycles from satellites deployed on one or more orbital planes whose inclination has been chosen close to tropical latitudes.

The dynamical behavior of a test-case constellation has been simulated numerically by means of GEODYN II software package, so to analyze the configuration and coverage evolution under the effects of the major perturbations.

## SINGLE SATELLITE REPEATING GROUND TRACK PATTERN

A single circular orbit satellite will perform a continuous ground track pattern; the geographical coordinates of its nadir trace for a uniformly rotating spherical earth are given as:

$$\begin{cases} \phi = \text{latitude} = \sin^{-1}(\sin i \sin u) \\ \lambda = \text{longitude} = \lambda_0 + \tan^{-1}(\cos i \tan u) - (\omega_E - \dot{\Omega})t \end{cases}$$

These relations are obtained by applying Napier's rules to the spherical triangle represented in Figure 1;  $\omega_E$  is the angular earth rotation,  $\dot{\Omega}$  the orbital nodal precession rate and  $u$  the argument of latitude.

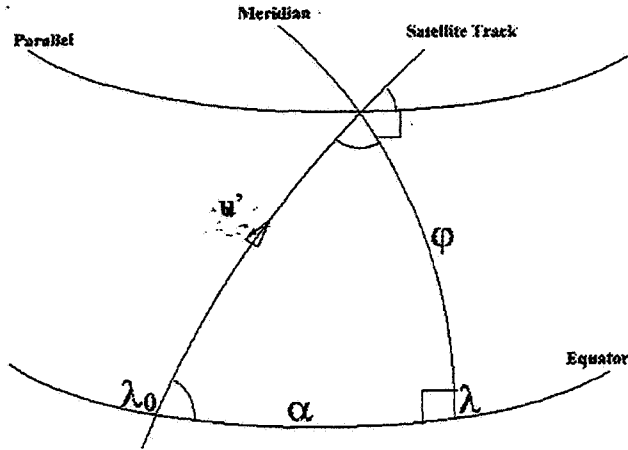


Figure 1 Geometry of satellite ground track

The westward longitudinal separation between consecutive equatorial crossing ( $S_t$ ) is given by:

$$S_t = T_n (\omega_E - \dot{\Omega}) \quad (1)$$

where  $T_n$  is the orbital nodal period, whose expression is

$$T_n = 2\pi \sqrt{\frac{a^3}{\mu}} \left[ 1 - \frac{K}{a^2 \sqrt{\mu}} (4 \cos^2 i - 1) \right] \quad (2)$$

where:

$$K = \frac{3}{2} J_2 R_E^2 \sqrt{\mu}$$

Unless using a sensor with a quite wide swath, the spatial gap between the consecutive revolutions of the track pattern does not guarantee a complete coverage in a period of the order of few days; on the other hand the condition for periodic coverage is that the nadir trace is duplicated after some definite period of time after which the previous pattern is retraced and so on indefinitely. The possibility to have the required coincidence of the  $R^{\text{th}}$  orbital node with the nodal earth rotation is accomplished by adjusting the satellite nodal period so as to produce exactly  $R$  revolutions in  $m$  nodal days ( $D_n$ ):

$$m D_n = R T_n \quad (3)$$

with

$$D_n = \frac{2\pi}{\omega_E - \dot{\Omega}} \quad (4)$$

When the apparent motion of the Sun ( $\Omega'_s$ ) is equal to  $\Omega'$  (sunsynchronous condition)  $D_n \equiv \text{solar day}$ .

Since  $m$  and  $R$  are restricted to integral values Eq. (3) tends to limit  $T_n$  (and then the corresponding altitudes) to a series of discrete values, taking also into account the necessity of considering periods of reasonable durations in order to locate satellites in low orbits (avoiding, however, excessive air drag). Substituting Eqs. (2) and (4) into Eq. (3) and expressing  $\Omega'$  as a function of  $a$  and  $i$ , we obtain the following polynomial in  $a$  for the periodicity condition:

$$C_1 a^{5.5} + C_2 a^4 + C_3 a^{3.5} + C_4 a^2 + C_5 = 0 \quad (5)$$

with

$$C_1 = \frac{\omega_E}{\sqrt{\mu}}; \quad C_2 = -\frac{m}{R}; \quad C_3 = -\frac{\omega_E}{\mu} K (4 \cos^2 i - 1)$$

$$C_4 = \frac{K}{\sqrt{\mu}} \cos i; \quad C_5 = -\frac{K^2}{\mu} \cos i (4 \cos^2 i - 1)$$

The coverage pattern also can be considered discrete (intermittent). The  $m$ -fold equatorial arc is evenly divided in two different ways: in  $m$  equal parts and also in  $R$  equal parts; the simplest single division mode which includes both the  $m$  and the  $R$ -fold divisions is the least common multiple of  $R$  and  $m$  or  $lcm(R, m)$ . This solution is unique; in practical applications the uniqueness requirement is met simply by assuming that only relatively prime  $m, R$  pairs are considered.

The number of orbits performed in one day is the repetition factor  $Q$  which can be split in two terms according to the relation

$$Q = N_i + N_f = N_i + \frac{k}{m} \quad (6)$$

where  $N_i$  is the integer number of orbits performed daily and  $N_f$  is its fractional part. Then the abovesaid possible solutions (pairs of  $R$  and  $m$ ) are given by the values of  $k$ , prime integer with  $m$  and  $1 \leq k \leq m-1$ ; it defines the ground track spacing according to the relationship:

$$\lambda_d = \lambda_0 + S_t \bmod \left( d \frac{k}{m} \right) \quad (7)$$

where  $\lambda_d$  represents the crossing longitude on day  $d$ ,  $\lambda_0$  is the co-rotating crossing longitude at the initial time ( $d = 0$ ) and the operator

$$\bmod(x) = \text{frac}(x) - \text{int} \left[ \text{frac}(x) + \frac{1}{2} \right]$$

allows to have subsequent crossings within  $\lambda_0 \pm S_t / 2$ , according to Hopkins' notation<sup>2</sup>. After  $m$  days, the longitudinal increment  $S_t$  will be divided in  $m$  equal increments of longitude  $S_m = S_t / m$ ; during the pattern development between two consecutive nodes, each day's nodal co-rotating crossing occurs east (or west) of the previous day's node by  $\pm k S_m$  where the sign is positive or negative if  $k < m / 2$  or  $k > m / 2$  respectively.

$S_m$  is related to the swath width of the instruments and influences the choice of a uniformly distributed ground tracks at the end of the repeat interval. In fact, coverage of the earth's equatorial region from a satellite is accomplished if the swath width on the earth's surface required for coverage is equal to the minimum longitudinal interval  $S_m$  between earth traces. If  $N_f = 0$  then the number of orbits performed must be an integer and the repeat interval  $m$  is only one day.

## UNIFORM HOMOGENEOUS CONSTELLATIONS

Our interest is limited to constellations consisting of satellites evenly deployed on circular orbits with the same altitude and inclination (Uniform Homogeneous Constellations - UHC). Previous works demonstrated that the addition of the number of satellites  $N$  on the same orbital plane and of the number of orbital planes  $P$  to a constellation has the potential of improving both revisit and spatial coverage<sup>3,4</sup>. Table 1 summarizes all the possible situations for single and multi-plane UHC.

**Table 1**  
**SINGLE AND MULTI-PLANE UHC**

	<u><math>r</math> (nodal days)</u>	<u><math>S_m</math> (km)</u>	<u><math>m/r</math></u>
$P$ (highest revisit frequency)	$\frac{lcm}{P \cdot N}$	$\frac{S_t}{lcm}$	$\frac{P \cdot m \cdot N}{lcm}$
$P$ (minimum ground track spacing)	$\frac{lcm}{N}$	$\frac{S_t}{P \cdot lcm}$	$\frac{m \cdot N}{lcm}$

where  $r$  is the repeat cycle of the constellation (nodal days) and  $lcm = lcm(N, m)$  is the least common multiple between  $N$  and  $m$  and  $S_m$  is the minimum ground track spacing.

## ORBIT SELECTION

In order to provide a service of continuous and global surveillance of the tropical regions the mission design must take into account several requirements in the orbit selection. The orbit periodicity (repetitivity), and the same geometry of illumination for remote sensing systems operating in the visible are the main ones.

The condition of multisunsynchronism (MSS) is obtained when the difference between the apparent solar motion  $\Omega_s'$  and the orbital nodal precession rate  $\Omega'$  is a submultiple of the difference between the angular earth rotation  $\omega_e$  and  $\Omega'$ . Since  $\Omega'$  depends on both the inclination  $i$  and the semi-major axis  $a$  of the orbit, the MSS condition can be expressed by the relation:

$$a^{7/2} = -K \frac{n \mp 1}{n \dot{\Omega}_s \mp \omega_E} \cos i \quad (8)$$

where  $n$  is the number of nodal days necessary to re-encounter the same geometry of illumination. The upper sign is valid for  $\dot{\Omega}' < \dot{\Omega}_s'$ , the lower one corresponds to  $\dot{\Omega}' > \dot{\Omega}_s'$ . In our specific case orbits with inclination around the tropical latitudes have been considered so that  $\dot{\Omega}' < 0$ , therefore the upper sign should be considered. Eq. (8) is represented in Figure 2 for inclinations between  $20^\circ$  and  $35^\circ$  and satellite altitudes between  $400 \text{ km}$  and  $1000 \text{ km}$  for various values of  $n$ .

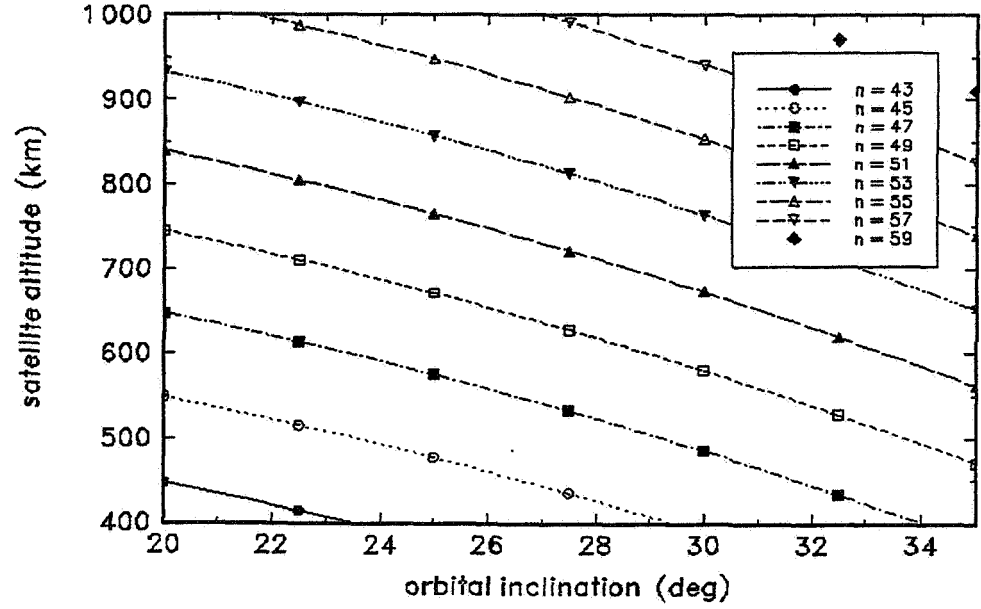


**Figure 2 Multi-sunsynchronous solutions from Eq. (8)**

Among all these solutions only periodic orbits should be considered. This can be obtained by solving simultaneously Eq. (5) and Eq. (8). Expliciting  $\cos i$  from Eq. (8) and substituting into Eq. (5) we obtain the following polynomial in  $a$  whose solutions are both periodic and MSS, provided that  $m$  is a submultiple of  $n$  and that  $R$  and  $m$  are prime.

$$C_1 a^7 + C_2 a^2 + C_3 a^{0.5} + C_4 = 0 \quad (9)$$

with

$$C_1 = \frac{4}{\mu K} \left( \frac{n\dot{\Omega}_s - \omega_E}{n-1} \right)^2; \quad C_2 = -\frac{1}{\sqrt{\mu}}$$

$$C_3 = -\frac{m}{R} \frac{n-1}{n(\dot{\Omega}_s - \omega_E)}; \quad C_4 = -\frac{K}{\mu}$$

To obtain reasonable values for the orbital altitude (say between *400 km* and *1100 km*) *R* should be given a value around  $(12 \div 14) \times m$ . Examples of solutions of Eq. (9) are shown in Table 2. The selection among all possible solutions has been done in accordance with the following criteria. The value of the illumination cycle *m* has been chosen to be the lowest possible, since a UHC constituted by an equal number of satellites has a revisit frequency of *1 nodal day*; the satellite altitude *h* has been limited between *400 km* and *1100 km* and the orbit inclination *i* between  $23.45^\circ$  and  $35^\circ$ . Then, for each solution found, the minimum instantaneous field of view (min. ifov) necessary to obtain the global coverage of the earth has been computed. The last column of Table 2 contains the distance between the ground tracks at the equator.

It should be noted that since the orbital inclination *i* does not appear in Eq. (9), its value will be computed by Eq. (8) once Eq. (9) has been solved for the value of the semi-major axis *a*. This means that also the orbital inclination can assume only discrete values in accordance with the integer numbers *m*, *n* and *R* that are used as input. Obviously appropriate triples of *m*, *n* and *R* can produce orbital inclination values in the desired range.

According to Table 1 the revisit frequency can be reduced to values below *1 nodal day* deploying a number *N* of satellites (equal to *m*) on each of *P* orbital planes. So, for example, in the cases with *m* = 2 a revisit frequency of  $\frac{1}{2}$  *nodal day* can be obtained with a UHC composed by 4 satellites, deployed on 2 orbital planes (2 satellites on each orbital plane) with ascending nodes at  $90^\circ$  apart. Of course the choice of a particular MSS orbit as reference trajectory for a surveillance constellation is the result of a trade-off process among several conflicting parameters such as the illumination cycle duration (that determines the number of satellites required to have a specific revisit frequency), the height of the orbit (and therefore the required instantaneous field of view to obtain global coverage), the inclination (determining the extension of the area to be covered) and the number of different illumination geometries. The requirements of each particular mission will determine, time by time, the conditions to be met by the constellation.

**Table 2**  
**MSS ORBITS WITH INCLINATION AROUND TROPICAL LATITUDE**

<u>m</u>	<u>n</u>	<u>h (km)</u>	<u>i (deg)</u>	<u>R</u>	<u>k</u>	<u>min. ifov (deg)</u>	<u>Sm (km)</u>
2	50	644.41	26.60	29	1	51.29	1381.90
2	54	648.18	35.14	29	1	63.06	1381.90
2	58	999.34	27.08	27	1	37.36	1484.26
2	60	1000.74	31.22	27	1	42.06	1484.26
3	48	588.20	24.21	44	2	35.22	910.80
3	51	700.59	26.08	43	1	32.60	931.98
3	54	703.31	32.81	43	1	39.50	931.98
3	57	937.63	28.01	41	2	27.51	977.44
3	60	939.82	33.83	41	2	32.29	977.44
3	60	1062.96	28.28	40	1	25.17	1001.88
4	48	561.48	25.85	59	3	29.55	679.24
4	52	565.56	34.86	59	3	37.88	679.24
4	52	729.52	27.07	57	1	24.74	703.07
4	56	906.85	27.30	55	3	20.88	728.64
4	60	1094.57	26.64	53	1	17.61	756.13
5	45	418.09	25.59	76	1	30.47	527.30
5	50	547.68	31.59	74	4	29.04	541.55
5	50	677.42	24.64	72	2	19.44	556.60
5	55	749.08	32.76	71	1	23.04	564.44
5	55	888.20	25.86	69	4	16.23	580.80
5	60	1037.91	29.50	67	2	16.15	598.13
6	48	431.73	32.61	91	1	30.74	440.38
6	48	535.03	27.38	89	5	21.91	450.28
6	54	759.56	30.23	85	1	17.76	471.47
6	54	875.54	23.91	83	5	12.75	482.83

## NUMERICAL SIMULATION AND ORBIT MAINTENANCE

To evaluate the influence of the main perturbations on the orbital parameters of a multi-sunsynchronous UHC, a particular test case has been considered for numerical integration. In order to guarantee a global coverage of the tropical regions with a revisit time of  $\frac{1}{2}$  *nodal day* (around 12 hours), a multi-sunsynchronous orbit with an altitude of 648.18 km and an inclination of 35.14° has been chosen as reference trajectory for the intended satellite constellation. Such an orbit gives rise to repetitive ground track with a revisit interval of 2 *nodal days* and a separation between adjacent tracks of 1382 km at the equator. In addition, every 54 *nodal days* the same place on the ground is flown over in the same illumination conditions. The relatively high inclination of this orbit implies the continuous coverage of a quite vast area. If, as in this case, this has to be obtained with a very limited number of satellites (only 4), this results in a large number of illumination and, being the ground tracks at the equator considerably far apart from each other (1380 km), a very wide instantaneous field of view of the sensor. The pattern of ground tracks for such an orbit during a complete *m-day* cycle is shown in Figure 3.



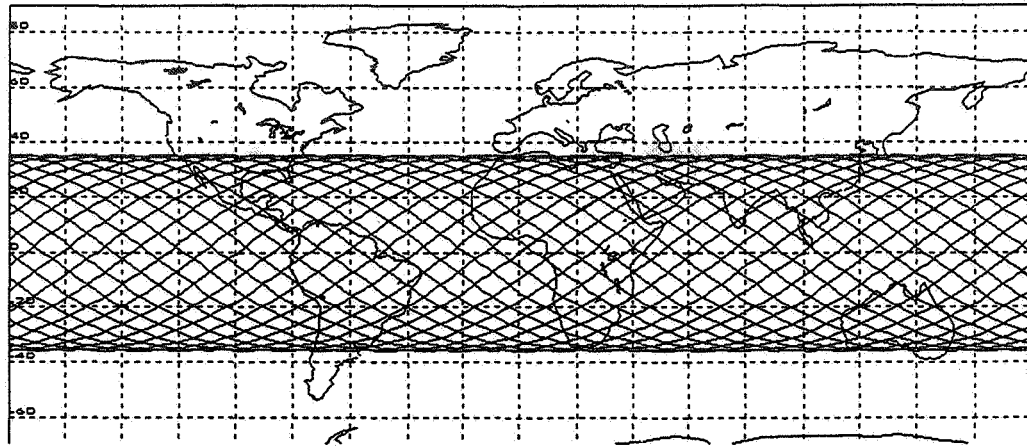


**Figure 3 Ground track pattern of the test case orbit during the  $m$ -day cycle**

The exact repeat of the satellite ground track pattern may be altered as a consequence of the variation of the nodal period, of the nodal precession rate and of the orbital inclination.

The major perturbations affecting the ground track repeatability are the atmospheric drag and the luni-solar gravitational potential. Luni-solar disturbances cause secular and long-period variations in the nodal period, the nodal precession rate and the inclination, while the atmospheric drag reduces systematically the semi-major axis, affecting both the nodal period (first order effect) and the nodal precession rate (second order effect).

To simulate the behavior of the constellation under the influence of the major perturbations a numerical integration of the motion of the satellites has been carried out by means of GEODYN II software for a time span of about *110 days*. All perturbations suitable for propagation of low earth orbits have been selected.

We have considered 4 satellites (mass = 300 kg, cross section area = 3 m<sup>2</sup> and  $C_D = 2.0$ ) uniformly deployed on 2 orbital planes with nodes equally spaced (90° apart). The evolution of the semi-major axis for the 4 satellites considered is represented in Figure 4. As expected we can notice a decrease in the semi-major axis at an almost constant rate due to the atmospheric drag. However, it is evident that the two planes of the constellation are affected in a different way by the aerodynamic resistance. Such a difference can be explained by the effect of the atmospheric diurnal bulge due to the heating of the atmosphere by direct illumination of the Sun. Nevertheless, because of the multi-sunsynchronicity of these orbits, the differential effect between the two planes is smoothed out in comparison with the case of corresponding sun-synchronous orbits that have constant geometry of illumination.

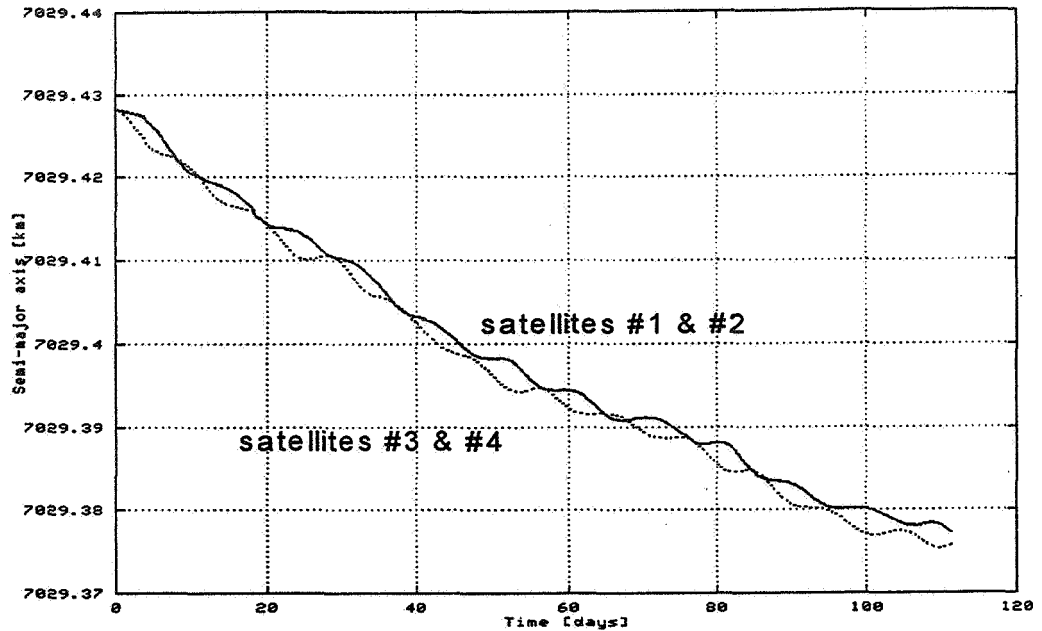


**Figure 4 Semi-major axis evolution for the 4 satellites of the constellation**

The maintenance of the operational orbit considered has been analyzed evaluating the maneuver requirements, taking into account that, at the altitude considered, the driving natural effect is the reduction of the nodal period due to the atmospheric drag. In fact, because of the constant reduction in the semi-major axis induced by the aerodynamic resistance, the satellite ground track slowly drifts to East. The knowledge of the nodal crossing drift is fundamental for planning the orbital corrections needed in order to keep the correct configuration of the constellation.

A possible strategy that maximizes the time interval between the maneuvers consists in starting the control cycle by placing each satellite on its eastern boundary of the longitude deadband, with a semi-major axis augmented by a suitable amount  $\Delta a$  with respect to the nominal value. If  $\Delta a$  is computed according to the expected semi-major axis decay, the sub-satellite ground track will drift westward, until will reach the western boundary of the deadband exactly when the semimajor axis is back to its nominal value. Afterwards, the further reduction in the semi-major axis will cause an inversion in the ground track drift eastward, and, as far as the drag force may be considered constant during a full control cycle, the eastern boundary of the deadband will be reached when the semimajor axis assumes a value that is lower than the nominal one by  $\Delta a$ . At that point the semi-major axis must be increased by  $2\Delta a$  by means of the propulsion system to repeat the control cycle and maintain the ground track within the required tolerance.

For circular orbits affected by a constant drag force, the velocity increment  $\Delta V_c$  required to restore the initial conditions at the end of each control cycle, the time interval between maneuvers and the corresponding  $\Delta a$  can be easily computed<sup>1</sup>:

$$\Delta V_c = \sqrt{\frac{B \rho V^3 \Lambda}{3 \omega_E R_E}} \quad (10)$$

$$T_c = \frac{4 \Delta V_c}{B \rho V^2} \quad (11)$$

$$\Delta a = \frac{B}{2} \rho \sqrt{\mu a} T_c \quad (12)$$

where  $\rho$  is the air density,  $B$  the ballistic coefficient and  $R_E$  the earth equatorial radius.

Considering a tolerance on the ground track  $\Lambda = \pm 1 \text{ km}$ , the Jacchia atmospheric model<sup>5</sup> with an exospheric temperature of  $1000 \text{ K}$ , and the assumption that monopropellant hydrazine would be used as fuel for the orbit control system the following values can be obtained for our test case from Eqs. (10), (11) and (12).

**Table 3**  
**CONTROL CYCLE RELEVANT FIGURES**

<u>Altitude (km)</u>	<u>T<sub>c</sub> (days)</u>	<u><math>\Delta V_c</math> (m/s per yr)</u>	<u>Fuel (kg/yr)</u>	<u><math>\Delta a</math> (m)</u>
648.18	19.1	0.4	0.1	18

The luni-solar disturbances affect the track repeatability, but can be taken into account by means of very small corrections to the semi-major axis control cycle. Nevertheless, due to the resonance existing between the sun motion and the nodal precession rate of multi-sunsynchronous orbits, long period and secular variations of the inclination could be expected.

An inclination variation involves a displacement of the sub-satellite track at higher or lower latitude. Therefore, an inclination control cycle should be envisaged as well if the track repeatability requirement has to be met everywhere along the orbital path.

## REFERENCES

1. C. Ulivieri and L. Anselmo, "Multi-Sun-Synchronous (MSS) Orbits for Earth Observation", *Advances in the Astronautical Sciences*, Vol. 76, Univelt Inc, San Diego, 1991 pp. 123-133.
2. R. G. Hopkins, "Long-Term Revisit Coverage Using Multi-Satellite Constellations", AIAA Paper N. 88-4276-CP, AAS/AIAA Astrodynamics Conference, Minneapolis, USA, 1988.
3. C. Ulivieri, G. Laneve and S. M. Hejazi Moghaddam, "UPH Constellations for Continuous Regional Surveillance", AAS 97-622, AAS/AIAA Astrodynamics Conference, Sun Valley, USA, 1997.
4. C. Ulivieri, G. Laneve and S. M. Hejazi Moghaddam, "Orbit Design Analysis for Remote Sensing Satellite Constellations", Paper presented at the IAF Workshop on Mission Design & Implementation of Satellite Constellations, Toulouse, France, November 1997.
5. L. G. Jacchia, *Revised Static Models of the Thermosphere and Exosphere with Empirical Temperature Profiles*, Smithsonian Astrophysical Observatory, Special report 332, 1971.

337507  
16P.53-18  
16 92 85

## MODELS AND ALGORITHMS FOR CONSTELLATION STATION KEEPING STRATEGIES AND SATELLITES REPLACEMENT

C. Brochet, J.M. Garcia, J.M. Enjalbert, T. Céolin<sup>†</sup>

During the mission of a constellation, maneuvers must be introduced periodically to reset the drifted satellites. Moreover some satellites may fail during the life of the constellation, and maneuvers have to be done to ensure the desired coverage.

In this paper, we propose several optimization models for this problem. For each model we present the most efficient resolution algorithm. Each model consists in minimizing the total consumption due to maneuvers. It takes into account the trajectory of each satellite and constraints on their relative positions. An additional constraint is introduced to limit the number of satellites that can be simultaneously controlled. Such an optimization problem is a Mixed Integer Non Linear Programming (MINLP). It contains boolean and real variables. Boolean variables determine which satellites can be thrust, and real variables correspond to the value of maneuvers.

The global problem is splitted on the basis of the generalized Bender's decomposition method (projection on the boolean variables space).

The first model is linear and differential (relative satellite positions). The sub-problem (calculation of the impulsive thrusts) is solved by a dual approach that finds the solution in a finite number of steps. It provides the global optimum in a very short computing time. This model is interesting in the case where the phasing of the constellation is not far from nominal conditions.

The second model is nonlinear and non differential. It represents the real problem without simplifications. The resolution of the sub-problem is done using a direct search approach (Hooke and Jeeves algorithm) to determine real variables in the sub-problem. This model is used to solve the station keeping problem and to determine optimal maneuvers to replace satellites in case of failure.

Numerical experiments and comparison between the two approaches are presented for various constellation configuration parameters.

### INTRODUCTION

Spatial projects are more and more numerous, and regularly, satellites are launched in orbit in order to begin a mission for many years. The objective of a constellation is for example to ensure a coverage that allows data communication between two satellites or between a satellite and a ground station. To avoid gaps in the required coverage, relative positions of these satellites must not exceed a fixed threshold. But many perturbations make the trajectory of satellites drifted, and it is necessary to regularly maneuver some of them. This process is called station keeping. These maneuvers have to be calculated in order to minimize the consumption of each satellites, since the mass of ergol is limited.

<sup>†</sup> LAAS-CNRS, 7 avenue du Colonel Roche, 31077 Toulouse cedex 04, France.

Moreover, since the number of simultaneous maneuvers is limited, additional constraints have to be taken into account. A same model can be used to calculate replacement maneuvers when a satellite fails.

Previous researches have been done on this subject. A linear model of the station keeping optimization problem has been stated, and a method to solve it has been proposed (Ref. 8 and 9). In this paper, we present new robust and efficient methods that can solve this linear problem. We also present a nonlinear station keeping optimization problem and an algorithm to solve it exactly.

In the first section, we present the problem modelling. The second section is devoted to the resolution of the mixed-variables problem. The method is decomposed into two levels: the master problem and the sub-problem. It needs successive resolutions of the sub-problem (real variables problem with boolean variables fixed). The two following sections present the resolution of the real variables problem, assuming that constraints can be linear or nonlinear. In the last section, numerical results and comparisons are presented.

## STATEMENT OF THE PROBLEM

### Station keeping problem

In this paper circular Walker constellations with  $N$  satellites are considered. The life of the constellation is decomposed into successive station keeping cycles. At each cycle, the station keeping optimization problem must be solved. It consists in finding the lowest values of maneuvers, that maintain the desired coverage, respecting operational constraints. These constraints mean that all satellites cannot be thrusted simultaneously, but just  $M$  among  $N$ . To take this into account, each station keeping cycle contains  $K$  steps. Only  $M$  maneuvers at the beginning of each step are allowed. That's why boolean variables  $\beta$  are introduced in the optimization problem. If  $\beta_i^k$  is equal to 1 then the corresponding satellite  $i$  is allowed to maneuver at the beginning of the step  $k$ , otherwise it cannot maneuver.

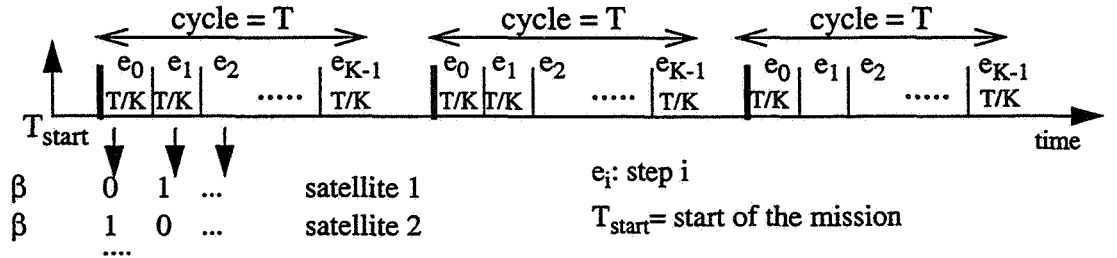


Figure 1 Station keeping cycles

Hence, solving the optimization station keeping problem, is to find for a cycle:

- Which satellite can maneuver at each step? Values of boolean variables:  $\beta_i^k$
- What are the values of these maneuvers? Values of real variables:  $\delta V_i^k$

Therefore, the problem is a mixed-variables problem. It contains  $K*N$  boolean variables and  $K*N$  real variables.

The general expression of this problem is the following:

$$\min_{\delta V, \beta} J(\delta V, \beta)$$

$$\begin{cases} |\Delta d_i^k| < \phi & \forall i, k & i \text{ denotes satellites whereas } k \text{ refers to steps} \\ \sum_{k=0}^{K-1} |\delta V_i^k| \leq \text{Cons}_i & \forall i & \text{Cons}_i \text{ is the maximal consumption authorized for satellite } i \\ \sum_{i=1}^N \beta_i^k \leq M & \forall k \\ (1 - \beta_i^k) \cdot \delta V_i^k = 0 & \forall i, k \end{cases} \quad (1)$$

The objective is to minimize the total consumption of each satellite. The problem has two sorts of constraints. The first one is a coverage constraint (distance between two satellites  $|\Delta d|$  must not exceed a threshold  $\phi$ ) and the three remaining constraints are operational constraints.

### Description of maneuvers

As it has been mentioned, we treat circular Walker constellations. Orbital parameters taken into account are  $[a, i, \Omega, \alpha]$  respectively semi-major axis, inclination, right ascension of the ascending node (RAAN) and mean anomaly.

The correction of the semi major axis and the mean anomaly can be done through in-plane maneuvers  $\delta V_t$ , whereas the correction of the inclination and the RAAN have to be done through a combination of in-plane and out of plane maneuvers  $\delta V_t$  and  $\delta V_w$  (Ref. 1 and 2).

### Criterion

In all station keeping models proposed, the objective is to minimize the total consumption of satellite maneuvers.

Possible objective functions are:

$$\begin{aligned} \min_{\beta, \delta V} J_1(\beta, \delta V) & \quad J_1(\beta, \delta V) = \sum_{k=0}^{K-1} \sum_{i=1}^N \beta_i^k \sqrt{(\delta V_{ti}^k)^2 + (\delta V_{wi}^k)^2} \\ \min_{\beta, \delta V} J_2(\beta, \delta V) & \quad J_2(\beta, \delta V) = \sum_{k=0}^{K-1} \sum_{i=1}^N \beta_i^k [|\delta V_{ti}^k| + |\delta V_{wi}^k|] \\ \min_{\beta, \delta V} J_3(\beta, \delta V) & \quad J_3(\beta, \delta V) = \sum_{k=0}^{K-1} \sum_{i=1}^N \beta_i^k [(\delta V_{ti}^k)^2 + (\delta V_{wi}^k)^2] \end{aligned} \quad (2)$$

The first criterion minimizes the sum of complete maneuvers.

The two others criteria minimize the sum of each component of each maneuvers.

In practice the choice of the criterion will depend on the physical possibility of doing maneuvers in both directions simultaneously or not.

### Resolution

The global optimization problem Eq. (1) can generally be written as follows:

$$\begin{cases} \min_{\delta V, \beta} f(\delta V, \beta) \\ g(\delta V, \beta) \leq 0 \\ h(\delta V, \beta) = 0 \\ \delta V \in \mathcal{R}^{KN} \quad \beta \in \{0, 1\}^{KN} \end{cases} \quad (3)$$

In this paper, this problem Eq. (3) will be called the mixed-variables problem. It belongs to the class of MINLP (Mixed Integer Non Linear Programming). This kind of problem is well studied in the literature (Ref. 3, 4, 5 and 6). All methods proposed, need successive resolutions of the real variables problem Eq. (4), that will be called the sub-problem (with fixed boolean variables).

$$\begin{cases} \min_{\delta V} f(\delta V) \\ g(\delta V) \leq 0 \\ h(\delta V) = 0 \\ \delta V \in \mathcal{R}^{KN} \end{cases} \quad (4)$$

The next section is devoted to the description of an exact method solving the mixed-variables problem Eq. (3). The resolution of the sub-problem Eq. (4) will depend on its characteristics. These methods will be described in the two following sections.

## THE RESOLUTION OF THE MIXED-VARIABLES PROBLEM

The resolution of the mixed-variables problem Eq. (3) consists in finding values of boolean variables and real one's. A natural method to solve this problem is to enumerate all boolean variables combinations. For each acceptable combination, the sub-problem is solved. Solutions of sub-problems, for each acceptable boolean combinations, are compared each others in order to determine the global optimum of the mixed-variables problem.

Such a method is too long to compute, that's why, we propose a more efficient method.

### Description

This method uses the generalized Bender's decomposition that Geoffrion extended to the non-linear case (Ref. 4). The mixed-variables problem is projected on the boolean variables space. It can be rewritten:

$$\text{Eq. (3)} \equiv \begin{cases} \min_{\beta} v(\beta) \\ \text{with} \quad v(\beta) = \begin{cases} \min_{\delta V} f(\delta V, \beta) \\ g(\delta V, \beta) \leq 0 \\ h(\delta V, \beta) = 0 \\ \delta V \in \mathcal{R}^{KN} \end{cases} \quad \text{Eq. (4)} \\ \beta \in V \cap \{0, 1\}^{KN} \\ V = \{\beta / (g(\delta V, \beta) \leq 0; h(\delta V, \beta) = 0)\} \end{cases} \quad (5)$$

Eq. (5) is called the master problem.

To have more details on this method, refers to (Ref. 4, 5 and 6).



## Algorithm

The objective of the algorithm is to make iteratively the lower bound (of the global minimum) increase and the upper bound decrease.

1. Select one acceptable combination of boolean variables  $\beta$ ;  $it=1$  (it is the current iteration)
2. Solve the sub-problem:

$$\max_{\mu} \min_{\delta V} f(\delta V, \beta) + \mu g(\delta V, \beta) + \lambda h(\delta V, \beta) \quad \delta V \in \mathcal{R}^{KN} \Rightarrow \begin{cases} \delta V_{it} \\ \mu_{it} \\ \eta_{max} \end{cases}$$

The solution is a new upper bound  $\eta_{max}$  of the global optimum of the mixed-variables problem.

3. A new constraint in the master problem can be added:

$$\eta_B \geq f(\delta V_{it}, \beta) + \mu_{it} g(\delta V_{it}, \beta) + \lambda_{it} h(\delta V_{it}, \beta)$$

4. Resolution of the master problem:

$$\begin{cases} \min_{\beta} \eta_B \\ \eta_B \geq f(\delta V_j, \beta) + \mu_j g(\delta V_j, \beta) + \lambda_j h(\delta V_j, \beta) \quad \forall j = 1 \dots it \\ \beta \in V \cap \{0, 1\}^{KN} \\ V = \{\beta / (g(\delta V, \beta) \leq 0)\} \end{cases} \Rightarrow \begin{cases} \beta_{min} \\ \eta_{min} \end{cases}$$

which provides a new lower bound  $\eta_{min}$  of the global optimum of the mixed-variables problem (concept of relaxation) and a new combination of boolean variables

5. If  $\eta_{min} \geq \eta_{max} + \varepsilon$  then stop, else return to 2.

Figure 2 The algorithm to solve the mixed-variables problem

## LINEAR AND DIFFERENTIAL OPTIMIZATION PROBLEM

### The linear and differential station-keeping problem

In this section we consider a differential and linear model of orbital parameters. The model is called differential since we consider the evolution of distance between a couple of satellites and not the evolution of each satellite (absolute model will be treated in the next section). Moreover the model is linear since constraints on distances between a couple of satellites are linear. In this case, the model Eq. (1) can be rewritten as follows:

The criterion can be one of the ones presented in Eq. (2).

Coverage constraints are the following:

$$\begin{cases} |\Delta a_i^{k+1}| = \left| \Delta a_i^0 + C_a \sum_{l=0}^k \Delta V_{ti}^l \right| < \phi_a & \text{with} \quad \Delta V_{ti}^l = \beta_{i+1}^l \delta V_{ti+1}^l - \beta_i^l \delta V_{ti}^l \\ |\Delta i_i^{k+1}| = \left| \Delta i_i^0 + C_i \sum_{l=0}^k \Delta V_{wi}^l \right| < \phi_i & \text{with} \quad \Delta V_{wi}^l = \beta_{i+1}^l \delta V_{wi+1}^l - \beta_i^l \delta V_{wi}^l \end{cases} \quad (6)$$

$$\begin{cases} \left| \Delta \alpha_i^{k+1} \right| = \left| \Delta \alpha_i^0 + C_\alpha^k + C_\alpha^a \cdot C_a \cdot \sum_{l=0}^k [(k+1-l) \Delta V_{ii}^k] + C_\alpha^i \cdot C_i \cdot \sum_{l=0}^k [(k+1-l) \Delta V_{wi}^k] \right| < \phi_\alpha \\ \left| \Delta \Omega_i^{k+1} \right| = \left| \Delta \Omega_i^0 + C_\Omega^k + C_\Omega^a \cdot C_a \cdot \sum_{l=0}^k [(k+1-l) \Delta V_{ii}^k] + C_\Omega^i \cdot C_i \cdot \sum_{l=0}^k [(k+1-l) \Delta V_{wi}^k] \right| < \phi_\Omega \end{cases} \quad \forall i, k$$

Assuming  $\Delta q_i^k = q_{i+1}^k - q_i^k$  whatever  $q = a, i, \Omega, \alpha$ .

Coefficients  $C_a, C_i, C_\alpha^k, C_\alpha^a, C_\alpha^i, C_\Omega^k, C_\Omega^a, C_\Omega^i$  are described in paper (Ref. 9). They have been calculated in order to take into account J2, atmospheric drags, and thrust effects.

$$C_\alpha^k = (k+1) \cdot (C_\alpha^a \cdot \Delta a_i^0 + C_\alpha^i \cdot \Delta i_i^0) \quad C_\Omega^k = (k+1) \cdot (C_\Omega^a \cdot \Delta a_i^0 + C_\Omega^i \cdot \Delta i_i^0)$$

Operational constraints are:

$$\begin{cases} \sum_{k=0}^{K-1} |\delta V_{ii}^k| \leq Cons_i \quad \forall i \quad \text{and} \quad \sum_{i=1}^N \beta_i^k \leq M \quad \forall k \\ (1 - \beta_i^k) \cdot (|\delta V_{ii}^k| + |\delta V_{wi}^k|) = 0 \quad \text{or} \quad (1 - \beta_i^k) \cdot ((\delta V_{ii}^k)^2 + (\delta V_{wi}^k)^2) = 0 \end{cases} \quad (7)$$

This mixed-variables problem can be solved with the previous method, but the resolution of the sub-problem Eq. (4) is required. The next sub-section is devoted to the resolution of the sub-problem Eq. (4) that contains linear constraints, like for example Eqs. (6) and (7).

## Resolution

The sub-problem Eq. (4) with linear constraints can be solved by the linear simplex algorithm (Ref. 8). However such a method implies the use of a software like Xpress and doesn't solve nonlinear problem with, for example, the criterion  $J_1$  or  $J_4$ . So we developed a specific approach based on analytical calculations. This method is also suitable for non-linear criteria.

*An analytical approach.* According to the theory of duality, Eq. (4) is similar to:

$$\max_{\mu \geq 0, \lambda} \min_{\delta V} L(\delta V, \mu, \lambda) = f(\delta V) + \mu^T g(\delta V) + \lambda^T \cdot h(\delta V) \quad (8)$$

The resolution of Eq. (8) provides the global optimum of the sub-problem Eq. (4).

The disadvantage of the equivalent problem Eq. (8) is that it contains two optimization problems and more variables than the sub-problem Eq. (4). Indeed, the problem Eq. (8) contains a maximization problem in  $\delta V$  variables (2KN variables) and a minimization one in  $\mu$  and  $\lambda$  (Lagrange multipliers) variables (X variables, if X is the number of constraints). However, we found solutions to reduce the complexity of the equivalent problem Eq. (8).

### 1. How to suppress the minimization problem?

In fact, the minimization problem can be solved using analytical expressions. Indeed, if we write stationnarity conditions Eq. (9) we can deduce relations Eq. (10) between  $\delta V$  optimal variables and other variables (Kuhn Tucker and Lagrange multipliers) of the problem.

$$\frac{\partial}{\partial \delta V} L(\delta V, \beta, \mu) = 0 \quad (9)$$

$$\delta V = \delta V(\mu, \lambda) \quad (10)$$

The calculation of the Hessian matrix shows that the expression of  $\delta V$  found with previous calculations corresponds to the global minimum of the problem.

So the solution of the minimization problem is analytical.

Note that:

$$-|\delta V| = \sqrt{(\delta V)^2}, \text{ so } \frac{\partial}{\partial \delta V} \sqrt{(\delta V)^2} = \text{sign}(\delta V) \quad \text{if} \quad \delta V \neq 0$$

- Case of criterion  $J_1$  or  $J_2$ , the relation Eq. (10) is not found directly. The way to obtain this kind of relation is to use the criterion  $J_1+J_3$  or  $J_2+J_3$  instead of  $J_1$  or  $J_2$ .

This is not a problem since values of  $|\delta V|$  are about  $10^{-4}$  (km/s), so values of  $(\delta V)^2$  are about  $10^{-8}$  (km/s) and we can conclude that  $(\delta V)^2 \ll |\delta V|$ . That's why criteria  $J_1$  or  $J_2$  are similar to  $J_1+J_3$  or  $J_2+J_3$ .

After having substituted  $\delta V$  by the expression found with Eq. (10) in the Lagrangian function, the new expression of the problem Eq. (8) is the maximization problem with Kuhn-Tucker and Lagrange variables:

$$\text{Eq. (8)} \equiv \max_{\mu, \lambda} L(\mu, \lambda) \quad (11)$$

2. How to reduce the number of variables of the problem Eq. (11)?

It is stated that a Kuhn Tucker multiplier is positive if the constraint is saturated and null otherwise. So there is no need to solve the problem with all Kuhn Tucker variables but just the ones that correspond to a constraint that will certainly be saturated. Others Kuhn Tucker parameters will be fixed to zero.

The way to find the variables of the problem is to plan what are the studied couples of satellites such that their relatives positions will have to be equal to the threshold.

When variables of the problem are determined, we can solve the problem Eq. (11).

If the criterion is  $J_1$  or  $J_3$  we can write stationnarity conditions:

$$\begin{cases} \frac{\partial}{\partial \mu} L(\mu, \lambda) = 0 & \text{if } \mu \neq 0 \\ \frac{\partial}{\partial \lambda} L(\mu, \lambda) = 0 & \forall \lambda \end{cases} \quad (12)$$

else, we must use a direct search algorithm (see next section) to solve the problem Eq. (11).

**Algorithm.** Case where all the saturated constraints are known before the resolution of the sub-problem, just one resolution of the problem Eq. (11) is needed. However, if we do not know which are the saturated constraints, we propose the following algorithm:

1.  $it=1$  (The variable  $it$  denotes the current iteration);  $\lambda=0$  and  $\mu=0$   
with these values calculate  $\delta V=\delta V(\mu, \lambda)$
2. what is the most violated constraint?  
The corresponding Lagrange multiplier becomes a variable  $\mu_{it}$  of the problem Eq. (11).  
The problem Eq. (11) contains now,  $it$  Kuhn-Tucker variables + all Lagrange variables.

3. Resolution of the equivalent problem Eq. (11) that provides optimal values of  $\mu_j$  ( $j=1..it$ ) and  $\lambda$ . with these values calculate  $\delta V = \delta V(\mu, \lambda)$
4. If the solution is feasible then  $it=it+1$  and return to 2, else stop.

**Figure 3 Linear station keeping optimization resolution**

*Example.* In this paper we just develop calculations, case when the sub-problem is the following:

$$\begin{cases} \min_{\delta V_{it}^k} & \sum_{k=0}^{K-1} \sum_{i=1}^N \beta_i^k (\delta V_{it}^k)^2 \\ \left| \Delta \alpha_i^0 + C_{\alpha}^k + C_{\alpha}^a \cdot C_a \cdot \sum_{l=0}^k [(k+1-l) \Delta V_{it}^k] \right| < \phi_{\alpha} & \forall i, \forall k \quad (1 - \beta_i^k) \cdot \delta V_{it}^k = 0 \end{cases}$$

The equivalent problem to solve is:

$$\begin{cases} \max_{\mu_1, \mu_2 \geq 0, \lambda} \min_{\delta V} L(\delta V, \mu_1, \mu_2, \lambda) & \text{with} \\ L(\delta V, \mu_1, \mu_2, \lambda) = \sum_{k=0}^{K-1} \sum_{i=1}^N \delta V_i^k{}^2 + \mu_{1i}^k \cdot \left\{ \Delta \alpha_i^0 + C_{\alpha}^k + C_{\alpha}^a \cdot C_a \cdot \sum_{l=0}^k [(k+1-l) \Delta V_{it}^k] - \phi_{\alpha} \right\} \\ + \mu_{2i}^k \cdot \left\{ -\Delta \alpha_i^0 - C_{\alpha}^k - C_{\alpha}^a \cdot C_a \cdot \sum_{l=0}^k [(k+1-l) \Delta V_{it}^k] - \phi_{\alpha} \right\} + \lambda_i^k \cdot \left\{ (1 - \beta_i^k) \cdot \delta V_i^k \right\} \end{cases}$$

The gradient and the hessian matrix of the lagrangian function are:

$$\begin{cases} \frac{\partial}{\partial \delta V_i^k} L(\delta V, \mu, \lambda) = 2\delta V_i^k + B \sum_{j=k}^{K-1} [(j+1-k)(\mu_{1i}^j - \mu_{1i}^j - \mu_{2i}^j + \mu_{2i}^j)] + \lambda_i^k \cdot (1 - \beta_i^k) = 0 \\ \frac{\partial^2}{\partial \delta V_i^k{}^2} L(\delta V, \mu, \lambda) = 2 > 0 \quad B = B(k, C_{\alpha}^a, C_a) \end{cases}$$

The new expression of  $\delta V$  is  $\delta V_i^k = -\frac{B}{2} \sum_{j=k}^{K-1} [(j+1-k)(\mu_{1i}^j - \mu_{1i}^j - \mu_{2i}^j + \mu_{2i}^j)] + \frac{\lambda_i^k \cdot (1 - \beta_i^k)}{2}$

The new problem to solve is:  $\max_{\mu_1, \mu_2 \geq 0, \lambda} L(\mu_1, \mu_2, \lambda)$

The gradient of this function is:

$$\begin{aligned} \frac{\partial}{\partial \mu_1^t} L(\mu_1, \mu_2, \lambda) = & fA(t, t+1) - \phi + \sum_{k=0; k \leq t}^{K-1} \frac{B}{2} \cdot (t+1-k) \cdot \left[ -\lambda_t^k \cdot (1-\beta_t^k) + \lambda_{t+1}^k \cdot (1-\beta_{t+1}^k) \right] \\ & - \frac{1}{2} B^2 \sum_{k=0}^{K-1} \left[ \sum_{j=0, j \leq t}^k (k+1-j)(t+1-j) \right] [\mu_1_{t-1}^k + \mu_1_{t+1}^k - 2\mu_1_t^k - \mu_2_{t-1}^k - \mu_2_{t+1}^k + 2\mu_2_t^k] \end{aligned}$$

By the same way,  $\frac{\partial}{\partial \mu_2^t} L(\mu_1, \mu_2, \lambda)$  and  $\frac{\partial}{\partial \lambda_t^t} L(\mu_1, \mu_2, \lambda)$  are calculated and the initial optimization problem has the same solution than the following linear system of equations:

$$\begin{cases} \frac{\partial}{\partial \mu_1^t} L(\mu_1, \mu_2, \lambda) = 0 & \forall \mu_1^t \neq 0 \\ \frac{\partial}{\partial \mu_2^t} L(\mu_1, \mu_2, \lambda) = 0 & \forall \mu_2^t \neq 0 \\ \frac{\partial}{\partial \lambda_t^t} L(\mu_1, \mu_2, \lambda) = 0 \end{cases}$$

## Conclusion

As a conclusion, the method presented in this section is very efficient since it can provide the global minimum (optimal maneuvers needed to ensure a good coverage) just resolving a linear equations system. This method can be applied to every station keeping problems such that the criterion is one of the ones quoted in Eq. (2), and with linear constraints in  $\delta V$ .

## NONLINEAR AND NON DIFFERENTIAL OPTIMIZATION PROBLEM

It can happen that perturbations on orbital parameters, makes the linear model not precise enough. That's why we propose a nonlinear model. This model is also absolute: all orbital parameters of each satellites are independently considered. This will allow not only to replace evenly satellites around the earth in station keeping, but also to correct some satellites too far from the nominal constellation.

In this section we present this new model and methods that can solve this nonlinear station keeping problem.

### Nonlinear and non differential station keeping problem

Criterion can be one of the ones of Eq. (2). The following criterion that minimizes the mass of consumption of ergol of all the N satellites of the constellation, can also be used:

$$\min_{\beta, \delta V} J_4(\beta, \delta V) \quad J_4(\beta, \delta V) = \sum_{i=1}^N m_{0i} \cdot \left( 1 - e^{\frac{\sum_{k=0}^{K-1} \beta_i^k \sqrt{(\delta V_{ti}^k)^2 + (\delta V_{wi}^k)^2}}{g \cdot Isp}} \right) \quad (13)$$

- $m_{0i}$  is the mass of ergol left of the satellite  $i$  at the beginning of the station keeping cycle considered,
- $g$  is the gravitational constant,
- $Isp$  is the specific impulsion.

Coverage constraints are the following:

$$\left\{ \begin{array}{l} |\Delta a_i^{k+1}| \leq \phi_a \\ |\Delta i_i^{k+1}| \leq \phi_i \\ |\Delta \alpha_i^{k+1}| \leq \phi_\alpha \\ |\Delta \Omega_i^{k+1}| \leq \phi_\Omega \end{array} \right. \quad \text{with} \quad \left\{ \begin{array}{l} a_i^{k+1} = a_i^k + \frac{2}{\sqrt{\mu}} \cdot (a_i^k)^{3/2} \delta V_{ti}^k \\ i_i^{k+1} = i_i^k + \cos \alpha \cdot \frac{(a_i^k)^{1/2}}{\sqrt{\mu}} \cdot \delta V_{wi}^k \\ \Omega_i^{k+1} = \Omega_i^k + \frac{F \cos i_i^{k+1}}{a_i^{k+1}{}^{7/2}} \cdot \Delta t + \frac{\sin \alpha}{\sin i_i^k} \cdot \frac{(a_i^k)^{1/2}}{\sqrt{\mu}} \cdot \delta V_{wi}^k \\ \alpha_i^{k+1} = \alpha_i^k + \left[ \sqrt{\mu} \cdot (a_i^{k+1})^{-3/2} - \frac{F(4 \cdot \cos^2 i_i^{k+1} - 1)}{a_i^{k+1}{}^{7/2}} \right] \cdot \Delta t + \frac{\sin \alpha}{\tan i_i^k} \cdot \frac{(a_i^k)^{1/2}}{\sqrt{\mu}} \cdot \delta V_{wi}^k \end{array} \right. \quad (14)$$

assuming that  $\begin{cases} \alpha = 0 \text{ or } \pi \text{ to control } i \\ \alpha = \pi/2 \text{ or } 3\pi/2 \text{ to control } \Omega \end{cases}$

Operational constraints are the same as in the previous model Eq. (7).

Constraints on absolute position of all satellites: satellites must not be too high or too low and must be close enough to the desired orbit inclination.

$$\left\{ \begin{array}{l} a_{\min} \leq a_i^k \leq a_{\max} \\ i_{\min} \leq i_i^k \leq i_{\max} \end{array} \right. \quad (15)$$

To balance the consumption of satellites, we can use either a new criterion ( $J_5$ ) or new constraints that will penalize the use of satellites for which the consumption of ergol is more important than for the others.

$$J_5(\beta, \delta V) = \sum_{k=0}^{K-1} \sum_{i=1}^N \left( P_i \cdot \beta_i^k \cdot \sqrt{(\delta V_{ti}^k)^2 + (\delta V_{wi}^k)^2} \right) \quad P_i = \text{Cons}_{\text{previ},i} + \sum_{k=0}^{K-1} \left( \beta_i^k \cdot \sqrt{(\delta V_{ti}^k)^2 + (\delta V_{wi}^k)^2} \right)$$

$\text{Cons}_{\text{previ},i}$  is the previous consumption of the satellite  $i$

## Resolution

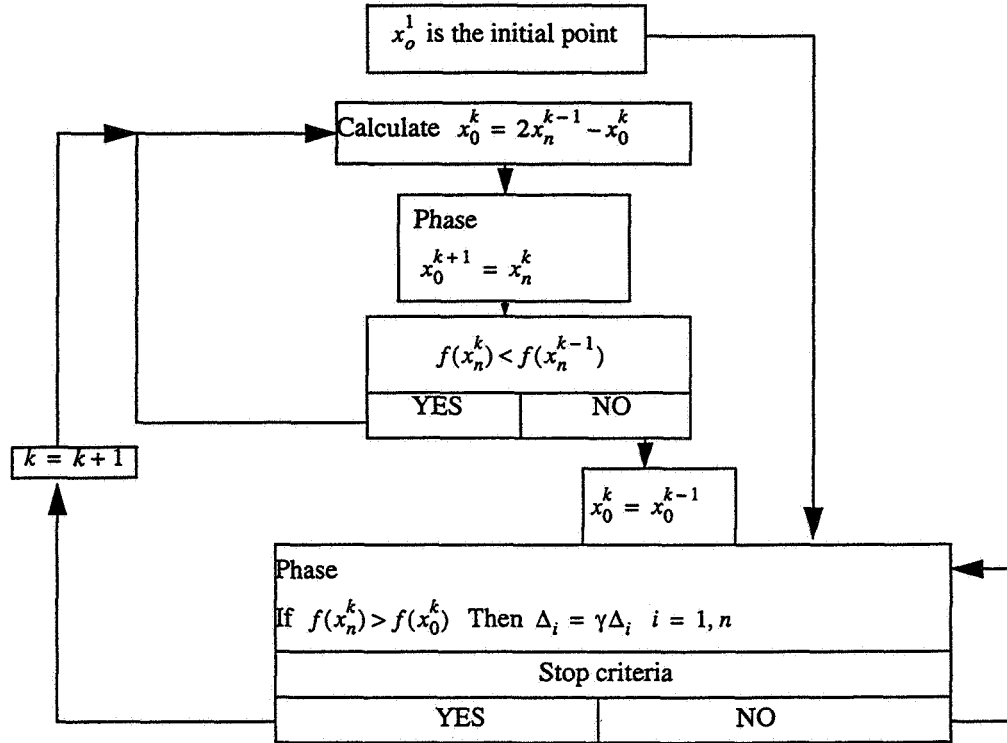
This sub-problem can be solved with a direct search algorithm.

A direct search method (Hooke and Jeeves) does not need the calculation of the gradient, but only a direct evaluation of the criterion on different points. To take into account constraints, the use of exact penalty functions is required:

$$(SP) \equiv \min_{\delta V} f(\delta V) + C_1 \cdot \max(0, g(\delta V)) + C_2 \cdot \max(0, |h(\delta V)|) \quad (16)$$

Such a method provides the global optimum of the sub-problem Eq. (4) if the optimal values of penalty coefficients  $C_1$  and  $C_2$  are well evaluated. It is difficult to get analytically exact value of penalty coefficients. However, there exists a way to get acceptable values for coefficients  $C_1$  and  $C_2$ , by solving in a first step the problem in the linear case.

Assuming  $f(x)$  is the objective function to minimize, the Hooke and Jeeves algorithm is the following (Ref. 7):



### Phase

For  $i = 1, n$

calculate  $x = x_{i-1}^k + \Delta_i e_i$

If  $f(x) < f(x_{i-1}^k)$  then  $x_i^k = x$

Else

calculate  $x = x_{i-1}^k - \Delta_i e_i$

If  $f(x) < f(x_{i-1}^k)$  then  $x_i^k = x$  else  $x_i^k = x_{i-1}^k$

Figure 4 Hooke and Jeeves algorithm

## The satellite replacement problem

*There exist two kinds of failure for the satellite.*

1. There is no ergol left, to make maneuver, but the satellite is able to work.

While its trajectory is not too far from the nominal trajectory, the satellite can be considered for the coverage study, but not for station keeping maneuvers.

2. The failure is a mechanic or an electronic's one: the satellite is thrust to a higher orbit, and cannot be considered any more for the study of coverage of the constellation.

This kind of failure is seldom predictable. When it happens, there are 3 solutions:

1. The redundancy makes the coverage of the constellation good enough, not to use another satellite, but maneuvers can be done to replace satellites evenly around the earth.

2. The satellite can be replaced by a stand-by satellite located on orbit. In this case, the spare satellite can be in the same orbital plane but at a lower altitude than the failed satellite (the altitude, and the mean anomaly have to be corrected), or in another orbital plane (the altitude, the mean anomaly, the RAAN and perhaps the inclination have to be corrected).

3. The satellite can be replaced by a satellite stored on the ground.

Case the satellite has to be replaced, if the failure has not been predicted, there's a constraint on the time length of the replacement, in order to minimize the time of damaged coverage (with gap in coverage).

*Optimization problem to replace a satellite.*

The solution consists in using the drift of the spare satellite in order to minimize the total maneuvers. Case when the spare satellite is located in the same orbital plane but at a lower altitude than the failed satellite, just the altitude, and the mean anomaly have to be corrected. That's why only, in-plane maneuvers and drifts are necessary to be controlled.

The optimization problem that consists in minimizing the total maneuvers has two sorts of variables: in-plane maneuvers (either just maneuvers of the spare satellite, or maneuvers of this satellite and all others satellites of the constellation) and the drifts time length. Constraints are the objective location of the spare satellite, and the maximum time length replacement of the failed satellite. Equations of evolution are non linear, since the spare satellite is first too far from its objective location in the constellation.

This model can be extended to the case when the spare satellite is not in the same orbit plane than the failed satellite.

*Conclusion*

This model can be used to determine optimal maneuvers needed to replace a failed satellite. However the way to choose the spare satellite to replace the failed one, has to be modeled. This will certainly be useful to the study of the design of a constellation, for choosing the location of spare satellites.

## Conclusion

As a conclusion, we can say that this new model is very interesting since it can solve the most complicated case: nonlinear mixed-variables problem. It's more precise than the linear one. It allows to take into account various constraints: on the position (relative or



absolute) of satellites, on the consumption that can be limited and on the balanced consumption.

This model can also be used to calculate optimal maneuvers needed to replace a failed satellite. A first approach to find optimal maneuvers has been presented. However, the global problem, including the choice of the spare satellite, has to be stated.

## NUMERICAL RESULTS AND COMPARISON

These numerical results concern constellations such that random perturbations have been added to initial values of orbital parameters of all the  $N$  satellites.

### Comparison of both methods to solve the mixed-variables problem

Methods described (enumeration and exact method splitted on the basis of the generalized Bender's decomposition) have been used to solve the mixed-variables station keeping problem.

Parameters of the example are the following:  $N=6$  satellites,  $K=2$  steps,  $M=3$ . In this example just the mean anomaly is corrected ( $\delta V_w=0$ ), the criterion is  $J_3$ , and constraints are linear. The sub-problem is solved using the analytical method Eq. (12).

The value of the global optimum, and the computing time of each method are presented in next table. The boolean combination found is obviously the same with both methods.

**Table 1**  
**COMPARISON BETWEEN ENUMERATION AND EXACT METHOD.**

<u>Type of result</u>	<u>Exact method</u>	<u>Enumeration</u>
Cost (meter/sec) <sup>2</sup>	2.66 10 <sup>-7</sup>	2.66 10 <sup>-7</sup>
Computing time (Sparc 5)	6 min 26	12 min 49

This example and many others confirm that the exact method provides the global optimum in a shorter computing time than the enumeration does.

### Comparison of analytical method and direct search algorithm

In this example, the mean anomaly of a constellation (such that  $N=16$  satellites,  $K=2$  steps), is corrected ( $\delta V_w=0$ ). The criterion is  $J_3$ , and constraints are linear.

We solved this station keeping problem using respectively these three methods: Algorithm 1 finds which constraints are saturated, Figure 3. The problem Eq. (11) is solved by the analytical method, i.e. the resolution of the system of equations: Eq. (12). Algorithm 2 also finds which constraints are saturated, Figure 3. The problem Eq. (11) is solved by the direct search approach, i.e. the Hooke and Jeeves algorithm. Algorithm 3 solves the problem Eq. (11) with all  $\mu$  and  $\lambda$  variables, using the Hooke and Jeeves algorithm.

**Table 2**  
**COMPARISON BETWEEN THE ANALYTICAL AND DIRECT SEARCH METHODS**

<u>Type of result</u>	<u>Algorithm 1</u>	<u>Algorithm 2</u>	<u>Algorithm 3</u>
Cost meter/sec - meter <sup>2</sup> /sec <sup>2</sup>	2,214 - 4.082	2,214 - 4.082	2,214 - 4,082
Computing time (UltraSparc)	6 sec	1h05'	1h40'
Number of optimization variables	11	11	96

Values of cost presented in table 2, proves that the direct search (Hooke & Jeeves) algorithm can provide the global optimal solution of a station keeping problem, even for an important number of variables. All maneuvers found, with the three methods, have the same value with both methods about  $\pm 10^{-6}$  m/s.

### Comparison of linear and nonlinear models

Let us consider two examples with basic parameters  $N=20$  satellites,  $K=3$  steps, altitude= $10^3$  meters, inclination= $53^\circ$ , Number of plane=5. The mean anomaly and the inclination are corrected, since we consider J2 effects. So in and out of plane maneuvers have to be calculated.

Example 1: parameters of the constellation are perturbed: random perturbations have been added on orbital parameters of each satellite such that

$$\sigma_a=10^3 \text{ meters}, \sigma_i=8.10^{-4^\circ}, \sigma_\alpha=10^{-1^\circ}, \sigma_\Omega=10^{-3^\circ}.$$

Example 2: parameters of the constellation are more perturbed:

$$\sigma_a=2.10^3 \text{ meters}, \sigma_i=1,2.10^{-3^\circ}, \sigma_\omega=2.10^{-1^\circ}, \sigma_\Omega=10^{-3^\circ}.$$

We solved these two examples with the linear model and using the analytical method. Optimal and feasible maneuvers found for each example have then been introduced in the nonlinear model. The first column of the next table presents thresholds that respectively  $|\Delta i|$  and  $|\Delta \alpha|$  must not exceed. The two remaining columns present the greatest values of  $|\Delta i|$  and  $|\Delta \alpha|$ , provided when optimal and feasible maneuvers found with the linear model have been introduced in the nonlinear model (for initial orbital parameters of examples 1 and 2).

**Table 3**  
**COMPARISON BETWEEN LINEAR AND NONLINEAR MODEL, EXAMPLES 1 & 2.**

	<u>Threshold</u>	<u>example 1</u>	<u>example 2</u>
$\Delta i$ maximum degrees	0.001	0.001	0.001
$\Delta \alpha$ maximum degrees	0.1	0.134	0.168

These results show that the linear model can be used and provides good results. However, when constellation parameters are far from the nominal positions, the linear model is not precise enough and the optimal linear solution can violate constraints.

## CONCLUSION

In this paper, a new robust and efficient method that can solve the linear station keeping optimization problem has been presented. This method provides the global optimum of the problem in a very short computing time. We also presented a nonlinear station keeping optimization problem and an algorithm to solve it. These models and methods are able to solve a large range of station keeping optimization problems: linear or nonlinear evolution model of orbital parameters, corrections of relative or absolute positions of satellites, operational constraints, constraints on the consumption of satellites, constraints on the consumption balancing of all the satellites, choice of the objective function that can minimize the sum of complete maneuvers or just the sum of components of maneuvers,...

Several researches will be devoted to the following items:

A hybrid method mixing both analytical approach and direct search method can be investigated in the case where the problem has both linear and nonlinear constraints.

Moreover, the choice of a stand-by satellite to replace a failed satellite has to be stated, and an optimization method has to be developed to solve this problem.

Researches on constellation design are also developed and will certainly provide informations on constraints of the station keeping problem.

## REFERENCES

1. O.Zarrouati, "Trajectoires spatiales", Cepadues Editions, 1987.
2. "Mécanique spatiale", Tome 1 Cepadues Editions, 1995.
3. Michel Minoux, "Programmation mathématique", Tomes 1&2, Dunod, 1983.
4. A. M. Geoffrion, "Generalized Benders decomposition", Journal of Optimization Theory and Applications, 10(4):237, 1972.
5. C. A. Floudas and V. Visweswaran, "A primal-relaxed dual global optimization approach", Journal of Optimization Theory and Applications, 78(2):187, 1993.
6. C. A. Floudas, "Nonlinear and mixed-integer Optimization", Oxford University Press, 1995.
7. R. Hooke and T. A. Jeeves, "Direct Search Solution of Numerical and Statistical Problems", Journal ACM, Vol. 8, pp. 212-229, 1961.
8. E. Lasserre, F.Dufour, J.L. Calvet, D.Arzelier, J.Foliard and M.Vincent, "Optimal approach to station acquisition and station keeping of satellite constellations", 20th International Symposium on Space Technology and Science, Gifu, Japan, May 19-25, 1996.
9. L. Lefebvre, A. Lamy, P. Brousse, M. Vincent, J. Foliard, F. Dufour, E. Lasserre and J. Bernussou, "Relative station keeping optimization for the starsys constellation", 12th International Symposium on Space Flight Dynamics, ESOC, Darmstadt, Germany, 2-6 June 1997.



337508  
10P.

54-13  
169286

## SCHEDULING TECHNIQUES FOR A CONSTELLATION VISIBILITIES

**Jean-Claude Agnès\*, Pascal Brousse†**

Many conception or scheduling problems of space systems are based on combinatorial optimization techniques. In this paper, we describe the application of these techniques to the resolution of the scheduling problem appearing in the choice of visibility windows of satellites of a constellation.

The problem we try to solve is described by:

- given a set of tracking antennas,
- one antenna can only follow one satellite at a time and needs a certain delay to allow reconfiguration before being able to track another satellite,
- satellites must all be tracked more than a certain time every day,
- as much as possible the load of the antennas must be equal.

Among all the visibility windows, the problem consist in choosing one set that satisfies theses constraints at best.

We describe several methods initially developed in the framework of the scheduling problem of imaging for the future Spot-5 satellite:

- exact methods like the so called «Russian dolls» based on a Depth First Branch and Bound algorithm to find an optimal solution at the price of a sometimes very large computation time,
- approximate methods like «greedy search» (iterative or random) to find a good solution with a very short computation time.

### INTRODUCTION

When designing a constellation of satellites, one of the many problems to solve consists in minimizing the ground station network taking into account the great number of satellites to track.

The needs can be summarized as follows:

- All satellites must be regularly tracked with a minimum duration for telemetry (for instance 5 minutes every 36 hours).
- This regular control must be compatible with a more important control on satellites in contingency (for instance a visibility on every orbit).

---

\* Space Mathematics Division, Numerical Analysis and Applied Mathematics Department, Toulouse Space Center, CNES, 18 avenue Edouard Belin, F-31401 Toulouse cedex, France. Email: Jean-Claude.Agnese@cnes.fr

† Space Mathematics Division, Mission Analysis Department, Toulouse Space Center, CNES, 18 avenue Edouard Belin, F-31401 Toulouse cedex, France. Email: Pascal.Brousse@cnes.fr

- When a problem occurs on a satellite, it is often necessary to reload the work plan of the whole set of satellites of the constellation within a short delay (for instance this can lead to the fact that half of the constellation must be visible within 3 hours and the other one within 6 hours).

To these constraints induced by exploitation and station-keeping can be added needs in visibility due to operations during the positioning phase following multiple launches and to de-orbiting operations.

Dimensioning the ground stations network for the control of a constellation requires then the use of efficient scheduling techniques to reach an optimized result.

## **PROBLEM MODELING**

### **The scheduling problem**

The visibility scheduling problem can be informally described as follows:

- Given a set of satellites of the constellation to be tracked;
- Given a set of antennas achieving tracking operations on these satellites;
- Given a reference time interval;
- Given a set  $S$  of visibility windows corresponding to the different ways to track a satellite by a particular antenna on the reference time interval; each window is assumed to meet the requirements (RF visibility, minimum duration...);
- Given a weight associated to each window which can be the result of an aggregation of several criteria like the importance of the satellite... typically for the standard problem of finding a visibility window for each satellite, the weight will be uniformly 1;
- Given a set of hard constraints which must be satisfied:
  - Only one visibility window needed for each satellite;
  - Non overlapping (one satellite tracked at a time) and respect of a minimal transition time (reconfiguration delay) between two successive tracking on the same antenna;
- The problem is to find a subset  $S'$  of  $S$  which is admissible (hard constraints met) and which maximizes the sum of the weights of the windows in  $S'$  (i.e. the number of satellites tracked). In addition, the best between two solutions, provided the fact they reach the same maximum will be the one which leads to the most equal load of the antennas and the most uniform repartition in time.

This problem belongs to the class of the Discrete Constrained Optimization Problems and more precisely is a Valued Constraint Satisfaction Problem<sup>1,2</sup>.

VCSP is an extension of the CSP framework where each problem can be characterized by:

- A set  $V$  of variables: a finite domain of values is associated to each variable and defines its possible instantiations;
- A set  $C$  of constraints: each constraint links a subset  $V'$  of the variables and defines forbidden combinations of values for the variables in  $V'$ ;
- A valuation set  $E$  (to value constraints and assignments) with a total order (to compare two valuations), a minimal element  $\perp$  (to represent constraint satisfaction) and a maximal one  $T$  (to represent violation of a hard constraint);
- A valuation function associating to each constraint  $c$  in  $C$  an element in  $E$  which represents the importance of the satisfaction of  $c$ ;
- An aggregation operator  $\otimes$  (to aggregate constraints valuations) which respects commutativity and associativity, monotonicity relatively to the order, and for which  $\perp$  is the identity element and  $T$  the absorbing one.
- Given an assignment  $A$  of all the problem variables, the valuation of  $A$  is the aggregation by the operator  $\otimes$  of the valuations of all the constraints not satisfied by  $A$ .

The standard objective is to produce an assignment with a minimal valuation. It is an NP-hard problem according to the complexity theory and then its worst-case complexity grows at least exponentially with the problem size.

### **Modeling as a Valued Constraint Satisfaction Problem**

The modeling of the visibility scheduling problem within the VCSP framework consists then in:

- Associating a variable  $v$  to each visibility window  $w$  which represents the possibility to track a specific satellite with a specific antenna; this window is defined by a time interval during which the satellite is in visibility of the antenna.
- Associating to  $v$  a domain  $d$  of values:  $d=\{0,1\}$  corresponding to the two possibilities to achieve (1) or not achieve (0) the tracking of the corresponding satellite on the associated antenna during this particular visibility window; the special value 0 corresponds to the possibility of not selecting  $w$  in the schedule;
- Associating to  $v$  a unary constraint forbidding the special value 0 with a valuation equal to the weight of  $w$  (the penalty for not selecting  $w$ );
- Translating as  $n$ -ary constraints with the maximal valuation  $T$  the requirement of tracking each satellite only once;
- Translating as binary constraints with the maximal valuation  $T$  the constraints of non overlapping and respect of the minimal transition time between two successive tracking on the same antenna (reconfiguration delay);
- Using as valuation set the set of integers between 0 (for  $\perp$ ) and an integer greater than the number of satellites to track (for  $T$ );

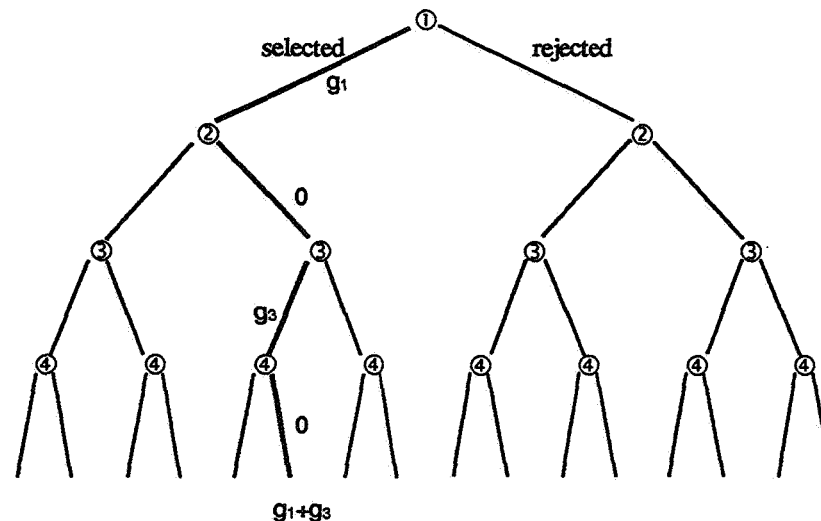
- Using as order the natural order on integers and as aggregation operator the usual + operator.

With this modeling the valuation of an assignment  $A$  is equal to  $T$  when a hard constraint is not satisfied or equal to the sum of the weights of the rejected windows when all the hard constraints are met. As it is always possible to produce an assignment where all the hard constraints are satisfied (for example by rejecting all the visibility windows), finding an assignment of minimal valuation is equivalent to finding an assignment satisfying all the hard constraints and minimizing the sum of the weights of the rejected windows i.e. the number of non tracked satellites in our case.

Except the unary constraints associated to each variable (the only ones which can be violated), all the other constraints are hard (valuation equal to  $T$ ). The valuation set and the aggregation operator induce an additive VCSP which is among the most difficult ones to solve.

## EXACT METHODS

Exact methods are systematic tree search procedures. The root of the tree, starting point for the search, is the empty assignment. At each node, the set of variables is partitioned into a set of instantiated variables and a set of uninstantiated variables. The children of a node corresponds to all possible extensions of the current assignment by instantiating a new variable. The leaves of the tree correspond to all the possible assignments. Variable instantiation ordering and value ordering can be used to guide the search. These methods are called exact because they are able to find an optimal solution provided that no running time limit is set. To avoid producing and evaluating all the possible assignments, optimistic evaluations of the partial assignments are used.





## Linear Programming in Integer Numbers

The first idea which comes to mind is to use commercial software. The problem can be seen as a linear programming problem in 0-1 numbers. So the modeling has been first implemented using XPRESS.

On a typical problem with a set of 870 initial windows, it has led to more than 380000 constraints. The only preprocessing took more than 1 hour on a SUN SS30 workstation and was very long to solve.

Thanks to previous studies on the scheduling of an earth observation satellite, specific methods developed in this context have been adapted to the visibility problem. They are described below.

## Depth First Branch and Bound

The most frequently used algorithm is the Depth First Branch and Bound which can be viewed as an extension to the VCSP framework of the backtrack algorithm widely used within the standard CSP framework.

Let us assume that the problem is to find an assignment with a minimal valuation less than  $\alpha_0$  and greater or equal to  $\beta$  (we suppose that it is known by other means that no assignment with valuation less than  $\beta$  exists). By default  $\alpha=T$  and  $\beta=\perp$ . The mechanism consists in performing a depth first search to find a complete assignment with a valuation less than  $\alpha$ . This bound initialized to  $\alpha_0$  strictly decreases during search. Each time a complete assignment with a valuation greater than or equal to the current bound is produced, a backtrack occurs. The algorithm stops when a complete assignment of valuation equal to  $\beta$  is found or when no complete assignment of valuation less than the current bound can be found.

This algorithm presents the following advantages:

- It only requires a limited space linear with respect to the number of variables;
- As soon as a first assignment with a valuation less than  $\alpha_0$  is found, the algorithm behaves like an anytime algorithm: if interrupted, the best solution found can be returned and its quality cannot but improve over time.

The main problem is that a depth first search can easily be stuck into a portion of the search space where no optimal assignment exists because of the first choices made during the search.

## Russian Dolls

This algorithm can be seen as an hybridization of Dynamic Programming and Branch and Bound. As it sequentially solves nested problems, it has been called Russian Dolls.

Given a problem with  $n$  variables, the method, which assumes a static variable ordering, consists in performing  $n$  searches, each one solving with the standard Depth First Branch and Bound algorithm a subproblem limited to a subset of the variables. The

$i^{\text{th}}$  problem is limited to the  $i$  last variables. Each problem is solved by using the same variable ordering, i.e. from variable  $n-i+1$  to  $n$ . The optimal valuation is recorded as well as the corresponding assignment. They will be used when solving the next problems to improve the valuation of the partial assignments and thus to provide better cuts: in other words, on the sub-tree issued from  $i$  you cannot find a better valuation than the one found when solving the  $i+1^{\text{th}}$  problem

This method which can be surprising since it multiplies by  $n$  the number of searches has proved to be very efficient. The main explanation is the quality of the valuation of the partial assignments provided by previous searches.

## **APPROXIMATE METHODS**

This section presents methods which aim at providing good solutions but cannot prove optimality. The counterpart is their efficiency in terms of computation time which becomes polynomial in the problem size.

### **Greedy search**

Visibility windows are first heuristically sorted. Then a solution is built by trying to insert each window in the current solution in the order of the sort and rejecting it if it is impossible. The algorithm is a one pass process and never comes back on its choices. The quality of the solution found greatly depends on the sort performed at the beginning. In the visibility problem, the best heuristic lies on a chronological order.

### **Iterative Greedy Search**

A way to improve the solution provided by this algorithm is to work in two phases:

- The first phase deals with the computation of a feasible solution using a greedy algorithm;
- The solution (result of the first phase) is then improved by a perturbation method based on an iterative inhibition of the selected windows. For each selected window, it consists in rejecting it and computing a new schedule from this point (the portion of schedule from the beginning up to that window being unchanged). If a better solution is found, the window is definitively rejected and the current solution updated else it is definitively selected.

This algorithm is a combination of greedy search (first phase) and limited local search (second phase).

### **Random Greedy Search**

Another way to more widely explore the search space is implemented in the Random Greedy Search:

- A upper loop modifies the set of windows in input, inhibiting some of them in a random way. The inhibition consists in randomly suppressing some of the visibility windows associated to a same satellite.

- The greedy algorithm is then used to compute a solution from this modified set.

This process is repeated as well. It always improves the solution found by a simple Greedy Search but there is no guarantee to find the optimal solution.

## IMPLEMENTATION

In order to standardize the computation process of the different algorithms, a set of basic functions as been implemented as shown on Figure 1. This functions deal with the basic manipulations necessary to build a solution and verify it. So scheduling algorithms can be easily interchanged.

They are based on two main data structures representing :

- The current assignment on which algorithms work and try to insert the different visibility windows;
- The best assignment which describes the best solution found.

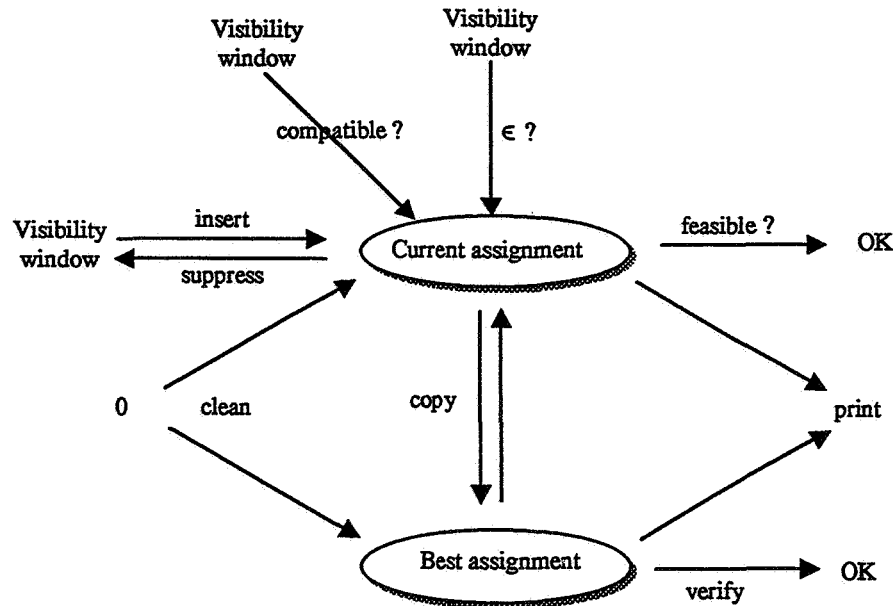


Figure 1: Basic functions of the scheduling algorithms

## RESULTS

On the next figures we give an example of the output of the scheduling process for 64 satellites (2 in contingency) tracked by 8 antennas in 4 stations on a period of 4 hours. Label C is for satellites in contingency which must be tracked as much as possible without holes of visibility longer than 2 hours. Label N is for specific satellites which must be viewed within the 2 first hours.

The algorithm has found a visibility for all satellites (included the one in contingency). The load of the different stations is almost equal. The entire process did not took more than a few minutes on the SUN SS30 workstation.

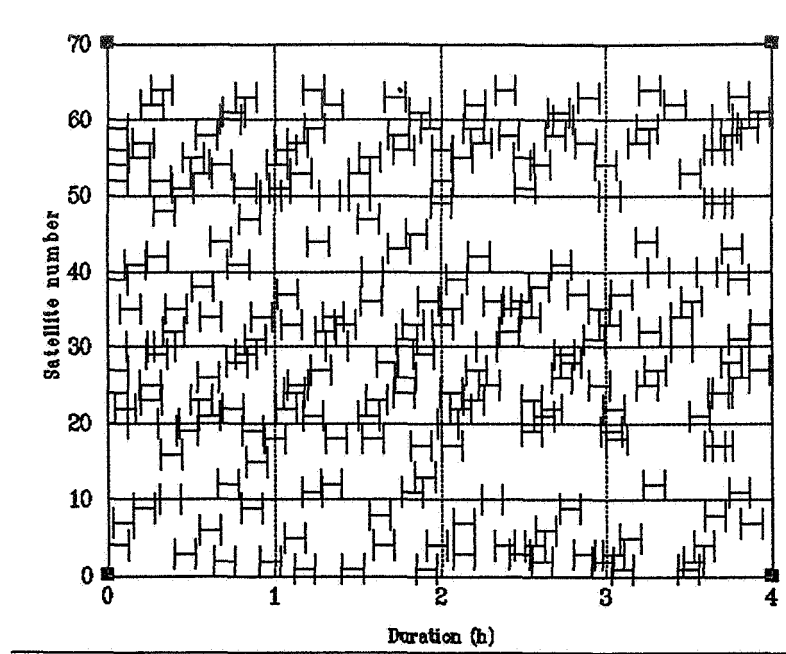


Figure 2: Set of possible visibility windows

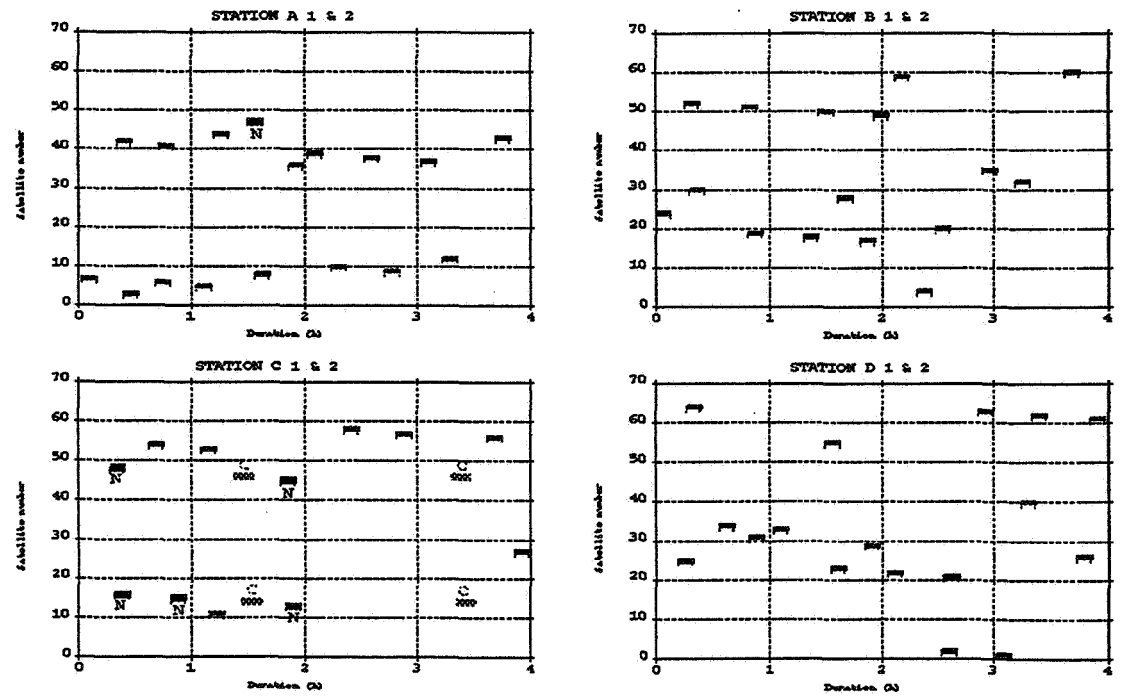


Figure 3: Output of the scheduling algorithm

## Elements of comparison between algorithms

Below, we give elements of comparisons between the different algorithms.

Algorithm	Notes	Quality	CPU time
Greedy Search	Often non optimal but very low CPU time	*	***
Iterative Greedy Search		*	**
Random Greedy Search	Best tradeoff	**	**
Linear Programming in Integer Numbers	Optimal solution, very long CPU time, large memory requirements	***	-
Russian dolls	Optimal solution but often prohibitive CPU time	***	-

## CONCLUSION

Exact methods like Russian Dolls or Linear Programming have the advantage to provide optimal solutions and to prove this optimality. Nevertheless they often fail on large size problems or in presence of high arity constraints in the sense that they cannot reach a solution in a reasonable computation time. When they fail, the systematic order they use to explore the search space prevents them to produce good quality solutions.

Approximate methods, like Random Greedy Search have the advantage to provide, within a limited time, good quality solutions thanks to their opportunistic way to explore the search space. But they have the drawbacks to provide no guarantee about this quality when some satellites remain untracked after a search for it is impossible to say that it is because the problem is unfeasible or because the algorithm has not found the solution.

In practice, these algorithms are intensively used for mission analysis in order to dimension the ground station network. When the constellation is operational, they will be integrated in the ground segment to plan the satellites tracking operations, both in nominal case and to reconfigure the constellation when some of them fall in contingency.

## REFERENCES

1. T. Schiex, "Préférences et incertitudes dans les problèmes de satisfaction de contraintes", Technical Report 2/7899 DERA, CERT, 1994.
2. T. Schiex, H. Fargier & G. Verfaillie, "Valued constraint satisfaction problems : hard and easy problems", in Proc. Of IJCAI-95, Montréal, Canada, 1995.
3. JC Agnès, "Logiciel ORVISK - Ordonnancement des visibilitées SkyBridge", *CNES Internal Technical Report*, DGA/T/TI/MS/MN/97-228, 1997.



# Design and Implementation of Satellite Formations and Constellations

David Folta<sup>o</sup>, Lauri Kraft Newman<sup>\*</sup>, and David Quinn<sup>+</sup>  
Navigation, Guidance, and Control Center  
Goddard Space Flight Center, NASA

14P.  
332509

The direction to develop small low cost spacecraft has led many scientists to recognize the advantage of flying spacecraft in constellations and formations to achieve the correlated instrument measurements formerly possible only by flying many instruments on a single large platform. Yet, constellations and formation flying impose additional complications on orbit selection and orbit maintenance, especially when each spacecraft has its own orbit or science requirements.

The purpose of this paper is to develop an operational control method for maintenance of these missions. Examples will be taken from the Earth Observing-1 (EO-1) spacecraft that is part of the New Millennium Program (NMP) and from proposed Earth System Science Program Office (ESSPO) constellations. Results can be used to determine the appropriateness of constellations and formation flying for a particular case as well as the operational impacts. Applications to the ESSPO and NMP are highly considered in analysis and applications.

After constellation and formation analysis is completed, implementation of a maneuver maintenance strategy becomes the driver. Advances in technology and automation by GSFC's Guidance, Navigation, and Control Center allow more of the burden of the orbit selection and maneuver maintenance to be automated and ultimately placed onboard the spacecraft, mitigating most of the associated operational concerns. This paper presents the GSFC closed-loop control method to fly in either constellations or formations through the use of an autonomous closed loop three-axis navigation control and innovative orbit maintenance support. Simulation results using AutoCon<sup>TM</sup> and FreeFlyer<sup>TM</sup> with various fidelity levels of modeling and algorithms are presented.

---

<sup>o</sup> Aerospace Engineer, Formation Flying Technology Lead, System Engineering Branch, NASA Goddard Space Flight Center, Greenbelt, Maryland, 20771.

<sup>\*</sup> Aerospace Engineer, EOS AM-1 Flight Dynamics Lead, Flight Dynamics Analysis Branch, NASA Goddard Space Flight Center, Greenbelt, Maryland, 20771.

<sup>+</sup> Aerospace Engineer, EO-1 GPS Lead, Flight Dynamics Analysis Branch, NASA Goddard Space Flight Center, Greenbelt, Maryland, 20771.

## INTRODUCTION

Missions such as those of the Earth System Science Program Office (ESSPO) and New Millennium Program (NMP) emphasize the use of multiple spacecraft to collect Earth-imaging scientific data.<sup>1,2</sup> These programs consist of multiple spacecraft in various orbits which include the Earth Observing System's EOS AM-1, EOS PM, EOS CHEM, and the EOS Laser Altimetry (ICESATs) missions. Other related spacecraft such as the next generation of Landsats are also considered part of this initiative. The EO-1 spacecraft of the NMP also is using the ESSPO requirements to promote technologies and correlated measurements. The orbit characteristics of several of these missions presented in the following table seem very similar in orbital mechanics terms, however the science goals are varied to achieve a wide range of Earth observations in the areas of ground imaging, atmospheric research, and ice sciences. These various spacecraft form a constellation of related spacecraft, potentially taking coincident or sequential measurements of the same location on the Earth's surface, or correlating measurements of related atmospheric phenomena. The reasons for these temporal measurements range from cross-calibration of the instruments as follow-on spacecraft are launched into the same orbit to sequential measurements made by instruments on spacecraft in different polar orbits.

Table - 1 Mission Characteristics

	EOS-AM	EOS-PM	Landsat-7	EO-1
Mean Altitude	705 km	705 km	705 km	705
Inclination	98.2	98.2	98.2	98.2
Repeat Cycle	16 days	16 days	16 days	16 days
MLT	10:30 am (desc) ± 15 min	1:30 pm (asc) ± 15 min	10:00 pm (desc) ± 15 min	N/A
Gndtrk control	± 20 km	± 10 km	± 5 km	± 3 km wrt L-7
Ground track Reference grid	WRS or previous repeat cycle track	WRS	WRS	Landsat-7 track
Sun- Synchronous?	Y	Y	Y	Y
Frozen?	Y	Y	Y	Y
Navigation	TONS	Ground/TDRS	Ground/TDRS	GPS
Constellation/ Formations Constraints	Constellation with Landsat-7	Constellation with AM, L-7	Constellation with EOS-AM	Formation Flying with Landsat-7
ELV	ATLAS	Delta	Delta	Delta
Launch Date	Oct., 1998	Dec., 2000	Dec., 1998	May 1999

As these programs mature, the maintenance of a constellation or formations of spacecraft drives the need for further analysis regarding the design of the spacecraft orbits. Analysis regarding the impacts of a design on subsequent missions and their requirements becomes more important and has highlighted challenges in determining the feasibility of proposed solutions to scientific questions, in accounting for monetary constraints, and in accommodating new technologies which have also posed challenges in the areas of orbit control and temporal observations. Extended analysis has also been driven by the imposition of constellation requirements on future low Earth orbiting spacecraft.

## FORMATION AND CONSTELLATION DESIGN DRIVERS

Design drivers for formations and constellations come from both scientific and technological disciplines, and include:<sup>3,4,5</sup>

- Small spacecraft flown as virtual platforms or ESSPO mission segments to meet instrument or scientific requirements.
- Navigation and communications requirements.
- Spacecraft and instrument operational considerations.



Constellations and formations offer the advantages of reduced launch risk per instrument, the separation of instrument and spacecraft bus schedules, and the implementation of new technology. However, the use of several spacecraft instead of one large spacecraft bus also has some disadvantages when coincident or sequential observations or calibration of instruments are required.<sup>6</sup> The use of one instrument's imaging data by another for planning, near-real time operations, or ground data processing can become a significant driver.

The proposed use of ground stations instead of the space network for communication support is another consideration in constellation and formation design.<sup>5</sup> ESSPO spacecraft are considering the use of X-band direct downlink for scientific data return. In order to assure that direct downlinking of data from numerous spacecraft will be possible without overlap in viewing from the ground station, an analysis was performed of the separation in a constellation which would minimize science data collection concerns<sup>5</sup>. Therefore, in considering the maintenance of a constellation or formation, fuel budgets must be analyzed. The goal is to minimize the required fuel for constellation maintenance by combining this maneuver with other maneuvers already planned to meet other mission requirements such as ground track control.

Navigation system selection also will impact the choice and design of constellations and formations not to mention the impact to the available onboard computer hardware and Attitude Control Systems (ACS). Recently, GPS has come to the forefront for real-time onboard navigation, but other technologies exist which may compliment the spacecraft hardware and provide a robust real-time navigation system. The technology of cross-links between spacecraft for both data communication and relative navigation has yet to be fully explored, but for a true closed-loop design, a real-time cross link must be available.

Orbit mechanics and the need to meet all mission orbit requirements place a great burden on the selection of the constellation and its maintenance. For example, most EOS missions have both ground track and mean local time (MLT) of node crossing control requirements. These orbital requirements must be met in order to successfully collect scientific data. Also, physical impossibilities will inhibit wishful thinking in the selection of some constellations or the achievement of the formations directly from the launch vehicle. Some constellations may take a long duration to establish and can impose increased constraints on the launch vehicle to meet injection targets. The operations associated with these maneuvers may also become a driver if the instruments are required to physically change their modes, such as covering up optics during maneuvers to protect against contamination or sun impingement.

### **Formation And Constellation Definitions**

While often used together, achieving and maintaining a constellation are independent concepts from that of formation flying.<sup>4,7</sup> A constellation is defined as two or more spacecraft in similar orbits that perform separate control of their orbits. They may provide global or localized science data, but mostly in a post-processing sense. They do not provide real-time communications between spacecraft. In general, a constellation could contain spacecraft that have no hard requirement concerning maintenance of a relative position. For a large difference in orbital anomalistic angles, relative cross track separations vary over the orbit since the spacecraft are really in different orbit planes. This orbit plane difference in nodal crossing is used as an advantage for constellation maintenance to meet sequential observations by accounting for the Earth rotation. The concern is that the result of relative drift in the along-track direction between two spacecraft yields a different sub-satellite point, thereby impeding the coincident observation requirement on every orbit. However, for the NMP problem, in order to achieve a higher percentage of coincident observations, the spacecraft have the additional requirement to maintain a formation within the constellation.

Formation flying is an orbital operations concept design in which a spacecraft maintains a predetermined trajectory relative to a reference position without making a physical attachment.<sup>7</sup> This reference position may be occupied by another spacecraft if desired. Consider two spacecraft placed in the same orbital plane and at the same altitude, with an initial anomaly separation angle small enough that atmospheric density and gravitational perturbations can be considered constant. These spacecraft will be similarly affected by atmospheric drag and by the gravitational potential field of the Earth provided that they have identical ballistic properties. Ballistic properties are defined here as the ratio of mass to the product of frontal area and coefficient of drag. If the spacecraft are separated in the radial direction, and the

respective ballistic properties are different, their orbit velocities are also different, and one spacecraft (the formation flyer) will appear to drift relative to the other (the reference flyer). The drift is most apparent in the along-track (orbital velocity) direction. The approach for determining the formation flying maintenance was formulated using basic orbital mechanics and formation flying concepts which are derived from Hill's or Clohessy-Wiltshire Equations of motion.<sup>8</sup>

## DESIGN METHODOLOGY

To consider the methodologies of maintaining constellations and formations, an example from each is discussed in detail. The first methodology discussed is the constellation.

### Constellation Design and Maintenance

The mean anomaly separation between spacecraft is used as the basis for our analysis. While some separations may seem exceedingly large, it is determined by the science temporal requirement for coincident/sequential observations and by communication requirements. Also, for spacecraft to observe the same location, their orbit planes must be oriented to account for the rotation rate of the Earth during the time lag between one spacecraft seeing the location and the other spacecraft passing over the same location. To characterize the definition of location, it is assumed that the sequential instrument fields of view are large enough to have an imaging expectancy of at least 80%.<sup>9</sup> A first order approximation to analyze the constellation was completed based on orbital mechanics found in any textbook. While high order Geopotential and third body effects can be ignored in the analytical results, they should be considered when verifying results. These values were verified in high order simulations using AI Solutions' AutoCon<sup>TM</sup>, or FreeFlyer<sup>TM</sup>.<sup>10</sup> The analysis of constellations was based on information in Table-1 and on the following assumptions and requirements:

- The spacecraft must maintain a minimum true anomaly separation.
- All spacecraft must meet their groundtrack requirements, therefore, maneuvers must be performed at intervals defined by the atmospheric conditions and not the constellation maintenance.
- The range of spacecraft ballistic coefficient differences are no larger than 15% with a baseline of 50 kg/m<sup>2</sup>.
- Atmospheric conditions are considered to be relatively uniform over the separation in the orbit planes and between spacecraft.
- The maximum separation in radial altitude to meet the maximum ground track requirement is 2 km (+/- 1 km about a reference altitude).

Other mission orbit requirements place additional constraints on the constellation maintenance. These are ground track control, frozen orbit control, inclination control, mean local time control, and repeating orbits. The principal driver of these is ground track maintenance, which has the most stringent orbit requirements. To meet science requirements for Earth observing instruments, the repeating groundtrack of the sub-satellite must be controlled. Ground track maintenance is performed by varying elements of the orbit to ensure that the orbit repeat cycle is met and reference points at the equator are over-flown each orbit. The ground track accuracy is maintained by changing the orbital nodal period with respect to the fixed Earth rotation rate. The nodal period is adjusted by changes to the semi-major axis. The number and times of the maneuvers to accomplish this are determined by atmospheric conditions. For ESSPO spacecraft, this maneuver frequency varies between one month and six months. Frozen orbit control can be accomplished through strategic placement of the ground maintenance maneuvers at no additional fuel cost. The other orbit parameters are rarely adjusted and are not considered here.

### Constellation Targets

To maintain the constellation, maneuvers must be performed to control the drifting between spacecraft due to the differential decay rates. The targets used for constellation maintenance are dependent upon the individual requirements of the science goals, operations, and constraints. An example of the targets used most often for polar orbiting ESSPO type missions are semi-major axis (sma) and eccentricity. One can maintain an ESSPO constellation by adjusting these parameters to control the individual orbit or to

maintain the constellation separation. A change to the sma will adjust the drifting in an orbit period between the spacecraft while the eccentricity can adjust the orientation of the relative orbit elements such as argument of periapsis. The sma can be targeted to meet the ground track requirements and to maintain the constellation.

#### Maintenance Using Ground Track Control

If one follows the ground track control theme then constellation maintenance is reduced to meeting the mission requirements. The ground track control is realized by a change to the sma and the adjustments made to this parameter will result in a differential drift in the relative mean anomaly. There is no control of the magnitude of the drift between the spacecraft as the drift distance is dependent upon when the maneuvers are performed for the ground track control. The targeted sma is the required sma to maintain the mission ground track which can be computed via differential correction methods in FreeFlyer™.

#### Maintenance Using Mean Anomaly Control

If one follows the differential mean anomaly rate theme, one can adjust the time it will take to transverse a delta mean anomaly between the spacecraft. The selection of the sma of the maneuvering spacecraft can be used as a target to bring about a controlled drift over a given delta anomaly in a given time. The derivation of this sma target is simply an algebraic expansion of the mean anomaly rates as shown below.

The mean anomaly difference over time can be computed as,

$$\Delta\theta = (n_1 - n_2)t \quad \text{where} \quad n_1 = \sqrt{\frac{\mu}{a_1^3}} \\ n_2 = \sqrt{\frac{\mu}{a_2^3}}$$

with  $a_n$  = mean sma,  $a_{n0}$  = initial mean sma,  $a_{nd}$  = sma decay rate,  $\mu$ =gravitational constant,  $n$  = mean motion, and  $t$ = time.

Using a desired angular difference and time, this can be expanded to,

$$\frac{\Delta\theta}{t} = \sqrt{\frac{\mu}{(a_{1o} \pm (a_{1d} \cdot t/2))^3}} - \sqrt{\frac{\mu}{(a_{2o} \pm a_{2d} \cdot t/2)^3}}$$

Solving for the target semi-major axis,  $a_{2o}$ , and using an assumption that the decay rates are subject only to the differential ballistic coefficients yields,

$$a_{2o} = \left[ \mu / \left( \sqrt{\frac{\mu}{(a_{1o} \pm (a_{1d} \cdot t/2))^3}} - \left( \frac{\Delta\theta}{t} \right) \right)^2 \right]^{1/3} + ((a_{1d} \cdot t/2) \cdot (Bc_1/Bc_2))$$

where,

$$a_{2d} = a_{1d} \cdot (Bc_1/Bc_2)$$

## Ground Track Control Results

To consider a sample scenario, this analysis assumes that ground track maintenance starts with one spacecraft half-way through the ground track maintenance cycle to account for the maximum radial separation (and therefore maximum in-track velocity difference) over time. Orbital decay rates were calculated at the solar flux maximum, based on +2 sigma predictions. If the ballistic coefficient ( $B_c$ ) is 50 kg/m<sup>2</sup>, the decay rate at 705 km at the beginning of the mission (June 1998) is approximately 0.0028 km/day. If the  $B_c$  equals 40 kg/m<sup>2</sup>, the decay rate is approximately 0.0034 km/day. Decay rates for the -2 sigma solar flux values can be orders of magnitude less (e.g.  $B_c=50\text{kg/m}^2$ , decay rate ~ 0.0003 km/day four years later) and could give significantly different results. The ground track maneuvers periodically change the relative semi-major axes of the spacecraft which results in a switching of the sign of the delta mean motion.

The maintenance of the ground track results in a repeating and somewhat uniform increasing and decreasing of the mean anomaly (along-track distance) between the spacecraft as maneuvers change the direction of the differential mean motion. The observed difference in the mean anomaly of each spacecraft varied by approximately  $\pm 15^\circ$  over a several month. This difference suggest that ESSPO type separation angle requirements of  $40^\circ$  can easily be met. Furthermore, results suggest that multiple spacecraft can be initially 'stationed' at intervals of  $60^\circ$  to allow for drift. These spacecraft do not need to be in co-planar orbits, since the above sequential observations and station coverage must be met. More importantly, the ground track control results of this analysis suggest that no additional propellant is required to maintain a constellation separation if the coincident observations can be reduced to occurring at smaller time intervals. In Figure 1, a mean anomaly separation angle is shown for spacecraft with the same  $B_c$  but with different ground track requirements of  $\pm 20$  km and  $\pm 5$  km. Figure 2 presents the separation angle for spacecraft that have the same ground track requirements, but the  $B_c$  of the formation flyer is 15% that of the reference spacecraft (40 kg/m<sup>2</sup> vs 50 kg/m<sup>2</sup>).

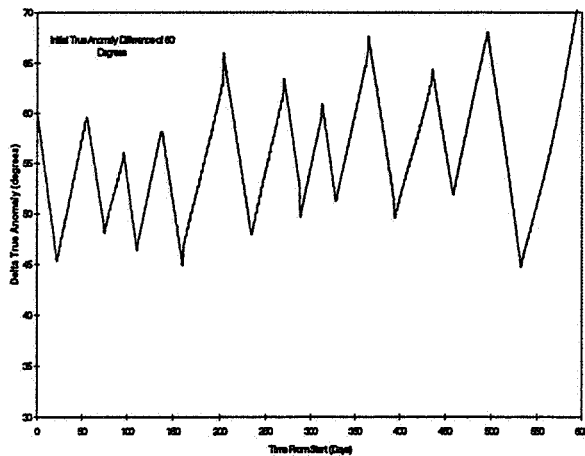


**Figure 1 - Constellation Drift of S/C with Different Groundtracks**

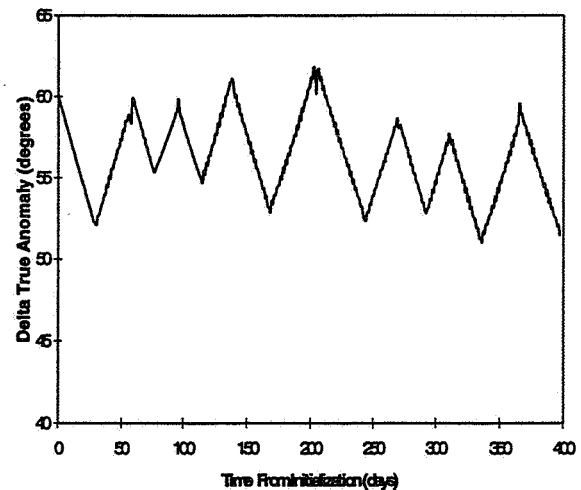


**Figure 2 - Constellation Drift of S/C with Same Groundtracks**

## Mean Anomaly Control Results

The results of using the equations derived above for the sma targets are shown in Figure 3 and 4. Figure 3 presents the required initial sma to drift a desired distance in a fixed time and the sma to drift a fixed distance in a desired time. Two examples in the figure show the effects of changing the fixed parameter. The results of this spreadsheet were numerically verified using the FreeFlyer™ system and the verified points are noted by the circles and squares. The initial reference sma was 7077 km, which represents a typical mean element of the sma of ESSPO orbits.

The mean anomaly control results of this analysis, while similar to the ground track results, suggest that any given constellation separation magnitude can be controlled. The separations and time can also be used as an input into the ground track control to minimize the separation drift distances and thereby increase the number of sequential instrument observations. The results suggest that ESSPO type separation angle requirements of 40° can easily be met. Furthermore, results suggest that multiple spacecraft can be initially 'stationed' at smaller separation angles. As with the ground track results, these spacecraft do not need to be in co-planar orbits, since the above sequential observations and station coverage must be met.

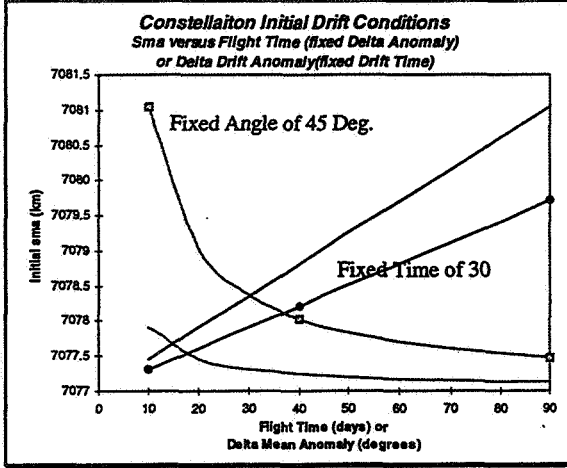


Figure 3 - Constellation Drift

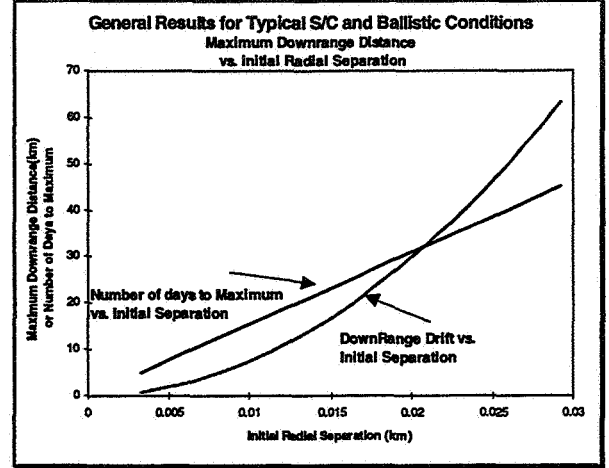


Figure 4 - Initial Return Drift Conditions

#### Analytical Drift Equations

Figure 4 presents a general analytical method to compute the initial radial separation for maintaining a constellations given a desire to control the along track separation. The equations for this plot are analytical and only a meant to given a representative case. The point is that a controlled drift in the along track direction, both away from and back toward a reference spacecraft cannot be achieved by using the generic drift equations previously described. The radial separation required for a controlled drift is an order of magnitude smaller than that for general drift over a given time period. Since the orbit decay is inversely proportional to the ballistic coefficient, the chase spacecraft will decay at an average decay rate similar to that of the reference and is given by,

$$\dot{r}_2 = \dot{r}_1 \cdot (Bc_1/Bc_2)$$

and the differential orbital decay rate will be

$$\Delta \dot{r} = \dot{r}_1 - \dot{r}_2$$

the initial radial separation can then be given by

$$\Delta \bar{r} = 0.5 \cdot \Delta \dot{r} \cdot t$$

The maximum downrange drift rate can then be given by substitution into the differential angular rates

$$\dot{D}_{\max} = 1.5 \cdot \sqrt{\mu/r^3} \cdot \Delta \bar{r}$$

and the maximum drift is then

$$D_{\max} = \dot{D}_{\max} \cdot 0.5 \cdot t$$

The equations are presented here as a general guideline and do not hold up under a high fidelity modeling which includes higher order Geopotential terms and differential orbital perturbations due to large angular separations. Figure 4 presents the drift and initial radial separation only for the decay rates used in the constellation analysis and need to be modified for each individual case.

## MECHANICS AND DEFINITIONS OF FORMATION FLYING

In order to meet the coincident observation requirement without a large variation in the anomaly as previously presented, a formation strategy must be developed and followed. Assuming that the fields of view of the instruments are circular (on the order of one kilometer in diameter) and nadir pointed, a control box can be determined to ensure that the FOVs will overlap to a given percentage<sup>9</sup>. It is assumed here that this control box is 50 kilometers in the along track direction, given the assumption that the ground error is equal to the along-track error for a sma of 7077 km. Therefore, to meet this two kilometer requirement, an initial altitude displacement for the formation flying spacecraft with respect to the reference is required to affect the formation flying theory.

Formation flying involves position maintenance of multiple spacecraft relative to measured separation errors. It involves the use of an active control scheme to maintain the relative positions of the spacecraft. Optimally, this process will be performed autonomously onboard the spacecraft and is called Enhanced Formation Flying, such as that which will be implemented by GSFC for the New Millennium EO-1 mission. A complete description of the fundamental of formation flying was previously published<sup>7,11</sup>. An example of the orbit dynamics of formation flying is shown in Figure 5.

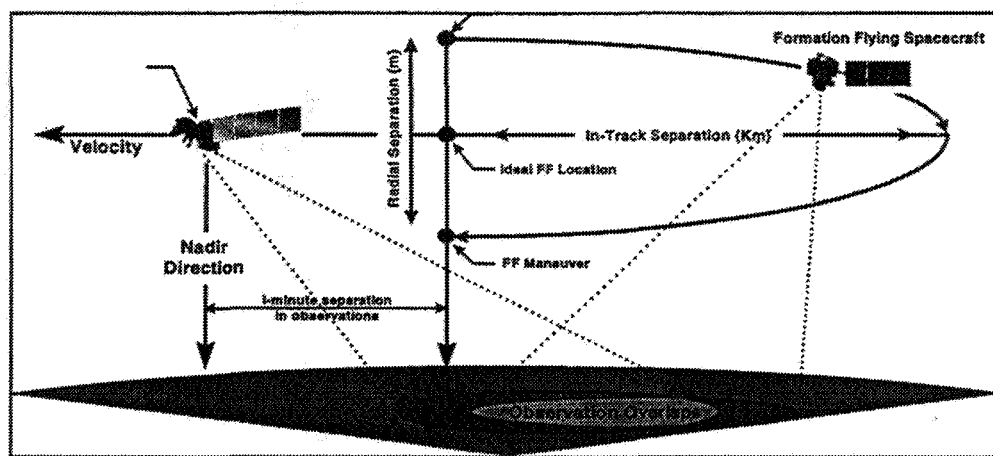


FIGURE 5. Formation Flying Example

Formation flying techniques can be used to meet a variety of mission separation requirements. When the mission requirements call for a tightly controlled separation (kilometer range), whether the overall separation is small or large, frequent control becomes necessary. Formations of spacecraft are identified using tight or loose control methods. While some separations may seem exceedingly large, they are determined by the science requirement to view coincident sites or a communication requirement of a ground station to view only one spacecraft at a time. For large separations, one must consider the rotation of the Earth if the formation is used to meet concurrent or sequential imaging of the same locations on the ground. Therefore, relative crosstrack separations are used to follow the reference ground track for any temporal requirement. A patent rights application was submitted to the GSFC patent counsel by two of the authors for the application of Autonomous Closed Loop 3-Axis Navigation Control Of Spacecraft.<sup>12</sup>

### Formation Flying and Targeting Algorithm Description

The algorithm enables the spacecraft to execute complex 3-axis orbital maneuvers autonomously. Figure 6 illustrates the basic sets of information required for formation targeting as it is incorporated into AutoCon<sup>TM</sup>. The algorithm is suited for multiple burn scenarios but is explained here in a two-burn approach for clarity. The simplest formation flying problem involves two spacecraft orbiting the Earth. One spacecraft, referred to as the control spacecraft, orbits without performing any formation flying maneuvers. The second spacecraft is the chase spacecraft. It monitors the control spacecraft, and performs maneuvers to maintain the desired formation phasing. The goal of the formation flying algorithm is to perform

maneuvers to move the chase spacecraft along a specified trajectory, called the transfer orbit, from its initial state  $S_0 = (r_0, v_0)$  at a given time  $t_0$  to a target state  $S_t = (r_t, v_t)$  at a later time  $t_t$ .

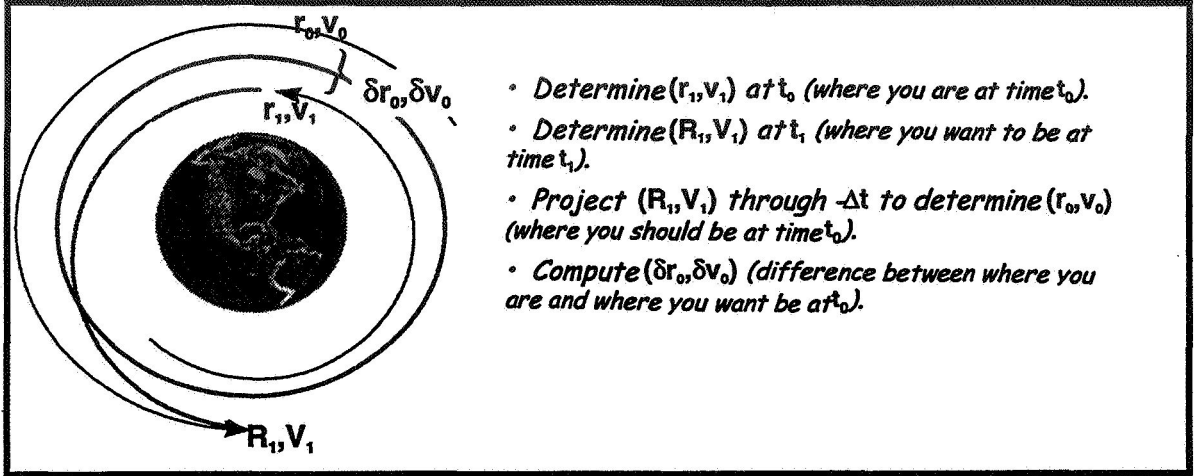


FIGURE 6. Formation Orbital Parameters

This goal is accomplished by finding the state the spacecraft would have at the current time in order to achieve the target state at the target epoch without maneuvering. This new state is called the desired state  $S_d = (r_d, v_d)$ ; it is the target state propagated backwards in time from the target epoch to the epoch of the initial state. The difference between the initial state and the desired state is:

$$\delta S = \begin{pmatrix} \delta r \\ \delta v \end{pmatrix} = \begin{pmatrix} r_0 - r_d \\ v_0 - v_d \end{pmatrix}$$

Then, following the derivation of the state transition matrix given in Battin<sup>13</sup>, the relevant state transition matrix submatrices are:

$$R(t_t) = \frac{|r_d|}{\mu} (1 - F) [(r_t - r_d) v_d^T - (v_t - v_d) r_d^T] + \frac{C}{\mu} [v_t v_d^T] + G [I]$$

$$\tilde{R}(t_t) = \frac{|r_t|}{\mu} [(v_t - v_d) (v_t - v_d)^T] + \frac{1}{|r_t|^3} [r_t | (1 - F) r_t r_d^T + C v_t r_d^T] + F [I]$$

The expressions for F, G, and C are derived from the universal variable. From these submatrices, the  $C^*$  matrix is computed as follows:

$$R^*(t_0) = -R^T(t_t)$$

$$V^*(t_0) = \tilde{R}^T(t_t)$$

$$C^*(t_0) = V^*(t_0) [R^*(t_0)]^{-1}$$

The expression for the impulsive maneuver follows immediately:

$$\Delta v = C^*(t_0) \delta r - \delta v$$

### Keplerian and Non-Keplerian Transfer Orbits

The transfer trajectory for constellations and formations does not need to be of a Hohmann type. Having established both actual and desired states of a spacecraft's location using any navigation filter, all that is needed is a means of autonomously zeroing the difference between the two states. Given two Keplerian trajectories and a chronologically defined maneuver window, a reference non-Keplerian trajectory may be determined which will smoothly transport the spacecraft from its position on the first Keplerian path at the beginning of the maneuver window to a desired position on the second Keplerian path

at the conclusion of the maneuver window. Control points on the reference trajectory in Figure 7 are calculated at regular time intervals consistent with the ability of the spacecraft to receive and process position data, fire its thrusters, and account for the effects of each firing. At each step in the process, the next control point on the reference path is examined and back-computed along a Keplerian path to determine small differences between spacecraft position and velocity on the reference path and determine which Keplerian path would intersect the reference path at the next control point. These differences are then fed into a system of linearized state transition matrices to determine the incremental  $\Delta V$  required to get the spacecraft to the next control position on the reference trajectory. At the conclusion of the maneuver window, a final burn is required to match the velocity required to maintain the new Keplerian trajectory. One can use single or multiple maneuvers to achieve the target condition

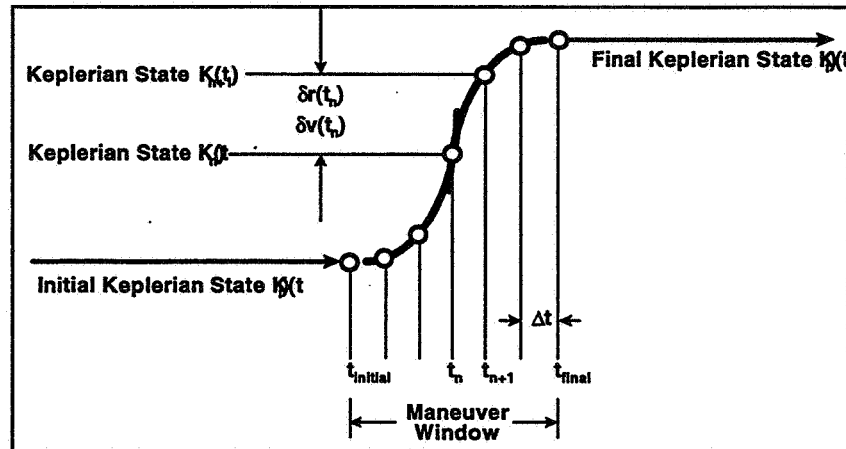


**FIGURE 7. Non-Keplerian Reference Trajectory During Maneuver**

#### Algorithm Targets

For the formation, the orbit target is described as a location relative to the reference so that the drifting due to ballistic coefficient difference can be utilized. For example, the EO-1 relative position has a three dimensional target that is 450 km behind the reference spacecraft in the along-track direction, a sub-kilometer altitude above the reference, and also a cross track differential to account for the rotation of the Earth to meet the observation requirements. This target can easily be misinterpreted as a simple rotation in true anomaly and altitude for the along-track direction and altitude and a node displacement for the cross track requirement. If a true anomaly is used to compute the along-track difference, a completely different orbit will be designed as the change on keplerian elements doesn't take into consideration the true orbit with the perturbations included. It can be shown that propagating an orbital element set with a delta true anomaly either before or after the change in altitude will not give the desired results. Therefore, if one wants the orbit or the formation flying spacecraft to 'fly' a predetermined trajectory, the following method can be used. This method will account for the cross track component as well.

- Initially use the reference orbit cartesian state
- Offset the altitude of the formation flyer by the desired amount
- Propagate (numerical methods suggested) the initial state backward/forward by the required time delta, e.g. plus or minus one minute.
- Change the Epoch of the final propagated state of the formation flyer to the original time to effect a change in the cross track to meet coincident observations
- Change the coordinate system into ECI from ECEF

#### Formation Flying Results

The following results are taken directly from the AutoCon<sup>TM</sup> ground system which utilizes the GSFC algorithm. The results are divided into two formation flying scenarios of two spacecraft which maintain either a close or a dynamic formation.<sup>7</sup> The initial conditions were derived from the orbit elements



for the Landsat-7 mission which has a sun-synchronous orbit with a descending node MLT of 10:00 a.m. and a ground track repeat of 233 orbits in 16 days. The results show formation flying evolution and the effect on the mission groundtrack requirements. Evolution Figures are presented in a control spacecraft rotating coordinate system with the radial direction being the difference in radius magnitude and the alongtrack direction being the arc between the position vectors.

### Close Formations

The first two figures present the maintenance of a formation that has a 10 meters radial separation only. Figure 8 presents the formation evolution in radial and separation distances for a period of 90 days. To re-initialize this orbit, two maneuvers are used in a Hohmann-like transfer. The first DV to re-establish the 10 m radial position separation by using the algorithm targeting method with a  $\frac{1}{2}$  orbit period and the second DV by using the same method with a .01 orbit period to adjust the velocity components. Figure 9 presents the ground track of these orbits. The initial orbital condition placed the ground track at the "0" error location for convenience.

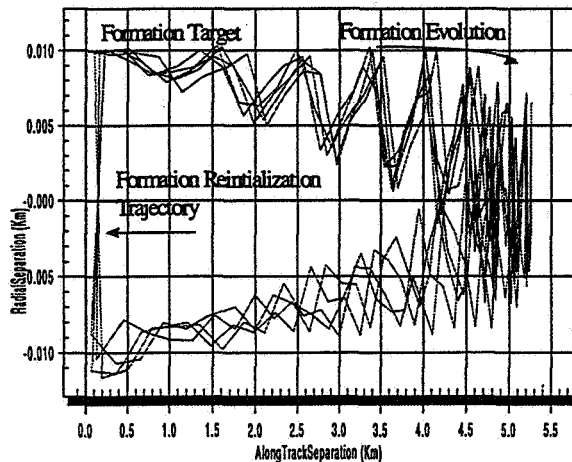


**Figure 8 - Close Formation Radial and Alongtrack Separation**

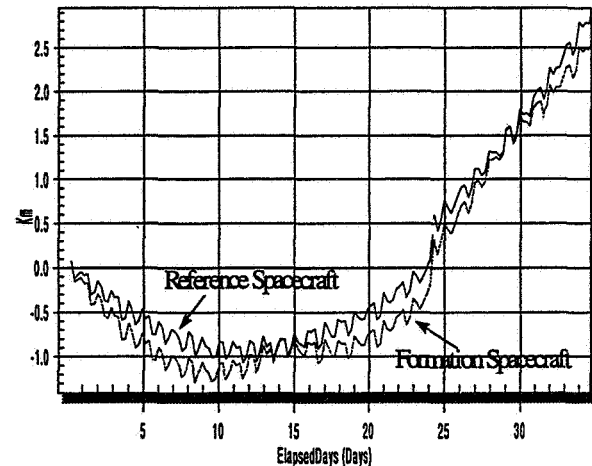


**Figure 9 - Close Formation Relative Groundtrack**

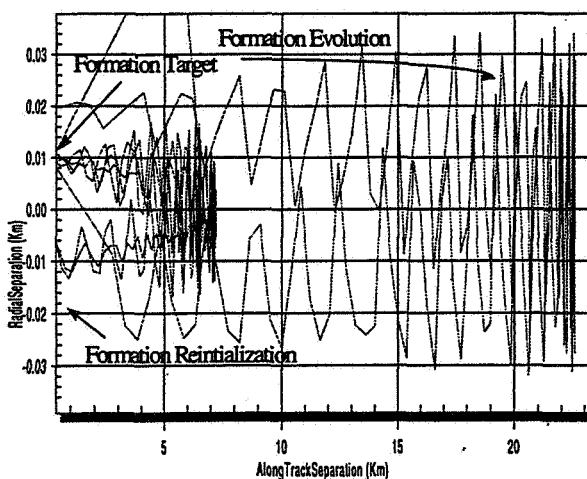


**Figure 10 - Close Formations with Reference S/C Groundtrack Maneuver**

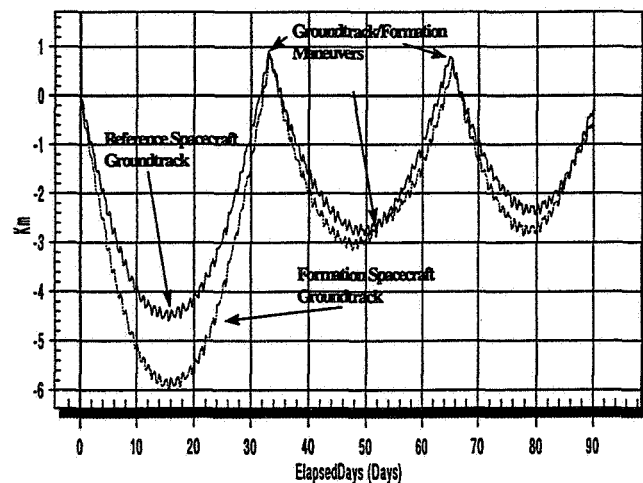


**Figure 11 - Close Formation Groundtracks with Maneuver**

Figures 10 and 11 present results of starting with an initial along track separation of 0 m and an initial radial separation of 20 m and then targeting to a 10 m radial and 0 along track separation whenever

either spacecraft performs a maneuver. Therefore, the first maneuver of the formation flyer is to adjust to both the groundtrack of the control spacecraft after its maneuver and to re-establish the initial formation parameters. Figure 10 presents the results when ground track maneuvers have occurred for the control spacecraft. As seen in Figure 11, a ground track maneuver takes place slightly before the time when the along track separation is near zero. The smaller parabola represent the maintenance of the formation to the 10 m radial separation. The formation evolution in radial and separation distances is presented for a period of 90 days.

### Dynamic Formations

The next simulation consists of maintaining a dynamic formation where the formation flying spacecraft was in a different orbit plane with an along track separation on the order of 450 km. To simulate this, the initial state of the control spacecraft was propagated backward for 1 minute (450 km at 7.5 km/s) and to maintain the ground track requirement the right ascension of ascending node was adjusted to account for a one minute Earth rotation. Figures 12 and 13 present the formation evolution in the radial versus along track and cross track versus along track separation for several days. The effect of the perturbations on the orbit elements has an immediate effect in the osculating orbital elements. This results in a very large radial separation approaching  $\pm 1$  km. A cross track of  $\pm 30$  km was anticipated since that is the effect of the node difference. As the formation evolved, a maneuver was required to re-established the formation at the initial separation of 0 m along track and 30 km cross track at a radial separation of 10 m. Figure 12 presents the trajectory of the formation flyer. The figure shows the radial separation change from approximately 500 m to +10 m and an along track separation from 450 km to 0 km. After this state was targeted, a maneuver was performed to maintain a formation similar to the close formation. Figure 13 presents formation evolution after the maneuver.-

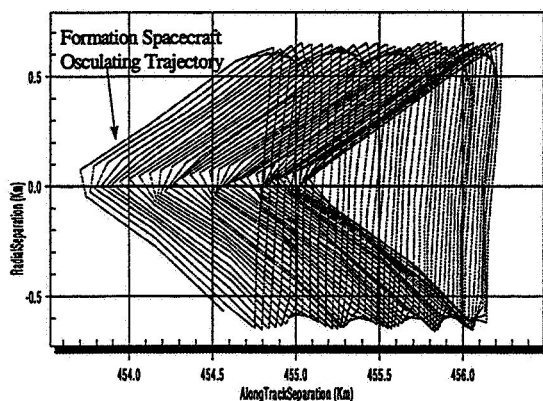


Figure 12 - Dynamic Formation Evolution

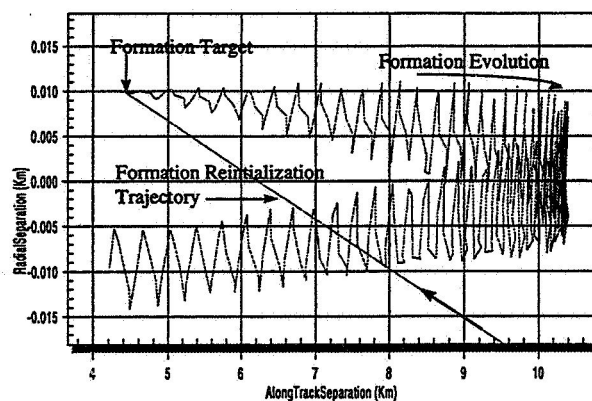


Figure 13 - Post Maneuver Trajectory and Evolution

### EFF TECHNOLOGY DESCRIPTION

The control of the constellations and formations mentioned above use an algorithm that is part of a new technology called AutoCon<sup>TM</sup>, which features flight software that is capable of autonomously planning, executing, and calibrating routine spacecraft orbital maneuvers<sup>10,14</sup>. The autonomous EO-1 formation flying control software AutoCon<sup>TM</sup> builds on this existing capability for the maneuver planning, calibration, and evaluation tasks. A fuzzy control engine is ideal for this application because it can easily handle conflicting constraints between spacecraft subsystems.

The AutoCon<sup>TM</sup> flight control system will need data from additional sensors and spacecraft subsystems such as propulsion, groundtrack, navigation, and attitude data. It will then be possible to autonomously generate, analyze, and execute the maneuvers required to initialize and maintain the formation between Landsat-7 and EO-1. Figure 14 shows a functional diagram of the AutoCon<sup>TM</sup> system. Because these calculations and decisions are performed onboard the spacecraft, the lengthy period of ground-based planning currently required prior to maneuver execution will be eliminated. The system is general and modular so that it can be easily extended to future missions. Furthermore, the AutoCon<sup>TM</sup> flight

control system is designed to be compatible with various onboard navigation systems (*i.e.* GPS, or an uploaded ground-based ephemeris). This formation flying technology will demonstrate the capability of EO-1 to fly over the same groundtrack as Landsat-7 within  $\pm 3$  kilometers at the equator while autonomously maintaining the formation for extended periods to enable paired scene comparisons between the two satellites.

### Autonomous Control Architecture Design

The Enhanced Formation Flying (EFF) system for the EO-1 application is designed by GSFC, AI Solutions, Inc., and the Hammers Company, who has responsibility for the EO-1 attitude control system (ACS). The flight software, AutoCon-Flight™ will serve as the overall architecture and execute the Goddard developed control algorithm for maneuver decision, design, and execution. This control algorithm will provide a delta-velocity magnitude, burn epoch, and duration to the ACS for execution. Maneuver implementation is the responsibility of the ACS. Maneuver calibration will be performed autonomously within AutoCon™. Integration testing and system verification will be performed with the ACS flight software prior to the mission to demonstrate technology readiness. Ground simulation equipment will be used for system integration, testing, and performance evaluation. Verification of the flight system performance during the operational phase will be conducted according to a validation plan. This validation will occur in several incremental steps starting with ground verification of the maneuver parameters that have been computed onboard, and will culminate with full onboard autonomous maneuver prediction, planning, and closed-loop onboard maneuver execution. A subsystem interface is shown in Figure 15.

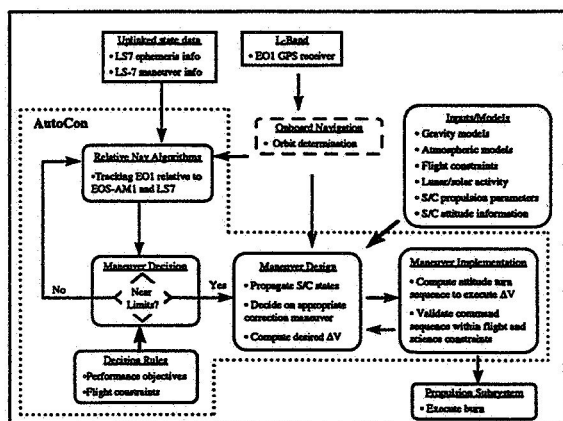


Figure 14 - AutoCon Functional Diagram

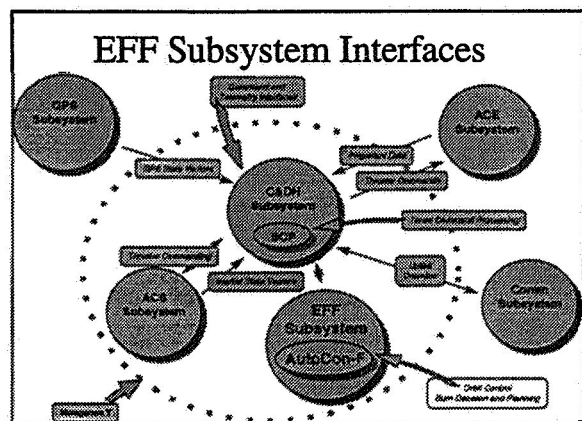


Figure 15 - AutoCon Sub-System Diagram

### CONCLUSIONS

In considering the use of constellations to meet scientific objectives, one must take into account the physical limitations and restrictions imposed. Our results suggest that no additional propellant is required to maintain a large constellation separation if the coincident observations can be reduced to occurring at small time intervals when the orbit mechanics would naturally provide this event. The maintenance of a constellation for constant coincident viewing can be quite complicated but is feasible if one manages and plans for this endeavor. This planning should assess emerging technology and the system engineering aspects of the spacecraft development. It should assess the spacecraft ballistic coefficient in particular as well as the amount of fuel required. The amount of coincident observations that are required to meet mission objectives versus the amount desired should be addressed. The formation can be established to provide coincident observations on a timed schedule, but may miss targets of opportunity for calibration or extra coverage.

This paper shows that the formation flying algorithm presented is a feasible technology that can be used in a closed-loop design to meet science and mission requirements of Low Earth Orbiting missions in the NMP and ESSPO. The algorithm is very robust in that it supports not only benign ground track control, but demanding 3-D control for inclination and non-Keplerian transfers. To best meet the NMP EO-1

requirements, this innovative technology will be flown onboard the spacecraft which launches in May 1999. The algorithms are being integrated into AutoCon™ for both ground support validation and closed-loop onboard autonomy. This system will be implemented as a close-loop flight code onboard the NMP Earth Orbiter-1 (EO-1) spacecraft thereby yielding the name of Enhanced Formation Flying while an open-loop system will be implemented on the ground for verification. The application of this algorithm and AutoCon™ system to other NMP or ESSPO programs is unlimited and can be used to fully explore the NASA mandate of faster, better, cheaper spacecraft.

## REFERENCES

1. G. Asrar, *NASA'S Mission To Planet Earth, Earth Observing System*, PAM-552, NASA Publication,
2. R. Ticker, "New Millennium Program's Earth Orbiter One Flight (NMP/EO-1) Opportunity for Industry Partnership", NASA, GSFC, Greenbelt, MD.
3. R. Carter, Internal memo of EO-1 Requirements, (1997), NASA GSFC Greenbelt, MD.
4. D. Folta, L. Newman, "Establishment And Maintenance Of A Constellation Of Multiple Spacecraft", Proceedings of the Flight Mechanics Estimation Theory Symposium, May, 1994
5. L. Newman, "EOS-PM Ground Station-to-Multiple Spacecraft Contact Study", memorandum to Mr. Wu, EOS-PM Project, May 1994.
6. D. Folta, F. Bordi, C. Scolese, "Considerations on Formation Flying Separations For Earth Observing Satellite Missions", Proceedings of the AIAA/AAS Spaceflight Mechanics Meeting, February 1992, Colorado Springs, Co.
7. Folta, D.C. and L. Newman (1996) "Foundations of Formation Flying For Mission To Planet Earth and New Millennium, AIAA 96-3645, AIAA Guidance, Navigation, and Control Conference and Exhibit, San Diego, CA
8. Clohessy and Wiltshire, *Terminal Guidance System for Satellite Rendezvous*, Journal of the Aerospace Sciences, Sept. 1960.
9. C. Scolese, D. Folta, and F. Bordi, "Field of View Location and Formation Flying For Polar Orbiting Missions", AIAA/AAS Spaceflight Mechanics Meeting, February, 1991, Houston, Tx.
10. R. Sperling, *AutoCon / FreeFlyer System Description and User's Guide*, (1997) AI Solutions, Inc., Greenbelt, MD. 20770
11. D. Folta and D. Quinn, "A 3-D Method for Autonomously Controlling Multiple Spacecraft Orbits", IEEE AeroSpace Conference, Aspen CO., March 21, 1998
12. D. Quinn, and D. Folta (1996) *Patent Rights Application and Derivations of Autonomous Closed Loop 3-Axis Navigation Control Of EO-1*.
13. Battin, R., *An Introduction to the Mathematics and Methods of Astrodynamics*, AIAA Education Series, (1987) Chapters 9 and 11.
14. F. Bauer, D. Quinn\*, K. Hartman†, D. Folta†, and John Bristow, "Enhanced Formation Flying Experiments For The New Millennium Program Earth Orbiter (EO)-1 Mission - Challenging Technology Program Management", AIAA, 5/97

56-18  
ABS. ONLY

AAS 98-305

169288

## NANOSAT CONSTELLATION MISSION DESIGN

Marco Concha and Robert DeFazio  
NASA Goddard Space Flight Center

337510

### ABSTRACT

1P

The NanoSat constellation concept mission proposes simultaneous operation of multiple swarms of as many as 22 identical 10 kg spacecraft per swarm. The various orbits in a NanoSat swarm vary from  $3 \times 5$  to  $3 \times 42 R_E$  in geometry. In this report the unique flight dynamics issues of this constellation satellite mission design are addressed. Studies include orbit design, orbit determination, and error analysis. A preliminary survey determined the orbital parameters that would yield a 100 minute shadow condition maximum while providing adequate ground station access for three ground stations.



## **A MODERNIZED APPROACH TO MEET DIVERSIFIED EARTH OBSERVING SYSTEM (EOS) AM-1 MISSION REQUIREMENTS**

**Lauri Kraft Newman**  
NASA GSFC, Code 572

**Mark E. Hametz, Darrel J. Conway**  
AI Solutions, Inc.

From a flight dynamics perspective, the EOS AM-1 mission design and maneuver operations present a number of interesting challenges. The mission design itself is relatively complex for a low Earth mission, requiring a frozen, Sun-synchronous, polar orbit with a repeating ground track. Beyond the need to design an orbit that meets these requirements, the recent focus on low-cost, "lights out" operations has encouraged a shift to more automated ground support. Flight dynamics activities previously performed in special facilities created solely for that purpose and staffed by personnel with years of design experience are now being shifted to the mission operations centers (MOCs) staffed by flight operations team (FOT) operators. These operators' responsibilities include flight dynamics as a small subset of their work; therefore, FOT personnel often do not have the experience to make critical maneuver design decisions. Thus, streamlining the analysis and planning work required for such a complicated orbit design and preparing FOT personnel to take on the routine operation of such a spacecraft both necessitated increasing the automation level of the flight dynamics functionality.

The *FreeFlyer*<sup>TM</sup> software developed by AI Solutions provides a means to achieve both of these goals. The graphic interface enables users to interactively perform analyses that previously required many parametric studies and much data reduction to achieve the same result. In addition, the fuzzy logic engine enables the simultaneous evaluation of multiple conflicting constraints, removing the analyst from the loop and allowing the FOT to perform more of the operations without much background in orbit design.

Modernized techniques were implemented for EOS AM-1 flight dynamics support in several areas, including launch window determination, orbit maintenance maneuver control strategies, and maneuver design and calibration automation. The benefits of implementing these techniques include increased fuel available for on-orbit maneuvering, a simplified orbit maintenance process to minimize science data downtime, and an automated routine maneuver planning process. This paper provides an examination of the modernized techniques implemented for EOS AM-1 to achieve these benefits.

## INTRODUCTION

The challenge in determining how best to support each mission is to not only look to the past to learn from successes and failures of previous missions, but to also look to the future to take advantage of new technologies. EOS AM-1 is no exception. In a similar fashion to the Landsat mission series, EOS AM-1 will fly in a Sun-synchronous, frozen orbit with a 16-day repeat cycle. This orbit necessitates frequent orbit maintenance maneuvers over the life of the mission. Modernized techniques were implemented for EOS AM-1 flight dynamics support in several areas, including launch window determination, orbit maintenance maneuver control strategies, and maneuver design and calibration automation. The benefits of implementing these techniques include increased fuel available for on-orbit maneuvering, a simplified orbit maintenance process to minimize science data downtime, and an automated routine maneuver planning process.

A cooperative effort with Lockheed Martin (the launch vehicle manufacturer) has resulted in an optimal use of the launch vehicle's capabilities that has enabled a greater than instantaneous launch window and has minimized the amount of corrective maneuvering required by the spacecraft. Once on orbit, analysis has shown that routine stationkeeping maneuvers executed as single burn maneuvers do not compromise orbital constraints. Additionally, in keeping with NASA's direction to reduce operations costs, the maneuver design process has been automated through the use of *FreeFlyer*<sup>TM</sup>. This paper details these modernized approaches to meeting the AM-1 requirements described above, including updated analysis methods, simplified maneuver alternatives, and automated operations.

## MISSION OVERVIEW

The Earth Observing System AM-1 (EOS AM-1) spacecraft is an Earth Systems Science Program Office (ESSPO) initiative to explore global change and the Earth's environment. EOS AM-1 will be launched no earlier than October 6, 1998 aboard an Atlas IIAS expendable launch vehicle (ELV) from the Western Range of Vandenberg Air Force Base. After the ascent maneuvers are executed to place EOS AM-1 in its mission orbit at 705 km mean equatorial altitude, the five science instruments aboard the spacecraft will begin taking measurements of the Earth's environment. These data will later be correlated with data from related instruments on other spacecraft to provide scientists with a more in-depth view of the phenomena under study.

The EOS AM-1 mission orbit is both frozen and Sun-synchronous with a 16-day repeating ground track. The ground track must be maintained to  $\pm 20$  km of the World Reference System (WRS). The frozen orbit condition must be maintained such that the altitude over a given latitude is within  $\pm 10/5$  km of the nominal value at all times. In addition, the Mean Local Time (MLT) of descending node must remain between 10:15 am and 10:45 am throughout the duration of the mission to maintain constant lighting over the Earth's surface. Passive control of the 98.2 degree nominal Sun-synchronous inclination prevents the need for out-of-plane maneuvers while maintaining the constant lighting within these mission tolerances. The inclination will be biased above the



nominal value to achieve a 10:15 MLT at beginning of life, and the inclination drift with time will cause the MLT to vary slowly over the course of the mission towards 10:45 and back to 10:15, requiring no maneuver to adjust the inclination actively. For more details on this technique, see Ref. 1.

## **METHODOLOGY IMPROVEMENTS**

In preparing to support the launch and operation of EOS AM-1, flight dynamics analysts have incorporated several techniques into the mission plan that, while not new, have not previously been used in an optimized manner. The first of these techniques is the use of guided targeting to achieve optimal inclination targets determined on board using a polynomial to widen the launch window. The second technique involves using one burn instead of the traditional Hohmann transfer to accomplish the combined ground track and frozen orbit maintenance. Performing one burn instead of two minimizes instrument down times and periods of less-accurate data while simplifying operations. The paragraphs below describe the benefits and concern associated with the use of these techniques and provides analysis verifying the accuracy and reliability of these methods.

### **Launch Window Widening**

To achieve a Sun-synchronous orbit, the spacecraft must be launched at the time that the desired orbit plane passes through the launch site longitude. This time occurs once per day in the appropriate (ascending or descending) direction. Ideally, this constraint would imply an infinitely small launch window to accurately achieve the desired MLT. The length of the window may be widened around the exact launch time by making use of the permissible error range on the MLT requirement. However, this error box is often better used to eliminate inclination maintenance maneuvers. The MLT drift throughout the mission may be kept to within the MLT limits by choosing the optimum inclination for a given MLT. This strategy eliminates the need for out-of-plane inclination maintenance maneuvers. Figure 1 (Ref. 2) shows the effects on MLT drift of the optimum inclination choices for EOS AM-1 for 10:20 am and 10:40 am beginning of life MLTs. This maintenance method for Sun-synchronous orbits is described more fully in Ref. 1. When these considerations are incorporated into the analysis, the desired launch target still requires achieving the optimum combination of inclination and MLT. Therefore, a virtually instantaneous launch window is once again required.

A second option is to make use of guided targeting when available from the ELV for widening the launch window by altering the target orbit parameters during powered flight. Guided targeting is a feature often used by a vehicle to accommodate needs of various payloads, such as azimuth targeting for deep space missions and minimum parking orbit inclination targeting for geosynchronous spacecraft. The Atlas IIAS vehicle that will be used to launch EOS AM-1 is capable of guided targeting implemented through the use of a polynomial in the flight code. EOS AM-1 is taking advantage of this capability to change the inclination and MLT targets depending on the actual minute within the launch window that the ELV lifts off. Using this method, the EOS AM-1 window was widened from instantaneous to a 20 minute launch opportunity. Although the EOS AM-1 MLT limits are between 10:15 and 10:45 am indicating that a 30 minute

window would be possible, the launch vehicle is restricting its target orbits to those between 10:20 am and 10:40 am MLT. This conservative approach will prevent exceeding the science requirements due to vehicle dispersions on the inclination, which would cause a high MLT drift rate at beginning of life. This high drift rate may cause an immediate violation of the MLT constraint.

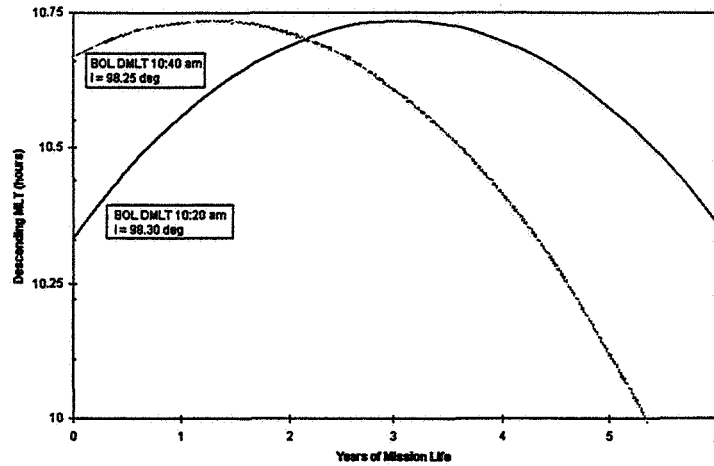


Figure 1: Optimum MLT and Inclination Targets for EOS AM-1

The Atlas flight code computes the inclination target in the following manner (Ref. 3). After launch occurs, the actual liftoff time is used to calculate the desired Greenwich Mean Time (GMT) of the descending node of the injection orbit from the equation:

$$\text{GMT}_{\text{DN}} = \text{GMT}_{\text{LO}} + \Delta t_1 + \Delta t_2 \quad (1)$$

where:  $\text{GMT}_{\text{LO}}$  is the GMT of liftoff in seconds.  
 $\Delta t_1$  is the nominal time of launch vehicle flight from liftoff to spacecraft separation (seconds)  
 $\Delta t_2$  is the nominal time from spacecraft separation to the descending node (seconds)

Because the exact actual powered flight times are not known before completion of that flight segment, values must be used for  $\Delta t_1$  and  $\Delta t_2$  that are determined pre-launch. In addition, the flight code cannot accept multiple values for these variables based on launch time, so the same constant values of  $\Delta t_1$  and  $\Delta t_2$  must be hard coded for use at all points in the launch window. Since the launch will most likely occur at the beginning of the launch window, the 10:20 values for these times were computed based on simulated powered flight trajectories by Lockheed Martin and set as constants in the flight code. Then, the  $\text{GMT}_{\text{DN}}$  computed in (1) may be used to compute  $\text{MLT}_{\text{DN}}$ , assuming a constant value for the longitude of descending node (LDN):

$$\text{GMT}_{\text{DN}} = \{\text{MLT}_{\text{DN}} - [\text{LDN} * (86400 \text{ sec}/360 \text{ deg})]\}_{\text{modulo } 24} \quad (2)$$

where: LDN is the longitude of descending node (deg East). It is the angle measured east of the Greenwich meridian to the descending node at the time of the descending node crossing.

Finally, the target inclination may be computed from a polynomial of the form:

$$INC_{TARG} = C_0 + C_1(MLT_{DN}) + C_2(MLT_{DN})^2 \quad (3)$$

where the  $MLT_{DN}$  is measured in hours computed using (2),  $INC_{TARG}$  is the target inclination in degrees, and the coefficients are computed before launch by fitting a curve to the optimal inclination and MLT targets for each minute of the launch window as shown in Figure 2 (Ref. 2). For the data in Figure 2,  $C_0 = 80.987296$ ,  $C_1 = 3.460392$ , and  $C_2 = -0.172758$ . These values of inclination and  $MLT_{DN}$  computed during flight augment the specified altitude target to fully determine the ELV target orbit.

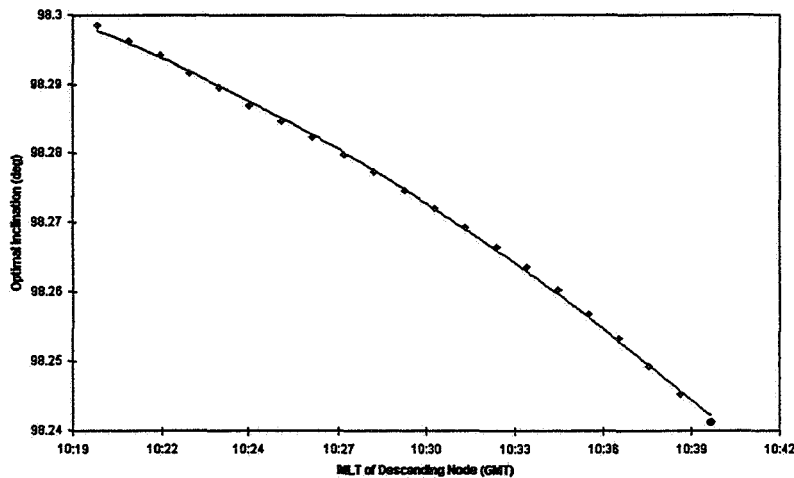


Figure 2: Optimum MLT targets for EOS AM-1 Injection

One issue raised about this technique is that when using a constant value for the  $\Delta t$ 's and the LDN in the above equations, the error caused by using one value over the whole launch window might outweigh the benefits of using the guided targeting. This concern arose because the inclination targets varied only  $0.05^\circ$  over the 20 minute launch window. It was eventually decided that holding the values constant did not cause a problem based on the analysis described below. Note that although the ELV is only contractually obligated to provide inclination accuracy within  $0.1^\circ$ , historical data has shown that Atlas vehicles routinely achieve inclination targets to within hundredths of a degree of the targeted value. Therefore, the targeted values are a reasonable goal for the mission. The closer the vehicle can place the spacecraft to its targeted inclination, the less fuel the spacecraft will have to spend on operationally complex out-of-plane inclination maneuvers to return to the optimum initial state.

Lockheed Martin supplied optimized trajectory runs for 10:20, 10:30, and 10:40 optimum  $MLT_{DN}$  and inclination targets. Flight Dynamics used these data and held the LDN and  $\Delta t$ 's from the 10:20 nominal trajectory constant over the whole launch window to compute the inclination target, as will be done in the flight code. The target

inclination was then computed using equations (1) - (3) for each minute of the window. Values for the beginning, middle, and end of the launch window are shown in Table 1.

Table 1  
INCLINATION TARGETS USING BEGINNING OF WINDOW LAUNCH  
CONSTANTS

MLT Targeted	GMT <sub>LO</sub>	$\Delta t_1$	$\Delta t_2$	GMT <sub>DN</sub>	LDN	LMST (hours)	INC Target
10:20	67065.8	820.3867	126.6371	68012.82	231.5716	10.333333384	98.29827
10:30	67665.8	820.3867	126.6371	68612.82	231.5716	10.500000051	98.27531
10:40	68265.8	820.3867	126.6371	69212.82	231.5716	10.666666717	98.24275

The worst case encountered in this analysis is a launch at the end of the window while achieving the  $3\sigma$  LDN dispersions on the target state. If the 98.24275° target 10:40 state above is compared with the optimum inclination of 98.2413°, the difference is -0.001446309° in inclination, well within the inclination dispersion allowance of 0.1°. If non-constant values of LDN and  $\Delta t$  had been used, the 10:40 target would be computed using the optimal 10:40 LDN and  $\Delta t$ 's, yielding 98.24115°, a difference of 0.00015° from the target computed using 10:20 constants.

The worst-case LDN dispersions computed by Lockheed Martin are  $\pm 0.060525^\circ$  for a 10:30 am target orbit. Applying these dispersions to the 10:20 data above (assuming similar dispersions regardless of when in the launch window liftoff occurs), the targets may be recomputed using the maximum ( $LDN_{1020} + 0.060525^\circ$ ) and minimum ( $LDN_{1020} - 0.060525^\circ$ ) LDNs. Results indicate that the maximum LDN dispersion case causes the 10:40 target to exceed the MLT box by  $10.66792605 - 10.66666666 = 0.00125939$  min, well within the 0.5 min allowable dispersion. For the minimum LDN dispersion case, the 10:20 target exceeds the MLT box by  $10.33333333 - 10.32652272 = 0.00681061$  min, also well within the 0.5 min allowable dispersion.

These analyses show that guided targeting as is used for the EOS AM-1 launch is a technique that works well for Sun-synchronous orbits. Thus a technique that is applied regularly to deep space and geosynchronous orbits has been shown to produce significant improvements in the low-Earth regime.

### Frozen Orbit Control

Having thus improved the launch and ascent process, the maintenance of the mission orbit was also examined for possible improvements. In addition to maintaining the ground track control grid, the science instruments on EOS AM-1 dictate that only small altitude changes can occur over any given latitude. Consequently, a frozen orbit is implemented to constrain the mean argument of perigee near 90 degrees. Freezing the orbit requires a mean eccentricity of 0.00116 for the mission altitude and inclination. If no ground track control maneuvers were required, some infrequent frozen orbit maintenance maneuvers would be required over the life of the mission to reshape the orbit. However, since the mission requires frequent altitude maneuvers, these maneuvers can be used to simultaneously restore the frozen orbit while performing ground track control. The key to utilizing the altitude maneuvers to simultaneously meet the frozen

orbit constraints is to perform the burns at a location in the orbit that will restore the orbit shape rather than degrade it. The location of the single burn within the orbit should be chosen to place the post-maneuver mean eccentricity and argument of perigee as close as possible to nominal values (0.00116 and 90 degrees, respectively). The maneuvers are placed alternately in the two locations, separated by about 180° anomaly, that the Hohmann transfer maneuvers would normally be placed to restore the frozen orbit.

Because it is desirable for operational reasons (less downtime for instruments, less data interruption, less maneuver planning) to perform the least number of maneuvers possible and still maintain the orbit within the science requirements, the technique of using only one maneuver instead of the traditional Hohmann transfer pair to maintain the AM-1 ground track was designed into the AM-1 support. A single maneuver has the same total  $\Delta V$  as the pair and is placed appropriately to maintain the frozen orbit condition. This technique was used with success to maintain the semi-frozen orbit of Landsat-5. AM-1 has a more stringent requirement to maintain its frozen altitude to within +10/-5 km mean altitude and  $\pm 20^\circ$  mean argument of perigee. Therefore, analysis was required to investigate the effects of the location of single ground track correction maneuvers within the orbit on the frozen orbit condition.

An algorithm was developed for the Flight Dynamics Analysis Branch that determines the best location to perform a single burn to drive the orbit back to the optimal frozen conditions. This algorithm was easily integrated into AI Solutions' object-oriented *FreeFlyer*<sup>TM</sup> product and is used as part of the automated ground track maintenance maneuver planning process. The algorithm (Ref. 5) requires as input the initial mean semi-major axis, argument of perigee, and eccentricity, as well as the values of the  $\Delta V$  and burn duration required for the ground track maintenance maneuver that will be accomplished in combination with the frozen orbit maintenance. First, the average orbit velocity is computed from the mean semi-major axis ( $a$ ) as:

$$V_{avg} = 1000 \sqrt{\frac{\mu_{Earth}}{a}} \text{ m/s} \quad (4)$$

Dividing the total desired  $\Delta V$  for the ground track maneuver by the burn duration yields a  $\Delta V$  per second,  $\delta v$ . Then the standard variations of Keplerian elements under this  $\Delta V$  are given by:

$$\Delta e = \frac{2\delta v(e + \cos MA)}{V_{avg}} \quad (5)$$

$$\Delta \omega = \frac{2\delta v \sin MA}{eV_{avg}} \quad (6)$$

Applying these equations iteratively over the duration of the maneuver allows the initial Keplerian elements to be coarsely propagated. After each iteration, the mean anomaly (MA) is calculated using:

$$MA^{(n)} = MA^{(n-1)} - \Delta\omega + \sqrt{\frac{\mu_{Earth}}{a^3}} \Delta t \quad (7)$$

The initial MA may then be varied parametrically to determine the value that best achieves the desired frozen orbit conditions. Figure 3 shows a scan over one orbit at 2° mean anomaly increments. The  $\Delta V$  is applied at each step and the post-burn eccentricity and argument of perigee computed. The area highlighted by the circle in Figure 3 shows where the set of post-burn solution points most closely intersects the target point of 0.00116 and 90°. This intersection point corresponds to a mean anomaly of 49°, where the computed values are 90.22° and 0.0011689, respectively. The point of 0° MA and the direction of increasing MA are both indicated in the figure.

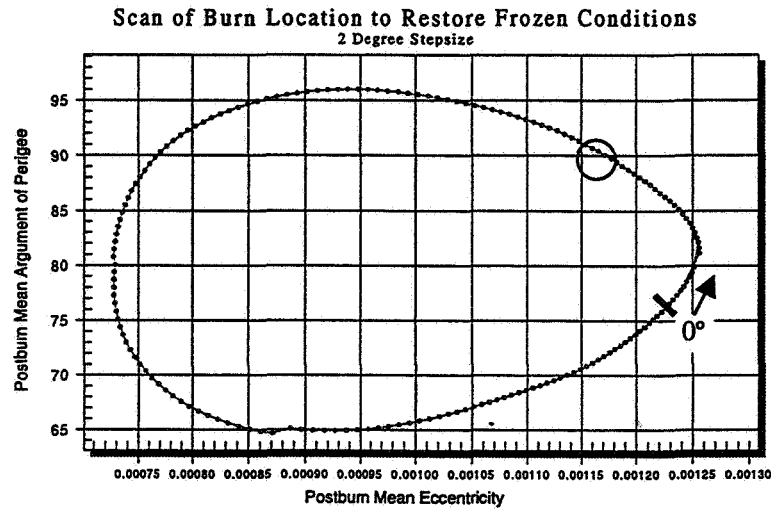


Figure 3: Optimum Mean Anomaly to Achieve EOS AM-1 Frozen Orbit

The frozen orbit evolution for an 18-month span with maneuvers determined using this algorithm is shown in Figure 4. The figure indicates that performing the single maneuver ground track corrections at the optimum frozen orbit restoration location achieved the maintenance of the mean argument of perigee to within the  $\pm 20^\circ$  allowed by the mission requirement. The straight line portions of the plot indicate places at which the maneuvers were performed.

The radial position constraint of +10/-5 km in mean altitude is then met by default, since the argument of perigee requirement is the more stringent of the two as described in Reference 4. This result may be easily seen when examining Figures 5 and 6 from Reference 4, which show the frozen orbit evolution for eccentricities that are increments of 0.002 higher (Figure 5) and lower (Figure 6) than the nominal 0.00116 value. The center ellipse in each figure is the nominal eccentricity, and ellipses moving out from the center are incrementally higher or lower, respectively. Based on both figures, the eccentricity must not deviate more than  $\pm 0.004$  from the nominal value. For an argument of perigee deviation of  $\pm 20^\circ$ , keeping the eccentricity deviation within these bounds requires constraining the altitude to within approximately +3.7 km/-2.3 km of the 705 km mean nominal, as shown in Figure 7 (Ref. 4). Since these altitude restrictions are

tighter than the required +10/-5 km limits, maintaining the argument of perigee will ensure that the radial position requirement is not violated.

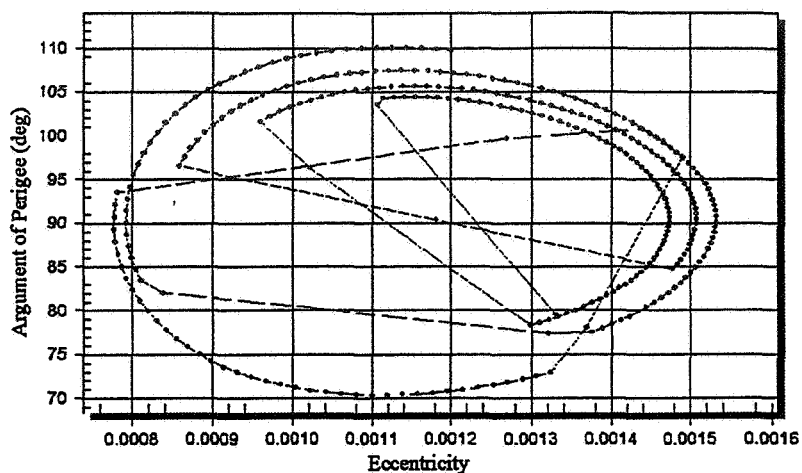


Figure 4: 18-Month Frozen Orbit Evolution

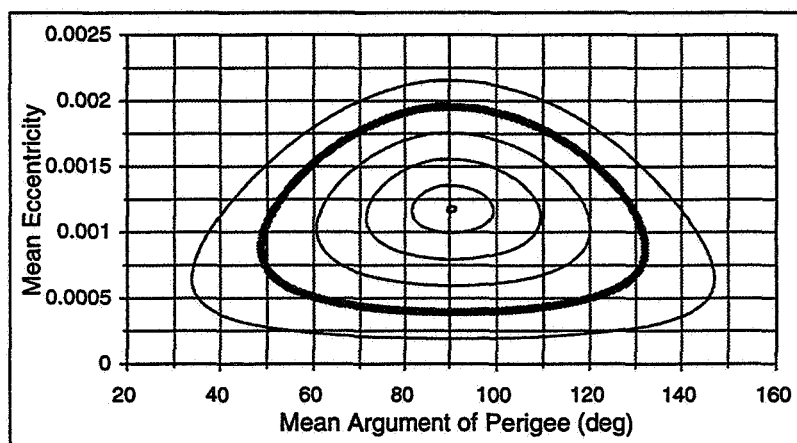


Figure 5: Frozen Orbit Evolution for Eccentricities of 0.0002 Increments Above Nominal

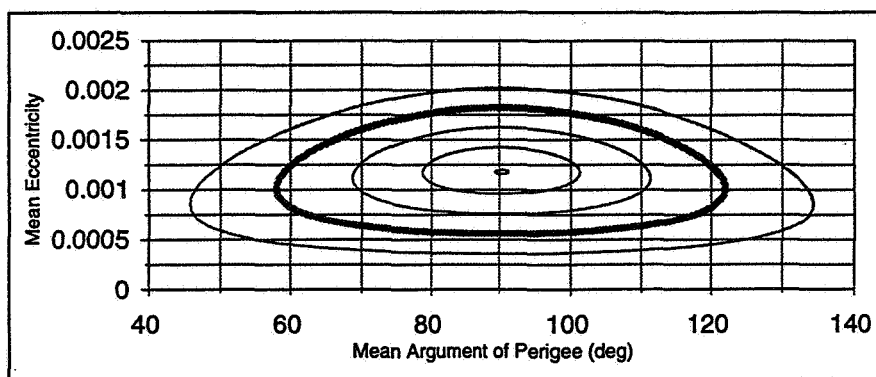


Figure 6: Frozen Orbit Evolution for Eccentricities of 0.0002 Increments Below Nominal

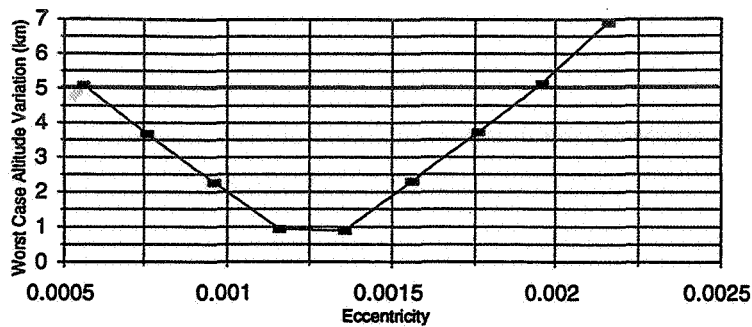


Figure 7: EOS AM-1 Altitude Variation vs. Eccentricity

## ADVANCEMENTS IN OPERATIONS TECHNIQUES

Flying a spacecraft with multiple orbital and operational constraints such as EOS AM-1 traditionally requires experienced personnel to design, plan, and execute maneuver control strategies. Current directions in NASA are driving towards more streamlined, “lights-out” environments in which spacecraft operators are only present during the day shift. This change of approach forces operators to perform a variety of functions more efficiently. The *FreeFlyer*<sup>™</sup> mission design and operations software, a commercial off-the-shelf (COTS) product developed by AI Solutions, Inc. under contract to NASA GSFC, provides the analyst with all the functionality required to design and test various control strategies. More importantly, this same strategy is then easily automated in the operations environment.

There are two factors that must be addressed in the mission design process. The first is examining the orbit mechanics to determine the best way to achieve and maintain an orbit that will meet the science requirements. The second, equally important factor is to address the real-world operational issues that must be included in any maneuver plan. For example, the basic physics behind the ground track control problem is to adjust the orbit period using altitude control. The operational constraints can include ground station viewing requirements and lighting constraints. *FreeFlyer*<sup>™</sup> is designed to include both types of considerations in the design process.

### The Physics - Ground Track Control

As described earlier, the ground track pattern for EOS AM-1 must remain within  $\pm 20$  km of the WRS grid. In order to use the full  $\pm 20$  km ground track control box, the orbit must be raised above the nominal altitude, causing the period to be greater than that of the nominal altitude. In that case, the spacecraft takes longer than nominal to reach the descending node, the Earth turns farther under the orbit plane, and the ground track drifts westward. When the nominal altitude is reached, there is no drift. As the period of the orbit continues to decrease, the spacecraft reaches the descending node earlier each orbit and the ground track error drifts eastward. The drift continues eastward to the edge of the control box. Consequently, periodic altitude raising maneuvers are required prior to reaching the eastern boundary to reset the ground track to the eastern edge of the box. After the maneuver, drag will again act on the orbit and will slow the westward drift rate



until it begins to drift eastward again. This repeated process of the ground track control problem appears as a scalloped-shaped plot as shown in Figure 8, where maneuvers are executed at the peaks and nominal altitude is reached in the troughs.

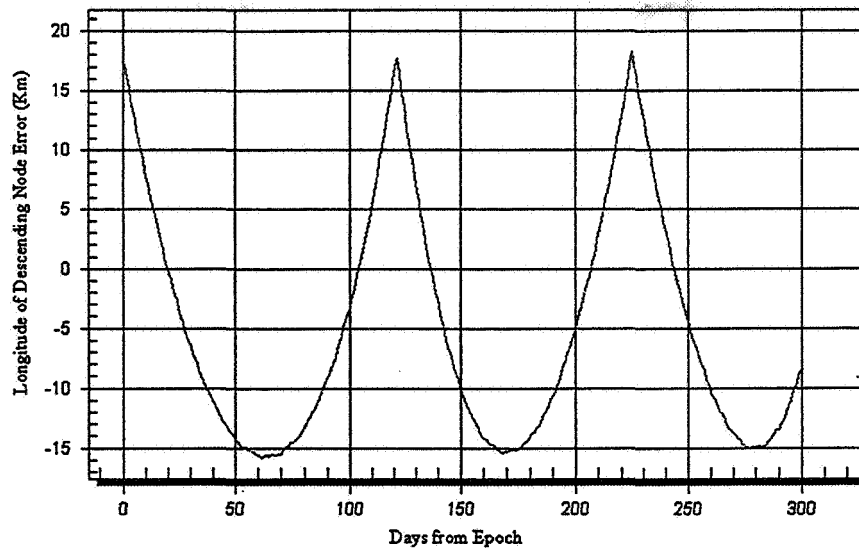


Figure 8: EOS AM-1 Ground Track Control for  $\pm 20$  km Error Box

Since the ground track drift is due largely to atmospheric drag effects and since the EOS AM-1 mission will span periods of both low and high solar flux, the frequency of the maneuvers will vary greatly over the mission lifetime. Also, the magnitude of the maneuvers can vary by factors of up to four between the solar maximum and the solar minimum. This variability has been handled historically by sizing the ground track maneuvers by hand to see what size burn will turn the drift westward while not overshooting the westward boundary. Stated differently, the analyst would test burn sizes until the turnaround point was at an acceptable limit near the western edge. This requires analyst knowledge of acceptable limits, drift rates, and flux predictions.

In *FreeFlyer*<sup>™</sup>, this process has been automated by numerically implementing the same strategy. The burn size is determined using an internal targeting algorithm based on a differential corrector incorporated into *FreeFlyer*<sup>™</sup>. Each iteration is evaluated by checking the longitude error at the turnaround point. This point is numerically defined as the location where the derivative equals zero. Since the longitude error data points contain small oscillations as shown in Figure 5, a running average of the data is first computed to smooth the curve so that a derivative may be calculated accurately.

Figure 9 shows the results of a maneuver targeted with the method described above. In this figure, an initial guess is tested in the curve labeled (1), a perturbation is applied along (2), and then the first iteration (3) is computed, tested, and accepted. This strategy minimizes the analysts' time pre-launch and allows the FOT to perform functions operationally without prior understanding of the problem.

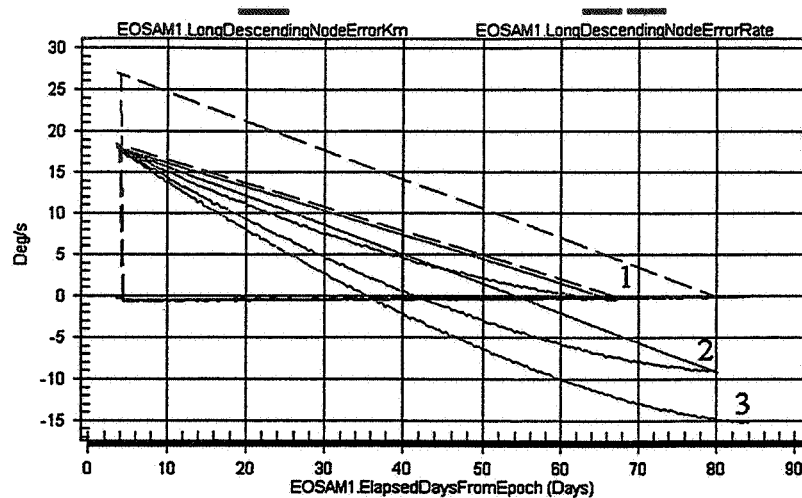


Figure 9: Ground Track Maneuver Targeting

In addition to designing and maintaining the orbit to meet science requirements, the operations environment places restrictions on the orbit design as well. These restrictions are often arbitrary and not related to the mechanics of the design itself.

*FreeFlyer*<sup>™</sup> is designed to automate operations by addressing both the physics and these operational requirements. The control language in the program allows the user to require any number of conditions to be met before performing an action. Therefore the user can state that if the need for a maneuver is detected and the spacecraft is in view of a ground station and the spacecraft is not in shadow, then the software should plan and execute the required maneuver.

However, since a maneuver plan will not always be comprised of true/false conditions, *FreeFlyer*<sup>™</sup> contains a fuzzy logic engine to resolve conflicting constraints or to allow constraint weighting. For example, if a soft boundary is reached, there may be time to wait for an ideal maneuver location. However, if the hard boundary is reached an immediate burn may be required. Some examples of these principles as they are being used for the EOS AM-1 mission are described in the remainder of this section.

### Operational Considerations – Calculable Parameters

A key component to automated maneuver planning is to include operational considerations, such as lighting conditions or maximum thruster on-times. While some constraints are either true or false, others may be approximate constraints. *FreeFlyer*<sup>™</sup> provides a mechanism that allows mission constraints to be defined and evaluated in terms of approximations. For instance, a basic maneuver to raise perigee would not necessarily need to occur exactly at apogee, but rather near apogee to allow other constraints (such as acquiring a ground station) to be satisfied.

*FreeFlyer*<sup>™</sup> contains a mechanism that allows combinations of constraints to be evaluated simultaneously and resolved into acceptable actions, even when these constraints appear to conflict. This mechanism is fuzzy logic. Fuzzy logic has been used

for control systems in cameras, subways, and automobiles to resolve conflicting control goals. *FreeFlyer*<sup>TM</sup> takes this technique and applies it in the orbit control regime.

Perhaps the least glamorous and yet most valuable example of an operational constraint utilizing fuzzy logic is time. With the staffing of the prime operations support shift during normal business hours, the scheduling of maneuver times is a key component of the EOS AM-1 control strategy. For AM-1 the FOT desired to restrict the maneuvers to occur mid-week during the late afternoon, allowing sufficient time to plan and execute the burn in a single shift. In *FreeFlyer*<sup>TM</sup>, the day of the week and time of the day for maneuvers can be added easily into the control logic of the maneuver plan.

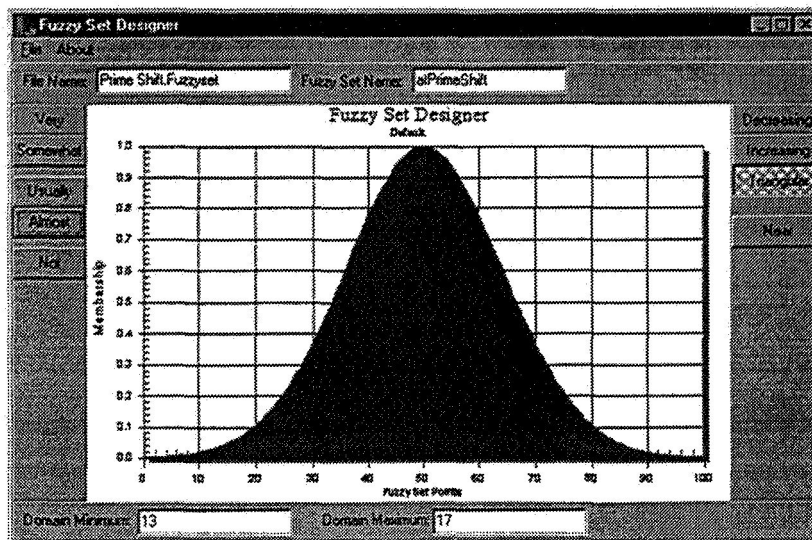


Figure 10: Fuzzy Set Utility in *FreeFlyer*<sup>TM</sup>

A fuzzy set representing the time of day is shown in Figure 10. The set is defined over a domain ranging from 13 to 17, representing the Greenwich Mean Time (GMT) of a day measured in hours. This domain was chosen to correspond to midday local time/EST. The shape of the set is used to weight the importance of the maneuver time in the control logic. Higher values (i.e. higher “degrees of membership” in the fuzzy logic sense) represent more acceptable solutions. This fuzzy set can then be used in *FreeFlyer*<sup>TM</sup> as a component of the decision algorithm configured by the user. More specifically, the user controls the maneuver plan using the following syntax:

```
If (AM1.LongitudeError > 18 and AM1.TimeOfDay is
atPrimeShift) then Maneuver EOSAM1
```

This command line (taken literally from a *FreeFlyer*<sup>TM</sup> control script, with slight modification for clarity) evaluates the error in the EOS AM-1 ground track and the time of day at the operations center for a modeled spacecraft epoch, and plans a maneuver if the error in the ground track is approaching the control boundary at a time of day that is acceptable for maneuver execution.

### Operational Considerations – Non-Calculable Parameters

The time of day, shadow conditions, or ground station coverage are events that can be readily computed in *FreeFlyer*<sup>TM</sup>. EOS AM-1 also requires the interpretation of man-made constraints. The requirement on the ground track control maneuvers is that EOS AM-1 must be in view of one of the TDRS satellites. For long-range planning, the location of the maneuver is tested to determine if the spacecraft is outside the TDRS zone of exclusion. For final maneuver plans, however, this is not sufficient.

A contact schedule for EOS AM-1 is delivered electronically on a weekly basis. This schedule contains the allotted contact opportunities with the TDRS system, a subset of the geometrically possible contacts computed in *FreeFlyer*<sup>TM</sup>. The contacts are approximately 10-minutes in duration and occur approximately twice per orbit. To ensure that the maneuver is planned within these scheduled passes, an ASCII file containing the weekly schedule is read by *FreeFlyer*<sup>TM</sup>, and is converted to fuzzy sets based on the spacecraft epoch. These fuzzy sets are then incorporated into the control script in a manner similar to that discussed above for the time of day constraint. The new control logic takes the form (Ref. 6):

```
Load InTDRSContact from TDRS_Schedule using AM1.Epoch;  
If (AM1.LongitudeError > 15 and AM1.Epoch is atPrimeShift  
and AM1.Epoch is InTDRSContact) then Maneuver EOSAM1
```

The analyst literally sets the control logic using this kind of near-natural language technique. The shapes of the fuzzy sets can easily be modified using extensions to the control language.

The flexibility provided by *FreeFlyer*<sup>TM</sup> for orbit control makes it an extremely powerful tool for mission analysis, planning and operations. The tool addresses needs in the user community that have been identified for a number of years, and moves the satellite control regime much closer to autonomous operations.

## CONCLUSION

EOS AM-1 has been able to realize cost savings in several areas. First, the expert flight dynamics personnel will only be required to support the mission post-launch in a consultation standing. FOT personnel will be able to include the routine flight dynamics activities into their daily schedule with a minimum of impact due to the high level of automation. Maneuvers will be restricted to the nominal work hours of the prime shift. In addition, time spent by the flight dynamics experts in planning special maneuvers, like the ascent sequence, has been drastically reduced by eliminating the need for running multiple pieces of software in parametric runs.

## REFERENCES

1. Folta, David C. and Lauri Kraft, "Methodology for the Passive Control of Orbital Inclination and Mean Local Time to Meet Sun-Synchronous Orbit Requirements",

AAS 92-143, AAS/AIAA Spaceflight Mechanics Meeting, Colorado Springs, CO, 24-26 Feb, 1992.

2. McIntosh, Richard, "EOS AM-1 Target Specification Preliminary Analysis," Computer Sciences Corporation, Feb. 1998.
3. Lockheed Martin, "EOS AM-1 / Atlas IIAS Interface Control Document," LMCA-ICD-95-004, Rev. C, 11 Nov. 1997.
4. Computer Sciences Corporation, CSC56816-02, "EOS AM-1 Ground-Track Control and Frozen Orbit Analysis" (memorandum), P. Noonan, September 9, 1996.
5. AI Solutions, Inc., "EOS AM-1 Mathematical Specifications," D. Conway and C. Schiff, March 31, 1998.
6. AI Solutions, Inc., "EOS AM-1 *FreeFlyer*<sup>TM</sup> Tutorial," Version 1.1, M. Hametz and P. Noonan, January , 1998.



58-18  
169290  
AAS 98-307

## SAC-A Satellite Control Design

21.

Roberto Alonso  
Pablo Anigstein  
Ricardo Sánchez Pena  
(CoNAE)

337542

### ABSTRACT

The SAC-A is a Low Cost – Short Schedule – Small Bus dedicated to test equipment and new technologies which may be used in operational or scientific missions with more immunity to failures. This satellite is planned to be launched in July, 1998 as part of the STS 88 mission.

The opportunity to fly in a low orbit for a reasonable period of time (at least 1 year), allows the characterization of the behavior of this new instrumentation in real world applications and also to compute performance.

The 68 kg satellite will have an almost octagonal configuration to be fitted within the Hitchhiker Motorized Door Canister with Hitchhiker Ejection System (HES) envelope. This volume is approximately a cylinder of 19 inches diameter by 20.5 inches maximum height.

The orbit will be circular @ 200 nm altitude with an inclination of 51.6 deg, the expected lifetime is about one year.

The experiments on board are:

- Differential Global Positioning System Receiver (DGPS)
- CCD Camera
- Tri Axial Magnetometer (TAM)
- Argentinian Si Cells
- UHF Receiver/VHF Transmitter.

From the mission design point of view, the on board power consumption plays a central role for the attitude strategy design: to supply the essential loads at least three solar arrays should be pointed most of the time to the sun. In addition, the DGPS receiver and the CCD camera should be pointed to the zenith-nadir direction. The other experiments do not impose any attitude constraints on the mission.

To fulfill all of the requirements several control modes are implemented. The paper explains in details the strategy adopted.

The sensors to accomplish the mission are:

**Six coarse sun sensors.** Six Argentinian Cells, placed on the satellite to cover the total sphere, although the configuration has some blind holes behind the solar panels.

**Tri-axial magnetometer.** It is the same fluxgate magnetometer used for the experiment, but the readings are taken only with 10 bits.

The actuators are:

**Momentum Wheel.** An in house made momentum wheel, located along the direction perpendicular to the sun line.

**Magnetic Torque Coils.** Three circular air core coils, one on each axis.

There are four identified operational modes along the lifetime of the satellite, listed below.

**Sun Pointing Mode.** The solar arrays are placed toward the sun to maximize the power generation. In this mode the whale tracker and the Argentinian Si Cells are tested. During eclipse, the sun signal is not available and the ACS enters in to eclipse submode.

**Picture Mode.** This mode allows to place the momentum bias normal to the nadir and sun vector to take Earth pictures, after a rotation around the wheel axis. The CCD camera is tested with this mode.

**DGPS Control Mode.** This mode allows to rotate the body Y axis around the sun line in order to point the antenna's boresight vector as close as possible to the zenith axis, required by the DGPS receiver to lock on the DGPS satellites. The DGPS and the triaxial magnetometer (because a very precise time and orbital position is needed to correlate the Earth magnetic field) are tested during this mode.

**Spinning Mode.** The satellite is spun along the momentum bias to check the DGPS performance in spinning satellites.

The Safe Hold Mode (with momentum wheel ON) is in effect the Sun Pointing Mode (from the power consumption and thermal equilibrium point of view). In case of momentum wheel failure, the satellite will enter in a "safe" spin mode along the sun line to preserve the necessary power generation.

The on board software has the capability to compute ephemeris, the magnetic field and sun vectors in inertial frame using theoretical models, attitude determination in real time and also detects failures which change the mode to Safe Hold. The software design is flexible enough to allow changes or patches on variables and modify areas of memory.

The proposed configuration is better than other possibilities considered in terms of safety and stability, because the precession of the momentum bias for Earth observation or to take pictures or to acquire the DGPS satellite is around the sun.



337543  
141. 59-18  
169291

# NEW METHODS IN ON-BOARD ATTITUDE CONTROL

Karlheinz Spindler<sup>†</sup>

In this paper we will derive control laws to perform attitude maneuvers which automatically avoid the pointing of a specified spacecraft axis into forbidden directions. These laws will be found by a control-theoretical approach using methods from differential geometry.

We will start by deriving a particularly simple control law maneuvering a spacecraft from rest to rest between prescribed attitudes in the absence of pointing constraints. Subsequently, we will show how maneuvers of this type can be concatenated in such a way that prescribed forbidden directions are guaranteed to be avoided. The control law obtained in this way does not take recourse to numerical methods and hence can be easily implemented in an on-board attitude control system, possibly for performing maneuvers in an emergency mode. Finally, we will propose an iterative scheme to optimize the solution.

## INTRODUCTION

The *attitude* or *orientation* of a spacecraft (modelled as a rigid body) is the matrix  $g \in \text{SO}(3)$  whose rows are the directions of the body's principal axes with respect to some reference coordinate system. Let us denote by  $I_1, I_2, I_3$  the moments of inertia, by  $\omega_1, \omega_2, \omega_3$  the angular velocities and by  $T_1, T_2, T_3$  the exerted torques about the principal axes. Then the attitude kinematics of the spacecraft are described by the equation

$$\dot{g}(t) = (\omega_1(t)E_1 + \omega_2(t)E_2 + \omega_3(t)E_3)g(t) \quad (1)$$

where

$$E_1 = \begin{bmatrix} 0 & 0 & 0 \\ 0 & 0 & 1 \\ 0 & -1 & 0 \end{bmatrix}, \quad E_2 = \begin{bmatrix} 0 & 0 & -1 \\ 0 & 0 & 0 \\ 1 & 0 & 0 \end{bmatrix}, \quad E_3 = \begin{bmatrix} 0 & 1 & 0 \\ -1 & 0 & 0 \\ 0 & 0 & 0 \end{bmatrix} \quad (2)$$

---

<sup>†</sup>Fachhochschule Wiesbaden, Fachbereich Mathematik, Naturwissenschaften, Datenverarbeitung und Umwelttechnik, Kurt-Schumacher-Ring 18, D - 65197 Wiesbaden, Germany. Phone: (49) 611-9495-377. FAX: (49) 611-9495-382. Electronic mail: spindler@r5.mnd.fh-wiesbaden.de.

whereas the dynamics are governed by Euler's equations

$$\begin{aligned} I_1 \dot{\omega}_1(t) &= (I_2 - I_3) \omega_2(t) \omega_3(t) + T_1(t), \\ I_2 \dot{\omega}_2(t) &= (I_3 - I_1) \omega_3(t) \omega_1(t) + T_2(t), \\ I_3 \dot{\omega}_3(t) &= (I_1 - I_2) \omega_1(t) \omega_2(t) + T_3(t). \end{aligned} \tag{3}$$

In this paper, we will study the problem of steering a spacecraft between given attitudes  $g(t_0) = g_0$  and  $g(t_1) = g_1$  while minimizing a cost functional which both measures the overall angular velocity and penalizes undesired attitudes during the maneuver. By choosing this cost functional judiciously, we will ensure that the angular velocities at the beginning and at the end of the maneuver take prescribed values and also that forbidden pointing directions are avoided during the maneuver.

## MATHEMATICAL BACKGROUND

Our approach is based on the observation that equation (1) can be considered as a control problem on the Lie group  $SO(3)$  (with the angular velocities  $\omega_i$  treated as control inputs). This observation will enable us to use differential geometric techniques in control theory<sup>1,2</sup>. The characteristic features of the situation are captured in the following problem formulation.

**Basic Control Problem.** *Let  $G$  be a Lie group with Lie algebra  $\mathfrak{g}$  and let  $(E_1, \dots, E_n)$  be a vector space basis of  $\mathfrak{g}$ . Consider a right-invariant dynamical system  $\dot{g}(t) = U(t)g(t)$  evolving on  $G$  where  $U(t)$  is the sum of a controlled term  $\sum_{i=1}^m u_i(t)E_i$  and a drift term  $\sum_{i=m+1}^n u_i E_i$  with given constants  $u_{m+1}, \dots, u_n$ . We will be interested in finding controls  $t \mapsto u_i(t)$  (where  $1 \leq i \leq m$ ) steering the system from  $g(t_0) = g_0$  to  $g(t_1) = g_1$ .*

To find suitable control laws which solve this motion planning problem, we propose to introduce a minimization condition which the controls are required to satisfy. This condition should be “reasonable”, but is not at all unique. The idea is not so much that the minimization of a specific cost functional is a strict requirement, but rather that introducing such a cost functional makes available methods from optimal control theory (specifically, Pontryagin’s Principle) as tools to find solutions to our problem. We first consider the special case that the cost functional does not explicitly depend on time.

**Theorem 1.** *In the control problem described above, let the controls  $u_i^*$  be chosen in such a way that a cost functional  $\int_{t_0}^{t_1} \Phi(g(t), u(t)) dt$  is minimized. Let  $t \mapsto g^*(t)$  be the resulting state trajectory in  $G$  so that  $\dot{g}^*(t) = U^*(t)g^*(t)$ . Then there exist a curve  $t \mapsto p^*(t)$  in  $\mathfrak{g}^* \setminus \{0\}$  and a number  $\varepsilon \in \mathbb{R}$  such that*

$$\dot{p}^*(t) = -\varepsilon \frac{\partial \Phi}{\partial g}(g^*(t), u^*(t)) - p^*(t) \circ \text{ad}(U^*(t)), \quad (4)$$

$$p^*(t)E_i = -\varepsilon \frac{\partial \Phi}{\partial u_i}(g^*(t), u^*(t)) \quad (1 \leq i \leq m). \quad (5)$$

If  $m = n$  (i.e., if the system is fully actuated) then necessarily  $\varepsilon \neq 0$  (absence of abnormal minimizers).

**Proof.** The Hamiltonian  $H : G \times \mathfrak{g}^* \times \mathbb{R}^n \rightarrow \mathbb{R}$  of the system is  $H(g, p; u) := \varepsilon \Phi(g, u) + \sum_{i=1}^n u_i p(E_i)$  where  $\varepsilon$  is either zero or an arbitrary nonzero number. Pontryagin's Principle shows that there is a curve  $t \mapsto p^*(t)$  in  $\mathfrak{g}^* \setminus \{0\}$  with

$$\begin{aligned} \dot{g}^*(t) &= \frac{\partial H}{\partial p}(g^*(t), p^*(t); u^*(t)) = U^*(t)g^*(t), \\ \dot{p}^*(t) &= -\frac{\partial H}{\partial g}(g^*(t), p^*(t); u^*(t)) - p^*(t) \circ \text{ad}(U^*(t)), \\ \frac{\partial H}{\partial u_i}(g^*(t), p^*(t); u^*(t)) &= 0 \quad (1 \leq i \leq m) \end{aligned}$$

for almost all  $t \in [t_0, t_1]$ . This establishes equations (4) and (5). If  $m = n$  then  $\varepsilon = 0$  would imply  $p^*(t) = 0$  (for almost all  $t$ ) according to equation (5), contradicting the choice of  $p^*$ . Hence  $\varepsilon \neq 0$  in this case. ■

We now consider a cost functional depending explicitly on time. The associated optimal control problem will be reformulated as one with a time-invariant cost functional by formally introducing time as an additional state variable. This reformulated control problem will automatically contain a drift term (even if the original control problem does not); hence the full generality of Theorem 1 is needed in obtaining our result.

**Theorem 2.** *In the control problem described above, let the controls  $u_i^*$  be chosen in such a way that a cost functional  $\int_{t_0}^{t_1} \Phi(g(t), u(t), t) dt$  is minimized. Let  $t \mapsto g^*(t)$  be the resulting state trajectory in  $G$  so that  $\dot{g}^*(t) = U^*(t)g^*(t)$ . Moreover, let  $\mathfrak{P}_1 : \mathfrak{g} \times \mathbb{R} \rightarrow \mathfrak{g}$  and  $\mathfrak{P}_0 : \mathfrak{g} \times \mathbb{R} \rightarrow \mathbb{R}$  be the canonical projections of the direct product  $\mathfrak{g} \times \mathbb{R}$ . Then there exist a curve  $t \mapsto \pi^*(t)$  in  $(\mathfrak{g} \times \mathbb{R})^* \setminus \{(0, 0)\}$  and a number  $\varepsilon \in \mathbb{R}$  such that*

$$\dot{\pi}^*(t) = -\varepsilon \frac{\partial \Phi}{\partial g}(g^*(t), u^*(t), t) \circ \mathfrak{P}_1 - \varepsilon \frac{\partial \Phi}{\partial t}(g^*(t), u^*(t), t) \circ \mathfrak{P}_0 - \pi^*(t) \circ \text{ad}(\overline{U}^*(t)), \quad (6)$$

$$\pi^*(t)\overline{E}_i = -\varepsilon \frac{\partial \Phi}{\partial u_i}(g^*(t), u^*(t), t) \quad (1 \leq i \leq m). \quad (7)$$

If  $m = n$  then  $\varepsilon$  can be chosen to be nonzero.

**Proof.** Let  $\theta(t) := e^t$ ; then any trajectory of the system  $\dot{g} = Ug$  determines a curve  $\gamma(t) := (g(t), \theta(t))$  in the direct product  $\Gamma := G \times \mathbb{R}^+$  which satisfies  $\dot{\gamma} = (\sum_{i=1}^n u_i \overline{E}_i + \overline{E}_0)\gamma$  where  $\overline{E}_0 := (0, 1)$ . Moreover, if  $P_1 : G \times \mathbb{R}^+ \rightarrow G$  and  $P_2 : G \times \mathbb{R}^+ \rightarrow \mathbb{R}^+$  denote the canonical projections, the cost functional can be written as  $\int_{t_0}^{t_1} \overline{\Phi}(\gamma(t), u(t)) dt$  where

$$\overline{\Phi}(\gamma, u) := \Phi(P_1(\gamma), u, \log(P_2(\gamma)))$$

does not explicitly depend on time any more. The claim then follows immediately by applying Theorem 1 to the control problem on  $\Gamma$  of steering  $\gamma$  from  $(g_0, e^{t_0})$  to  $(g_1, e^{t_1})$  while minimizing  $\int_{t_0}^{t_1} \overline{\Phi}(\gamma(t), u(t)) dt$ .

If  $m = n$  we can choose  $\varepsilon \neq 0$ . Otherwise an optimal control would be necessarily independent of the cost functional, which implies that we could replace the time-dependent cost functional by a time-invariant one. But for a time-invariant cost functional the absence of abnormal minimizers was established in Theorem 1 already. ■

## ATTITUDE MANEUVERS

We will now apply the above results to attitude control. To keep things simple, let us consider the case that a spacecraft shall be steered from rest to rest between prescribed attitudes. (The method to be presented can, with a little extra effort, also be applied to maneuvers between arbitrarily prescribed rotational states.) Moreover, let us assume that certain state constraints have to be taken into account (such as the need to avoid the pointing of specified spacecraft axes into forbidden directions or the requirement to stay close to a desirable reference trajectory). We will formally treat the angular velocities as control inputs and try to plan a maneuver which is “as smooth as possible” in the sense that a cost functional measuring the overall angular velocity during the maneuver is minimized. To deal with the state constraints we introduce a term in the cost functional which penalizes undesirable attitudes during the maneuver. (This is reminiscent of a Lyapunov approach using artificial potential functions with peaks about undesired attitudes.<sup>3</sup>) Moreover, in order to guarantee that a rest-to-rest maneuver is being planned, we impose infinite penalties on nonzero angular velocities at the beginning and at the end of the maneuver. Thus we are led to the optimal control problem of determining the angular velocities  $t \mapsto \omega_i^*(t)$  which steer the spacecraft between the prescribed attitudes while minimizing a cost functional of the form

$$\int_{t_0}^{t_1} \left( \frac{q(t)}{2} \sum_{i=1}^3 \omega_i(t)^2 + F(g(t), t) \right) dt \quad (8)$$

where  $F$  is chosen according to the nature of the constraints to be considered and where  $q$  is a positive weighting function with singularities at the start time  $t_0$  and at the end time  $t_1$ . (A typical choice for  $q$  is depicted in Figure 1 below.)

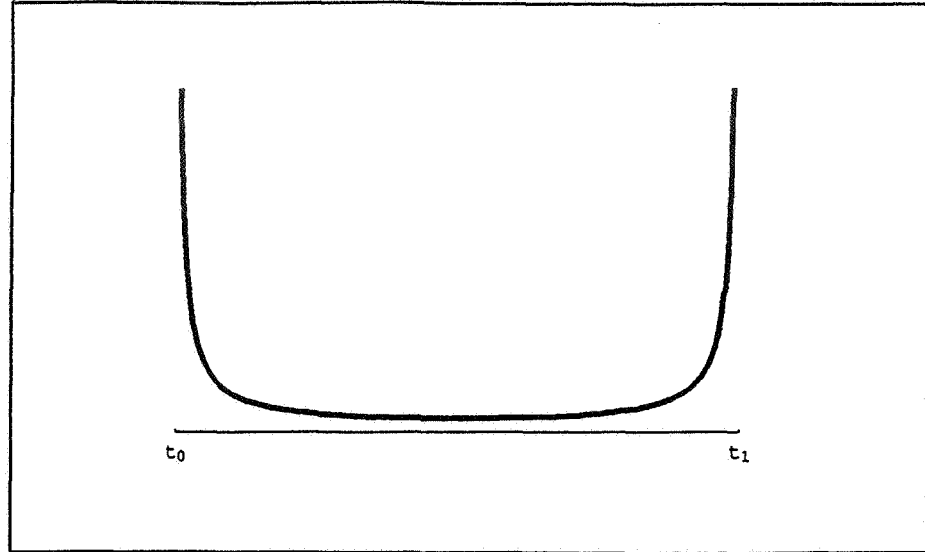


**Figure 1:** Typical choice for the weighting function  $q$ .

We will now apply Theorem 2 to solve this optimal control problem. Once this is done, the torques required to implement the desired maneuver are found by simply plugging the angular velocities  $t \mapsto \omega_i^*(t)$  into Euler's equations (3).

**Theorem 3.** *Consider the problem of steering a three-axis controlled spacecraft between two specified attitudes  $g(t_0) = g_0$  and  $g(t_1) = g_1$  such that the cost functional (8) is minimized. Denote the optimal angular velocities by  $t \mapsto \omega_i^*(t)$  and let  $t \mapsto g^*(t)$  be the resulting attitude evolution. Then the functions  $\Omega_i(t) := q(t)\omega_i^*(t)$  satisfy the differential equations*

$$\begin{aligned}\dot{\Omega}_1(t) &= (\partial F / \partial g)(g^*(t), t)[E_1] =: \Phi_1(g^*(t), t), \\ \dot{\Omega}_2(t) &= (\partial F / \partial g)(g^*(t), t)[E_2] =: \Phi_2(g^*(t), t), \\ \dot{\Omega}_3(t) &= (\partial F / \partial g)(g^*(t), t)[E_3] =: \Phi_3(g^*(t), t).\end{aligned}\tag{9}$$

**Proof.** Applying Theorem 2 with  $\varepsilon := -1$ , we obtain a curve  $t \mapsto \pi^*(t)$  in  $(\mathfrak{so}(3) \times \mathbb{R})^* \setminus \{(0, 0)\}$  such that for  $1 \leq i \leq 3$  we have  $\pi^*(t)\overline{E}_i = \Omega_i(t)$  on the one hand and

$$\dot{\pi}^*(t)\overline{E}_i = \frac{\partial F}{\partial g}(g^*(t), t)[E_i] - \underbrace{\pi^*(t)(\omega_1^*(t)[\overline{E}_1, \overline{E}_i] + \omega_2^*(t)[\overline{E}_2, \overline{E}_i] + \omega_3^*(t)[\overline{E}_3, \overline{E}_i])}_{=0}$$

on the other hand; here the last term vanishes because of the bracket relations

$$[E_1, E_2] = -E_3, \quad [E_2, E_3] = -E_1, \quad [E_3, E_1] = -E_2.$$

This yields the claim. ■

Combining the scalar functions  $\Omega_i$  and  $\Phi_i$  to vector-valued functions  $\Omega$  and  $\Phi$ , respectively, and writing

$$L(w) := w_1 E_1 + w_2 E_2 + w_3 E_3 = \begin{bmatrix} 0 & w_3 & -w_2 \\ -w_3 & 0 & w_1 \\ w_2 & -w_1 & 0 \end{bmatrix} \quad (10)$$

for all  $w \in \mathbb{R}^3$ , we can succinctly formulate our result by stating that if the angular velocities  $t \mapsto \omega_i^*(t)$  are optimally chosen with respect to the cost functional (8) and if  $t \mapsto g^*(t)$  is the corresponding attitude evolution, then the functions  $t \mapsto g^*(t)$  and  $t \mapsto \Omega^*(t)$  are solutions of the following system of coupled differential equations:

$$\begin{aligned} \dot{g}(t) &= q(t)^{-1} L(\Omega(t)) g(t), \\ \dot{\Omega}(t) &= \Phi(g(t), t). \end{aligned} \quad (11)$$

## BOUNDARY CONDITIONS

In addition to the differential equation (11), the two boundary conditions  $g(t_0) = g_0$  and  $g(t_1) = g_1$  have to be satisfied. This is accomplished by following a shooting procedure which we now describe. For  $s \in \mathbb{R}^3$  let  $t \mapsto (g_s(t), \Omega_s(t))$  be the unique solution of the initial value problem

$$\begin{aligned} \dot{g}(t) &= q(t)^{-1} L(\Omega(t)) g(t), & g(t_0) &= g_0, \\ \dot{\Omega}(t) &= \Phi(g(t), t), & \Omega(t_0) &= s. \end{aligned} \quad (12)$$

We want to adjust  $s$  in such a way that  $g_s(t_1) = g_1$ . To do so, we have to investigate how the functions  $t \mapsto (g_s(t), \Omega_s(t))$  vary in dependence of the parameter  $s$ . Therefore, we introduce the functions

$$\alpha_i(t, s) := \frac{\partial}{\partial s_i} g_s(t) \quad \text{and} \quad \beta_i(t, s) := \frac{\partial}{\partial s_i} \Omega_s(t) \quad (13)$$

for which we will now derive differential equations. First,

$$\begin{aligned} \dot{\alpha}_i(t, s) &= (\partial/\partial s_i) \dot{g}_s(t) = (\partial/\partial s_i) q(t)^{-1} L(\Omega_s(t)) g_s(t) \\ &= q(t)^{-1} L(\beta_i(t, s)) g_s(t) + q(t)^{-1} L(\Omega_s(t)) \alpha_i(t, s). \end{aligned} \quad (14)$$

Second,

$$\begin{aligned} \dot{\beta}_i(t, s) &= (\partial/\partial s_i) \dot{\Omega}_s(t) = (\partial/\partial s_i) \Phi(g_s(t), t) \\ &= (\partial\Phi/\partial g)(g_s(t), t) [\alpha_i(t, s) g_s(t)^{-1}]. \end{aligned} \quad (15)$$

These differential equations are accompanied by the obvious initial conditions

$$\begin{aligned} \alpha_i(t_0, s) &= (\partial/\partial s_i) g_s(t_0) = (\partial/\partial s_i) g_0 = 0, \\ \beta_i(t_0, s) &= (\partial/\partial s_i) \Omega_s(t_0) = (\partial/\partial s_i) s = e_i. \end{aligned} \quad (16)$$

From (1) and (14) we see that the functions  $A_i(t) := \alpha_i(t, s) + g_s(t)\alpha_i(t, s)^T g_s(t)$  satisfy the differential equations  $\dot{A}_i(t) = q(t)^{-1} L(\Omega_s(t)) A_i(t)$  and thus, in view of the initial condition  $A_i(t_0) = 0$ , vanish identically; hence

$$g_s(t)\alpha_i(t, s)^T = -\alpha_i(t, s)g_s(t)^T. \quad (17)$$

This last equation is, in fact, trivial because it simply expresses the fact that  $\alpha_i(t, s)g_s(t)^{-1}$  is an element of  $\mathfrak{so}(3)$ , which is clear from the very definition of  $\alpha_i$ . The evaluation of the right-hand side of (15) is simplified by noting that (17) can be rewritten in the form

$$g_s(t)^T \alpha_i(t, s) g_s(t)^{-1} = -\alpha_i(t, s)^T. \quad (18)$$

The desired value of  $s$  is such that  $g_s(t_1) = g_1$ . The strategy is to first find a reasonable initial guess  $s^{(0)}$  and then apply a Newton-type algorithm to produce improved values  $s^{(1)}, s^{(2)}, \dots$  until the condition  $g_s(t_1) = g_1$  is satisfied within the desired accuracy. Inserting the approximation

$$g_{s+\Delta s}(t_1) \approx g_s(t_1) + \sum_{i=1}^3 (\Delta s_i) \alpha_i(t_1, s) \quad (19)$$

into the target equation  $g_{s+\Delta s}(t_1) = g_1$ , we see that the update equation in the Newton-type iteration is given by

$$\sum_{i=1}^3 (\Delta s_i) \alpha_i(t_1, s) = g_1 - g_s(t_1). \quad (20)$$

In the next paragraph we will show how to find a reasonable initial estimate  $s^{(0)}$ . This paragraph is interesting in its own right, because it yields a very simple algorithm to perform a rest-to-rest maneuver between prescribed attitudes in the absence of state constraints.

## CONSTRAINT-FREE MANEUVERS

Let us for a moment ignore the presence of state constraints. Then we can choose  $F \equiv 0$  in the cost functional, and the equations (9) simply state that the functions  $\Omega_i$  remain constant during the maneuver. The contents of the following theorem is that the constants can be explicitly written down as functions of the initial attitude  $g_0$  and the target attitude  $g_1$ .

**Theorem 4.** *Suppose we want to steer the spacecraft from the attitude  $g(t_0) = g_0$  to the attitude  $g(t_1) = g_1$  while minimizing the functional*

$$\int_{t_0}^{t_1} q(t) (\omega_1(t)^2 + \omega_2(t)^2 + \omega_3(t)^2) dt. \quad (21)$$

Let  $\gamma := g_1 g_0^{-1}$  and  $\alpha := \arccos((\text{tr}[\gamma] - 1)/2)$  and let  $Q$  be an antiderivative of  $1/q$ . Define constants  $c_i^*$  as follows:

$$\begin{bmatrix} c_1^* \\ c_2^* \\ c_3^* \end{bmatrix} = \frac{\alpha}{2 \sin \alpha (Q(t_1) - Q(t_0))} \begin{bmatrix} \gamma_{23} - \gamma_{32} \\ \gamma_{31} - \gamma_{13} \\ \gamma_{12} - \gamma_{21} \end{bmatrix}. \quad (22)$$

Then the optimal controls are given by  $\omega_i^*(t) = c_i^*/q(t)$  for  $1 \leq i \leq 3$ , and the torques which lead to these angular velocities are given by

$$\begin{bmatrix} T_1(t) \\ T_2(t) \\ T_3(t) \end{bmatrix} = \frac{-1}{q(t)^2} \begin{bmatrix} I_1 c_1^* \dot{q}(t) + (I_2 - I_3) c_2^* c_3^* \\ I_2 c_2^* \dot{q}(t) + (I_3 - I_1) c_1^* c_3^* \\ I_3 c_3^* \dot{q}(t) + (I_1 - I_2) c_1^* c_2^* \end{bmatrix}. \quad (23)$$

The maneuver is such that any body-fixed axis  $b \in \mathbb{R}^3$  rotates about the axis  $\mathbb{R}a$  where

$$L(a) = g_0^T g_1 - g_1^T g_0. \quad (24)$$

**Proof.** From (9) we know that the functions  $\Omega_i = q\omega_i^*$  are constants, say  $\omega_i^*(t) = c_i/q(t)$ . Let  $C := c_1 E_1 + c_2 E_2 + c_3 E_3$ ; then the optimal trajectory  $t \mapsto g^*(t)$  in  $\text{SO}(3)$  satisfies  $\dot{g}^*(t) = q(t)^{-1} C g^*(t)$ . This equation can be explicitly integrated. In fact,  $Q$  being an antiderivative of  $1/q$ , we have

$$g^*(t) = \exp\left((Q(t) - Q(t_0))C\right) g_0. \quad (25)$$

The constants  $c_i$  must be such that  $g(t_1) = g_1$  which means that  $\exp([Q(t_1) - Q(t_0)]C) = g_1 g_0^{-1} = \gamma$ . Rodrigues' formula then shows that  $c_i = c_i^*$  for  $1 \leq i \leq 3$ . (Note that the equation  $\cos \alpha = (\text{tr}[\gamma] - 1)/2$  does not determine  $\alpha$  uniquely. However, since our optimization criterion requires  $c_1^2 + c_2^2 + c_3^2$  and hence  $\alpha$  to be as small as possible, we really have  $\alpha = \arccos((\text{tr}[\gamma] - 1)/2)$ ; whence the claim.) The torques  $T_i$  are then obtained by plugging in  $\omega = \omega_i^*$  in Euler's equations (3).

If  $b \in \mathbb{R}^3$  is a body-fixed direction (i.e., if  $b_1, b_2, b_3$  are the body-coordinates of a unit vector rigidly attached to the spacecraft) then the motion of this axis in space between  $u := g_0^T b$  and  $v := g_1^T b$  is given by

$$\begin{aligned} g^*(t)^T b &= g_0^T \exp(-(Q(t) - Q(t_0)) L(c^*)) b \\ &= g_0^T \exp(-(Q(t) - Q(t_0)) L(c^*)) g_0 g_0^T b \\ &= \exp(-(Q(t) - Q(t_0)) g_0^T L(c^*) g_0) g_0^T b \\ &= \exp(-(Q(t) - Q(t_0)) L(g_0^T c^*)) u \end{aligned} \quad (26)$$

where we used the fact that  $C = L(c^*)$ . This shows that the body-axis rotates about the axis spanned by  $\hat{a} := g_0^T c^*$ . Note that if  $\lambda := 2(Q(t_1) - Q(t_0))(\sin \alpha)/\alpha > 0$  and if  $a := \lambda \hat{a}$  then

$$\begin{aligned} L(a) &= \lambda \cdot L(g_0^T c^*) = \lambda \cdot g_0^T L(c^*) g_0 = g_0^T (\gamma - \gamma^T) g_0 \\ &= g_0^T (g_1 g_0^T - g_0 g_1^T) g_0 = g_0^T g_1 - g_1^T g_0. \end{aligned} \quad (27)$$

■



## CONSTRAINED MANEUVERS

We now consider the case that certain forbidden directions have to be avoided during the maneuver. More precisely, we assume that a number of spacecraft axes (expressed in terms of unit vectors  $b_j \in \mathbb{R}^3$  with respect to the body-fixed principal axes system) and a number of pointing directions (expressed in terms of vector-valued functions  $t \mapsto d_j(t) \in \mathbb{R}^3$  with respect to the inertial reference system) are specified in such a way that the  $j$ -th spacecraft axis is forbidden to coincide with the  $j$ -th pointing direction at any time; in fact, the angle between these two axes may be required to exceed a minimum angle  $\varphi_{\text{safe}}$ . Now it is easy to verify whether or not a maneuver as in Theorem 3 meets this requirement. In fact, as was shown before, each body-axis  $b_j$  rotates about an axis  $\mathbb{R}a$  (uniquely determined by the initial attitude and the target attitude) as shown in Figure 2, and the closest possible angle between the rotating axis and a fixed space direction  $d_j$  is given by  $|\theta_j - \delta_j|$  where  $\theta_j := \angle(u_j, a) = \angle(v_j, a)$  and  $\delta_j := \angle(a, d_j)$  (see Figure 3); hence the maneuver given in Theorem 2 is safe if  $|\theta_j - \delta_j| > \varphi_{\text{safe}}$  for all  $j$ .

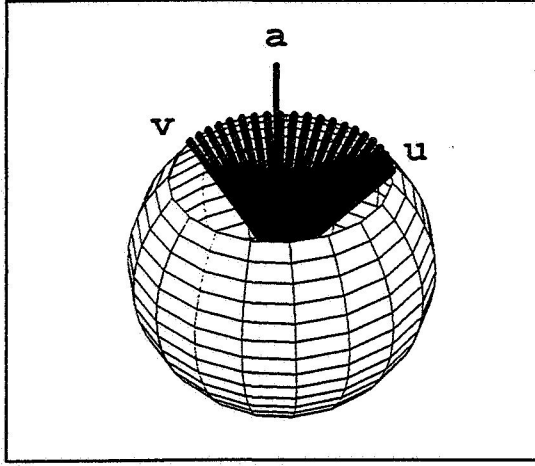


Figure 2: Motion of a body-axis during the maneuver.

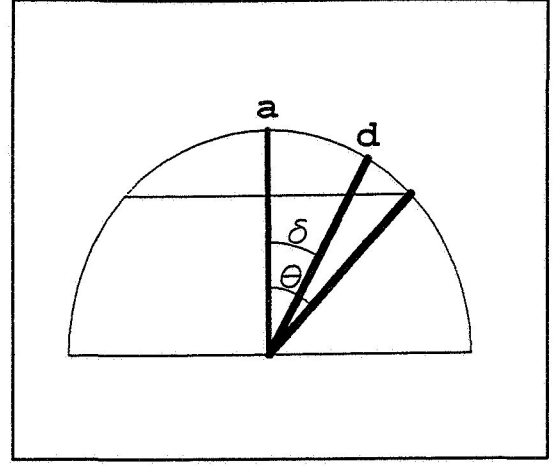


Figure 3: Checking the pointing constraints.

If the maneuver is not safe, then we can simply concatenate several maneuvers of the same type each of which avoids the forbidden directions. We will explicitly do so in the case that there is one axis for which there are two forbidden directions, having in mind a cryogenically cooled space telescope for which the telescope direction is forbidden to coincide with either the sun or the moon direction. If the circle  $C$  along which a maneuver as in Theorem 4 would carry the telescope axis is found to be not safe due to one of the forbidden directions, say  $d_1$ , then the other forbidden direction  $d_2$  can make only one of the two regions bounded by  $C$  unsafe, but not both; hence (after replacing  $a$  by  $-a$  if necessary) we can assume that the region containing  $a$  is safe for operations. (This is the case if  $\langle d_2, a \rangle < 0$ .) The idea is now to slew the telescope axis from its initial position  $u$  to the axis direction  $a$  and from there to the target direction  $v$ . The next theorem shows how to find a safe intermediate attitude  $g_i$ .

**Theorem 5.** Suppose we want to steer the spacecraft from the initial attitude  $g_0$  to the target attitude  $g_1$ . Let  $u := g_0^T b$  and  $v := g_1^T b$  be the initial and the target direction of the telescope axis  $b$  in space. Let  $a \in \mathbb{R}^3$  be such that  $L(a) = g_0^T g_1 - g_1^T g_0$ . (This is the rotation axis for the maneuver as in Theorem 4.) Let  $A$  be the matrix with columns  $a$ ,  $u$  and  $a \times u$  and let  $B$  be the matrix with columns  $b$ ,  $2\langle u, a \rangle b - g_0 a$  and  $g_0(a \times u)$ , respectively. Then  $g_i := BA^{-1}$  is a safe intermediate attitude; i.e., performing two maneuvers as in Theorem 4 (first from  $g_0$  to  $g_i$ , then from  $g_i$  to  $g_1$ ) avoids the forbidden directions.

**Proof.** The idea is to slew the telescope from  $u = g_0^T b$  to  $a$  (which requires  $a = g_i^T b$ , i.e.,  $g_i a = b$ ) along the great-circle through  $u$  and  $a$  (which requires  $c \cdot L(u \times a) = g_0^T g_i - g_i^T g_0$  with a constant  $c \neq 0$ ). Then necessarily

$$\begin{aligned} g_i u &= g_0(g_0^T g_i - g_i^T g_0)u + g_0 g_i^T g_0 u = c \cdot g_0 L(u \times a)u + g_0 a \\ &= c \cdot g_0 (\langle u, a \rangle u - a) + g_0 a = (1 - c) \cdot g_0 a + c \cdot \langle u, a \rangle b \end{aligned}$$

and hence

$$\begin{aligned} 1 &= \|g_i u\|^2 = (1 - c)^2 + 2c(1 - c) \langle u, a \rangle \langle g_0 a, b \rangle + c^2 \langle u, a \rangle^2 \\ &= (1 - c)^2 + \langle u, a \rangle^2 (2c - c^2) = 1 + c(c - 2) \|u \times a\|^2 \end{aligned}$$

which implies  $c = 2$ . Consequently,  $g_i u = 2\langle u, a \rangle b - g_0 a$ . Since  $g_i \in \text{SO}(3)$  we then have

$$\begin{aligned} g_i(a \times u) &= g_i a \times g_i u = b \times (2\langle u, a \rangle b - g_0 a) \\ &= b \times (-g_0 a) = g_0 a \times b = g_0 a \times g_0 u = g_0(a \times u). \end{aligned}$$

Hence  $g_i$  necessarily maps  $a$  to  $b$ ,  $u$  to  $2\langle u, a \rangle b - g_0 a$  and  $a \times u$  to  $g_0(a \times u)$ ; this determines  $g_i$  uniquely. Since  $A$  maps  $e_1$  to  $b$ ,  $e_2$  to  $u$  and  $e_3$  to  $a \times u$  and since  $B$  maps  $e_1$  to  $b$ ,  $e_2$  to  $2\langle u, a \rangle b - g_0 a$  and  $e_3$  to  $g_0(a \times u)$ , this implies  $g_i = BA^{-1}$ . ■

## MANEUVER OPTIMIZATION

The maneuver proposed in the previous paragraph is a safe option (and possibly useful in an on-board emergency mode), but does not yield an overall smooth motion, as the spacecraft is artificially brought to rest at the maneuver midpoint. Therefore, we propose to find a better solution by using a shooting procedure as described above, taking as a starting point the maneuver determined in the constraint-free case. As before, let  $b_j$  be the spacecraft directions which are not allowed to coincide with the forbidden directions  $d_j$ . If  $t \mapsto g(t)$  denotes the spacecraft attitude evolution then the angle  $\varphi_j$  between  $b_j$  and  $d_j$  is given by  $\cos \varphi_j(t) = \langle g(t)^T b_j, d_j(t) \rangle$ . Hence we will introduce a term of the form  $\sum_j \chi(\langle g(t)^T b_j, d_j(t) \rangle)$  in the cost functional where  $\chi : [-1, 1] \rightarrow [0, \infty)$  is an increasing function taking relatively large

values for arguments close to 1; such a term penalizes attitudes at which any of the axes  $b_j$  is close to the corresponding forbidden direction  $d_j$ . (One may be tempted to simply choose a function  $\chi : [-1, \cos \varphi_{\text{safe}}) \rightarrow [0, \infty)$  with a singularity at  $\cos \varphi_{\text{safe}}$ , thereby introducing a term which imposes infinite penalties on violations of the pointing constraints. However, such a choice is not feasible, because the solutions of the resulting differential equations usually run into singularities and hence do not yield a solution of our control problem.) To guide the resulting spacecraft motion, we will introduce an additional term which penalizes deviations from the reference attitude evolution found for the unconstrained case, where the penalty is low close to the forbidden attitudes and high in safe regions. This penalty term may explicitly depend on time, imposing higher penalties on deviations towards the end of the maneuver. Thus in the cost functional (8) we will use a control term of the form

$$F(g, t) := \sum_j \chi(\langle g^T b_j, d_j(t) \rangle) + \rho \left( \sum_j \chi(\langle g^T b_j, d_j(t) \rangle), t \right) \|g - g_{\text{ref}}(t)\|^2 \quad (28)$$

where the matrix norm  $\|\cdot\|$  is the one derived from the inner product  $\langle\langle A, B \rangle\rangle := \text{tr } A^T B = \sum_{i,j} a_{ij} b_{ij}$ .

## SIMULATION RESULTS

As an example, let us take the initial attitude  $g_0 = 1$  (identity matrix) and the target attitude

$$g_1 = \begin{bmatrix} 0.03154 & -0.11772 & 0.99255 \\ 0.25689 & -0.95873 & -0.12187 \\ 0.96593 & 0.25882 & 0.00000 \end{bmatrix}.$$

Choosing the normalized time interval  $[t_0, t_1] = [0, 1]$  and the weighting function  $q(t) := 1/(t - t^2)$ , Theorem 4 yields the maneuver whose angular velocity evolutions are given in Figure 4.

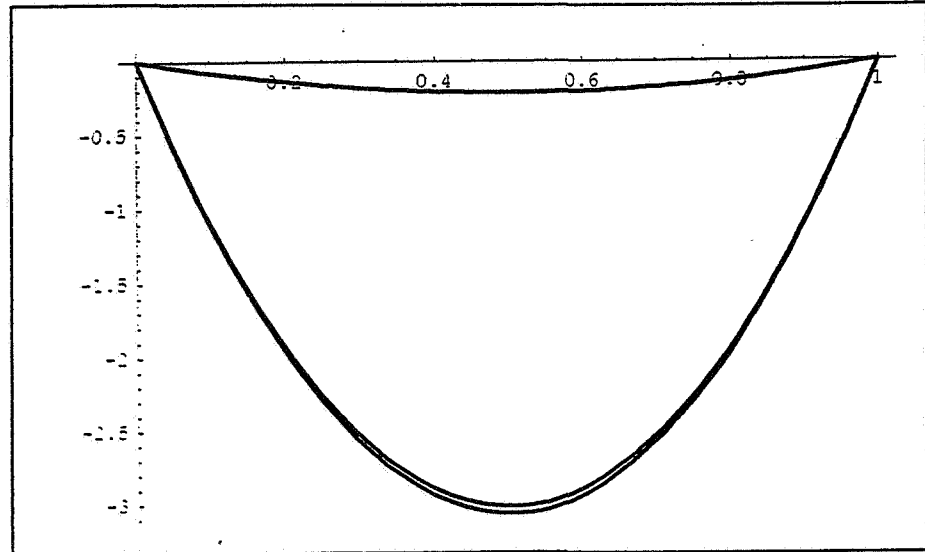
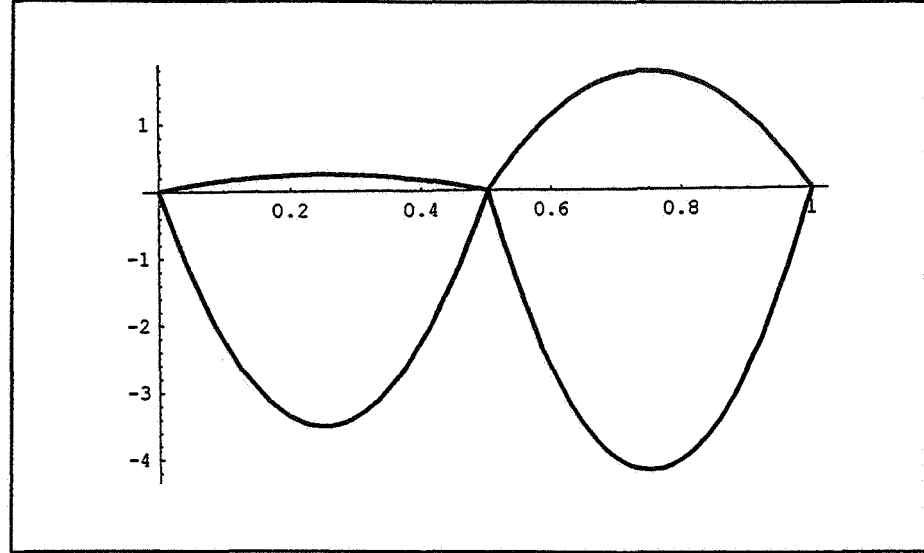


Figure 4: Angular velocities during one-leg maneuver.

We now declare the direction  $d := (0.38209, 0.73555, 0.55943)^T$  to be a forbidden direction for the body-axis  $b := (0, 0, 1)^T$  which we can interpret as a telescope direction; here  $d$  is chosen as the direction of the telescope axis at time  $t = 0.5$  during the above maneuver. To obtain a safe spacecraft motion, we split this maneuver into two; following the procedure described in Theorem 5 we obtain a two-leg maneuver whose angular velocity evolutions are given in Figure 5 below.



**Figure 5:** Angular velocities during two-leg maneuver.

The pointing requirement which is violated during the one-leg maneuver (see Figure 6) is now met during the two-leg maneuver (see Figure 7).

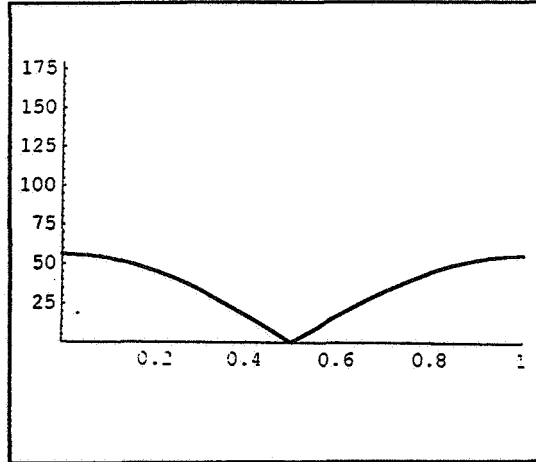


**Figure 6:** Angle between telescope axis and forbidden direction during one-leg maneuver.

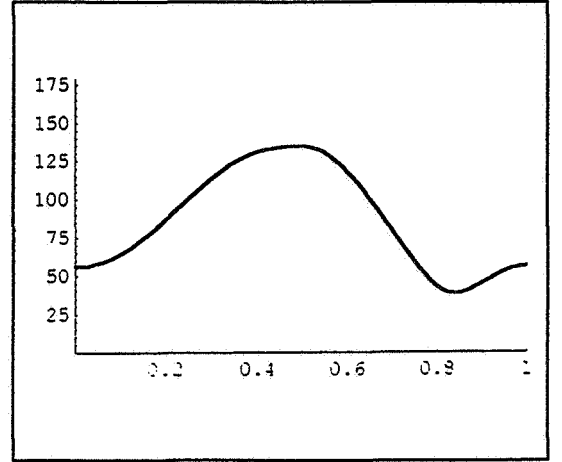


**Figure 7:** Angle between telescope axis and forbidden direction during two-leg maneuver.

It is instructive to compare how the target attitude  $g_1$  is approached in both maneuvers. To do so, we plot the deviation  $t \mapsto \|g(t) - g_1\|$  in both cases. (See Figure 8 and Figure 9 below.)

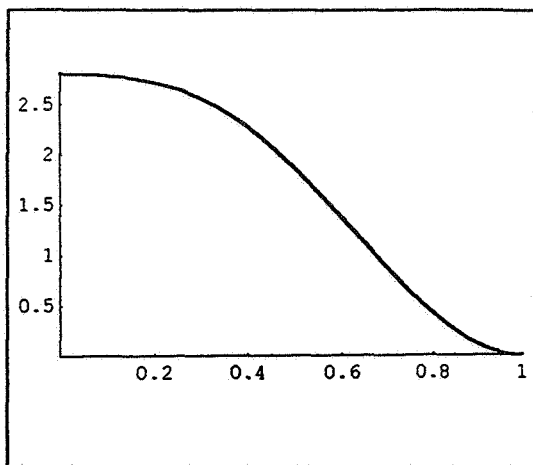


**Figure 8:** Deviation between current attitude and target attitude during one-leg maneuver.

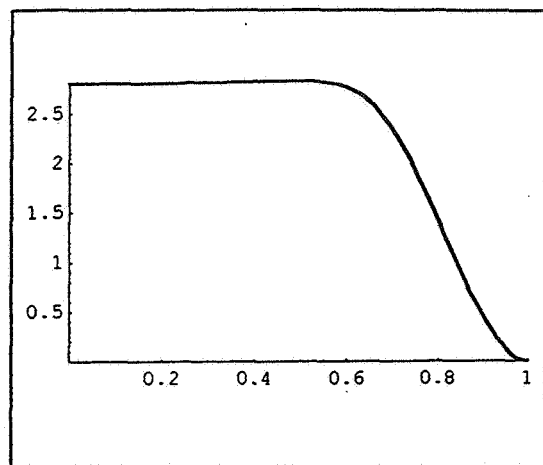


**Figure 9:** Deviation between current attitude and target attitude during two-leg maneuver.

Finally, we introduce a penalty term of the form (28) in the cost functional by choosing  $\chi(x) := 100 \cdot \exp(x - 0.8)$  and  $\rho(x, t) := 1/x$ . The reference trajectory  $t \mapsto g_{\text{ref}}(t)$  is the one obtained for the one-leg maneuver described above, and the initial values of the functions  $t \mapsto q(t)\omega_i^*(t)$  for the first iteration are taken from this maneuver. The shooting method described before converges fast; the angular velocities of the resulting solution are given in Figure 10 below.

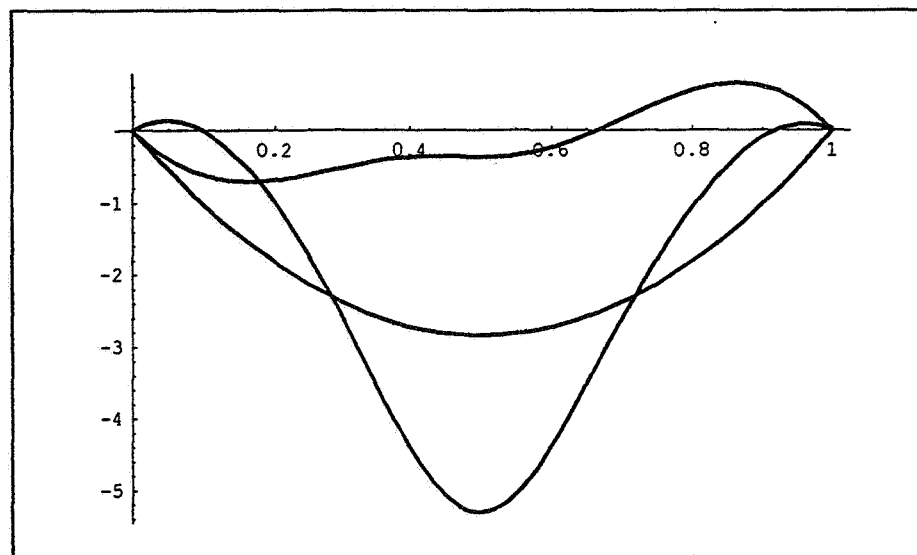


**Figure 10:** Angular velocities during optimized maneuver.

Figure 11 shows how the target attitude is approached, and Figure 12 gives the angle between the telescope axis and the forbidden space direction during the maneuver. As shown, the forbidden direction is only barely avoided (by about  $0.13^\circ$ ). Avoidance by a larger safety margin can be achieved by modifying the cost functional.

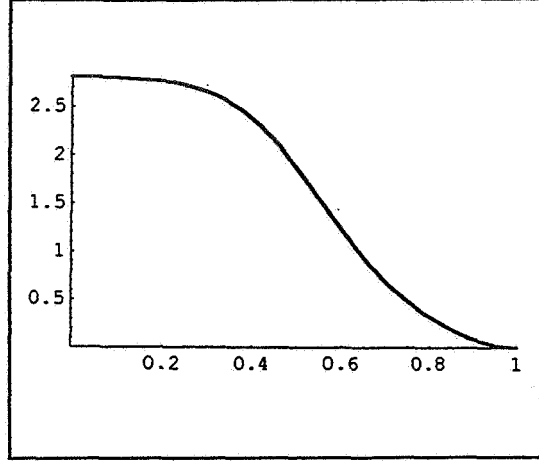


**Figure 11:** Deviation between current attitude and target attitude during optimized maneuver.

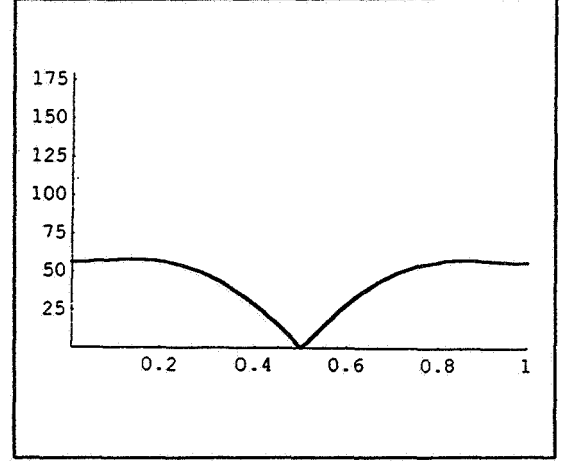


**Figure 12:** Angle between telescope axis and forbidden direction during optimized maneuver.

To understand the scale in the deviation plots, we note that the maximum deviation between two elements of  $SO(3)$  is given by

$$\begin{aligned}
 \max_{g, h \in SO(3)} \|g - h\| &= \max_{g, h \in SO(3)} \|gh^{-1} - 1\| = \max_{\gamma \in SO(3)} \|\gamma - 1\| \\
 &= \max_{\gamma \in SO(3)} \sqrt{\|\gamma\|^2 - 2\text{tr}(\gamma) + \|1\|^2} \\
 &= \max_{\gamma \in SO(3)} \sqrt{6 - 2\text{tr}(\gamma)} = \max_{\varphi \in \mathbb{R}} \sqrt{6 - 2(1 + 2\cos\varphi)} \\
 &= \max_{\varphi \in \mathbb{R}} \sqrt{4 - 4\cos\varphi} = \sqrt{8} \approx 2.828.
 \end{aligned} \tag{29}$$

## REFERENCES

1. Roger W. Brockett, R. S. Milman, Hector J. Sussmann, *Differential Geometric Control Theory*, Birkhäuser 1983
2. Velimir Jurdjevic, *Geometric Control Theory*, Cambridge University Press 1996
3. Colin R. McInnes, *Large Angle Slew Maneuvers with Autonomous Sun Vector Avoidance*, Journal of Guidance, Control, and Dynamics, Vol. 17, No. 4, July-August 1994, pp. 875-877

168.  
337544  
AAS 98-309  
510-18  
169292

## **AN APPROACH TO THE DESIGN AND IMPLEMENTATION OF SPACECRAFT ATTITUDE CONTROL SYSTEMS**

**James R. O'Donnell, Jr., Ph.D.  
David J. Mangus  
Goddard Space Flight Center, Code 572  
Greenbelt, Maryland USA 20771**

Over 39 years and a long list of missions, the guidance, navigation, and control (GN&C) groups at the Goddard Space Flight Center have gradually developed approaches to the design and implementation of successful spacecraft attitude control systems. With the recent creation of the Guidance, Navigation, and Control Center at Goddard, there is a desire to document some of these design practices to help to ensure their consistent application in the future.

In this paper, we will discuss the beginnings of this effort, drawing primarily on the experience of one of the past attitude control system (ACS) groups at Goddard (what was formerly known as Code 712, the Guidance, Navigation, and Control Branch). We will discuss the analysis and design methods and criteria used, including guidelines for linear and nonlinear analysis, as well as the use of low- and high-fidelity simulation for system design and verification of performance. Descriptions of typical ACS sensor and actuator hardware will be shown, and typical sensor/actuator suites for a variety of mission types detailed. A description of the software and hardware test effort will be given, along with an attempt to make some qualitative estimates on how much effort is involved. The spacecraft and GN&C subsystem review cycles will be discussed, giving an outline of what design reviews are typically held and what information should be presented at each stage. Finally, we will point out some of the lessons learned at Goddard.

### **INTRODUCTION**

Throughout its history, the Goddard Space Flight Center has had a number of attitude control system (ACS) branches and organizations devoted to the design, development, testing, and operation of the attitude control and determination subsystems of spacecraft. During the many years and many projects with which these groups have been involved, a number of practices, approaches, and lessons learned have been developed that have led to a great many successful missions.

With the recent reorganization of engineering groups at Goddard, a number of attitude control and navigation groups have been merged and combined within the new Guidance, Navigation, and Control Center (GNCC). The approaches and material discussed in this paper primarily reflect the heritage of only one of the antecedent groups to the GNCC, what was formerly Code 712, the Guidance, Navigation, and Control Branch. Code 712 had primary responsibility for the mid-range and larger spacecraft designed and

built at Goddard. Other groups, also part of the new GNCC, designed the ACS subsystems for the smaller missions or were involved in ACS on-orbit operations. A paper written from the points of view of these groups would reflect many of the same general approaches, though it would likely differ in emphasis.

The goal of this paper is to begin the work of documenting the different aspects of the ACS subsystem design process. The paper will cover many topics very broadly in an attempt to give an overview of our work and some feeling for our design approach. It is hoped that this effort will continue in a much more complete and rigorous way, so that the ACS design heritage and expertise of the Goddard ACS groups can be preserved for the future.

## **ACS SUPPORT FOR SPACECRAFT PROJECT PHASES**

A typical spacecraft project goes through at least five general phases, four of which require the direct, full participation of ACS engineers. These first four phases are the spacecraft conceptual design, development, integration and test, and launch and early operations. Once a spacecraft is on-orbit and operating, ACS involvement usually is limited to support for special events such as orbit maneuvers, anomaly resolution, and participation in end-of-life and other engineering tests.

Following is a list that summarizes many of the tasks that are performed by members of the ACS subsystem throughout these phases of a spacecraft's life.

- 1. Spacecraft ACS Conceptual Design**
  - Support GN&C systems engineering in defining high-level analysis support
  - Support GN&C systems engineering in determining contractor support
  - Review project-level requirements with scientists
  - Develop GN&C mission-level requirements from project-level requirements
  - Define ACS hardware requirements
  - Define ACS software requirements
  - Define attitude knowledge and control requirements
  - Define trajectory requirements
  - Design GN&C mission scenario
  - Develop control mode block diagrams
  - Develop control mode error budgets
- 2. System Development**
  - Verify control mode rigid body stability margins
  - Develop a low-fidelity time domain simulation (LoFi)
  - Verify control mode pointing performance using LoFi
  - Perform structure modal reduction analysis
  - Perform control mode flexible body stability margins analysis
  - Develop high-fidelity models of selected sensor and actuator hardware
  - Develop a nonlinear high-fidelity time domain simulation (HiFi)
  - Verify control mode error budget using HiFi
  - Verify control mode transitions using HiFi
  - Present at the Critical Design Review
  - Develop the ACS Algorithm Document
  - Support the definition of the flight software test facility
  - Write software test procedures that verify control mode requirements
  - Perform and evaluate results of control mode software testing
  - Support hardware procurement and hardware and software design reviews
- 3. Integration and Test (I&T)**
  - Develop and support spacecraft-level ACS hardware aliveness tests
  - Develop and support spacecraft-level ACS hardware functionality test procedures
  - Develop and support spacecraft-level ACS hardware phasing test procedures



- Develop and support spacecraft-level ACS end-to-end tests
  - Develop on-orbit ACS procedures
  - Develop and support ACS level Comprehensive Performance Tests
4. **Launch and Early Operations**
- Determine on-orbit sensor and actuator calibration requirements
  - Develop mission operation center ACS telemetry page layouts
  - Support pre-launch mission operations
  - Support launch and early on-orbit activities
  - Support on-orbit sensor and actuator calibrations

The remainder of this paper will discuss these phases, and the different work that occurs in each, in some more detail. The main concentration, again reflecting the experience of the authors and Code 712, will be on the development and I&T phases, with a little discussion on the systems engineering and conceptual design phase.

## SYSTEMS ENGINEERING AND DESIGN

ACS support for spacecraft development begins in the initial systems engineering and design effort, which very often begins a number of *years* before a project is even approved. There are usually a variety of study and “pre-Phase A” efforts involved in the very early spacecraft design; once a project is approved, it enters a much more formal period of development and test.

During the early systems efforts, systems engineers and those who work directly with the ACS subsystem begin the initial design task, taking the science and other mission requirements and using them to design ACS requirements and a subsystem concept that will allow the spacecraft to successfully achieve its science objectives. This early ACS design comprises the following steps:

1. **Mission Concept Design:** In this design phase, the object is to develop a concept that will allow for the successful completion of the mission’s science objectives, within the imposed budgetary, time, and other constraints. This mission concept encompasses all phases of the project, from initial design and development, through test, launch, and operations. Specific to the ACS, an initial design of the subsystem is created—including control modes and preliminary hardware sensor and actuator complement—that will allow the mission concept to be successfully implemented.
2. **ACS Level Requirements:** Once the mission concept is developed, the mission-level requirements must be used to generate subsidiary requirements for each subsystem. For the ACS, this will typically mean requirements for pointing accuracy and stability, momentum management, and orbit maneuvering and maintenance; as these requirements are developed and refined, they can have a direct impact on the subsystem design, both algorithmic and hardware.
3. **Error Budgets:** With numerical ACS subsystem requirements in hand, it is necessary to develop error budgets that parcel out the required performance goals and allowable errors to the different parts of the subsystem. These budgets will define the type and quality of ACS hardware required, as well as imposing performance and stability requirements on the control algorithms developed in the design process.
4. **Trade Studies:** It is usually necessary to iterate on all of the above steps, generating a number of options and possibilities for the different aspects of the design. Decisions made at the subsystem level, both in the ACS subsystem and others, can have potential impacts in other subsystems and on the system as a whole. The object of the early stages of the design is for the systems engineers, aided by specialists in the different subsystem areas, to generate a viable preliminary design and attainable set of requirements so that the design and development effort can continue with an expectation of success.

## ACS ANALYSIS AND DESIGN

In the ACS analysis and design phase, the requirements and mission concept generated in the early systems engineering effort is turned into reality—at least a mathematical and algorithmic reality, at this point. The first step is to define the control modes—and relationships between modes—that can implement the mission concept defined in the conceptual design of the spacecraft ACS. Then, for each mode, a linear controller design and analysis must be performed.

For the majority of spacecraft attitude control systems, initial design is performed assuming a PD or PID controller. Because of the relatively benign disturbance environment for most space missions, this simple controller usually proves to be sufficient. Using a PD or PID controller and a linear  $J/s^2$  plant to model the spacecraft, beginning the design of controller gains and analysis of ACS performance is very straightforward. As the physical design of the entire spacecraft becomes more mature, and mathematical models of it more complete, a flexible mode analysis is done to ensure that the spacecraft ACS will not excite any uncontrolled oscillations during operation. Throughout the design process, simulations are developed and run to verify the time-domain performance of the spacecraft.

A final aspect of the ACS algorithmic design does not apply specifically to the spacecraft performance within a specific mode, but looks at the management of angular momentum across all modes. Depending on the mission, all spacecraft will encounter a variety of disturbance inputs—aerodynamic, gravity gradient, solar pressure, and magnetic, to name the most common—that, over time, can cause a buildup of system angular momentum within the spacecraft. A system for managing and off-loading this momentum must be designed, as it will eventually affect the performance of the spacecraft ACS.

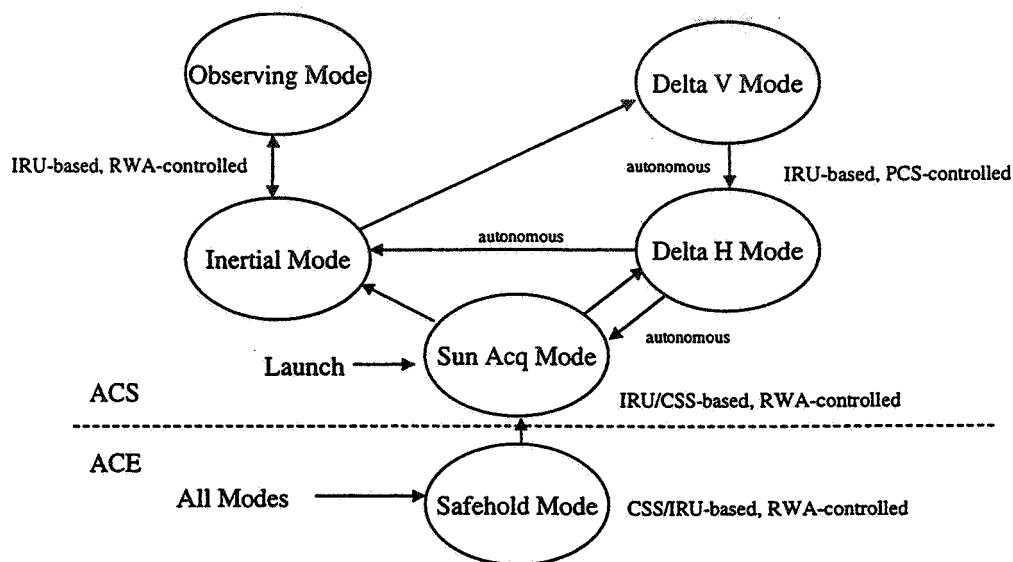
### Control Mode Definition

Figure 1 shows an example control mode diagram from the MAP spacecraft. The six modes, five in the spacecraft main ACS processor and one in the separate attitude control electronics (ACE) box, were designed to meet the requirements derived from the mission requirements and concept for the MAP ACS subsystem.

### Linear System Design and Stability

It is during the linear ACS design and analysis phase of a project that the work most commonly associated with the ACS *analyst* is done. For the large majority of spacecraft, the control laws used as the basis for ACS design remain the same as those used 20 years ago. The initial design and stability analysis is mainly concerned with using the available tools to decide what control law is needed, determine the controller gains and other parameters needed to implement that control law, and then to verify its performance and stability. As more information—such as system inertia matrices and flexible mode analyses—becomes available, further analysis is performed to verify that sufficient performance and stability margins still exist.

The bulk of the engineering judgement and expertise of the ACS analyst with respect to the linear design come into play in two main areas. First, the initial design must include sufficient performance and stability margins so that, as more information about the system becomes known and more fidelity is included in the design models, the design continues to satisfy all performance and stability criteria. Second, the control law and linear ACS design must be created and translated in such a way so that it can be turned into physical hardware and software on the spacecraft.



**Figure 1 MAP Control Modes**

*Design and Analysis Tools.* Many of the design and analysis concepts used by today's ACS analyst haven't changed from those used by his or her predecessor, 20 or 30 years ago. The same collection of methods used to characterize the performance and stability of systems modeled with linear equations has been used in the aerospace industry for as long as it has been around. Of course, the way these tools are implemented has changed quite a bit with the advent and increasing power of the computer. Today's analyst may be creating root locus, Bode, and Nichols plots much like analysts of the past, but he or she is generating them a lot more quickly.

Figure 2 shows a collection of plots that represent some of the typical means of designing and analyzing attitude control systems modeled with linear equations. Root Locus plots allow the designer to work directly with the open- and closed-loop poles and zeros of the linear system; well-known relationships can then be used to derive frequency- and time-domain characteristics, such as natural frequency and damping ratio, rise time and settling time, for the resulting system. Bode and Nichols plots (as well as Nyquist plots, an example of which is not shown) are alternate methods of displaying the same frequency-domain information and characteristics of a system. The most important of these characteristics, as relates to system stability, are the system gain and phase margins. These margins give a measure of how much more or less gain and how much more phase lag a system can handle before it goes unstable. Adequate margin is needed when designing a system modeled with linear equations to ensure that the real system will remain stable and have acceptable performance in actual operation.

The final design tool used by the ACS analyst is the time-domain simulation. Through a variety of simulations of varying degrees of fidelity, the performance of the control system is analyzed and verified.

As mentioned above, many of the design techniques used by ACS designers has remained the same. The way in which the designer generates and makes use of these tools has changed, and is beginning to change a lot more quickly, as computers become faster. For instance, using a software tool such as the Interactive Control Design Module from Integrated Systems, the linear equations for a system and a baseline controller can be set up, and the controller parameters can be changed and the resulting system performance viewed in real-time.

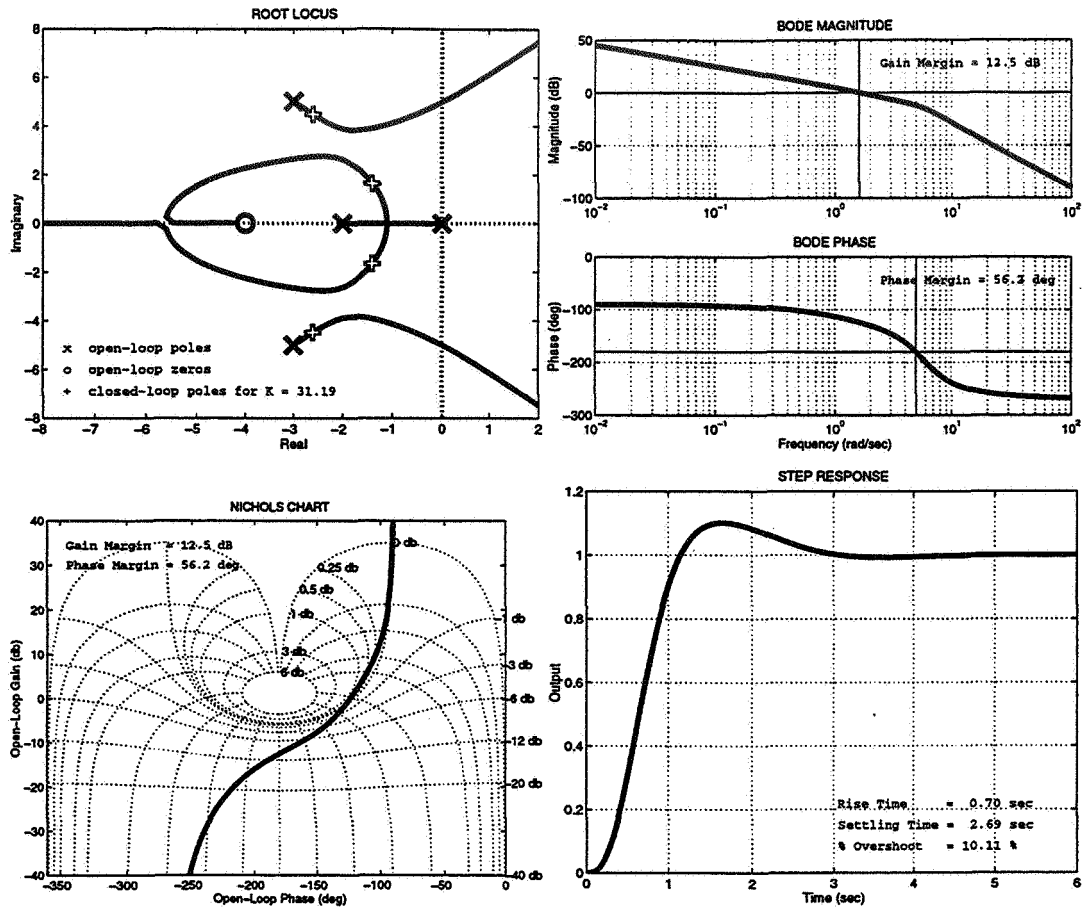


Figure 2 Linear Analysis and Design Techniques

**Rigid Body Stability.** The initial ACS design and analysis is usually done with a simple linear model of the spacecraft, using only rigid body dynamics. At this stage of a project, it is usually not possible to accurately model any better than this. It is not until the physical design of spacecraft bus and instrument become more mature that details of the flexible body characteristics of the system become available.

There are a number of design criteria that can be applied to a rigid body design. Of course, most of the time-domain criteria are dictated by the requirements of the mission; these include things like slew rate and pointing performance. Controller designs must first satisfy these requirements. However, there are a number of criteria that determine the stability of a system that also must be satisfied. The criteria used are the gain and phase margins of the system<sup>1</sup>. The margins that we typically use, which must be found with respect to any commandable gain within the control system (i.e., controller gains, reaction wheel or other actuator scale factors, etc.), are a gain margin of 12 dB and a phase margin of 40°.

**Flexible Body Stability.** Flexible body analysis is generally performed starting with a NASTRAN (or other such) model of a system that gives the flexible mode frequencies and modal gains of a system. This list of modes is reduced, based on the modal frequencies and gains compared to the bandwidth of the control system, into a number of modes used for linear analysis. These modes are then included in the linear model of the system as a series of second-order systems of the form:

$$\frac{K_i}{s^2 + 2\zeta\omega_i s + \omega_i^2} \quad (1)$$

The parameters  $K_i$  and  $\omega_i$  in Eq. (1) are the modal gain and frequency of mode  $i$ , respectively. The parameter  $\zeta$  is the damping ratio of the flexible modes, which is conservatively set to 0.001 (this translates to an impulse response that takes approximately  $5\tau = 5/\zeta\omega_i = 5000/\omega_i$  seconds to die out<sup>2</sup>). With the flexible modes in place, stability analysis is performed using the same desired gain and phase margins as used above.

## Performance

Along with determining the stability of a system, generally using frequency-domain techniques such as Bode or Nichols plots, the performance of a system must be determined using time-domain simulations of the system. Generally, three types of simulations are created and used during a project for analysis and design. The first of these is a simple linear simulation, using the same linear model as that used for frequency-domain analysis. Time-domain performance of such a model can be calculated analytically by the same design package that is used to create Bode or Nichols plots, and is typically used as a first cut during the early stages of the design.

Aside from simple linear models of a system, nonlinear models and simulation tools are used with both low-fidelity (LoFi) and high-fidelity (HiFi) models of a system

*Low Fidelity Simulations.* Low-Fidelity (LoFi) simulations, like simple linear models, are typically used during the early stages of an ACS design and analysis effort to broadly characterize the performance of the system. LoFi simulations differ from linear models in that they typically include some nonlinear elements, particularly mixed discrete and continuous systems to model the physical environment and dynamics of a spacecraft along with the discrete controller.

Typically, the LoFi simulation is used during the early design stages when there is likely to be a lot of iteration back and forth between design and performance verification, and so a quick turnaround is highly desirable. The intent of the LoFi is to show broad performance characteristics, enough to verify that the design can meet the pointing, slew rate, and other criteria.

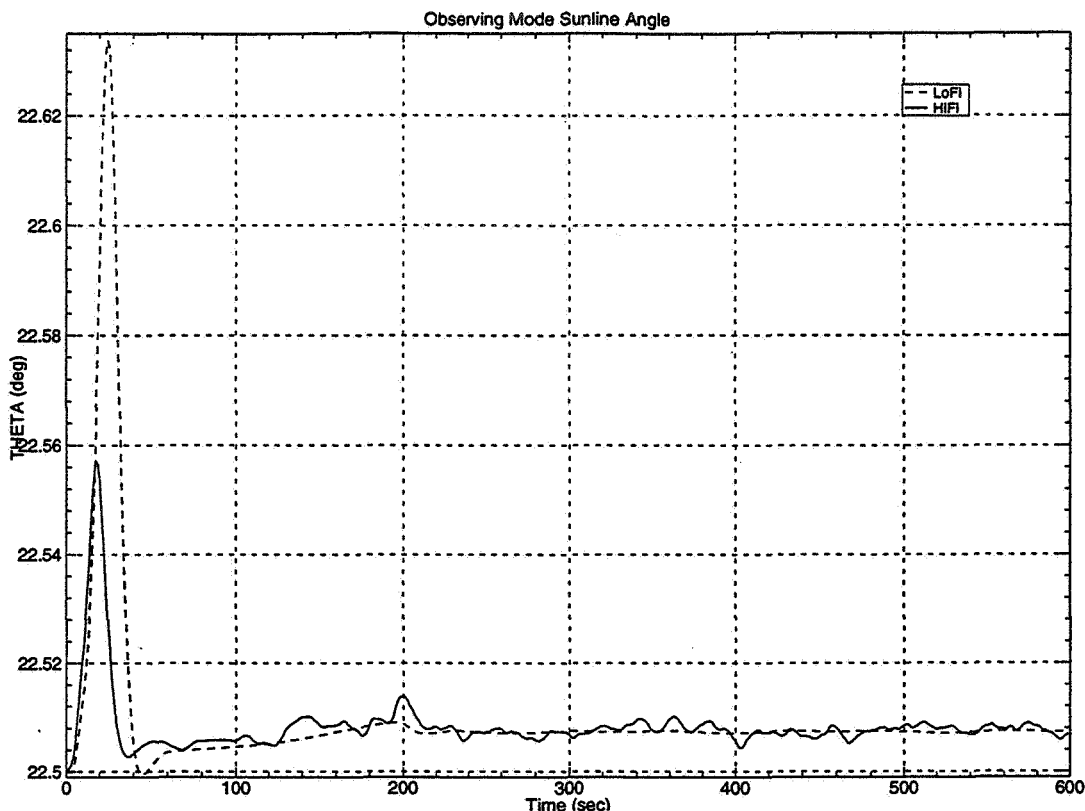
*High Fidelity Simulations.* Whereas a LoFi simulation is primarily a design tool, a high-fidelity (HiFi) simulation is mainly used for design verification. HiFi simulations are created by including as much detail into the simulation as possible, including such things as sensor and actuator performance and noise models, environmental disturbances, quantization error, and even the ability to model non-ACS specific events such as ACS processor warm and cold restarts. Also, as will be discussed in the ACS Flight Software section later in this paper, automatic code generation tools can even allow the HiFi to be used to generate actual flight software.

Figure 3 shows an example of a LoFi and HiFi spacecraft simulation. Notice that the LoFi shows a fairly accurate portrayal of the “macro” performance of the control system. The HiFi, which is plotted on a much tighter scale, gives a better view on the “micro” level, showing the details of the system response in the presence of noise and other disturbances.

## Momentum Management

Design and analysis of the momentum management component of the ACS begins in the initial study phase of a spacecraft design, and continues as the spacecraft design matures and the mathematical models used for it continue to be developed. The following considerations and rules of thumb are used in its design:

1. Identify the external torques that contribute to a build-up of system momentum. Typically, these torques are gravity gradient, aerodynamic, and solar pressure. In low-Earth orbits, gravity gradient and aerodynamic torques are the most significant; at higher orbits, the most significant external torque is usually from solar pressure.



**Figure 3 Low- and High-Fidelity Simulations**

2. Select a momentum unloading control law. The two control laws generally used are referred to as “**B dot**” and “**HxB**”. **B dot** does not require any hardware other than magnetic torquer bars and a magnetometer, but leaves a residual spacecraft body rate equivalent to one or two revolutions per Earth orbit, and will not dump momentum stored in the wheels. **HxB**, on the other hand does not leave the spacecraft with a residual rate, but it also requires system momentum information (typically from gyros and reaction wheel tachometers).
3. Using past missions in a similar orbit, analysis of worst-case environmental disturbance torques, and LoFi simulations as a guide, make a first cut at magnetic torquer bar sizing.
4. Select torquer bar sizes including 100% margin. Inertia ratios, and other parameters that influence the spacecraft response to environmental torques, will typically rise by more than 30% from the initial sizing studies to launch.
5. Test the final design using the HiFi simulation. It is best to use a 36-hour test, so that a full 24 hours is covered to allow the Earth magnetic dipole to rotate in inertial space, with an additional six hours of overlap on each side.

A similar approach, using similar margins, is taken when magnetic momentum unloading impractical or impossible. Two other possible approaches to momentum unloading are using thrusters (which is very quick and efficient, but requires expendable fuel) or, in higher orbits where the dominant disturbance torque is solar pressure, by trimming the orientation of the solar panels with respect to the sunline.

## ACS HARDWARE

As the ACS is being designed by analysts, other ACS subsystem engineers are selecting and procuring the hardware to be used to implement that design on the spacecraft. The hardware needed for the ACS

subsystem can be divided up into three categories: flight hardware shared by the ACS and other spacecraft subsystems, the ACS sensor, actuator, and other electronic hardware, and the hardware needed on the ground to integrate and test the ACS system.

Depending on the design of a given system, the ACS will usually be implemented within the main spacecraft processor, within a separate attitude control electronics (ACE) box, or sometimes both. The main processor, along with the hardware and software that comprise the command and data handling (C&DH) subsystem, are integral parts necessary for the successful operation of the ACS. Similarly, the attitude control electronics, used as an interface between the control algorithms implemented in either the main processor or a dedicated ACE processor and the sensor and actuator hardware. Also, instrument data is sometimes used for fine position sensing within the ACS.

## Flight Sensor Hardware

There is a wide variety of ACS sensor and actuator hardware available for spacecraft missions—each piece of hardware has different characteristics of performance, cost, lifetime, and other criteria, that make it applicable to a subset of the possible missions. In this section of the paper, we will give examples of some of the major types of sensors and actuators. At the end of the section we will show a table containing some representative mass, power, and performance numbers for some of the sensor types discussed.

*Earth Sensor:* Earth sensors detect the Earth's horizons (actually, an infrared radiation band from the CO<sub>2</sub> layer slightly above each horizon) as seen from space to provide two axes of attitude information with respect to the geodetic nadir vector from the spacecraft to the Earth. Earth sensors cannot measure the yaw angle about this vector. These sensors are very often used as the primary attitude sensors for Earth-pointing spacecraft; even when the pointing requirements of the mission exceed the capabilities of an Earth sensor, they are often used for Earth acquisition after launch and other maneuvers.

There are two general classes of Earth sensors. The first type, scanning Earth sensors, use a moving optical head to detect where the horizon is. Static Earth sensors, on the other hand, are built to operate at a given altitude range and have a fixed field-of-view designed to intersect the Earth horizon at one or more points. In general, scanning sensors are heavier, use more power, and cost more (in addition to causing attitude disturbances that may affect the science payload), but also have a larger range of operation and greater pointing performance.

*Digital Sun Sensor:* Digital sun sensors are generally used to detect the orientation of a spacecraft with respect to the vector from the spacecraft to the sun. Like an Earth sensor, sun sensors cannot measure the orientation of the spacecraft about this vector. Digital sun sensors can be used to give two axes of information, and are generally used with other attitude measurements as part of a general attitude determination algorithm, or to provide attitude updates to a Kalman filter.

*Inertial Reference Unit:* Inertial reference units are gyro/accelerometer packages that can be used as an angular rate and acceleration sensor (to save cost, weight, and power, the accelerometers are often left out, unless there is a structural resonance issue). They can also be used to propagate an attitude estimate between measurements from an attitude sensor. Gyros are available in a wide range units, varying considerably in mass, power, and capabilities.

*Star Tracker:* Star trackers are used to detect and track stars. By correlating measurements of the line of sight vectors to multiple stars, the spacecraft's current orientation with respect to an inertial reference frame can be determined (the particular inertial frame used depends on that used to specify the star positions).

Most star trackers currently operate by providing information to the spacecraft processor about line-of-sight vectors and magnitudes to detected stars. Algorithms in the processor, using an onboard star catalog, identify the stars detected and use their defined positions to calculate the spacecraft attitude. In the event of a spacecraft where this information is only needed for attitude knowledge, and not attitude control, this processing may also be done on the ground. However, some of the newest star trackers now becoming available are so-called "quaternion output" trackers—they have their own processor and built-in star

catalog, and can directly output a quaternion expressing the orientation of the star tracker boresight with respect to an inertial reference frame.

	Mass (kg)	Power (W)	Performance
Earth Sensor (static)	0.69	0.5–2	20° field of view 0.25° accuracy
Earth Sensor (scanning)	2.5	8	45° field of view 0.05–0.1° accuracy
Digital Sun Sensor	2	1.05	±32° field of view 0.017° accuracy 0.0039° resolution
Inertial Reference Unit (two-axis unit)	1.6–5.8	7.5–12	0.1–1 arcsec/pulse
Star Tracker	8.1	12	8×8° field of view 3 arcsec accuracy

*Other Sensors:* In addition to the sensors discussed above, which are the typical sensors usually used by the ACS mission mode controller, there are a number of other sensors that are generally included or can be used on a spacecraft. These sensors fall into two general categories:

First, there are sensors used for a special purpose on a spacecraft, other than a normal mission mode control. Two examples of this would be the course sun sensor, usually used as a part of a minimum hardware sun acquisition control mode, and the three-axis magnetometer, usually used along with magnetic torquer bars for momentum unloading. (It is interesting to note that algorithms, such as the “Contingency Mode” developed for the TRMM spacecraft, have been developed and implemented that use magnetometer measurements, along with measurements from other sensors, such as digital sun sensors, to generate a mission mode attitude estimate.)

Second, there are a number of new technology attitude sensors that are in development and/or at the experimental stage. These include the use of GPS signals in a differential mode to generate attitude information, and a number of integrated star tracker/inertial reference unit sensors that generate both attitude and attitude rate information.

## Flight Actuator Hardware

Most spacecraft use one of two types of actuators for most of their flight actuator requirements. Propulsion systems and thrusters are included on a spacecraft to perform orbit maneuvering and stationkeeping, as well as for momentum management on spacecraft where magnetic torquer rods are not sufficient (or usable, for non-Earth orbiting or high-Earth orbiting spacecraft). The ACS groups work closely with the propulsion groups at Goddard to design a thruster system, where needed, that will satisfy all spacecraft requirements for attitude, orbit, and momentum management. In general, though, most spacecraft require reaction or momentum wheels as their primary actuator.

*Reaction Wheel:* A reaction wheel is used to apply or remove a rate from a spacecraft by making use of the conservation of angular momentum. When torque is applied to a reaction wheel to get it to change its rotation rate about a given axis, a corresponding torque and angular rate change is generated in the spacecraft in the opposite direction. Two of the most important ways that reaction wheels are characterized is through their momentum capacity and their torque authority—in general, larger wheels have more capacity and can generate a larger torque, at the expense of more mass, power, and cost.

	Mass (kg)	Power (W)	Performance
Reaction Wheel “Type A”	2.55	5.5–9 (orbit average) 25 (peak)	0.012–0.02 Nm torque authority 4 Nms momentum capacity
Reaction Wheel “Type E”	10.5	15–40 (orbit average) 280 (peak)	0.3 Nm torque authority



Momentum wheels are similar to reaction wheels; generally, they provide lower torque, but have a higher efficiency. Lastly, in addition to thrusters and wheels, magnetic torquer bars are often used by spacecraft in low-Earth orbit for momentum management.

## Test Hardware

In addition to the flight hardware that must be acquired to implement an ACS design on a spacecraft, there is a large amount of additional hardware that is required for ground test purposes. Figure 4 shows an example of the hardware used for a hybrid dynamic simulator (HDS), used to provide ground-test capability for a spacecraft, both software algorithms and flight hardware, from low-level testing through final integration and test.

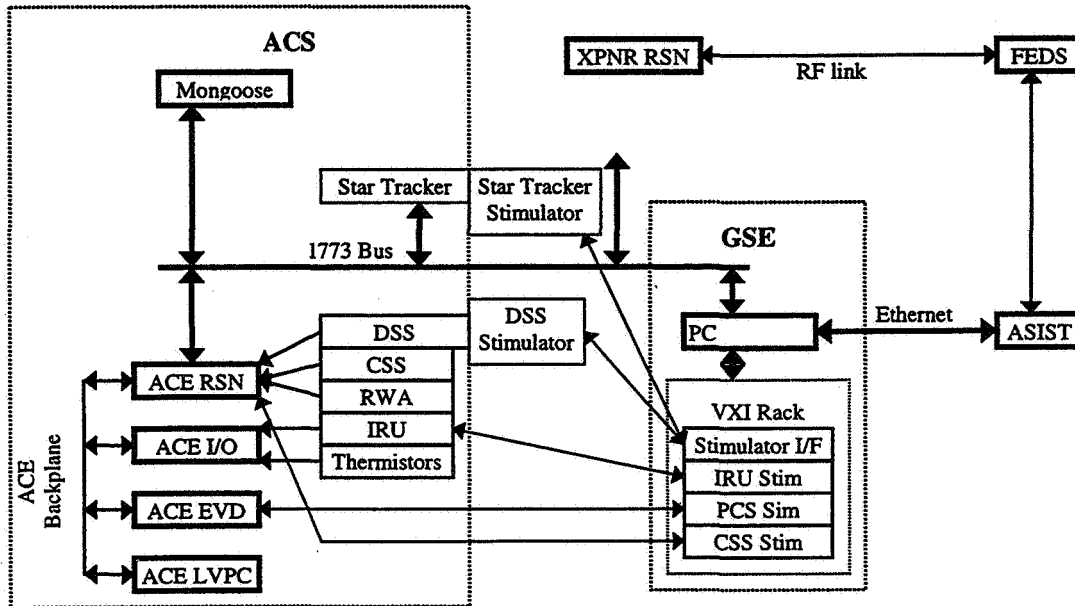


Figure 4 HDS Hardware for ACS Testing

Multiple hardware test setups are typically required for many missions, allowing the ability to concurrently test the main spacecraft processor, the independent attitude control electronics (if present), as well as the ability to stimulate all flight hardware and hardware interfaces. The production of breadboard and engineering test units (ETU) for many of the flight components adds to the cost and effort involved. Depending on how the test effort is scheduled, very often completely different test “strings” are required to allow for testing of ACS and C&DH functionality separately. When all of this additional hardware required for the testing effort is considered, it becomes a significant fraction of the cost and effort associated with the flight hardware.

## ACS FLIGHT SOFTWARE

There are three major phases in the production of ACS flight software used to implement the control laws developed to support the spacecraft mission. The first phase bridges the gap from the ACS design described above to the flight software developers, usually through the means of an algorithm document. Next, the ACS algorithms, along with all of the other necessary flight software functions, are developed for the specific processors and hardware architecture selected for the spacecraft. Finally, perhaps most importantly, software (and hardware, as discussed above) is developed and run to fully test the functions of the flight software.

## ACS Algorithm Document

For the TRMM project, ACS analysts converted the algorithms needed to implement the controller into FORTRAN-like syntax used in the TRMM ACS Algorithm Document<sup>3</sup>. This document was then provided to the ACS flight software developers who used it as a guide to develop the C language routines necessary to implement the algorithms on the spacecraft main and ACE processors.

One of the lessons learned from the TRMM experience is that the FORTRAN vs C syntax used for the algorithm document and flight software, respectively, hampered the ability of the developers to correctly interpret the algorithm document, as well as making it more difficult for the ACS designers to verify the correctness of the code. Using similar syntax—which in this case would have meant using C-like syntax in the algorithm document—would have made the process a lot easier.

Taking advantage of some of the advances in the technology of the control system design tools, a slightly different approach to that used by TRMM is now possible. Products such as DocumentIt from ISI allow documentation to be generated automatically from a system model, such as a HiFi simulation. The documentation generated for the MAP ACS uses the software tool's ability to create output meant for display on the Web.

The ability to automatically generate documentation is only a small part of what is becoming possible with the newest generation of ACS design tools. As will be discussed in the next section, there are several tools available now that will automatically generate flight software from a system model, thus skipping the algorithm to algorithm document to flight software translation process altogether.

## Automatically-Generated Code

Figure 5 shows an example block diagram from the MAP HiFi simulation, depicting the Observing Mode controller. Instead of translating this controller into a written algorithm, which would then be coded by the ACS flight software developers, by using ISI's AutoCode ACS development tool, flight code for this controller can be automatically generated.

There are a number of potential benefits to automatic code generation. Primarily, once confidence in the code-generation tool is established, it should strengthen the testing effort. Because it is possible to generate some of the flight code much more quickly using this method, it is possible to begin testing earlier, and thus test more thoroughly. Also, because the algorithms are proven within the simulation environment first, before the code is generated, a great deal of lower-level testing can be avoided.

The MAP program is one of the first at Goddard to use automatically generated flight software. Because of this, the scope of what parts of the ACS were chosen to be AutoCoded was limited; even so, approximately 1/3 of the MAP ACS flight software was automatically generated. The consulting group at ISI, which has a lot more experience using automatic code generation, and the ISI tools in particular, has reported even greater percentages of automatically generated code and improvements of the flight software design cycle for the MSTI-1, MSTI-2, and MSTI-3 programs<sup>4</sup>.

## Development vs Testing

Based on the experiences that we have had across many missions, it is safe to say that the flight software testing effort is always underestimated. Just as software is developed to implement ACS algorithms for flight, software test procedures are needed to test that software throughout the development and integration and test phases of the project. The relative amount of effort needed for ACS flight software development vs testing is roughly a 50/50 split between the two. This includes the manpower and time to develop the software, either flight or test, and to run the tests; it doesn't include ACS analyst support, but that also tends to be pretty evenly split between the two activities.

The relative effort assessments discussed above do not include that involved for configuration management and maintenance of a system for tracking ACS parameters and for filing discrepancy reports (DRs) for the different ACS subsystem components. One of the lessons learned from past programs that is currently being applied is the use of a central database for maintaining the DRs and parameters used throughout the ACS subsystem: HiFi simulation, flight software, and HDS. Because of this, it is fair to consider this effort as a general overhead important to both the development and testing effort.

## DESIGN REVIEW CYCLE

Each spacecraft goes through a number of design reviews, each of which has a different emphasis and reflects a different stage in the design process. While the specific names of the reviews for each project may vary, the general topics covered at each stage tend to be the same. Some of the typical reviews and topics covered, as they relate to the ACS subsystem, over the course of a project are discussed in this section.

There is some overlap from one review to another, and a number of topics that will be covered in each. In particular, every review will discuss design changes (and their impacts) and action items (and their resolutions) since the last review, as well as outstanding issues and concerns.

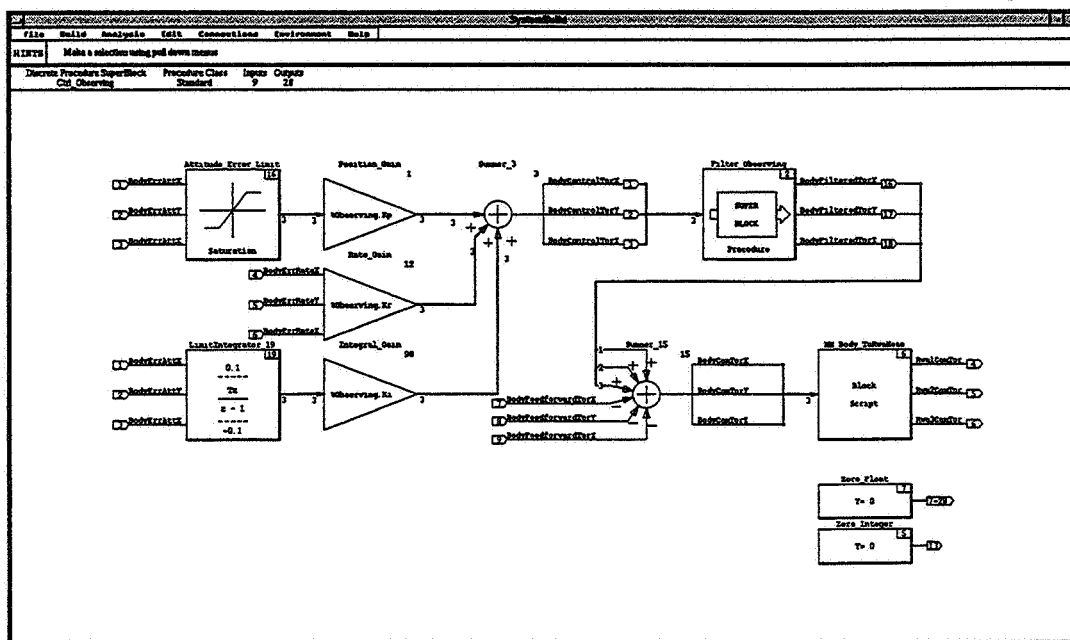


Figure 5 MAP Observing Mode Controller to be AutoCoded

## Preliminary Design Review (PDR)

The first formal review is usually the Preliminary Design Review, or PDR. This is typically conducted after enough time has passed for a first cut at an ACS subsystem design has been done. The purpose of the initial design and review is to develop a preliminary design for the complete ACS subsystem and to determine the viability of the mission concept. If the mission has any “show stoppers”—mission requirements that cannot be met within the budgetary, time, or other constraints imposed on the project—they should be identified by the PDR. Also, major design issues should be identified. A list of topics typically covered in a PDR is as follows:

1. Requirements
2. Subsystem Analysis

- Analyses Performed
  - ACS Modes
    - Descriptions
    - Stability
    - Performance
  - Other Topics (Attitude Determination/Error Budgets, Momentum Management)
3. Hardware
    - Procured Components
    - In-House Development
  4. Software
  5. Operations
  6. Testing

## **Critical Design Review (CDR)**

The Critical Design Review (CDR) is the last subsystem-specific review conducted. By the time it is conducted, the ACS design should be completed, analyzed, and tested to the point that it can be said and demonstrated with confidence that the design will meet all requirements. Issues identified at the PDR should be addressed and closed at the CDR. The design of other parts of the spacecraft should have matured by subsystem CDR so that flexible mode analysis is possible. The CDR will cover much of the same material as the PDR, though the design should be more mature and finalized.

1. Requirements
2. Subsystem Analysis
  - Status
    - Stability Analyses
    - Flexible Mode Analyses
    - ACS Mode Description and Performance Summaries
  - Other Topics (Attitude Determination/Error Budgets, Momentum Management)
3. Noncompliance Summary/Open Issues
  - Hardware
  - Software
4. Failure Detection and Correction
5. Operations
6. Testing

Once all subsystems have had their CDRs, there is a spacecraft-level CDR that covers the complete spacecraft, at a higher level. It is through this review, either on its own or with a separate confirmation review, that it is decided whether or not the spacecraft design is complete and good enough to justify continuing with the integration and test process.

## **Pre-Environmental Review (PER)**

A Pre-Environmental Review (PER) is conducted immediately prior to the full spacecraft going into environmental testing. The purpose of the review is to ensure that all outstanding issues from previous reviews and I&T have been closed, and that a plan is in place for successfully testing spacecraft aliveness and functionality as it goes through the different environments. Items typically covered in a PER include:

1. Hardware Qualification and Testing
  - For Each Component:
    - Hardware Description and Part Number
    - Component Specification Document
    - Manufacturer Environmental Testing and Total Running Time
    - Delivery Date

- Waivers
- Functional/Aliveness Bench Tests
- Electrical Integration Procedure
- Performance Tests
- 2. Spacecraft Level Testing
  - Aliveness, Functional, and Phasing Tests
  - Comprehensive Performance Testing CPT)
  - Dynamic Simulator Testing
- 3. Is the Spacecraft Ready for Environmental Testing?

## **Pre-Ship Review (PSR)**

A review is conducted before a spacecraft is shipped to its launch site to determine if it is ready for launch. This Pre-Ship Review would cover the following types of topics:

1. Events since PER
  - Spacecraft Tests w/Dates
    - Results
    - Completion Status
  - Flight Hardware Operating Hours
  - Anomalies Since PER
    - Problem
    - Cause of problem
    - Current status
2. Is the Spacecraft Ready for Launch?

## **CONCLUSION**

This paper has attempted to cover a lot of material very broadly, to give an idea of what is involved in one approach to a successful spacecraft design. It is by no means the only approach to how to design a spacecraft, nor is this paper meant to be a detailed blueprint of the design process. It is, instead, a summary of some of the experiences that we have had at Goddard over the years, and is hopefully the first step in a larger effort to document the design expertise currently present in the Guidance, Navigation, and Control Center.

## **ACKNOWLEDGEMENTS**

The authors would like to gratefully acknowledge Robert Spagnuolo, Otilia Rodriguez-Alvarez, Debbie Henretty, Maureen Bartholomew, Nelson Rubin, and Martin Frederick, all members of Goddard's Guidance, Navigation, and Control Center, for their assistance in the preparation of this paper.

## **REFERENCES**

1. G. E. Mosier and J. W. Croft, "XTE Linear Analysis Objectives Plan", Goddard Space Flight Center, Code 712, Internal Memo.
2. R. J. Richards, "An Introduction to Dynamics and Control", Longman Group Limited, London, 1979.
3. J. Bracken, J. San, J. D'Agostino, and K. Barnes, "TRMM ACS Algorithm Document", Goddard Space Flight Center, Code 712, Build 5.5, September 16, 1997.
4. F. Tubb, R. McEwen, J. Farazian, and A. Waddell, "MSTI-3 Spacecraft Attitude Control Software Development using Automatic Code Generation", Integrated Systems, Inc.



## Disturbance Accommodating Sliding Mode Controller for Spacecraft Attitude Maneuvers

Jongrae Kim\*, Jinho Kim†, John L. Crassidis‡

In the absence of an external disturbance and uncertainty, sliding mode (variable structure) control is guaranteed to asymptotically stabilize a system, which is provided by using a correction control input calculated using a Lyapunov-type condition i.e., sliding mode existence condition. When bounded unmodeled external torques are added, the closed-loop system is no longer globally asymptotically stable since steady-state errors are present. The error can be minimized by increasing the correction control gain or decreasing the thickness of boundary layer of sliding mode control. But for limited actuator capability the maximum control gain and the minimum thickness of boundary layer being allowed may be restricted.

Disturbance accommodating control is a signal synthesis adaptive control. For a short time interval the disturbance is assumed to be modeled by a linear combination of previously selected basis functions. A disturbance accommodating observer can be used to identify unmeasurable internal and external disturbances. In this paper, sliding mode control is combined with disturbance accommodating control (i.e., Disturbance Accommodating Sliding Mode Control) in terms of modified Rodrigues parameters for a spacecraft attitude regulation and tracking maneuvers. The presented disturbance accommodating sliding mode control has the following advantages: 1) the design procedure is more effective than the traditional sliding surface stabilizing problem since steady-state errors are reduced, 2) the designed disturbance accommodating observer is linear, and 3) the robustness of sliding mode is guaranteed in the range of actuator capability. Simulation results are shown that use the disturbance accommodating sliding mode control to reduce steady-state errors in the case of applied external disturbances.

## INTRODUCTION

Spacecraft attitude control for large-angle slewing maneuver poses a difficult problem, including the nonlinear characteristics of the governing equation, modeling

\*Graduate Student, Dept. Mechanical Eng., The Catholic University of America, 73gim@pluto.ee.cua.edu

†Associate Professor, Dept. Aerospace Eng., Inha University, Inchon, Korea, jhkim@dragon.inha.ac.kr

‡Assistant Professor, Dept. Mechanical Eng., The Catholic University of America, jlc@pluto.ee.cua.edu

uncertainty and unexpected external disturbances. Sliding mode (variable structure) control provides robustness with respect to modeling errors and is an effective method for handling the nonlinear characteristics for attitude control. Variable structure control for multi-axial spacecraft attitude maneuvers was first presented by Dwyer and Rammirez.<sup>1</sup> In their paper, the sliding surface is defined by the Rodrigues parameters (gibbs vector). The Rodrigues parameters provide a minimal (i.e., three-dimensional) parameterization. However, the Rodrigues parameters have a singularity for 180 deg rotations. Vadali presented an optimal sliding manifold using error quaternions.<sup>2</sup> For large angle maneuvers, quaternion feedback was presented by Wie and Barba.<sup>3</sup> A quaternion feedback regulator was also presented by Wie, Weiss and Arapostathis.<sup>4</sup> Quaternions are nonsingular for any rotation, however, the use of quaternions requires an extra parameter that leads to a nonminimal parameterization. Crassidis and Markley developed a sliding mode controller for regulation and tracking problems of spacecraft attitude control based on the modified Rodrigues parameters.<sup>5</sup> The advantages of using modified Rodrigues parameters include the following: 1) rotations up to 360 deg are possible, and 2) the parameters form a minimal parameterization.<sup>5</sup> Therefore, in this paper, sliding mode control based on modified Rodrigues parameters is adopted. All of the above control laws are robust with respect to variations in the moment of inertia tensor on the order of 10 - 20 %.<sup>6</sup>

One of the drawbacks of sliding mode control is the chattering problem due to disturbance and modeling imprecision. For spacecraft attitude control, chattering may excite the higher frequencies of spacecraft and cause structural failure. Chattering can be settled by smoothing the control input using boundary layer or bandwidth-limited sliding mode control, which was presented by Dwyer and Kim<sup>7</sup>. However, a globally suitable boundary layer thickness cannot be easily determined. Moreover, for spacecraft attitude control it may be difficult to predict the external disturbances acting on body. When bounded unmodeled external torques are added, the closed-loop system is no longer globally asymptotically stable since a steady-state error is present. The error can be minimized by increasing the correction control gain or decreasing the thickness of boundary layer of sliding mode control. In this paper we derive this relation using a Lyapunov function. But for limited actuator capability the maximum correction control gain and the minimum thickness of boundary layer being allowed may be restricted. Though the steady-state errors are usually small, in a high-precision attitude pointing or tracking systems, these errors may not be tolerable for satisfying a mission requirement.

In this paper, we adopt disturbance accommodating control to minimize steady-state errors in sliding mode control. The disturbance accommodating control concept was first proposed by Johnson.<sup>9,10</sup> External disturbances  $w(t)$  are assumed to satisfy  $d^{m+1}w(t)/dt^{m+1} = 0$  differential equation where the external disturbances are represented as  $m$ th-degree polynomials in time  $t$  with unknown coefficients.<sup>10</sup> Design procedures and existence of the disturbance observer are presented in (Ref. 11, 12).



This is extended to internal disturbances arising from uncertain plant parameter variations in (Ref. 13). Some design examples are shown in (Ref. 14), and applied to the Hubble Telescope in (Ref. 15). A tutorial presentation of disturbance accommodating control is shown in (Ref. 16). In these papers, a disturbance accommodating observer is combined with a control method that provides linear behaviors in the responses of the systems. Advantages of using disturbance accommodating observer include the following: 1) it is linear, and 2) it also compensates the error due to modeling uncertainty.

Combining sliding mode control with a disturbance accommodating observer (i.e., Disturbance Accommodating Sliding Mode Control) was presented by Kim, and was applied to a robot manipulator for reducing the upper bound of bandwidth of sliding mode control.<sup>17</sup> In this paper sliding mode control based on modified Rodrigues parameters is adopted for spacecraft attitude control. Also, a disturbance accommodating observer is combined with sliding mode control for reducing steady-state errors due to external disturbances. Simulation results that use the disturbance accommodating sliding mode control to reduce the steady-state error are shown for the case of regulation and tracking maneuvers.

The organization of this paper proceeds as follows. First, a brief summary of the kinematics and dynamics of a spacecraft is presented. Then, a brief overview of the sliding mode control based on modified Rodrigues parameters is shown. Next, a robust analysis of the sliding mode control with respect to external disturbances is accomplished using a Lyapunov function. A disturbance accommodating observer is derived for reducing the steady-state error. Also, sliding mode control and disturbance accommodating observer are combined. Finally, simulation results are shown for regulation and tracking of a spacecraft.

## PROBLEM FORMULATION

In this section, a brief review of the kinematic equations of motion using modified Rodrigues parameters, the rigid body dynamics, and sliding mode control based on the kinematics is shown.

### Attitude Kinematics and Dynamics

The modified Rodrigues parameters are defined by<sup>5</sup>

$$\mathbf{p} \equiv \hat{\mathbf{n}} \tan (\theta / 4) \quad (1)$$

where  $\mathbf{p}$  is a  $3 \times 1$  vector,  $\hat{\mathbf{n}}$  is a unit vector corresponding to the axis of rotation and  $\theta$  is the angle of rotation. The kinematic equations of spacecraft attitude motion described in modified Rodrigues parameters are derived by using the spacecraft's angular velocity ( $\boldsymbol{\omega}$ ), given by<sup>5</sup>

$$\dot{\mathbf{p}} = 1/4 \left\{ \left( 1 - \mathbf{p}^T \mathbf{p} \right) I_{3 \times 3} + 2 [\mathbf{p} \times] + 2 \mathbf{p} \mathbf{p}^T \right\} \boldsymbol{\omega} \quad (2)$$

where  $\mathbf{p}^T$  is the transpose of  $\mathbf{p}$ ,  $I_{3 \times 3}$  is a  $3 \times 3$  identity matrix, and  $[\mathbf{p} \times]$  is a  $3 \times 3$  cross product matrix defined by

$$[\mathbf{p} \times] = \begin{bmatrix} 0 & -p_3 & p_2 \\ p_3 & 0 & -p_1 \\ -p_2 & p_1 & 0 \end{bmatrix} \quad (3)$$

The dynamic equation of motion for a rigid body with external disturbance ( $\mathbf{w}$ ) is given by Euler's equation, defined by

$$\dot{\boldsymbol{\omega}} = J^{-1} [J\boldsymbol{\omega} \times] \boldsymbol{\omega} + J^{-1} \mathbf{u} + J^{-1} \mathbf{w} \quad (4)$$

where,  $J$  is the spacecraft's inertia ( $3 \times 3$ ) matrix,  $J^{-1}$  is the inverse matrix of  $J$ , and  $\mathbf{u}$  is the control input torque ( $3 \times 1$ ) vector.

### Sliding Mode Control

In this paper it is assumed that measurements of both the spacecraft attitude and angular rate are available and the dynamics of actuator is neglected. The nonlinear model for spacecraft motion is summarized by<sup>5</sup>

$$\dot{\mathbf{p}} = F(\mathbf{p}) \boldsymbol{\omega} \quad (5)$$

$$\dot{\boldsymbol{\omega}} = \mathbf{f}(\boldsymbol{\omega}) + J^{-1} \mathbf{u} + J^{-1} \mathbf{w} \quad (6)$$

where

$$F(\mathbf{p}) \equiv 1/4 \left\{ (1 - \mathbf{p}^T \mathbf{p}) I_{3 \times 3} + 2 [\mathbf{p} \times] + 2 \mathbf{p} \mathbf{p}^T \right\} \quad (7)$$

$$\mathbf{f}(\boldsymbol{\omega}) \equiv J^{-1} [J\boldsymbol{\omega} \times] \boldsymbol{\omega} \quad (8)$$

Sliding mode control introduces velocity vector fields directed toward the sliding surface or manifold ( $\mathbf{s} = 0$ ) in its immediate vicinity, where  $\mathbf{s}$  is given by<sup>1</sup>

$$\mathbf{s} \equiv \boldsymbol{\omega} - \mathbf{m}(\mathbf{p}) \quad (9)$$

The quantity  $\mathbf{m}(\mathbf{p})$  is defined using a desired vector field from the kinematic equation, given by<sup>1</sup>

$$\mathbf{m}(\mathbf{p}) = F^{-1}(\mathbf{p}) \mathbf{d}(\mathbf{p}) \quad (10)$$

where

$$F^{-1}(\mathbf{p}) = 4 (1 + \mathbf{p}^T \mathbf{p}) \left\{ (1 - \mathbf{p}^T \mathbf{p}) I_{3 \times 3} + 2 [\mathbf{p} \times] + 2 \mathbf{p} \mathbf{p}^T \right\} \quad (11)$$

The quantity  $\mathbf{d}(\mathbf{p})$  is formed by allowing a linear behavior in the sliding motion, given by<sup>5</sup>

$$\mathbf{d}(\mathbf{p}) = \Lambda (\mathbf{p} - \mathbf{p}_d) \quad (12)$$

where  $\mathbf{p}_d$  is the desired reference trajectory and  $\Lambda$  is a diagonal matrix with negative elements. The input by sliding mode control is divided into two parts. The first is the equivalent control  $\mathbf{u}_{eq}$  for satisfying the ideal sliding mode conditions (i.e., invariant

conditions). The second is the correction control  $u_{cr}$  for satisfying the sliding mode existence conditions.<sup>1</sup> As a result, the control input is given by<sup>1</sup>

$$u = u_{eq} + u_{cr} \quad (13)$$

where

$$u_{eq} = -J \left\{ f(\omega) - \frac{\partial m}{\partial p} F(p) [m(p) + s] \right\} \quad (14)$$

$$u_{cr} = -JK \text{sat}(s, \epsilon) \quad (15)$$

where  $K$  is a  $3 \times 3$  positive definite diagonal matrix. The saturation function is used to minimize chattering in the control torques. The function is defined by

$$\text{sat}(s_i, \epsilon) \equiv \begin{cases} 1 & \text{if } s_i > \epsilon \\ s_i/\epsilon & \text{if } |s_i| \leq \epsilon \\ -1 & \text{if } s_i < -\epsilon \end{cases} \quad (16)$$

The detail descriptions of the quantities  $m(p)$  and  $\partial m/\partial p$  for the regulation and the tracking problems can be found in (Ref. 5).

## CONTROL DESIGN

In this section a robust analysis of the sliding mode control with respect to a external disturbance is accomplished using a Lyapunov function. A disturbance accommodating observer is also derived for reducing the steady-state error. Finally sliding mode control and disturbance accommodating observer are combined.

### Robust Analysis of Sliding Mode Control

We use the following candidate Lyapunov function  $V$  to study global stability of the motion by sliding mode control.<sup>8</sup>

$$V = \frac{1}{2} s^T J s \quad (17)$$

Define an error torque  $\Delta w$  using an estimated external disturbance  $\hat{w}$  and the actual external disturbance through<sup>8</sup>

$$\Delta w = \hat{w} - w \quad (18)$$

The first time derivative of the candidate Lyapunov function with the control input reduces to<sup>8</sup>

$$\dot{V} = -s^T JK \text{sat}(s, \epsilon) - s^T \Delta w \quad (19)$$

Note that in the absence of an external disturbance estimation error, this system is guaranteed to be globally asymptotically stable. If bounded unmodeled disturbances are added, but not compensated for in the control law, the system is no longer asymptotically stable. If  $K$  is large enough so that  $s^T JK \text{sat}(s, \epsilon)$  is larger than  $s^T \Delta w$ , then

$\dot{V}$  is guaranteed to be negative. Substituting the control torque into the first time derivative of sliding function, the following dynamics is obtained<sup>8</sup>

$$\dot{s} = -K \text{sat}(s, \epsilon) - J^{-1} \Delta \mathbf{w} \quad (20)$$

We assume that the thickness of boundary layer  $\epsilon$  is sufficiently small and the correction control gain  $K$  is sufficiently large to keep the time derivative of Lyapunov function negative-definite with bounded external disturbances in the region of the outer boundary layer. In the boundary layer the dynamics of sliding function is given by

$$\dot{s} = -\frac{K}{\epsilon} s - J^{-1} \Delta \mathbf{w} \quad (21)$$

If the estimation error of external disturbance settles to a value and the sliding function  $s$  must settle to a finite constant steady-state value  $s_{ss}$ . Setting the derivative in the dynamics of sliding function to zero we obtain<sup>8</sup>

$$0 = -\frac{K}{\epsilon} s_{ss} - J^{-1} \Delta \mathbf{w} \quad (22)$$

Therefore the steady-state value of sliding function (i.e., tracking error) will converge to the following finite offset<sup>8</sup>

$$s_{ss} = -\frac{\epsilon}{K} J^{-1} \Delta \mathbf{w} \quad (23)$$

The tracking error will not converge to zero but to a finite offset. This offset can be reduced to fall within acceptable limits by decreasing the boundary layer thickness  $\epsilon$  or increasing the correction control gain  $K$ . However, decreasing the boundary layer or increasing the correction control gain will limit the error recovery performance by saturating the actuator or will cause high frequency chattering in the actuator.<sup>8</sup> For high-precision attitude tracking, this small error offset or the high gain may not be acceptable. The steady-state error can also be reduced by making  $\Delta \mathbf{w}$  smaller.

### Disturbance Accommodating Observer

The uncertainty associated with some internal and external disturbances  $\mathbf{w}(t)$  is represented by a semideterministic waveform-model description of the generalized spline-function type, given by<sup>16</sup>

$$\mathbf{w}(t) = \mathbf{c}_1 f_1(t) + \mathbf{c}_2 f_2(t) + \cdots + \mathbf{c}_m f_m(t) \quad (24)$$

where the basis functions  $f_1(t)$ ,  $f_2(t)$ ,  $\cdots$   $f_m(t)$  are completely known and the constant weighting coefficient vectors  $\mathbf{c}_1$ ,  $\mathbf{c}_2$ ,  $\cdots$   $\mathbf{c}_m$  are totally unknown and may jump in value from time to time. Without loss of generality, it is further assumed that the basis functions  $f_i(t)$  satisfy a linear differential equation. As a consequence, there exists a linear dynamical “state model” representation as follows:<sup>16</sup>

$$\dot{\mathbf{w}}(t) = \mathbf{H}(t) \mathbf{z} \quad (25)$$

$$\dot{\mathbf{z}} = D(t)\mathbf{z} + \sigma(t) \quad (26)$$

where  $H(t)$ ,  $D(t)$  are completely known and  $\sigma(t)$  is a vector of impulse sequences representing jumps in the  $\mathbf{c}_i$  which are sparse but otherwise totally unknown. The waveform and state models have been successfully used to represent plant model errors associated with the following items:<sup>16</sup>

1. coulomb and other complex forms of nonlinear damping
2. uncertain external input disturbances
3. plant parameter model errors
4. coupling effects in reduced-order state models

The basis functions can be chosen as power series in time  $t$  or as orthogonal polynomials commonly used in approximation theory.<sup>16</sup> The design procedure and the existence problem of the appropriate observer with the stabilizing gain was shown in (Ref. 12).

### Disturbance Accommodating Sliding Mode Control

In this paper we divide the control input into the equivalent control input  $\mathbf{u}_{eq}$  and the correction control input  $\mathbf{u}_{cr}$  of the sliding mode control and the disturbance accommodating control input  $\mathbf{u}_{dac}$  for canceling the effects of external disturbances.<sup>16,17</sup>

$$\mathbf{u} = \mathbf{u}_{eq} + \mathbf{u}_{cr} + \mathbf{u}_{dac} \quad (27)$$

After applying the control input to the dynamics of the sliding function, the dynamics and the disturbance model can be written in the following state-space form:<sup>16,17</sup>

$$\dot{\mathbf{s}} = J^{-1}\mathbf{u}_{cr} + J^{-1}\mathbf{u}_{dac} + J^{-1}\mathbf{w} \quad (28)$$

$$\dot{\mathbf{z}} = D(t)\mathbf{z} + \sigma(t) \quad (29)$$

$$\mathbf{w} = H(t)\mathbf{z} \quad (30)$$

The appropriate disturbance accommodating observer is given by<sup>12</sup>

$$\dot{\hat{\mathbf{z}}} = D(t)\hat{\mathbf{z}} - K_0(\mathbf{z} - \hat{\mathbf{z}}) \quad (31)$$

$$\dot{\hat{\mathbf{w}}} = H(t)\hat{\mathbf{z}} \quad (32)$$

where,  $K_0$  is the observer gain ( $9 \times 9$ ) matrix which provides sufficient time constants in the observer. We adopt the three basis functions as 1,  $t$ ,  $t^2$  for each body axis (i.e.,  $i = 1, 2, 3$ ).

$$w_i(t) = c_1 + c_2t + c_3t^2 \quad (33)$$

We assume that the time derivative of the jerk of external disturbance is zero (i.e.,  $d^3w_i(t)/dt^3 = 0$ ), so that  $H_i$ ,  $D_i$  are given by

$$H_i = \begin{bmatrix} 1 & 0 & 0 \end{bmatrix} \quad (34)$$

$$D_i = \begin{bmatrix} 0 & 1 & 0 \\ 0 & 0 & 1 \\ 0 & 0 & 0 \end{bmatrix} \quad (35)$$

All the matrices in the observer are constant, however, the observer in Eq. (31) cannot be directly implemented due to the unmeasurable state  $z$ . Define a new state variable  $Q$  as follows:<sup>17</sup>

$$Q = \hat{z} - K_1 s \quad (36)$$

where  $K_1$  is a gain matrix ( $9 \times 3$ ). The gain  $K_1$  can be tuned to satisfy the following condition:<sup>17</sup>

$$K_0 + K_1 H = 0 \quad (37)$$

Finally, the modified observer composed by the measurable or known states is derived as follows:<sup>18</sup>

$$\dot{Q} = (D + K_0)Q + (D + K_0)K_1 s - K_1 J^{-1}(u_{cr} + u_{dac}) \quad (38)$$

where the initial condition is given by  $Q(0) = -K_1 s(0)$ . Then, the estimation error dynamics becomes<sup>18</sup>

$$\Delta \dot{Q} - (D + K_0) \Delta Q = -\sigma(t) \quad (39)$$

where

$$\Delta Q = (\hat{z} - K_1 s) - (z - K_1 s) \quad (40)$$

If the gain  $K_0$  is large enough so that the error dynamics is stable and converges fast, then the tracking error offset is reduced. The designed observer is linear and it can be easily implemented in digital software. One of drawbacks of the observer is that the sensor noise is amplified by the gain at the output of the observer. In this case we cannot use the reduced observer form, and have to implement a observer to estimate the state  $s$ .

A brief description of the control and system is shown in Figure 1. The estimated states  $\hat{z}$ ,  $\hat{w}$  and  $u_{dac}$  are calculated by the following relation:<sup>16,17</sup>

$$\hat{z} = Q + K_1 s \quad (41)$$

$$\hat{w} = H \hat{z} \quad (42)$$

$$u_{dac} = -\hat{w} \quad (43)$$

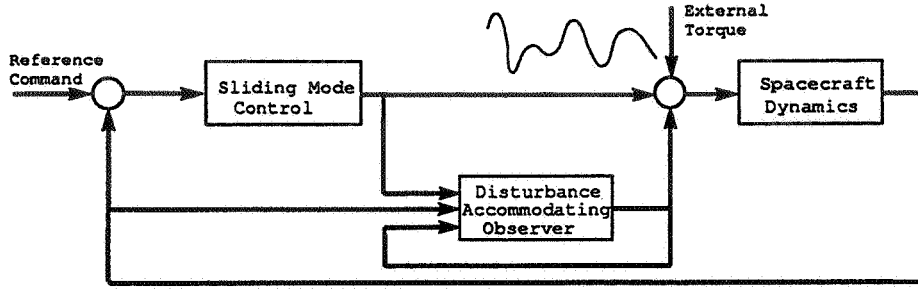


**Figure 1 System Block Diagram**

## **SIMULATION**

The inertia matrix of the simulated spacecraft is given by<sup>5</sup>

$$J = \text{diag} \begin{bmatrix} 114 & 86 & 87 \end{bmatrix} [kg \ m^2] \quad (44)$$

The initial conditions for the angular velocity are set to zero. The boundary layer thickness  $\epsilon$  in the saturation controller is set to 0.01.<sup>5</sup> Also, the control torques are limited to 1.0 N-m.<sup>5</sup> The simulations are performed by Runge-Kutta 5 method in simulink in MATLAB with a maximum step size of 1 sec, minimum step size of 0.0001 sec and a tolerance  $1.0 \times 10^{-6}$ . The external disturbances applied to each body axis are set to  $0.3 \sin(t/10)$  N-m. The observer gain  $K_{0i}$  for each body axis (i.e.,  $i = 1, 2, 3$ ) is calculated using a pole-placement method as the following:

$$K_{0i} = \begin{bmatrix} -30.0 & 0 & 0 \\ -300.0 & 0 & 0 \\ -1000.0 & 0 & 0 \end{bmatrix} \quad (45)$$

Simulation cases for the regulation and tracking problems are given by

1. Case A: Sliding Mode Control without the external disturbances
2. Case B: Sliding Mode Control with the external disturbances
3. Case C: Disturbance Accommodating Sliding Mode Control with the external disturbances

## **Regulation**

The initial conditions for the modified Rodrigues parameters are given by

$$p(0) = \begin{bmatrix} -0.1 & 0.5 & 1.0 \end{bmatrix}^T \quad (46)$$

The rotation for the initial conditions is approximately 206 deg. The diagonal elements of the correction control gain  $K$  are all set to 0.0015 and the constant  $\lambda$

(the diagonal term of  $\Lambda$ ) is set to  $-0.015 \text{ sec}^{-1}$ . The sliding function trajectories of modified Rodrigues parameters for each case are shown in Figure 2. As shown in Figure 2, the trajectory of Case B oscillates in the boundary layer. In Case C, when disturbance accommodating sliding mode control applied the trajectory is almost the same as the one of Case A. The estimation errors,  $\Delta \mathbf{w}$ , are shown in Figure 3. The maximum estimation errors for each body axes are smaller than 1.7 % with respect to the maximum external torques.

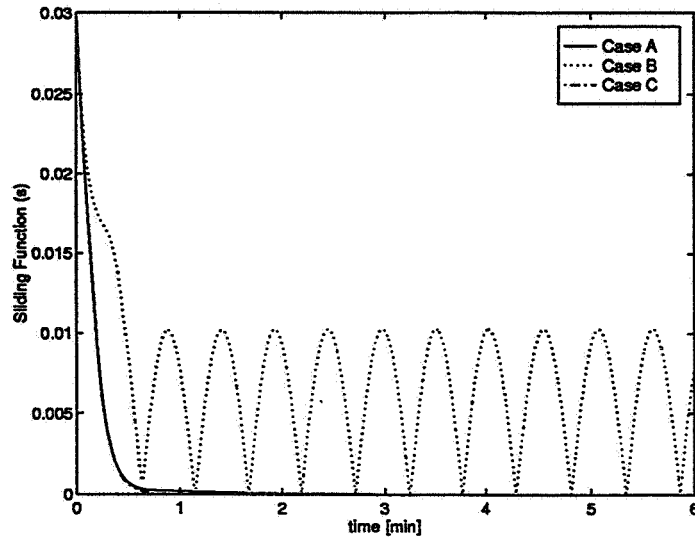


**Figure 2 Regulation: Sliding Function Trajectories**

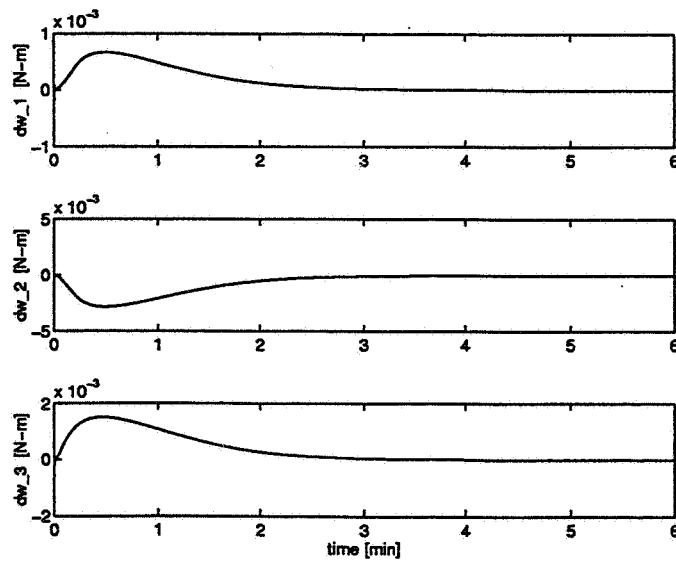


**Figure 3 Regulation: Estimation Errors  $\Delta \mathbf{w}$**



## Tracking

The initial conditions for the angular velocity and the modified Rodrigues parameters are set to zero. The diagonal elements of the correction control gain  $K$  are set to 0.03 and the constant  $\lambda$  is set to  $-0.3 \text{ sec}^{-1}$ . The desired trajectories of modified Rodrigues parameter  $\mathbf{p}_d$  are given by

$$p_{d1} = 0.05 \sin(0.005t) \quad (47)$$

$$p_{d2} = 0.05 \sin(0.006t) \quad (48)$$

$$p_{d3} = -0.05 \sin(0.007t) \quad (49)$$

The sliding function trajectories for each case are shown in Figure 4. As shown in Figure 4, the trajectory of Case B oscillates up and down through the trajectory of Case A. In Case C, when disturbance accommodating sliding mode control applied the trajectory is almost the same as the one of Case A. The estimation errors,  $\Delta \mathbf{w}$ , are shown in Figure 5. The maximum estimation errors for each body axes are smaller than 17 % with respect to the maximum external torques.

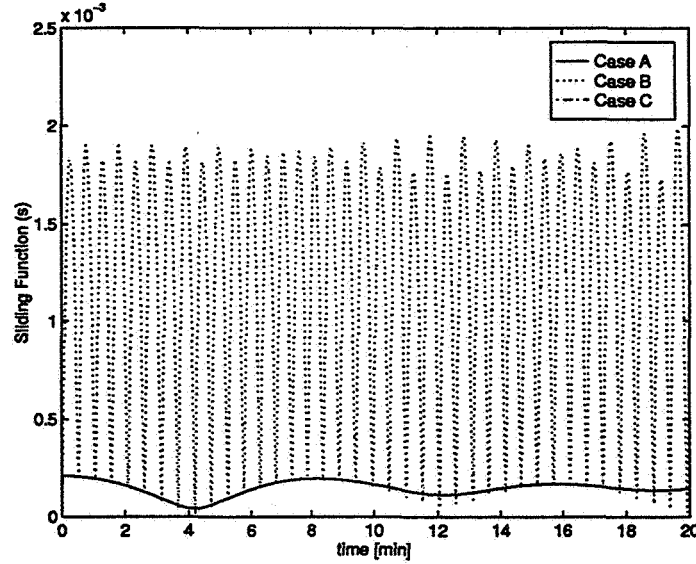
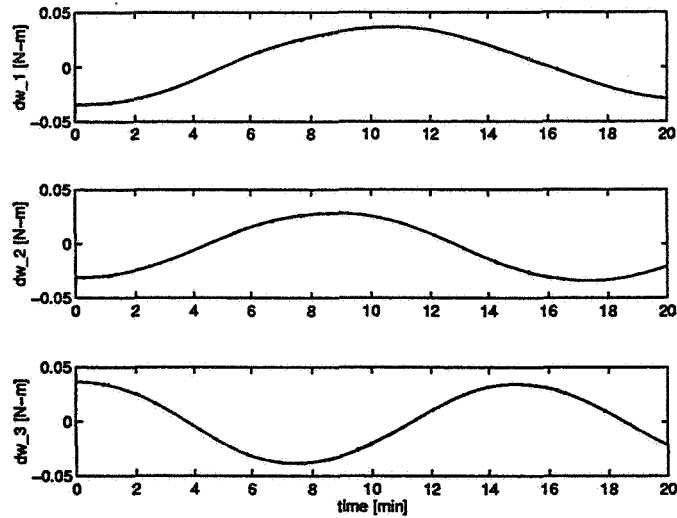


Figure 4 Tracking: Sliding Function Trajectories

## CONCLUSION

A method for compensating the steady-state error of sliding mode control due to external disturbance was presented and applied to spacecraft attitude maneuvers. The presented disturbance accommodating sliding mode control include the following advantages: 1) the design procedure is more effective than the traditional sliding surface stabilizing problem since steady-state errors are reduced, 2) the designed disturbance accommodating observer is linear allowing the use of many design and

analysis methods for linear systems, and 3) the robustness of sliding mode is guaranteed in the range of actuator capability. Simulation results indicate that the new algorithm was able to reduce the upper bound of the steady-state error.



**Figure 5 Tracking: Estimation Errors  $\Delta w$**

## REFERENCES

1. Dwyer, T. A. W., and Ramirez, H. S., "Variable-Structure Control of Spacecraft Attitude Maneuvers", *Journal of Guidance Control & Dynamics*, Vol. 11, No. 3, 1988, pp. 262 - 269.
2. Vadali, S. R., "Variable-Structure Control of Spacecraft Large-Angle Maneuvers", *Journal of Guidance Control & Dynamics*, Vol. 9, No. 2, 1986, pp. 235 - 239.
3. Wie, B., and Barba, P. M., "Quaternion Feedback for Spacecraft Large Angle Maneuvers", *Journal of Guidance Control & Dynamics*, Vol. 8, No. 3, 1985, pp. 360 - 365.
4. Wie, B., Weiss, H., and Arapostathis, A., "Quaternion Feedback Regulator for Spacecraft Eigenaxis Rotations", *Journal of Guidance Control & Dynamics*, Vol. 12, No. 3, 1989, pp. 375 - 380.
5. Crassidis, J. L., and Markley, F. L., "Sliding Mode Control Using Modified Rodrigues Parameters", *Journal of Guidance Control & Dynamics*, Vol. 19, No. 6: *Engineering Notes*, 1996, pp. 1381 - 1383.
6. McDuffie, J. H., and Shtessel, Y. B., "A Sliding Mode Controller and Observer for Satellite Attitude Control", *AIAA Conference 1997*, AIAA-97-3755, 1997, pp. 1613 - 1619.

7. Dwyer, T. A. W., and Kim, J., "Bandwidth-Limited Robust Nonlinear Sliding Control of Pointing and Tracking Maneuvers", Proc. of American Control Conference, Vol. 2, 1989, pp. 1131 - 1135.
8. Schaub, H., Robinett, R. D., and Junkins, J. L., "Adaptive External Torque Estimation by Means of Tracking a Lyapunov Function", The Journal of the Astronautical Sciences, Vol. 44, No. 3, Jul. - Sep., 1996, pp. 373 - 387.
9. Johnson, C. D., "Optimal Control of the Linear Regulator with Constant Disturbances", IEEE Transactions on Automatic Control, Aug. 1968, pp. 416 - 421.
10. Johnson, C. D., "Further Study of the Linear Regulator with Disturbances - The Case of Vector Disturbances Satisfying a Linear Differential Equation", IEEE Transactions on Automatic Control, Apr. 1970, pp. 222 - 228.
11. Johnson, C. D., "Accommodation of External Disturbances in Linear Regulator and Servomechanism Problems", IEEE Transactions on Automatic Control, Vol. Ac-16, No. 6, Dec. 1971, pp. 635 - 644.
12. Johnson, C. D., "On Observer for Systems with unknown and inaccessible Inputs", International Journal of Control, Vol. 21, No. 5, 1975, pp. 825 - 831.
13. Johnson, C. D., "Adaptive Controller Design using Disturbance Accommodation Technique", International Journal of Control, 1985, Vol. 42, No. 1, pp. 193 - 210.
14. Johnson, C. D., "Application of Linear Adaptive Control to Some Advanced Benchmark Examples", Proc. of American Control Conference, 1989, pp. 460 - 465.
15. Addington, S. I., and Johnson, C. D., "Dual-Mode Disturbance Accommodating Pointing Controller for Hubble Space Telescope", Journal of Guidance Control and Dynamics, Vol. 18, No. 2, Mar. - Apr. 1995, pp. 200 - 207.
16. Johnson, C. D., "A New Approach to Adaptive Control", Control and Dynamic Systems, Academic Press Inc., 1988, pp. 1 - 69.
17. Kim, J., "Disturbance Accommodating Sliding Mode Control", Proc. of American Control Conference, 1992, pp. 888 - 890.
18. Kim, J., and Kim, J., "Disturbance Accommodating Spacecraft Attitude Control Using Thruster", AIAA/AAS Astrodynamics Conference, 1996, pp. 800 - 805.



**Globally Asymptotically Stable Reorientation Controller with  
Control Constraint and Slew Rate Limit**

**Dr. Hans Seywald\*, Dr. Renjith Kumar\*, Dr. Min Qu\***

**ABSTRACT**

This paper introduces a nonlinear reorientation and attitude controller based on feedback linearization. Besides user-prescribed maximum and minimum gain values, the controller requires no tuning, and is applicable to arbitrary rigid spacecraft configurations. The user needs to input only data pertaining to the physical problem setup, such as the spacecraft's inertia matrix, initial conditions, target orientation, target angular velocity, control constraint, and slew rate limit. Global asymptotic stability is guaranteed. The controller is computationally inexpensive, and numerical tests show excellent performance in terms of transient behavior and overall maneuver time.

---

\* Analytical Mechanics Associates



513-13  
169295  
AAS 98-312  
161.  
337577

## IMPROVEMENT OF ORBIT DETERMINATION AND PREDICTION ACCURACY OF ADEOS/RIS

Mina Ogawa<sup>†</sup>, Maki Maeda<sup>†</sup>, Mikio Sawabe<sup>†</sup>, Masao Hirota<sup>†</sup>,  
and Yousuke Yamamoto<sup>††</sup>

The Advanced Earth Observing Satellite (hereafter ADEOS) was launched on August 17th, 1996 and its operation was terminated on the end of June 1997. The ADEOS carries a large aperture laser-reflector, referred as "Retroreflector-In-Space"(RIS). In order to hit laser properly onto the RIS, we need a trajectory prediction with accuracy of about 100 m. The flight-dynamics team at the NASDA/TACC (Tracking and Control Center) ordinarily derives a satellite trajectory with Range and Range Rate (RARR) measurements using S-band radio wave. However, the trajectory prediction is expected to be only as accurate as 1 km for the ADEOS. This uncertainty is not acceptable for the RIS.

Although the operation of the ADEOS was terminated, NASDA keeps on making every effort to improve the accuracy of trajectory determination and propagation of the ADEOS/RIS with Satellite Laser Ranging (SLR) data obtained at world-wide SLR ground stations. As a result, we achieved a hundred-fold and a ten-fold improvement on accuracy of orbit determination and prediction respectively.

This paper presents the summary of the experiment and the latest results. A brief discussion of the post-ADEOS mission plan will be found in this paper as well.

### INTRODUCTION

Satellite laser ranging (SLR) measurement with a pulse laser beam is one of means for measuring a distance between a ground station and a satellite. SLR measurement provides more accurate trajectory than that derived from the Range and Range Rate (RARR) measurement with radio wave.

The Advanced Earth Observing Satellite (ADEOS), launched into space on August 17, 1996, by National Space Development Agency of Japan (NASDA), and its operation was terminated on the end of June 1997. One of the sensors on board the ADEOS is a hollow laser reflector called Retroreflector-In-Space (RIS) (see Figure 1) provided by the Japanese Environment Agency (EA).

---

<sup>†</sup> National Space Development Agency of Japan (NASDA), Sengen 2-1-1, Tsukuba, Ibaraki, 305-8505, Japan

<sup>††</sup> Fujitsu Limited, Nakase 1-9-3, Mihama-ku, Chiba-shi, Chiba, 261-8588, Japan

The effective diameter of the RIS is 0.5 m (see Figure 1) and the large surface area enables it to reflect back a large fraction of energy throughput of a laser beam from a ground station without being suffered from satellite jittering. The ADEOS/RIS is originally designed to measure absorption spectrum in a reflected laser beam due to a small amount of Ozone, Methane, and other compounds found in the atmosphere. With the RIS on board the ADEOS, we plan to develop a prototype scheme of advanced trajectory determination system for future NASDA satellite missions. The finalized scheme, called "Global and high accUracy Trajectory determination System" (GUTS) will be designed to utilize both SLR and differential GPS (Global Positioning System) measurement, and would be able to derive a satellite orbit within a accuracy of 25 cm when a satellite is in orbit at altitude of about 800 km. The finalized scheme will be in operation by the year of 2003. Final goal of our system is a accuracy of 20 cm using SLR short arc data obtained multi-stations' simultaneously.

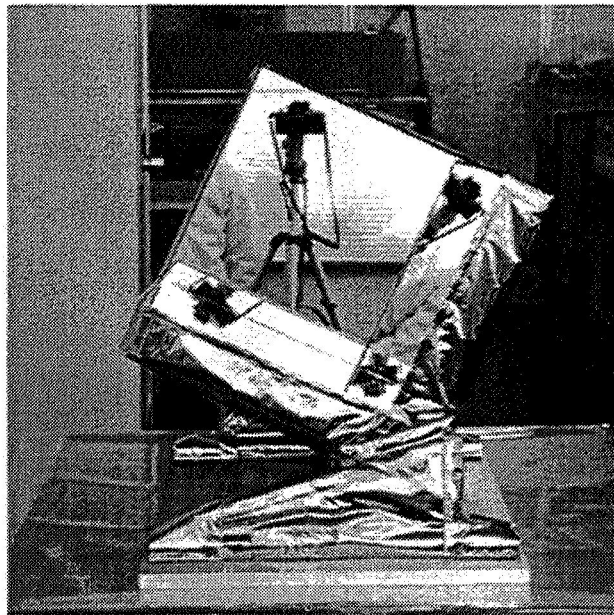


**Figure 1 Retroreflector-In-Space**

In this paper we discuss the following items:

- Data delivery system for the ADEOS/RIS.
- Observations with the ADEOS/RIS.
- Accuracy of trajectory determination using long arc data.
- Accuracy of trajectory prediction.
- Effects on accuracy of trajectory determination by each observation and force model.
- Comparison of trajectory determination accuracy using SLR data and using RARR data.



## DATA DELIVERY SYSTEM FOR THE ADEOS/RIS

In order to point a laser beam accurately to the RIS, we must provide high precision orbital parameters to a designated SLR station. Currently uncertainty of a satellite's position must be as small as 100 m for a successful SLR observation, and the orbital solution is also expected to be valid as long as a time interval of 3 days.

As a mean to deliver such a high precision trajectory ephemeris, the NASDA and the Communication Research Laboratory (CRL) have established a data delivery link for the ADEOS/RIS experiment (Figure 2). The CRL is responsible for distributing and archiving of every SLR data taken with the ADEOS/RIS, while the NASDA develops a scheme for estimating accurate trajectory of the ADEOS satellite and predicting its position prior to the next RIS observation.

First, SLR data obtained at SLR stations around the world (Figure 3) are collected at the CRL through E-mail and/or anonymous file transfer protocol (FTP) via Internet. Second, all of the SLR data are automatically transmitted to the Tsukuba Space Center (TKSC), NASDA, via the Earth Observation Center (EOC), NASDA, by using also E-mail and FTP through a network dedicated for this purpose (the data transfer rate is about 1.5 Mbps).

Then, after accumulating sufficient amount of the SLR data, the NASDA analyzes all of the collected data and make available estimated satellite's orbital parameters with high precision prior to the next SLR measurement.

These parameters are provided in a standard format for transferring Tuned Interrange Vector (TIRV) and time bias function. TIRV contains orbital elements estimated at a certain epoch, and predicted orbital elements derived at every 0 UTC. Time bias function is defined as a difference expressed in terms of time between the latest estimated orbital element and the latest observation. Using these information, SLR station is tracking the spacecrafts.

The predicted orbital positions are weekly transmitted back from the NASDA to each SLR station in a reverse order of the passage mentioned above. TIRV is derived once per week and time bias function is derived two times per week<sup>1</sup>.

If the SLR data collected in one week are not enough to determine the ADEOS orbit, TIRV should be derived from RARR measurement with S-band radio wave or 2-line elements received from the GODDARD Space Flight Center, NASA.

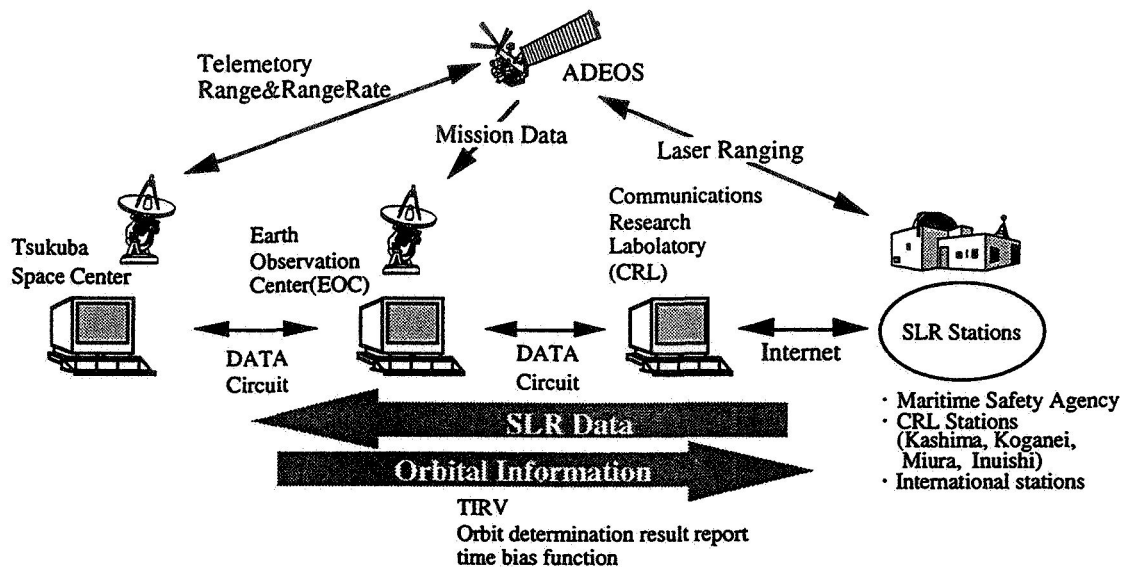


Figure 2 ADEOS/RIS Delivery Network System

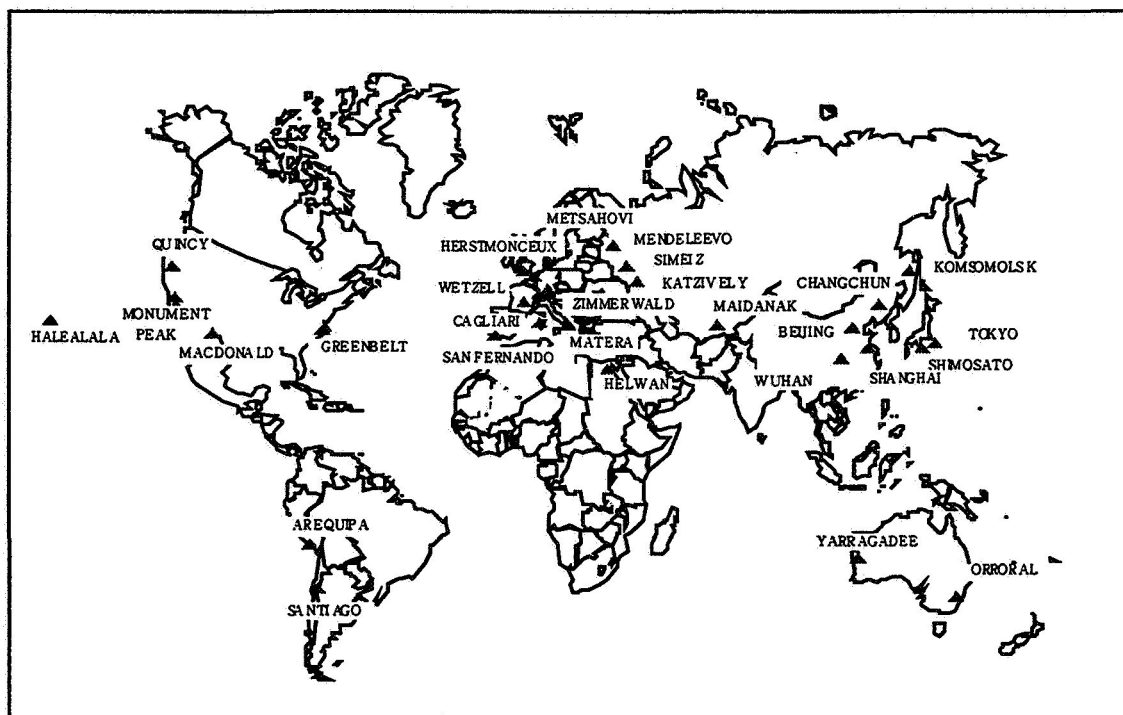


Figure 3 ADEOS/RIS SLR Network

## OBSERVATION WITH THE ADEOS/RIS

We have been collecting the ADEOS/RIS SLR data since October 30, 1996. The collected data number as of April 1, 1998, are 762 passes from 28 SLR stations, including 5 passes obtained after the end of ADEOS's operation. Some of the data were gathered from NASA Crustal

amics Data Information System (CDDIS). Those data were not used for tracking ADEOS/RIS only for analyses. Table 1 shows the summary of the ADEOS/RIS data obtained at each SLR on, from October 30, 1996 to June 30, 1997 and after the termination of the ADEOS operation.

**Table 1**  
**SUMMARY OF THE ADEOS/RIS DATA**

STATION ID	STATION NAME	1996.10.30-1997.6.30		1997.7.1-		AVERAGE of RMS(mm)*
		NUMBER of PASSES	NUMBER of DATA	NUMBER of PASSES	NUMBER of DATA	
1864	MAIDANAK	25	192			138.0
1868	KOMSOMOLSK	15	61			58.1
1870	MENDELEEVO	44	279	1	4	75.3
1873	SIMEIS	7	37			28.0
1893	KATSIVELY	2	9			12.3
7080	FORT DAVIS	17	85			17.5**
7090	YARAGADEE	8	50			8.6
7105	WASHINGTON	22	142	1	12	10.1**
7109	QUINCY	4	23			7.3**
7110	MONUMENT PEAK	47	242			9.0
7210	MAUI	13	66			10.1
7236	WUHAN	1	4			8.9
7237	CHANGCHUN	52	414			58.6
7249	BEIJING	38	271			46.2
7308	TOKYO	7	68			53.1
7403	AREQUIPA	13	53			8.7
7404	TLRS-2(SANTIAGO)	1	6			33.3
7548	CAGLIARI	11	55			14.7
7805	METSAHOVI	52	390	1	3	33.1
7810	ZIMMERWALD	1	15			1.0
7824	SAN FERNANDO	43	447	1	6	50.5
7831	HELWAN	1	10			25.3
7837	SHANGHAI	5	18			36.5
7838	SIMOSATO	48	578			33.9
7840	HERSTMONTCHIEUX	126	579	1	1	9.9
7843	CANBERRA	84	564			8.4
7939	MATERA	30	172			84.6
8834	WETTZELL	40	360			2.6
TOTAL		757	5190	5	26	

\* Average of RMS of normal point data

\*\* after data rejection

## TRAJECTORY DETERMINATION AND PREDICTION

### Trajectory Accuracy Improvement

The NASDA keeps on improving the accuracy of orbit determination and prediction of the ADEOS/RIS by updating the software models of the ADEOS/RIS analysis system. At first, we applied Tropospheric refraction correction<sup>2</sup>, center of mass correction, and GEM-T3 which is more accurate geopotential model than that for the ADEOS routine operation ( Ref. 3, 4 ), and achieved a ten-fold improvement on accuracy of trajectory determination. For further improvement, we applied much more accurate geopotential model JGM-3 and earth radiation pressure, and reduced the uncertainty of SLR station position.

In this chapter, the latest models and results of the ADEOS/RIS trajectory determination and prediction will be reported.

### Condition of Trajectory Determination and Prediction

We determined the ADEOS/RIS trajectory using a few days data arc with about one day of overlap between data arcs (Figure 4). During the ADEOS/RIS operation, the NASDA used 3 days data arc and 0.5 days of overlap. Estimated parameters are an orbital element, solar radiation pressure modification rate  $\Gamma_1$ , and air drag modification rate  $\rho_1$ .

$$\rho_a = \rho_m(1 + \rho_1) \quad \rho_a: \text{actual atmosphere density} \quad \rho_m: \text{model atmosphere density}$$

$$\Gamma_a = \Gamma_m(1 + \Gamma_1) \quad \Gamma_a: \text{actual solar radiation pressure} \quad \Gamma_m: \text{model solar radiation pressure}$$

The NASDA used the NASDA Orbit Computing System ( NOCS on a main frame or NOCS2 on EWSs ) for the ADEOS routine operation, and uses proto-type GUTS for the ADEOS/RIS analysis. Parameters and software models considered in the ADEOS operation and our analysis are shown in Appendix A. The conditions of trajectory determination are mostly according to the ADEOS/RIS Tracking Standards <sup>1</sup> and the IERS standards 1992<sup>5</sup>.

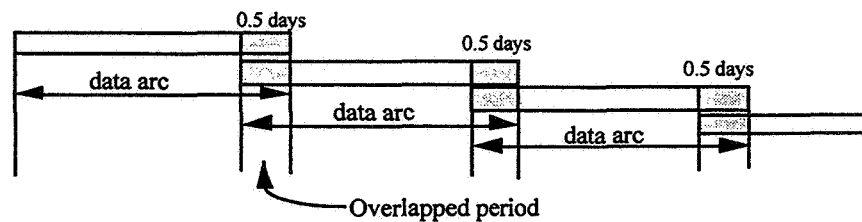


Figure 4 Data Span for Trajectory Determination (long arc)

### Accuracy of Trajectory Determination using Long Arc Data

We investigate accuracy of trajectory determination by comparing orbits during time span where one data arc and the next data arc overlap, since a trajectory of a spacecraft must be continuous. In order to get enough pass in the period of overlap between data arcs, in this section we use 4 days data arc with 1 day of overlap. Table 2 shows sample of SLR data taken with the ADEOS/RIS, its O-C and the estimated value of  $\rho_1$  and  $\Gamma_1$  scale factor parameters using the latest and full software models. Table 3 shows the accuracy of trajectory determination, and Figure 5 shows the difference between the trajectory derived from arc No. 1 and that from arc No. 2.

The uncertainty for a trajectory position in the along track is determined to be about 0.4 to 2 meters for the ADEOS (Table 3). A similar analysis conducted using 3.5 days data arc with 0.5 days of overlap resulted in 20 to 75 meters as uncertainty in the along track (Ref. 4). So, we can say that we achieved a ten-fold improvement on accuracy of trajectory determination from former analysis in Reference 4.

**Table 2**  
**DATA SPAN, O-C RMS AND ESTIMATED PARAMETERS**

Arc No.	Start (UTC)	End (UTC)	Pass	Site	Data	O-C RMS(m)	$\rho_1$	$\Gamma_1$
1	1996/10/30 3h	1996/11/02 12h	15	8	101	0.303	0.301	0.449
2	1996/11/02 3h	1996/11/05 11h	10	7	61	0.210	0.298	0.408
3	1996/11/05 8h	1996/11/08 21h	14	8	83	0.366	0.350	0.440
4	1996/11/08 2h	1996/11/11 19h	16	8	100	0.232	0.410	0.492

**Table 3**  
**ACCURACY OF TRAJECTORY DETERMINATION**

Arc No.	Overlap span (UTC)				Difference in Position(m)			
	Start (UTC)	End (UTC)	Pass	Site	Radial	Along Track	Cross Track	RSS
1-2	1996/11/02 0h - 1996/11/03 0h		3	3	0.130	0.446	0.275	0.540
2-3	1996/11/05 0h - 1996/11/06 0h		2	2	0.725	2.022	1.323	2.523
3-4	1996/11/08 0h - 1996/11/09 0h		5	5	0.126	0.402	1.392	1.454

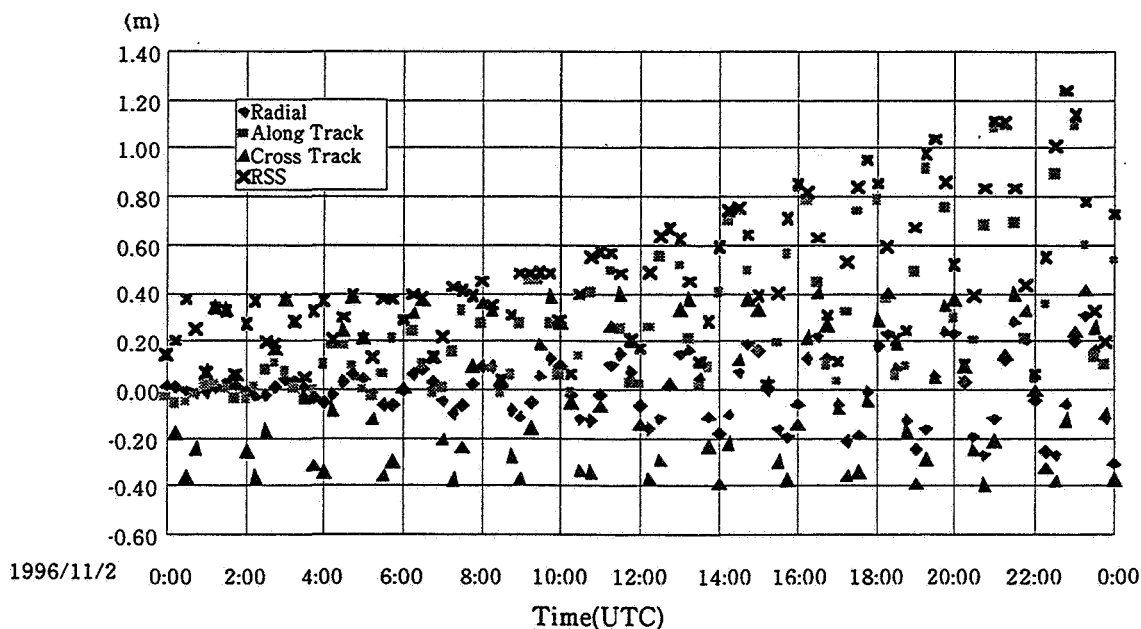


**Figure 5 Comparing orbits during the overlapped period**

### Accuracy of Trajectory Prediction

We use orbital parameters determined with 4 days arc data (Table 2) in order to investigate an error of a trajectory prediction. For an example, difference between orbital parameters in the data arcs No. 1 and No. 2 is defined as an error of trajectory prediction for the next three days, and difference between No. 1 and No. 3 is defined as an error for the next six days (see Figure 6). This scheme provides prediction errors for a total of 9-days period.

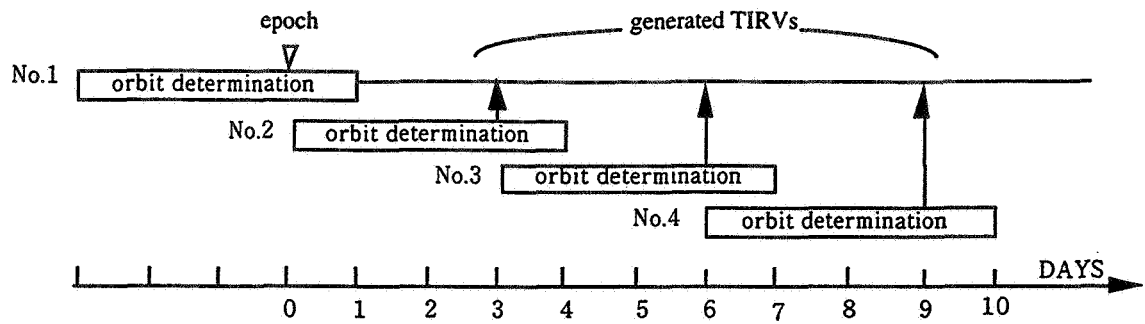


**Figure 6 Scheme for estimating an error of trajectory prediction**

In Table 4, one of examples for the error estimate is shown. "Epoch" is the point which evaluate two orbital element and that is the epoch of determined orbital element, too.

The orbit predicted from the orbital element No. 1 differs about 2.6 m from the orbital element No. 2. In other words, the prediction accuracy is 2.6 m in three days. Although the other data show different values in the accuracy, the values are constantly under 30 meters that satisfies our main requirement for a successful SLR measurement. However, we must note that this result is only accurate for a period of low solar activity.

**Table 4**  
**DIFFERENCE BETWEEN PREDICTED ORBIT AND REFERENCE ORBIT (m RMS)**

Epoch	Reference orbit	Predicted orbit from No.1	Predicted orbit from No.2	Predicted orbit from No.3
1996/11/02 0h	No.1	-	0.152	8.117
1996/11/05 0h	No.2	2.551	-	2.223
1996/11/08 0h	No.3	9.416	26.595	-
1996/11/11 0h	No.4	83.425	98.300	12.713

#### **Effects on Accuracy of Trajectory Determination by Each Observation and Force Model**

In order to confirm effects of both various force and observation models, we choose several case studies (see Table 5). For the other models, for example, solar radiation pressure model, air drag model and tidal effect comparing, please see Reference -4. From O-C and difference of position and velocity of each case, we evaluate a degree of effects on trajectory determination by each model.

**Table 5**  
**SELECTED CASES FOR STUDYING EFFECTS OF VARIOUS MODELS**

case No.	a	b	c	d	e
earth gravity model	A	B	A	A	A
center of mass correction	○	○	×	○	○
earth radiation pressure	○	○	○	×	○
tropospheric reflection model	○	○	○	○	×

A: JGM-3 B: GEM-T3 ○: considered ×: not considered

All of the significant observation and force models are considered in the case a. In cases from b to e, one of the models is omitted from modeling for trajectory determination. Since, the case a should define the best O-C RMS value (provided that all the selected model is defined accurately), exclusion of one of the selected models should result in a larger value for the O-C RMS and a degree of its derivation of the O-C RMS from the case a may be used as a sensitive indicator for determining the importance of the excluded model.

Table 6 shows O-C RMS and estimated parameters  $\rho_1$  and  $\Gamma_1$ , of data arc No. 1 and arc No. 2 for each case. Table 7 and table 8 show the accuracy of trajectory determination and prediction respectively.

**Table 6**  
**O-C RMS, ESTIMATED  $\Gamma_1$  AND  $\rho_1$**

Arc No.	Case No.	Start (UTC)	End (UTC)	Pass	Site	Data	O-C RMS(m)	$\rho_1$	$\Gamma_1$
1	a	1996/10/30 3h	1996/11/02 12h	15	8	101	0.303	0.301	0.449
1	b	1996/10/30 3h	1996/11/02 12h	15	8	101	2.090	0.209	0.370
1	c	1996/10/30 3h	1996/11/02 12h	15	8	101	0.439	0.304	0.438
1	d	1996/10/30 3h	1996/11/02 12h	15	8	101	0.304	0.296	0.359
1	e	1996/10/30 3h	1996/11/02 12h	15	8	101	1.845	0.287	0.534
2	a	1996/11/02 3h	1996/11/05 11h	10	7	61	0.210	0.298	0.408
2	b	1996/11/02 3h	1996/11/05 11h	10	7	61	0.730	0.362	0.431
2	c	1996/11/02 3h	1996/11/05 11h	10	7	61	0.360	0.295	0.391
2	d	1996/11/02 3h	1996/11/05 11h	10	7	61	0.209	0.293	0.314
2	e	1996/11/02 3h	1996/11/05 11h	10	7	61	2.037	0.298	0.421

**Table 7**  
**DIFFERENCES IN TRAJECTORY POSITION DURING THE OVERLAPPED PERIOD**

Case No.	Radial	Along Track	Cross Track	RSS
a	0.130	0.446	0.275	0.540
b	0.939	2.152	0.672	2.442
c	0.117	0.654	0.121	0.675
d	0.223	0.495	0.095	0.551
e	0.370	1.846	0.375	1.920

**Table 8**  
**POSITION ERROR OF TRAJECTORY PREDICTION FOR THREE DAYS**

Case No.	Radial	Along Track	Cross Track	RSS
a	0.937	2.325	0.476	2.551
b	-1.145	-38.503	-1.107	38.536
c	0.745	5.034	0.241	5.094
d	0.902	2.726	0.194	2.878
e	2.684	-14.868	0.171	15.109

Figure 7 shows the difference in position between the trajectory derived being corrected the center of mass and that not being corrected. According to the figure 7, the difference in the along track is about 2 meters that is corresponding to the center of mass offset.

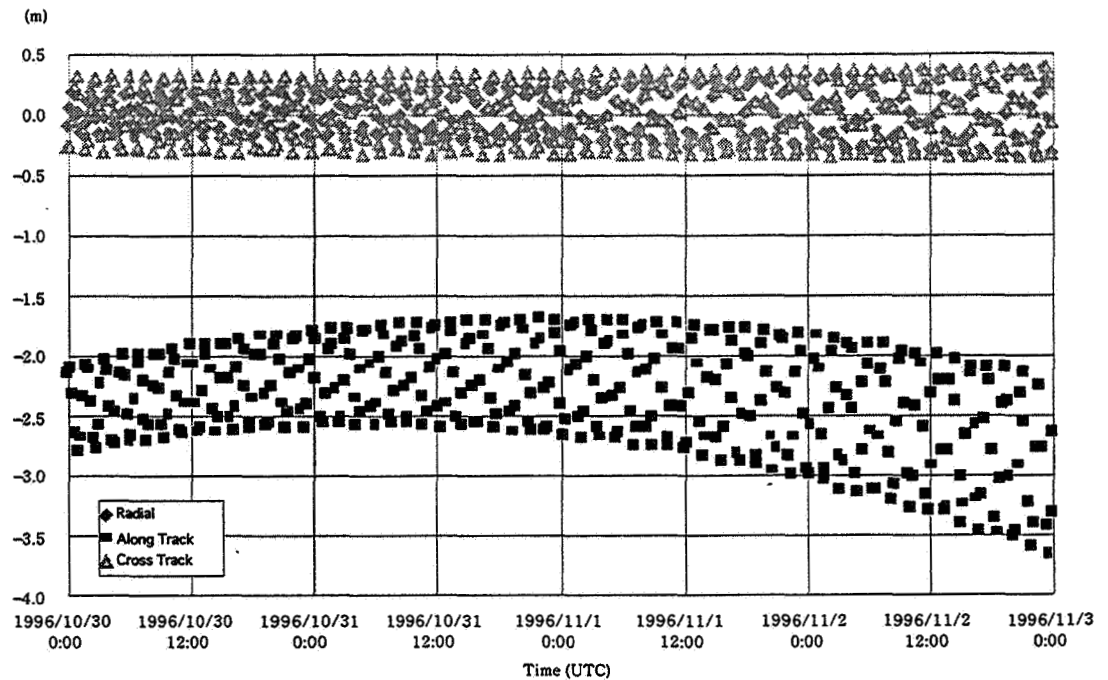


**Figure 7 Difference in position  
( Center of mass corrected VS Center of mass not corrected)**

Uncertainty for the earth radiation pressure model has only a minor impact to O-C RMS. The acceleration by the earth radiation pressure model is so small that the effect may included in the accuracy of trajectory determination by this ADEOS/RIS analysis system.

When all the models considered, O-C RMS is 0.5m to 2.5m, therefore, the position accuracy may be 10 meters or better.

#### **Comparison of Trajectory Determination Accuracy using SLR Data and using RARR Data**

In this section, we discuss accuracy of determined and predicted trajectories using SLR data or RARR data. The solution obtained by the RARR measurement with S-band radio wave were provided to all the ADEOS users together with the ADEOS mission data during the ADEOS operation period. Using the SLR data and the RARR data in table 9, we estimated the ADEOS/RIS trajectory with the conditions showed in Appendix. Table 10 and table 11 illustrate difference in position between those solutions. The difference grows at a alarming rate as each arc passes, which implies that a larger error may propagate through the RARR method.



**Table 9**  
**SELECTED SLR DATAARC AND RARR DATAARC**

SLR					RARR				
Arc No.	Start(UTC)		End(UTC)		Arc No.	Start(UTC)		End(UTC)	
1S	1996/10/30	3h	1996/11/02	12h	1R	1996/10/31	0h	1996/11/02	18h
2S	1996/11/02	3h	1996/11/05	11h	2R	1996/11/03	1h	1996/11/05	18h
3S	1996/11/05	8h	1996/11/08	21h	3R	1996/11/05	1h	1996/11/07	20h
4S	1996/11/08	2h	1996/11/11	19h	4R	1996/11/08	2h	1996/11/10	19h

**Table 10**  
**DIFFERENCE IN TRAJECTORY POSITIONS**  
**( DERIVED FROM THE RARR VS DERIVED FROM SLR)**

Arc No.	Time Span (UTC)		Difference in Position (m)			
	Start(UTC)	End(UTC)	Radial	Along Track	Cross Track	RSS
1S vs 1R	1996/10/31 0h	- 1996/11/03 0h	6.166	22.259	12.274	26.156
2S vs 2R	1996/11/03 0h	- 1996/11/06 0h	7.753	19.385	14.346	25.332
3S vs 3R	1996/11/05 0h	- 1996/11/08 0h	6.629	16.054	16.301	23.82
4S vs 4R	1996/11/08 0h	- 1996/11/11 0h	5.647	28.679	21.716	36.413

**Table 11**  
**DIFFERENCE BETWEEN PREDICTED ORBIT AND REFERENCE ORBIT (m RMS)**

Epoch(UTC)	Reference orbit	Predicted orbit	Predicted orbit	Predicted orbit
		from 1R	from 2R	from 3R
1996/11/02 0h	1S	18.549	47.51	188.202
1996/11/05 0h	2S	156.699	16.78	18.446
1996/11/08 0h	3S	423.923	208.242	32.609
1996/11/11 0h	4S	822.053	640.769	150.481

## POST-ADEOS MISSION

The NASDA plans to launch the ADEOS-II, which succeeds the ADEOS, in the summer of 1999. The ADEOS-II will also carry Laser Reflector which has 9 individual cube-corners arranged to provide a quasi-hemispherical array on the pole nadir orientation. A center cube-corner will be oriented toward the nadir normal, and the 8 remaining cube corners will be positioned radially. This configuration will enable us to make an SLR observation in nearly all visible ranges (except a shade part of bus equipment). Its visible ranges is expected to be larger than that of the ADEOS.

Table 12 shows the NASDA spacecrafts that are planning to be launched with carrying Laser Reflector in future.

**Table 12**  
**NASDA'S SPACECRAFT CARRYING LASER REFLECTOR**

<u>S/C NAME</u>	<u>Launch year</u>	<u>Orbit type</u>	<u>Altitude (km)</u>	<u>Onboard LR type</u>
ADEOS	1996, SUMMER	LEO	800	horror
ADEOS-II	2000	LEO	800	prism array
ETS-VIII	2002	GEO	36500	TBD
ALOS	2003	LEO	700	prism array

LEO : Low Earth orbit

GEO : Geostationary Orbit

We provide an estimate of accuracy for trajectory determination and prediction during the low solar activity period.

Accuracy of predicting a trajectory is less than 30 meters and the accuracy is valid for a period of three days after the calculation. Although the accuracy changes quite randomly from 3 to 30 meters, we achieve our main purpose that accuracy of trajectory prediction must be under 100 m for the defined period. For tracking the RIS for its original scientific experiment, our derived TIRVs are sufficient for a successful run.

For accuracy of trajectory determination, we achieve accuracy of about 3 meters in the along track. Uncertainty for a trajectory position of low earth orbiter results mainly from an uncertainty in the along track direction. Therefore, the accuracy of 3 meters in along track direction provides a good measure for the overall accuracy in position. Since accuracy of trajectory determination prior to this experiment was about 150 meters, the accuracy for the ADEOS is improved significantly.

However, approximately from the year of 1999, the solar activities will become more significant. Then it will become difficult to satisfy the requirement for accuracy of trajectory prediction since an effect of air drag onto trajectory determination is poorly understood. Unfortunately, we have no means to verify the above assumption for accuracy of trajectory determination and prediction owing to ADEOS operation termination. It would be necessary to determine and predict the trajectory more frequently.

#### **ACKNOWLEDGMENT**

We wish to thank all of personnels, particularly those who are involved at SLR stations and SLR networks both supporting the ADEOS/RIS experiment and the ADEOS operation.

#### **REFERENCES**

1. ADEOS/RIS Tracking Support Coordination Group, "ADEOS/RIS Tracking Standards", 1996
2. Marini J. W., and Murray C. W., "Correction of Laser Range Tracking Data for Atmospheric Refraction at Elevations Above 10 Degrees", NASA GSFC X-591-73-351, 1973

3. M. Maeda, M. Ogawa, M. Sawabe , M. Hirota and H. Kunimori, "ADEOS/RIS LASER TRACKING EXPERIMENTS", *12th International Symposium on Space Flight Dynamics*, ESA SP403, 1997, pp. 131-136
4. M. Maeda, M. Ogawa, M. Sawabe, M. Hirota and H. Kunimori, "ACCURACY OF TRAJECTORY DETERMINATION AND PREDICTION OF ADEOS WITH RIS EXPERIMENT", *Laser Radar Ranging and Atmospheric Lidar Techniques*, SPIE Vol. 3218, 1997, pp. 31-39
5. McCarthy, Dennis. D., "IERS Standards (1992)", IERS Technical Note 13, 1992

## APPENDIX SOFTWARE MODELS

SOFTWARE MODEL	ADEOS operation by NOCS/NOCS2	ADEOS/RIS experiment by proto-type GUTS
<b>ASTRONOMICAL CONSTANTS</b>		
Speed of Light	$2.99792458 \times 10^8$ m/s	$2.99792458 \times 10^8$ m/s
Astronomical unit	$1.4959787 \times 10^8$ km	$1.4959787066 \times 10^8$ km *
Equatorial radius of the Earth	6378.138 km (GEM-10B)	6378.137 km(WGS-84) *
Flattening of the Earth	1/298.257 (GEM-10B)	1/298.257(GEM-10B)
Mean spin rate of Earth	$7.292115 \times 10^{-5}$ rad/s	$7.292115 \times 10^{-5}$ rad/s
<b>TIME SYSTEMS</b>		
Inner	TAI	TAI
Input/Output	UTC	UTC
UT1 - TAI	from IERS Bulletin B	from IERS Bulletin B
<b>COORDINATE SYSTEMS</b>		
Inertial	Mean equator and equinox of J2000.0	Mean equator and equinox of J2000.0
Input/Output	True equator and equinox of date	True equator and equinox of date, Tuned Interange Vector (TIRV) *
Precession	Newcomb theory	Newcomb theory
Nutation	developed by Woolard (JPL-DE200 used )	developed by Woolard (JPL-DE200 used)
Polar motion	from IERS Bulletin B	from IERS Bulletin B
Geodetic coordinate system	WGS-84, C-7	WGS-84, C-7
<b>FORCE MODELS</b>		
Geopotential		
Geopotential model	GEM-10B to degree and order 36 GEM-T3 to degree and order 50	GEM-T3 to degree and order 50 JGM-3 ( $C_{21}$ , $S_{21}$ rate and $J_2$ rate is not included) *
Tidal effect	GM: $398600.44 \text{ km}^3/\text{s}^2$ (GEM-10B)	GM: $398600.436 \text{ km}^3/\text{s}^2$ *
luni-Solar gravity	only solid Earth tide by sun and moon (not IERS)	only solid Earth tide by sun and moon (not IERS)
luni-Solar ephemeris	JPL-DE200	JPL-DE200
Moon-Earth mass ratio:	0.01230002	0.012300034(DE200) *
Sun-Earth mass ratio:	$3.329460 \times 10^5$	$3.32946045 \times 10^5$ (DE200) *
Atmospheric drag		
Atmospheric density model	Jacchia-Nicolet (geomagnetism not considered), Jacchia-Roberts, Modified Harris-Priester, MSIS86	Jacchia-Nicolet (geomagnetism not considered)
Radiation pressure		
Solar Radiation	Solar constant = $4.57 \times 10^{-6} \text{ N/m}^2$ at 1AU Cylindorical model for Earth and Moon shadow	Solar constant = $4.560 \times 10^{-6} \text{ N/m}^2$ at 1AU * Cylindorical model for Earth and Moon shadow
Earth Ratiation	N/A	Second degreezonal model *
Reflection model	single plate for Solar, Earth radiation and atmospheric drag	single plate for Solar, Earth radiation and atmospheric drag

SOFTWARE MODEL	ADEOS operation by NOCS/NOCS2	ADEOS/RIS experiment by proto-type GUTS
<b>MEASUREMENT MODELS</b>		
Range	In use( Light time equation is solved by instantaneous range difference method)	In use ( Light time equation is solved by instantaneous range difference method)
Range rate	In use	none *
Antenna angles (AZ,EL)	In use	none *
(X , Y )	In use	none *
1-way Doppler	In use	none *
Data correction		
Tropospheric refraction	GTDS <sup>†</sup> Algorithms	Marini and Murray model *
Ionospheric refraction	Tsuchiya Model	N/A *
Center of mass	N/A	Considered *
Site displacement	N/A	only Solid Earth tide by Sun and Moon *
<b>NUMERICAL INTEGRATION</b>		
Method	Adams-Cowell method	Adams-Cowell method
predictor- corrector	first order: Adams-Bashforth predictor Adams-Moulton corrector second order: Stormer predictor Cowell corrector	first order: Adams-Bashforth predictor Adams-Moulton corrector second order: Stormer predictor Cowell corrector
<b>ESTIMATION METHOD</b>		
Basic method	Weighted least squares estimation	Weighted least squares estimation
Iterative procedure	Iteration of cholesky method equations	Iteration of cholesky method equations
<b>ESTIMATION PARAMETERS</b>		
Orbital elements	Cartesian Keplerian	Cartesian Keplerian
Force model Parameters	Scale factor of amospheric drag $\rho_1$ Scale factor of solar radiation $\Gamma_1$	Scale factor of amospheric drag $\rho_1$ Scale factor of solar radiation $\Gamma_1$
Observation biases	Range bias and so on	Range bias and so on
Station Location biases	(Xb, Yb, Zb)	(Xb, Yb, Zb)

<sup>†</sup>GTDS : Goddard Trajectory Determination System

\* Difference between the ADEOS operation system and the ADEOS/RIS experiment system



331548

128

5/4-13

AAS 98-313

169296

## NEXT DAY PRECISE ORBITS FOR TOPEX/POSEIDON USING DORIS

Jean-Paul Berthias<sup>†</sup>, Sabine Houry<sup>‡</sup>

Until now, TOPEX/Poseidon precise orbits were needed only for the production of Geophysical Data Record files, and thus were not required until about 5 weeks after data acquisition. Recent developments in operational oceanography now require the rapid delivery of precise altimeter data within days, and possibly hours, of data acquisition. The processing of the altimeter measurements can be accomplished according to this schedule, and the only difficulty rests with the production of the precise orbit ephemerides.

The long delay involved in the current production scheme results from the necessity to collect laser tracking data from ground stations and also from the need to wait for the final and most accurate values of the solar activity and Earth orientation parameters. A reduction in the orbit production delay forces the processing to deal with DORIS data only and with predicted values for the parameters. In addition, this reduces the amount of validation that can be performed before delivery.

Fortunately, the spatial and temporal coverage of the DORIS tracking system is such that the DORIS data by itself is sufficient to produce a precise orbit. Also, predictions of solar activity and Earth orientation parameters have improved considerably over the last few years, so that using them instead of actual data does not significantly degrade the orbit accuracy.

Using this strategy, DORIS orbits have been computed on a daily basis within 24 to 48 hours of data acquisition. And since the beginning of October 1997, these orbits have been included on the Poseidon Interim Geophysical Data Record files for all cycles when this altimeter is on. Evaluations of these daily orbits reveal that their radial accuracy is very close to that of the standard precise orbits ephemerides.

## INTRODUCTION

The DORIS (Doppler Orbitography and Radiopositioning Integrated by Satellite) tracking system was designed and developed by the Centre National d'Etudes Spatiales (CNES), in collaboration with the Institut Géographique National (IGN) and the Groupe de Recherches en Géodésie Spatiale (GRGS), to achieve the very high level of orbit

---

<sup>†</sup> Manager, Orbit Metrology Group, Centre National d'Etudes Spatiales, 18 avenue E. Belin, 31401 Toulouse Cedex 4, France

<sup>‡</sup> Member of the technical staff, Orbit Metrology Group, Centre National d'Etudes Spatiales, 18 avenue E. Belin, 31401 Toulouse Cedex 4, France

determination accuracy required by the joint NASA-CNES altimeter mission TOPEX/Poseidon (T/P).

The two T/P altimeters measure the distance between the spacecraft and the ocean surface with a precision of about 2 cm<sup>1</sup>. In order to derive the absolute sea surface height from these observations, the altitude of the spacecraft has to be known with the same level of precision. To reach this goal a major effort was launched as part of the T/P Precise Orbit Determination (POD) activities. It included, among others things, improvements to geopotential models<sup>2</sup>, the development of sophisticated surface force models<sup>3</sup>, and the installation of the DORIS tracking system<sup>4,5</sup>.

These efforts have resulted in an orbit precision never achieved before for a large satellite in low Earth orbit. The error level of the T/P Precise Orbit Ephemerides (POE) that are routinely produced by NASA and CNES does not exceed 2 to 3 cm RMS in the radial direction as demonstrated by various tests: tracking data residual analysis, especially high elevation laser ranging residuals, comparisons of orbits computed with different data sets (in particular DORIS and laser versus GPS), and altimeter crossover residual analysis<sup>6,7,8,9</sup>.

DORIS is a one-way, ascending Doppler system which utilizes a set of ground beacons that broadcast continuously and omnidirectionally on two frequencies of 2036.25 and 401.25 MHz. Each beacon contains an ultrastable quartz oscillator (USO), as well as sensors for monitoring the temperature, pressure and humidity. The broadcast message, which is transmitted every 10 seconds, consists of the meteorological data, the beacon identification number, a short status report and a synchronization signal. The receiver on-board the satellite receives the dual frequency signal and computes the integrated Doppler count over intervals of 7 or 10 seconds. The receiver is programmed in advance to multiplex the signals from several commonly viewed beacons.

The current DORIS network consists of about 50 beacons covering the entire surface of the Earth, with the exception of the Southern Pacific ocean. It is routinely used to track three satellites, SPOT 2 (since 1990), T/P (since 1992) and the recently launched SPOT 4, and produces more than 250 passes of data per satellite and per day. With this network, the DORIS system provides on a daily basis a uniquely spatially and temporally dense set of high precision ground-based tracking data.

DORIS is a centralized tracking system, in which all the data are collected on-board of the spacecraft. This makes it possible to compute the orbit either on-board in real-time, or on the ground in near real-time. The real-time capability is now operational on SPOT 4, while the near real-time processing is routinely used to compute daily 1-day orbits for T/P. The key accomplishment was to improve the precision of these orbits to a level comparable to that of the POE.

## **RATIONALE FOR FAST PRECISE ORBIT PRODUCTION**

Until now, precise orbits were only needed for the production of Geophysical Data Record (GDR) files, which are designed for the scientific community, and are distributed with a two month delay. Thus POEs were not required until about 5 weeks after data acquisition. The Interim GDR (IGDR) files, which were provided to users requesting fast service, were generated using lower precision operational orbits.



Recently, there has been a lot of interest in operational oceanography, which involves the processing of altimeter data within days, and even hours, of data acquisition. And for some applications, the availability of accurate products is crucial to the quality of the result.

The French MERCATOR project<sup>10</sup>, which is supported in part by CNES, is a leading project in this field. Its goal is the implementation within five to seven years of a pre-operational high resolution global ocean model which assimilates satellite and in situ data. One of the by-products should be the demonstration of the operational need for space based oceanography data, with real-time availability as one of the key factors.

Looking to the future, near real-time altimeter data should become one key component of the global ocean observation system. Quick assimilation of this data into global meteorological models could improve weather forecast, both on a short term and seasonal basis (e.g. El Niño). It could also help predictions of near-surface conditions for the open ocean, which would in turn benefit fishing or transportation industries while improving safety. Even local forecast of coastal currents would be improved through a better knowledge of the deep ocean boundary conditions.

## **CHALLENGES OF FAST PRECISE ORBIT PRODUCTION**

These new requirements for fast precise orbit production creates new challenges. The long delay involved in the current production scheme makes it possible to collect laser ranging data from ground stations, and also to benefit from the final and most accurate values for the solar activity and Earth orientation parameters. A reduction in this delay forces the precise orbit production system to deal with DORIS data only and with predicted values for the parameters. In addition, this reduces the amount of validation which can be performed before delivery.

Fortunately, when available, the DORIS data by itself is sufficient to produce precise orbits. In addition, atmospheric drag is very small at the altitude of T/P, and short term predictions of solar fluxes and geomagnetic indices have improved considerably over the last few years, so that using them instead of actual data does not significantly degrade the orbit accuracy.

Similarly, the quality of predictions for Earth orientation parameters has also improved, but it is still not sufficient<sup>†</sup> at the level of accuracy that we deal with. However, the DORIS data is powerful enough to accurately determine the orbit in the Earth based frame in which the station locations are known, even though it is not known how to precisely relate this frame to the inertial frame in which the equations of motion are integrated.

There are two elements that contribute to this success. The first one has to do with the ability to recover the Earth orientation parameters while computing the orbit. However, the quality of the result is not sufficient to ensure centimeter level accuracy. The second one is the fact that when the T/P orbit and the DORIS station coordinates are expressed in the

---

<sup>†</sup> The factor of two improvement in the quality of the IERS Bulletin A short term predictions<sup>11</sup>, introduced in early March, might change this conclusion. It is currently under investigation. This change was implemented to improve the quality of GPS orbit predictions.

same frame, the only way that the Earth orientation parameters play a role is through the non-inertial nature of the frame. This then translates into two effects, one which has to do with dynamics, and involves the appearance of fictitious forces, the other one which appears in the computation of the propagation time of signals between the beacon and the spacecraft. Both of these effects are small, and therefore the error induced by the use of approximate Earth orientation parameters is of second order. But, in addition, the reduced dynamics stochastic correction technique<sup>12</sup> (ELFE) used in the CNES precise orbit production strategy corrects the dynamical errors using measurements.

## **ORBIT PRODUCTION STRATEGY**

### **Description**

The near real-time precise orbits are produced at CNES using the tools that were developed for the POE. The ZOOM software is used for all the computations, and the Voyager user interface and procedures are used to activate and monitor the various steps of the processing<sup>13,14</sup>.

A short summary of the strategy is as follows:

- Perform a standard orbit determination using a complete dynamical model. Corrections to the IERS predictions for polar motion parameters are added to the standard state vector (initial conditions, multiplicative coefficients for solar radiation pressure and atmospheric drag, frequency and troposphere bias per pass, constant along-track and once-per-revolution along-track and cross-track empirical forces). The result is a fully dynamical orbit ephemeris expressed in the true-of-date reference frame.
- Apply the reduced dynamics stochastic correction technique to adjust a piecewise constant empirical force that follows a first order Markovian evolution scheme. The result is a corrected orbit ephemeris, still expressed in the true-of-date reference frame.
- Convert both dynamical and corrected ephemeris to the IERS Terrestrial Reference Frame (ITRF) using the estimated value of the Earth orientation parameters. It is only in this frame that the orbit is accurate, so these are the products which are delivered and archived.
- Validate the orbit using data residual analysis, comparison of two successive orbits in the overlapping region, and comparison with the previous day's extrapolated orbit.

Other verifications, including comparisons with respect to the POE and altimeter crossover residual statistics, are conducted routinely, as soon as these products become available.

### **Products**

T/P DORIS data is received at CNES in daily batches in the morning. On day D the orbit is actually computed using data from days D-2 and D-1, and covers 30 hours. This includes a two hour margin at both ends, where the stochastic correction degrades the orbit rather than improving it: this is due to the lack of past information on the correlated stochastic process at the beginning, and to the lack of future information at the end. This leaves 26 hours of usable ephemeris, covering the period from 8 p.m. on day D-2 to 10 p.m.

on day D-1. The first two hours, 8 to 10 p.m. on day D-2, are a repeat of the previous day's orbit and are used for validate using overlap statistics.

In the operational process, the orbit which is delivered on day D actually covers days D-2 through D. This is the result of the merging of the precise orbits computed following the above procedure on days D-1 and D, as well as 2 hours coming from the purely dynamical solution of day D, from 10 p.m. to midnight, and 24 hours of extrapolation.

These composite orbits are delivered to the Centre de Traitements DORIS/Poseidon (CTDP) which reformats them before providing them to AVISO. They are then added to the fast IGDR products and sent to the Service Hydrographique et Océanographique de la Marine, and to its US counterpart, NAVOCEANO. During the periods when the Poseidon altimeter is on, these orbits are also used to produce the standard IGDR.

## **Operations**

The processing chains are activated automatically on a daily basis by Unix cron processes. The activation takes place at the same time every day; however, there are sometimes delays in the reception of the DORIS data from NASA's Jet Propulsion Laboratory, or in the preprocessing performed by the CTDP. In this case, the procedure switches to a sleep state and checks for data arrival at regular intervals. Once the data are available the entire processing takes less than one hour on the SUN Ultrasparc Enterprise E5000 of the CNES central computing facilities.

At the end of the processing an E-mail message is sent to the supervising engineer. It contains the status of the individual steps, as well as the results of the various verification tests. Simplified global status messages are available for display on the terminal of an operator. However, during the current development phase, no operator is available to monitor the orbit determination processes during weekends. As a temporary solution, a copy of the final mail message is sent to the private mailbox of one of us (S.H.) who can thus remotely monitor the status of the system, and take appropriate action.

Many of the internal validation tests are associated with expected ranges for results. Whenever values are out of range, processing is stopped. This prevents delivery of incorrect orbits to the end user. Using the Voyager monitor, the supervising engineer can intervene manually in the system, and resume the processing at any point. He can skip steps, override options, and perform step by step processing, or chained operations.

Many parameters are generated during the daily processing. They are archived for long term monitoring of the orbit quality. In the near future, an automated quality assessment report will be generated based on these parameters and provided to users along with the orbits.

## **ACCURACY ASSESSMENT**

Near real-time DORIS orbits have been computed over the last few months, using various configurations. Hence, results vary slightly as a function of the configuration used at the time. However, this has no significant impact on the analysis which is presented here.

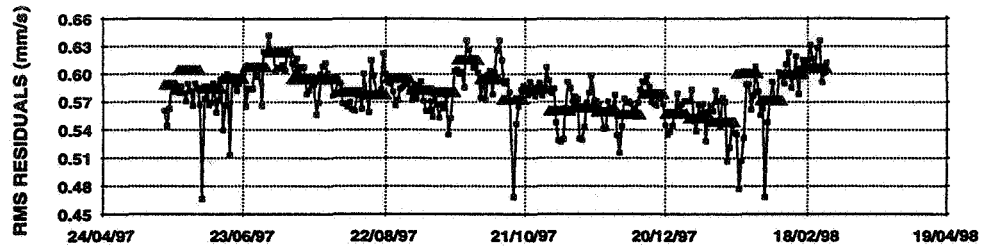


Figure 1 DORIS residuals RMS value

The statistical analysis of the data residual is a good tool to evaluate the quality of the processing. In the case of DORIS, the data appear noise limited around the level of 0.55 mm/s. RMS values of the DORIS data residuals are plotted on Figure 1. Daily solution residuals (squares) are at least as good, if not better, than residuals of the POE (triangles). In particular, daily residuals are lower during fixed yaw periods, when cross-track and along-track directions remain constant relative to the satellite body. In this case, the adjusted once-per-revolution parameters absorb poorly modeled surface forces more easily.

Successive orbits overlap over a 2-hour period. Comparison of the two solutions over this period provides a good estimate of the orbit error. RMS values of these differences are plotted on Figure 2.

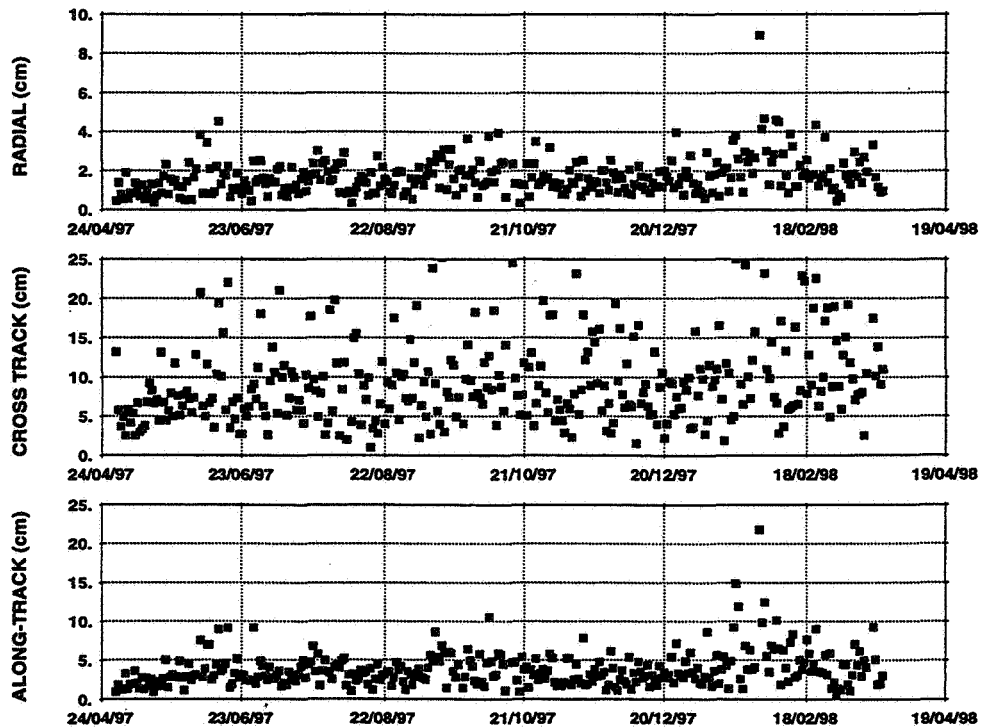


Figure 2 Orbit overlap differences RMS values

In the radial direction (top curve) differences rarely exceed 4 cm. Their mean value is below 2 cm. The large overlap differences in the cross-track direction, and to a lesser extent in the along-track direction, are a consequence of the daily changes in the solved-for polar motion parameters. The quality of the corrections to the polar motion parameters computed during the orbit production process can be estimated a posteriori when IERS final solutions become available about 4 weeks later. The RMS of the differences over a few months are 2.6 and 2.2 milliarcseconds for the  $u$  and  $v$  components, which correspond respectively to 7.8 cm and 6.6 cm. These values are consistent with the observed level of cross-track and along-track error.

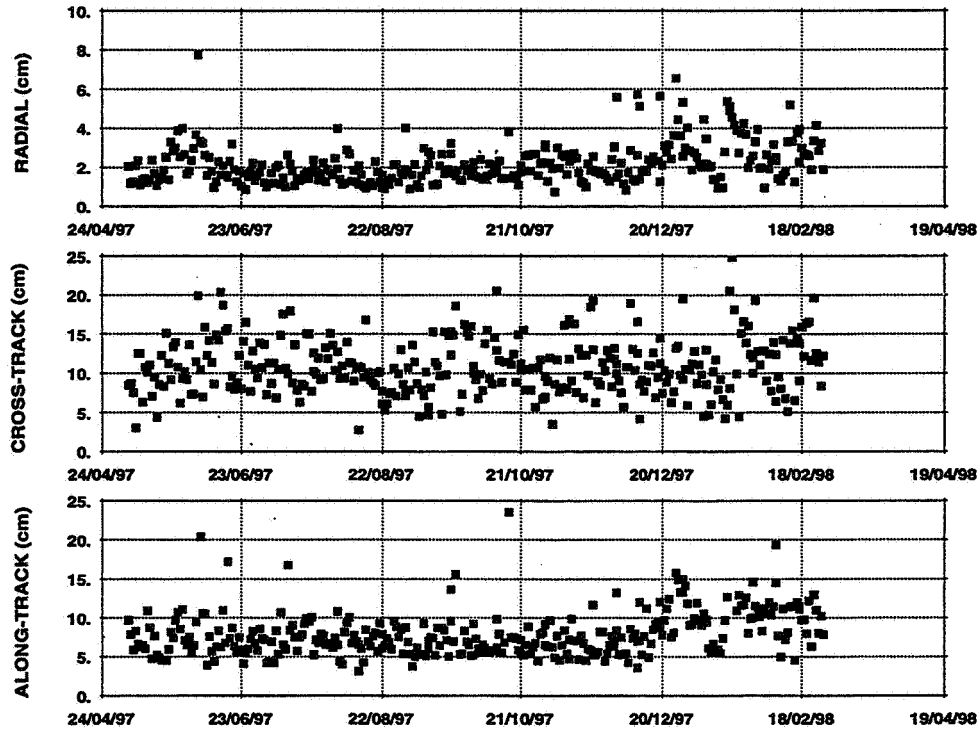


Figure 3 RMS differences between daily orbits and the POE

RMS values of the radial differences between daily orbits and the corresponding POE are also about 2 cm (Figure 3). This is comparable to the radial error level in the POE itself, thus, in the radial direction, daily orbits appear to be about as accurate as the POE. Cross-track and along-track differences are significantly larger, respectively about 10 cm and 7 cm RMS. Here again, these differences are mostly the result of inaccuracies in the Earth orientation parameters.

The larger differences observed since December 1997 are due to a change in the reference system used to generate the near real-time orbits. Originally, these orbits and the POE used the same reference system, based on a set of station coordinates computed at CNES. In December of last year, the reference system of the daily orbits was switched to the ITRF 96 solution<sup>15</sup>. The almost 5 cm offset along the  $Z$  direction between the two frames adds to the difference between the orbits in the radial and along-track directions.

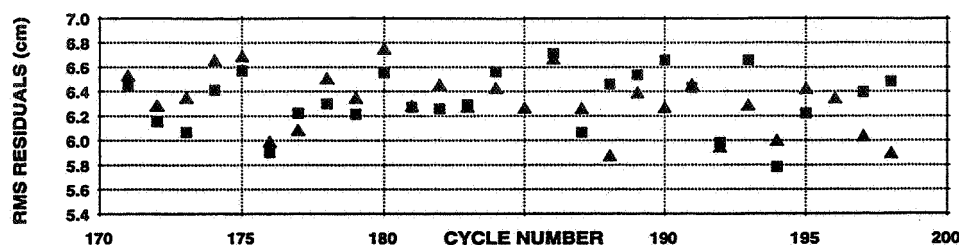


Figure 4 Altimeter crossover residual RMS value

The computation of altimeter crossover residuals provides the best external test of the quality of the orbits as this data is not used to compute the orbit. Figure 4 presents the result of these evaluations. Crossover residuals computed using a combination of 10 daily orbits to produce a full repeat cycle are represented by squares, while crossover results for the POE are represented by triangles. Full cycle crossover residuals for daily orbits and precise orbits are roughly the same. This confirms that the radial orbit error level in the daily orbits and in the POE are nearly identical. However, this test does not provide any reliable estimate of the error level, as the residual signal is dominated by ocean variability, altimeter data noise and tide model errors.

## PERSPECTIVES FOR REAL-TIME PRECISE ORBIT DETERMINATION

In 1991, CNES started the development of a DORIS based space borne orbit determination system for the SPOT 4 satellite<sup>16</sup>. The core of the system is a standard DORIS receiver to which a new function has been added to process measurements in real-time and produce an orbit. Positions and velocities are then added to the image data in the spacecraft telemetry and downloaded to the ground image processing centers.

This on-board orbit determination system, DIODE (Détermination Immédiate d'Orbite par DORIS Embarqué), is now fully operational. Figure 5 shows a comparison of the SPOT 4 positions computed on-board and received in the telemetry with a ground based reference orbit. This plot corresponds to the first week of operations.

The current results of DIODE are an excellent proof of its quality and reliability. The accuracy of the results, a few meters 3D at 1 sigma, is well within the requirements of most space missions, including SPOT.

However, technically, this version of the orbit determination software is obsolete in terms of precision. It was delivered to the project in mid 1995, and since then major improvements have been brought to the software to support the development of the new DORIS receivers. These instruments will offer an order of magnitude improvement in precision over the current version<sup>17,18</sup>. Work is on-going to try to retrofit the SPOT 4 software to benefit from this improvement in accuracy, as well as other new functions such as the ability to initialize autonomously.

### DIODE/SPOT4 First three days on orbit

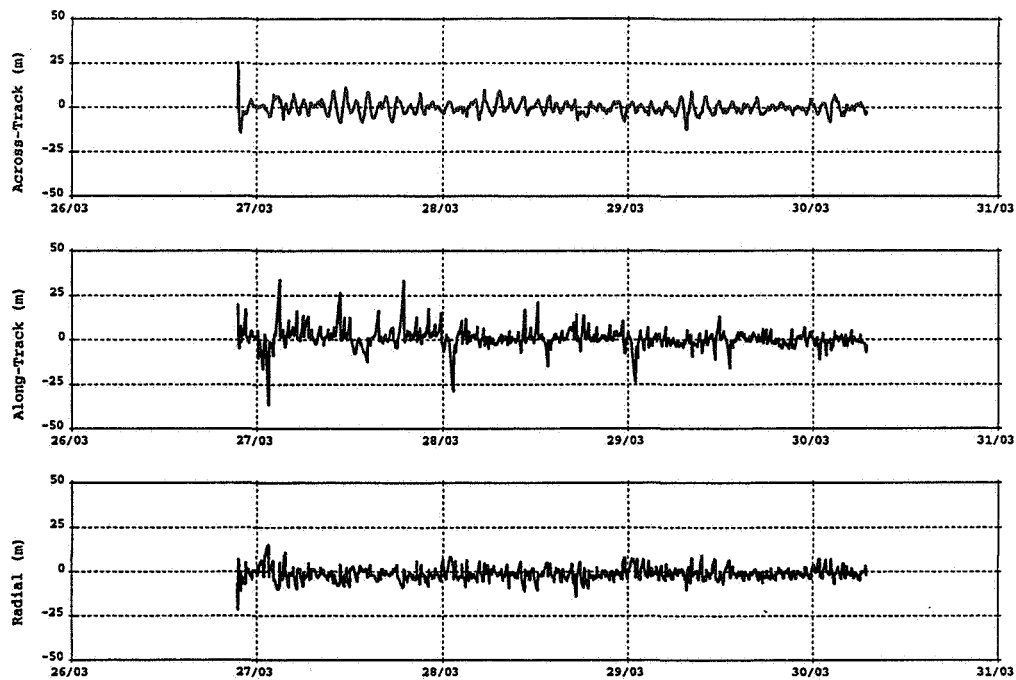


Figure 5 First comparisons of the on-board orbit with a ground-based reference

One key factor for this progress is the fact that both the real-time on-board orbit determination software and the operational full precision ground-based orbit determination program, ZOOM, are developed within the same group. Thus, challenges arising from the requirements of operational oceanography have stimulated the development of new and more precise real-time processing strategies.

The latest version of DIODE was designed for the European ENVISAT satellite. When adapted to take into account the rather complex attitude control of the T/P spacecraft, it provides orbits with a radial error level of between 10 and 20 cm RMS. This is not sufficient for the very precise operational applications, but can be used to produce auxiliary wind and wave products.

However, improved modeling techniques and a better tuning of the filter have led to significantly better results in some test cases<sup>19</sup>. These results still need to be confirmed. If they can be generalized, there is hope that, in the future, real-time precise orbits can be produced.

## CONCLUSION

Evaluations of near real-time daily orbits computed for T/P using DORIS data reveal that their radial accuracy is roughly identical to that of the POE. Their introduction into the fast IGDR products, and into the Poseidon IGDR, hence their availability to the

oceanographic community, should contribute significantly to the development of operational altimeter data processing.

Jason, the follow on to the T/P mission, will support operational oceanography by providing users with IGDRs based on the near real-time DORIS orbits, and with an even faster delivery product, the Operational Science Data Record (OSDR) based on the real-time on-board orbits. It is hoped that these new developments will help secure the future of operational oceanography, so that we can all benefit from its extraordinary potential contribution to weather and marine state forecasting.

## ACKNOWLEDGMENT

The authors wish to thank Eric Julien and Véronique Lefrère of CISI, Aeronautics and Space Branch, Toulouse, France, for their implementation of the complex computer procedures required to produce the near real-time orbits. They also thank Christian Jayles and Patrick Broca for providing them with the first results of the DIODE experiment on-board of SPOT 4.

## REFERENCES

1. L.L. Fu, E.J. Christensen, C. A. Yamarone, M. Lefevre, Y. Ménard, M. Dorrer, P. Escudier, "TOPEX/POSEIDON mission overview", *Journal of Geophysical Research*, Vol. 99, No. C12, 1994, pp 24369-24381
2. B.D. Tapley, et al, "The JGM-3 geopotential model", *Journal of Geophysical Research*, Vol. 101, B12, 1996, pp 28029-28049
3. J.A. Marshall, S.B. Luthcke: "Modeling radiation forces acting on TOPEX/POSEIDON for precision orbit determination", *Journal of Spacecraft and Rockets*, Vol. 31, No. 1, 1994, pp 89-105
4. F. Nouël, J. Bardina, C Jayles, Y. Labrune, B. Truong, "DORIS: a precise satellite positioning doppler system", *Astrodynamics 1987, Advances in the Astronautical Sciences*, J.K. Solder et al. (eds), Vol. 65, 1988, pp. 311-320
5. F. Nouël, J.-P. Berthias, P. Broca, A. Comps, M. Deleuze, A. Guitart, C. Jayles, P. Laudet, C. Pierret, A. Piuze, D. Pradines, D. Taburiau, C. Valorge, "Precise orbit determination with the DORIS/SPOT 2 system: first results", *Proceedings of the ESA Symposium of Spacecraft Flight Dynamics*, Darmstadt, Germany, September-October 1991, pp. 91-95
6. F. Nouël, J.P. Berthias, M. Deleuze, A. Guitart, P. Laudet, A. Piuze, D. Pradines, C. Valorge, C. Dejoie, M.F. Susini, D. Taburiau: "Precise CNES orbits for TOPEX/POSEIDON: Is reaching 2 cm still a challenge?", *Journal of Geophysical Research*, Vol. 99, No. C12, 1994, pp. 24405-24419
7. B.D. Tapley, J.C. Ries, G.W. Davis, R.J. Eanes, B.E. Schutz, C.K. Shum, M.M. Watkins, J.A. Marshall, R.S. Nerem, B.H. Putney, S.M. Klosko, S.B. Luthcke, D. Pavlis, R.G. Williamson, N.P. Zelesnki, "Precision orbit determination for TOPEX/POSEIDON", *Journal of Geophysical Research*, Vol. 99, No. C12, 1994, pp. 24383-24404
8. B.D. Tapley, J.C. Ries, "Recent advances in precision orbit determination", *Proceedings of the 1997 AIAA GNC, AFM, and MST Conference and Exhibit*, New-Orleans, Louisiana, August 1997



9. J.-P. Berthias, S. Houry, A. Piuze, "How good is DORIS for precise orbit determination?", *Proceedings of the DORIS Days Meeting*, Toulouse, France, April 1998
10. P. Courtier, "The MERCATOR project and the future of operational oceanography", *Proceedings of the International Symposium "Monitoring the oceans in the 2000s: an integrated approach"*, Biarritz, France, October 1997
11. J. Ray and B. Luzum, "Improved polar motion predictions", *IGS Electronic Mail*, Message no 1816, February 1998
12. B. Barotto and J.-P. Berthias, "First results of Reduced Dynamics with DORIS on TOPEX/Poseidon and SPOT", *Journal of Guidance and Control*, Vol. 19, No. 6, pp. 1296-1302
13. F. Nouël, M. Deleuze, P. Laudet, C. Valorge: "Operational aspects of precise orbit determination of SPOT and TOPEX/Poseidon satellites with DORIS", *Spaceflight Dynamics, Advances in the Astronautical Sciences*, J. Teles et al. (eds), Vol. 84, 1993, pp. 279-290
14. E. Julien, J.P. Berthias, P. Broca, A. Comps, M. Deleuze, A. Guitart, S. Houry, C. Jayles, P. Laudet, F. Nouël, A. piuzzi, D. Pradines: "The DORIS orbit computation service", *Proceedings of the 11<sup>th</sup> International Astrodynamics Symposium*, Gifu, Japan, May 1996
15. C. Boucher, Z. Altamimi, P. Sillard, "The ITRF96 realization of the International Terrestrial Reference System", *Proceedings of the IAG Scientific Assembly*, Rio de Janeiro, Brazil, 1997
16. J.-P. Berthias, C. Jayles, D. Pradines, "DIODE: a DORIS based real-time on-board orbit determination system for SPOT 4", *Spaceflight Dynamics, Advances in the Astronautical Sciences*, J. Teles et al. (eds), Vol. 84, 1993, pp. 125-138
17. J.-P. Berthias, P. Broca, J. Fourcade, C. Jayles, D. Pradines, D. Laurichesse, "General characteristics of real-time on-board orbit determination", *Proceedings of the 12<sup>th</sup> International Symposium on Space Flight Dynamics*, Darmstadt, Germany, June 1997, pp. 267-274
18. C. Jayles, P. Broca, J.P. Berthias, D. Laurichesse, "Navigation autonome temps réel", *Proceedings of the DORIS Days Meeting*, Toulouse, France, April 1998
19. D. Laurichesse, private communication



169.  
337550

S15-18  
169 277

## High-Precision Altimetry Products from Envisat-1

F. M. Martínez Fadrique, GMV  
R. C. A. Zandbergen, Logica  
D. Navarro Reyes, GMV

ESA / European Space Operations Centre  
Robert Bosch Strasse 5, 64293 Darmstadt, Germany

The Earth observation satellite Envisat-1 will be controlled by the European Space Operations Centre (ESOC). This paper addresses ESOC's orbit determination activities for Envisat, and more particularly the possibility of obtaining high-precision altimetry products for near-real-time ocean surface topography monitoring.

First, this paper presents the current ESOC capabilities in the area of Precise Orbit Determination (POD) and ocean surface model computation, based on the most recent ERS-2 data. A detailed analysis of the models used for ERS and the possibilities of implementing newly developed ones is discussed in order to identify potential improvements. Since the precise tracking devices on board Envisat provide further sources of improvement compared to ERS, this paper also presents the advantages which may be expected from Envisat for obtaining better orbits and models.

Finally, the new Navigation Package for Earth Observation Satellites (Napeos), which will perform both the operational and precise orbit determination, will be described in a few words

## INTRODUCTION

Continuing its Earth observation programme, ESA will launch Envisat-1 in November 1999. Envisat, with its improved instruments and tracking devices, will still resemble in many aspects the remote sensing satellites currently in operation. The satellite will be controlled by ESOC, which will also be responsible for all Flight Dynamics activities. These activities include routine operational orbit determination, orbit prediction and orbit maintenance (manoeuvre planning) but also very precise orbit determination resulting in the availability of high-precision altimetry products.

The aim of ESOC Flight Dynamics is not to produce scientific data. Rather, its requirements on orbit determination, prediction and control stem from the need to control the spacecraft and its instruments, and to maintain the ground track of the satellite within a narrow deadband. In addition to these near-real time activities, precise orbit determination (POD) is performed for the evaluation of the routine orbit determination and the performance of the altimeter instrument. POD is aided by the presence of the laser retro-reflector (LRR) and, as a new instrument compared to ERS, the DORIS system (Doppler Orbitography and Radiolocation Integrated by Satellite). These tracking systems shall provide the possibility of obtaining an accuracy of around 5 cm in the radial direction. The altimeter height measurements, when properly

processed, also provide a source of tracking data, and the ocean surface topography models obtained in this processing are a valuable spin-off of the Envisat POD.

As the result of several years of experience with the POD of ERS and Topex/Poseidon, the Envisat mission can build on the knowledge of very accurate models and processing techniques. Of special interest is the processing of altimeter data, while the nearly complete coverage by precise DORIS tracking will allow the computation of more accurate orbits in zones of major interest like the Pacific ocean, where no simultaneous altimetry and precise tracking data were available for ERS. Unfortunately, at the same time Envisat will suffer the consequences of flying during the solar maximum, which will make air drag modelling much more challenging.

ESOC's current capabilities in the area of POD and ocean surface model computation will first be evaluated using the most recent ERS-2 data. Subsequently, the accuracy which may be expected from Envisat will be explored, with a view to establishing the accuracy of the altimetry by-products of the ESOC Envisat POD.

## **CURRENTLY IMPLEMENTED MODELS FOR ERS**

Two parallel activities will exist in the Envisat orbit support: operational and high-precision orbit determination.

The operational orbit determination is based on requirements of near-real time orbit determination with maximum stability and reliability and relatively modest accuracy. The dynamic models and tracking data processing models currently used for ERS yield the required accuracy specified for orbit determination and prediction, both for ERS and Envisat, even in the period of increased solar activity. This orbit determination scenario is not subject to dramatic improvements, mainly due to the accuracy limitations of the S-band tracking system itself. This activity includes the estimation of optimised manoeuvre sequences in order to maintain the ground track within one km from the reference ground track throughout the mission.

Precise orbit determination follows a completely different approach. The most accurate models available are used in order to obtain orbits as accurate as possible. The tracking data used for this purpose are also the most accurate available (satellite laser ranging (SLR) and Precise Range and Range-rate Equipment (PRARE)) with state of the art data processing models. This scenario is subject to continuous improvement, both in the environmental modelling and in the processing of the tracking data. Of particular interest is the analysis and implementation of models for the correction of altimeter observations.

Although the main objective of the ESOC POD is the processing of ERS data and the generation of ERS high-precision orbits, data from other satellites equipped with different tracking devices are processed. This allows the verification of algorithms and models which may be used for ERS and the generation of auxiliary data (e.g. station coordinate solutions) for which the ERS orbit configuration is not optimal.

## **Dynamics and tracking data processing models**

The following setup, currently used for POD of ERS, Topex/Poseidon, SPOT and Lageos also forms the basis for the processing of other (future) satellite and tracking configurations:

### **Reference frame**

- Mean equator and equinox of J2000.0
- Nutation (Wahr model)
- Earth rotation (EOP IERS Bulletin A)
- SLR station coordinates from an ERS and Lageos multiarc solution aligned to the ITRF
- DORIS station coordinates from ITRF

### **Dynamics**

- JGM-3 (70,70) gravity model

- MSISE-90 air density model. Detailed drag modelling based on spacecraft geometry and aerodynamic flow; scale factor estimated every twelve hours.
- Luni-solar gravity
- Frequency-dependent solid Earth tides (Wahr model)
- Ocean tides (Schwiderski)
- Direct solar radiation pressure model. Detailed modelling based on spacecraft geometry
- Albedo and infrared radiation perturbations
- Manoeuvre modelling with scale factor estimation
- One cycle per revolution (cpr) along-track and cross-track empirical acceleration. One set of coefficients per arc.

#### **Tracking data processing**

- Murray- Marini tropospheric correction (laser)
- Centre of mass correction
- Tropospheric, ionospheric and centre of mass corrections from dataset for DORIS
- Tropospheric, ionospheric, centre of mass, antenna phase, station mechanical and external corrections for the Precise Range and Range-rate Equipment (PRARE) tracking data.
- SLR range station bias
- PRARE range station bias and pass atmospheric scale factor

### **Altimeter data processing**

#### **Ocean surface:**

- Solid Earth tide correction, Schwiderski model
- Permanent tide correction, Wahr model
- Ocean tide correction, Schwiderski NSWC model
- Ocean loading, Schwiderski model
- Mean Sea Surface, OSU-91A plus ERS-1/ESOC correction model
- Dynamic Sea Surface Topography, ERS/ESOC model

#### **Propagation:**

- Dry tropospheric correction, Saastamoinen 1972 and ECMWF pressure field
- Wet tropospheric correction, ESOC model
- Ionospheric correction, Rawer-Bent model

#### **Other:**

- Electromagnetic bias correction from Fast-Delivery products
- Centre of mass
- Altimeter instrument bias

Some of the models used in the processing of altimetry were developed in-house (*ERS-2 Altimeter Calibration at ESOC, Romay-Merino et al.*); the altimeter data generated in the geodetic phase of ERS-1 gave the possibility of generating a global solution for the mean sea surface with resolution of 0.3 degrees and accuracy better than 10 cm. A spherical harmonic expansion for the altimetry wet tropospheric correction was also computed based on meteorological data from the ECMWF.

### **Precise Orbit Determination Implementation**

Satellite laser ranging observations and altimeter normal points are the tracking data types used in the ERS-2 POD. A parallel POD activity for evaluation purposes uses PRARE as precise tracking data. Both orbit determination activities use five-day arcs overlapping the previous and following arcs by one day each (two-day effective overlap). The three days in the middle of each arc are kept as the precise solution (see Figure 1). With this strategy one can eliminate boundary effects from ill-determined parameters like aerodynamic coefficients. Comparisons of the one-day arcs centred in each of the two-day overlap periods are made in order to verify internal consistency between successive arcs.

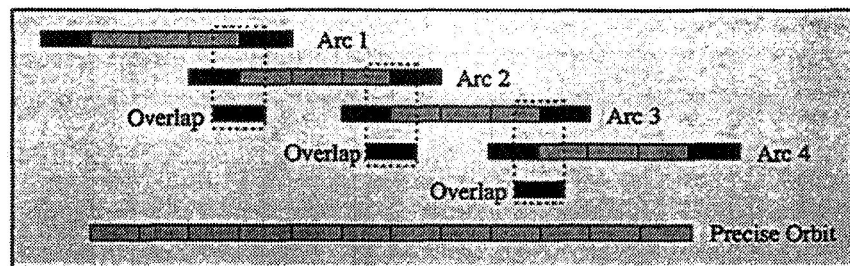


Figure 1: Precise Orbit Determination Strategy

## ERS-2 precise orbit determination results

Since the launch of ERS-1 in 1991, and subsequently for ERS-2, the ESOC precise orbit determination has seen a gradual improvement in the dynamics and data processing models with a corresponding improvement in the accuracy of the orbit solutions for these satellites. A major step was achieved at the occasion of the relative calibration of the ERS-1 and ERS-2 altimeter instruments during the ERS-2 commissioning phase (*ERS-2 Altimeter Calibration at ESOC, Romay-Merino et al.*).

The first step in the generation of precise altimetry products is the generation of a high-precision orbit solution. This is accomplished by the simultaneous processing of SLR quick-look data from the EUROLAS and CDDIS data servers and altimetry. The SLR station coordinates used for ERS are based on multi-arc solutions incorporating ERS and Lageos data, where the scale and orientation of these solutions have been made to match the current ITRF solution. The latest solution is based on two years of Lageos and ERS data and coincides in scale and orientation with ITRF-96.

Unfortunately, the ERS-1 PRARE tracking device failed soon after its activation. For ERS-2, the processing of PRARE data has received a lot of attention from the international POD community, and after two years solutions with an accuracy comparable to those based on satellite laser ranging (SLR) and altimetry, but independent of the altimeter data, have become possible (cf. e.g. *Incorporation of PRARE data in ERS-2 orbit computation, Visser et al.*).

Typical one-way rms values of ERS-2 SLR residuals are shown in Figure 2. They are an indication of the total satellite position accuracy during the periods of visibility by a laser station.

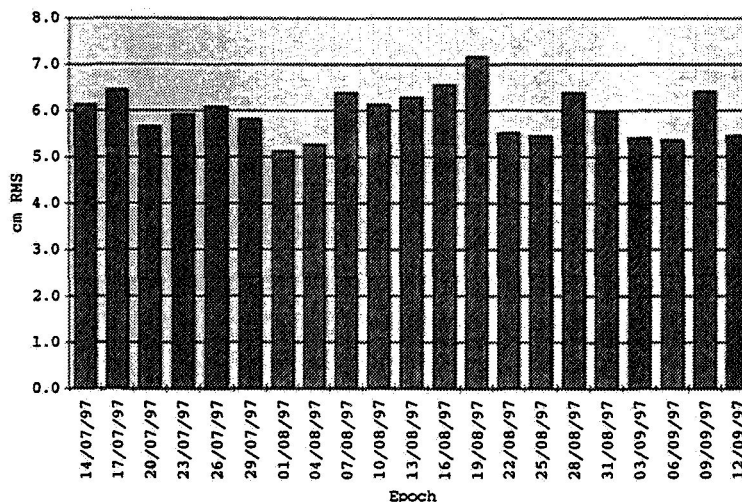
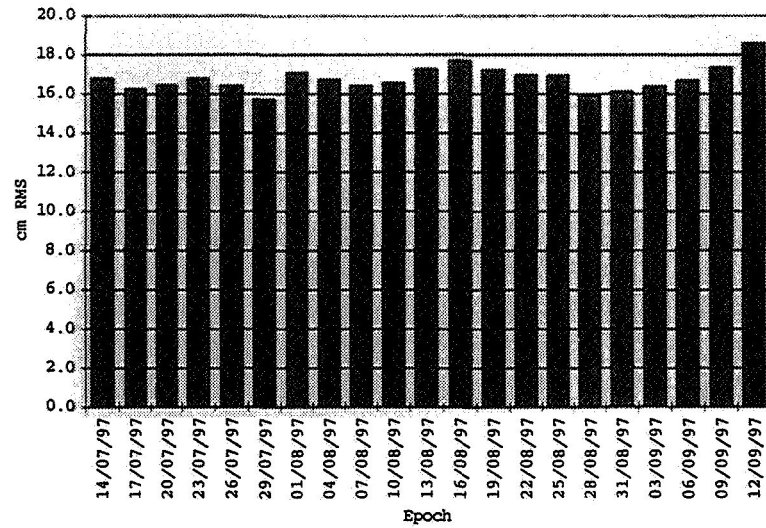


Figure 2: ERS-2 POD SLR Residuals

The altimetry residuals, of which rms statistics are shown in Figure 3, are an indication of the combined radial accuracy of the orbits and the models used in the processing of the altimeter data.



**Figure 3: ERS-2 POD Altimetry Residuals**

Another indication of the orbit accuracy is the consistency between consecutive orbit determinations. The rms difference in the overlapping arcs give an idea of the consistency of the solutions. For the SLR/altimetry combination these values are below 5 cm.

Orbits based on (revision five) PRARE data are yielding fits of the tracking data of about 7 cm RMS in range (one-way) and 0.8 mm/s RMS in range-rate (see Figure 4).

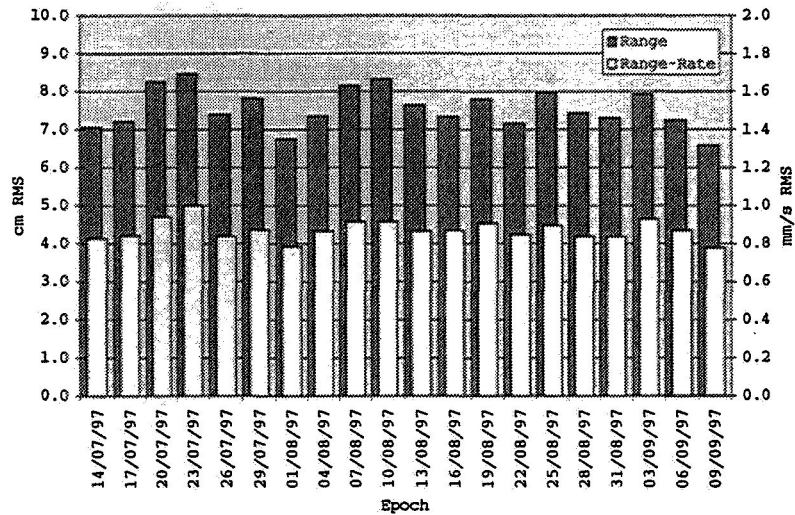


**Figure 4: ERS-2 POD PRARE Residuals**

ERS-2 altimeter products from PRARE/SLR orbits are being generated at ESOC and shown at its Internet web site (<http://nng.esoc.esa.de/>). A similar future activity will be based on DORIS/SLR orbits for Envisat. The extension of the PRARE MEX station network at the beginning of this year improved the accuracy and consistency of orbits independent from altimetry. The radial internal consistency goes from 5.7

cm for the SLR solution to 1.9 cm for the PRARE/SLR combination. The combination SLR/altimetry stays in between with 3.3 cm (see Figure 5). The problem related with the SLR solution is due to the lack of data in the first part of the analysed period, which is typical for SLR in seasons of bad weather in the northern hemisphere.

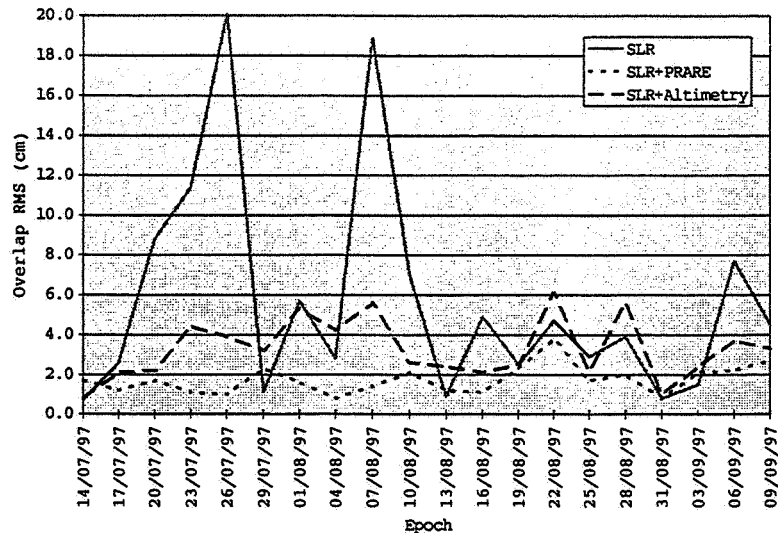


**Figure 5: ERS-2 Orbit Radial Internal Consistency for Various Tracking Scenarios**

The radial orbit comparison between the altimetry/SLR and PRARE/SLR solutions has an rms of 3.0 cm. Given that the maximum accuracy that can be obtained with the JGM3 model has been estimated to lie around 8 cm, the accuracy of the PRARE/SLR solution should be sufficient for obtaining altimeter products.

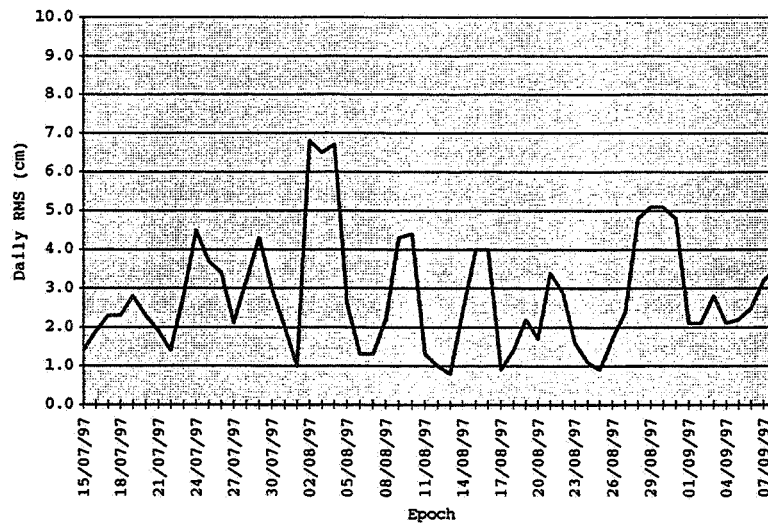


**Figure 6: ERS-2 Radial Orbit Comparison: Altimetry/SLR vs. PRARE/SLR**

## ENVISAT ORBIT DETERMINATION

ESOC Flight Dynamics is now preparing for the support of the Envisat mission. The similarities between the two spacecraft and their orbits make it possible to reuse most of the existing ERS systems for Envisat. It is important, however, also to identify the differences between the two missions in order to make the appropriate adjustments in order to maintain the existing performance and improve it where possible.



## The Envisat Tracking Devices

Four tracking devices are available on Envisat for the purpose of operational and precise orbit determination. These are:

- S-band transponder: This system provides 2-way range and range difference data from ESA's Multi-Purpose Tracking System (MPTS). This is the main source for the operational orbit determination. Its relative low accuracy (of the order of 1 meter after pre-processing) makes it unsuitable for POD.
- Laser Retro-Reflector: This is a passive device which provides a capability for high-precision 2-way ranging from the SLR network. The coverage of this network is limited to populated areas of the Earth (Europe, North America, etc.) and it is very sensitive to meteorological conditions.
- Doppler Orbitography and Radiolocation Integrated by Satellite (DORIS): This system replaces the PRARE system used on ERS. DORIS provides high precision one-way range rate observations from a very uniformly distributed network with a nearly global coverage. The device mounted on-board Envisat incorporates the second generation of the DORIS tracking system.
- Radar altimeter: Although not a tracking device in the first place, it provides height measurements above the instantaneous sea surface, which can be used to improve the operational orbit determination.

The main advantage of Envisat with respect to ERS is the global tracking data coverage provided by DORIS. Also the DORIS station co-ordinates are computed as part of the ITRF from Spot and Topex/Poseidon solutions.

## Precise Orbit Determination Prospect

To demonstrate the accuracy achievable in Envisat POD it is necessary to simulate a scenario with a similar satellite, orbit and tracking data. This is most easily achieved by using an existing mission whose characteristics are close to those of Envisat. Missions carrying a DORIS instrument are SPOT and Topex/Poseidon. Although Topex/Poseidon is more attractive because it also carries two radar altimeters and a laser retro-reflector, the SPOT orbital height is much closer to that of Envisat, and this will be the deciding factor in the achievable orbit determination accuracy. For the analysis, six arbitrarily selected months of SPOT-2 DORIS data were selected. The models used in the analysis are basically those from ERS except for the variable area table for drag and radiation pressure. The station coordinates set was taken directly from the ITRF94.

The potential accuracy of the orbits is to certain extent represented by the level of residuals in the orbit fits. For the analysed data a value of 0.56 mm/s was computed, which is equivalent with a noise in 20-second one way range normal points of 2 cm. This means that the achievable accuracy is of the same order of an orbit computed with SLR, limited by the JGM-3 geopotential to 7-8 cm in the radial direction.

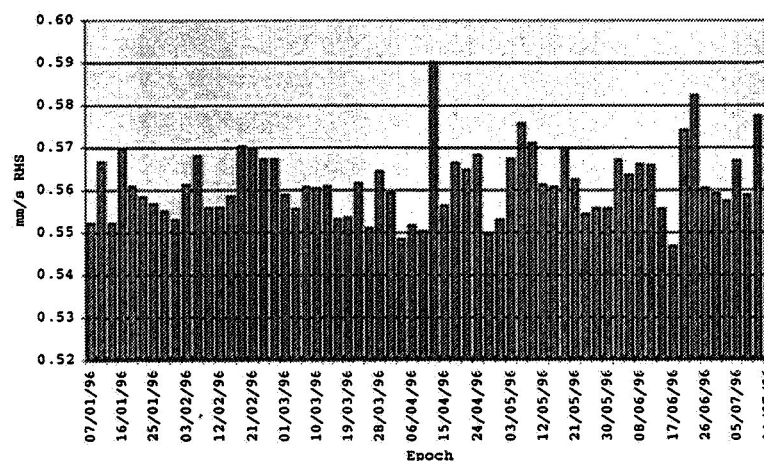
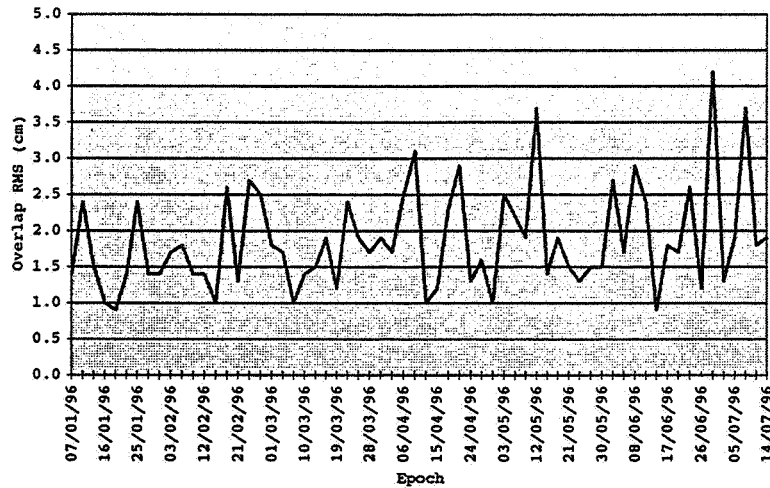


Figure 7: SPOT-2 DORIS Residuals

The internal consistency of the solutions in overlapping arcs, for the analysed period, yielded a value of 1.7 cm, which compares very favourably with the aforementioned values of 2.68 cm for altimetry/SLR solutions and 1.9 cm for PRARE/SLR solutions for ERS.



**Figure 8: SPOT-2 DORIS Orbit Internal Consistency**

## New Models for Envisat

The high solar activity expected during the Envisat mission will have two major consequences. Most importantly, the increased error in air density prediction leads to a larger error in the along-track position and velocity restitution. Secondly, the higher solar activity increases the ionospheric delay effects on the tracking data, which are not easy to model properly. The first problem is partially compensated by the higher ballistic coefficient of Envisat compared to ERS. The ionospheric modelling problem does not affect the SLR data, and can be mostly eliminated from the DORIS and altimeter instruments because both are dual-frequency systems. Still, it will be of some interest to compare the performance of the old Rawer-Bent model with that of the International Reference Ionosphere (IRI), which incorporates data from the latest period and a prediction for the next few months. Another possibility is to use GPS derived ionospheric products from the ESOC GPS analysis facilities. This has the major advantage that the very latest state of the ionosphere can be used, taking then into account any abrupt fluctuation of solar flux and geomagnetic index.

Other important areas with a potential for improvement are the gravity model, the ocean tide model and the mean and dynamic sea surface topography models.

The gravity model currently used for ERS is JGM-3, which is complete to degree and order 70. This model places a limit on the achievable radial orbit accuracy of around 7-8 cm. More recent models with acclaimed accuracies of 5 cm in the radial direction for ERS are the general-purpose TEG-3 model from the University of Texas in Austin and the ERS-tailored DGM-E04 from the Delft University in the Netherlands. These three models may be compared using ERS-2 and SPOT-2 orbit determination. Table 1 shows a summary of the results, clearly indicating that tracking data residuals are reduced significantly and so are the orbit consistency value.

		JGM-3	TEG-3	DGM-E04
SLR	SLR Residual (cm)	6.6	5.2	5.1
	Overlap (cm)	5.7	3.1	4.9

**Table 1: Gravity Models Comparison**

		JGM-3	TEG-3	DGM-E04
Altimetry/SLR	SLR Residual (cm)	6.0	5.1	5.5
	Altimetry Residual (cm)	16.0	15.3	9.7
	Altimeter Bias (cm)	9.9	9.7	9.7
	Overlap (cm)	3.3	2.1	2.4
PRARE/SLR	SLR Residual (cm)	6.6	6.2	5.8
	PRARE Range Residual (cm)	7.4	6.3	6.7
	PRARE Range-rate Residual (mm/s)	0.86	0.73	0.76
	Overlap (cm)	1.9	1.3	2.0
DORIS (SPOT-2)	Residual (mm/s)	0.56	0.55	0.55
	Overlap (cm)	1.7	1.4	1.4

Table 1: Gravity Models Comparison (contd.)

Figure 9 shows that the radial orbit consistency is especially improved using the more recent gravity model(s) if the tracking data is sparse.

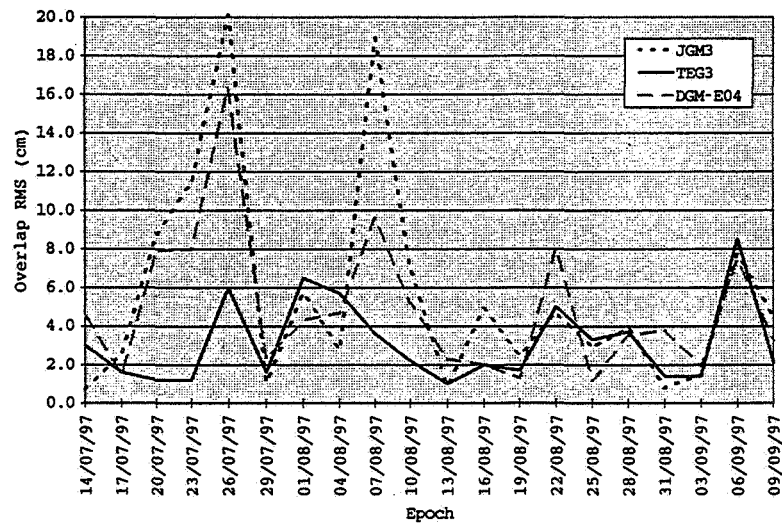


Figure 9: ERS-2 SLR Orbit Radial Internal Consistency Geopotential Models Comparison

For Envisat it is of interest to predict what the effect of using these gravity models is going to be. The radial comparisons between the orbits computed with JGM-3, TEG-3 (CST/UT) and DGM-E04 (DEOS) for different tracking scenarios (see Figures 10a, 10b and 10c) show that differences are driven by the change in model and not by the tracking data. The worst scenario (SLR only) is not much different from the best scenario (SLR + PRARE). It is also noteworthy that the differences between TEG-3 and DGM-E04 orbits computed at ESOC are not far from the differences between the CSR and DEOS computed orbits.

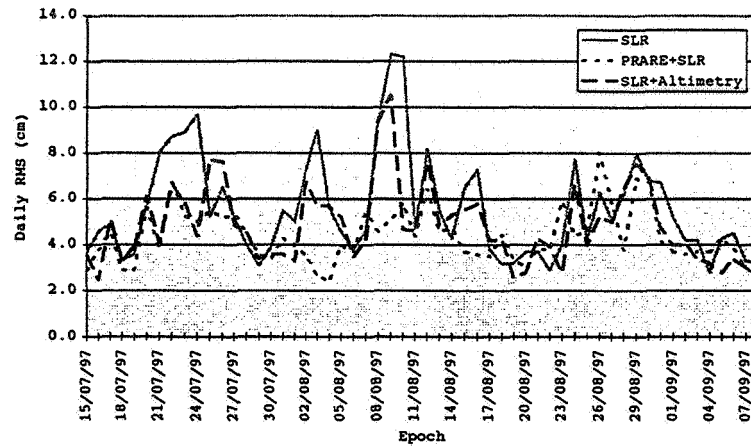


Figure 10a: Orbit Comparisons : JGM3 vs. TEG3

Figure 10a: Radial Orbit Comparisons: JGM-3 vs. TEG-3

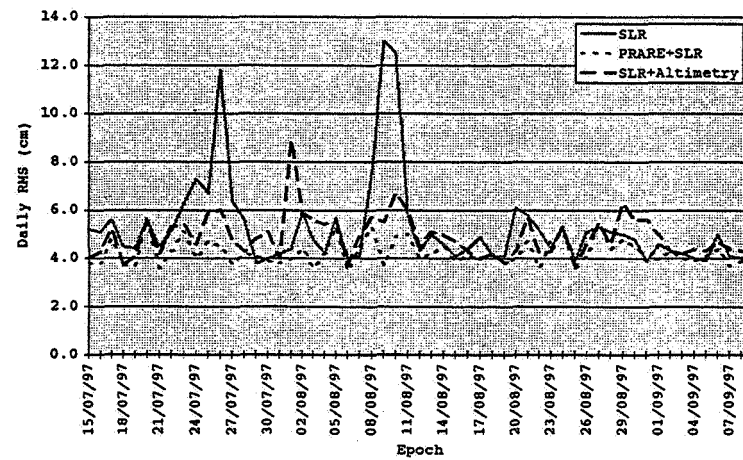


Figure 10b: Radial Orbit Comparisons: JGM-3 vs. DGM-E04

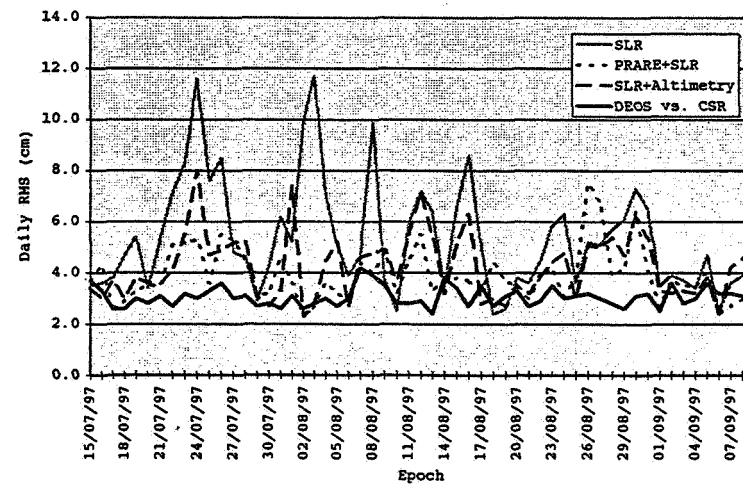
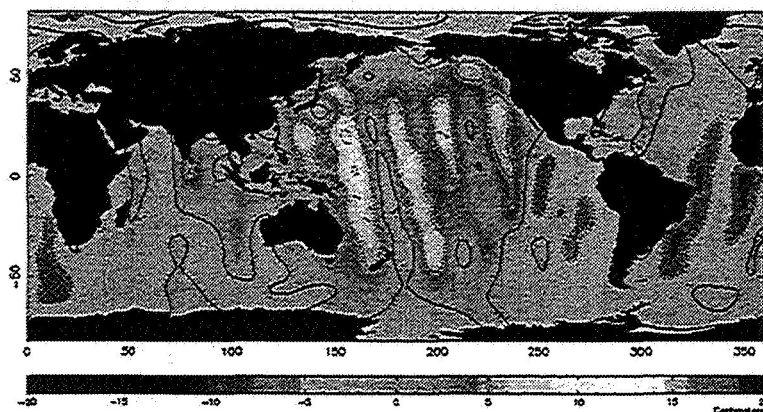
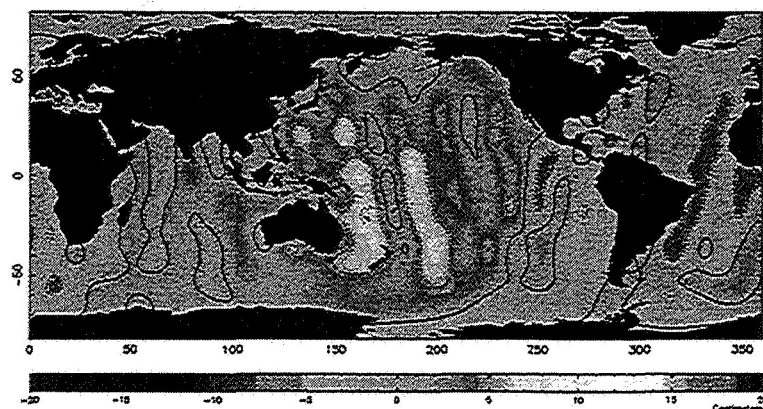


Figure 10c: Radial Orbit Comparisons: DGM-E04 vs. TEG-3

Another important effect of the use of these improved gravity models is the reduction in geographically correlated error. One can see this computing the differences between Sea Surface Topographies (SST) calculated with JGM-3 and the more recent models. Figures 11a and 11b show that this effect is essentially independent of the type of tracking used in the computation.



**Figure 11a: SST Differences (PRARE/SLR)**



**Figure 11b: SST Differences (Altimetry/SLR)**

The next important area of improvement when computing precise altimetry products is the processing of the altimetry data itself. Two significant areas for improvement are the ocean tides model and the ionospheric model. For ocean tides, the CSR 3.0 model was compared with Schwiderski using ERS-2 data. For the ionosphere, IRI-95 was tested against the Rawer-Bent model.

Altimeter residuals drop from 16.7 cm RMS using Schwiderski to 16.0 cm RMS using CSR 3.0. The altimeter bias increases by 0.3 cm although no clearly defined trend can be observed in the different arcs.

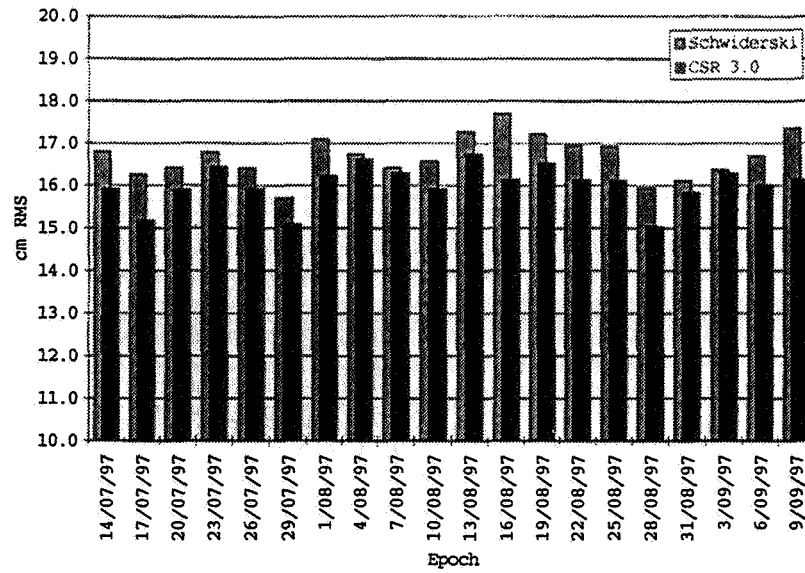


**Figure 12: ERS-2 Altimeter Residuals: Schwiderski vs. CSR 3.0 Ocean Tide Model**

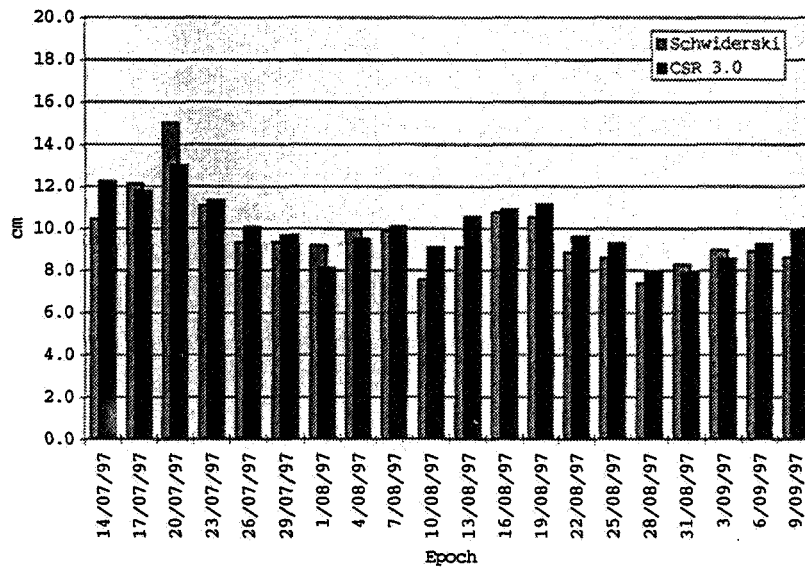


**Figure 13: ERS-2 Altimeter Bias: Schwiderski vs. CSR 3.0 Ocean Tide Model**

The impact of the detail in the ocean tide modelling in the evaluation of sea surface topographies can add up locally to several centimetres as can be seen in Figure 14.

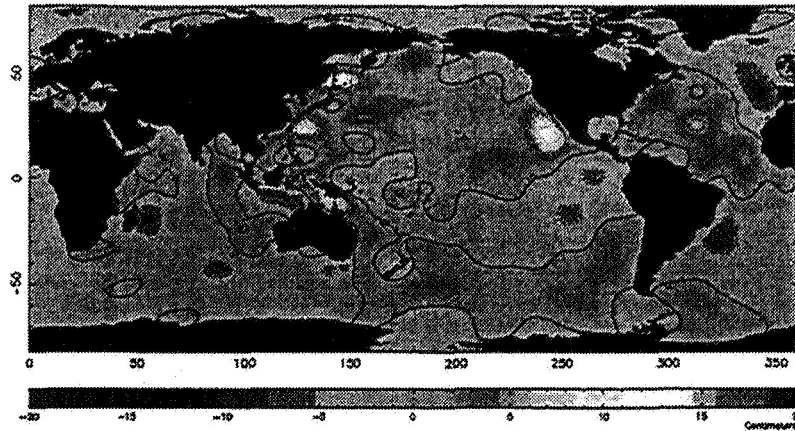


**Figure 14: Schwiderski vs. CSR 3.0 Ocean Tide Model**

The impact of the ionospheric correction is practically negligible, most likely due to the very low current solar activity that makes this correction very small. In periods of high solar activity, like for Envisat, in which this correction should become larger, the use of more accurate models than Bent should bring noticeable improvements.

### **Altimetry Products from ERS and Envisat**

In order to obtain precise altimetry products, the orbit determination should ideally not use the altimeter data as tracking data, such that aliasing of the models used in the processing into these products is avoided. A typical example is the ESOC mean sea surface model used in the processing of the ERS POD solutions, whose errors risk being propagated into the monthly dynamic topography models which are estimated and published on the WWW.

For ERS routine operational orbit determination, altimeter data are an extremely valuable addition to the set of tracking data. For this purpose, a mean sea surface model like the one derived at ESOC is ideally suited, as long as it is used with a consistent dynamic SST model. This model computed on a grid with size of  $0.3^\circ$  is based on ERS-1 altimetry data from the geodetic phase and produces much better residuals than the existing geoid models. Similarly, for ERS-2 POD using laser data, the processing of the altimeter data in the same way results in the best possible precise for verification of the routine operational products. The ESOC mean sea surface model was also ideally suited for the relative altimeter calibration between ERS-1 and ERS-2.

The dynamic SST models computed monthly from ERS-2 POD are affected by the accuracy of the ESOC mean sea surface model. The latter agrees with state-of-the-art geoid models up to degree and order 17, and no significant errors must be expected here. The SST models are computed to degree and order 23, and a constant (with time) error in these higher-degree terms will be aliased into each of the monthly solutions. This will have no discernible impact on the variations which are observed between the different months, and which have very clearly shown the effects of the well-known recent El Nino event.

It has been demonstrated that with the ERS-2 PRARE data, a precise solution independent from altimetry, but with a very similar accuracy, can nowadays be obtained and it is expected that this will be even more the case for Envisat, thanks to the almost complete global coverage from DORIS. The ESOC mean sea surface model will again be a valuable tool in the relative calibration of the ERS-2 and Envisat altimeter instruments, after which a continued production of monthly dynamic topography models with a delay of less than a few weeks will be possible. If more detailed geoid models from dedicated gravity missions become available during the lifetime of Envisat, absolute dynamic topography maps data can be obtained in near-real time from the Envisat POD carried out at ESOC.

# THE NAVIGATION PACKAGE FOR EARTH OBSERVATION SATELLITES (NAPEOS)

Aiming to support the Envisat mission with the highest level of accuracy both in data processing and environmental modelling, ESOC is developing the Navigation Package for Earth Observation Satellites (Napeos). This package, based on several years of experience in precise orbit determination and the processing of tracking data, shall be responsible all orbit and manoeuvre related activities for Envisat, from the retrieval of the data to the dissemination of both operational and precise products.

Napeos shall inherit from the ERS flight dynamics software the knowledge in precise orbit determination and orbit control, including the experience in automatic spacecraft operations and real time product generation. Based on this experience Napeos has been designed as a self-contained package capable of performing all activities required for spacecraft operations, from the data acquisition and pre-processing to the orbit determination (operational and precise), precise product generation and multi-arc physical parameter estimation. On top of this, the most advanced software engineering techniques and the extensive use of standardisation should make of Napeos a product easy to maintain and enhance.

## CONCLUSIONS

Based on the experience accumulated during the ERS missions, ESOC is capable of computing orbits with an accuracy equalling those of the world leaders in this field. This experience, combined with the use of the latest available models, will ensure the availability of high-precision orbits and altimetry products for Envisat, within days from data take.

The various analyses and comparisons shown in this paper further demonstrate the capability at ESOC to accommodate new models and tracking data types as they become available. This will be further improved by the use of the Napeos package, for which the capability to implement new models was one of the design-driving features.

## REFERENCES

1. Tapley, C. K. Shum, J. C. Ries, S. R. Poole, P. A. M. Abusali, S. V. Bettadpur, R. J. Eanes, M. C. Kim, H. J. Rim, B. E. Schutz.  
*The TEG-3 Geopotential Model*  
Center for Space Research, The University of Texas at Austin, Austin, TX 78712 USA
2. M. M. Romay Merino, R. Piriz, R. Zandbergen, J. M. Dow  
*ERS-2 Altimeter Calibration at ESOC*  
ESA/European Space Operations Centre, Robert-Bosch Strasse 5, 64293 Darmstadt, Germany
3. P. N. A. M. Visser, R. Scharroo, R. Floberhagen, B. A. C. Ambrosius  
*Impact of PRARE on ERS-2 Orbit Determination*  
Delft Institute for Earth-Oriented Space Research (DEOS), Kluyverweg 1, 2629 HS, Delft, The Netherlands
4. P. N. A. M. Visser, R. Scharroo, B. A. C. Ambrosius,  
*Incorporation of PRARE on ERS-2 Orbit Computation*  
AGU 1997 Spring Meeting, May 1997, Baltimore, Maryland  
Delft Institute for Earth-Oriented Space Research (DEOS), Kluyverweg 1, 2629 HS, Delft, The Netherlands
5. P. N. A. M. Visser, R. Scharroo, B. A. C. Ambrosius, R. Noomen  
*Incorporation of PRARE on ERS-2 Orbit Computation*  
EGS XXII General Assembly, April 1997, Vienna, Austria  
Delft Institute for Earth-Oriented Space Research (DEOS), Kluyverweg 1, 2629 HS, Delft, The Netherlands



6. F. M. Martinez Fadrique, R. C. A. Zandbergen, R. Piriz, J. Dow  
***ERS-2 Orbit Determination with PRARE***  
 EGS XXII General Assembly, April 1997, Vienna, Austria  
 ESA/European Space Operations Centre, Robert-Bosch Strasse 5, 64293 Darmstadt, Germany
7. R. Scharroo, P. N. A. M. Visser  
***Precise Orbit Determination and Gravity Field Improvement for the ERS Satellites***  
 Delft Institute for Earth-Oriented Space Research (DEOS), Kluyverweg 1, 2629 HS, Delft, The Netherlands
8. R. J. Eanes, R. and S. Bettadpur  
***The CSR 3.0 Global Ocean Tide Model***  
 Technical Memorandum, CSR-TM-95-06, December 1995  
 Center for Space Research, The University of Texas at Austin, Austin, TX 78712 USA
9. M. Rutkowska, M. M. Romay Merino  
***Estimation of the Borowiec Station Position***  
 OAD Working Paper 546  
 ESA/European Space Operations Centre, Robert-Bosch Strasse 5, 64293 Darmstadt, Germany
10. ***ERS Technical Note 21: "ERS Convention 1996"***  
 Paris, July 1996
11. ***PRARE Weekly Reports***  
 GeoForschungsZentrum, Potsdam, Germany
12. ***DORIS System Description***  
[www-project.cst.cnes.fr:8060](http://www-project.cst.cnes.fr:8060)  
 CNES, 18 Avenue Edouard BELIN, 31055 Toulouse Cedex, France



128.  
337551  
516-13  
169298

# Isolation of Tracking Error Sources within Orbit Determination

F. Delhaise\*, O. Mikkelsen† and S. Pallaschke  
ESA/ESOC, Robert-Bosch-Strasse 5, D-64293 Darmstadt, Germany

The orbit determination programs often apply a least squares estimator which provides good statistical information on the quality of the obtained solution, but does not provide adequate means for the identification of error sources. Isolation of error sources may be achieved with certain difficulty, e.g., by selecting specific sets of the tracking data and varying the solve-for parameters in successive runs.

However, the obtained results of this trial-and-error process are often ambiguous and unhelpful in the identification of the source for the degraded orbit determination result. This paper summarizes an investigation into additional functionality for the detection of unmodeled orbit determination errors such as station or transponder delay biases or an unexpectedly high noise level for a particular station. The respective merits of two different basic approaches involving extensions to the common least squares method or, conversely, alternatives to the least squares estimator, were studied.

## INTRODUCTION

The trajectory determination problem can be defined as the estimation of a set of  $p$  parameters denoted by a  $p$ -dimensional vector  $\vec{x}$  given an  $m$ -dimensional observation vector  $\vec{y}$  (with  $m \gg p$ ), the equations of motion  $\vec{f}$ , and the statistical properties of the random noise  $\vec{\epsilon}$ :

$$\vec{y} = \vec{f}(\vec{x}) + \vec{\epsilon} \quad (1)$$

The orbit determination software used in the Flight Dynamics division at ESOC uses a Gauss-Newton iterative procedure based on a weighted least squares estimator. After linearization around an initial estimate  $\vec{x}_0$ , the estimate of the differential correction is given by:

$$\Delta \vec{x} = (F^T W F)^{-1} F^T W \Delta \vec{y} \quad (2)$$

where  $F$  is the matrix of partial derivatives of  $\vec{f}$  with respect to  $\vec{x}$  evaluated at  $\vec{x} = \vec{x}_0$ ,  $\Delta \vec{y}$  is the vector difference between the observations vector and the computed measurements vector

\*. EDS Industrien (Deutschland) GmbH, based at ESOC

†. TERMA, Copenhagen, Denmark

(residuals vector) and  $W$  is a weight matrix which is taken as diagonal.

Potential error sources in the orbit determination process are usually identified via the statistical properties of the solution of the linearized problem: the loss function, mean and the root mean squares values of the residuals and covariance matrix of the estimation error. The value of the loss function is a useful measure of the degree to which the solution fits the observed data. The mean value and the root mean square (r.m.s.) of the residuals can indicate major causes of a poor fit such as unmodeled biases or a high level of observation noise. For a converged solution, the diagonal elements of the error covariance matrix indicate the dispersion of the estimated parameters while the off-diagonal elements represent the interdependence (correlation) among errors in the solve-for parameters.

These statistics alone are however sometimes insufficient to identify sources of error in the orbit estimation process. The purpose of this paper is to investigate additional functionality for detection of unmodeled orbit determination errors. Two different basic approaches were investigated (see Ref. 5 for further details).

- Extensions to the common least squares method
- Alternative to the least squares estimator

## EXTENSIONS TO THE LEAST SQUARES METHOD

The Gauss-Newton algorithm based on the least squares estimator (also called the  $l_2$  estimator) is widely used for solving the orbit determination as it constitutes a good compromise between efficiency and complexity. The main justification for using a least-squares estimator results from the Gauss-Markov theorem. It states that under the following hypothesis of the measurement noise distribution:

- the matrix of the partial derivatives  $F$  has full rank,
- the measurement noise has zero mean,
- the measurement noise has a covariance matrix positive definite known up to a multiplicative factor,

then the weighted least-squares estimator is an unbiased linear estimator. If furthermore the weight matrix is the inverse of the noise covariance matrix then the least-squares method constitutes the minimum variance estimator within the class of all unbiased linear estimators. A further mathematical justification for the least squares criterion is that it is the maximum likelihood estimator corresponding to a Gaussian distribution of the random noise.

In practice, however these necessary conditions are hardly ever completely fulfilled. In the context of this study, further investigations have been performed to find a way to diagnose the potential following problems:

- poor choice for the weight matrix (the covariance of the measurement noise is usually not perfectly known),
- poor observability of one or more solve-for parameters,
- non-zero mean value of noise,
- outliers and bias in the observations data,
- convergence problems in the strongly non-linear case.

Before investigating possible solutions to the above problems, the so-called “hat” matrix is introduced. This is particularly useful because it yields a measure of the observations quality.

## Measurement Quality - "Hat" matrix

The least squares residuals can be formulated as (see Ref. 8):

$$\begin{aligned}\hat{\mathbf{r}} &= \hat{\mathbf{y}} - \hat{\mathbf{f}}(\hat{\mathbf{x}}) \\ \hat{\mathbf{r}} &= (\mathbf{I} - \mathbf{V}) \hat{\mathbf{y}}\end{aligned}\tag{3}$$

where  $\mathbf{I}$  is the identity matrix and  $\mathbf{V}$  is the  $W$ -orthogonal projection matrix of the measurements space to the range  $\langle \mathbf{F} \rangle$  of the Jacobian matrix  $\mathbf{F}$ . This is the so-called "hat" matrix and is formulated as:

$$\mathbf{V} = \mathbf{F} (\mathbf{F}^T \mathbf{W} \mathbf{F})^{-1} \mathbf{F}^T \mathbf{W}\tag{4}$$

The matrix  $\mathbf{V}$  is a  $(m \times m)$  idempotent matrix with trace and rank  $p$ . It is an important matrix which occurs repeatedly in regression work. Its diagonal elements play a key role in determining the variance of the residuals. It can be shown that (see Ref. 8):

$$\text{Var}(r_i) = (1 - v_{i,i}) \sigma^2 / w_i\tag{5}$$

where  $v_{i,i}$  is the  $i$ -th diagonal element of the hat matrix,  $w_i$  is the weight associated to the  $i$ -th measurement and  $\sigma^2$  is the variance of the measurement noise.

The diagonal elements of the hat matrix (called here the leverage values) are a good indicator of the geometry quality of the measurements combined with their given weight value. The higher the value of the diagonal element  $v_{i,i}$ , the higher the impact of the corresponding measurement on the estimated solution. The measurements whose diagonal elements of the hat matrix exceed  $3p/m$  are called leverage measurements.

As an example, the leverage values  $v_{i,i}$  are printed in Table 1 for a typical Ariane Geostationary Transfer Orbit (GTO) simulated over a tracking interval of about 11 hours. This example consists of 2-ways ranges from Malindi (Kenya) and Villafranca (Spain) and antenna angles from Perth (Australia). The corresponding weighted partial derivatives of each measurement with respect to each solve-for-parameter evaluated at the initial estimate is also given in the defined range from 1 to 9. The maximum value of the partial derivatives for all measurements with respect to a particular solve-for parameter is set to "9" and its minimum value is set to "1".

The highest quality in terms of geometry and weight is reached by the measurements numbered 1 (Malindi), 52 (Malindi) and 55 (Villafranca), 2-ways ranges made at the start and at the end of the tracking interval. These are the computed observations which are the most sensitive to a slight change in the initial estimate. This is confirmed by the corresponding large values of the weighted Jacobian matrix.

Table 1 also shows that the leverage values of the angular data are very small, demonstrating that these observations will not really influence the obtained solution. This is explained by the fact that the angular data are much less accurate measurements than the 2-ways ranges.

The following additional information can easily be retrieved from the printed weighted Jacobian matrix. The semi-major axis is essentially estimated by the range measurements which are at the end of the tracking interval. The reason is that the semi-major axis is directly correlated to the mean motion and the longer the tracking interval, the better the mean motion estimate. The inclination is poorly estimated by the station Malindi which lies close to the equator (the

weighted Jacobian values are below 2) but it is better estimated by Villafranca's range which is furthermore taken rather far away from perigee and apogee (its weighted partial derivative w.r.t. inclination reaches its maximum).

**Table 1: Residuals - Leverage Values - Weighted Jacobian Matrix<sup>a</sup>**

no	time hh:mm	stat.	type	V deg	observat. (km, deg)	raw res (km)	stand.	student	lever.	Jacobian AEINWV
1	23:12	MAL	RNG	101	20983.690	0.0082	0.318	0.453	0.507	1 6 2 9 9 9
2	23:32	MAL	RNG	120	32167.450	0.0064	0.250	0.287	0.238	1 2 2 9 9 7
3	23:33	PER	AZI	120	323.118	0.0147	-0.573	-0.573	0.000	1 1 1 1 1 1
4	23:33	PER	ELE	120	45.778	0.0108	-0.420	-0.420	0.000	1 1 1 1 1 1
5	23:52	MAL	RNG	131	41097.270	0.0008	-0.031	-0.033	0.137	1 1 2 9 9 6
11	00:32	MAL	RNG	145	54534.538	0.0152	-0.590	-0.616	0.080	1 4 2 9 9 5
16	01:32	MAL	RNG	159	67443.624	0.0195	-0.756	-0.789	0.081	2 5 1 9 9 3
17	01:52	MAL	RNG	162	70316.844	0.0017	0.067	0.070	0.084	2 6 1 9 9 3
20	02:12	MAL	RNG	166	72590.097	0.0131	-0.509	-0.533	0.086	2 6 1 9 9 3
21	02:32	MAL	RNG	169	74307.738	0.0078	-0.303	-0.317	0.086	2 7 1 9 9 2
25	03:12	MAL	RNG	175	76203.585	0.0141	-0.548	-0.571	0.079	3 7 1 8 8 2
27	03:52	MAL	RNG	180	76186.637	0.0180	0.698	0.723	0.066	3 8 1 8 8 1
28	03:53	PER	AZI	180	320.816	0.0149	-0.580	-0.580	0.000	1 1 1 1 1 1
29	03:53	PER	ELE	180	45.421	0.0202	-0.785	-0.785	0.000	1 1 1 1 1 1
30	04:12	MAL	RNG	183	75491.652	0.0057	-0.223	-0.230	0.061	4 8 1 8 8 1
31	04:13	PER	AZI	183	318.223	0.0936	3.628	3.629	0.000	1 1 1 1 1 1
32	04:13	PER	ELE	183	43.706	0.0088	0.343	0.343	0.000	1 1 1 1 1 1
34	04:52	MAL	RNG	189	72747.763	0.0163	-0.634	-0.653	0.058	4 8 1 8 8 2
38	05:32	MAL	RNG	195	68170.470	0.0661	2.562	2.666	0.076	5 9 1 7 7 2
42	06:12	MAL	RNG	202	61659.378	0.0160	-0.622	-0.662	0.116	6 9 1 7 7 3
44	06:52	MAL	RNG	210	53040.764	0.0066	-0.258	-0.281	0.160	7 9 1 7 7 3
47	07:12	MAL	RNG	216	47879.329	0.0008	0.031	0.034	0.169	8 9 1 7 7 4
49	07:52	MAL	RNG	230	35915.199	0.0179	0.697	0.803	0.246	9 7 2 8 8 4
52	08:12	MAL	RNG	242	29556.943	0.0081	-0.315	-0.626	0.746	9 4 2 8 9 4
55	10:11	VIL	RNG	125	37818.158	0.0135	-0.525	-2.042	0.933	9 6 9 6 7 4

- a. Column 5 lists the true anomaly (deg) corresponding to each measurement; columns 8 and 9 list the standardized and studentized residuals respectively; column 10 lists the leverage values and the last column gives the scaled partial derivatives of all measurements w.r.t. each of the solve-for parameters: A: semi-major axis, E: eccentricity, I: inclination, N: right ascension of the ascending node, W: argument of perigee and V: true anomaly.

## Weighting Errors

If the number of measurements is large enough for each measurement type and ground-station, a possible weighting problem can be diagnosed by comparing the quadratic mean of the standardized residuals block by block. Measurements are defined to belong to the same block if they are of identical type and from the same station. A standardized residual  $s_i$  is defined as:

$$s_i = \sqrt{\frac{w_i}{\hat{\sigma}^2}} r_i; \quad \text{where} \quad \hat{\sigma}^2 = \frac{1}{m-p} \hat{r}^t W \hat{r} \quad (6)$$

where  $w_i$  is the weight value of the  $i$ -th measurement. The ratios of the quadratic means should be close to 1 if the weighting correctly reflects the measurement noise.

A reasonable weighting value of each block can be deduced from the obtained residuals. A suggested weight value for block "k" is:

$$p_k = A / \hat{\sigma}_k^2 ; \text{ where } \hat{\sigma}_k^2 = \frac{1}{m_k - p} \hat{r}_k^T W \hat{r}_k \quad (7)$$

where A is an arbitrary positive constant,  $m_k$  is the number of measurements in block "k" and  $\hat{r}_k$  is the residuals vector of block "k".

For the orbit determination run described in Table 1, the suggested weights are: 1.03 for Malindi, 1.02 for Villafranca and 1.05 for Perth which is ideal. But when assuming a random noise for Malindi half of the actual one, the suggested weights are 0.25 for Malindi, 1.02 for Villafranca and 1.05 for Perth which corresponds to the exact correction to bring to the assumed noise level of the three stations.

### The Problem of Observability

Multicollinearities among the solve-for parameters (i.e. they are highly correlated) result in much larger variances and correlations for the least squares estimators. This implies a much greater likelihood of a poor estimate of their respective parameters. Knowledge of multicollinearities and their attendant problems is the first step in correcting its deleterious effects. Numerical comparison of the magnitudes of the estimated solve-for parameters and their variance and covariance must be made with standardized variables in order to remove the distortions due to different scales. In the normalized space, a measure of the inflation of the variance of least squares estimators due to multicollinearities is done via the so-called Variance Inflation Factor (V.I.F.). These elements are the diagonal elements of the inverse matrix of R which is a (p x p) matrix defined as (see Ref. 4, Ref. 8):

$$R = K^{-1}(F^T W F) K^{-1} \quad (8)$$

where K is the diagonal matrix formed by the square root of the W-norm of each column of the Jacobian matrix F.

Another fundamental diagnosis of lack of observability is based on the spectral analysis of R and especially of the smallest eigenvalue of R ( $\mu_{\min}$ ). It can be demonstrated that the large components in the (standardized) eigenvectors corresponding to eigenvalues near zero identify the solve-for parameters that are involved in the multicollinearity (see Ref. 4, Ref. 8).

The factor by which the magnitude of the solve-for parameters vector is increased due to multicollinearity can be deduced from the following formula (see Ref. 10):

$$E[\hat{x}^N \hat{x}^N] = \hat{x}_T^N \hat{x}_T^N + \sigma^2 \sum_j \frac{1}{\mu_j} \quad (9)$$

where  $\hat{x}^N$  is the estimated solve-for parameters vector in the normalized space,  $\hat{x}_T^N$  is the exact solution in the normalized space,  $\sigma^2$  is the variance of the measurement noise and  $\mu_j$  are the eigenvalues of the matrix R.

As an illustration, the variance inflation factors, the eigenvalues and eigenvectors of the matrix R and the "expansion" factor of formula (9) are printed for three simulated orbit determination runs applied to:

- a GTO orbit determination with coverage from four ground-stations,
- a geostationary (GEO) orbit determination with a coverage from the four ground-stations,

- a GEO orbit determination with coverage from a single station lying at the equator.

**Table 2: Variance Inflation Factors**

	a	e	i	$\Omega$	$\omega$	f
GTO (4 stat)	5	2	1	189	188	3
GEO (4 stat)	2	3	3	$4 \times 10^3$	$2 \times 10^6$	$2 \times 10^6$
GEO (1 stat)	2	2	4	$2 \times 10^5$	$2 \times 10^6$	$9 \times 10^6$

**Table 3: Eigenvalues of the matrix R**

GTO (4 stat)	0.002	0.1	0.4	0.9	1.5	2.9
GEO (4 stat)	$3 \times 10^{-7}$	0.0002	0.3	0.6	1.4	3.6
GEO (1 stat)	$4 \times 10^{-7}$	$8 \times 10^{-6}$	0.4	0.5	0.9	4.2

Table 2 shows a clear lack of observability of the right ascension of the ascending node  $\Omega$ , the argument of perigee  $\omega$  and the true anomaly  $f$  for the geostationary orbits which is well explained by its small inclination and eccentricity values. For the first GEO for which the coverage is performed by 4 stations, only one eigenvalue is close to zero while the GEO covered by a single station shows two direction of lack of observability. These directions given by the corresponding eigenvectors of R are the following:

$$\begin{aligned}
 \text{GEO-1:} \quad \hat{e}_1 &= -0.6i + 0.6\Omega - 0.4f \\
 \text{GEO-2:} \quad \hat{e}_1 &= 0.6\Omega + 0.7\omega - 0.3f \\
 \hat{e}_2 &= 0.7\Omega - 0.6\omega + 0.3f
 \end{aligned} \tag{10}$$

The expansion factor of equation (9) is also a relevant indicator of an eventual lack of observability of certain parameters. The value of this factor is much larger for the GEO orbit types (it equals 1 and 6, respectively) than for the GTO ( $= 2.10^{-4}$ ). In conclusion, it is clear that the three angles  $\Omega$ ,  $\omega$  and  $f$  are very poorly observable, only the sum of the three angles can be determined with accuracy. This is a well known result for the orbit determination of geostationary orbits but this illustrates the utility of these additional parameters in diagnosing the attainable degree of accuracy.

### Accommodation to multicollinearities

Hoerl (Ref. 9) first suggested using a ridge-regression like algorithm to control the inflation and general instability associated with the least squares estimates. This algorithm minimizes the sum of squares of residuals with the constraint:

$$\|\Delta \hat{x}\|_{K^2} < \alpha \tag{11}$$

where  $\alpha$  is a positive real number and K is the matrix defined for the equation (8). The relationship of a ridge regression estimate to an ordinary estimate is given by a form of the following kind (see Ref. 10 for further details):



$$\Delta \hat{x}^* (\kappa) = Z_{\kappa} \Delta \hat{x} \quad (12)$$

The ridge estimators are defined as a function of a ridge parameter  $\kappa$ , whose value can be selected by the operator. The popularity of ridge regression is explained by the fact that if  $\kappa$  is chosen suitably small not only will the effects of the multicollinearities be reduced but the ridge estimator will be closer than the least squares estimator (closer in terms of the total squared errors).

In our software, an approach like the one given by equation (11) was selected. The operator has the possibility to give an initial estimate of the covariance matrix of the initial estimate  $P_{\Delta x_0}$  different from infinity. In this case, the least squares differential correction is computed at each iteration as:

$$\widehat{\Delta \hat{x}}_{\text{new}} = (F^T W F + P_{\Delta x_0}^{-1})^{-1} [F^T W \Delta \hat{y} + P_{\Delta x_0}^{-1} \Delta \hat{x}_{\text{old}}] \quad (13)$$

This solution accounts for the fact that the initial estimate  $\hat{x}_0$  is known to be accurate to a confidence level given by  $P_{\Delta x_0}$ . Therefore, any solution is constrained to satisfy the a-priori realization  $\hat{x}_0$  to within the limits of its uncertainty so that equation (11) is guaranteed to be verified.

This algorithm is especially useful when the orbit has to be estimated based on only a few measurements, e.g. shorter after separation or after a long-duration manoeuvre.

A comparison between the two methods (12) and (13) has been performed. Solution (13) has certainly the advantage that it does not depend on a tuning parameter  $\kappa$ . However, (13) only ensures convergence to a solution close to the initial estimate. It will not ensure that the obtained estimate is more accurate than the least squares estimator. Therefore (13) is suitable only when the least squares estimator cannot yield any solution at all. In other situations of real multicollinearities, a ridge estimate given by (12) is more favourable in order to ensure a more accurate solution than the usual least squares estimate.

### Outliers-Leverage Measurements

An outlier among residuals is one that is far greater than the rest in absolute value. We must distinguish carefully between a large residual caused by an inadequate model and a large residual caused by poor data (like incorrect operations of measuring means). The former can be remedied by improving the model; the latter has no remedy. A criterion such as that of least squares is very sensitive to large residuals. A few large outliers can transform a potentially useful solution to nonsense (e.g. a negative air-drag coefficient). It is therefore important in least squares estimation to detect outliers and attempt either to eliminate them or to improve the model so that they do not influence the estimation.

In our software, this problem is tackled in two ways. On one side it may automatically reject an outlier and on the other side it may use a so-called robust  $l_2$  estimator to proceed to a gentle elimination of large residuals.

The automatic rejection of outliers is based on the absolute values of the standardized residuals. The measurement is rejected if this absolute value is larger than a given threshold. Alternatively the studentized residuals could also be used as rejection criteria. These are the raw residuals  $r_i$  scaled by their estimated standard deviation:

$$t_i = \sqrt{\frac{w_i}{(1 - v_{i,i})\hat{\sigma}^2}} r_i \quad (14)$$

This studentized criterion has the advantage to be based on residuals following more closely the normal distribution than the raw or standardized residuals. But according to our tests it is not always an acceptable rejection criterion. The reason is that the leverage measurements have, by definition, a large value of the studentized residual. Therefore they are easily rejected even if they are just slightly off which is easily the case for leverage measurements which are very sensitive to the initial estimate. See, for example, the high value of the studentized residual of measurement 55 of Table 1 which is not an outlier.

Automatic rejection is not always advisable. Sometimes large residuals provide information which other data points cannot. They may indicate physical effects which are not included in the mathematical model of the orbit propagation.

As a compromise, we may consider that a large residual indicates that the observation is improbable and it should be assigned small weight (no cutoff is used). Such a robust estimator which is by definition less sensitive to large errors has been implemented as a possible option. The basic idea of this algorithm is to define the weight value of each measurement as function of the value of its standardized residual from the previous iteration (see Ref. 3, Ref. 4). This then yields to a reduction of the weight value for the measurements that have large residuals at the previous iteration. The reweighting at each iteration is defined as:

$$w_i = \begin{cases} 1 & \text{if } r_i = 0 \\ \frac{s}{r_i} \psi\left(\frac{r_i}{s}\right) & \text{if } r_i \neq 0 \end{cases} \quad (15)$$

where  $s$  is also calculated from the residuals. It is taken as the median deviation of the residuals (Ref. 4). The HAMPEL function  $\psi$  is defined as follow:

$$\psi(x) = \text{sign}(x) \begin{cases} |x| & \text{if } (0 \leq |x| \leq a) \\ a & \text{if } (a \leq |x| \leq b) \\ \frac{c - |x|}{c - b} a & \text{if } (b \leq |x| \leq c) \\ 0 & \text{if } (|x| > c) \end{cases} \quad (16)$$

with the values  $a=1.7$ ,  $b=3.4$  and  $c=8.5$ .

Being less sensitive to measurements with large residuals, this algorithm might in some cases point out better than the common least squares algorithm the error sources such as a station bias or an abnormal large measurement noise for a particular station. As an illustration, a GTO orbit was simulated over one orbital revolution with 2-ways range from four stations: Perth (66 meas.), Kourou (60 meas.), Villafranca (78 meas.) and Malindi (58 meas.). A station range bias of 600 meters was introduced for Kourou. Table 4 lists the mean and r.m.s. values obtained by

each of the two methods after convergence.

**Table 4:  $l_2$ , robust  $l_2$  and  $l_1$  comparison**

	Common $l_2$ -method		Robust $l_2$ -method		$l_1$ -method		sum of leverage values
	mean	r.m.s.	mean	r.m.s.	mean	r.m.s.	
<b>Perth</b>	-103	127	-3	19	-8	20	2.17
<b>Kourou</b>	473	477	593	593	588	588	0.67
<b>Villaf.</b>	-140	143	-3	19	-8	22	1.60
<b>Malindi</b>	-78	110	0	20	0	20	1.56

Table 4 shows that the Kourou bias is detectable in a nearly exact way by the robust  $l_2$  method via the mean and r.m.s. values. This method consequently yields a solution of a higher degree of accuracy than the common  $l_2$  method. This is a distinct advantage of this robust estimator.

However, in order to be able to pinpoint error sources such as individual station biases the following requirements must be fulfilled. The quality in terms of geometry and weight (which can be expressed as the sum of the leverage values) of the error-free measurements should be sufficiently large for the algorithm to converge to the solution primarily defined by these error-free measurements. Thus, the residuals of the faulty measurements will become large. They are subsequently automatically downweighted by the robust estimator and will then no longer influence the solution.

### Convergence

When starting the iterative process defined by equation (2) with an initial estimate far from the solution, the actual contours of the non-linear loss function are not well approximated by the linearization. The Gauss-Newton procedure may converge very slowly, it may oscillate widely around the solution or it may even fail to converge altogether. An alternative to Gauss-Newton linearization procedure is the so-called steepest descent method. The basic idea is to move from an initial estimate into the direction of the "steepest" descent of the loss function. This direction changes continuously as the path is followed. Although this method initially converges rapidly, it slows down when the solution approaches the vicinity of the minimum. Marquardt (Ref. 13) proposed an algorithm which performs an optimal interpolation between the two techniques.

The implementation of the Marquardt algorithm has been performed as a possible option, by adding a constant  $\lambda_k$  to the diagonal elements of the normal matrix. The sequence of positive real number  $\lambda_k$  has to decrease rapidly enough after each iteration to ensure convergence. The following sequence was chosen (Ref. 4):

$$\lambda_k = \frac{\gamma_k^2}{(k+1)^2}, \quad k \text{ is the iteration number} \quad (17)$$

with  $\gamma_k^2$  the diagonal elements of the normal matrix at iteration "k".

Test runs have shown that the Marquardt algorithm can provide convergence where the Gauss Newton method failed, i.e. reaching a negative semi-major axis and an eccentricity value larger than 1. However due to its reduced rate of convergence, using the Marquardt algorithm appears advisable only when the original algorithm would have failed.

## ALTERNATIVE TO THE LEAST SQUARES METHOD

### $l_1$ -Estimator

One major drawback of the least squares method is its lack of robustness (i.e. its sensitivity to large errors). The  $l_1$  and  $l_\infty$  norms are two possible alternatives for minimizing the vector of residuals of the regression equation (1) (other choice for the norm are possible but seldom used):

$$\text{Min} \|\vec{y} - \vec{f}(\vec{x})\|_p; \quad \text{for } p=1, 2 \text{ or } \infty \quad (18)$$

For the orbit determination with eventual large errors within the tracking data, the  $l_\infty$  criterion must be rejected because it assigns high weight to large residuals (since the  $l_\infty$  criterion is to minimize the largest residual).

In the opposite, the  $l_1$  criterion aims to minimize the sum of the absolute value of the residuals. It is therefore much less influenced by large residuals than  $l_\infty$  or even  $l_2$ .  $l_1$  solution is the maximum likelihood estimator corresponding to a distribution of the error which goes to zero far more slowly than the normal distribution. It, therefore, encompass large residuals that would be extremely improbable with the least squares criterion.

In our software, two weighted  $l_1$  algorithms may be used as a possible alternative to the usual least squares method: either a modification of the simplex method as implemented by Barrodale and Roberts (Ref. 2) or a modification of the dual simplex algorithm as proposed by Abdelmalek (Ref. 1). These two algorithms produced results with a comparable degree of accuracy and computing time.

The weighted  $l_1$  method was tested on numerous example cases with conditions such as a bias on the station or transponder delay, a bad initial estimate or a high noise level for a particular station. These examples showed that a degree of accuracy similar to the common least squares method is attained by the  $l_1$  solution. The rate of convergence is only slightly lower, especially in the proximity of the approaching the solution. Like the iteratively reweighted least squares method (see above) the solution is not influenced by a high noise level of a particular station. Furthermore, and contrary to the least squares method, the exact noise level of each station is exactly reflected after convergence by each station's r.m.s values. The  $l_1$  method can also be used to indicate the exact value of a previously unknown station bias (see Table 4), where least squares would tend to even out the residuals for all stations.

## ACKNOWLEDGMENT

The authors wish to acknowledge the invaluable assistance of Wolfgang Peterhänsel (EDS Industrien Deutschland GmbH, based at ESOC) in setting up the test environment and simulating tracking data.

## REFERENCES

- R1. Abdelmalek N.N. "An Efficient Method for the Discrete Linear  $l_1$  Approximation Problem. Math. Comput. 29, 844-850, 1975.
- R2. Barrodale I., Roberts F.D.K. "An Improved Algorithm for Discrete  $l_1$  Linear Approximation", SIAM J. Numer. Anal. 10, 839-848, 1973.
- R3. Branham R.L. "Scientific Data Analysis, An Introduction to Overdetermined Systems", Springer-Verlag New-York Inc, 1990.
- R4. Carrou J.P. "Spatial Mechanics", Vol 1, CNES, 1995
- R5. Delhaise F. et al. "Study of Fault Detection, Isolation and Recovery Based on Tracking Data", ESOC Final Report, to be issued, 1998.
- R6. Deutch R. "Estimation Theory", Prentice-Hall Inc, 1965
- R7. Draper N.R. and Smith H. "Applied Regression Analysis", John Wiley & Sons, Inc, 1966
- R8. Gunst R. and Mason R. "Regression Analysis and its Application", Dekker, Inc, 1980
- R9. Hoerl A.E. "Application of Ridge Analysis to Regression Problems" Chemical Engineering Progress 58, p. 54-59, 1962
- R10. Hoerl A.E. and Kennard R. W. "Ridge Regression: Biased Estimation for Nonorthogonal Problems", Technometrics, Vol 12, No.1, 1970.
- R11. Hubert M. and Rousseeuw P. "Robust regression with both continuous and binary regressors", 1998
- R12. Koch K. "Parameter Estimation and Hypothesis Testing in Linear Models", Springer-Verlag, 1987.
- R13. Marquardt D. W. "An Algorithm for Least-Squares Estimation of Non-linear Parameters", SIAM, Vol. 11, p. 431, 1963.
- R14. Meyer S.L. "Data Analysis for scientists and Engineers", John Wiley & Sons, Inc, 1975
- R15. Robison. E.A. "Least Squares Analysis in Terms of Linear Algebra", Goose Pond press, 1981
- R16. Soop E.M. "Handbook of Geostationary Orbits", Kluwer Ac. Publishers, 1994.



141.  
332553

## ACCURACY MODELING FOR SHORT-ARC DETERMINATION OF LOW EARTH ORBITS

S. Kawase\*

A concise accuracy model is derived for orbit determination and prediction. Optical and radar tracking, in the form of single-site single-pass observation, are evaluated. Orbit prediction errors are formulated analytically as functions of tracking arc length and prediction time length. The relative merits of the optics and radars are clarified through the analysis. These results offer a basis for discussing short-term strategies of spacecraft near-miss avoidance in low earth orbits.

### INTRODUCTION

Suppose a manned space station in a low earth orbit receives a warning of close approach by another orbiting object, probably a satellite no longer in service. Urgent tracking and orbit determination of the object will be needed, to analyze the approaching geometry and to work out an avoidance maneuver. It will be essential to assess the accuracy of the tracking and orbit determination, because the planning of the avoidance maneuver depends entirely on that accuracy.

It would be best if we could model the accuracy of orbit determination for every possible form of tracking, but this would be a difficult task if the tracking may involve multiple observation passes using multiple sensors at multiple sites. A viable, concise model of the orbit determination accuracy does not seem likely. However, if the orbit determination is "urgent" as mentioned above, then its tracking period must be short, probably with single-site single-pass observation, and this may change the situation. The present paper will show that the orbit determination accuracy can be modeled in concise formulations for that kind of short arc tracking.

In the present paper we first derive the accuracy model for optical tracking. The derivation is analytic, with its geometrical meaning clarified. The accuracy model is next modified to cover radar tracking, and finally the analytical results are checked against numerical evaluations.

### OPTICAL OBSERVATION AND ORBIT DETERMINATION

Assume that the earth is spherical with radius  $R$  and the tracked object is in a near-circular orbit of altitude  $h$ , as illustrated in Figure 1. The orbital path is assumed, for ease of analysis, to pass near the zenith of the tracking station,  $T$ . (This restrictive assumption will be relaxed later.) Tracking observations are made when the object is at  $P_2$ , which is directly above  $T$ , and when it is at  $P_1$  and  $P_3$ , which are at angle  $\theta$  from  $P_2$ . Thus we have three observation points, with  $\theta$  specifying the length of the observation arc. Although actual tracking will try to acquire as many data points as possible

---

\* Space Systems Section, Communications Research Laboratory, Kashima, Ibaraki 314-0012 Japan.  
Phone: +81 299 84 7149, Fax: +81 299 84 7160, e-mail: kawase@crl.go.jp.

during the observation pass, here we assume only three points because the smoothing effect of multiple data points is out of the scope of our interest.

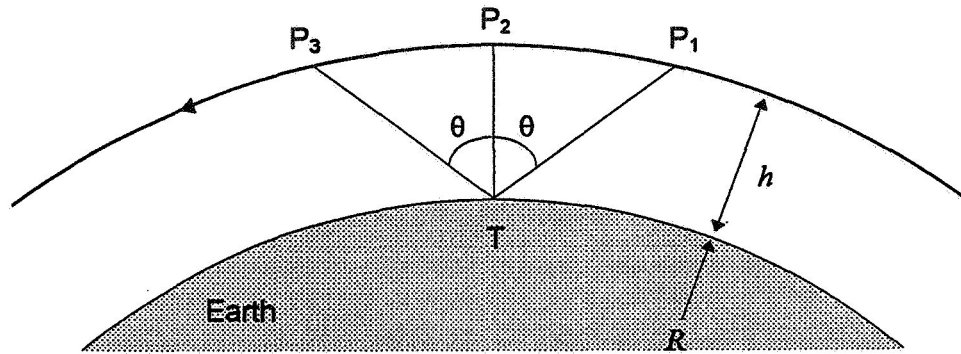


Figure 1 Tracking Geometry

Optically observed are two angles  $u$  and  $v$  as illustrated in Figure 2, where  $u$  measures the object's angular position along the flight path, and  $v$  measures that across the path. A positive  $v$  in Figure 1 would point toward the back of the page.

Any orbit determination needs an a-priori orbit of the object and this is assumed to come from cataloged orbits with a typical accuracy of several kilometers.<sup>1</sup> We assume here, for ease of analysis, that the observations made at  $P_1$ ,  $P_2$ , and  $P_3$  are so accurate that these observations newly determine the orbital elements. The sole exception is the semi major axis (SMA), which cannot be determined from single-pass tracking. The SMA has to be improved by comparing the predicted time of arrival into the observer's field of view against the actual time. So the determination of SMA is left out of our discussion and the other five orbital elements are assessed of the accuracy of determination. The reference time of the orbit determination is set at the time the object passes the zenith point  $P_2$ .

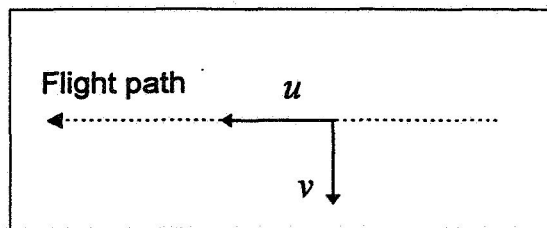


Figure 2 Optical Observations

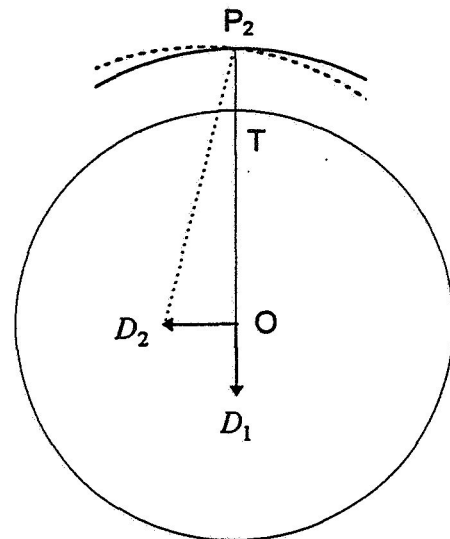


Figure 3 Center-Shift Components



## IN-PLANE ORBIT DETERMINATION

The shape of an orbit with small eccentricity can be approximated with a center-shifted circle, as shown in the Appendix. The center-shift has two orthogonal components  $D_1$  and  $D_2$ , as illustrated in Figure 3, where  $D_2$  is orthogonal to OT. Besides this, the object can have a constant displacement  $M$  along its flight path, so we have three orbital elements  $(D_1, D_2, M)$  to define the in-plane orbital motion. Suppose these elements were initially all zero. If each varies from zero slightly, then variations arise in the tracking observations; this is examined in detail below.

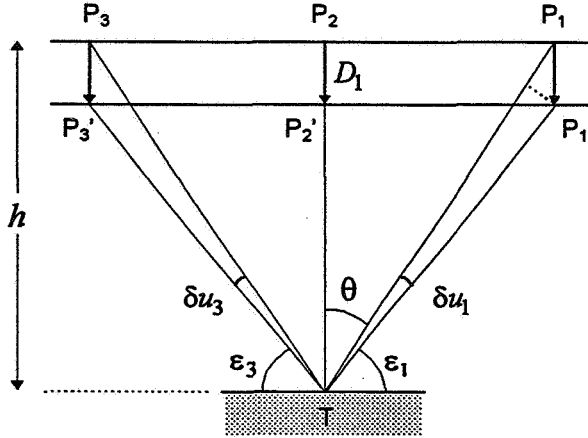


Figure 4 Observation Variation due to  $D_1$

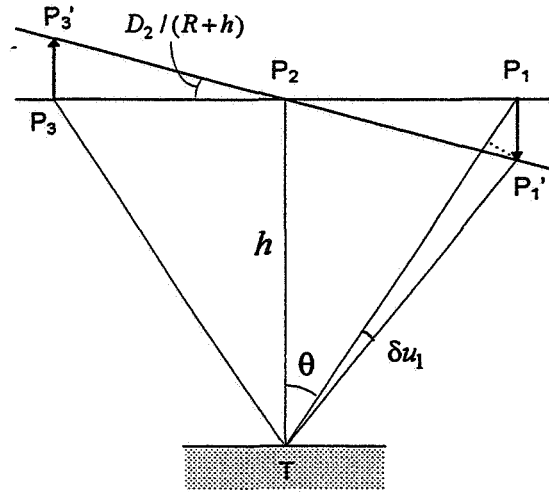


Figure 5 Observation Variation due to  $D_2$

An orbital arc visible to the tracking station is short if the orbital altitude is low. Our observation points  $P_1$ ,  $P_2$ , and  $P_3$  then lie nearly in a line as illustrated in Figure 4, and a small fictitious center-shift  $D_1$  makes these points move down by  $D_1$  to  $P_1'$ ,  $P_2'$ , and  $P_3'$ . Strictly speaking,  $P_1'P_3'$  exceeds  $P_1P_3$  because displacements arise along the path—see Eq. (A2) of the Appendix—but this excess is small so that the change from  $(P_1, P_2, P_3)$  to  $(P_1', P_2', P_3')$  may be regarded as a parallel displacement. Displacement  $P_1P_1'$  is detected at T through its transversal component  $D_1 \sin \theta$ ; dividing this by the distance  $TP_1 = h / \cos \theta$  makes the following variation arising in the observed  $u$  of  $P_1$ :

$$\delta u_1 = -(D_1 / h) \sin \theta \cos \theta \quad (1)$$

The observed  $u$  of  $P_2$  has no variation, so

$$\delta u_2 = 0 \quad (2)$$

while  $P_3P_3'$  causes the same variation as  $P_1P_1'$  but with a change of sign:

$$\delta u_3 = (D_1 / h) \sin \theta \cos \theta \quad (3)$$

Orbital perturbation and the earth's rotation are neglected because the object's time of flight from  $P_1$  to  $P_3$  is short. Consider next the center-shift  $D_2$  and assume that this shift is a "modified center-shift" as defined in the Appendix. That is to say, the orbital circle is regarded as rotating slightly, as illustrated in Figure 3, around fixed  $P_2$ . This causes the flight path near  $P_2$  to incline from being horizontal, as illustrated in Figure 5. The linear arrangement of  $P_1$ ,  $P_2$ , and  $P_3$  then inclines by  $D_2 / (R+h)$ , thus causing a displacement in  $P_1$  by  $P_1P_1' = D_2 / (R+h) \cdot h \tan \theta$ , and its contribution to the observation variation is

$$\delta u_1 = -\frac{D_2}{R+h} \sin^2 \theta \quad (4)$$

This is the same for  $P_3$ , while  $P_2$  does not move, so that

$$\delta u_2 = 0 \quad (5)$$

$$\delta u_3 = -\frac{D_2}{R+h} \sin^2 \theta \quad (6)$$

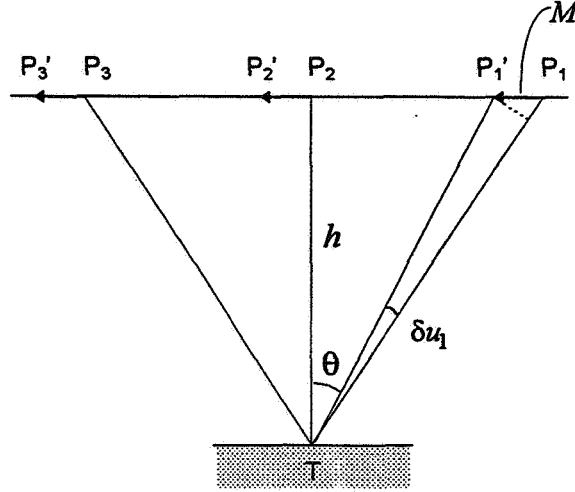


Figure 6 Observation Variation due to  $M$

Finally consider  $M$ , the along-path displacement (see Figure 6). Its transversal component causes the following variations to the observed  $u$  of  $P_1$ ,  $P_2$ , and  $P_3$ :

$$\delta u_1 = (M/h) \cos^2 \theta \quad (7)$$

$$\delta u_2 = M/h \quad (8)$$

$$\delta u_3 = (M/h) \cos^2 \theta \quad (9)$$

Eqs. (1) through (9) are combined to form

$$\begin{pmatrix} \delta u_1 \\ \delta u_2 \\ \delta u_3 \end{pmatrix} = \frac{1}{h} \begin{pmatrix} -sc & -s^2/A & c^2 \\ 0 & 0 & 1 \\ sc & -s^2/A & c^2 \end{pmatrix} \begin{pmatrix} D_1 \\ D_2 \\ M \end{pmatrix}$$

where  $s = \sin \theta$ ,  $c = \cos \theta$ , and  $A = (R+h)/h$ . Note that  $D_1$ ,  $D_2$ , and  $M$  do not cause variations in the observed  $v$ ; this allows us to invert the relationship, thereby obtaining

$$\begin{pmatrix} D_1 \\ D_2 \\ M \end{pmatrix} = h \begin{pmatrix} -\frac{1}{2sc} & 0 & \frac{1}{2sc} \\ -\frac{A}{2s^2} & \frac{Ac^2}{s^2} & -\frac{A}{2s^2} \\ 0 & 1 & 0 \end{pmatrix} \begin{pmatrix} \delta u_1 \\ \delta u_2 \\ \delta u_3 \end{pmatrix} \quad (10)$$

which ascribes the orbital element variations to the observation variations. (The left-hand side in this context should be  $\delta D_1$ ,  $\delta D_2$ , and  $\delta M$  while we omit “ $\delta$ ”s for simple notation.) Now regard  $\delta u_1$ ,  $\delta u_2$ , and  $\delta u_3$  as denoting observation errors; then Eq. (10) evaluates the error in the in-plane orbit determination.

## ORBIT PREDICTION ERROR

Evaluate next the error in predicted orbits. Suppose the object has revolved in its orbit as much as angle  $\psi$  from  $P_2$ . (This  $\psi$  may be mean anomaly or true anomaly without difference since the orbit is nearly circular.) The orbital element errors  $D_1$  and  $D_2$  of Eq. (10) give rise to an along-path error. This error equals the sum of the  $\delta l$ s of Eqs. (A2) and (A4) of the Appendix, which makes  $2D_1 \sin \psi + 2D_2 (\cos \psi - 1)$ , and this is rewritten, by using Eq. (10), as

$$(h/sc)(-\delta u_1 + \delta u_3) \sin \psi + (Ah/s^2)(-\delta u_1 + 2c^2 \delta u_2 - \delta u_3)(\cos \psi - 1).$$

Evaluating this quantity in standard deviation is our final step. Assume that  $\delta u_1$ ,  $\delta u_2$ , and  $\delta u_3$  are independent of each other and have identical normal distributions with standard deviation  $\sigma_u$ ; we then have the error evaluation of

$$\text{along-path: } h\sigma_u \frac{\sqrt{2}}{\sin \theta} \sqrt{\frac{\sin^2 \psi}{\cos^2 \theta} + A^2 \frac{1 + 2\cos^4 \theta}{\sin^2 \theta} (\cos \psi - 1)^2} \quad (11)$$

Next, for the radial error component, sum up the  $\delta r$ s of Eqs. (A3) and (A5) of the Appendix, to make  $-D_1 \cos \psi + D_2 \sin \psi$ . Rewrite this by using Eq. (10) to have

$$\frac{h}{2sc}(\delta u_1 - \delta u_3) \cos \psi + \frac{Ah}{2s^2}(-\delta u_1 + 2c^2 \delta u_2 - \delta u_3) \sin \psi,$$

and evaluate this in standard deviation in the same manner as the above, to obtain the evaluation of

$$\text{radial: } \frac{h\sigma_u}{\sqrt{2} \sin \theta} \sqrt{\frac{\cos^2 \psi}{\cos^2 \theta} + A^2 \frac{1 + 2\cos^4 \theta}{\sin^2 \theta} \sin^2 \psi} \quad (12)$$

Recall that Eq. (10) contains the relationship  $M = h \delta u_2$ , indicating that a bias error exists along the path. Evaluating this in standard deviation makes another error evaluation of

$$\text{along-path, bias: } h\sigma_u \quad (13)$$

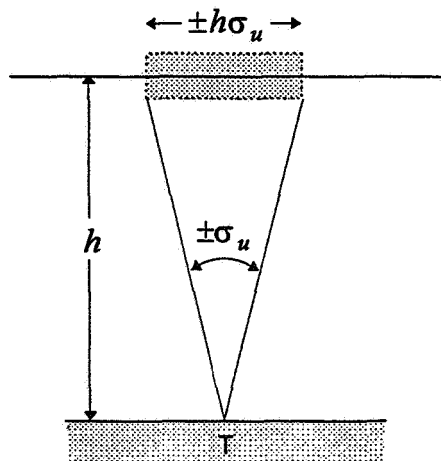
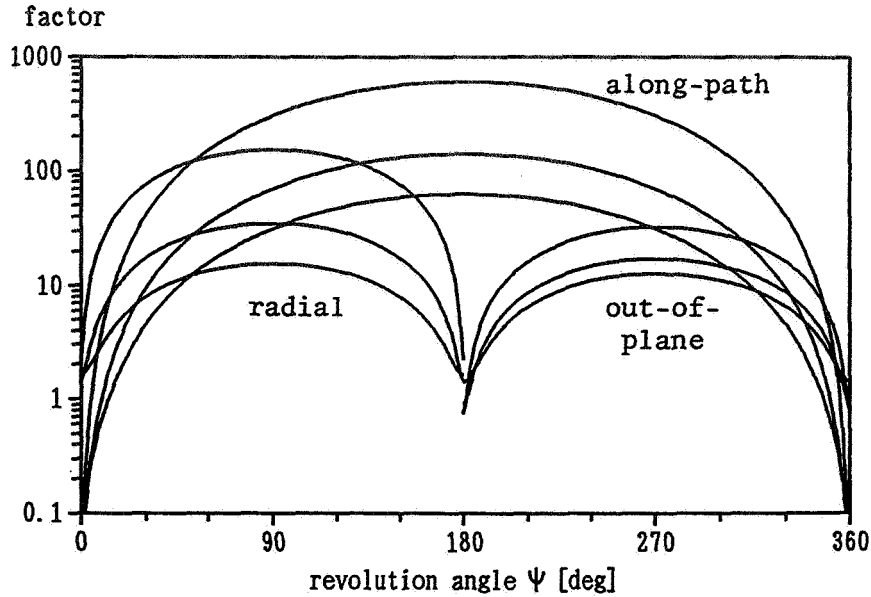


Figure 7 Basic Transversal Resolution

Evaluations (11), (12), and (13) have the following physical meaning: If we look upward from station T and project the angle observation error to the flight path (see Figure 7), then the projection



**Figure 8 Magnification Factor for Optical Tracking.**  
**From top to bottom in each group are for  $\theta = 20, 40, 60$  deg**

falls onto the width of  $\pm h\sigma_u$  along the path. We call this width the “basic transversal resolution” and it is equal to the along-path bias (13). Evaluations (11) and (12) both have the form of “basic transversal resolution  $\times$  magnification factor”, and the factors vary with  $\psi$  and  $\theta$ . At the altitude of the space station ( $h = 435$  km),  $A$  is 15.7 so that the terms with  $A$  become dominant in the square roots of evaluations (11) and (12). The along-path error thus takes its maximum at half a revolution after the orbit determination, and the radial takes its maximum at 1/4 and 3/4 of a revolution. The along-path error maximum is four times larger in magnitude than the radial maximum. By recalling the dominance of the  $A$ -terms and looking at Eq. (10) once more, we see that the orbit prediction error originates mainly from the  $D_2$ -determination error. That is to say, determining the flight path’s inclination against the horizontal plane (refer to Figure 5) is the major difficulty in determining the orbit. The observation arc  $\theta$  affects the magnification factors as shown in Figure 8, where the radial for 180 deg through 360 deg is omitted because it is periodic. A smaller  $\theta$  may cause a problem in that the newly determined and predicted orbits become less accurate, in some region of  $\psi$ , than the a-priori orbit. This problem could be avoided by weighting the a-priori orbit, but at the cost of discarding our accuracy model. The along-path factor in Figure 8 becomes less than one near  $\psi = 0$  and  $\psi = 360$  deg, at which points the bias error (13) becomes dominant.

## OUT-OF-PLANE ERROR EVALUATION

The inclination of the orbital plane has two degrees of freedom. Consider first an inclination such that the orbit-normal vector leans towards T (see Figure 9) by a small angle  $i_1$ . This causes the points  $P_1$ ,  $P_2$ , and  $P_3$  to move uniformly by  $(R+h)i_1$  to  $P_1'$ ,  $P_2'$ , and  $P_3'$ , all in parallel to the local horizontal plane of T. Accordingly, the observed  $\nu$  of  $P_1$  varies by  $P_1P_1'/TP_1$ , and the same occurs for the observed  $\nu$  of  $P_3'$ , so that we have

$$\delta\nu_1 = \delta\nu_3 = A \cos\theta \cdot i_1 \quad (14)$$

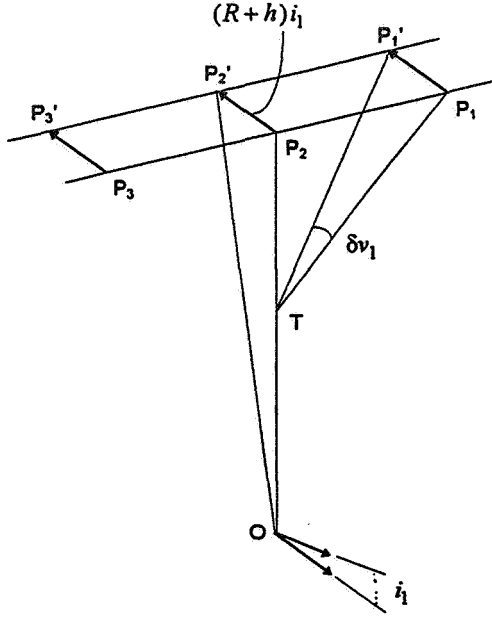


Figure 9 Observation Variation due to  $i_1$

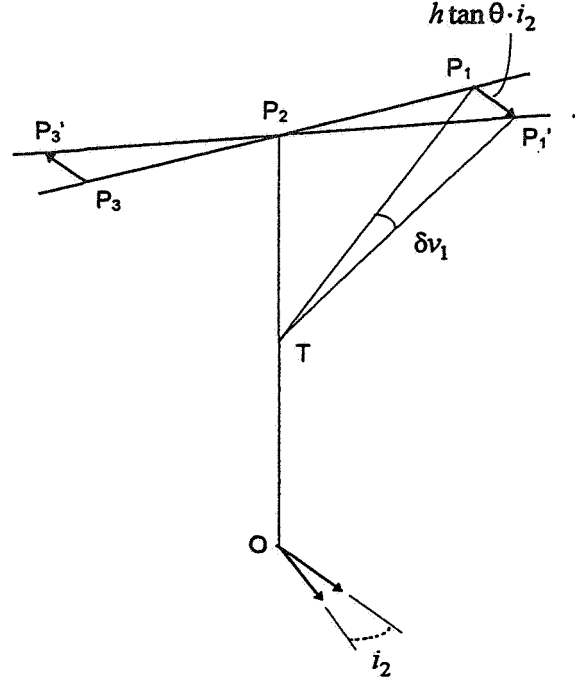


Figure 10 Observation Variation due to  $i_2$

The other inclination is illustrated in Figure 10, where the orbital plane rotates around the axis OT by  $i_2$ , and this makes the linear arrangement of  $P_1$ ,  $P_2$ , and  $P_3$  change its orientation horizontally by  $i_2$  with  $P_2$  being fixed. The displacement  $P_1P_1' = h \tan \theta \cdot i_2$  then causes a variation in  $v_1$  as

$$\delta v_1 = -\sin \theta \cdot i_2 \quad (15)$$

and the same, with an inverted sign, in  $v_3$  as

$$\delta v_3 = \sin \theta \cdot i_2 \quad (16)$$

Only two observation points  $P_1$  and  $P_3$  are considered because we are determining two orbital elements. Note that  $i_1$  and  $i_2$  cause no variations in the observed  $u$ . Equations (14), (15), and (16) are combined to form

$$\begin{pmatrix} \delta v_1 \\ \delta v_3 \end{pmatrix} = \begin{pmatrix} A c & -s \\ A c & s \end{pmatrix} \begin{pmatrix} i_1 \\ i_2 \end{pmatrix}$$

This can be inverted in order to evaluate the out-of-plane orbit determination errors:

$$i_1 = (\delta v_1 + \delta v_3) / (2A \cos \theta) \quad (17)$$

$$i_2 = (-\delta v_1 + \delta v_3) / (2 \sin \theta) \quad (18)$$

The orbital element errors  $i_1$  and  $i_2$  cause an orbit prediction error that points out of the plane. This error equals, at a revolution angle  $\psi$  from  $P_2$ ,  $(R+h)(i_1 \cos \psi + i_2 \sin \psi)$ , and this is rewritten, by applying Eqs. (17) and (18), as

$$(R+h) \left( \frac{\delta v_1 + \delta v_3}{2A \cos \theta} \cos \psi + \frac{-\delta v_1 + \delta v_3}{2 \sin \theta} \sin \psi \right).$$

Evaluating this in standard deviation assumes the same statistics for  $\delta v_1$  and  $\delta v_3$  as those for  $\delta u$ s, resulting in the evaluation of

$$\text{out of plane: } \frac{h\sigma_v}{\sqrt{2}} \sqrt{\frac{\cos^2 \psi}{\cos^2 \theta} + \frac{A^2 \sin^2 \psi}{\sin^2 \theta}} \quad (19)$$

where  $\sigma_v$  is the standard deviation of the  $v$ -observation error. The out-of-plane magnification factor has the same periodicity as the radial. It is shown, with its first period omitted, in Figure 8. If  $\sigma_u = \sigma_v$ , the out-of-plane error is always smaller than the radial at the same revolution angle  $\psi$ . Evaluations (11), (12), (13), and (19) thus model the accuracy of the optically tracked orbit determination and prediction.

The orbital accuracy may be affected by inaccurate modeling of the orbital dynamics, and such inaccuracy originates in most cases from the atmospheric drag for low altitude objects. This kind of inaccuracy however, gives rise first to a change in SMA, and through this then to a change in the along-path motion. Since the determination of SMA was left out of our present discussion, we analyzed the error relationship only between observations and orbital elements.

## RADAR OBSERVATION

Radar provides observations of range  $\rho$ , azimuth  $\alpha$ , and elevation  $\epsilon$ . Variations arising in these observations are examined here, and the tracking geometry of Figure 1 and Figures 4, 5, and 6 are again referred to. We need only two observation points,  $P_1$  and  $P_3$  in Figure 1, because the radar observation  $(\rho, \alpha, \epsilon)$  has one more degree of freedom than the optics. The other assumptions made so far do not change.

Consider first the in-plane orbital elements. Figure 4 shows that variations in the elevations  $\epsilon_1$  and  $\epsilon_3$  of  $P_1$  and  $P_3$  are written in terms of  $u$  simply as  $\delta\epsilon_1 = \delta u_1$  and  $\delta\epsilon_3 = -\delta u_3$ , so that we have the following:

$$\delta\epsilon_1 = -(D_1/h)\sin\theta\cos\theta \quad (20)$$

$$\delta\epsilon_3 = -(D_1/h)\sin\theta\cos\theta \quad (21)$$

$$\delta\epsilon_1 = -\frac{D_2}{R+h}\sin^2\theta \quad (22)$$

$$\delta\epsilon_3 = \frac{D_2}{R+h}\sin^2\theta \quad (23)$$

$$\delta\epsilon_1 = (M/h)\cos^2\theta \quad (24)$$

$$\delta\epsilon_3 = -(M/h)\cos^2\theta \quad (25)$$

Next refer to Figures 4, 5, and 6 and see that the displacement  $P_1P_1'$  creates, through its line-of-sight component, variations in the range  $\rho_1$  of  $P_1$ , as

$$\delta\rho_1 = -D_1\cos\theta \quad (26)$$

$$\delta\rho_1 = -\frac{D_2h}{R+h}\sin\theta \quad (27)$$

$$\delta\rho_1 = -M\sin\theta \quad (28)$$

and similarly to that of  $P_3$ , with some sign changes, as

$$\delta\rho_3 = -D_1\cos\theta \quad (29)$$

$$\delta\rho_3 = \frac{D_2h}{R+h}\sin\theta \quad (30)$$

$$\delta\rho_3 = M\sin\theta \quad (31)$$

The optical angles can be calibrated accurately to the reference positions of the fixed stars seen in the observational field of view. This is not the case for radar, as its elevation measurement may be affected by an unknown bias error. What the radar actually does is thought to be the following. Let  $\hat{\epsilon} = \epsilon_1 - \epsilon_3$ , the difference between the two elevations, make our tracking observation. The bias error commonly existing in  $\epsilon_1$  and in  $\epsilon_3$  then cancel out so that an accurate observation of  $\hat{\epsilon}$  can be made. Accordingly, Eqs. (20) through (25) reduce to the following three equations:

$$\delta\hat{\epsilon} = 0 \cdot D_1 \quad (32)$$

$$\delta\hat{\epsilon} = -\frac{2D_2}{R+h} \sin^2 \theta \quad (33)$$

$$\delta\hat{\epsilon} = (2M/h) \cos^2 \theta \quad (34)$$

Combine Eqs. (26) through (34) and denote  $s = \sin \theta$ ,  $c = \cos \theta$ , and  $A = (R+h)/h$  to make

$$\begin{pmatrix} \delta\rho_1 \\ \delta\rho_3 \\ \delta\hat{\epsilon} \end{pmatrix} = \begin{pmatrix} -c & -s/A & -s \\ -c & s/A & s \\ 0 & -2s^2/(Ah) & 2c^2/h \end{pmatrix} \begin{pmatrix} D_1 \\ D_2 \\ M \end{pmatrix}$$

and invert it as

$$\begin{pmatrix} D_1 \\ D_2 \\ M \end{pmatrix} = \frac{1}{2} \begin{pmatrix} -1/c & -1/c & 0 \\ -Ac^2/s & Ac^2/s & -Ah \\ -s & s & h \end{pmatrix} \begin{pmatrix} \delta\rho_1 \\ \delta\rho_3 \\ \delta\hat{\epsilon} \end{pmatrix} \quad (35)$$

in order to evaluate the in-plane orbit determination error due to the observation errors  $\delta\rho_1$ ,  $\delta\rho_3$ , and  $\delta\hat{\epsilon}$ .

Evaluating the orbit prediction errors from Eq. (35) proceeds in the same way as that for the optics. Set the error standard deviations of range and elevation to  $\sigma_\rho$  and  $\sigma_{\hat{\epsilon}}$ , and the resulting evaluations are

$$\text{along-path: } \sigma_\rho \sqrt{2} \sqrt{\frac{\sin^2 \psi}{\cos^2 \theta} + A^2 \left( \frac{\cos^4 \theta}{\sin^2 \theta} + \frac{k^2}{2} \right) (\cos \psi - 1)^2} \quad (36)$$

$$\text{radial: } \frac{\sigma_\rho}{\sqrt{2}} \sqrt{\frac{\cos^2 \psi}{\cos^2 \theta} + A^2 \left( \frac{\cos^4 \theta}{\sin^2 \theta} + \frac{k^2}{2} \right) \sin^2 \psi} \quad (37)$$

These now have the form of "range resolution  $\times$  magnification factor." The constant  $k = h\sigma_{\hat{\epsilon}}/\sigma_\rho$  is the ratio of the elevation's basic transversal resolution to the range resolution, which depends on each radar and on the orbital altitude. Except for this dependency on  $k$ , the way that errors (36) and (37) vary with the revolution angle  $\psi$  is similar to errors (11) and (12), eliminating the need to plot them. Particular to the radar is the absence of  $1/\sin \theta$  at the head and this makes the radar highly accurate when the observation arc is short.

The along-path bias error from Eq. (35) is  $M = (-\sin \theta \cdot \delta\rho_1 + \sin \theta \cdot \delta\rho_3 + h\delta\hat{\epsilon})/2$ , which is evaluated in standard deviation as

$$\text{along-path, bias: } \sigma_\rho \sqrt{\frac{\sin^2 \theta}{2} + \frac{k^2}{4}} \quad (38)$$

Finally, there is the out-of-plane error evaluation. In Figure 9, the displacement  $P_1P_1'$  causes a

variation in azimuth by angle  $\angle P_1 P_2 P_1'$ , which is larger than  $\delta v_1$  the optically observed variation. But it is larger simply because of the radar's azimuth-elevation mechanism, and the azimuth observations are thus physically equivalent to  $v_1$  and  $v_3$ . Therefore the out-of-plane evaluation can be based on (19), as

$$\text{out of plane: } \frac{h\sigma_\alpha}{\sqrt{2}} \sqrt{\frac{\cos^2 \psi}{\cos^2 \theta} + \frac{A^2 \sin^2 \psi}{\sin^2 \theta}} \quad (39)$$

where  $\sigma_\alpha$  is the azimuth error standard deviation. Evaluations (36) through (39) thus model the accuracy of the radar-tracked orbit determination and prediction.

## NUMERICAL TEST

Our analysis is based on a number of assumptions and approximations. The analytical results were therefore checked against more exact numerical error-evaluations.

The assumptions of two-body orbits along with two or three observation points is the same. Again, the earth's rotation is neglected. The orbital element variations propagate, without approximations, to the observation variations through the numerical processing of satellite motions and tracking observations. This provides the normal equation of the least square method, from which an exact error covariance matrix of  $5 \times 5$  can be used to evaluate the orbital element errors. These errors are then Kepler-propagated in order to evaluate the orbit prediction error; this makes our check-reference. The error standard deviations of optical and radar angles are all assumed to be 10 arcsec and that of radar range to be 21 m, and the orbital altitude to be 435 km; this makes constant  $k=1$ .

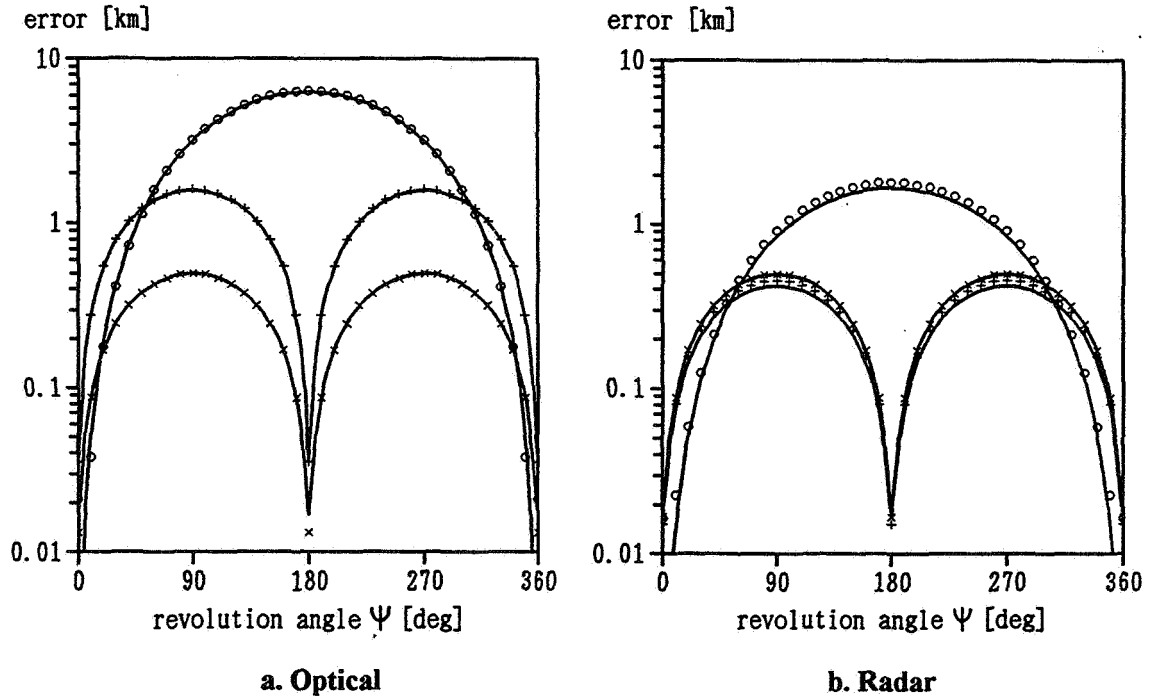


Figure 11 Numerical Test

— is analytical; o (along-path), + (radial), x (out-of-plane) are numerical;  $\theta=28$  deg



The analytical and numerical evaluations were compared. Figure 11 shows that the evaluations agree each other with small discrepancies, if any. The analytical and numerical evaluations were compared at the error-maximums (i.e., at  $\psi=180$  deg for along-path and at  $\psi=90$  or  $270$  deg for radial and out-of-plane) while the observation arc  $\theta$  was being varied. The results, shown in Figure 12, indicate the practical validity of our analytical model.

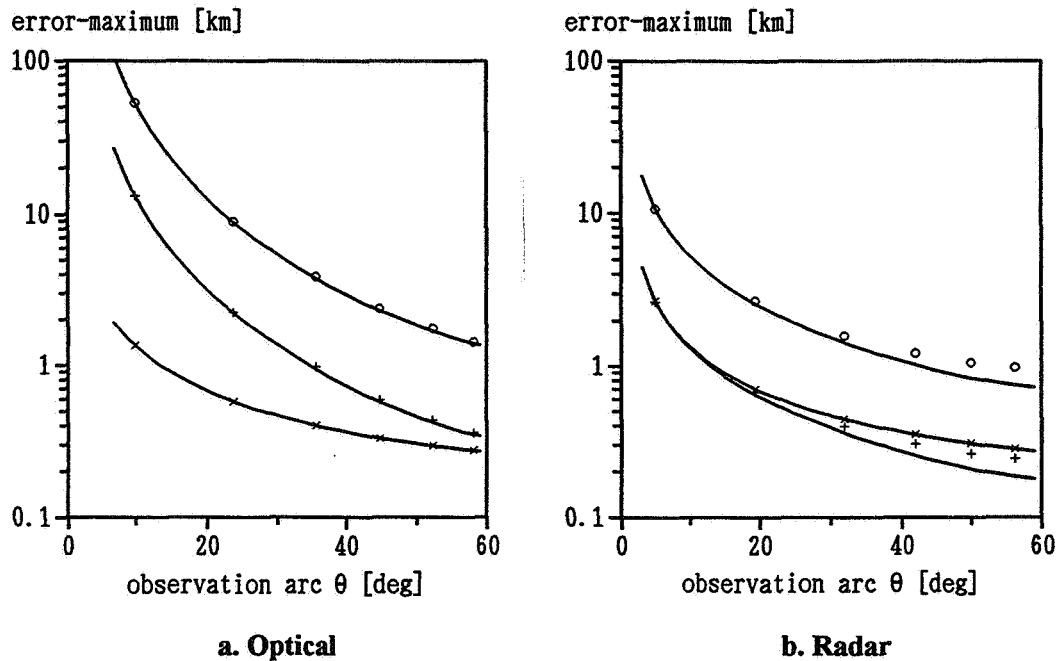
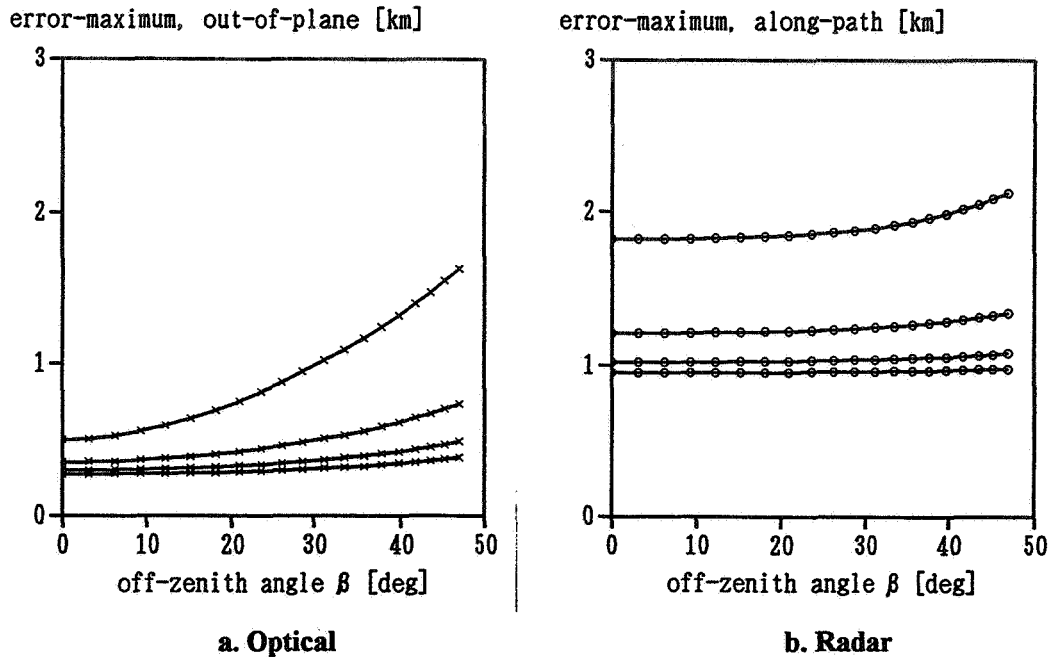


Figure 12 Numerical Test

— is analytical,  $\circ + x$  (same as in Figure 11) are numerical

The “zenith passing path” has been the most restrictive of our assumptions. Let the orbital path be off the zenith by angle  $\beta$  as viewed from T. This causes the numerical evaluation for the optics to differ from what appears in Figure 11(a). This difference, which was seen only in the out-of-plane error, caused the evaluation plot to elongate and have an increased maximum. (Its minimum changed little.) This increase in the error-maximum, which is shown in Figure 13(a), depends on  $\beta$  and  $\theta$ . The same thing also occurs with the radar, where the along-path error suffers the increase in error-maximum as shown in Figure 13(b). The results suggest that, practically speaking, our analytical model still works for non-zenith passing paths, except for optical tracking with a short observation arc and a large off-zenith angle.



**Figure 13 Effect of Off-Zenith Path (Numerical Evaluation)**

From top to bottom are for  $\theta = 28, 42, 52, 60$  deg

## SUMMARY

Although restricted to a particular case of single-site single-pass tracking, we have established orbit determination accuracy models for optical and radar observations. The principal difference between the optics and the radar, in terms of our analysis was the radar's superior accuracy of in-plane orbit determination when the observation arc is short. Otherwise, the orbit prediction errors that arose were common to optics and radars, with major error sources commonly being the difficulty in determining the flight path's inclination.

That the orbital prediction errors take their maximums and minimums at particular points of a revolution will be worth notice when near-miss avoidance strategy is discussed. More precise modeling obviously needs to consider the error in SMA. Its effects, however, will stay small in short-term orbital predictions.

The present accuracy modeling will offer a basis for discussing short-term strategies of near-miss warning and avoidance in low earth orbits.

## REFERENCES

1. S. A. Chamberlain, T. A. Slauenwhite, "United States Space Command Space Surveillance Network Overview", Proceedings of the First European Conference on Space Debris, Darmstadt, Germany, 5-7 April 1993.

## APPENDIX

### Shape Of Near-Circular Orbit

Consider an elliptical orbit with semi major axis  $a$  and small eccentricity  $e$ , with its focus at  $O$  in Figure A1 and perigee at  $P$ . Let  $S$  be a satellite at true anomaly  $f$ , and  $O'$  a point away from  $O$  by  $ae$  to the opposite of  $P$ . Find then the distance from  $O'$  to  $S$ .

The formula for the satellite radius is  $r = a(1 - e^2)/(1 + e \cos f)$ , which is approximated for small  $e$  by

$$r = a - ae \cos f \quad (A1)$$

The distance in question is then written as  $O'S = \sqrt{r^2 + (ae)^2 - 2rae \cos(\pi - f)}$ , which reduces, with  $e^2$  being neglected, to  $O'S = a$ . The shape of our orbit is therefore a circle with radius  $a$ , centered at  $O'$ , which is shifted from  $O$  by  $D = ae$ .

### Position Variation due to Center-Shift

Suppose we have a satellite in a circular orbit, and this satellite is at mean anomaly  $m$ . And suppose that the eccentricity changes from its initial zero to a small  $e$  resulting in a center-shift by  $D = ae$ . Find how much the satellite's position varies.

Satellite true anomaly  $f$  is related to the mean anomaly  $m$  by  $f - m = 2e \sin m$ . The position thus varies, along the orbital path, by

$$\delta l = a(f - m) = 2ae \sin m = 2D \sin m \quad (A2)$$

As for radial variation, see Eq. (A1) and set  $\delta r = r - a = -ae \cos f$ . Approximate  $e \cos f \cong e \cos m [1 - (f - m) \sin m] \cong e \cos m$ , since  $e(f - m)$  is small to the order of  $e^2$ . The variation is then written as

$$\delta r = -ae \cos m = -D \cos m \quad (A3)$$

We regard this  $D$  in Eqs. (A2) and (A3) as causing the satellite position variation.

### Modified Center-Shift

Suppose we have a satellite in a circular orbit, to which the following two events occur:

- The center shifts by  $D$ .
- The satellite displaces along the path by  $-2D$ .

This combined set of events is referred to as a "modified center-shift," and it makes Eq. (A2) change to  $\delta l = 2D(\sin m - 1)$ , while the  $\delta r$  in Eq. (A3) remains valid with little error. Let  $m' = m - 90^\circ$  and use this  $m'$  to rewrite  $\delta l$  and  $\delta r$  as

$$\delta l = 2D(\cos m' - 1) \quad (A4)$$

$$\delta r = D \sin m' \quad (A5)$$

What we are doing is better understood by looking at Figure A2 as follows: Our initial orbit is centered at  $O$ , with  $Q$  being a quarter revolution point.  $S$  is a satellite at revolution angle  $m'$  from  $Q$ . Now event a) occurs so that our new orbital circle becomes centered at  $O'$ , while the new orbit passes  $Q$  because event b) assures  $\delta l = \delta r = 0$  for a satellite at  $Q$ . Satellite  $S$  then experiences a position variation that obeys Eqs. (A4) and (A5). Note that  $O'Q$  is a radius of the new orbital circle, while the length  $O'Q$  is virtually equal to  $OQ$  for a small  $D$ .

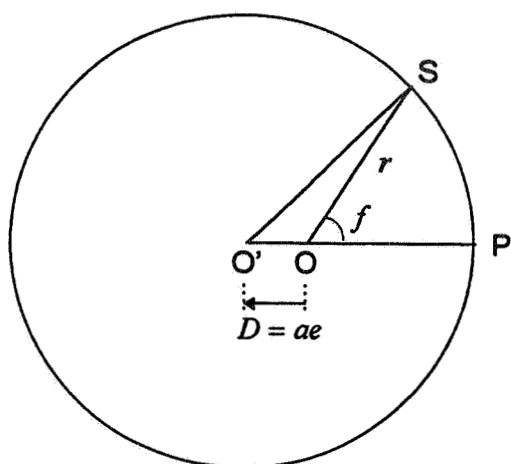


**Figure A1** Shape of the Orbit

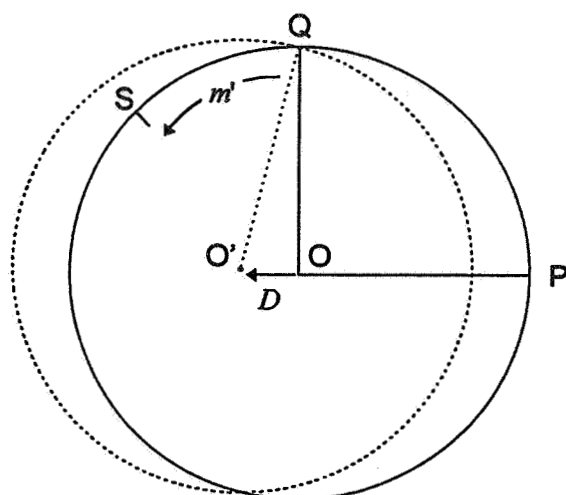


**Figure A2** Modified Center-Shift

337557 121. 5/8-13  
169300

## ORBITAL PERTURBATIONS USING GEOPOTENTIAL COEFFICIENTS UP TO HIGH DEGREE AND ORDER: HIGHLY ECCENTRIC ORBITS

Rodolpho Vilhena de Moraes\* and Edwin Wnuk†

Several methods have been proposed for calculations of the eccentricity function for a high value of the eccentricity, however they cannot be used when the high degree and order coefficients of gravity fields are taken into account. The method proposed by Wnuk<sup>1</sup> is numerically stable in this case, but when is used, a large number of terms occurs in formulas for geopotential perturbations.

In this paper we propose an application of expansions of some functions of the eccentric anomaly  $E$  as well as Hansen coefficients in power series of  $(e - e^*)$ , where  $e^*$  is a fixed value of the eccentricity derived by Da Silva Fernandes<sup>2,3,4</sup>. These series are convergent for all  $e < 1$ .

### INTRODUCTION

Recent applications of artificial satellites needs the description of the orbital motion under a precision of centimeters. For example, the radial component of position of altimetric satellites such as ERS-1, ERS-2 and TOPEX/POSEIDON must be determined with a precision of a few centimeters in order that the altimetric measurements can be conveniently used.

Also, in order to avoid collisions of important and big spacecraft, such as future space stations, the position of objects (active satellites and space debris) must be computed with a precision of the order of meters.

Taking into account the perturbations due to the geopotential, theories of motion of satellites must be developed, as well as models for the potential, to attain the expected level of description of the satellite's motion.

Within this aim, the well-known Kaula's geopotential perturbations theory<sup>5</sup> can be slightly modified (Wnuk<sup>6</sup>) introducing the lumped coefficients which group terms with the same frequency. Lumped coefficients simplifies the derivation of the expressions for the perturbations and enable us to consider a great number of geopotential coefficients.

\* Grupo de Dinâmica Orbital e Planetologia, DMA-FEG-UNESP, 12500-000, Guaratinguetá, SP, Brazil, e-mail: rodolpho@feg.unesp.br

† Astronomical Observatory of the Adam Mickiewicz University, Poznań, Poland, e-mail: wnuk@phys.amu.edu.pl

Orbits with a high eccentricity ( $e \sim 0.5 - 0.8$ ), besides near circular ones, are very popular and are used in many satellite missions. For example, some artificial Earth satellites, like Molnya type satellites, are placed in orbits with  $e \cong 0.6 - 0.7$ , geostationary transfer orbits (GTO) have the same eccentricity, and orbits with the similar eccentricity are used in some planet's missions (e.g. past and future Mars' missions, Galileo mission). Usually numerical integration of the equations of motion is applied in calculation of orbits with a such high eccentricity. However, in some applications one needs an analytical description of the satellite motion.

Analytical theories of an artificial satellite motion give formulas for perturbations that are in a closed form for the eccentricity only in a case of perturbations due to some zonal harmonic coefficients. In the general case, when an arbitrary degree and order spherical harmonic coefficients have to be taken into account, series of expansions in the eccentricity have to be used in formulas for perturbations. Some difficulties occur when the analytical theory of a satellite motion is used in calculations of a precise position on a highly eccentric orbit. The source of these difficulties is the calculation of the eccentricity functions (Hansen's coefficients) and their derivatives. The Kaula's formula for the eccentricity function is not numerically stable for a large values of eccentricity and simultaneously large values of indices.

Several methods were proposed for calculations of the eccentricity function for a high value of the eccentricity ( e.g. Szeto and Lambeck<sup>7</sup>, Gooding and King-Hele<sup>8</sup>, Rosborough and Lemoine<sup>9</sup>), however they cannot be used when the high degree and order coefficients of gravity fields are taken into account. The method proposed by Wnuk<sup>1</sup> is numerically stable in this case, but when is used, a large number of terms occurs in formulas for geopotential perturbations.

In this paper we propose an application of expansions of some functions of the eccentric anomaly  $E$  as well as Hansen coefficients in power series of  $(e - e^*)$ , where  $e^*$  is a fixed value of the eccentricity derived by Da Silva Fernandes<sup>2,3,4</sup>. These series are convergent for all  $e < 1$ .

## PERTURBATIONS DUE TO THE GEOPOTENTIAL

The geopotential  $V$  expressed in orbital elements can be put in the following form (Wnuk<sup>6</sup>):

$$V = \frac{GM}{r} + \frac{GM}{a} \sum_{m=0}^N \sum_{k=-N}^N \sum_{q=-Q}^Q \gamma_{km} (C_m^{kq} \cos \psi_{mkq} + S_m^{kq} \sin \psi_{mkq}), \quad (1)$$

where

$$\begin{aligned} C_m^{kq} &= \sum_{j=j_1}^N {}^* Q_{jm}^{kq} \bar{C}_{jm}, \\ S_m^{kq} &= \sum_{j=j_1}^N {}^* Q_{jm}^{kq} \bar{S}_{jm}, \end{aligned} \quad (2)$$

are the generalized lumped coefficients,  $\bar{C}_{l,m}$  and  $\bar{S}_{l,m}$  are normalized geopotential coefficients,

$$Q_{jm}^{kq} = \left( \frac{a_e}{a} \right)^l A_{jm}^k G_{j,(j-k)/2,q} \quad (3)$$

are functions of the normalized inclination function  $\bar{A}_{lm}^k(I) = \bar{F}_{l,m,(l-k)/2}(I)$  and of the eccentricity function  $G_{lpq}(e)$  (Kaula<sup>5</sup>),

$$\begin{aligned} \psi_{mkq}(\omega, \Omega, M, \Theta) &= k\omega + (k+q)M + m(\Omega - \Theta) + (k-m)\frac{\pi}{2}, \\ j_1 &= \max [k_1 k_1 + 2E((m-k_1+1)/2)], k_1 = |k| + 2(\delta_{0k} + \delta_{1k}), \\ \gamma_{km} &= (1)E^{[(k-m+1)/2]}, \end{aligned} \quad (4)$$

$N = \max l$ ,  $Q = \max |q|$ ,  $E(x)$  is the Entier function and the symbol  $\sum^*$  stands for summation with step 2.

The general form of the formulas for the first order geopotential perturbations in the quantity  $\varepsilon$  (an orbital element or a component of the radius vector) is the following (Wnuk<sup>1,10</sup>, Wnuk and Breiter<sup>11</sup>):

$$\Delta \varepsilon = \sum_{m=0}^N \sum_{k=-N}^N \sum_{q=-Q}^Q \left( A_{mkq}^1 \cos \psi_{mkq} + B_{mkq}^1 \sin \psi_{mkq} \right), \quad (5)$$

where the amplitudes  $A_{mkq}^1(a, e, I)$ ,  $B_{mkq}^1(a, e, I)$  are functions of generalized lumped coefficients  $C_m^{kq}$ ,  $S_m^{kq}$ .

As an example, Fig. 1 shows the perturbations due to the geopotential for the Brazilian satellite SCD1. The perturbations obtained are given as function of the order  $m$  of the harmonics. The 70x70 JGM-3 (Nerem et al.<sup>12</sup>) geopotential model has been used in calculations. The spectrum of the perturbations shows that coefficients of high degree and order must be taken into account if it is necessary to attain precision of centimeters. Estimated values of perturbations in components of the radius vector (the radial,

transverse and normal components) are plotted on fig.2. Figure 3. shows differences between numerical integration and the analytical method for the orbit of SCD1 satellite in the case of tesseral harmonic perturbations. One can see very good agreement, on a level of 1 cm, of the analytical theory with numerical integration.

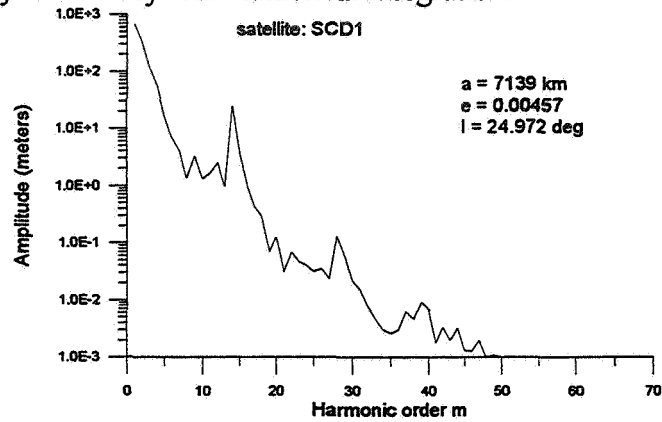


Fig.1. Total perturbations due to the geopotential for the Brazilian satellite SCD1.

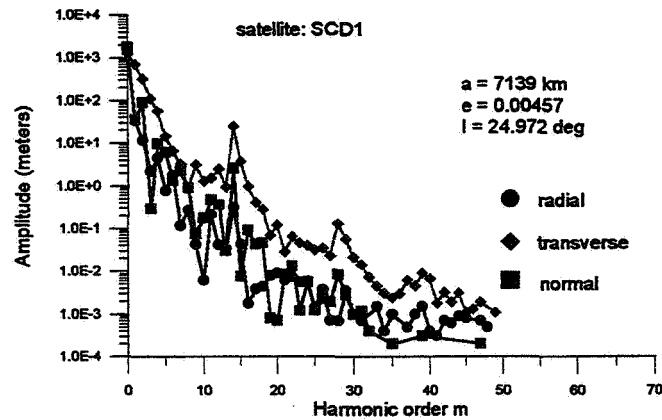


Fig.2. Perturbations in components of the radial vector for the Brazilian satellite SCD1.

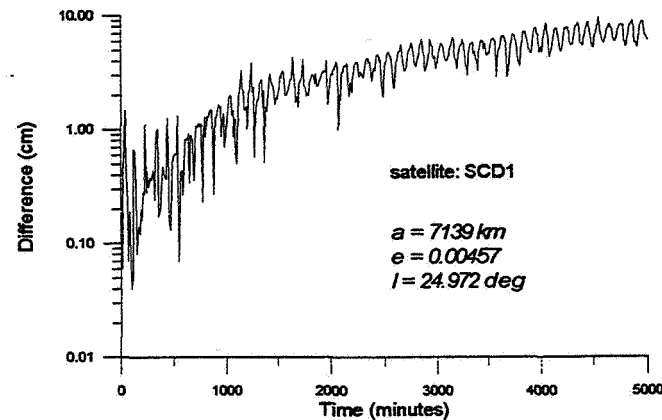


Fig.3. Differences between numerical integration and the analytical method for the low eccentricity orbit of the Brazilian satellite SCD1.



## HIGHLY ECCENTRIC ORBITS

The Kaula's eccentricity function  $G_{l,p,q}(\epsilon)$  is related to the Hansen's coefficients  $X_k^{n,m}(\epsilon)$  by the following equation:

$$G_{l,p,q} = X_{l-2p+q}^{-(l-1)(1-2p)}(\epsilon). \quad (6)$$

The Tisserand<sup>13</sup> (1889) definition of the Hansen's coefficients  $X_k^{n,m}(\epsilon)$  as well as the Kaula's<sup>5</sup> (1966) formula for the  $G_{l,p,q}(\epsilon)$  function are sums of terms, which include factorials and binomial coefficients. This formulation is not numerically stable at the higher eccentricities. In the case of high eccentricities Wagner<sup>14</sup> and Gooding and King-Hele<sup>8</sup> replaced Kaula's formula by an integral formula, which was next used by Rosborough and Lemoine<sup>9</sup> in the sensitivity studies of Mars orbiters for Mars gravity recovery. The integral formula works very well for high eccentricities, however because of computation time and some numerical instabilities, its practical application is limited when indices  $l$ ,  $p$ ,  $q$  reach high values.

Following Da Silva Fernandes<sup>3,4</sup> we propose to calculate the Hansen's coefficients  $X_k^{n,m}(e)$  from the following power series of  $(e - e^*)$ :

$$X_k^{n,m}(e) = \sum_{l=1}^{\infty} \frac{(e - e^*)^{l-1}}{(l-1)!} \frac{d^{l-1}}{de^{l-1}} X_k^{n,m}(e) \Big|_{e=e^*}, \quad (7)$$

where  $e^*$  is a fixed value of the eccentricity. This series is convergent for all values of the eccentricity  $e < 1$  such that  $|e - e^*| < \rho(e^*)$ . The values of the convergence radius  $\rho(e^*)$  are given by Da Silva Fernandes<sup>3</sup>. The values of Hansen's coefficient of the larger eccentricity  $e$  are calculated from the power series with coefficients of derivatives of Hansen's coefficients of the smaller eccentricity  $e^*$ .

The derivatives of the Hansen's coefficients are calculated with the use of the following formulas (Giacaglia<sup>15</sup>):

$$X_k^{n,m}(e) = \sum_{s=0}^{s_1} \sum_{j=-s}^{j_1} \binom{n-m+1}{s} \binom{n+m+1}{s+j} f_{n,s,j}(\beta) J_{k-m+j}(ke), \quad (8)$$

where  $J_l(x)$  is the Bessel function,

$$f_{n,s,j}(\beta) = (1 + \beta^2)^{-n-1} (-\beta)^j \beta^{2s}, \quad \text{with} \quad \beta = \frac{e}{1 + \sqrt{1 - e^2}} \quad (9)$$

$$\text{and } s_1 = \begin{cases} n - m + 1 & \text{if } n - m + 1 \geq 0 \\ \infty & \text{if } n - m + 1 \leq 0 \end{cases} \quad j_1 = \begin{cases} n + m + 1 - s & \text{if } n + m + 1 \geq 0 \\ \infty & \text{if } n + m + 1 \leq 0 \end{cases}$$

The function  $f(\beta)$  may be expressed as the following power series of the eccentricity  $e$  (Jarnagin<sup>16</sup>):

$$f_{n,s,j}(\beta) = \sum_{i=0}^{\infty} \left[ 2 \binom{-n+2i-2+j+2s}{i} - \binom{-n+2i-1+j+2s}{i} \right] \left( \frac{e}{2} \right)^{2i+j+2s} \quad (10)$$

The derivatives

$$\frac{d^l}{de^l} X_k^{n,m}(e) = \sum_{s=0}^{s_1} \sum_{j=-s}^{j_1} \binom{n-m+1}{s} \binom{n+m+1}{s+j} \left[ \sum_{r=0}^l \binom{l}{r} \frac{d^r}{de^r} f(\beta) \frac{d^{l-r}}{de^{l-r}} J_{k-m+j}(ke) \right] \quad (11)$$

may than be easy obtained, if we use the following relations for derivatives of the Bessel functions:

$$\frac{d^t}{de^t} J_l(x) = \frac{1}{2^t} \sum_{r=0}^t (-1)^r \binom{t}{r} J_{l-t+2r}(x). \quad (12)$$

Using the above formulas one may calculate Hansen's coefficients for an arbitrary values of the eccentricity and arbitrary values of indices. This method of calculation of the eccentricity function enables to obtain geopotential perturbations for orbits with high values of the eccentricity and high order and degree geopotential coefficients. As an example, fig.4 shows geopotential perturbations for the orbit with the eccentricity of 0.73. One can see that even for the harmonic order of 40 perturbations are on a level of meters, and resonance effects have to be taken into account for the higher orders. Because of the resonance effects the comparison with numerical integration (fig.5) is a bit worse then in the case of near circular orbits, but still is on a level of a few meters.

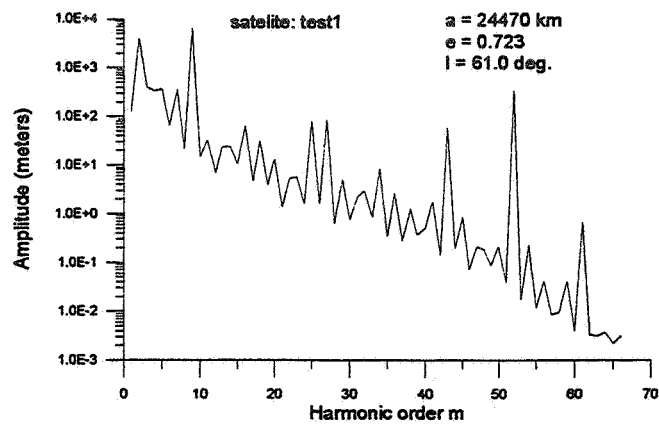


Fig.4. Total perturbations for the high eccentricity satellite orbit.

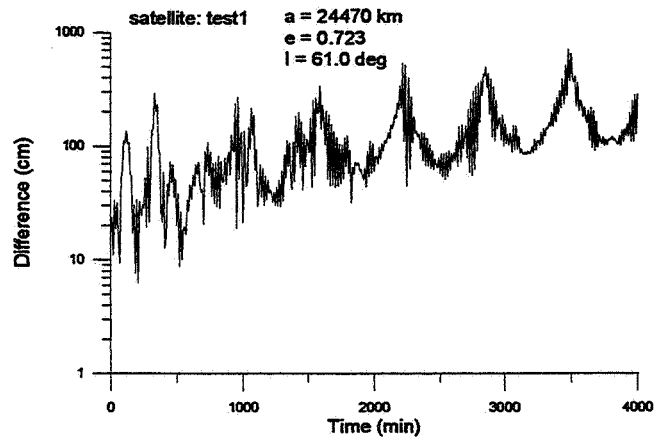


Fig.5. Differences between numerical integration and the analytical theory for the high eccentricity satellite orbit.

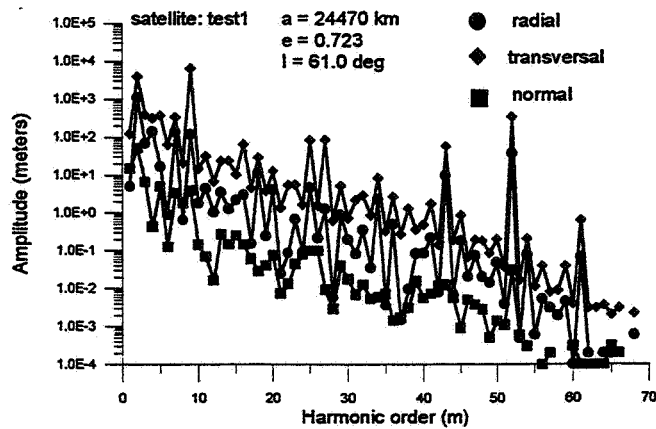


Fig.6. Perturbations in components of the radius vector for the high eccentricity orbit.

## PERTURBATIONS IN COMPONENTS OF THE RADIUS VECTOR

Formulas for geopotential perturbations in the radial, transverse and normal components published by Wnuk and Breiter<sup>11</sup> has some functions of the eccentric anomaly as factors. Due to the simultaneous presence of the eccentric and mean anomalies in these formulas some difficulties occur. In order to overcome this difficulty let us consider the  $H(E)$  functions introduced by Da Silva Fernandes<sup>3</sup> given as

$$H(E) = -m \sum_{n=1}^{\infty} \frac{1}{n} \sum_{s=0}^{\infty} \frac{\Delta z^s}{s!} \left[ \frac{d^s}{de^s} J_{n+m}(ne) \Big|_{e=e^*} H(-nM) - \frac{d^s}{de^s} J_{n-m}(ne) \Big|_{e=e^*} H(nM) \right], \quad (13)$$

where  $H(E)$  is an analytical function of the eccentric anomaly  $E$ ,  $e^*$  is a given value for the eccentricity  $e$  and  $\Delta z = (e - e^*)$ . This expression is convergent for every  $M$  as long as  $|e - e^*| < \rho(e^*)$ , being  $\rho(e^*)$  a positive real number (Da Silva Fernandes<sup>2</sup>).

Using the  $H(E)$  functions, and after a lengthy calculation, the formulas for the radial component  $\Delta r$ , the transverse component  $\Delta \lambda$  and the binormal components  $\Delta b$  can be expressed by the following series, convergent for high eccentricities:

$$\Delta r = a n \sum_{m=1}^N \sum_{k=-N}^N \sum_{q=-Q}^Q \gamma_{km} \{ r_1 \sin \psi + \frac{1}{2} \sum_{s=1}^L \sum_{t=1}^L \{ r_2 \cos(\psi + sM) + r_3 \cos(\psi - sM) + r_4 \sin(\psi + sM) + r_5 \sin(\psi - sM) \} \}, \quad (14)$$

where

$$r_1 = (T_{mkq}^1 - \frac{T_{mkq}^2}{2} e + T_{mkq}^3 e) \cos \psi + (R_{lkq}^1 - \frac{R_{lkq}^2}{2} e + R_{lkq}^3 e),$$

$$r_2 = \frac{T_{mkq}^2}{e} (c_{st} + c_{s,L+1}) - T_{mkq}^3 (c_{st}^1 + c_{s,L+1}^1) - T_{mkq}^4 b_{st}^1,$$

$$r_3 = \frac{T_{mkq}^2}{e} (c_{st} + c_{s,L+1}) - T_{mkq}^3 (c_{st}^1 + c_{s,L+1}^1) + T_{mkq}^4 b_{st}^1,$$

$$r_4 = -R_{lkq}^4 b_{s,t}^1 + \frac{R_{mkq}^2}{e} (c_{st} + c_{s,L+1}) - R_{mkq}^3 (c_{st}^1 + c_{s,L+1}^1),$$

$$r_3 = R_{mkq}^4 b_{s,t}^1 + \frac{R_{mkq}^2}{e} (c_{st} + c_{s,L+1}) - R_{mkq}^3 (c_{st}^1 + c_{s,L+1}^1).$$

$$\Delta\lambda = an \sum_{m=1}^N \sum_{k=-N}^N \sum_{q=-Q}^Q \gamma_{km} \{ \lambda_1 \cos \psi + \lambda_2 \sin \psi +$$

(15)

$$\frac{1}{2} \sum_{s=1}^L \sum_{t=1}^L \{ \lambda_3 \cos(\Psi + sM) + \lambda_4 [\cos(\Psi - sM) + \lambda_5 \sin(\psi + sM) + \lambda_6 \sin(\psi - sM)] \}$$

where

$$\lambda_1 = -3e \frac{R_{mkq}^5}{2} + R_{mkq}^6,$$

$$\lambda_2 = 3e \frac{T_{mkq}^5}{2} + T_{mkq}^6,$$

$$\lambda_3 = R_{mkq}^5 (c_{st}^1 + c_{s,L+1}^1) + \frac{R_{mkq}^5}{e} - R_{mkq}^6 (a_{st}^1 + a_{s,L+1}^1) - \frac{R_{mkq}^7}{1-e^2} b_{st} - R_{mkq}^7 b_{st}^1,$$

$$\lambda_4 = R_{mkq}^5 (c_{st}^1 + c_{s,L+1}^1) + \frac{R_{mkq}^5}{e} + R_{mkq}^6 (a_{st}^1 + a_{s,L+1}^1) + \frac{R_{mkq}^7}{1-e^2} b_{st} - R_{mkq}^7 b_{st}^1,$$

$$\lambda_5 = T_{mkq}^5 (c_{st}^1 + c_{s,L+1}^1) - \frac{T_{mkq}^5}{e} (c_{st} + c_{s,L+1}) + T_{mkq}^6 (a_{st}^1 + a_{s,L+1}^1) + \frac{T_{mkq}^7}{1-e^2} b_{st} + T_{mkq}^7 b_{st}^1,$$

$$\lambda_6 = T_{mkq}^5 (c_{st}^1 + c_{s,L+1}^1) - \frac{T_{mkq}^5}{e} (c_{st} + c_{s,L+1}) + T_{mkq}^6 (a_{st}^1 + a_{s,L+1}^1) - \frac{T_{mkq}^7}{1-e^2} b_{st} - T_{mkq}^7 b_{st}^1.$$

$$\Delta b = \frac{an}{4} \sum_{m=1}^N \sum_{k=-N}^N \sum_{q=-Q}^Q \gamma_{km} \{ b_1 \cos(\psi + \omega) + b_2 \cos(\psi - \omega) + b_3 \sin(\psi + \omega) + b_4 \sin(\psi - \omega) \}$$

$$b + \sum_{s=1}^L \sum_{t=1}^L \{ b_5 \cos(\psi + \omega + sM) + b_6 \cos(\psi + \omega - sM) + b_7 \cos(\psi - \omega - sM) \\ + b_8 \cos(\psi - \omega + sM) + b_9 \sin(\psi + \omega + sM) + b_{10} \sin(\psi + \omega - sM) \\ + b_{11} \sin(\psi - \omega + sM) + b_{12} \sin(\psi - \omega - sM) \},$$

where

$$b_1 = -e(3R_{mkq}^8 - \sqrt{1-e^2}R_{mkq}^8 + 3R_{mkq}^9),$$

$$b_2 = -e(3R_{mkq}^8 - \sqrt{1-e^2}R_{mkq}^8 - 3R_{mkq}^9),$$

$$b_3 = e(3T_{mkq}^8 + \sqrt{1-e^2}T_{mkq}^8 + 3T_{mkq}^9),$$

$$b_4 = -e(3T_{mkq}^8 - \sqrt{1-e^2}T_{mkq}^8 + 3T_{mkq}^9),$$

$$b_5 = -R_{mkq}^8 d_{st} - \frac{\sqrt{1-e^2}}{e} R_{mkq}^8 (c_{st} + c_{s,L+1}) + R_{mkq}^9 d_{st} - R_{mkq}^9 \sqrt{1-e^2} b_{st},$$

$$b_6 = -R_{mkq}^8 d_{st} - \frac{\sqrt{1-e^2}}{e} R_{mkq}^8 (c_{st} + c_{s,L+1}) + R_{mkq}^9 d_{st} + R_{mkq}^9 \sqrt{1-e^2} b_{st},$$

$$b_7 = R_{mkq}^8 d_{st} + \frac{\sqrt{1-e^2}}{e} R_{mkq}^8 (c_{st} + c_{s,L+1}) + R_{mkq}^9 d_{st} + R_{mkq}^9 \sqrt{1-e^2} b_{st},$$

$$b_8 = R_{mkq}^8 d_{st} - \frac{\sqrt{1-e^2}}{e} R_{mkq}^8 (c_{st} + c_{s,L+1}) - R_{mkq}^9 d_{st} + R_{mkq}^9 \sqrt{1-e^2} b_{st},$$

$$b_9 = T_{mkq}^8 d_{st} + \frac{\sqrt{1-e^2}}{e} T_{mkq}^8 (c_{st} + c_{s,L+1}) - T_{mkq}^9 d_{st} - T_{mkq}^9 \sqrt{1-e^2} b_{st},$$

$$b_{10} = T_{mkq}^8 d_{st} - \frac{\sqrt{1-e^2}}{e} T_{mkq}^8 (c_{st} + c_{s,L+1}) - T_{mkq}^9 d_{st} + T_{mkq}^9 \sqrt{1-e^2} b_{st},$$

$$b_{11} = -T_{mkq}^8 d_{st} - \frac{\sqrt{1-e^2}}{e} T_{mkq}^8 (c_{st} + c_{s,L+1}) - T_{mkq}^9 d_{st} + T_{mkq}^9 \sqrt{1-e^2} b_{st},$$

$$b_{12} = -T_{mkq}^8 d_{st} + \frac{\sqrt{1-e^2}}{e} T_{mkq}^8 (c_{st} + c_{s,L+1}) - T_{mkq}^9 d_{st} - T_{mkq}^9 \sqrt{1-e^2} b_{st}.$$

Here,  $\psi$  stands for  $\psi_{mkq}$ . The coefficients  $R_{mkq}^i$  and  $T_{mkq}^i$ ,  $i=1,\dots,9$ , as defined in (Wnuk and Breiter<sup>11</sup>), are functions of the lumped coefficients and it is worthwhile to mention that their expressions have  $\psi$  in the denominator. The terms  $a_{st}^1, b_{st}, c_{st}, c_{st}^1$  and  $d_{st}$  are functions of the eccentricity  $e$  defined as follows (Da Silva Fernandes<sup>4</sup>):

$$\begin{aligned}
b_{st} &= \frac{2(e-e^*)^{t-1}}{s(t-1)!} \frac{d^{t-1}}{de^{t-1}} \left[ \frac{J_s(se)}{e} \right]_{e=e^*}, & b_{st}^1 &= \frac{2(e-e^*)^{t-1}}{s(t-1)!} \frac{d^t}{de^t} \left[ \frac{d}{de} J_s(se) \right]_{e=e^*}, \\
c_{st} &= \frac{2(e-e^*)^{t-1}}{s^2(t-1)!} \frac{d^{t-1}}{de^{t-1}} \left[ e \frac{d}{de} J_s(se) \right]_{e=e^*}, & c_{st}^1 &= -\frac{(e-e^*)^{t-1}}{(t-1)!} \frac{d^{t-1}}{de^{t-1}} \left[ \frac{2(1-e)}{e} J_s(se) \right]_{e=e^*}, \\
a_{st}^1 &= 2 \frac{(e-e^*)^{t-1}}{(t-1)!} \frac{d^{t-1}}{de^{t-1}} [J_s(se)]_{e=e^*}, & d_{st} &= \frac{2(e-e^*)^{t-1}}{s^2(t-1)!} \frac{d^t}{de^t} \left[ \frac{d}{de} J_s(se) \right]_{e=e^*}.
\end{aligned}$$

where  $J_n(x)$  are the Bessel functions of order  $n$  for the variable  $x$ .

## CONCLUSIONS

New formulas for computation of the orbital perturbations due to the geopotential in radial, transverse and binormal components, valid for highly eccentric orbits, were derived. The formulas were transformed to the form  $\sum A_i \frac{\cos}{\sin} \varphi_i$  as it is usual in perturbation theory.

## ACKNOWLEDGMENTS

This work was supported by FAPESP (96/0612-9, 98/00791).

## REFERENCES

1. Wnuk, E. "Highly Eccentric Satellite Orbits," *Adv. Space Res.*, Vol. 19, No. 11, 1997, pp 1735.
2. S. Da Silva Fernandes, "Some Expansions of the Elliptic Motion to High Eccentricities," *Celestial Mechanics and Dynamical Astronomy*, 1994, Vol. 58, pp 297-308.
3. S. Da Silva Fernandes, "Some Expansions of the Elliptic Motion to High Eccentricities," *Celestial Mechanics and Dynamical Astronomy*, 1995, Vol. 62, pp 305-321.

4. S. Da Silva Fernandes, *Celestial Mechanics and Dynamical Astronomy*, 1996, Vol. 63, pp 375.
5. W. Kaula, *Theory of Satellite Geodesy*, Blaisdell, Waltham, Mass., 1966.
6. E. Wnuk, "Tesseral Harmonic Perturbations for High Order and Degree Harmonics," *Celest. Mech.* vol.44, 1988 pp. 179-191.
7. K. Szeto and K. Lambeck "On Eccentricity Function for Eccentric Orbits", *Celest. Mech.*, vol. 27, 1982, pp. 325-338
8. R. H. Gooding and D. G. King-Hele, "Explicit Forms of Some Functions Arising in the Analysis of Resonant Satellite Orbits," *R.A.E. Technical Report*, No. 99035, 1988.
9. G. W. Rosborough, and F.G. Lemoine, "Sensitivity Studies of Mars Orbiters for Mars Gravity" Recovery, *J. Astronautical Sciences*, vol.39, No.3, pp. 327-357, 1991
10. E. Wnuk, "Tesseral Harmonic Perturbations in the keplerian Orbital Elements", *Acta Astronomica*, Vol. 40, 1990 pp 191.
11. E. Wnuk, E. and S. Breiter: "Tesseral Harmonic Perturbations in Radial, Transverse and Binormal Components", *Celestial Mechanics*, Vol. 48, 1990, pp. 375.
12. R. S. Nerem and 21 others, "Gravity Model Development for TOPEX/Poseidon: Joint Gravity Models 1 and 2", *J. Geophys. Res.*, vol. 99 No. C12, pp. 24,421-24,447 (1994).
13. F. Tisserand, *Traite de Mechanique Celeste*, Gauthier - Villars et Fils, Paris (1889).
14. C. A. Wagner "Spectra From the Tracking of Planetary Orbiters", *J. Geophys. Res.* vol.84, No.B12, pp. 6891-6908 (1979).
15. G.E.O. Giacaglia, "A Note on Hansen's Coefficients in Satellite Theory", *Celestial Mechanics*, Vol 14, 1976, pp. 515.
16. M. P. Jarnagin Jr. 1965, Expansions in-Elliptic Motion, *Astron.papers Am Eph.naut.Almanac*, Vol.18, 1965, XXXVI.



5/9-13  
ABS ONLY  
AAS 98-318  
169301

## ON THE ANALYSIS OF LUNAR ALBEDO EFFECTS ON LOW LUNAR ORBIT AND GRAVITY FIELD DETERMINATION

Rune Floberghagen

Pieter Visser

Frank Weischede

Massimiliano Vasile

337559  
1P.

### ABSTRACT

A force model for the lunar albedo effect on low lunar orbiters is developed on the basis of Clementine imagery and absolute albedo measurements. The model, named the *Delft Lunar Albedo Model 1* (DLAM-1), is a 15 x 15 spherical harmonics expansion, and is intended to improve force modeling for low satellite orbits, and moreover to help avoid aliasing of non-gravitational force model defects in future lunar gravity solutions from satellite tracking data.

The development of the model from the available lunar albedo data sources is described, followed by a discussion on its calibration using absolute albedo measurements. Further interpretation of the model is based on a comparison with main selenological features. Next, the implementation of DLAM-1 in satellite force computations is outlined, with emphasis on computation costs. DLAM-1 is also applied in low lunar orbit determination, and results for typical orbits of current and prospective satellite missions are presented. Finally, the effect of lunar albedo on future solutions for the gravitational potential of the Moon is presented. In this regard, particular interest is on gravity mapping from global data sets, e.g. satellite-to-satellite tracking, which is expected to be one of the experiments of coming lunar missions. It is shown that albedo-induced orbit perturbations have a magnitude and frequency signature which are non-negligible for precise orbit and gravity modeling. Radial orbit errors are in the order of 1-2 m for one week arcs.

used the content  
table of  
for org. source  
and world of  
learning for  
HP



526-13  
169302

AAS 98-319

12P.

337560

## NAVIGATION AND GUIDANCE ERROR ANALYSIS OF SELENE LUNAR LANDER CONSIDERING ORBIT DETERMINATION ERROR

Hayato Oono<sup>†</sup>  
Shinich Ishikawa<sup>†</sup>  
Ken Nakajima<sup>††</sup>  
Kentaro Hayashi<sup>††</sup>  
Rie Odaka<sup>††</sup>

Generally, to achieve the high accurate navigation, both the radar altimeter and the inertial measurement sensors consisting of the accelerometers and the gyros are used during the powered decent to the lunar surface. In the current conceptual design, the SELENE (SELenological ENgineering Explorer) lander is considered to have no way to use the radar altimeter during the most part of the powered decent from the restriction of cost, weight, etc.. Therefore, the initial navigation error of the lander at the start of the powered decent brings about an important influence on a safe landing. This initial state error corresponds to the accuracy of the orbit determination in the ground system. To relax the effect of this initial state error, we carried out the accuracy analysis of the orbit determination by using the satellite-to-satellite tracking via a lunar relay satellite. The obtained results are then used in the navigation and guidance error analysis. It can be shown that there is the adequate possibility of the safe landing by the navigation with the only inertial measurement sensors during the braking phase. In this paper, the nominal trajectory, the guidance method and the results of error analyses mentioned above are reported.

### INTRODUCTION

The SELENE (SELenological ENgineering Explorer) mission will be carried out by a probe combination in the beginning of the next century. The probe is composed of a Lunar relay satellite, a Lunar observation satellite and a Lunar lander. They will be launched by an H-IIA rocket in the summer of 2003 year. The lander will be on a Lunar circular orbit with the lunar observation satellite and will be operated for a period of about one year, the end of the program of the Lunar surface scientific observation. After that, the lander will be released from the lunar satellite and after the de-orbit maneuver initiated the powered decent from its perilune point at an altitude of about 15 kilometers. We call a phase from an altitude of about 15km to reaching an altitude of about 4km BRAKING phase.

<sup>†</sup> Guidance and Propulsion Technology Laboratory, Office of Research and Development, National Space Development Agency of Japan, Tsukuba Space Center, Sengen 2-1-1, Tsukuba-city, Ibaraki, 305 Japan

<sup>††</sup> Mitsubishi Space Software Co., Ltd.

In this phase, the navigation of the lander is based on the data from an inertial measurement unit. This unit is consisted of accelerometers and gyros. Therefore, the initial state error at the Powered Decent Initiation (PDI) brings about a great influence on its terminal point state. The cause of this initial state error at PDI is the error of the ground base orbit determination. Especially, the uncertainty of the lunar gravity potential influences the accuracy of the orbit determination seriously.

We performed the orbit determination analysis considering the uncertainty of the lunar gravity potential and the navigation and guidance error analysis based on the above result to confirm it's feasibility as the primary analysis of SELENE lunar lander mission . Figure 1 shows the flow of these analyses we performed.

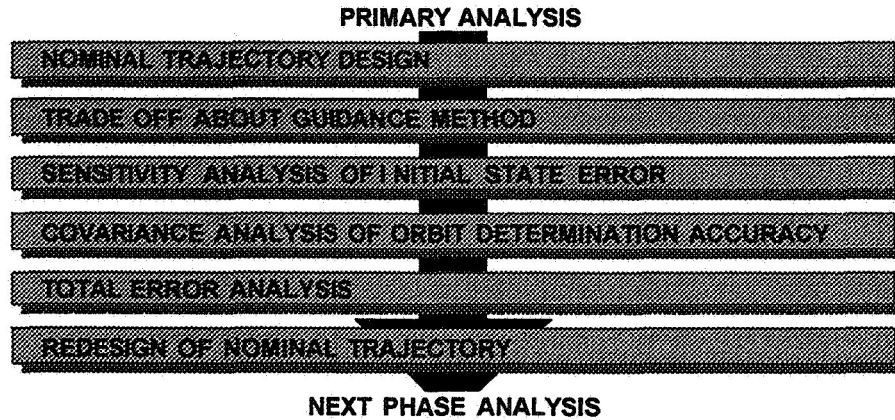


**Figure 1 Flow of the Primary Analyses**

First, we performed the trade off study about the powered decent guidance, and selected a candidate one from this result. To clarify the tolerance of position and velocity error at the powered decent initiation (PDI), using the selected guidance method, we carried out the sensitivity analysis of initial state error with respect to the state at the powered flight terminal point.

Next, we tried the covariance analysis of orbit determination accuracy for the lander including the tracking system with a lunar relay satellite. In this covariance analysis, especially, we considered the error of Lunar potential model Lun60D (Ref. 1). Then we performed the total error analysis considering the initial state error, the thruster error and the error of onboard inertial measurement sensors. Finally, we redesigned the nominal trajectory to land safely from the results of the above analyses.

## **NOMINAL TRAJECTORY**

Table 1 shows the lander characteristics, In Figure 2, we depict the preliminary nominal trajectory of the braking phase in powered decent we assumed.

**Table 1  
LANDER CHARACTERISTICS**

<u>Initial Mass (kg)</u>	<u>Thrust Force (N)</u>	<u>Exhaust Velocity (m/s)</u>
856.000	1700.000	3098.901

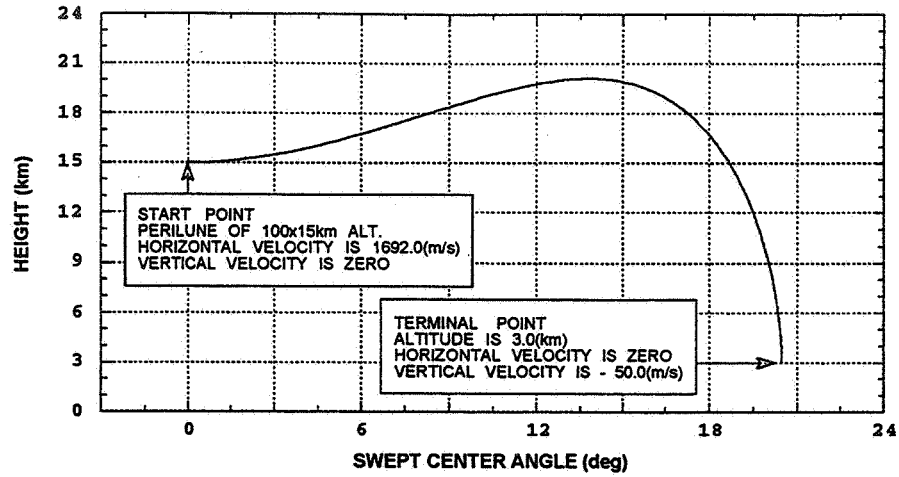


**Figure 2 Preliminary Nominal Trajectory**

This trajectory was designed using the bilinear tangent law to minimize the time transfer under the restriction of along track is free and the thrust magnitude is fixed (Ref. 2).

## POWERED GUIDANCE

As the candidates of guidance method for the braking phase, we prepared for the following three types of guidance method.

The first is Proportional Guidance (G1), this guidance scheme is represented by the following equation.

$$\ddot{r}_D(t) = r_0 + r_1 t \quad (1)$$

Here,  $r_D$  is desired selenocentric radius.  $r_0$  and  $r_1$  are constants.

The second guidance is based on Linear Tangent law (G2). In this guidance scheme, the desired thrust direction vector  $X_D$  is

$$X_D(t) = \frac{-X_G + (p + qt) Y_G}{\sqrt{1 + (p + qt)^2}} \quad (2)$$

where  $X_G$ ,  $Y_G$  indicate the along track direction vector, radial direction vector respectively, and  $p$ ,  $q$  are constants. The minus sign before  $X_G$  in Eq.(2) means this guidance is the braking of velocity.

The final guidance (G3) desires the thrust direction  $X_D$  as

$$X_D(t) = X_G \cos(\theta + \omega t) + Y_G \sin(\theta + \omega t) \quad (3)$$

where  $\theta$  and  $\omega$  are constants. We obtain this Eq.(3) by the parameter transformation of the desired thrust direction vector used in the Space Shuttle Powered Explicit Guidance (Ref. 3).

In the guidance scheme G2 and G3, we must predict the increment of position and velocity due to the thrust acceleration  $a_T$ . These prediction are represented by the following integrals.

$$\Delta r_T = \int_0^T dt \int_0^t a_T(s) X_D(s) ds \quad (4)$$

$$\Delta v_T = \int_0^T a_T(t) X_D(t) dt \quad (5)$$

The thrust acceleration  $a_T$  under the assumption that the thrust force and the weight flow rate are constant value is

$$a_T(t) = \frac{C^*}{\tau_m - t} \quad (6)$$

where  $C^*$  is the effective exhaust velocity,  $\tau_m$  is the mass zero time.

In G2 scheme, Eq.(4) and Eq.(5) can be expressed by some elementary functions. On the other hand, these equations in G3 scheme can not be expressed by any elementary functions, however we can calculate them with sufficient accuracy using the series expansion etc..

In Table 2 and Figure 3, we show the comparison results of each guidance method.

**Table 2**  
**CAPABILITY OF EACH GUIDANCE METHOD**

	<u>Time of Flight(sec)</u>	<u>Fuel Consumption(kg)</u>	<u>Sweep Angle(deg)</u>
NOMINAL	693.9	380.6	20.4
G1	696.2	381.9	20.7
G2	694.0	380.7	20.5
G3	693.9	380.6	20.4

We thought the adaptability for the nominal trajectory was important and selected G3 method as the guidance during the braking phase. Though G2 also has the adaptability, G3 has the applicable wide range for the thrust direction and the swept center angle in comparison with G2.

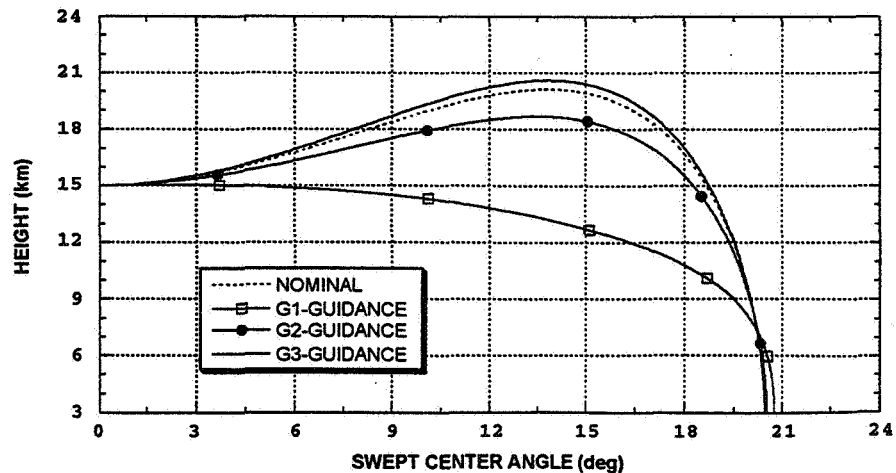


**Figure 3 Comparison of Nominal Trajectory**

## SENSITIVITY ANALYSIS

In the preliminary nominal trajectory, the terminal point of the braking phase is 3 km altitude from the lunar surface. If the initial state (onboard navigation) error is very large, there is possibility that the height at the braking phase termination is under the lunar surface. To make clear this situation, we analyzed the sensitivity of each state at the terminal point with respect to each initial state error using G3 guidance method. Table 3 shows results of the sensitivity analysis. Here, H,C and L indicate radial, cross and along track direction respectively, and DH,DC and DL indicate the time derivative of H,C and L. The evaluation of sensitivities in the cross track direction are excluded from Table 3, this is because we do not consider the control for the out of a trajectory plane in this analysis.

**Table 3**  
**RESULTS OF SENSITIVITY AT TERMINAL POINT**

A Priori Error	H(km)	L(km)	DH(m/s)	DL(m/s)
H±1(km)	-/+1.351	±0.134	-/+1.399	±0.014
L±1(km)	-/+0.383	±0.058	-/+0.233	±0.557
DH±1(m/s)	-/+0.713	±0.025	-/+1.397	±0.320
DL±1(m/s)	-/+0.246	±0.000	-/+0.464	±0.748

In the present investigation, we assume that the recoverable error after the braking phase is the position error in H of about 2km, therefore we obtain the error tolerance at PDI as shown in Table 4 under the condition that each initial state error occurs independently.

**Table 4**  
**ERROR TOLERANCE AT PDI**

<u>H(km)</u>	<u>L(km)</u>	<u>DH(m/s)</u>	<u>DL(m/s)</u>
±1.48	±5.22	±2.80	±8.13

## ORBIT DETERMINATION

In SELENE lander, the state at PDI is uplinked from the ground station, and this uplinked state is based on the result of orbit determination. Therefore the state error at PDI corresponds to the error of orbit determination. Here we describe the results of analysis about the orbit determination and propagation accuracy.

The accuracy of orbit determination is computed with the pseudo epoch estimator using Kalman filter algorithm. Then we must consider the effect of uncertainty parameters, because the degradation of the accuracy is mainly dominated by these uncertainty parameters. In particular, the degraded effect due to the uncertainty of Lunar potential is well-known. We treat this uncertainty as the considered (unadjusted) parameters. These algorithm (Ref. 4) are

$$K = PA_x^T [A_x PA_x^T + P_v]^{-1} \quad (7)$$

$$P = (I - KA_x) P (I - KA_x)^T + KP_v K^T \quad (8)$$

$$S = S - K (A_x S + A_y) \quad (9)$$

$$A_x = \frac{\partial z}{\partial x_0}, \quad A_y = \frac{\partial z}{\partial y} = \frac{\partial z}{\partial x} \frac{\partial x}{\partial y} \quad (10)$$

where  $\mathbf{x}_0$  is the satellite state (position and velocity) at epoch which is the estimated parameters,  $\mathbf{x}$  is the satellite state at time  $t$ ,  $\mathbf{y}$  is the considered parameters that are treated as systematic error sources ( $\mathbf{y}$  corresponds to the error of potential coefficients mentioned above),  $\mathbf{z}$  is the modeled measurements,  $P$  is the error covariance matrix,  $P_y$  is the measurement variances,  $K$  is the Kalman gain and  $S$  is the sensitivity matrix in  $\mathbf{y}$  on the estimated parameters. The propagation of error covariance including the effect of the considered parameters are

$$P(t) = \frac{\partial \mathbf{x}(t)}{\partial \mathbf{x}_0} P \left( \frac{\partial \mathbf{x}(t)}{\partial \mathbf{x}_0} \right)^T + \left( \frac{\partial \mathbf{x}(t)}{\partial \mathbf{y}} + \frac{\partial \mathbf{x}(t)}{\partial \mathbf{x}_0} S \right) P_y \left( \frac{\partial \mathbf{x}(t)}{\partial \mathbf{y}} + \frac{\partial \mathbf{x}(t)}{\partial \mathbf{x}_0} S \right)^T \quad (11)$$

where  $P_y$  is the diagonal covariance matrix for the considered parameters.

The lander will be released from an altitude of about 100km circular polar orbit of the lunar satellite and after de-orbit maneuver, initiated the powered decent from its perilune point at an altitude of about 15 kilometers. Considering these sequences and landing to Mare Serentitatis, for covariance analysis, we set up the schedule of measurements and operations as shown in Figure 4.

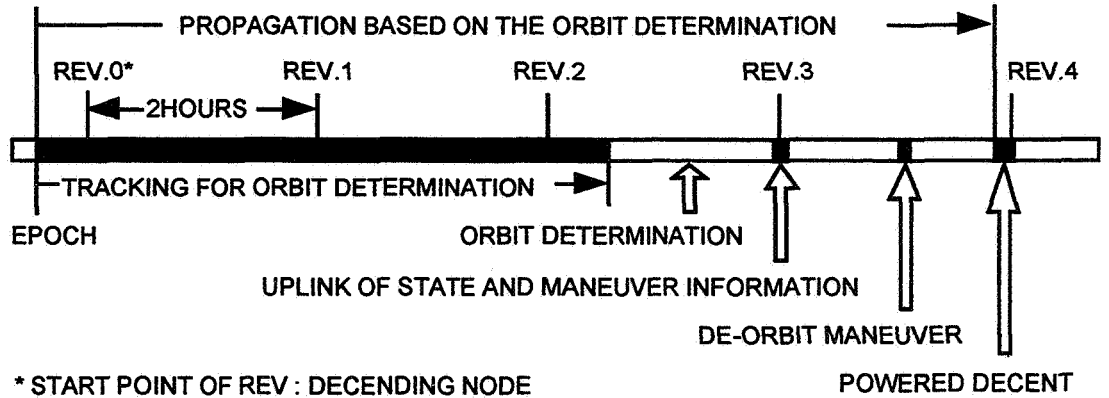


**Figure 4 Schedule of Measurement and Operation**

Here we describe the scenarios of measurements and operations. The tracking station that is one of the domestic stations tracks the lunar orbiter and measures range and range rate in the duration of three passes of the lunar orbiter. The orbit determination process is carried out from the final Loss-Of-Sight(LOS) of tracking to the next Acquisition-Of-Sight(AOS). Timing, orientation and velocity increments for the de-orbit maneuver, and timing, initial orientation and initial state at PDI are uplinked to the lander.

Therefore, to evaluate the initial state error at PDI, we need to propagate the error covariance of orbit determination from epoch to PDI for about 9 hours, of course, then we must take into account the effect of the considered parameters. Table 5 shows the error sources used in covariance analysis, and Figure 5 shows the error analysis results under the above scenarios.



**Table 5**  
**ERROR SOURCES USED COVARIANCE ANALYSIS**

Parameter	1-Sigma A priori Uncertainty
Lunar orbiter state vectors at Epoch	100 km in each position component 100 m/s in each velocity component
Lunar potential	full coefficients error in Lun60D
Lunar gravity constant	0.004 km <sup>3</sup> /sec <sup>2</sup>
Earth gravity constant	0.004 km <sup>3</sup> /sec <sup>2</sup>
Solar gravity constant	450000 km <sup>3</sup> /sec <sup>2</sup>
Earth position	10 m in each of X,Y, 20m in Z
Solar position	2000 m in each of X,Y,Z
Range bias	10 m
Range noise	10 m
Range-rate noise	0.5 cm/s

The results in Figure 5 indicate that the position accuracy in the cross track direction is too bad. Because the measurements have no sensitivity of the cross track direction in order that the orbit plane is parallel to the Earth-Moon line in the duration of tracking just before landing. Accuracy of the other elements are also not good.

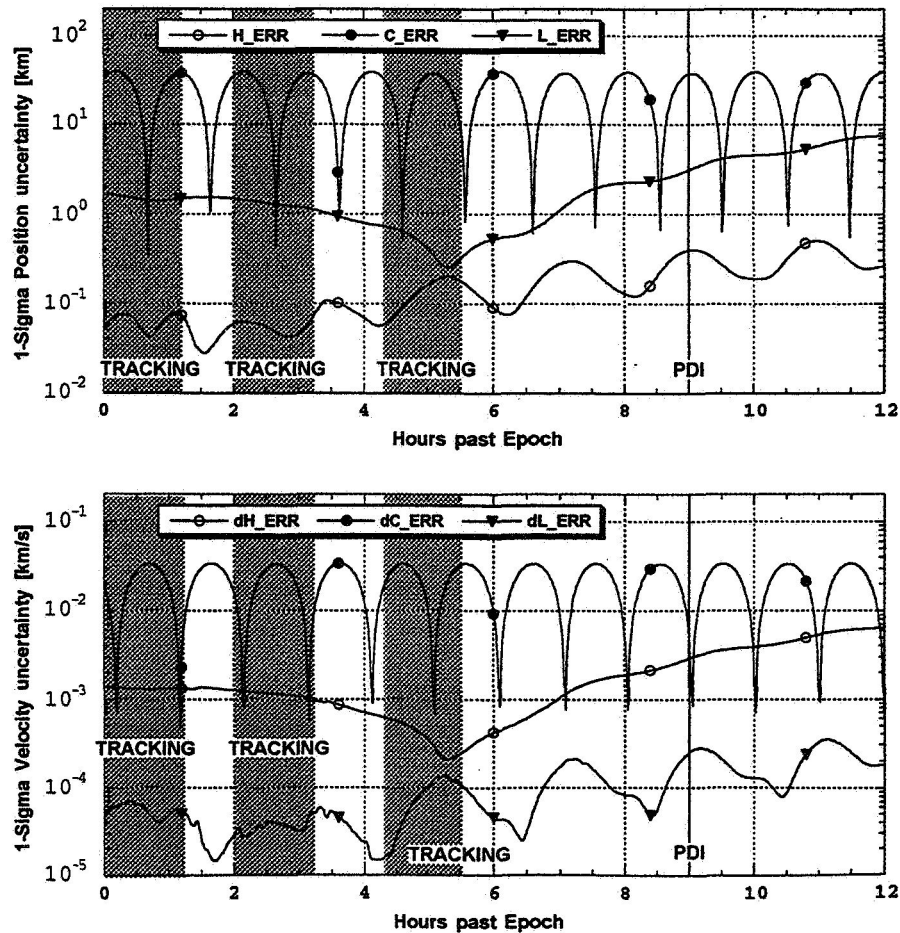


**Figure 5 Propagation Error of Orbit Determination Accuracy**

To improve the propagation accuracy at PDI, we tried the covariance analysis of an orbit determination using satellite-to-satellite tracking. The SELENE mission consists of a relay, an orbiter and a lander satellite. The initial trajectory of the relay satellite is the same inclination and the perilune height as the orbiter and the apolune height of about 2500km. Figure 6 shows the results of the error propagation using the satellite-to-satellite tracking. A priori uncertainty of relay satellite state uses the results obtained by the another analysis about the relay satellite. The other conditions are the same as the above case (see Table 5).

The time span from epoch to PDI in Fig.6 is different from it in Fig.5, but the time span from the end of tracking to PDI that is the most important point in this analysis is the same as both cases.

In the case shown in Fig.6, to be the difference of ascending node between the relay and the orbiter satellite of about 27 deg, the position and velocity error in cross track direction are improved in comparison with the case shown in Fig. 5.

Table 7 shows the propagation results of orbit determination accuracy at PDI of the above two cases.

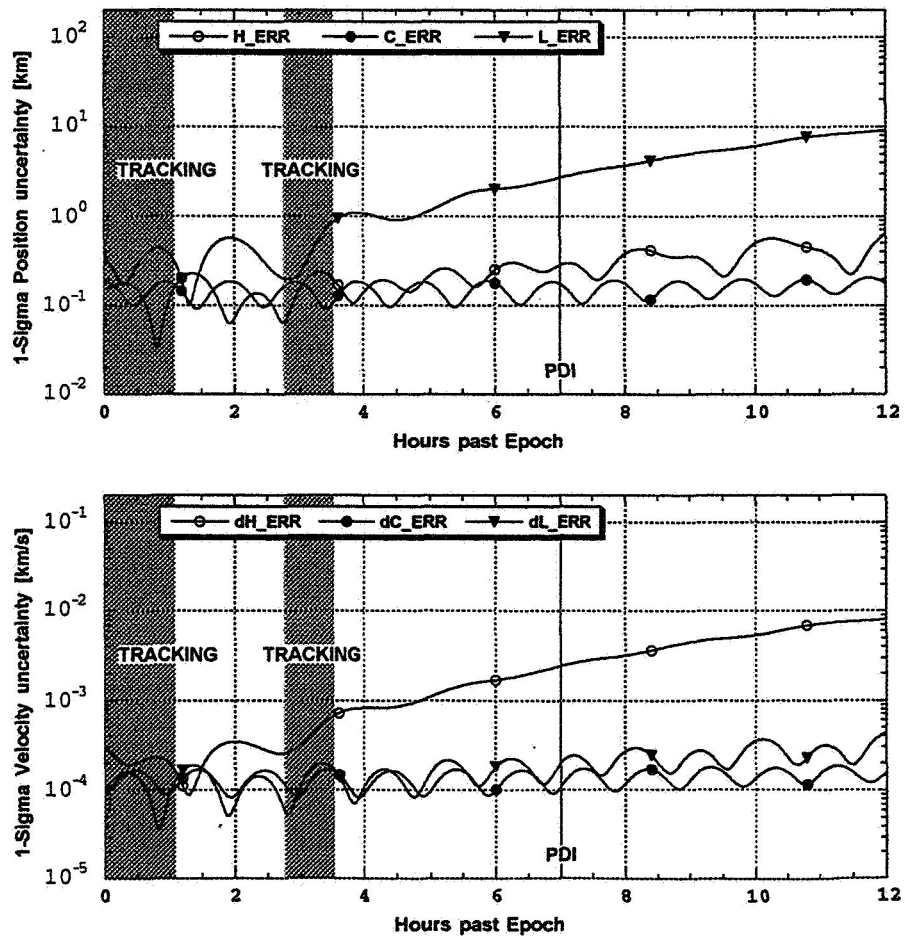


**Figure 6 Propagation Error using Satellite-to-Satellite Tracking**

**Table 7**  
**3-SIGMA LEVEL PROPAGATION ERROR AT PDI**

CASE	H(km)	C(km)	L(km)	DH(m/s)	DC(m/s)	DL(m/s)
Station-Orbiter	1.182	111.861	9.411	8.764	14.469	0.736
Station-Relay-Orbiter	0.855	0.526	8.150	7.422	0.331	0.600

It is clear that the error of position in L and velocity in H at PDI shown in Table 7 are not satisfied with the error tolerance at PDI shown in Table 4. However, by reasons that the correlation coefficient between position error in L and velocity error in H is about minus one, and the error of same sign in L and DH at PDI occurs the position error of same sign in H at terminal point (see Table 3), there is possibility that these two error factors offset each other. In next section, we describe the total error analysis considering this cancelled effect.

### NAVIGATION AND GUIDANCE ERROR ANALYSIS

As mentioned above, we selected the guidance method of the braking phase in powered decent, and defined a priori state error at PDI. And we performed the error analyses using these results. Figure 7 shows the outline of this analysis.

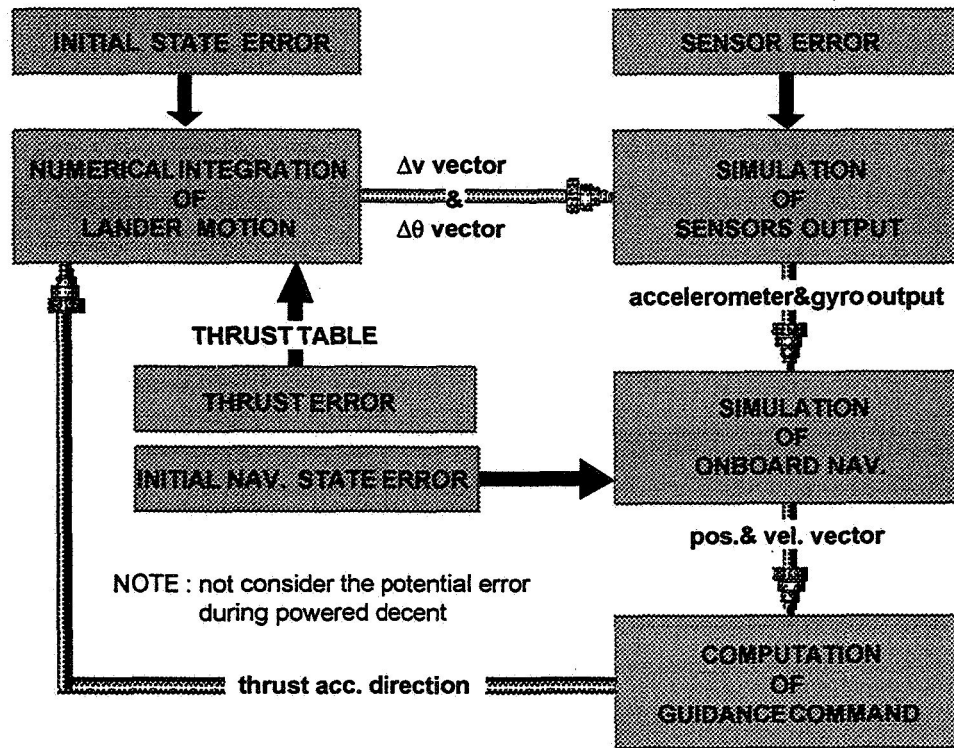


**Figure 7 Outline of Navigation and Guidance Error Analysis**

In this simulation, the terms integrated numerically are the acceleration due to the thrust force and the lunar gravity constant. The perturbation due to the lunar potential is not considered. And the time of flight during the braking phase is in short of about 700sec, the error sources on the environment influenced the lander motion shown in Table 5 are disregarded.

**Table 8**  
**ERROR SOURCES USED ERROR ANALYSIS IN BRAKING PHASE**

<u>Parameter</u>	<u>3-Sigma A priori Uncertainty</u>
Initial position in H	±855.0 (m)
Initial position in L and velocity in H	±8150.0 (m) and -/+7.422 (m/s)
Initial velocity in L	±0.600 (m/s)
Initial attitude	±0.0406 (deg) in each Roll, Pitch and yaw
Thrust variation	±9.0 (%)
Isp variation	±9.0 (%)
Tail-off impulse	±450.0 (N sec)
Initial nav. pos. in H	±855.0 (m)
Initial nav. pos in L and vel. in H	±8150.0 (m) and -/+7.422 (m/s)
Initial nav. vel. in L	±0.600 (m/s)
Initial nav. attitude	±0.0406 (deg) in each Roll, Pitch and yaw
Accelerometer bias	±100.0 (μg) in each axis
Accelerometer scale	±300.0 (ppm) in each axis
Gyro bias	±0.015 (deg/hour) in each axis

Table 8 shows the main error sources used the navigation and guidance error analysis of the braking phase. In Table 8, we used the propagation results obtained by satellite-to-satellite tracking, because we can not evaluate the effect of large error in cross track direction appropriately to be the lack of the control for the out of plane.

In Table 8, initial position or velocity indicates the error sensed in the onboard navigation system, and initial nav. position or velocity error indicates the error non-sensed in the onboard navigation system. And the position error in L and the velocity error in H are treated as a composite error case by reason of the strong correlation.

Actually, we executed the analyses for total 43 error (86 cases considering the sign) sources such as the inertial measurement sensors, the thruster characteristics, the initial state and the onboard navigation state. Table 9 shows the results of the navigation and guidance error analysis including the effect due to the error sources besides those shown in Table 7.

**Table 9**  
**3-SIGMA ERROR AT TERMINAL POINT (ALT.=3KM)**

<u>Parameter</u>	<u>Unit</u>	<u>3-Sigma RSS</u>	<u>Main Error Source</u>
Time of Flight	sec	80.4	Thrust force variation
Fuel Consumption	kg	25.9	Isp variation
Position in H	km	2.8	Initial nav. L pos. & DH vel.
Position in C	km	0.7	Initial C pos.
Position in L	km	67.7	Thrust force variation
Velocity in H	m/s	8.8	Initial nav. attitude in pitch
Velocity in C	m/s	1.5	Initial nav. attitude in yaw
Velocity in L	m/s	2.5	Initial nav. L pos. & DH vel.

Considering 3-sigma error sources, Table 9 indicates that the altitude at terminal point of the braking phase is  $3 \pm 2.8$  km and this result is not satisfied with the altitude requirement over 1 km at the terminal point. Accordingly, we should modify the altitude of about 3 km into 4 km at the terminal point to secure from impacting on the surface. By this modification, the range of the altitude at terminal point considering 3-sigma error is the value of about 1.2 km to 6.7 km. We tried to analyze again using new terminal altitude and confirmed to be satisfied with the requirements for the fuel consumption etc..

## CONCLUSION

From the above analyses, if some conditions such as using satellite-to-satellite tracking data and modifying the altitude into 4km at the terminal point of the braking phase are met, we obtained the conclusion there is the adequate possibility of the safe landing by the navigation with the only inertial measurement sensors during the braking phase.

Lunar landing is the first experiment for us, we must still study about many things to accomplish the SELENE mission.

In the next phase analysis, we are going to perform more detailed analysis about the orbit determination accuracy with the lunar potential model Glgm2 or improved by the Lunar Prospector Mission.

## REFERENCES

1. A. S. Konopliv, W. L. Sjogren, R. N. Wimberly, R. A. Cook and A. Vijayaraghavan, "A High Resolution Lunar Gravity Field and Predicted Orbit Behavior," AAS 93-622, 1993
2. A. E. Bryson, Jr and Yu-chi Ho, "Applied Optimal Control," Hemisphere Publishing Co., New York, 1975
3. R. F. Jagers, "An Explicit Solution to the Exoatmospheric Powered Flight Guidance and Trajectory Optimization Problem for Rocket Propelled Vehicles," AIAA 77-1051, 1977
4. G. J. Bierman, "Factorization Methods for Discrete Sequential Estimation," Academic Press, New York, 1977



521-13

AAS 98-320

169303

## TRAJECTORY DESIGN OF SELENE LUNAR ORBITING AND LANDING

Yasuhiro Kawakatsu\*  
Yutaka Kaneko\*  
Yoshisada Takizawa\*

337561  
120

This paper focuses on the three topics related to the trajectory design of SELENE. The first is the orbit maneuver of the orbiter. The altitude of the orbiter is 100km and the orbit is strongly perturbed by high order term of the gravity potential. In order to satisfy the mission requirements, ten maneuvers are scheduled during one year mission. The second topic is the orbit design of relay satellite. The relay satellite has no propulsion system and has no orbit maneuver capability. The orbit of the relay satellite is perturbed mainly by earth's gravity and the shape of the orbit changes through the one year mission. The initial orbit is selected carefully to meet the mission requirements through the mission considering the effect of perturbation. The third topic is the trajectory design of the landing mission. The navigation error in the landing phase is expected to be large value. Main reason of the error is orbit determination error and long duration of inertial navigation. The landing trajectory is designed to permit this navigation error and assure the safe landing.

### INTRODUCTION

SELENE (SELenological and Engineering Explorer), the first ISAS & NASDA joint mission to the Moon will be launched by H-IIA rocket in 2003. SELENE is a lunar polar orbiter of 100km altitude with a relay satellite for far-side tracking coverage. The orbiter is composed of two modules, the Mission Module (MM) and the Propulsion Module (PM). PM works for attitude and orbit control of the orbiter system for one year during the global observation. After this observation period, PM separates from the MM and demonstrates soft-landing on the surface, namely it is operated as Lunar Lander in the mission.

---

\* Advanced Mission Research Center, National Space Development Agency of Japan.  
Sengen 2-1-1, Tsukuba-city, Ibaraki, 305-8505, Japan

This paper focuses on the three topics related to the trajectory design of SELENE. The first is the orbit maneuver of the orbiter to maintain its altitude within the required range. The second is the orbit design of relay satellite and the third is the trajectory design of the landing mission. Details of these topics are described from the next section.

## **ORBIT ANALYSIS OF LUNAR POLAR ORBITER**

### **Orbit Perturbation Analysis**

Lunar Polar orbiter is orbited on the 100km circular orbit with inclination of 95 degree. It is required from the science mission group to maintain the altitude of the orbiter within the range of  $100\text{km} \pm 30\text{km}$ . In other words, the eccentricity of the orbit is required to keep under the value of 0.016.

The orbit of SELENE orbiter in the low lunar orbit is perturbed by several factors. Those are irregularness of lunar gravity potential, the gravity of the earth or the sun, solar pressure, and so on. However, the most dominant factor is the irregularness of lunar gravity potential and the other effect of the other factors is relatively low. In this section, the perturbation caused by the irregularness of lunar gravity potential is solely taken into account.

As a lunar gravity potential model, Lun60d(1993)<sup>1</sup> is adopted in this paper. It is composed of 60 degrees of zonal and non-zonal coefficients with their estimation error. Data source for the gravity potential estimation are the orbit determination data of Lunar Orbiter and Apollo subsatellites.

One of the mission objectives of Lunar Prospector which now activates is the precise determination of the lunar gravity potential model. New gravity potential model based on the Lunar Prospector data will be reflected to the SELENE design no sooner than it will be published.

Here we want to take up the movement of the eccentricity vector of the orbit under the perturbation of the lunar gravity potential high order term. The eccentricity vector mentioned here has the magnitude of the orbit eccentricity and the direction of the orbit perilune direction. The movement of the tip of the eccentricity vector for the duration of two month is described in Figure 1. As is shown in the figure, the movement of the eccentricity vector is highly complicated in case the whole gravity potential coefficients are taken into account. It is difficult to analyze systematically with the whole potential coefficients taking into account. In the following analysis, we take the effect of the zonal term and non-zonal term separately in order to make the systematic analysis. Considering the non-linear effect between the zonal term and non-zonal term, this analysis, which take them into account separately, does not give the precise results. However, the following results indicates that the effect of nonlinearity between the zonal and non-zonal term is not so significant.

If the zonal term is only taken into account, the time variance of the eccentricity vector can be calculated analytically<sup>2</sup>.

Figure 2 shows the drift of the eccentricity vector under the effect of zonal term. The requirements from the science mission, that is to keep the altitude within the range of 100



$\pm 30\text{km}$ , is described by the circle with the radius of 0.016. It shows that in case only the zonal term is taken into account, the eccentricity vector get out of the admissible range in 120 days.

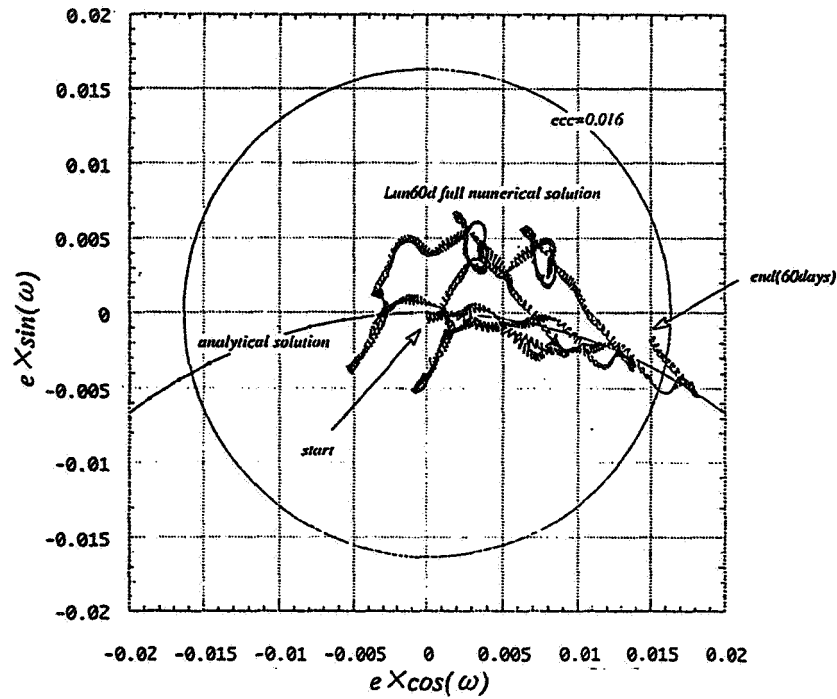


**Figure 1 Drift of the Eccentricity Vector under the Perturbation**

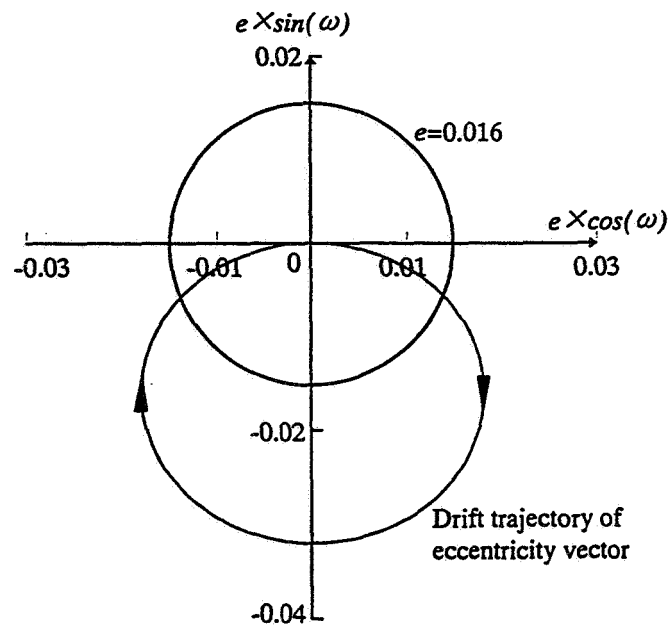


**Figure 2 Drift of Eccentricity Vector in the Effect of Zonal Term**

In the other hand, the time drift of the eccentricity vector under the effect of non-zonal term cannot be expressed in the form of the fundamental function. To analyze the effect of the non-zonal term, the numerical simulation is inevitable. Figure 3 shows the drift of the eccentricity vector for each 1 lunar month (27.3 days). The shape of the each 1 month's drift trajectory resembles well. Additionally, the center of the trajectory drifts along the ellipse shown in figure 1, that is the drift trajectory drawn under the effect of the zonal term only.

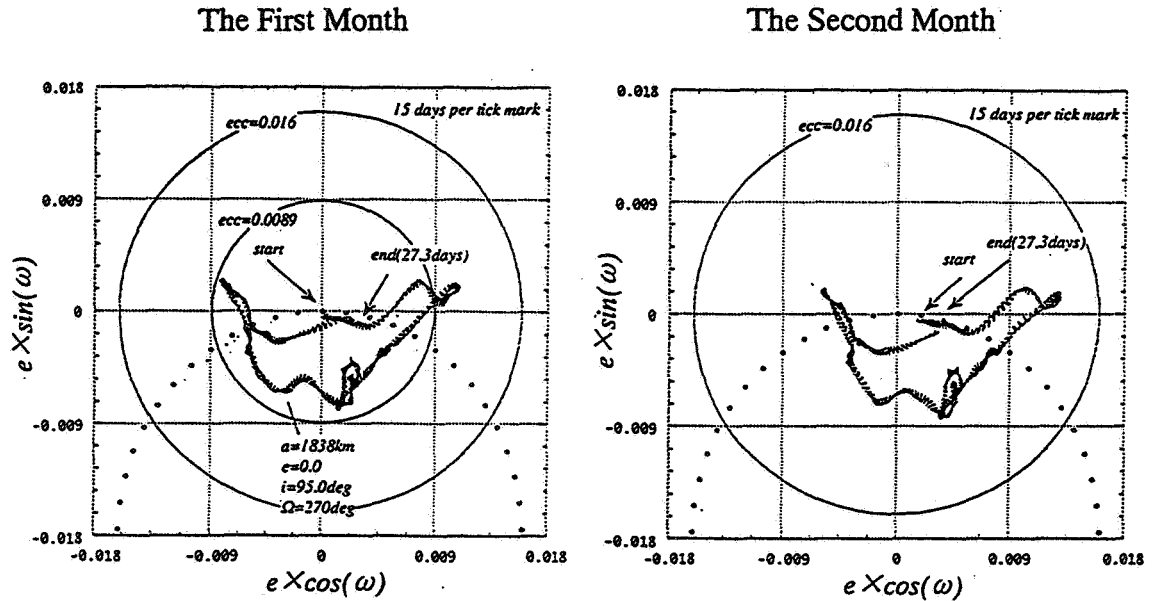


**Figure 3 Drift of Eccentricity Vector of Each Month**

If the effect of the non-zonal term is represented by its enclosing circle, the drift of the eccentricity vector can be estimated as a circular region drifting along the perturbation ellipse by the zonal coefficient. In case of the orbit altitude 100km and orbit inclination 95 degree, the radius of the enclosing circle is about 0.008.

In the gravitational potential model, the error of the coefficient has been written additionally. For the system design, it is desirable to consider the worst case in range of the coefficient error. In this perturbation analysis, it is necessary to rightly estimate the effect of the gravitational potential coefficient error on the eccentricity vector drift.

As to the zonal coefficient, it is possible to calculate analytically the sensitivity of the zonal coefficient error against the feature of the eccentricity vector perturbation. In the altitude maintenance control analysis mentioned after, the worst case from the point of maneuver interval and maneuver quantity is estimated. Figure 4 shows the drift trajectory of the eccentricity vector in the worst case considering the zonal coefficient error. "The

worst case” means the case in which the altitude becomes the limit of the permissible altitude- $(\pm 30\text{km})$  in the shortest time. It corresponds to the case in which the drift trajectory reaches the limitation circle of radius 0.016 in the figure the shortest time. In case using the nominal coefficient, it takes 120 days for the eccentricity vector to reach the limit. However, it takes only 67 days for the eccentricity vector to reach the limit circle in the worst case.

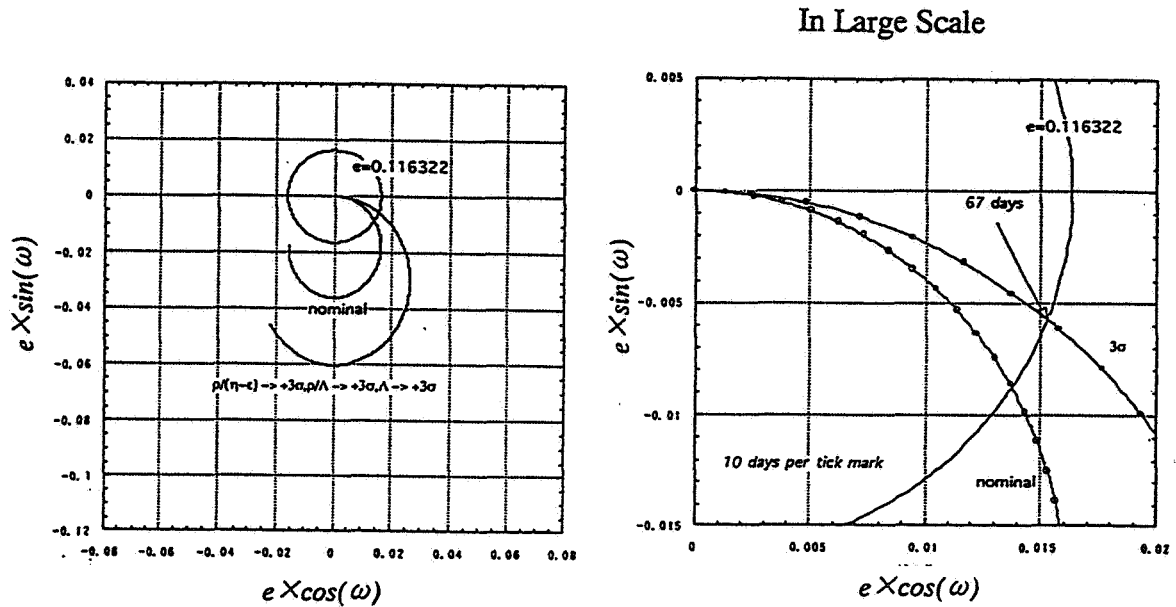


**Figure 4**  
**Drift of Eccentricity Vector Considering Zonal Coefficient Error**

Since the sensitivity of the non-zonal coefficient error cannot be calculated analytically, the worst case of the eccentricity vector perturbation cannot be specified. In the altitude maintenance maneuver analysis mentioned below, the non-zonal coefficient error is not taken into account when the eccentricity vector perturbation is analyzed. Instead, in order to cope with the non-zonal coefficient error, 20% margin for the whole orbit maneuver  $\Delta V$  is appropriated.

### Altitude Maintenance Control Analysis

The orbit maneuver  $\Delta V$  necessary for maintaining permission altitude which is a demand from the observation mission is discussed here. It is considered in the worst case including the zonal coefficient error.

The approach of the altitude maintenance control is shown in figure 5. The

perturbation of the eccentricity vector by a gravitational potential is considered as an enclosing circle-drifting on the perturbation ellipse only considering the zonal coefficient. The effect of the non-zonal coefficient is represented by the circular region. Since the eccentricity vector exists somewhere in the circle, the altitude limitation will never violated if appropriate maneuver is executed when the enclosing circle touch the limitation circle. In case of the figure, the enclosing circle touches the tolerance limits in the right side. Then the maneuver is carried out to move the eccentricity vector as left as possible in order to gain the maximum maneuver interval. The objective point is the center of the enclosing circle which touches the tolerance limits at the left. By this way, the tolerance limits will never be violated even if the eccentricity vector exists anywhere in the enclosing circle.  $\Delta V$  necessary for moving the eccentricity vector in the way mentioned above becomes a controlled quantity per 1 maneuver. Non-zonal coefficient error is not yet considered in this stage.

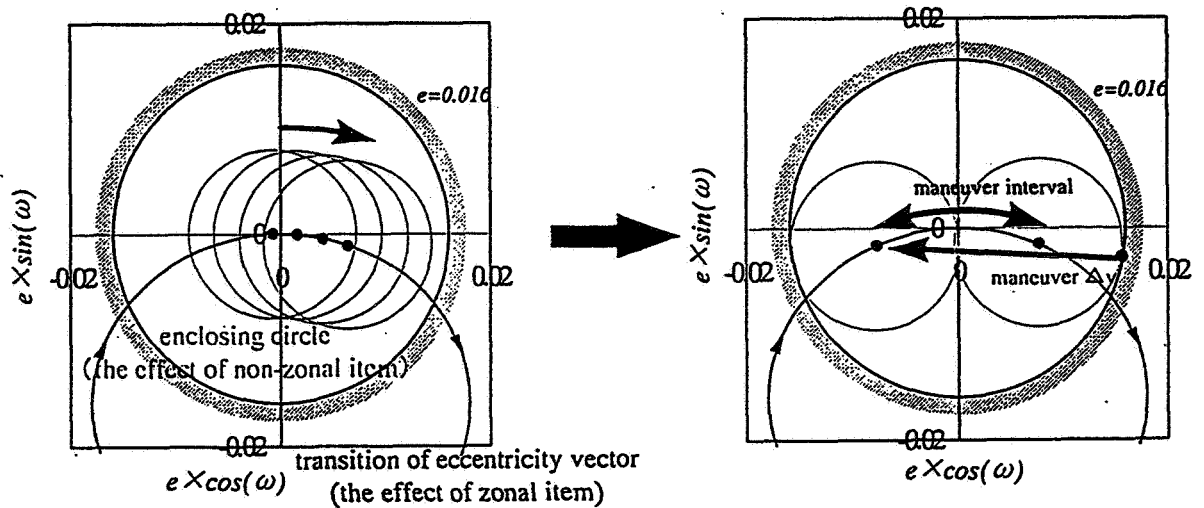


**Figure 5 Maneuver Interval and  $\Delta V$  in Altitude Maintenance Control**

The result of the altitude maintenance control analysis is shown in table 1. It is a result of the worst case considering the zonal term coefficient error. 20% margin for the Non-Zonal term coefficient error is contained in the  $\Delta V$  for 1 year mission.

**Table 1**  
**RESULT OF ALTITUDE MAINTENANCE CONTROL ANALYSIS**

<u>Used Model</u>	<u>Maneuver Interval</u>	<u><math>\Delta V</math> for one maneuver</u>	<u><math>\Delta V</math> for 1 year maneuver</u>
LUN60d	66 days	19.6m/s	118m/s

The result of the altitude maintenance control analysis is shown in table 1. It is a result of the worst case considering the zonal term coefficient error. 20% margin for the Non-Zonal term coefficient error is contained in the  $\Delta V$  for 1 year mission.

## **ORBIT ANALYSIS OF RELAY SATELLITE**

The relay satellite does not have the orbit maneuver capability, and its orbit through whole mission duration (1 year and 2 months) is decided by the condition at the relay satellite separation. In the initial orbital elements of the relay satellite, ascending node  $\Omega$ , argument of perilune  $\omega$ , and inclination  $i$  (that means the perilune direction and the orbital plane) equals to those of the orbiter when the lunar orbit injection sequence of the relay satellite is considered. Additionally, perilune altitude equals to 100km which is the altitude of the orbiter. As a result, free design parameter in relay satellite orbit elements is only semimajor axis  $a$  (or eccentricity  $e$ ).

### **Orbit Settings of Relay Satellite**

It is necessary to take in mind two roles of the relay satellite, when setting the relay satellites orbit.

The first is to relay signals to the orbiter at the far side of the moon. The signals include command, telemetry, Doppler shift measurements and ranging. Four way Doppler shift measurements relayed by the orbiter and the relay satellite will determine the gravitational mapping of the far side of the moon with high resolution and sensitivity. The coverage of lunar gravimetry for the far side is principally restricted by the limited opportunity of four way communication link. From this point of view, the orbit of the relay satellite is required to be visible for long duration from the orbiter at the far side of the moon. In other words, the apolune altitude of the relay satellite's orbit is required to be sufficiently high.

The second role of the relay satellite is the radio sources for Delta VLBI observation. The radio sources will be also loaded on the propulsion module of the SELENE orbiter which will be separated and land on the near side of the moon surface after the polar orbital mission period for one year. Delta VLBI observation using radio sources loaded on the relay satellite and the propulsion module on the moon surface will be made for two months after the propulsion module will be landed. The data will be analyzed to derive the precise orbits of the relay satellite and contribute to determine precisely the gravimetry and the libration of the moon. From this point of view, the average altitude of the relay satellite is required to be sufficiently low so that the effect of gravity can be observed clearly.

The semimajor axis of the relay satellite was set to 3000km considering the conditions mentioned above.

## Relay Satellite Perilune Altitude Analysis

Delta VLBI mission will be carried out for 2month after the landing of the propulsion module on the lunar surface. This means that the mission period is set from 1 year to 1 year and 2 months after from the orbit injection of the relay satellite. It is required from the delta VLBI mission to keep the perilune altitude of the relay satellite at 0km~600km during the mission period. In this section, the result of the perilune altitude analysis during the delta VLBI mission period is shown.

There is no orbit maneuver executed for the relay satellite after the separation from the orbiter. Therefore, the orbit through the whole mission duration of the relay satellite is determined by the initial state in the orbit injection.

Firstly, the date of the relay satellite injection is an important factor. Since the main perturbation factor to the relay satellite orbit is the earth's gravity, and the positional relation of the earth and relay satellite orbit changes by the injection date. Next, for the orbital element,  $a$ ,  $e$  are set to the above-mentioned value and  $i$ ,  $\Omega$  are set to the value equal to those of the orbiter. For the remaining element,  $\omega$ , it is also decided from the closest approach condition of the translunar trajectory, when the injection date is designated. In short, the free parameter as an initial state is only the injection date, and the orbit of the relay satellite through the whole mission duration will be determined for the injection date.

As a result, the perilune altitude during the delta VLBI mission period will be also determined for the injection date. Figure 6 plots the perilune altitude at the 360th and the 420th day from the relay satellite orbit injection. Horizontal axis indicates the assumed launch date in the summer 2003. "360" and "420" is the day when the delta VLBI mission starts and ends. It indicates that, for some launch date, the perilune altitude at the 420th day becomes negative, and the relay satellite collides with the lunar surface during the delta VLBI mission period. From this result, it can be concluded that, there are only 17 days which can satisfy the requirements of the delta VLBI mission.

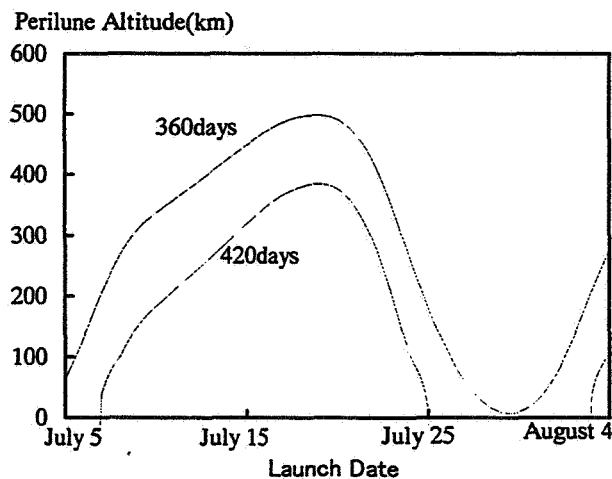


**Figure 6 Perilune Altitude of the Relay Satellite**

The launch window for SELENE is also constrained from the other constraints such as the  $\Delta V$  in the lunar orbit injection, the launch condition of the rocket, the eclipse on the translunar trajectory, etc.. Assuming the launch in summer, 2003, launch window of 12 days in one month remain.

## LANDING TRAJECTORY

After the one year observation, the payload module separates from the mission module and demonstrates soft-landing on the lunar surface, namely it is operated as lunar lander in the mission.

Landing sequence of the propulsion module is shown in figure 7. The propulsion module separates from mission module on a circular orbit of altitude 100km. The propulsion module executes de-orbit maneuver and it is injected into the elliptical orbit of whose apolune altitude 100km and perilune altitude 15km. After the coasting phase for half way of elliptical orbit, the powered descent phase starts. In the powered descent phase, the maneuver which mainly cancels the horizontal velocity is executed and terminal condition of velocity 0m/s and altitude 4km is achieved. Vertical attitude is established within short seconds in the beginning, and the vertical descent maneuver is carried out to achieve soft landing on the lunar surface.

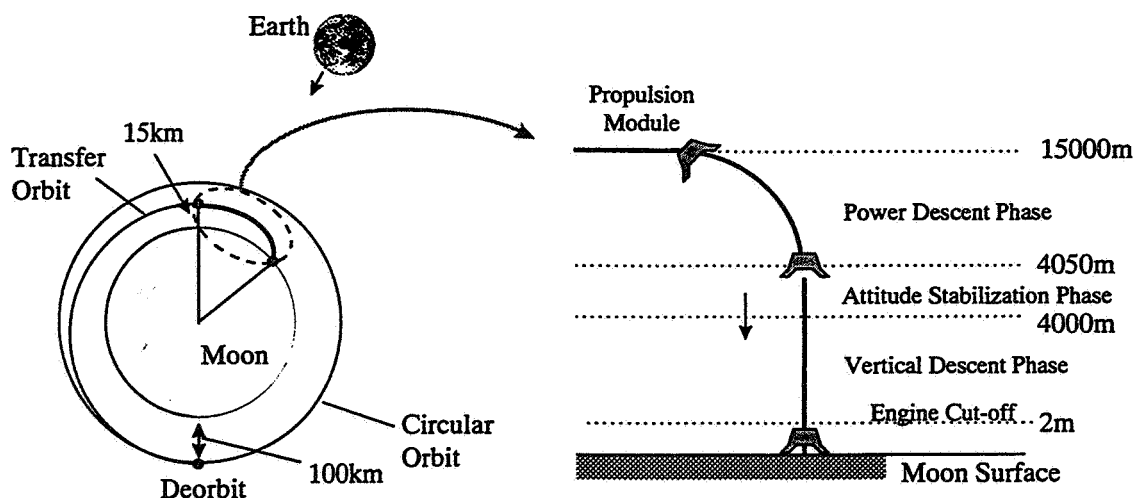


**Figure 7 Landing Sequence**

Precise sequence of each phase are described in the following.

### Before Separation

Orbit and attitude determination are carried out before the propulsion module separation. The summary of the orbit determination sequence is shown in figure 8. 5 or 6 passes are visible in one day from the tracking station in Japan. The visible duration in

each pass is about one hour. That is to say, the satellite passes the near side of the moon for 5 or 6 times in the visible duration from Japan. The orbit determination is carried out using the tracking data of the first 3 passes, and the orbit determination value is transmitted in the fourth pass. The landing is carried out in the fifth pass. The sixth pass is unavailable for the landing, because the transmission time after landing is insufficient for sending image data in this case. The attitude determination is carried out using the star sensor mounted on the mission module. The orbit determination value sent from the ground and the attitude determination value from star sensor are used as an initial value of the inertial navigation system of the landing phase.

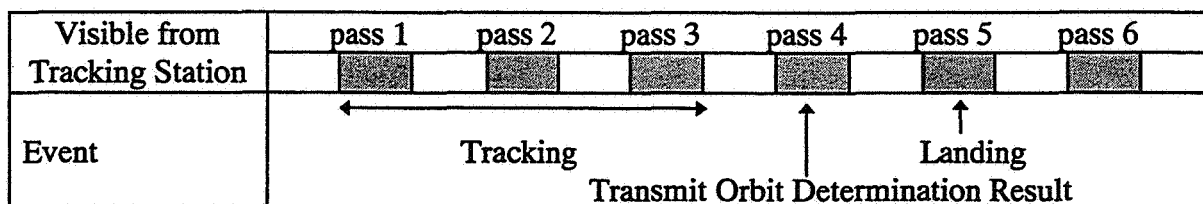


**Figure 8 Orbit Determination Sequence**

For the reduction of navigation error, the orbit determination had better be carried out after the propulsion module is injected into the elliptical orbit. However, the power of the propulsion module is supplied from its battery, and its capacity is not enough for long hours operation. For the sufficient orbit determination accuracy, at least 3 visible pass, that is, about 6 hours of orbit determination period is necessary. This duration is too long to supply power only by the battery on the propulsion module. This is the reason why the orbit determination is carried out before separation. It is about 1 hour after the attitude determination in the time to the landing, and the drift error of the gyro is negligible. There is no problem in carrying out the attitude determination in this stage.

### Separation and De-orbit of Propulsion Module

"Mare Serentitatis" in the near side of the moon is planned to be landing point (about 20 degE and 25 degN). As mentioned above, the propulsion module coast half way of the elliptical orbit before the powered descent phase. Therefore, the injection to the elliptical orbit is carried out in the back side of the moon. The separation of the propulsion module is carried out just before the elliptical orbit injection in order to shorten the operation time of the propulsion module as possible.

The separation velocity is about 10cm/s, and the navigation error produced in this phase is negligible.  $\Delta V$  necessary for the elliptical orbit injection is about 20m/s. At this maneuver, an output of the accelerometer is referred, and the engine is cut off at the timing when the required velocity increment is acquired. As a result, the elliptical orbit injection is achieved without producing large  $\Delta V$  error in spite of thrust error, etc..



## Coasting Descent Phase

The propulsion module is injected into the elliptical orbit whose apolune altitude 100km and perilune altitude 15km, and coasts for half way of the orbit. Its position and velocity are propagated on the onboard inertial navigation system. The powered descent is started when the vertical velocity becomes zero, in other words, at the perilune passage point.

## Powered Descent Phase

The navigation during the powered descent phase is also done only according to the information of inertial measuring unit (IMU). Though there is a radio altimeter/velocitymeter installed in the propulsion module underside, it is not yet available in this phase. The reason is that the attitude of propulsion module is almost horizontal, and measurement direction is out of range. As a guidance system, the explicit guidance method to optimize the propellant consumption is used. The descent trajectory is almost reverse of the ascent trajectory of the rocket, and various guidance method used in the rocket launch is applicable for the guidance method in this phase. There is no significant difference in the guidance performance among each method. Only the altitude (4km) and velocity (horizontal/vertical direction 0m/s) are designated as a terminal condition. The horizontal position is not designated as a guidance target. From the result of the guidance error analysis, the guidance error has fallen within the enough small value. This fact shows that the propulsion module can be guided to the goal point in its own navigation system, even in the existence of the thrust error, etc.. However, the navigation error is a different problem. Since the IMU is the only available sensor after the orbit determination, the navigation error considerably increases., For example, the altitude error at the end of the powered descent phase is estimated as 3.6km for  $3\sigma$ . In short, even if the guidance system works well and the propulsion module is guided accurately to the target on the inertial navigation system, the actual altitude of the propulsion module disperses in the range of 0.4km~7.6km for  $3\sigma$  at the end of the powered descent phase.

## Vertical Descent Phase

The attitude of the propulsion module at the end of the powered descent phase leans 70 degrees from the vertical direction. Vertical attitude establishment phase for about 7 seconds is set in the beginning of the vertical descent. It falls about 50m in this phase. The radio altimeter/speedometer is available at this moment, and actual altitude information can be used in the navigation system for the first time. Combined navigation system which uses the information of the IMU and the radio altimeter/velocitymeter is used in this phase. From the result of the navigation error analysis, there is about 2m/s ( for  $3\sigma$  ) horizontal velocity error in the beginning of the vertical descent phase. The horizontal velocity error cannot be removed only by the altimeter information. Therefore, in order to satisfy the landing condition, the radar velocitymeter is necessary. The vertical descent phase is basically a sequence using free fall and the maximum thrust deceleration. A breaking line which is set at the beginning of the vertical descent phase considering the

mass and thrust error. The on-off signals of the main engines is set referring this line. As a result of these sequence, the soft landing is achieved.

## **CONCLUSION**

Three topics related to the trajectory design of SELENE are introduced. The feasibility of the mission is verified through the conceptual design study. The SELENE project is phased up to the preliminary design phase this spring and more detailed studies, tests and simulations will be done to confirm the system feasibility.

## **ACKNOWLEDGEMENT**

We thank the SELENE project team members for their contribution to the work described in this paper.

## **REFERENCES**

1. A. S. Konopliv, W. L. Sjogren, R. N. Wimberly, R. A. Cook and A. Vijayaraghavan, "A High Resolution Lunar Gravity Field and Predicted Orbit Behavior," AAS 93-622, 1993
2. R. A. Cook, "The Long-Term Behavior of Near-Circular Orbits in a Zonal Gravity Field," AAS 91-463, 1991

# OPTIMAL TRAJECTORIES FOR LUNAR LANDING MISSIONS

MASSIMILIANO VASILE\*, RUNE FLOBERGHAGEN#

**Abstract** In this paper a temporal finite element method is developed for dynamics and optimal control problems. The approach is here proposed in order to determine the optimal initial conditions, and the optimal control law to perform the desired soft landing on the South Pole of the Moon. The spacecraft is modeled as a point mass subject to gravity forces due to the Moon, the Earth and the Sun, and controlled by an ideal throttleable thrust. An estimation of total propellant consumption is presented taking into account possible errors arising from a poor knowledge of the present force model. Finally an optimal control strategy for obstacles avoidance is proposed. Some sample problems show the effectiveness of the proposed approach.

## INTRODUCTION

Various space agencies are presently studying or approving several new missions to the Moon. The demonstration of landing technologies is an essential feature of all these new mission plans (Lunar-A, SELENE<sup>1</sup>).

In particular the mission target is to perform a precise soft landing in a morphological complex area on the South Pole of the Moon. In order to achieve this mission goal and to lead the project to success it is necessary to minimize risks of a hard landing, reducing costs in term of weight budget.

As demonstrated in previous works<sup>2</sup> this is a challenging task due to the strongly non uniform and yet not well known gravity field of the Moon which will give great dispersion in final results. Thus the consequences of a wrong force field prediction on the design of a landing trajectory should be analyzed.

The landing problem can be handled as a typical boundary values problem in which the final position and a series of constraints on the trajectory must be met.

In this paper a Spectral Elements in Time (SET) approach is proposed in order to determine the optimal initial conditions, and the optimal control law to perform the desired soft landing on the South Pole of the Moon. The spectral elements approach is based on a variational method coupled with a spectral elements discretization of the solution which leads to a fast and compact memory algorithm and allows the introduction of several constraints conditions in order to fulfill all the requirements of this kind of mission.

The landing mission is here divided in two phases: a coast phase and a homing phase. The analysis of the coast phase is performed considering the GLGM-2 gravity

\* Dipartimento di Ingegneria Aerospaziale Politecnico di Milano, via Golgi 40, 20133 Milano, Italy

#DEOS, Delft Institute for Earth-Oriented Space Research, Kluyverweg 1, 2629 HS, Delft, The Netherlands

model and the perturbing effects of the Earth and the Sun; however, as stated before, the uncertainty on present gravity models could lead to major errors in coasting trajectory predictions. Thus different possible coasting orbits with different geometry have been studied.

A wrong prediction in the coasting trajectory endpoint propagates through a variation of the homing trajectory which could lead to a hard landing. The extra mass and thrust requirements to correct the final descent are analyzed here imposing an error in the gravity model and computing a new optimal homing descent.

The error is estimated considering both the uncertainty on the GLGM-2 coefficients - obtained from the covariance analysis - and a completely different gravity model.

The second phase is characterized by a poor knowledge of the landing site, therefore altimeter data and images should be processed during the mission in order to determine the landing area correctly. Thus an optimal control law is introduced in order to correct the descending trajectory on the basis of real time data acquisition.

Finally some results proving the effectiveness of the proposed approach will conclude this paper and possible initial conditions and control law, to conduct a soft landing, are presented.

## SPACECRAFT AND FORCE MODEL

The basic set of equations of motion of the spacecraft subject to a generalised force function  $\mathbf{f}$  and to a control  $\mathbf{u}$  can be expressed in the following general form:

$$\dot{\mathbf{x}} = \mathbf{f}(\mathbf{x}, \mathbf{u}) \quad (1)$$

The state vector  $\mathbf{x}$ , in a Cartesian reference frame (see Figure 1), can be expressed in terms of displacements  $\mathbf{q}$  and momenta  $\mathbf{p}$  as follows

$$\mathbf{x} = \{p_x, p_y, p_z, q_x, q_y, q_z\}^T; \quad (2)$$

while the function  $\mathbf{f}(\mathbf{x}, \mathbf{u})$  is defined as

$$\mathbf{f} = \left\{ \frac{\partial U(\mathbf{q})}{\partial q_x} + \frac{u_x}{(1+m_R)}, \frac{\partial U(\mathbf{q})}{\partial q_y} + \frac{u_y}{(1+m_R)}, \frac{\partial U(\mathbf{q})}{\partial q_z} + \frac{u_z}{(1+m_R)}, p_x, p_y, p_z \right\}^T \quad (3)$$

where  $u_x, u_y, u_z$  are the three components of the control along the Cartesian axis X,Y,Z.

The mass ratio  $m_R$  is defined as  $m_p/m_s$ , where  $m_p$  is the propellant mass and  $m_s$  is the dry mass of the spacecraft. Furthermore a linear mass flow equation is added to the differential system in order to take into account the dependency of the mass on the thrust modulus  $\|\mathbf{u}\|$ :

$$\dot{m}_R = -\|\mathbf{u}\| / c \quad (4)$$

where  $c$  is the exhaust gas velocity  $c = I_{sp}g_0$ , with  $I_{sp}$  the specific impulse and  $g_0$  the gravity acceleration on Earth surface.

The function  $U$  is the potential due to the gravity forces acting on the spacecraft, namely the gravity field of the moon and third body perturbations.

In a selenocentric reference frame (see Figure 1), the potential of the lunar gravity field given as expansion into spherical harmonics is a sum of the potential of a sphere and the perturbation accounting for all the deviations of a real body from a sphere:

$$U(\mathbf{q}) = \frac{\mu_M}{r(\mathbf{q})} + R_M(\mathbf{q}) \quad (5)$$

$$R_M(\mathbf{q}) = \frac{\mu_M}{r(\mathbf{q})} \sum_{l=2}^{+\infty} \left( \frac{R_M}{r(\mathbf{q})} \right)^l \sum_{m=0}^l P_{lm} \left( \frac{q_z}{r(\mathbf{q})} \right) \left[ C_{lm} \cos \left( m \arctan \left( \frac{q_y}{q_x} \right) - m\theta \right) + S_{lm} \sin \left( m \arctan \left( \frac{q_y}{q_x} \right) - m\theta \right) \right] \quad (6)$$

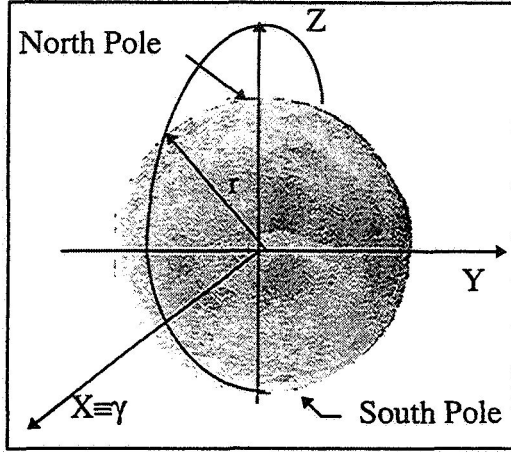


**Figure.1. Selenocentric reference frame**

where  $\mu_M$  is the gravity parameter of the Moon,  $R_M$  is the mean equatorial radius and  $\theta$  is the phase of lunar rotation, namely the angle between some body fixed direction along the equator and some inertial direction along the equator.

The perturbing function due to the presence of the Earth and the Sun can be developed in terms of the displacements  $\mathbf{q}$  and of the position of the planet relative to the local coordinate frame as follows<sup>3</sup>:

$$R_B(\mathbf{q}) = \mu_B \left( \frac{1}{d_B} - \frac{\langle \mathbf{q}, \rho_B \rangle}{\rho_B^3} \right) \quad (7)$$

where  $\mu_B$  is the gravity parameter of the third body, namely the Earth or the Sun,  $\rho_B$  is the selenocentric position radius of the third body and  $d_B$  is defined as follows:

$$d_B = (\rho_B^2 + q^2 - 2\rho_B q \cos \delta)^{1/2} \quad (8)$$

where  $\delta$  is the angle between  $\rho$  and  $q$ .

## OPTIMAL CONTROL FORMULATION

Let consider a performance index of the form:

$$J = \varphi(\mathbf{x}(t_f), t_f) + \int_{t_i}^{t_f} L[\mathbf{x}(t), \mathbf{u}(t), t] dt \quad (9)$$

where  $\varphi(\mathbf{x}, t)$  is a discrete function of the states and time at the final time and  $L(\mathbf{x}, \mathbf{u}, t)$  is an integrand performance index.

The problem is to find a state function  $\mathbf{x}: [t_0, t_f] \rightarrow \mathcal{R}^n$  and a control function  $\mathbf{u}: [t_0, t_f] \rightarrow U \subset \mathcal{R}^m$ , that minimize (or maximize) the cost function (9), subject to conditions (1), (4) and to the following conditions on final boundaries:

$$\Phi(\mathbf{x}, t) = 0 \quad (10)$$

Adjoin<sup>4</sup> the system differential equations (1) and (4) and boundary conditions (10) to  $J$ , respectively with multiplier functions  $\lambda(t)$  and  $v$ :

$$J = [\varphi(\mathbf{x}, t) + v^T \Phi(\mathbf{x}, t)] \Big|_{t_i}^{t_f} + \int_{t_i}^{t_f} [L + \lambda^T (\mathbf{f} - \dot{\mathbf{x}}) + \lambda_m (\dot{m}_R + \|\mathbf{u}\|_c)] dt \quad (11)$$

For convenience, define a scalar function  $H$  as follows:

$$H[\mathbf{x}(t), \mathbf{u}(t), \lambda(t), t] = L[\mathbf{x}(t), \mathbf{u}(t), t] + \lambda^T(t) \mathbf{f}[\mathbf{x}(t), \mathbf{u}(t), t] + \lambda_m(t) \|\mathbf{u}(t)\|_c \quad (12)$$

Taking the first variation of  $J$ , considering also differential changes in the terminal time  $t_f$ , the following is obtained:

$$\delta J = \left[ \frac{\partial \varphi}{\partial \mathbf{x}} + \mathbf{v}^T \frac{\partial \Phi}{\partial \mathbf{x}} \right] \delta \mathbf{x} + \delta \mathbf{v}^T \Phi \Big|_{t_i}^{t_f} + \delta t_f \left( \lambda^T \mathbf{f} + L + \frac{\partial \varphi}{\partial t} + \mathbf{v}^T \frac{\partial \Phi}{\partial t} \right) \Big|_{t_f}^{t_i} + \int_{t_i}^{t_f} [\delta L - \delta \lambda^T \dot{\mathbf{x}} + \delta \lambda^T \mathbf{f} - \lambda^T \delta \dot{\mathbf{x}} + \lambda^T \delta \mathbf{f} + \delta \lambda_m (\dot{m}_R + c \|\mathbf{u}\|) + \lambda_m \delta \dot{m}_R + \lambda_m c \frac{\partial \|\mathbf{u}\|}{\partial u} \delta \mathbf{u}] dt = 0 \quad (13)$$

In order to have boundary conditions of the weak type the following terms<sup>5</sup> are adjoined to expression (13):

$$\delta \lambda^T (\mathbf{x} - \mathbf{x}^b) + \lambda^b \delta \mathbf{x} \Big|_{t_i}^{t_f} + \delta \lambda_m^T (m_R - m_R^b) + \lambda_m^b \delta m_R \Big|_{t_i}^{t_f} \quad (14)$$

with the costates boundary values at final time  $\lambda_f^b$  defined<sup>4</sup> as follows:

$$\frac{\partial \varphi(\mathbf{x}, t)}{\partial \mathbf{x}} + \mathbf{v}^T \frac{\partial \Phi(\mathbf{x}, t)}{\partial \mathbf{x}} \equiv \lambda_f^b \quad (15)$$

The resulting equation takes the form:

$$\delta J = \lambda^b \delta \mathbf{x} \Big|_{t_i}^{t_f} + \delta \mathbf{v}^T \Phi \Big|_{t_i}^{t_f} + [\delta \lambda^T (\mathbf{x} - \mathbf{x}^b) + \delta \lambda_m (m_R - m_R^b) + \lambda_m^b \delta m_R] \Big|_{t_i}^{t_f} + \delta t \left( \frac{\partial \varphi}{\partial t} + \mathbf{v}^T \frac{\partial \Phi}{\partial t} + L + \lambda^T \mathbf{f} \right) \Big|_{t_f}^{t_i} + \int_{t_i}^{t_f} [\delta L - \delta \lambda^T \dot{\mathbf{x}} + \delta \lambda^T \mathbf{f} - \lambda^T \delta \dot{\mathbf{x}} + \lambda^T \delta \mathbf{f} + \delta \lambda_m (\dot{m}_R + c \|\mathbf{u}\|) + \lambda_m \delta \dot{m}_R + \lambda_m c \frac{\partial \|\mathbf{u}\|}{\partial u} \delta \mathbf{u}] dt = 0 \quad (16)$$

After an integration by parts of the term  $\delta \lambda^T \dot{\mathbf{x}}$ , the expression (16) reduces to the form:

$$\delta J = \lambda^b \delta \mathbf{x} \Big|_{t_i}^{t_f} + \delta \mathbf{v}^T \Phi \Big|_{t_i}^{t_f} + (-\delta \lambda^T \mathbf{x}^b + \delta \lambda_m m_R^b) \Big|_{t_i}^{t_f} + \delta t \left( \frac{\partial \varphi}{\partial t} + \mathbf{v}^T \frac{\partial \Phi}{\partial t} + L + \lambda^T \mathbf{f} \right) \Big|_{t_f}^{t_i} + \int_{t_i}^{t_f} [\delta L + \delta \dot{\lambda}^T \mathbf{x} + \delta \lambda^T \mathbf{f} - \lambda \delta \dot{\mathbf{x}} + \lambda^T \delta \mathbf{f} - \delta \dot{\lambda}_m m_R + \lambda_m \delta \dot{m}_R + \delta \lambda_m \|\mathbf{u}\| c + \lambda_m c \frac{\partial \|\mathbf{u}\|}{\partial u} \delta \mathbf{u}] dt = 0 \quad (17)$$

The controls, both at boundary and at internal nodes, have to satisfy necessary condition  $H_u(x, \lambda, u, t) = 0$  and Legendre-Clebsch condition  $H_{uu}(x, \lambda, u, t) \geq 0$ .

## THE SET APPROACH

The finite elements in time method (FET) has been successfully applied to a large number of problems in computational mechanics, spacing from rigid body dynamics to structural mechanics, wave propagation, fluid dynamics and optimal control<sup>5,7,8</sup>.

In this paper we propose a slightly different approach using, instead of FET, Spectral Elements in Time (SET) a high-order finite element technique that combines the geometric flexibility of finite elements with the high accuracy of spectral methods. Spectral method, pioneered in the mid 1980's by Anthony Patera<sup>9</sup> at MIT for fluid dynamics problems, is here applied to the integration of ODEs in the time domain, being spectral elements in time more accurate and efficient in finding the solution for our problems involving less memory space and less computational cost.

Both FET and Spectral Elements methods offer some interesting features that make them attractive in automated numerical procedures:

- Through the use of spectral basis for shape functions, high order methods can be constructed, therefore allowing the development of automated  $p$  and  $hp$  adaptive procedures.
- Using a time assembly process, they allow the solution of general boundary-value problems. Besides the computation of the system response, this technique provides at a negligible extra computational cost an approximation of the transition matrix that allows to perform a linearised stability analysis of the solution<sup>7</sup>.
- The variational framework is an ideal context for developing constrained formulations for mechanics<sup>8</sup>, leading to schemes characterized by robust numerical behavior.

The variational principle (17) is the governing equation for the weak Hamiltonian method for optimal control problems. This formulation provides the base for the development of the SET discretization for general boundary problems.

Now let the time domain  $D(t_i, t_{i+1}) \subset \mathcal{R}$  be decomposed into  $N$  finite time elements:

$$D = \bigcup_{j=1}^N D_j(t_i, t_{i+1}) \quad (18)$$

The parametric approximations of the trial functions  $(\mathbf{x}, \lambda, \mathbf{u}, m_R)$  and test functions  $(\delta \mathbf{x}, \delta \lambda, \delta \mathbf{u}, \delta m_R)$  are developed within the space of the polynomials of order  $k-1$  and  $k$  respectively:

$$\begin{Bmatrix} \mathbf{x} \\ m_R \end{Bmatrix} = \sum_{s=1}^k f_s(t) \begin{Bmatrix} \mathbf{x}_s \\ m_{Rs} \end{Bmatrix} \quad \begin{Bmatrix} \lambda \\ \lambda_m \\ \nu \end{Bmatrix} = \sum_{s=1}^k f_s(t) \begin{Bmatrix} \lambda_s \\ \lambda_{ms} \\ \nu_s \end{Bmatrix} \quad (19)$$

$$\begin{Bmatrix} \delta \mathbf{x} \\ \delta m_R \end{Bmatrix} = \sum_{s=1}^{k+1} g_s(t) \begin{Bmatrix} \delta \mathbf{x}_s \\ \delta m_{Rs} \end{Bmatrix} \quad \begin{Bmatrix} \delta \lambda \\ \delta \lambda_{ms} \\ \delta \nu \end{Bmatrix} = \sum_{s=1}^{k+1} g_s(t) \begin{Bmatrix} \delta \lambda_s \\ \delta \lambda_{ms} \\ \delta \nu \end{Bmatrix} \quad (20)$$

$$\mathbf{u} = \sum_{s=1}^k f_s(t) \mathbf{u}_s \quad \delta \mathbf{u} = \sum_{s=1}^k f_s(t) \delta \mathbf{u}_s \quad (21)$$

where the functions  $f$  and  $g$  are defined as follows:

$$f \in P^{k-1}(D_j) ; \quad g \in P^k(D_j) \quad (22)$$

and the quantities  $\mathbf{x}_s, \lambda_s, \mathbf{u}_s$  and  $m_{Rs}$  are internal node values.

In a more general way we could decompose the domain  $D$  as a union of smooth images of the reference time interval  $[-1, 1]$  where we define a reference parameter  $v$ :

$$\nu = 2 \frac{t - t_{i+1/2}}{t_{i+1} - t_i} = 2 \frac{t - t_{i+1/2}}{\Delta t} \quad (23)$$

The basis functions  $f$  and  $g$  can be constructed by using Lagrangian interpolants associated with the internal Gauss-Lobatto node<sup>9</sup>. Thus if  $\{\xi_i\}_{i=1}^k$  are the set of Gauss-Lobatto points on the reference interval  $[-1, 1]$ ,  $f_i(v)$  will be the Lagrangian interpolating polynomial vanishing at all the Gauss-Lobatto nodes except at  $\xi_i$  where it equals one. Each integral of the continuous form (17) is then replaced by a Gauss quadrature sum:

$$\begin{aligned}
& \sum_{i=1}^n \sigma_i \left[ \delta \dot{\lambda}(\xi_i)^T x(\xi_i) + \delta \lambda(\xi_i)^T f(\xi_i) \frac{\Delta t}{2} \right] \\
& \sum_{i=1}^n \sigma_i \left\{ -\lambda(\xi_i)^T \delta \dot{x}(\xi_i) + \left[ \frac{\partial L(\xi_i)}{\partial x} + \lambda(\xi_i)^T \frac{\partial f(\xi_i)}{\partial x} \right] \delta x(\xi_i) \frac{\Delta t}{2} \right\} \\
& \sum_{i=1}^n \sigma_i \left[ -m_R(\xi_i) \delta \dot{\lambda}_m(\xi_i) + c \|u(\xi_i)\| \delta \lambda_m(\xi_i) \frac{\Delta t}{2} \right] \\
& \sum_{i=1}^n \sigma_i \left[ \lambda_m(\xi_i) \delta \dot{m}_R(\xi_i) + \lambda(\xi_i)^T \frac{\partial f(\xi_i)}{\partial m_R} \delta m_R(\xi_i) \frac{\Delta t}{2} \right] \\
& \sum_{i=1}^n \sigma_i \left[ \frac{\partial L(\xi_i)}{\partial u} + \lambda(\xi_i)^T \frac{\partial f(\xi_i)}{\partial u} + \lambda_m(\xi_i) c \frac{\partial \|u(\xi_i)\|}{\partial u} \right] \delta u(\xi_i) \frac{\Delta t}{2}
\end{aligned} \tag{24}$$

where  $\sigma_i$  is the weight associated with  $\xi_i$ .

By the discrete form (24) two distinct procedures can be derived:

- An implicit time marching self-starting integration obtained for initial value problems
- An assembled process developed for boundary value problems, obtained by matching the final boundary state of each element with the initial state of the subsequent element.

Both approaches are taken into account in this effort: while the assembled system is used to solve the optimum problems, the time marching integrator is used to propagate the initial condition bounds, forward and backward in time.

By the SET discretization the differential problem is transformed into a system of non-linear algebraic equations. Then a numeric optimization process can be used to minimize the objective function satisfying the differential constraints. All the additional constraints on the state and on the control are discretized and directly implemented into the optimization process. Here a Newton algorithm with line search is adopted to solve the non-linear system arising from discretization. Linearised algebraic equations for a single spectral element yield:

$$J_{(e)} * \Delta y_{(e)} = -R_{(e)} \tag{25}$$

where  $J_{(e)}$  is the elemental tangent matrix,  $R_{(e)}$  the elemental residual vector,  $\Delta y_{(e)} = (\Delta x, \Delta \lambda, \Delta u, \Delta m_R)_{(e)}$  are increments to nodal states, costates and controls, while the subscript  $(.)_{(e)}$  refers to elemental quantities. The global matrix formulation can then be obtained through the standard finite element assembly process performed on the corresponding elemental matrices:

$$J * \Delta y = -R \tag{26}$$

The matrix  $J$  is highly sparse<sup>10</sup> and can be conveniently stored in a compressed format and solved by an iterative sparse solver.

## CONVERGENCE ANALYSIS

The validation of the optimization algorithm has been performed on several problems taken from Ref.4. In particular we compare our results to two sample problems presented in Ref.5 where a finite elements techniques is developed for



optimal dynamics problems. The first optimal control problem is a transfer of a particle on a rectilinear path with fixed time. The thrust angle is the control and the particle has constant mass and constant acceleration modulus:

$$\mathbf{f}(\mathbf{x}, \mathbf{u}, t) = \{a \cos(u), a \sin(u), p_x, p_y\}^T \quad (27)$$

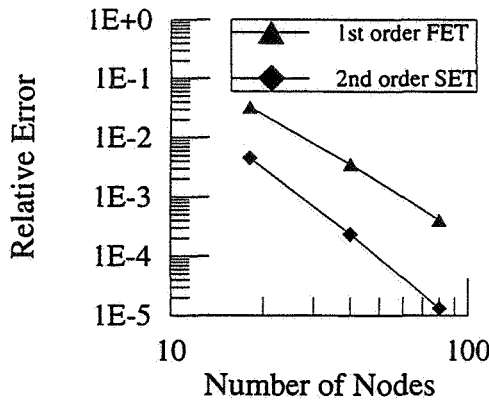


**Figure 2. Relative error on final thrust inclination, versus computational cost**

The objective function is the final horizontal component of velocity that should be maximized:

$$J = \varphi(\mathbf{x}(t), t) \Big|_t^f = p_x^b \Big|_t^f \quad (28)$$

Initial conditions are fixed and there are also two terminal constraints on state: fixed final height and final vertical component of velocity, which must be zero:

$$\Phi(\mathbf{x}, t) \Big|_t^f = \{0, (q_y - h), p_y, 0\}^T \Big|_t^f \quad (29)$$

In Figure 2 a comparison in final solution accuracy is made between the solution obtained using a spectral discretization with polynomials of the 2nd order, both for the

control and the state, and the results reported in Ref.5 in which finite elements of the first order for the state and of order zero for the control have been used.

As can be seen increasing the order of the polynomials, especially for the control, reduces the over all cost. Spectral basis for the generation of polynomials of high order guarantees numerical stability of the integration algorithm allowing p adaptivity<sup>10</sup>, where the solution is continuous, and flexible h adaptivity where it's not.

## THE LANDING PROBLEM

In order to make the right choice for the best landing maneuver two main drivers have been identified: the overall cost, in terms of weight budget, and the reliability. Thus two are the main problems analyzed here:

- find a reliable orbit, for the coast phase, which can be used as safety path in case of landing abort
- evaluate the propellant consumption and the maximum thrust needed to perform the desired homing trajectory, taking into account errors arising from non correct modeling of the present force field.

### Coast Phase

A stable periodic orbit for the coast phase would reduce the risk of a hard landing even without a huge amount of propellant, and could be a reliable parking orbit in case of a landing abort. However the lack of data on the real gravity field of the moon gives a meaningful uncertainty on the frozen/periodic orbit location. This can be clearly seen in Figures 3-7 where three different solutions, generated<sup>11</sup> using respectively Lemoine's GLGM-2 model, Konopliv's Lun60d and GLGM-2 plus uncertainties (sigmas) on harmonics coefficients, are represented. In particular the huge variation of 180° in frozen periselenium anomaly should be noted.

Thus different possible orbits with different orbital elements have then been analyzed and three specific cases are discussed here: a direct descent from a 100x100 km parking orbit down to a 100x20 km orbit with the periselenium over the South Pole; a direct descent from a 100x100 km parking orbit down to a 70x20 km frozen/periodic orbit with the periselenium over the South Pole; a two-steps maneuver which exploits an intermediate 50x20 frozen/periodic orbit with the periselenium over the North Pole. Exact orbital elements are reported in Table 1, while in Figure 9 orbit geometry for the three coasting trajectories are represented and, for each maneuver, ignition time and thrust modulus  $u$  (constant) reported. Table 2 summarizes the propellant consumption budget for the coast phase, taking into account extra propellant necessary to come back on a stable orbit in case of landing abort.

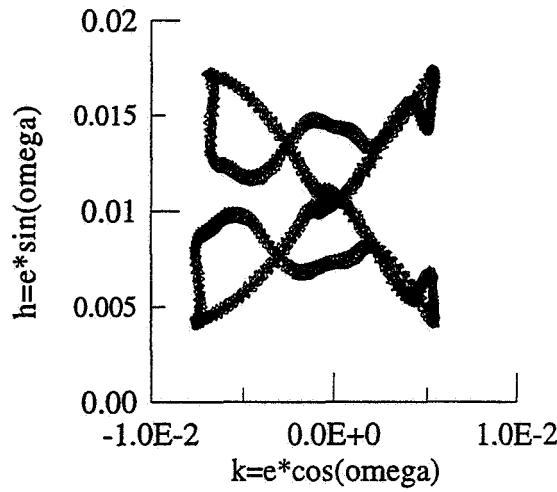


**Figure 3. Periodic solution, osculating h-k plane:  $a=1788$  km,  $T=2$  months, Lemoine's GLGM-2.**

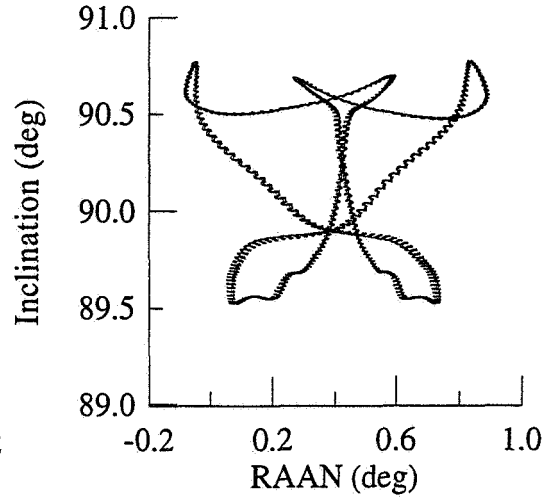


**Figure 4. Periodic solution, osculating i- $\Omega$  plane:  $a=1788$  km,  $T=2$  months, Lemoine's GLGM-2.**

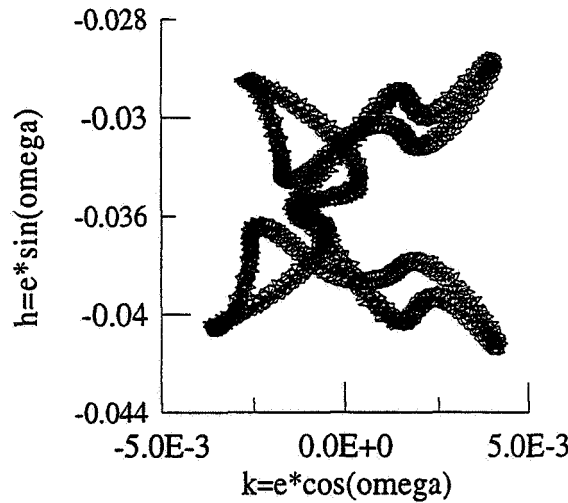


**Figure 5. Periodic solution, osculating h-k plane:  $a=1788$  km,  $T=2$  months, Konopliv's Lun60d.**

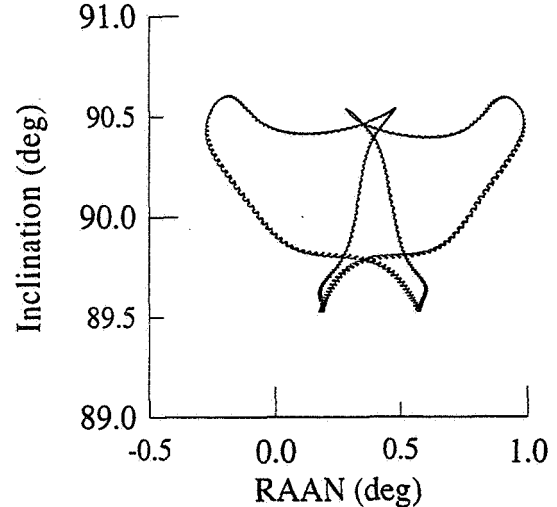


**Figure 6. Periodic solution, osculating i- $\Omega$  plane:  $a=1788$  km,  $T=2$  months, Konopliv's Lun60d.**

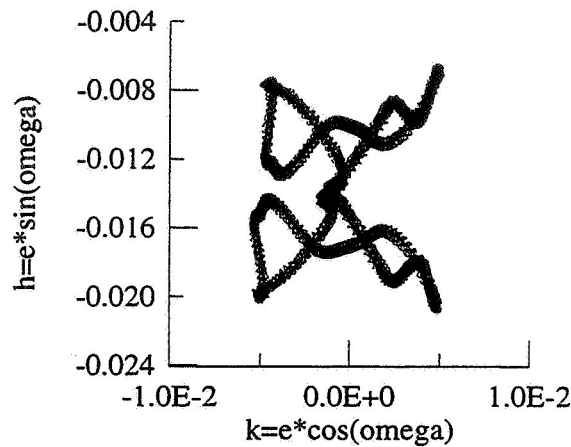


**Figure 7. Periodic solution, h-k plane:**  
a=1788 km, T=2 months, Lemoine's  
GLGM-2+sigmas

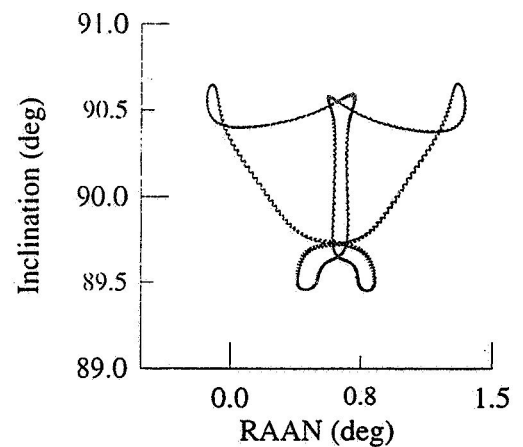


**Figure 8. Periodic solution, i-Ω plane:**  
a=1788 km, T=2 months, Lemoine's  
GLGM-2+sigmas

After designing the desired coasting orbit using an estimated force model, computed initial conditions are propagated forward in time using a different gravity model, taken to be true. As estimated force model we take at first Lun60d, using Lemoine's as true one, and then we take Lemoine's as estimated and GLGM-2 plus sigmas as true one. Errors in final state vector computed in this phase will represent uncertainties in initial state vector for the following homing phase.

**Table 1. Coasting Orbit Keplerian Elements**

	Direct 100x100	Periodic 70x20	Periodic 50x20
a (km)	1798	1784.16	1772.63
Node Longitude (deg)	0.14	179.136	0.145
Ω (deg)	0.14	0.1342	0.145
e	0.0222	0.014368	0.008264
i (deg)	90	90.12	89.96
ω (deg)	-90	-96.37	-89.7

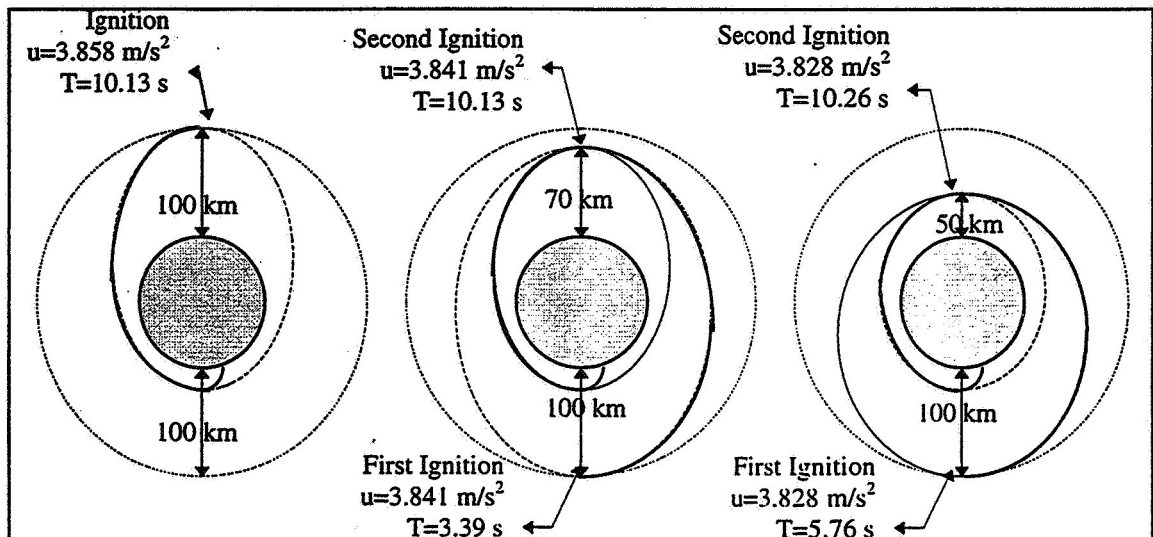


**Figure 9. Coasting Trajectories Geometry and Orbital Maneuvers**

Table 2. Coasting Maneuvers

Maneuver	Propellant Consumption (m <sub>R</sub> )	Max Thrust (m/s <sup>2</sup> )	Extra Propellant (m <sub>R</sub> )
Direct 100x20	0.01242	3.8582	0.0116
Frozen/periodic 49.3x20	0.01953	3.8283	0.0124
Frozen/periodic 70x20	0.01653	3.8412	0

## Homing Phase

An optimum criterion aimed to minimize the thrust is adopted for the homing phase: a low maximum thrust will reduce engines dimension and weight and the overall propellant consumption. An optimal trajectory is designed for an estimated force model taking into account a number of constraints characterizing the homing phase.

A landing site placed on a circle of 86° of latitude south on the near side has been selected and different approaching directions have been analyzed in order to identify the best moment to begin the homing maneuver. Final altitude is fixed at 2 m above the ground, where thrusters are cut off and the residual vertical velocity of the spacecraft is 3 m/s. Initial conditions are constrained to be on a given coasting trajectory with given orbital keplerian parameters:

$$\Phi(\mathbf{x}, t) \Big|_i = \left\{ \begin{array}{l} v^2 + \frac{\mu}{a} - \frac{2\mu}{r} \\ r^2 - [a(1-e^2) - e(q_x \cos\omega - q_z \sin\omega)]^2 \\ \mathbf{v} \wedge \mathbf{r} - \mathbf{h} \\ \langle \mathbf{v}, \mathbf{r} \rangle + rr \end{array} \right\} \Big|_i \quad (30)$$

where  $\mathbf{v}=\mathbf{v}(\mathbf{p})$  is the velocity vector,  $\mathbf{r}=\mathbf{r}(\mathbf{q})$  the radius,  $a, e, \omega$  and  $\mathbf{h}$  the semi-major axis, the eccentricity, the periapsis and the angular velocity of the coasting orbit respectively. A specific impulse  $I_{sp}=317$ s is here adopted. From 10 km to 0.002 km an alignment constraint is imposed on the state vector in order to reduce the tangential velocity to zero and to direct the thrust to the ground before the final break. This constraint is implemented by means of an additional weighted objective function  $w_v$ , of the form:

$$L = \frac{1}{2} u^2 + w_v(\mathbf{p}) \quad (31)$$

From 5 km to 0.002 km an obstacles avoidance strategy is turned on in order to guide the spacecraft to a suitable place. Results for the homing trajectory, computed using 8 elements with polynomials of the 6th order both for state and control vector, are shown in Figures 10,11,12 and 13. The velocity modulus and the velocity angle  $\alpha$  relative to the ground are represented in Figures 14 and 15. The maneuver begins 559.637 km before the landing site and lasts 856 s. It should be noted how, approaching to the ground,  $\alpha$  turns to 270°. The thrust modulus and the thrust angle  $\beta$

relative to the ground are represented in Figures 16 and 17 respectively, while in Figure 18 the propellant consumption history is plotted.

The specific thrust modulus stays always under  $3.912 \text{ m/s}^2$  and reaches its maximum value when the alignment constraint on velocity vector is turned on. At this point two subsequent maneuvers reduce the velocity component tangential to the ground to zero. A final maneuver is performed to reduce the velocity to  $3 \text{ m/s}$ . In order to evaluate the effects of force model errors, initial conditions are forced to be equal to the final conditions taken from the coast phase analysis and a new optimal solution is computed taking into account different gravity models. The result in term of extra thrust and extra propellant mass for the homing phase is summarized in Table 3.

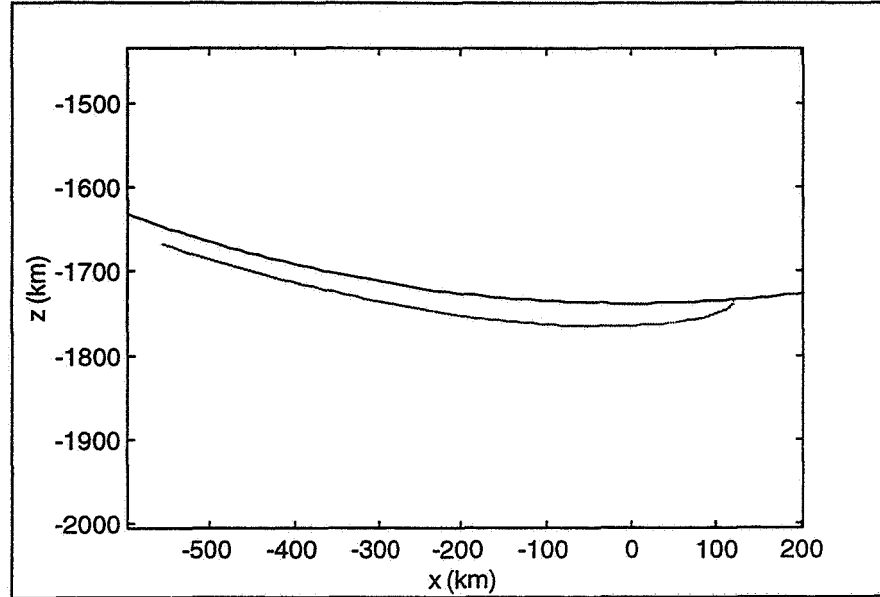


**Figure.10. Homing trajectory relative to the Moon surface: z-x plane**

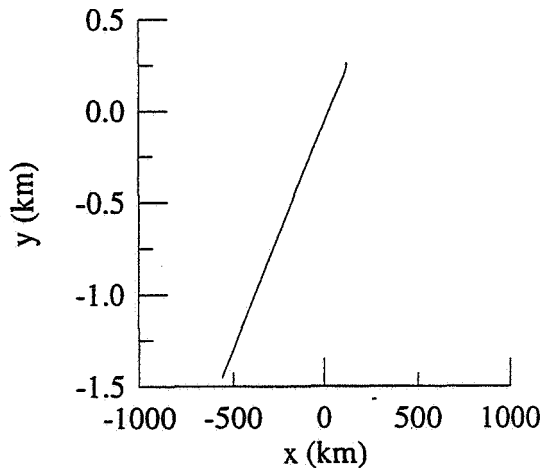


**Figure.11. Homing: y-x plane**

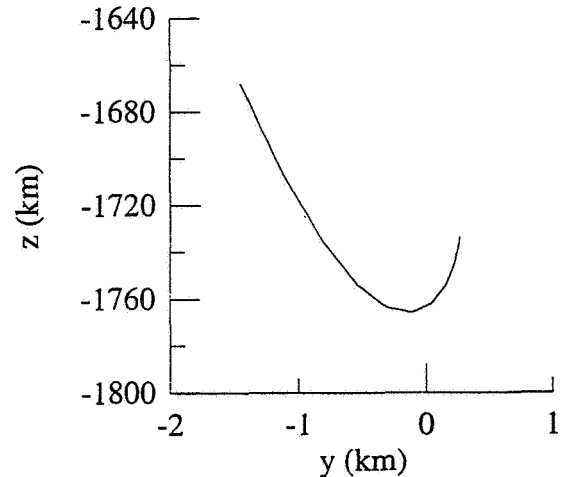


**Figure.12. Homing: z-y plane**

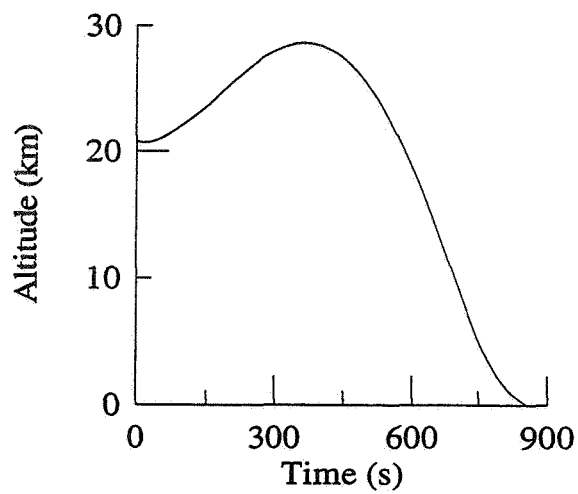


**Figure.13. Altitude vs. time**

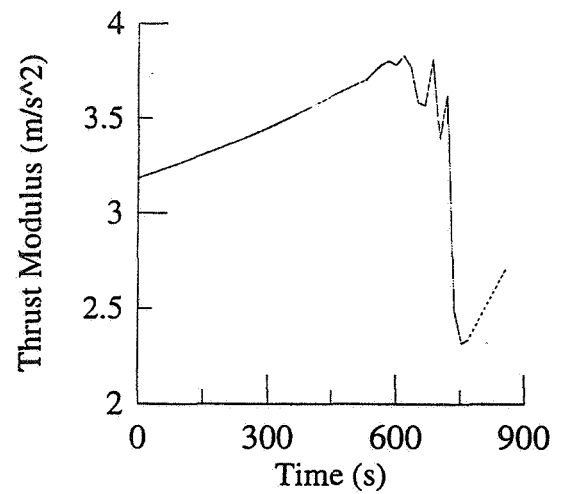


**Figure.16. Thrust modulus vs. time**

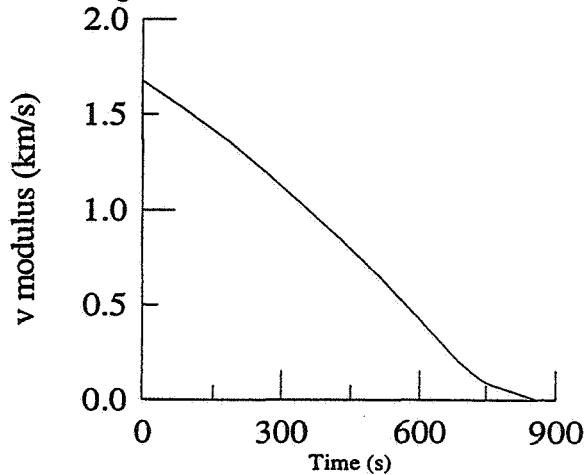


**Figure.14. Homing: velocity modulus vs. time**

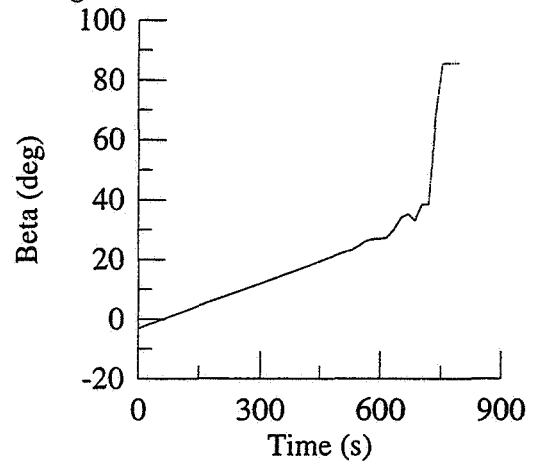


**Figure.17. Thrust inclination relative to the ground**

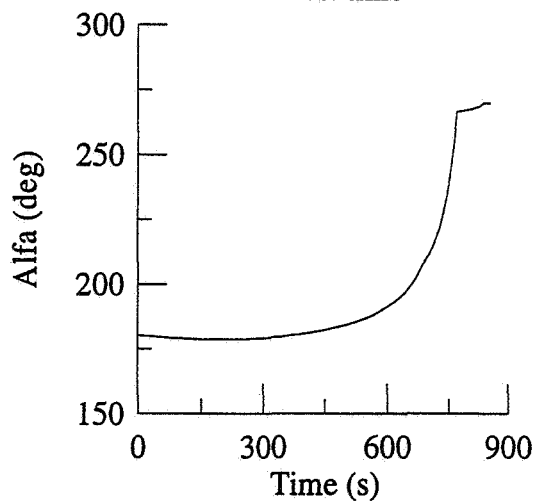


**Figure.15. Velocity inclination relative to the ground.**

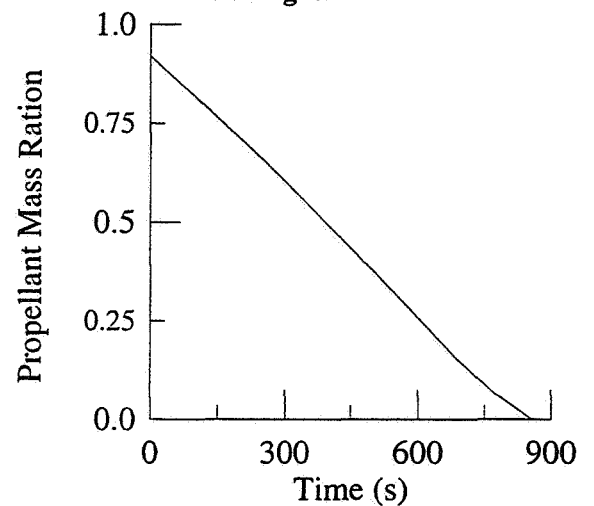


**Figure.18. Propellant mass consumption vs. time.**

## Obstacles Avoidance Strategy

The strategy for obstacles avoidance is implemented directly into the optimization process: the objective function  $L$  is modified introducing an additional term which is function of the distance  $d_o$  from obstacles. In this way the new optimal solution will maximize the distance from obstacles, minimizing the thrust needed to perform the maneuver. The new objective function is defined as follows:

$$L^* = \frac{1}{2} u^2 + k_v d_o(q) \quad (32)$$

where  $k_v$  is a weight parameter which characterizes the priority of maneuvers on thrust minimization: the higher  $k_v$  is the more the maneuvers are fast and expensive.

The distance  $d_o$  is evaluated superimposing a characteristic shape function on obstacles as shown in Figure 19.

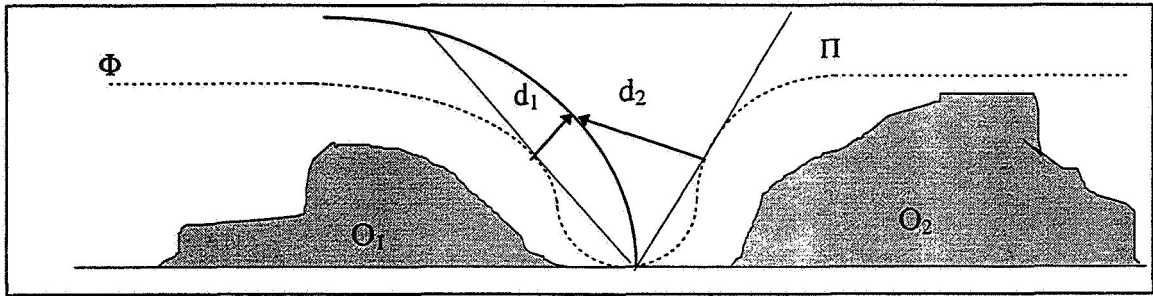


**Figure 19. Example of shape function for obstacles avoidance maneuver: shape function  $\Phi$  is superimposed on obstacles  $O_1$  and  $O_2$ . Distance  $d_1$  and  $d_2$  are evaluated from the surface of the tangent cone  $\Pi$ .**

In order to provide a real time control, the differential problem and the additional objective functions are linearized in a neighbour of an initial optimal solution. In the linearized model the shape function is substituted by a sequence of cones tangent (see Figure 19) to the original shape function. In this way at each step  $\Delta t$  the optimization algorithm has to evaluate just one sparse matrix inversion to reach an accuracy on the solution of  $1e-6$ . The weight parameter  $k_v$  is a function of the amplitude of cones, scaled to the dimension of the thrust modulus.

As test cases, different scenarios have been generated with different random distribution of obstacles of several dimensions, ranging from mountains of few kilometers to rocks of some meters. The cone parameter  $k_v$  becomes a function of obstacles position, altitude and width, and of the estimation of the landing site position, which represents the cone vertex location. Every  $\Delta t$  seconds, during the descent, the cone geometry is updated on the basis of new data on landing site and obstacles nature. To prove the robustness of the algorithm, different temporization for data acquisition have been simulated, taking into account possible delays. In Figure 20 three possible obstacles avoidance maneuvers are shown, each starting with different initial conditions and characterized by a temporization  $\Delta t = 8.56$  s. These solutions are integrated using 10 elements with polynomials of the 2nd order both for state and control vector. In Figures 21 and 22 specific thrust modulus and inclination as to the ground are plotted.

On trajectory number 3, the spacecraft detects obstacle 3 at 3.5 km and obstacle 2 only at 1 km from the ground, thus, as can be seen in Figure 20, two subsequent fast maneuvers are necessary to avoid them both. On the contrary, on trajectory number 2 the spacecraft detects obstacle 3 at 3.5 km and obstacle 2 at 2.5 km allowing a more smooth maneuver. On trajectory number 1 obstacle 1 is detected immediately while obstacle 2 is detected below 1 km, requiring a fast maneuver with a thrust angle of  $51^\circ$ .

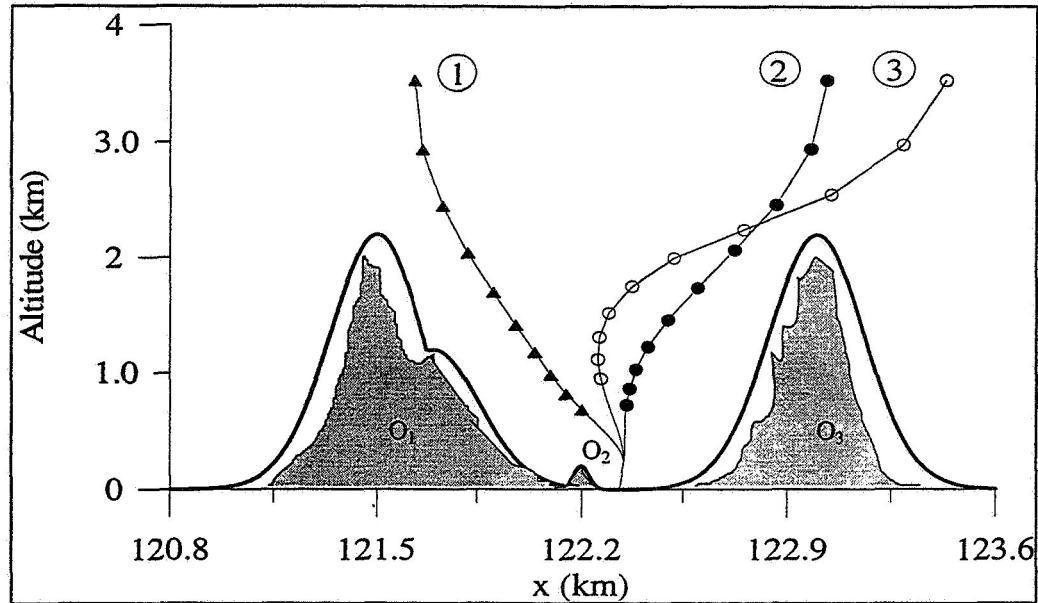


Figure.20. Example of obstacle avoidance maneuvers

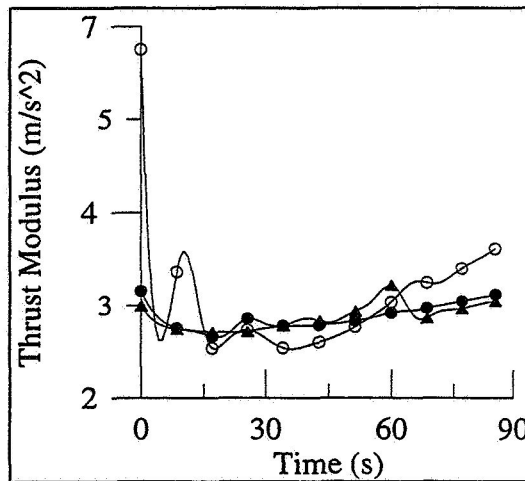


Figure.21. Thrust modulus

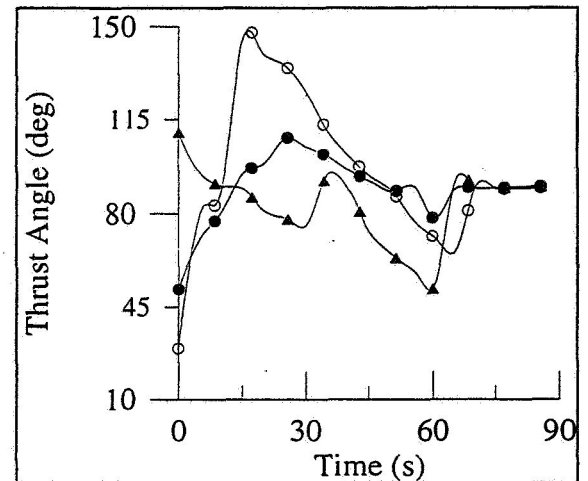


Figure. 22. Inclination relative to the ground

Table 3. Overall Homing Costs

Maneuver	Propellant Consumption ( $m_R$ )	Max Thrust ( $m/s^2$ )	Extra Propellant ( $m_R$ )	Extra Thrust ( $m/s^2$ )
Homing from 100x20	0.927	3.8582	0.003137	0.02445
Homing from 70x20	0.923	3.8412	0.000269	0.00807
Homing from 49.3x20	0.920	3.8283	0.000123	0.00856



## CONCLUSIONS

In this paper a numerical approach based on the spectral elements in time technique is presented for optimal control problems. An optimal set of initial conditions and an optimal control law has been derived to perform a soft landing on the South Pole of the Moon. For the final descent a control strategy for obstacles avoidance has been proven to be effective, leading to a fast and simple control in real time. Taking into consideration errors arising from gravity perturbations and uncertainties on landing site location, a total mass ratio of  $0.951 \pm 0.003137$  of propellant is estimated to be necessary with a maximum specific thrust of  $3.858 \text{ m/s}^2 \pm 0.02445 \text{ m/s}^2$ . From this preliminary analysis a 70x20 frozen/periodic orbit seems to be the optimal coasting orbit, both for cost and reliability. However this aspect must be investigated further on the basis of more reliable gravity data: if the actual periselenium was at  $90^\circ$ , a mission aimed to a soft landing on the North Pole would be recommended.

Future developments aimed to enhancing the model of the spacecraft are at present being studied, in particularly to define a pulsed thrust and to introduce the attitude control in the optimization process.

## REFERENCES

1. Kinoshita T., Itagaki H., Moriuma H., Namura E. *Outline of the experimental Lunar Lander in SELENE Project*. ESA SP-403 ISBN 92-9092-295-8 August 1997.
2. Floberghagen R., Visser P., Vasile M.. *Low Lunar Orbits Analysis, determination and selection for soft landing on the lunar South Pole*. ESA SP-403 ISBN 92-9092-295-8 August 1997.
3. Sanso F., Rummel R. *Theory of Satellite Geodesy and Gravity Field Determination*. Lecture Notes in Earth Sciences. Vol.25, Springer-Verlag, 1988.
4. Bryson A.E. Jr., Ho Yu-Chi. *Applied Optimal Control*. Blaisdell Publishing Company, Waltham, Massachusetts, 1969.
5. Hodges D.H., Bless R.R.. *A Weak Hamiltonian Form for Optimal Control*. Jan 01, 1989, NASA-CR-185336, NAS 1.26:185336.
6. Bulirsch R., Miele A., Stoer J., Well K.H.. *Optimal Control, Calculus of Variation, Optimal Control Theory and Numerical Methods*. ISNM Vol. 111, Birkhauser Verlag 1993
7. Borri M. *Helicopter Rotor Dynamics by Finite Elements Time Approximation*. Comp.&Maths. with Appls., vol.12A, No.1, 1986, pp. 149-160
8. Borri M., Bottasso C.L., Mantegazza P. *Basic Features of the Time Finite Elements Approach for Dynamics*. Meccanica, Vol.27, 1992, pp. 119-130.
9. Karniadakis G.E., Bullister E.T. and Patera A.T.. *A Spectral Elements Method for Solution of Two- and Three-dimensional Time-dependent Navier-Stokes Equations*. Proc. Europe-U.S. Conf. on Finite Element Methods for Nonlinear Problems, Springer-Verlag, p.803, 1985.
10. Pavarino L.F.. *Preconditioned Mixed Spectral Elements Methods for Elasticity and Stokes Problems*. AMS(MOS) subject classifications 65f10.
11. Finzi A.E., Vasile M.. *Numerical Solution for Lunar Orbits*. IAF-97-A.5.08, 48th International Astronautical Congress, October 6-10, 1997, Torino, Italy.



## HIGH-ORDER STATE ESTIMATION FOR APPROACH AND LANDING OF LUNAR OR PLANETARY SPACECRAFT \*

Shuji ONO<sup>†</sup>

This paper presents a new algorithm for the independent estimation of the high-order state vector of attitude, angular rate, thrust, and dynamic parameters, needed for the spacecraft control in the approach and landing to the moon or a planet. Without aid of the inner information of a gyroscope and an accelerometer, the constructed algorithm uses only the outer information ( range & range rate ) of the tracking station measurement or the topographical measurement by the reflection wave, for the multi-beams emitted from several antennas equipped on a vehicle. The simulation results well verify the effectiveness of this algorithm, even in place of an attitude sensor. The new excellent result is especially obtained by the topographical assumption of a ground surface model. This paper gives one of fundamental guidelines not only for the new design of the navigation system and the ground control system of an aircraft, a future space-plane, or a planet-surveyor, but also for the identification of a planetary surface model.

### INTRODUCTION

The approach and landing on the moon or a planet presently depends upon the on-board control system of an un-manned vehicle; due to an uncertain topographical information and a communication delay upto the Earth. Therefore the right or wrong, namely, the landing rocket and the on-board control system normally operated or not, the landed point was nominal or not, there were any damages in the vehicle or not, must be waited until the end of the postflight data analyses for several hours or some days. In the near future, if the interplanetary communication and tracking network and the detailed topographical data will be arranged, the unmanned on-board system will be reliable and safe. Moreover the flight situation will be independently seized and judged in realtime if the manned station will be constructed nearby.

This paper, on the premise of the above arrangements in the near future, aims the independent estimation of the high-order state vector, separated from the vehicle inner information, that is, for the purpose of evaluating the Inertial

\* Prepared for 13<sup>th</sup> International Symposium on Space Flight Dynamics at Goddard Space Flight Center, May 1998.

† Doctor of Engineering, Tsukuba Computer Center, Tsukuba Space Center, National Space Development Agency of Japan ( NASDA ), 2-1-1 Sengen, Tsukuba city, Ibaragi-ken, JAPAN, Tel. (81)298-52-2488, Fax. (81)298-52-2394.

Measurement Unit ( IMU ) system of a gyroscope, an accelerometer, and an attitude sensor. The high-order state vector of attitude, angular rate, thrust, and dynamic parameters, is necessary for the vehicle control in an approach and landing on the moon or a planet. The new algorithm is constructed only with use of the outer information ( range & range rate ), measured by the tracking station of the known position and velocity, or measured by the reflection wave from the known topographical model, for the multi-beams emitted from the several antennas on a vehicle.

The first analyses by the tracking station use the previous algorithms for the stochastic estimation and the geometrical determination <sup>[1-4]</sup>. The stochastic algorithm adopts the extended Kalman filter commonly used in the on-board system. The geometrical algorithm determinates the high-order state vector by the relative position and velocity amongst the spacecraft antennas and the tracking stations. Moreover the introduction of the relation of several antennas locations on the vehicle ( Fixed Frame method ) realizes a high accurate determination. The dynamic model of 19 dimensional state vector considers the vehicle dynamics of powered flight. The atmospheric effect is ignored for simplicity. The measurement model of 24 dimensional vector is formulated in order to discriminate each antenna datum of range and range rate. The measurement by several antennas is assumed to be sequential or simultaneous. As the target of analysis is for the Mars, the imaginary tracking stations are supposed to be GTS ( Geostationary Tracking Satellite ) on a geostationary orbit of 17000 km altitude, TS ( Tracking Satellite ) on a circular orbit of 10000 km altitude around the Mars.

In the second analyses by the reflection wave from the ground, two topographical algorithms for the stochastic estimation and the geometrical determination were newly constructed with use of the map data with a mountain and a river for example, developed from the assumption of a planetary surface model of sphere. And the Mars is also the target. The stochastic algorithm was constructed by the replace of the new measurement model of topographics from the previous algorithm. The geometrical algorithm was also newly constructed under the condition of the optimum evaluation function to be minimum.

In both simulations, each stochastic estimation results that the estimated error variances (  $\sigma$  ) of state vector have the excellently converging tendency, and each geometrical determination also shows that the obtained state very narrowly varies around the Nominal state change. The simulation indicates the independent and high accurate estimation of high-order flight state only by assuming the tracking network or only by the premise of the topographical ground surface model. The effectiveness of these algorithms with several antennas equipment, is well verified, even in place of an attitude sensor. Moreover the application of this technique to the Earth mission is very easy, because of the conditions already arranged in the tracking network and also about the detailed topographical model of the Earth.

This paper gives one of fundamental guidelines not only for the new navigation system design of an airplane, a helicopter, moreover a future space-plane, or a planet-surveyor in the re-entry or the approach and landing phase, which demand the independent attitude estimation without use of the ordinary inertial navigation system, but also for the identification of a planetary surface model.

# HIGH-ORDER STATE ESTIMATION BY TRACKING STATION

This chapter presents the assumption and the result of the analyses. The detailed algorithms for the stochastic estimation or the geometrical determination only by the outer information measured at the tracking station of the known position and velocity, are shown in the previous papers<sup>[2-4]</sup>.

Figure 1 is the relation between the Mars and a spacecraft in an boost phase. The spacecraft body coordinate and the Mars centered inertial coordinate are also defined. Four antennas are located in front and rear of the fuselage, and also on both wingtips. The imaginary tracking stations GTS, TS are assumed around the Mars. The configuration of the vehicle is only imaginary and used only from the relation to the previous papers<sup>[1-4]</sup>.

Table 1 is the apriori parameters. The simulation is performed for the de-orbit phase from an initial circular orbit around the Mars. The simulation time is 80 seconds. The de-orbit motor is assumed to be ignited at 5 seconds after the calculation start. The motor burning time is 70 seconds. The initial values of the attitude Euler angles ( roll/ pitch/ yaw ) and of their rates (  $\omega_1, \omega_2, \omega_3$  ), defined by the nominal attitude of de-orbit direction, are all zero. The initial motor thrust parameter is  $\eta_{k=0} = 100$  ( % ). The initial thrust off-set is (  $\varepsilon_2, \varepsilon_3$  )  $_{k=0} = 0$  ( mm ). The diagonal elements of the initial error co-variance matrix  $P_{k=0}$  adopt the values of Table 1. The initial non-diagonal elements are all zero.

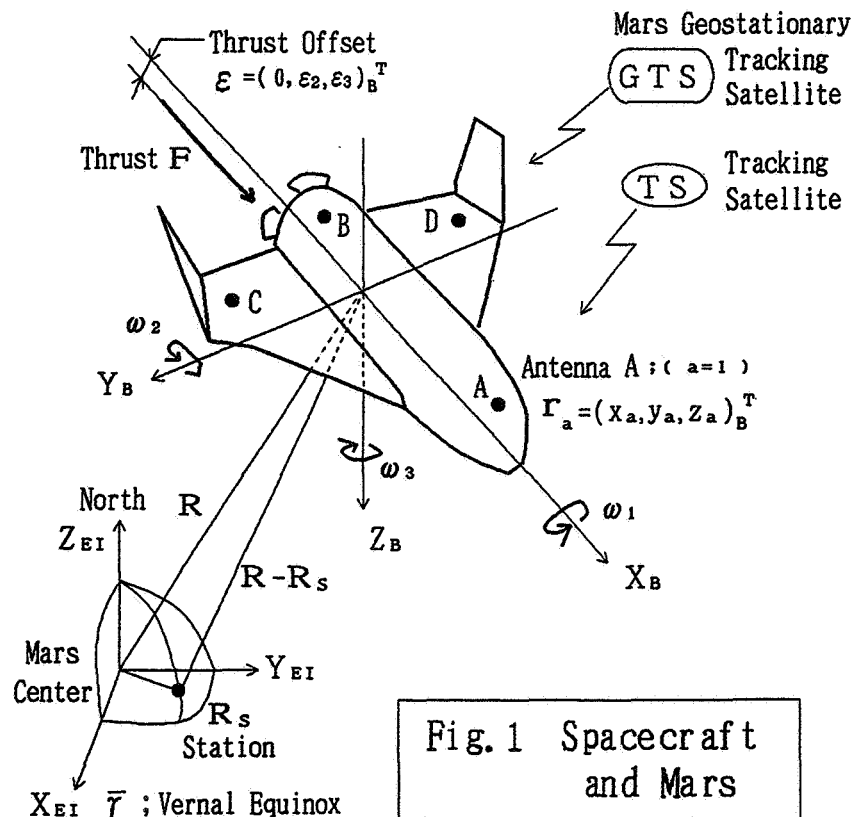


Fig. 1 Spacecraft and Mars

Table 2 depicts the locations of four antennas ( A, B, C, D ) and four liquid fuel tanks in the instantaneous body coordinates.

Body Scale 1 is the standard antenna layout for the assumed vehicle. Each location of Scale 2 is twice larger than that of Scale 1.  
Scale 0 means all antennas locations on the origin of the body coordinates.

The measurement data are generated by adding the normal random numbers to the Nominal data of range and range rate, between each antenna on a vehicle and each tracking station of GTS, TS and the Mars station. The time span of measurement is 0.1 seconds.

The normal random numbers were calculated with the random errors in Table 1.

Table 1 Apri'ori Parameters

<u>Orbit Condition</u> ; Height $h = 20 \text{ km}$ < Circular > Inclination $i = 1.0 \text{ deg}$	
<u>Mars Spacecraft</u> ; Mass $M = 700 \text{ kg}$	
<u>Approach Motor</u> ; Thrust $F = 1000 \text{ N}$ Specific Impulse $I_{sp} = 320 \text{ sec}$	
<u>Errors of Measurement Data</u> ;	
----- < Random Error > -----	
Range	1 m
Range Rate	0.01 m/s
<u>Initial Covariance Matrix ( <math>P_{k=0}</math> ) ;</u>	
Position	$\sigma_{x, y, z} = 1.0 \text{ km}$
Velocity	$\sigma_{\dot{x}, \dot{y}, \dot{z}} = 0.1 \text{ km/s}$
Euler Angle	$\sigma_{\phi, \theta, \psi} = 10.0 \text{ deg}$
Angular Rate	$\sigma_{\omega_1, \omega_2, \omega_3} = 1.0 \text{ deg/s}$
Thrust Offset	$\sigma_{\varepsilon_2, \varepsilon_3} = 10.0 \text{ mm}$
Moment of Inertia	$\sigma_{I_{xx}, I_{yy}, I_{zz}} = 1.0 \text{ kgm}^2$
Mass	$\sigma_M = 10.0 \text{ kg}$
Thrust Parameter	$\sigma_\eta = 1.0 \%$

Table 2 Body Scale & Tanks Location

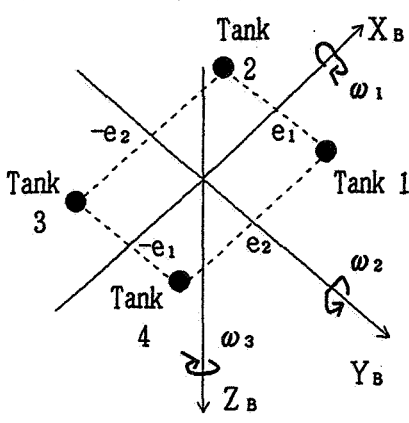
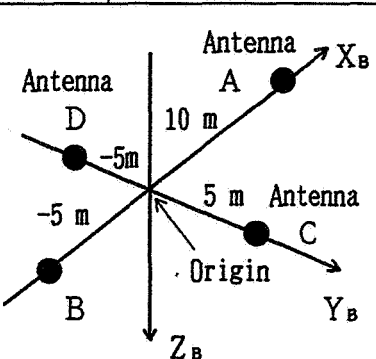
Antenna	Body Scale	Location of Liquid Fuel Tanks	
	1		
A	10 m	$e_1$	0.5 m
B	-5 m	$e_2$	0.2 m
C	5 m		
D	-5 m		
			

Figure 2 is the simulation results of the stochastic estimation by the assumed tracking station. The Kalman filter starts to operate at  $T = 5$  seconds after the simulation start. The estimated error variances ( $\sigma$ ) of state vector have the excellently converging tendency. Otherwise in the geometrical determination, the obtained state is shown very narrowly to vary around the Nominal state change.

Both simulations by each algorithm indicate the high accurate estimation and the effectiveness of the several antennas equipment.

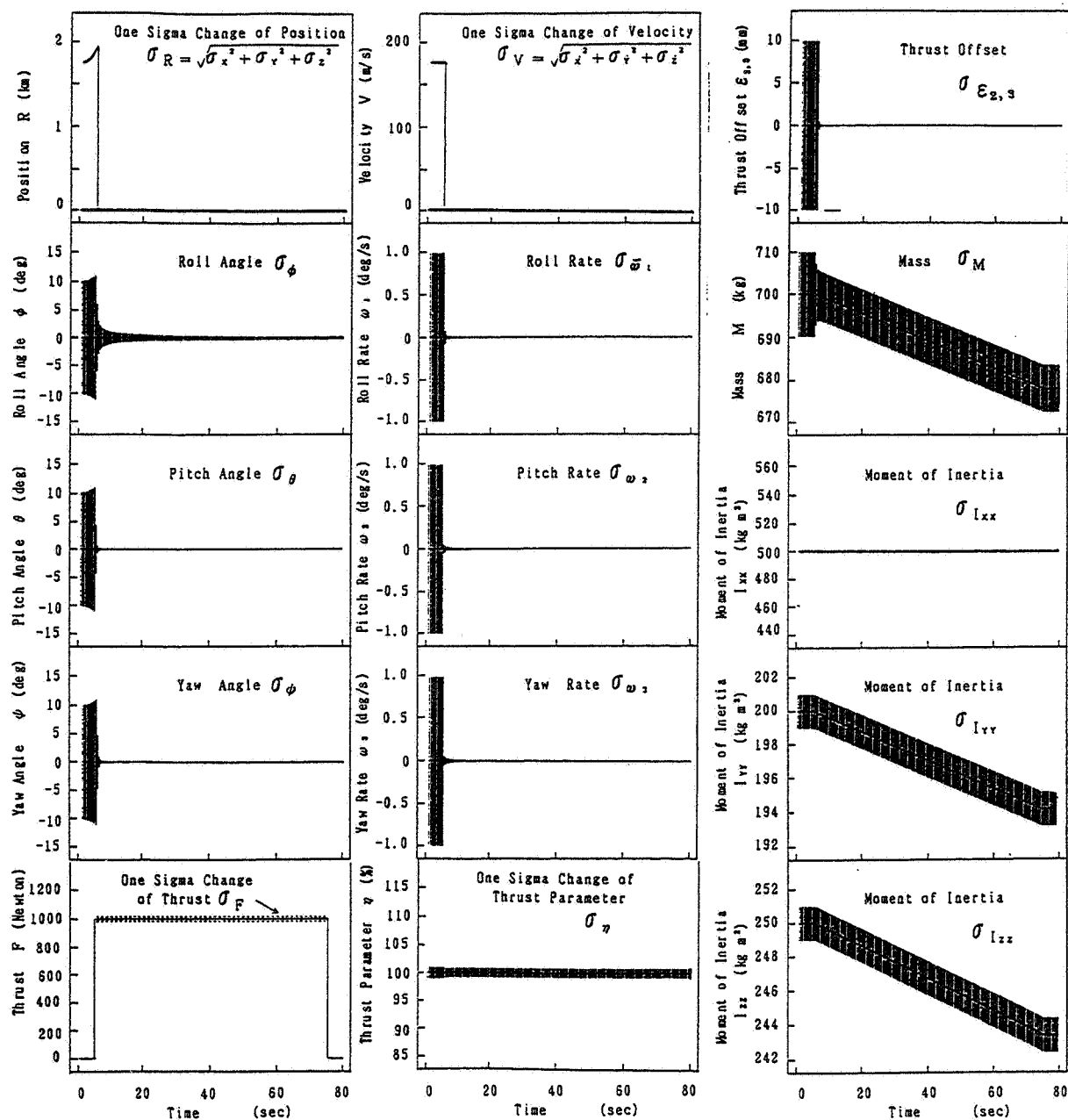


Fig.2 Stochastic Estimation by Tracking Station  
( Mars Approach Phase ; case MB-20A )

Figure 3 is the effects of Body Scale to the precision of estimation. The figure (a) is the results of the stochastic estimation, and shows the changes of the error variances at  $T = 80$  seconds in accordance with Body Scale. The figure (b) is the geometrical result. The change of the standard deviation processed over the whole time of calculation, is also shown in accordance with Body Scale.

Both results indicate that the precision remarkably ameliorates as the vehicle scale becomes bigger.

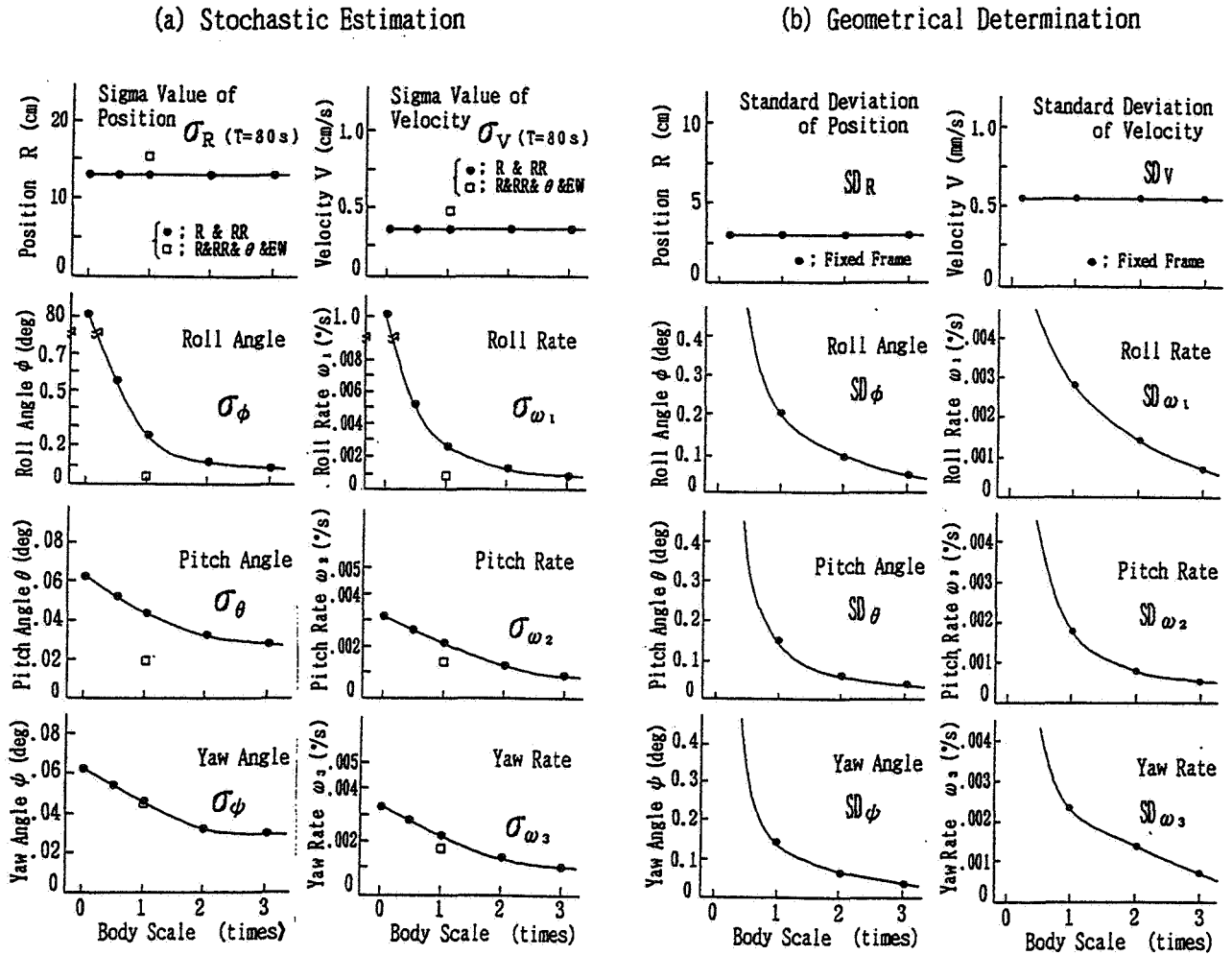


Fig. 3 Effects of Body Scale  
( Mars Approach Phase )



# HIGH-ORDER STATE ESTIMATION BY TOPOGRAPHICAL REFLECTION WAVE

## ( Topographical Algorithm )

Fig.4 shows a spacecraft during a motor burn on a planetary ground surface. Three beams of each different direction are assumed to be emitted from 4 antennas on a vehicle. The algorithm to estimate the flight state vector by the measurement data ( range and range rate ) of the reflection wave from the ground, is described as follows.

Fig.5 shows the spacecraft flight path and the locus of antenna beam on the assumed topographical model of a planetary ground surface. The spacecraft state vector, considering a boost phase dynamics, is position, velocity, Euler angle, angular velocity, thrust, and dynamic parameter, same as the previous chapter. Each reflection wave is assumed as the same time measurement. The measurement model is constructed so as to distinguish each antenna beam. The range is obtained to calculate the intersecting point of beam direction within a planer element of the topographical surface. The range rate is the time derivative of the range.

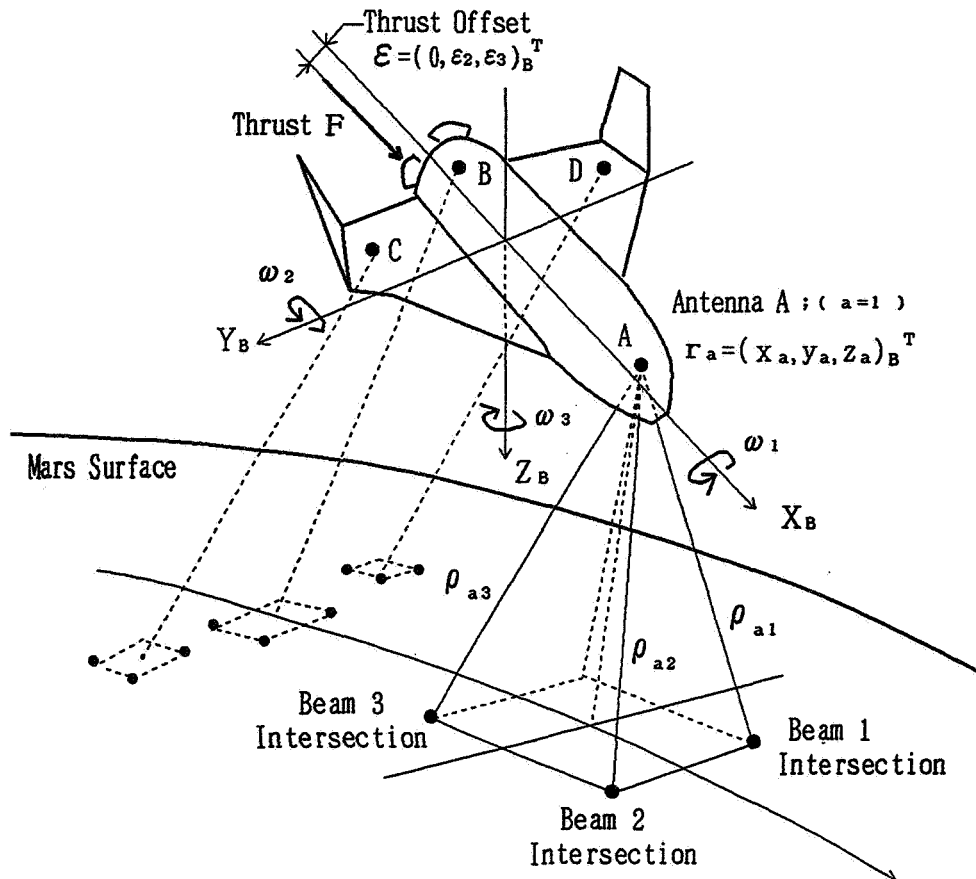


Fig.4 Spacecraft and Beam Reflection

The stochastic algorithm was constructed from that of the previous chapter by the recomposition of the measurement model considering the topographical information.

Table 3 is the topographical algorithm for the geometrical determination. Step 1 is the measurement data generation of range and range rate by addition the measurement errors (the random numbers) to the nominal data of antenna beam reflection. Step 2 is the generation of the spacecraft flight state with errors by the addition of the random numbers. This state value becomes the initial condition in Step 3. Step 3 is the state determination of position, velocity, Euler angle, and angular rate ( 12 dimensions ) by the Newton method under the condition of the evaluationnal function( S ) minimum. The other high-state vector can be estimated by an iteration of state propagation.

Fig. 5 Flight Path and Beam Locus on Topographical Model

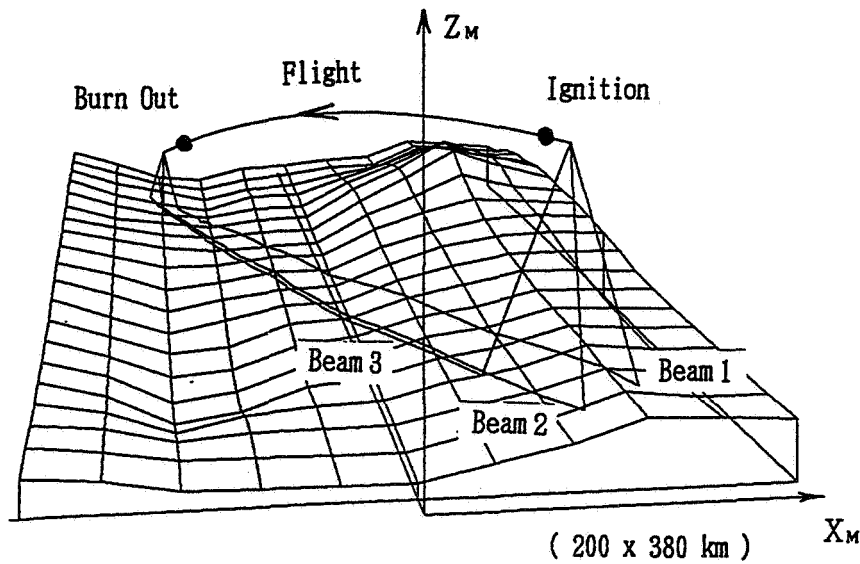


Table 3 Outline of Determination Algorithm

Step 1	Generation of Measurement Data with Random Numbers ; Topographical Reflection Waves for 4 Antennas / 3 Beams.
Step 2	Addition of Random Numbers to Nominal State Change of Spacecraft.
Step 3	Determination of Flight State ( Position, Velocity, Euler Angle, Angular Rate ) by Newton Method with the following condition ; $S = \sum_{a=1}^4 \sum_{b=1}^3 [(\rho^* - \rho)^2 + (\dot{\rho}^* - \dot{\rho})^2]_{ab} \rightarrow \text{Minimum}$

where  $\rho^*, \dot{\rho}^*$  ; Range & Range Rate in Step 1,  $a=1, 2, 3, 4$  ; Antenna Number,  
 $\rho, \dot{\rho}$  ; Range & Range Rate in Step 3,  $b=1, 2, 3$  ; Beam Number.

( Topographical Estimation Results )

The simulation of topographical estimation by this new algorithm was performed for the same case of de-orbit from a circular orbit of altitude 20 km around the Mars as the previous chapter.

Fig.6 is the stochastic results of the estimated position, velocity, attitude, attitude rate, and so on. The Kalman filter starts to operate at  $T=5$  seconds after the simulation start. From these figures, the error variances ( $\sigma$ ) of the state

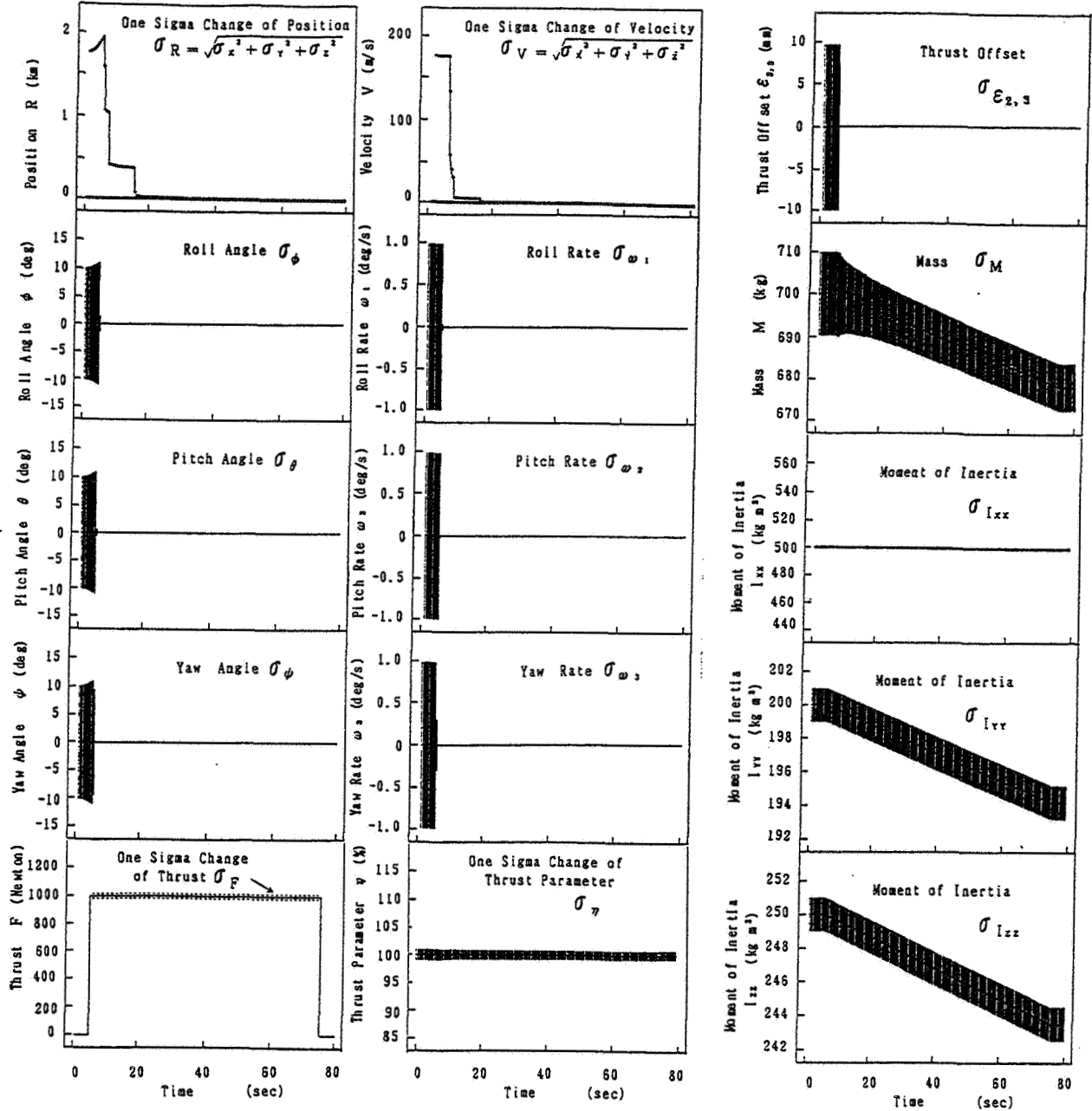


Fig. 6 Stochastic Estimation by Topographical Wave  
( Mars Approach Phase ; Case Mars-1 )

vector, except the moment of inertia, have the excellent covering tendencies.

Fig.7 is the geometrical results. The algorithm of geometrical determination also starts to operate at  $T = 5$  seconds. The simulation shows that the determined state varies very narrowly around the Nominal change.

Table 4,5 are the simulation conditions of both algorithms and the results. The converged error variances ( $\sigma$ ) at the end of simulation  $T = 80$  seconds, and the standard deviations calculated from the differences between the Nominal state and the determined value over the simulation time, are both very small.

The high accurate estimation only by the topographical information and the effectiveness of several antennas equipment, are also indicated.

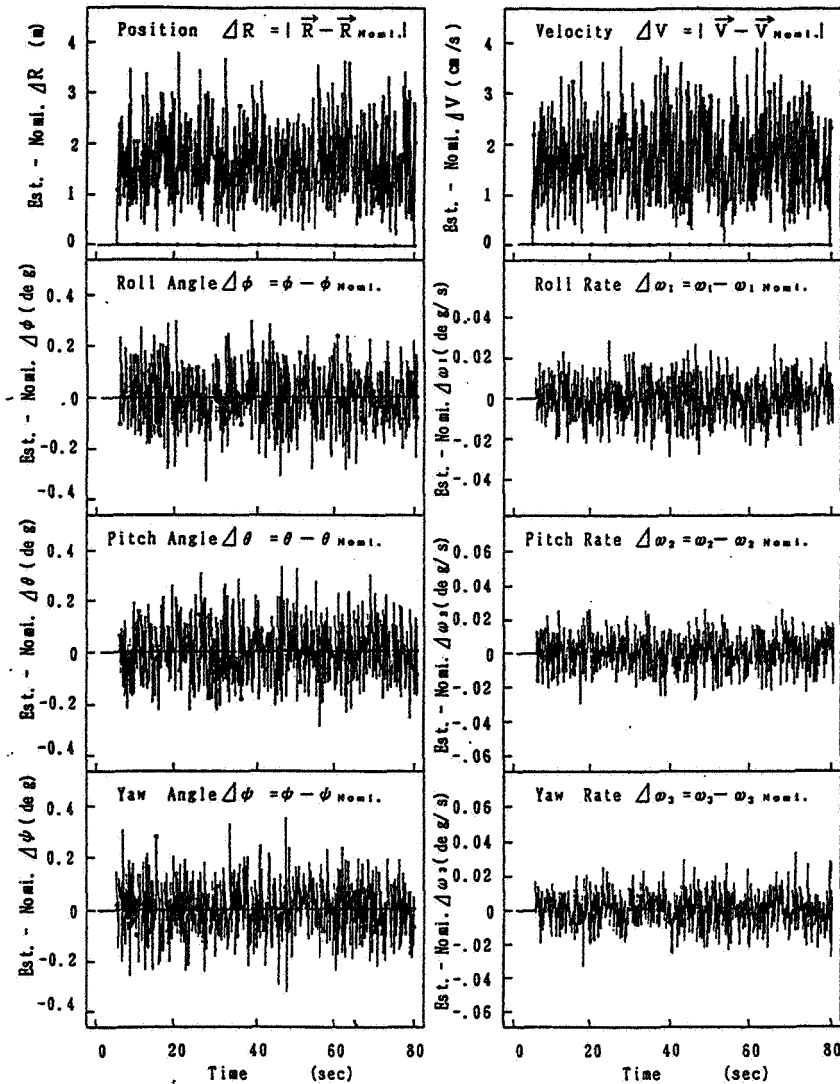


Fig. 7 Geometrical Determination by Topographical Wave  
( Mars Approach Phase ; Case Mars )

In general, it has been thought that the estimation of yaw angle only from the reflection wave is difficult. But this newly constructed algorithm was shown to be able to estimate the high-order flight state especially including the yaw angle with high precision.

This analysis uses the rough ground model, and the change of range and range rate is discontinuous. Therefore in the initial operation of Kalman filter, the estimation of position and velocity is not smooth. But the estimation becomes smooth with time and very accurate at the end of operation. Although the next analysis targets for the continuous ground model, the results of the detailed model are the same as the fundamental results and tendencies of this paper.

From the above, the new algorithms are both verified effectively to operate.

Table 4 Stochastic Estimation Results  
by Reflection Wave  
( Mars Approach Phase )

Run Condition & Result	Run Case	Mars-1
Flight Phase		Mars Approach
Dynamic Model ( dimension )		19
Measurement Model ( dimension )		24
(Range & R.Rate) (combination)		R&RR
Equipments ; Doppler Radar, etc		4
Random Noise of Measurement ;		
Range Noise $\sigma_R$ ( m )		1.0
Range Rate Noise $\sigma_{RR}$ (cm/s)		1.0
Location of 4 antennas & Measurement by antennas & Body Scale ( Times )		Each Point Same Time 1
Time Interval DT (sec)		0.1
Results of Estimated $\sigma$ Error ;		
Position $\sigma_R$ ( m )		2.60
Velocity $\sigma_V$ (cm/s)		6.940
Roll Angle $\sigma_\phi$ (deg)		0.00093
Pitch Angle $\sigma_\theta$ (deg)		0.00064
Yaw Angle $\sigma_\psi$ (deg)		0.01229
Roll Rate $\sigma_{\omega_1}$ (°/s)		0.00002
Pitch Rate $\sigma_{\omega_2}$ (°/s)		0.00001
Yaw Rate $\sigma_{\omega_3}$ (°/s)		0.00016
Thrust Off-set $\sigma_{\varepsilon_2}$ ( mm )		0.00002
Thrust Off-set $\sigma_{\varepsilon_3}$ ( mm )		0.00001
Thrust Param. $\sigma_\eta$ ( % )		0.821
Mass $\sigma_M$ ( kg )		5.59

Table 5 Geometrical Determination Results  
by Reflection Wave  
( Mars Approach Phase )

Run Condition & Result	Run Case	Mars
Flight Phase		Mars Approach
Measurement Model ( dimension )		24
(combination)		R&RR
Equipments ; Doppler Radar, etc		4
Generation of Random Noise for R&R ;		
Range Noise $\sigma_R$ ( m )		1.0
R.Rate Noise $\sigma_{RR}$ (cm/s)		1.0
Data Smoothing		No Smoothing
Location of 4 antennas & Measurement by antennas & Body Scale ( Times )		Each Point Same Time 1
Generation of Random Noise for $X_i$ ;		
Position Nois $\sigma_{x,y,z}$ ( m )		1.0
Velocity Nois $\sigma_{\dot{x},\dot{y},\dot{z}}$ (cm/s)		1.0
Euler Angle Nois $\sigma_{\phi,\theta,\psi}$ (deg)		0.1
Anguler Rate Nois $\sigma_{\omega_1,\omega_2,\omega_3}$ (°/s)		0.01
Time Interval DT (sec)		0.1
Result of Estimated $\varepsilon$ Errors ;		
Position $\varepsilon_R$ ( m )		1.6528
Velocity $\varepsilon_V$ (cm/s)		1.6613
Roll Angle $\varepsilon_\phi$ (deg)		0.09515
Pitch Angle $\varepsilon_\theta$ (deg)		0.09479
Yaw Angle $\varepsilon_\psi$ (deg)		0.09877
Roll Rate $\varepsilon_{\omega_1}$ (°/s)		0.00972
Pitch Rate $\varepsilon_{\omega_2}$ (°/s)		0.00959
Yaw Rate $\varepsilon_{\omega_3}$ (°/s)		0.00947

## CONCLUSIONS

This paper concludes that the high-order state vector of spacecraft attitude, angular rate, thrust, and dynamic parameters, besides position and velocity, can be independently estimated with high precision by several antennas equipments on a vehicle, only from the outer measurement data of tracking stations or topographical reflection wave, separated from the vehicle inner information ( IMU ).

The new topographical algorithms was also verified effectively to operate in place of an attitude sensor. The next target is the estimation for the atomospheric flight on the detailed ground model. Although the detailed analysis is expected to become higher accurate, the results of the detailed model are the same as the fundamental results and tendencies of this paper.

This paper gives one of newly technical guidelines not only for the design of the new navigation system and the ground control system, where the future aircrafts and the spacecrafts demand the high-order state estimation separated from the vehicle inner information of the ordinary navigation system and IMU data, but also for the identification of a planetary surface model.

Moreover the application of this technique to the Earth around mission is very easy, because of the conditions already arranged in the tracking network and also about the detailed topographical model of the Earth.

## REFERENCES

- 1) ONO S., " High-Order State Estimation for Space-Plane with Several Antennas", Proceedings of the International Symposium on Spacecraft Ground Control and Flight Dynamics ( SCD1 ), Journal of the Brazilian Society of Mechanical Sciences, Vol.XVI, Special Issue, ISSN 0100-7386, P.513-520, (1994)
- 2) ONO S., " Stochastic Algorithm for High-Order State Estimation of Space-Plane without IMU Data , Transactions of The Japan Society for Aeronautical and Space Sciences, Vol.38, No.121, pp.207-227, (1995).
- 3) ONO S., " Geometrical Algorithm for High-Order State Determination of Space-Plane without IMU Data, Transactions of The Japan Society for Aeronautical and Space Sciences, Vol.38, No.121, pp.228-242, (1995).
- 4) ONO S., " A Study of Unsteady Dynamics and of High-Order State Estimation for Space Flight Vehicle System ", Thesis for Doctorate in Engineering, Nagoya University, No.1326, pp.1-175, (1997).

524-13

169306

## LUNAR PROSPECTOR MISSION DESIGN AND TRAJECTORY SUPPORT

**David Lozier & Ken Galal**  
**Space Projects Division**  
**Ames Research Center, NASA**

**David Folta & Mark Beckman**  
**Guidance, Navigation, and Control Center**  
**Goddard Space Flight Center, NASA**

The Lunar Prospector mission is the first dedicated NASA lunar mapping mission since the Apollo Orbiter program which was flown over 25 years ago. Competitively selected under the NASA Discovery Program, Lunar Prospector was launched on January 7, 1998 on the new Lockheed Martin Athena II launch vehicle.

The mission design of Lunar Prospector is characterized by a direct minimum energy transfer trajectory to the moon with three scheduled orbit correction maneuvers to remove launch and cislunar injection errors prior to lunar insertion. At lunar encounter, a series of three lunar orbit insertion maneuvers and a small circularization burn were executed to achieve a 100 km altitude polar mapping orbit.

This paper will present the design of the Lunar Prospector transfer, lunar insertion and mapping orbits, including maneuver and orbit determination strategies in the context of mission goals and constraints. Contingency plans for handling transfer orbit injection and lunar orbit insertion anomalies are also summarized. Actual flight operations results are discussed and compared to pre-launch support analysis.

### INTRODUCTION

#### Mission Overview

The January 7, 1998 launch of the Lunar Prospector spacecraft marked the return of America's space program to the moon, picking up where the Apollo program left off with a low altitude polar orbiting mission to map the entire surface of the moon. In contrast to the Apollo program, however, Lunar Prospector was a modest spacecraft funded at a cost of \$63 million (including the launch vehicle) by NASA's Discovery Program<sup>1</sup>. Six science experiments were flown to map the composition of the lunar surface, study the moon's gravity and magnetic fields, investigate levels of tectonic and volcanic activity, and search for evidence of water ice at the lunar poles.

## Spacecraft Description

The Lunar Prospector spacecraft (Figure 1) is a spin-stabilized graphite-epoxy drum, 1.4 meters in diameter by 1.22 meters in height, with three radial instrument booms located 120 degrees apart. Power is provided by solar arrays mounted on the outside of the drum. Attitude, spin rate, and velocity control are provided by a blowdown monopropellant hydrazine propulsion subsystem using six 22 N thrusters. Attitude and spin rate determination are provided by a sun sensor and an Earth/Moon limb sensor. Telemetry and command functions are provided by redundant S-band transponders through either a medium gain or an omni-directional low gain antenna mounted on a mast aligned the spacecraft spin axis.

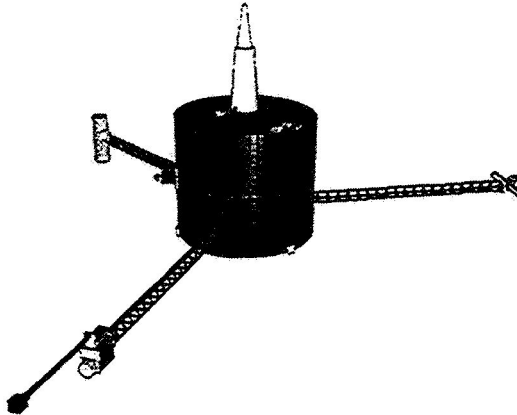


**Figure 1: Lunar Prospector Spacecraft with Instrument Booms Deployed**

The nominal Lunar Prospector telemetry rate is 3.6 kbps real-time with no onboard tape recorder. However, a 53.3 minute delayed transmit capability at the spacecraft permits ground capture of telemetry data taken from the backside of the Moon. The total spacecraft mass at launch was 296.4 kg, including 137.7 kg of hydrazine propellant.

## NOMINAL MISSION PROFILE

Table 1 provides a summary of the nominal mission profile designed for the Lunar Prospector mission. The Lunar Prospector spacecraft was launched on January 7, 1998 at 02:28:44 GMT from the Eastern Test Range. A Lockheed Martin Athena II vehicle placed the payload (spacecraft and injection stage) in a nominal 100 nautical mile circular parking orbit after a 13-minute flight. Following a 42-minute coast to a translunar injection point over North-Western Australia, the payload was released and a Star 37FM motor was used to apply a nominal 3142 m/s delta-V over the course of a 64 second burn. The design flight time to the moon was 105 hrs from injection. A series of three lunar insertion burns were designed to place the spacecraft into its 100 km polar mapping orbit about the moon.

### Launch Date Selection and Transfer Orbit Design

The approach taken by the Lunar Prospector project for establishing launch dates was to limit launch opportunities to a single set of consecutive prime and backup days each month. This approach was motivated in part by a desire to limit launch vehicle preparation costs, as well as a desire to only select launch dates which provided the best geometry in terms of minimizing both operational risk to the mission and overall propellant consumption. Monthly launch dates were identified beginning in September of



1997. Possible earlier launch dates were rejected in order to avoid the September 16, 1997 lunar eclipse by the Earth, which would have lasted several hours and necessitated a larger battery.

Table 1  
LUNAR PROSPECTOR NOMINAL MISSION DESIGN PARAMETERS

Launch Conditions	Nominal Launch Date/Time .....	January 7, 1998 02:28:42.7 UTC
	Launch Vehicle .....	Athena-II
	Launch Azimuth .....	97 deg E (29.2 deg inclination)
	Parking Orbit .....	87.7 x 102.7 nmi
Injection Conditions	TLI Motor .....	STAR37FM
	TLI Velocity .....	3142 m/sec
	TLI Payload Mass .....	1521.2 kg
	Total LP Spacecraft Mass .....	296.4 kg
	LP Propellant Mass .....	137.7 kg
	Trans-lunar Injection Time .....	L+56 min
	SC Separation .....	L+57 min
	TDRS Acquisition .....	at SC Sep
Transfer Orbit Conditions	DSN Acquisition .....	Sep+22 min
	Transfer Orbit Flight Time .....	105 hr
	Reorientation Maneuver to Cruise Attitude .....	92 deg
	Spin Down Maneuver .....	-30 rpm (from 57 at TLI)
	Post-Boom Deployment Spin Up .....	+5 rpm
	1st Trajectory Correction Maneuver .....	TLI+4.5 hr
	2nd Trajectory Correction Maneuver .....	TCM1 +24 hr
Lunar Orbit Insertion Conditions	3rd Trajectory Correction Maneuver .....	LOI-1 -24 hr
	Epoch of Arrival .....	1/11/98 12:00 UTC
	Radius of Closest Approach .....	1819 km
	Lunar Orbit Inclination .....	89.8 deg
	Reorientation Maneuver to LOI Attitude .....	22 deg
	LOI#1 .....	354 m/sec
	LOI#2 .....	274 m/sec at LOI-1 +24 hours
	LOI#3 .....	264 m/sec at LOI-2 +24 hours
	Reorientation Maneuver to Mapping Attitude .....	30 deg

In the Fall of 1997, two sets of prime and backup launch dates consisting of January 6/7 and February 4/5 were selected as candidate launch opportunities for the Lunar Prospector mission. These launch dates and the associated transfer trajectories were selected on the basis of the following factors:

- **Sun Angle Geometry:** A favorable sun angle of close to 90 degrees relative to the spacecraft z-axis was desired during translunar injection (TLI) and lunar orbit insertion (LOI) for power, thermal and attitude determination considerations.
- **Shadowing:** In order to minimize risk to the spacecraft, it was desired that the spacecraft be in sunlight following TLI, and for the duration of the 2-day LOI sequence to place the spacecraft into its low altitude mapping orbit. Additionally, transfer orbit geometries (for both nominal and contingency orbits) whereby the s/c-Earth-sun angle approached 180 degrees were to be avoided due to the possibility of long shadow periods (up to 9 hours in some cases) while in the transfer orbit.
- **Transfer Orbit Inclination:** A low transfer orbit inclination with respect to the Earth/Moon plane was desired in order to minimize LOI costs.

- **Moon Position:** Lunar orbit insertion with the moon close to apogee yields a slightly lower DV cost (up to 38 m/s).
- **Attitude Maneuvers:** To minimize propellant consumption and risk to the spacecraft, transfer orbit trajectories that required small turn angles to get from the transfer orbit cruise attitude to the LOI attitude and from the LOI attitude to the mapping orbit attitude were chosen.
- **Post TLI Station Acquisition:** While the station look angle changes rapidly near Earth for a given inertial TLI attitude and antenna configuration, certain trajectories enable post-TLI station coverage sooner than others. Minimizing the time to acquire telemetry and command capability was a goal in order to minimize the time to correct launch and transfer orbit dispersions.
- **LOI Station Coverage:** As a goal, the periselene arrival time was to be maintained such that dual station coverage was available during LOI#1. Furthermore, it was desired that all subsequent LOI burns be conducted in view of a station (a 64 minute delayed command timer was available for doing burns in the blind when necessary).

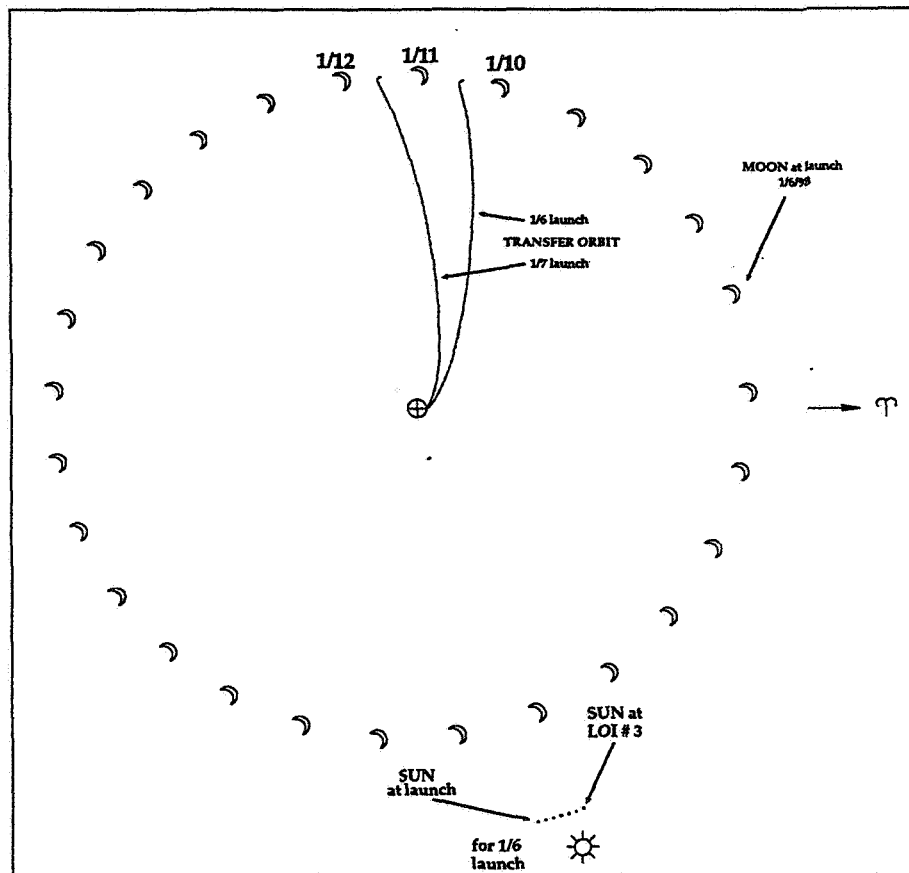


**Figure 2: Lunar Prospector Transfer Orbit Geometry for Prime and Backup Launch Dates**

From a given launch site, a launch to the moon is possible on each day of the month, with two launch times (roughly 12 hours apart) available on each launch date<sup>2</sup>. The launch date establishes the sun/Earth/moon geometry for the transfer orbit. The selection of the launch time, for a given launch date, establishes the inclination of the transfer orbit plane relative to the Earth-moon plane, and influences lighting and station coverage conditions at injection. On a given day, the transfer orbits corresponding to the two possible launch times are typically distinguished by the length of the coast time in the parking orbit

(i.e. short coast or long coast), or alternatively, by the proximity of the injection point to the ascending vs. descending node. As a final option in transfer orbit design, for each launch date/time, two lunar insertion conditions are available over either the northern or southern lunar hemisphere. The selection of the lunar approach geometry affects the required LOI thrust direction and hence the magnitude of attitude turns required as part of LOI operations. Through a careful consideration of the launch date, launch time, and lunar approach geometry, transfer orbits for prime and backup launch dates (Figure 2) were arrived at that minimized both the risk to the Lunar Prospector spacecraft and the propellant required to get into orbit about the moon. The resulting transfer orbits selected were low heliocentric inclination orbits with injections near ascending node and lunar insertion in the northern lunar hemisphere.

### **Transfer Orbit Maneuver Strategy**

The nominal Lunar Prospector transfer orbit maneuver plan called for a total of three trajectory correction maneuvers (TCMs) with TCM#1 planned at 4.5 hours after separation, TCM#2 at 24 hours after TCM#1, and finally, TCM#3 at 24 hours prior to lunar orbit insertion. A total of 80 m/s was nominally allocated to cover corrections to possible launch and TLI dispersions.

Key to this maneuver strategy was a desire to execute TCM#1 as soon as possible after TLI in order to minimize losses associated with burning away from perigee. It was felt that given all the spacecraft events that had to occur before a nominal burn could take place (e.g. 90 deg reorientation to the cruise attitude, boom deployment, orbit/attitude determination, maneuver planning, command load generation/execution), a burn 4.5 hour into the mission was an achievable goal, assuming a nominal post-separation timeline of events. Ideally, for this maneuver time, the required correction for any launch/TLI dispersions would have grown by a factor of 3.5 by the time of the maneuver. However, given Lunar Prospectors attitude and thruster firing mode (where both axial and tangential thrusters are fired in a vector mode), and a desire to maintain a fixed time of flight to the moon, it was expected that a 1 m/s launch/TLI error would require 4.5 m/s of equivalent propellant to correct for an orbit maneuver at 4.5 hours after TLI.

TCM#2 was nominally scheduled 24 hours after TCM#1 in order to provide sufficient time to collect tracking data for an orbit solution and plan the maneuver, as well as to permit the prime operations shift to rest between burns. TCM#3 was scheduled 24 hours prior to lunar insertion to provide any required final corrections to the approach trajectory.

### **Lunar Orbit Insertion Maneuver Strategy**

Three LOI maneuvers were designed to capture the spacecraft into lunar orbit and lower apoapsis most of the way into the nominal 100 km polar mapping altitude. Each LOI burn was to be performed from an inertial attitude using 2 axial jets along the aft side of the spacecraft (axial jets on the antenna end of the spacecraft could not be used for long burns due to antenna heating concerns). The LOI maneuver sequence was designed with the following goals/constraints in mind:

- **S/C Pointing:** There was a desire to maintain a single attitude throughout the LOI maneuver sequence in order to minimize propellant use and operational complexity. By maintaining a fixed argument of periapsis for each intermediate orbit in the LOI sequence, no attitude maneuvers would be required.
- **Maneuver Duration and Frequency:** While there was no hardware limitation on the maximum time to burn during each LOI maneuver, burn efficiency considerations suggested keeping the burns as small as possible in order to minimize thrust losses over the burn arc. On the other hand, operational considerations suggested keeping the overall number of burns at a manageable number.
- **Intermediate Orbit Perturbations:** It was recognized that smaller LOI#1 burns would result in an initial capture orbit that was more susceptible to third body perturbations (largely from the Earth, and affecting mostly orbit inclination). Such perturbations can be nullified to some degree by biasing the lunar orbit insertion conditions to counteract the anticipated evolution of the orbit. However, the

possibility always exists that unforeseen delays might result in an extended stay in the initial capture orbit, whereby excessive orbit errors could accumulate which would require subsequent correction.

Based on the above guidelines, a three-burn LOI sequence was designed to first capture the spacecraft into a 12 hour period orbit, lower it into a 3.5 hour period orbit, and finally drop apoapsis most of the way into the 100 km nominal mapping altitude. This sequence resulted in three LOI maneuvers of roughly equal size (approximately 30 minutes each), with an initial orbit that experienced relatively small perturbations. The lunar arrival conditions were biased slightly from the nominal 90 degree inclination and 1838 km periselene radius (to 89.8 deg and 1829.7 km, respectively) to allow for inclination growth due to third body perturbations while in the 12 hour capture orbit, and to allow for expected growth in periapsis altitude resulting from LOI finite burn losses. A constant argument of periapsis was targeted for the first two burns to avoid the need for attitude maneuvers between burns.

### Orbit Determination Strategy

The orbit determination strategy for Lunar Prospector was broken into two phases: cislunar phase and mapping phase. Both phases were analyzed pre-mission using covariance analysis and simulated tracking data. The simulations assumed tracking by the Deep Space Network (DSN) stations in California, Australia, and Spain. The DSN stations were expected to provide range, Doppler, and XY angle (DSN 26 m stations only) measurements.

There were two primary goals during the transfer/LOI phase: (1) provide predicted ephemerides for mission planning and trajectory design, and (2) provide near-real-time assessments of orbit maneuver performance. During the transfer/LOI phase, there were seven maneuvers nominally planned: four deterministic (TLI and LOI#1-3) and three corrective (TCM#1-3). During this phase, it was expected that the spacecraft would be continuously tracked by the DSN. After each maneuver, range, Doppler, and XY angles (only for DSN 26 m stations) would be collected and processed to determine the new trajectory. Due to reduced dynamics as the spacecraft moved away from perigee, the time required to obtain an accurate converged solution increased with each maneuver in the transfer orbit. Once captured in lunar orbit, the required convergence time was mostly a function of the orbit period. Table 2 shows the expected tracking arc required after each maneuver to obtain a full state batch orbit estimation.

**Table 2**  
**LUNAR PROSPECTOR ORBIT DETERMINATION TURN-AROUND TIMES**

Maneuver	TLI	TCM-1	TCM-2	TCM-3	LOI-1	LOI-2	LOI-3
Planned Post-Maneuver OD Time	30 min*	6 hrs	8 hrs	12 hrs	4 hrs	3 hrs	2 hrs

Following each LP orbit maneuver, an updated orbit state was computed in support of preliminary maneuver planning of subsequent burns. The state would be updated several hours prior to the upcoming maneuver as an input to the final maneuver plan. In each case, the predicted velocity uncertainty of the solution at the time of a maneuver was at least an order of magnitude less than the planned delta-V for that maneuver. This ensured that the maneuver plan was not corrupted by trajectory uncertainties.

The capability for near-real-time maneuver assessments was required in support of Lunar Prospector contingency plans --- particularly in support of the critical TLI and LOI-1 burns. The near-real-time

---

\* Use of combined tracking data from TDRSS (available at TLI and lasting approximately 45 minutes) and the DSN (available starting at 19 minutes after TLI) would have enabled a preliminary solution to be computed within 30 minutes of TLI and a final solution 2 hrs after TLI.

assessment would be made by monitoring DSN Doppler residuals. Once a final maneuver plan was available several hours before an upcoming maneuver, the predicted finite burn ephemeris was used to generate simulated nominal Doppler measurements. These Doppler measurements were processed using orbit estimation software and compared to the pre-maneuver state in order to generate a baseline plot of the expected Doppler residual signature over time. Next, simulated finite burn ephemerides were generated assuming a hot or cold maneuver, and corresponding Doppler residuals from these off-nominal cases were also plotted. Once the maneuver began, Doppler residuals were compared in near-real-time against the previously generated plots to enable a quick assessment of the maneuver performance. Pre-mission analysis had indicated that for each of the planned deterministic maneuvers, the difference between residual signatures for a nominal and a 5% off-nominal maneuver was greater than the expected residuals associated with state/measurement uncertainties during that maneuver. Thus, any deviation in maneuver performance of 5% or greater would be observable.

During the mapping phase of the mission, the main challenge to orbit determination support was that of meeting accuracy requirements. The mission requirement for post-processed solutions (using LP derived lunar gravity models) was 1 km 1-sigma position accuracy in each of radial, cross-track, and along-track directions. A pre-launch covariance analysis indicated that the lunar potential model was the leading source of orbit estimation error. The lunar potential model to be used initially was GLGM-2 developed at Goddard by F. Lemoine using tracking data from the 1994 Clementine mission<sup>3</sup>. The covariance analysis indicated that the mission requirements could only be partially met using this model, and only with extensive post-processing. For certain geometries (e.g. when orbit normal was perpendicular to the Earth-Moon line and lunar occultation occurred) the mission requirements would not likely be met<sup>4</sup>.

As part of one of the experiments to be conducted by Lunar Prospector, tracking measurements were to be used by A. Konopliv at JPL to develop a new lunar potential model. It was planned that a switch to the new potential model would be made when the model became available (approximately two months into the mapping mission) and that LP definitive orbit data would be regenerated using the new model to ensure that orbit accuracy requirements could be met. The actual orbit accuracy attainable using the new model would not be known until it became available.

### Contingency Planning

Several orbit contingency plans were devised to handle possible off-nominal performance of the spacecraft, ground system, and launch/injection sequence. Naturally, Lunar Prospector orbit contingency plans centered around critical mission phases consisting of transfer orbit injection and lunar orbit insertion and included the following:

- **Emergency Post-TLI Correction:** In the event of a TLI overburn by greater than 20 m/s, or a TLI underburn of between 20 and 35 m/s, an emergency correction burn was to be executed approximately 40 minutes following spacecraft separation from the TLI stage.
- **Contingency Phasing Orbit:** In the event of a TLI under-performance by more than 35 m/s, a plan was devised whereby the spacecraft would be initially left in its anomalous orbit about the Earth, then placed into a phasing orbit for several revolutions, with an attempt to capture into lunar orbit approximately one lunar sidereal month (27 days) beyond the nominal capture date.
- **LOI #1 Under-Performance Contingency:** In the event that a near-real-time assessment of the LOI#1 maneuver indicated a significant under-performance, plans were in place to extend the burn via command upon completion of the nominal LOI burn duration.
- **Delayed LOI #1 Contingency (3 hours or less):** For delays in the nominal start time of LOI#1 of 3 hours or less, it was planned that a maneuver with a  $\Delta V$  essentially along the negative velocity vector of the outgoing hyperbola would be executed to capture into a 2-day period (or less) lunar orbit. For a 3 hour delay in LOI#1 start time, it was estimated that a penalty on the order of 400 m/s would be incurred, which would severely jeopardize the mission.

- **Delayed LOI #1 Contingency Delay (greater than 3 hours):** For delays in the nominal start time of LOI#1 longer than 3 hours, it was found that a direct capture was not the most efficient method to get into lunar orbit. Instead, for the nominal Lunar Prospector January 7 launch trajectory, it was more efficient to delay any orbit correction until 3 days past periselene and target for a lunar insertion 41 days after periselene 1. The propellant penalty associated with this contingency strategy is approximately the same as that of a direct capture after a 3-hour delay in LOI#1 start time (400 m/s).

Key to these plans was the early detection of anomalous maneuver conditions through near-real-time orbit assessment using the Doppler residual method described in the previous section. In preparation for these contingencies, procedures and data bases of required attitude and burn conditions as a function of time were prepared for quick implementation in the event of a contingency.

## LP MANEUVER RESULTS

Table 3 contains a history of orbit conditions following each maneuver in the transfer and lunar orbit insertion phases of the mission. It should be noted that target maneuver  $\Delta V$  values listed in the table may in some cases be slightly different from ideal  $\Delta V$  values expected from a propagation of the pre-maneuver state with nominal maneuver end states targeted. This is due to the existence of slightly different Lunar Prospector propulsion models (all consistent to within a few percent) that were available during the mission. As a result, in some cases the selected burn time was based on an average of the models in an effort to provide an added measure of safety (e.g. a slightly longer burn was used during LOI#1). The estimated performance values in Table 3 are based on the trajectory team's baseline propulsion model and are computed relative to actual commanded maneuver times and the best available thrust calibration estimates going into each burn. Possible calibration error sources include attitude uncertainties and propulsion system adiabatic cooling effects. All post-maneuver states are represented in terms of Mean-of-J2000 Keplerian elements relative to the equatorial plane of the central body indicated.

**Table 3**  
**LUNAR PROSPECTOR MANEUVER SUMMARY**

	<b>TLI</b>	<b>TCM#1</b>	<b>TCM#2</b>	<b>LOI#1</b>	<b>LOI#2</b>	<b>LOI#3</b>	<b>MOC#1</b>
<b>Target Maneuver <math>\Delta V</math></b>	3142 m/s	50.2 m/s	7.4 m/s	364.4 m/s	271.8 m/s	262.3 m/s	12.1 m/s 2.6 m/s
<b>Estimated Performance</b>	99.7%	99%	99%	99.3%	99.1%	97.6%	100.4%
<b>Post-<math>\Delta V</math> State</b>	1/ 7/98	1/ 7/98	1/ 8/98	1/11/98	1/12/98	1/13/98	1/16/98
<b>Epoch (GMT):</b>	03:30:00	12:30:00	8:45:00	12:20:00	12:05:00	12:10:00	00:00:00
<b>a (km):</b>	182799	197202	196231	6014.6	2712.2	1860.4	1838.3
<b>e :</b>	0.96403	0.96727	0.96886	0.69714	0.32713	0.01653	0.00046
<b>i (deg):</b>	29.20	29.27	29.26	89.72	89.87	90.01	90.55
<b><math>\Omega</math> (deg):</b>	318.58	318.20	318.16	192.59	192.49	192.39	192.76
<b><math>\omega</math> (deg):</b>	318.09	318.70	318.32	150.37	150.32	147.86	224.02
<b>MA (deg):</b>	0.14	13.34	43.74	10.63	90.13	59.16	317.04
<b>Period (hrs):</b>	216.1	242.1	240.3	11.63	3.52	2.000	1.965
<b>R<sub>Apoapsis</sub> (km):</b>	359023	387949	386351	10207.6	3599.4	1891.2	1837.8
<b>Central Body</b>	Earth	Earth	Earth	Moon	Moon	Moon	Moon

## Launch and Trans-Lunar Injection

Lift-off of the Lunar Prospector mission occurred on time — approximately 2 seconds into its 4-minute launch window. Following a nominal launch and parking orbit insertion of the Athena II launch vehicle, the STAR37 motor burned for 64 seconds to place the spacecraft into its transfer orbit to the moon. The computed post-TLI orbit state vector is presented in Table 3, while the target injection state (impulsive) is shown in Table 4. The TLI burn occurred over the North-Western coast of Australia (LON = 125 E, LAT = 18 S). The ground track from launch to TLI +18 hours is shown in Figure 3. The solid arc just east of Florida consists of the 13 minute boost phase. The ground track for the 42 minute coast in the parking orbit (represented by the dashed line beginning at the end of the boost phase) crosses over southern Africa and ends at the TLI point on the NW coast of Australia. The post TLI ground track is labeled with tic marks every hour and is shown for the first 18 hours of the transfer orbit. The combination of Lunar Prospector launch and injection errors is estimated at  $-9.1$  m/s. Planar orbit dispersions (i.e., inclination, ascending node, and argument of perigee) were very small --- on the order of a few hundredth of a degree.

**Table 4**  
**LUNAR PROSPECTOR NOMINAL TRANSFER ORBIT INJECTION STATE**

injection epoch, January 7, 1998	03:25:02 GMT
semi-major axis	200240.3 km
eccentricity	0.967225
inclination	29.184 deg
longitude of ascending node	318.534 deg
argument of periapsis	318.068 deg
True Anomaly	.207 deg

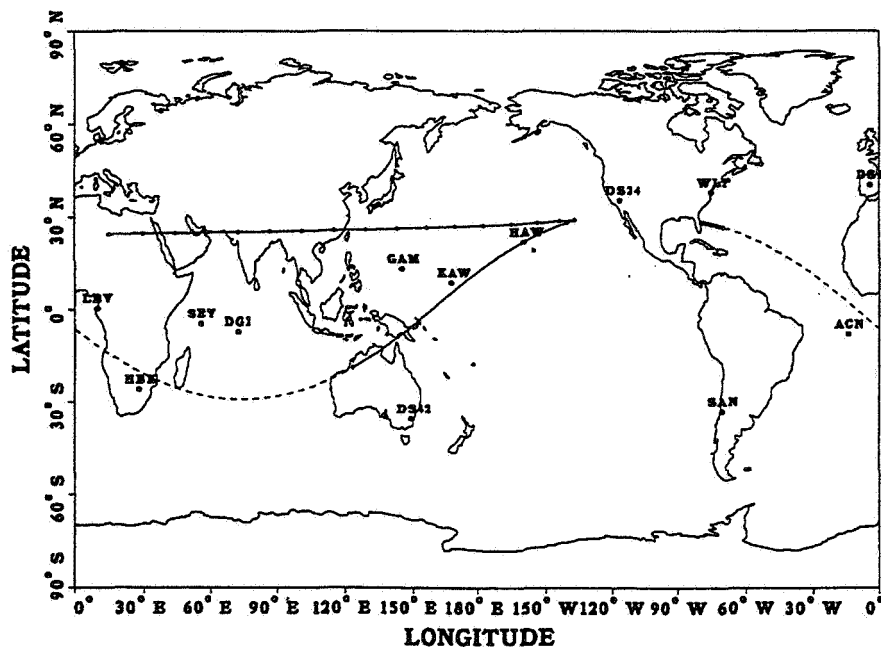


**Figure 3: Lunar Prospector Launch and Transfer Orbit Injection Ground Track**

## Transfer Orbit Maneuvers

Table 5 lists the timeline of key events in the transfer orbit. TCM#1 was nominally planned for TLI + 4.5 hours, however, a number of factors conspired to delay the maneuver until 8.5 hours after TLI. The nominal post-TLI timeline called for immediate acquisition of the spacecraft in 2-way mode using NASA's Tracking and Data Relay Satellite (TDRS) – West spacecraft and for use of the telemetry and Doppler to verify the health of the Lunar Prospector s/c and the performance of the TLI burn. The TDRS support was planned on a best effort basis as part of an on-going effort to establish the potential use of TDRS to support non-TDRS (i.e. not equipped with a TDRS-compatible transponder) missions. Unfortunately, due to limited test data on the LP transponder frequency characteristics, and the limited sweep capability of the TDRS spacecraft, TDRS was initially unable to lock up on the LP telemetry stream. At TLI + 21 minutes, the Deep Space Network's Goldstone station locked on the LP transmit signal in two-way mode, and within a few minutes, data from the 300 bits per second (bps) telemetry stream was received. However, the telemetry data observed was noisy (due to a combination of the low bit rate and marginal LP antenna aspect angle geometry\*) and commanding was suspended until the antenna geometry improved and the health of the spacecraft could be ascertained.

**Table 5**  
**TRANSFER ORBIT TIMELINE OF KEY EVENTS**

<b>Event Start</b>	<b>Time Relative to TLI (dd hh:mm)</b>
LP Separation	TLI + 00 01:00
DSN Acquisition	TLI + 00 00:21
Receipt of First Telemetry (Noisy)	TLI + 00 00:24
90 deg LP Reorientation to Cruise Attitude	TLI + 00 02:27
Spin Down from 51 to 31 rpm	TLI + 00 03:05
Science Boom Deployment	TLI + 00 03:44
21 deg Attitude Adjustment Maneuver	TLI + 00 05:58
Trajectory Correction Maneuver (TCM) #1	TLI + 00 08:30
Trajectory Correction Maneuver (TCM) #2	TLI + 01 04:50
31 deg Reorientation to LOI Attitude	TLI + 02 03:05
Periselene	TLI + 04 08:35

After the successful DSN acquisition of LP in two-way mode, TDRS was able to lock up on the telemetry stream. However, as TDRS visibility was expected to end a short time later, mission controllers were reluctant to risk re-configuring the ground system to accept the data, and instead decided to concentrate on the Goldstone coverage.

About an hour later, with the antenna geometry improving and engineers reassured that the LP attitude, orbit and subsystems were nominal, spacecraft commanding was resumed. At TLI + 02:27, the spacecraft

---

\* The marginal antenna angle geometry was expected, but it was hoped that data quality would hold up until the spacecraft could be commanded into its cruise attitude. It is suspected that poor geometry was only partially to blame for the noisy data, and that another factor was the low transmit bit rate in use initially to improve chances for TDRS acquisition. The LP transponder was an off-the-shelf item with a 1024 kHz subcarrier frequency designed for higher bit rates. At the 300 bps telemetry rate the LP subcarrier to data rate ratio was not optimal for ensuring ground station acquisition, despite pre-launch efforts to configure ground equipment in such a way as to maximize performance using this signal.



was re-oriented 90 degrees toward its cruise attitude and commanded to its nominal 3600 bps telemetry rate. As a result of the delays and concerns over cooling of the spacecraft boom deployment mechanisms, a decision was made to alter the target cruise attitude by approximately 10 degrees in order to provide additional solar heating of those areas. The science booms were successfully deployed at TLI + 03:44. A 21 degree attitude trim maneuver was performed at TLI + 05:58 for thermal reasons.

As a result of these delays in the timeline, the first trajectory correction maneuver was not performed until TLI + 8.5 hours. This delay raised the required  $\Delta V$  magnitude of the correction from 38 m/sec (for a TCM#1 at TLI + 4.5 hours) to 50 m/sec. However, this was still well within the budgeted 80 m/sec allocated for transfer orbit maintenance. TCM#1 consisted of a vector burn with a 13 m/s axial component and 48.5 m/s tangential component.

TCM#2 took place on schedule and consisted of a 7.4 m/s vector burn (1.2 m/s axial and 7.3 m/s tangential). A final TCM#3 was scheduled to take place at LOI - 24 hours, but was called off when a propagation of the post-TCM#2 state yielded a projected periselene condition within 10 km of the target radius and .1 deg of the target inclination.

### **Lunar Orbit Insertion Maneuvers**

Lunar Prospector LOI maneuvers occurred according to plan, with the propulsion system performing to between 1 and 3 percent repeatability. LOI burns #1 and #2 placed the spacecraft into an 11.63 hour, then a 3.52 hour orbit, and LOI#3 dropped apoapsis down to within 50 km of the target mapping orbit altitude. LOI#3 was purposely targeted 3% short as an extra margin of safety, since it was predicted that a 9% hot LOI#3 burn would have dropped apoapsis down to lunar radius. A final mapping orbit correction (MOC-1) maneuver on January 15, 1998 circularized the orbit at a 100 km altitude. This maneuver consisted of two axial burns to lower apoapsis and raise periapsis to a target radius of 1838 km. The second burn was executed slightly off-apses to permit DSN coverage of the burn.

### **Mapping Orbit Maintenance**

The strategy for maintaining the LP 100 km altitude polar orbit was developed with the following goals:

1. Maintain an altitude band of 100 km +/- 20 km
2. Conduct maneuvers in view of a ground station
3. Minimize the number of maneuvers
4. Use axial maneuvers instead of vector burns if possible

The last goal was established for reasons of operational simplicity, since LP vector burns cannot be performed readily during shadow periods for lack of a reference sun pulse. Since the nominal LP spin-axis attitude is within a few degrees of the ecliptic normal (and therefore almost normal to the lunar equator), this goal required that the argument of periapsis be close to zero degrees to allow axial maneuvers to take place parallel to the velocity direction at periapsis/apoapsis. Furthermore, as LP maneuvers consist of a two-burn Hohmann sequence, the second goal requires that maneuvers be conducted when the orbit plane is normal to the Earth/moon line — a condition that occurs approximately every 14 days.

Figure 4 shows a history of the LP orbit periapsis/apoapsis altitude and argument of periapsis through the first orbit maintenance maneuver in the mapping orbit, followed by a prediction of the orbit evolution assuming no further maneuvers are conducted. The dashed vertical lines reflect the actual date of the first LP MOC maneuver (MOC#2) and the planned date of the second (56 days apart and coincident with periods of full station coverage). Furthermore, as the plot of orbit argument of periapsis shows, the maneuver dates occur when the line of apsides is within 15 degrees of the equator, allowing axial

maneuvers to take place with only minor losses in efficiency. Without maneuvers, the orbit could be expected to impact the moon within approximately 150 days.

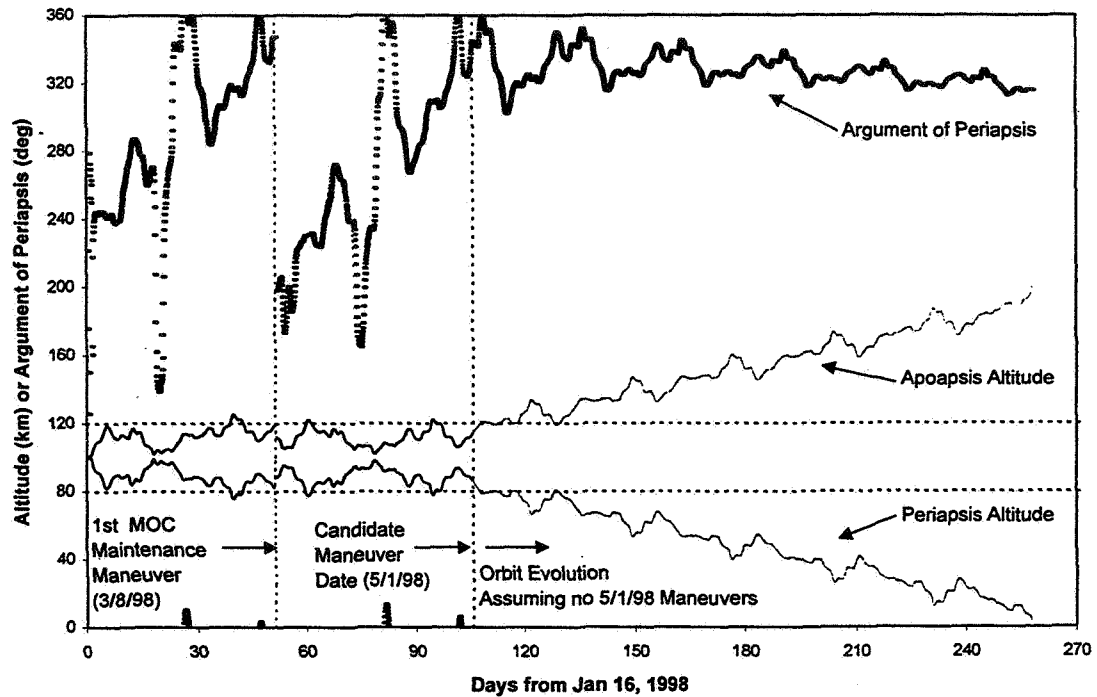


**Figure 4: LP Orbit Evolution of Apoapsis/Periapsis Altitude and Argument of Periapsis Beyond the First Mapping Orbit Maintenance Maneuver (LP75D lunar potential model)**

A 56 day interval between maneuvers was chosen to minimize the number of maneuvers performed, from the standpoint of reducing operational risk to the mission and minimizing perturbations to science data collection. Therefore, the goal of each mapping orbit correction was to adjust the orbit eccentricity and argument of periapsis in order to maintain an altitude variation within  $\pm 20$  km over the next 56-days. The phase space approach of plotting argument of periapsis and eccentricity discussed in References 5 and 6 is a useful tool in understanding LP orbit evolution. Figure 5 contains such a polar plot with eccentricity plotted along the radial direction and argument of periapsis plotted along the angular direction. In this plot, LP orbit evolution is plotted for a 1-year duration, starting with the initial 100 km circular orbit attained after MOC#1 on January 15, 1998. Figure 5 describes how eccentricity grows with time, as argument of periapsis gravitates toward a value of 270 degrees. In order to limit excursions beyond the  $\pm 20$  km range, initial values of 180 deg for argument of periapsis and approximately 0.0065 for eccentricity (88 x 112 km orbit) were targeted as maneuver end conditions for subsequent maneuvers. This forced the orbit to evolve through the zero eccentricity point and permitted a longer time between maneuvers. It is expected that such a strategy will figure even more prominently during the extended mission phase when frequent maneuvers will be required to maintain the 10 km periapsis altitude.

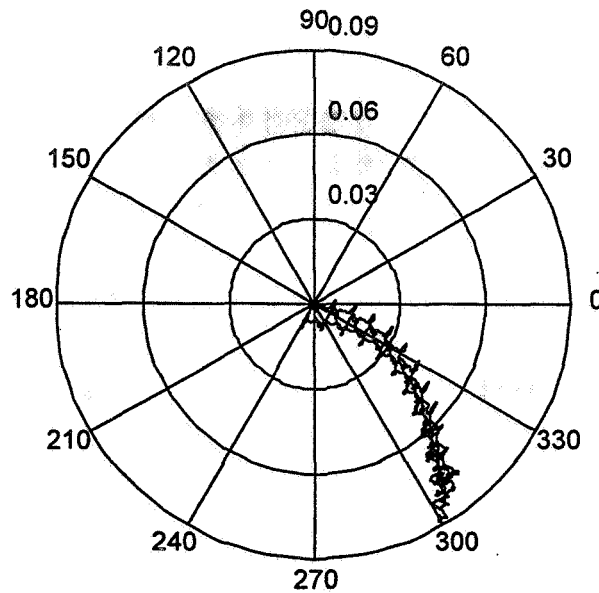


**Figure 5: Lunar Prospector Mapping Orbit Eccentricity and Argument of Periapsis Evolution**  
[Eccentricity along radial direction and argument of periapsis along angular direction]

## LP ORBIT DETERMINATION RESULTS

Upon launch of the LP spacecraft, the first task of the orbit team was to assess the performance of the TLI maneuver. The failure to acquire TDRSS data delayed that assessment. When coherent DSN Doppler was received, approximately 23 minutes after TLI, the residuals indicated a slightly cold burn. The expected residuals for several off-nominal cases, along with the actual residuals obtained, are shown in Figure 6. The off-nominal cases modeled are -20 and -35 m/s TLI magnitude error and  $\pm 0.8$  and -2.4 deg in argument of perigee error.

The first full state estimate was not obtained until 2.5 hrs after TLI due to the failure to acquire TDRSS tracking data and due to dropouts in the DSN data. The calibrated TLI magnitude error was estimated at -9.1 m/s, which matched the near-real-time Doppler assessment data fairly well. TCM#1 was not preformed until 8.5 hours after TLI.

After each of the TCMs, a Doppler assessment was made in near-real-time. In each case, the assessment indicated that the maneuver was slightly cold. The final calibrated efficiencies of these maneuvers (Table 3) are consistent with these initial Doppler-based assessments. The first orbit solution after TCM#1 was obtained after seven hours. The goal was to obtain this solution within six hours of the maneuver, however since TCM#1 was performed much farther away from perigee than planned, additional data were needed for a solution. After TCM#2, the first orbit estimate was available eight hours later — exactly as expected. TCM#3 was cancelled, which meant the orbit trajectory would be well determined for the LOI#1 maneuver.

During the 30 minute LOI#1 maneuver, the DSN lost coherent lock on the spacecraft. As a result, no Doppler data were obtained until immediately after the maneuver. A Doppler assessment at that point indicated a successful lunar capture with only a slightly cold burn. A full orbit state was obtained 1.5 hrs after LOI#1, which was slightly over 2 hours earlier than expected.

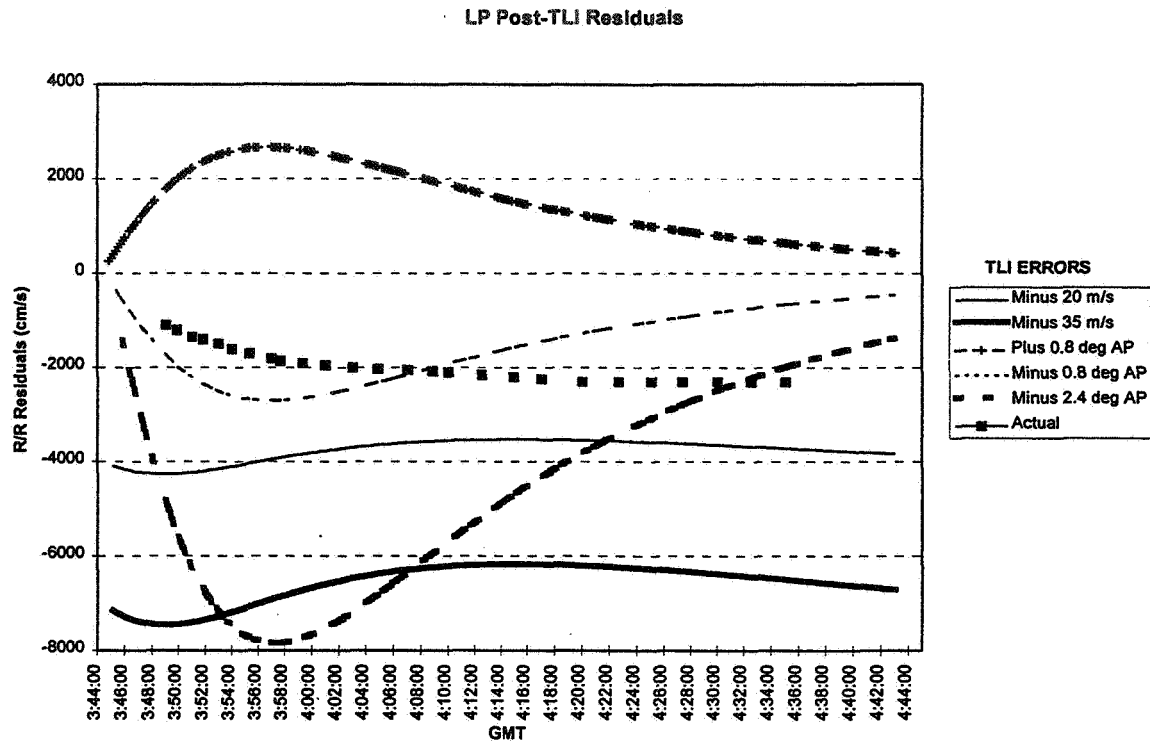


**Figure 6: Lunar Prospector Doppler Residual Signatures for Post-TLI Maneuver Assessment**

LOI#2 and LOI#3 were nominal. Doppler assessments were used during each maneuver to estimate maneuver efficiency. In particular a near-real-time assessment of LOI#3 was performed out of concern for an over-burn beyond the 100 km target apoapsis altitude. Full state estimates were available 2 hrs after LOI#2 and 3.5 hrs after LOI#3. The trend for the amount of tracking data needed to converge after LOI#1, 2 & 3 was exactly opposite of what was expected. This has been attributed to the inadequacy of the GLGM-2 potential model at lower altitudes. This effect was not seen in the covariance analysis.

Once the mapping orbit was achieved, different batch arc lengths were attempted with the goal of extending them as long as possible to reduce the amount of processing time (since it was expected that definitive ephemerides would be regenerated with the new potential model at a later date). A 14 hr tracking arc was chosen with a 2 hr overlap between two consecutive tracking arcs. Thus two 12 hr definitive ephemerides per day were placed on the Goddard Lunar Prospector web site (<http://fdd.gsfc.nasa.gov/lp/>) for use by the LP mission control center and science community.

The first updated LP potential model was available after just two weeks in the mapping orbit. The new model, LP75A, was developed by A. Konopliv of the Jet Propulsion Laboratory. A final model, LP75D<sup>7</sup>, was available after one month and was used to generate updated ephemerides. A comparison of the orbit accuracy achievable with each of these three models is shown in Table 6. The orbit accuracy is measured as the difference between two consecutive definitive ephemerides over the period of overlapping tracking data. The LP75A solutions consisted of 26 hr arcs with a 2 hr overlap. The LP75D solutions consisted of 55 hr arcs with a 7 hr overlap.

Clearly the LP75D solutions meet the LP mission requirements. As of February 23, updated definitive ephemerides were being generated using the LP75D model. The regeneration of the first five weeks of

definitive ephemerides will be completed by mid-April. The entire lunar mapping orbit definitive ephemeris history is available on the Goddard Lunar Prospector web site.

**Table 6**  
**LUNAR PROSPECTOR MAPPING ORBIT DETERMINATION ACCURACY**

Model	Radial RMS	Cross-track RMS	Along-track RMS	Position RMS	Maximum Position	Average Doppler Residual
GLGM-2	475 m	4.0 km	4.4 km	6.6 km	31.6 km	21 cm/sec
LP75A	NA	NA	NA	1.9 km	7.3 km	5.5 cm/sec
LP75D	11 m	192 m	169 m	240 m	532 m	8.3 mm/sec

## CONCLUSION

Lunar Prospector orbit operations occurred largely according to plan and resulted in the successful attainment of the 100 km altitude polar mapping orbit within budgeted orbit maneuver propellant allocations. A large share of the credit for the success of the Lunar Prospector mission can be attributed to the straightforward design of the spacecraft and the overall mission, and to a well-built and well-tested spacecraft that performed flawlessly. In particular, the spacecraft propulsion system was well modeled and provided excellent repeatability. Finally, a robust orbit determination strategy, characterized by accurate solutions and fast-turnaround, was also an important factor that contributed to maneuver targeting accuracy and low propellant consumption.

## ACKNOWLEDGMENTS

Special thanks to Greg Marr, Karen Richon, Marco Concha, Osvaldo Cuevas, Pat Johnson and Joe Toth of NASA/Goddard, and to Marcie Smith of NASA/Ames, Dan Swanson of Lockheed Martin, Mark Ryne and Alex Konopliv of JPL and Dr. Alan Binder of the Lunar Research Institute for their excellent contributions to the success of Lunar Prospector trajectory operations.

## REFERENCES

1. Hubbard, G. S., et al., "The Lunar Prospector Discovery Mission: A New Approach to Planetary Science", IAF-97-Q.4.01, October 1997.
2. Clarke, V. C., Jr., "Design of Lunar and Interplanetary Ascent Trajectories," AIAA Journal, Vol. 1, No. 7, July 1963.
3. Lemoine, F. G., et al., "A 70th Degree Lunar Gravity Model (GLGM-2) from Clementine and Other Tracking Data," Journal of Geophysical Research Vol. 102, No. E7, Pgs 16339-16,359 July 25, 1997
4. Folta, D., et al., "Lunar Prospector Mission Design," Flight Mechanics Symposium, Greenbelt, MD, May 19-21, 1997.
5. Cook, R. A. and Sweeter, T. H., "Orbit Maintenance for Low Altitude Near-Circular Lunar Orbits", AAS Paper 92-185, February 1992.
6. Konopliv, A. S., et al., "A High Resolution Lunar Gravity Field and Predicted Orbit Behavior", AAS Paper 93-622, August 1993.
7. Konopliv, A. S., "Lunar Prospector Gravity Results", to be presented at AGU Spring Meeting, May 26-29, 1998, Boston, MA.



525-17  
169307  
337565  
101.

# GPS PERFORMANCE FOR GEO's AND HEO'S THE EQUATOR-S SPACECRAFT MISSION

**Werner Enderle, Michael Schmidhuber, Eberhard Gill,  
Oliver Montenbruck, Armin Braun',  
Bernd Eisfeller, Oliver Balbach'**

The successful usage of spaceborne GPS receivers for orbit- and attitude determination has in the past mainly been applied for spacecraft in near-circular Low Earth Orbits (LEO), e.g. TOPEX/POSEIDON, RADCAL.

However, no experience exists of using GPS signals for spacecraft navigation in altitudes above the GPS (20.000 km), such as the Geostationary Orbit (GEO) or the Geo Transfer Orbit (GTO). In this context, EQUATOR-S with its highly elliptical orbit offers a unique possibility in order to increase significantly the experience concerning GPS visibility, signal reception and GPS based navigation.

The application of GPS based spacecraft navigation in GEO's and HEO's will bring advantages in many aspects. Besides orbit/attitude determination, GPS offers a potential for increasing command capabilities and decreasing ground station support. This will lead to a reduction of mission cost especially for LEOP phase of geostationary satellites.

This paper describes first experiences in operating a GPS receiver in a highly elliptical orbit and presents first results of GPS visibility and signal reception conditions within this orbit.

## INTRODUCTION

EQUATOR-S (see Figure 1) is a scientific satellite for the investigation of the magnetosphere of the sun under the responsibility of the Max-Planck-Institut fuer Extraterrestrische Physik (MPE) in Garching, Germany. EQUATOR-S was launched on December 2, 1997 into the Geostationary Transfer Orbit (200 km x 36000 km) together with a Japanese Communication Satellite JC-SAT 5 on an Ariane 4 (44P) from Kourou in French Guyana. EQUATOR-S is under the control of DLR's German Space Operations Center (GSOC). Following a nine day LEOP phase the spin stabilized satellite was boosted (see Figure 2, Table 1) into the final low inclination HEO (500 km x 67000 km). Besides several scientific payloads, EQUATOR-S carries also a GPS receiver (incl. two antennas, cables and interface box) as a technological experiment.

---

\* German Space Operations Center (GSOC), DLR, D-82230 Wessling, Germany.  
Phone: +49 (8153) 28 17 52, Fax +49 (8153) 28 14 60, E-mail: werner.enderle@dlr.de  
† Institute of Geodesy and Navigation (IfEN), University FAF Munich, Germany.

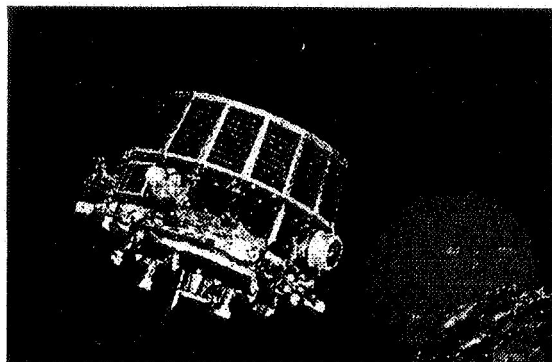


**Figure 1: EQUATOR-S**

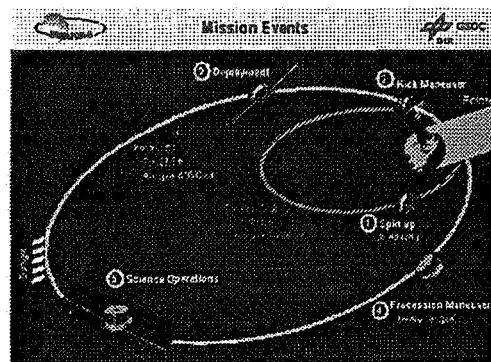


**Figure 2: Mission Events**

**Table 1: EQUATOR-S Orbital Elements**

Element	Unit	GTO	Final Orbit
		Epoch 1997/12/02 23:16:42 UT	Epoch 1997/12/11 18:38:30 UT
Semi major axis	[km]	24467.7	40084.9
Eccentricity	[-]	0.7311	0.828791
Inclination	[deg]	3.999	3.999
R.A. Asc. Node	[deg]	232.561	225.667
Arg. Perigee	[deg]	178.045	195.769
Mean Anomaly	[deg]	3.840	6.738
Perigee Height	[km]	200.8	484.8
Apogee Height	[km]	35978.3	67275.3

## SCIENCE OBJECTIVES

The science objectives of the GPS experiment on-board of EQUATOR-S are the GPS data reception conditions in very high altitudes including the topics of GPS satellite visibility (geometry, link budget, side lobe usage) and measurement quality (position, pseudo range, carrier phase). Another field of interest concerns the orbit determination (OD) in highly eccentric orbits which can be subdivided into OD from GPS navigation solution and OD from GPS raw data (pseudo range, carrier phase).

Further science objectives are the determination of the spin axis orientation, verification of ionospheric signal path models and special emphasis is given to near-geostationary altitudes in view of potential applications for autonomous orbit/attitude determination and control of future geostationary satellites.



## PROBLEMS OF USING GPS IN HEO'S AND GEO

The GPS system is designed for applications on Earth, above Earth surface in very low altitudes (e.g. airplanes) and satellites in LEO. For this reason the GPS antennas directed towards the Earth with an half cone angle of  $21.3$  [deg] (L1). Application of GPS in GEO's and HEO's are therefore outside the original GPS specifications. The main problems of using GPS in this orbits are given by the visibility limitations of GPS satellites at high altitudes (geometry), signal reception at high altitudes caused by poor signal strength (link budget) and a wide range of Doppler due to highly variable velocities particularly for HEO's around perigee.

The reception and using of GPS signals in HEO's and GEO (see Figure 3) will only be possible if the following criteria will be fulfilled at the same time

- the line of sight from host satellite (EQUATOR-S) to the GPS satellite is not blocked by the Earth
- the line of sight from host satellite (EQUATOR-S) to the GPS satellite is not blocked by a spacecraft component
- the signal strength of the received GPS signal is strong enough, so that the receiver can track the signal (the Signal to Noise Ratio (SNR) is the key factor)

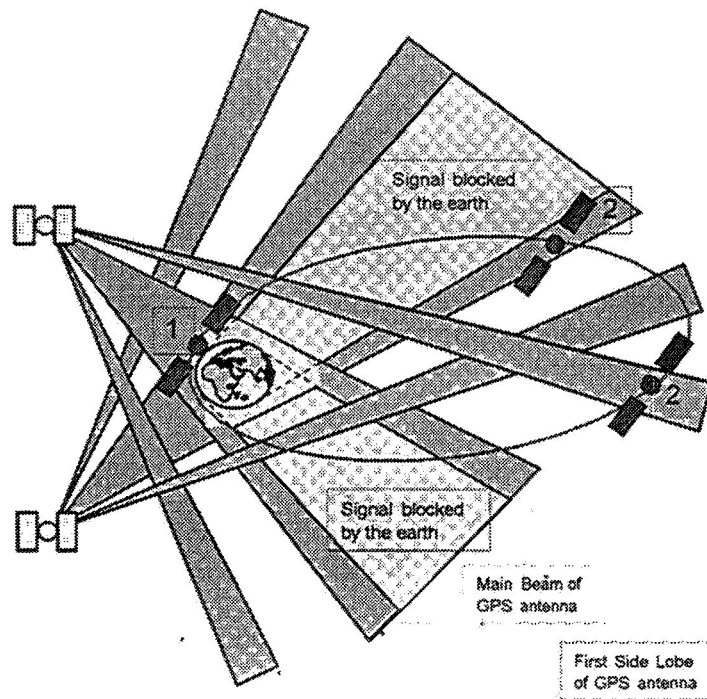


**Figure 3: Visibility of GPS satellites in HEO's and GEO**

## GPS RECEIVER ON-BOARD EQUATOR-S

The GPS technology experiment on-board EQUATOR-S has been equipped with a Motorola Viceroy 12 channel parallel receiver (see Figure 4), capable of L1-band, C/A-code and carrier phase measurements. The receiver features 2 x 6 channels connected to the two antennas. For visibility reasons (covering the entire sphere) one antenna is attached at the top of EQUATOR-S and one at the bottom (see Figure 5). Considering that the Viceroy receiver has originally been designed and build for the use on three-axis stabilized satellites in LEO, constrains apply for it's operation on a spinning satellite in a HEO.

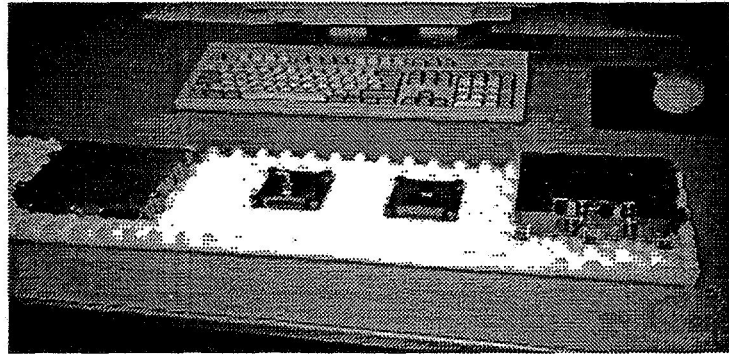


**Figure 4: Motorola Viceroy receiver, antennas and interface box**

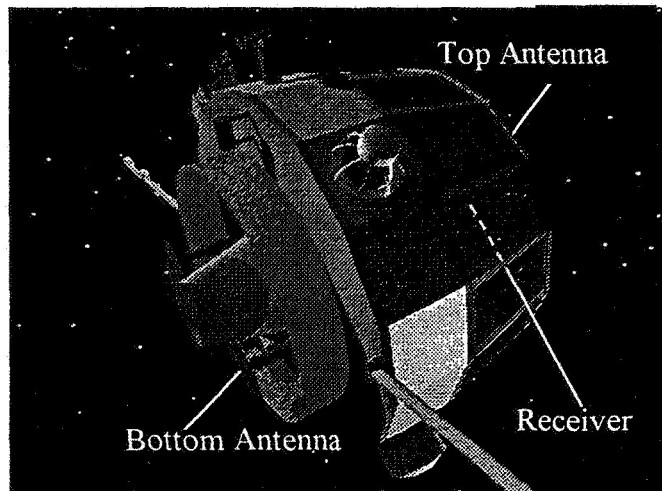


**Figure 5: Location of the GPS antennas on-board EQUATOR-S**

## **OPERATIONS CONSTRAINS**

Apart from the exciting scientific aspects, the GPS experiment furthermore faces a challenging operations concept due to the given constraints relating the operations. Some of the constraints are EQUATOR-S specific e.g. no Earth pointing attitude at high altitudes (poor GPS visibility), during the GTO the bottom antenna was obstructed by the kick motor, this results in a restricted field of view and limited TM/TC system capabilities. Considering the constraints given by the receiver, the expected Doppler shift between the GPS satellites and the receiver is internally computed from a set of orbital elements using a simple orbit model. Therefore, new reference orbit elements must be uploaded from ground after each perigee transit. Since there is a high risk to the receiver electronics from the hard radiation in the higher altitudes, the receiver shall be switched off above 40.000 km. The automatic selection of GPS satellites is based on their elevation above the user satellite's local horizontal plane. For high altitudes and an inertial fixed antenna lobe, the selection algorithm fails and has to be replaced by a manual assignment of GPS satellites to the various receiver channels.

Despite these restrictions, which could at least partially be compensated by appropriate operations procedures, the receiver was successfully switched-on and initialized soon after the separation.

## **VISIBILITY PREDICTION - VISIBILITY TOOL 'HEOVIS'**

Considering that the automatic search algorithm fails in high altitudes, the necessity for a highly reliable GPS visibility predict tool was essentially for successfully operations in high altitudes and also for analysis. For this reason a GPS visibility predict tool has been developed. The calculation of the GPS visibility includes the geometric visibility conditions and a link budget [3], [4] computation. Implemented in this software is besides the orbit dynamic of the GPS satellites also the complete orbit and attitude dynamic of EQUATOR-S [2]. The link budget calculation applies all relevant aspects including the antenna pattern of the GPS satellites emitting antennas and the receiver antenna (see Figure 6 and 7). Detailed description are given in [1]. Some visibility predict results are given in the Figures 8-11.

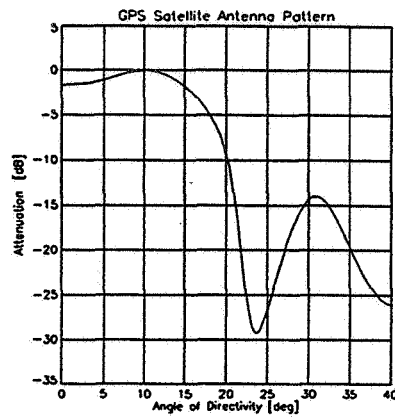


Figure 6: Emitting antenna pattern

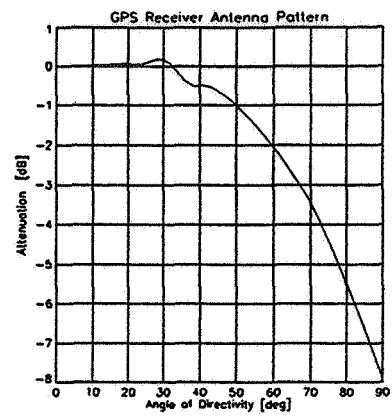


Figure 7: receiver antenna pattern

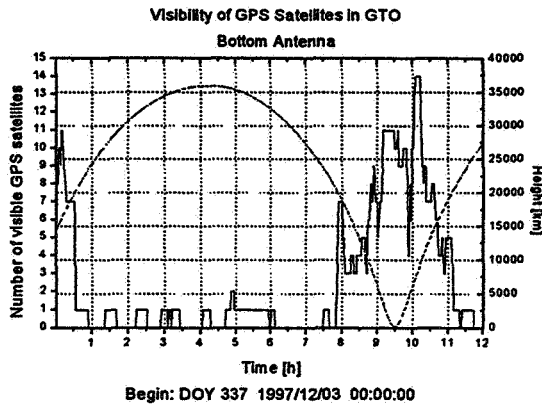


Figure 8: Predict number of visible GPS

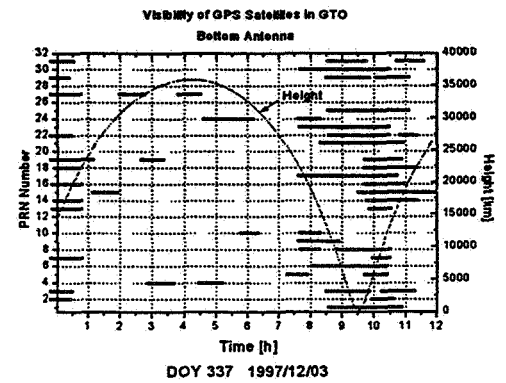


Figure 9: Predict visible PRN

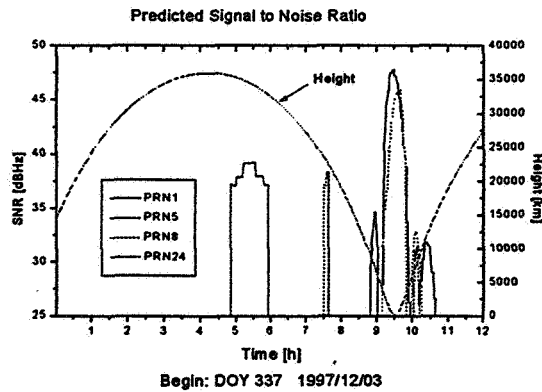


Figure 10: Predict of SNR

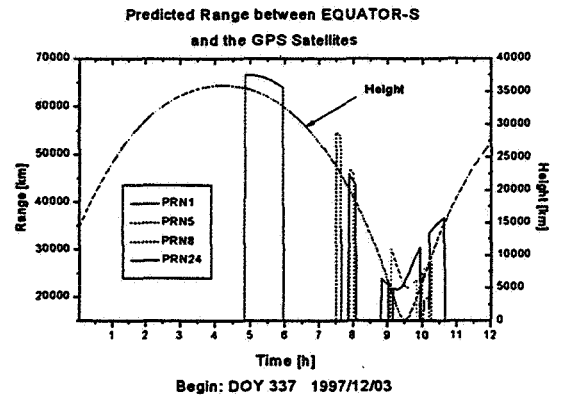


Figure 11: Predict of range

## RESULTS

The first result was the first GPS satellite which has been tracked (PRN 24) by the bottom antenna (two channels simultaneously) for a duration of 03:52 min in an altitude of about 34.000 km. As far as we know, this was the first time that a GPS satellite has been tracked around the GEO altitude. The precise information of this event is given in Figure 12. The most critical parameter for the GPS signal acquisition and tracking in high altitudes is the SNR. Unfortunately the SNR value is not given by the Viceroy receiver in a physically unit. The output of this information is a so called SS parameter (Figure 13 a) ). By using a formulae, given by Motorola for Earth application this SS parameter was converted into the SNR with the physically unit [dBHz] (Figure 13 b)). Comparing this value with from HEOVIS predicted SNR value (38 dBHz) shows, that the converted SNR lies ca. 4dBHz below the predicted SNR. The predicted SNR corresponds with information from Motorola for expected initial acquisition of the GPS signal SNR numbers. Figure 13 c) shows the integrated carrier phase measurements and Figure 13 d) displays the pseudo range obtained from the receiver. The values of the pseudo range measurements shows that the tracked GPS PRN 24 must have been in the opposite of the Earth, seen from EQUATOR-S. The predicted pseudo range for the tracked GPS PRN24 fit very well with the pseudo range measurements.

The second result presented here is the tracking a GPS satellite (PRN04) within a the first side lobe of the GPS emitting antenna. The ability of signal reception from the first side lobe increases in HEO's the number of visible GPS satellites especially in altitudes > 20.000 km significantly. The Figure 14 displays the tracking of a GPS satellite in the first side lobe.

The last result presented here shall be the GPS tracking with the longest duration (40 min). In Figure 15 a) – 15 f) are the displayed the main parameters of this measurement. The GPS PRN29 was tracked for about 40 min from an altitude of 15.000 km up to an altitude of 22.000 km (Figure b)). The total number of visible GPS satellites was between four and five (Figure a)). In Figure d) one could see that the converted SNR decrease with increasing altitude. The values at the end of the curves indicate a loss of signal. The parameter values of PRN03 were also plotted in all Figures, this was done in order to compare the values obtained by a different tracking mode status. While PRN29 would have been used for a position solution algorithm (mode status 8), PRN03 would not have been used (mode status 7).

It should also mentioned that the maximum number of simultaneously tracked GPS satellites was three and therefore no receiver position solution is available.

Orbit determination results based on C/A-code and carrier phase measurements are expected to be available very soon.

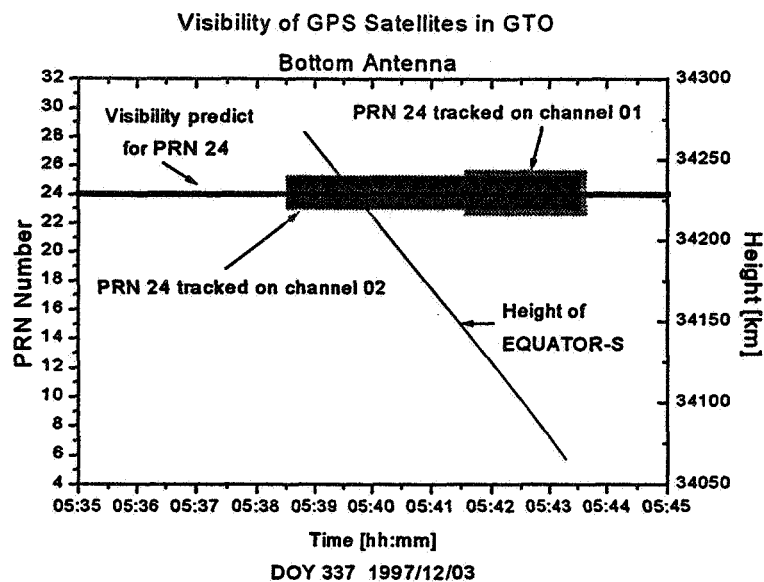


**Figure 12: First tracking of a GPS satellite in GEO altitude**

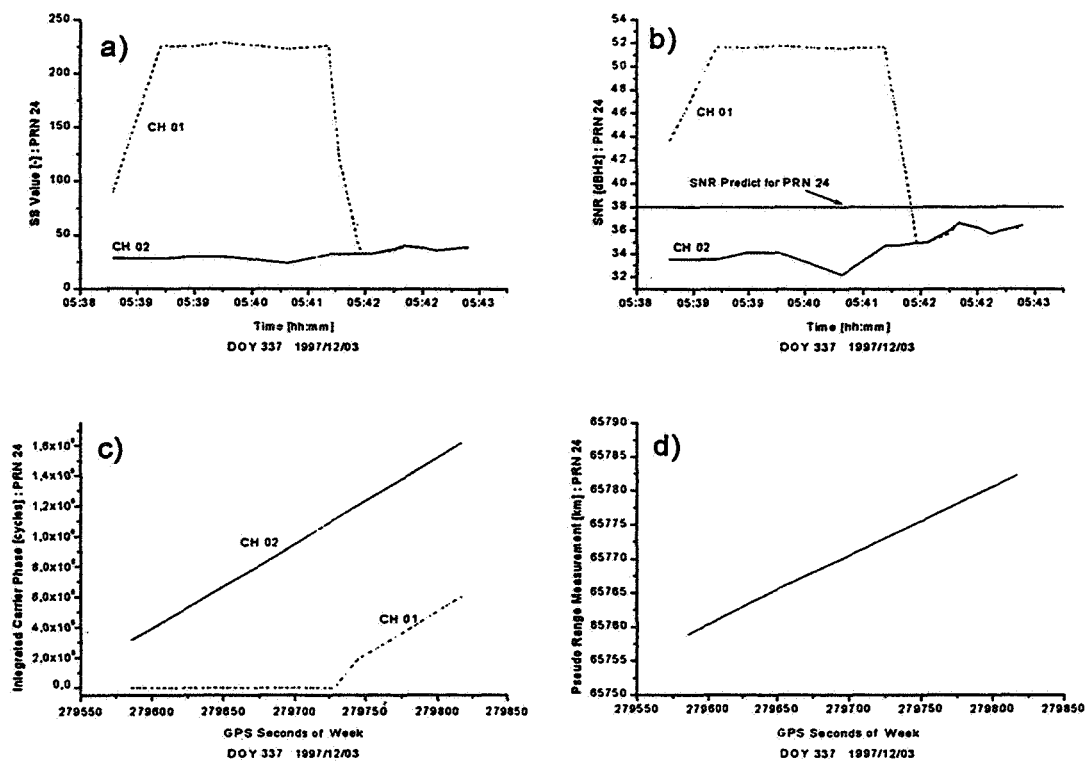


**Figure 13: PRN24 measurements**

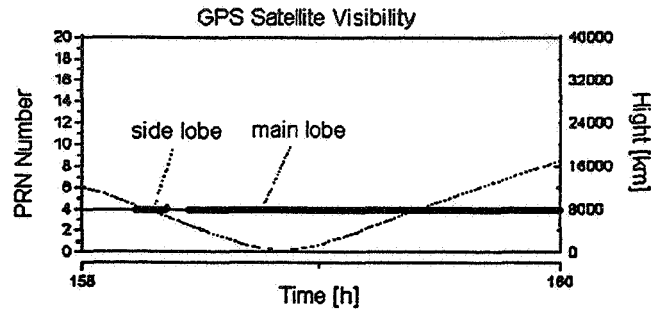


Figure 14: Tracking of PRN04 in the side lobe

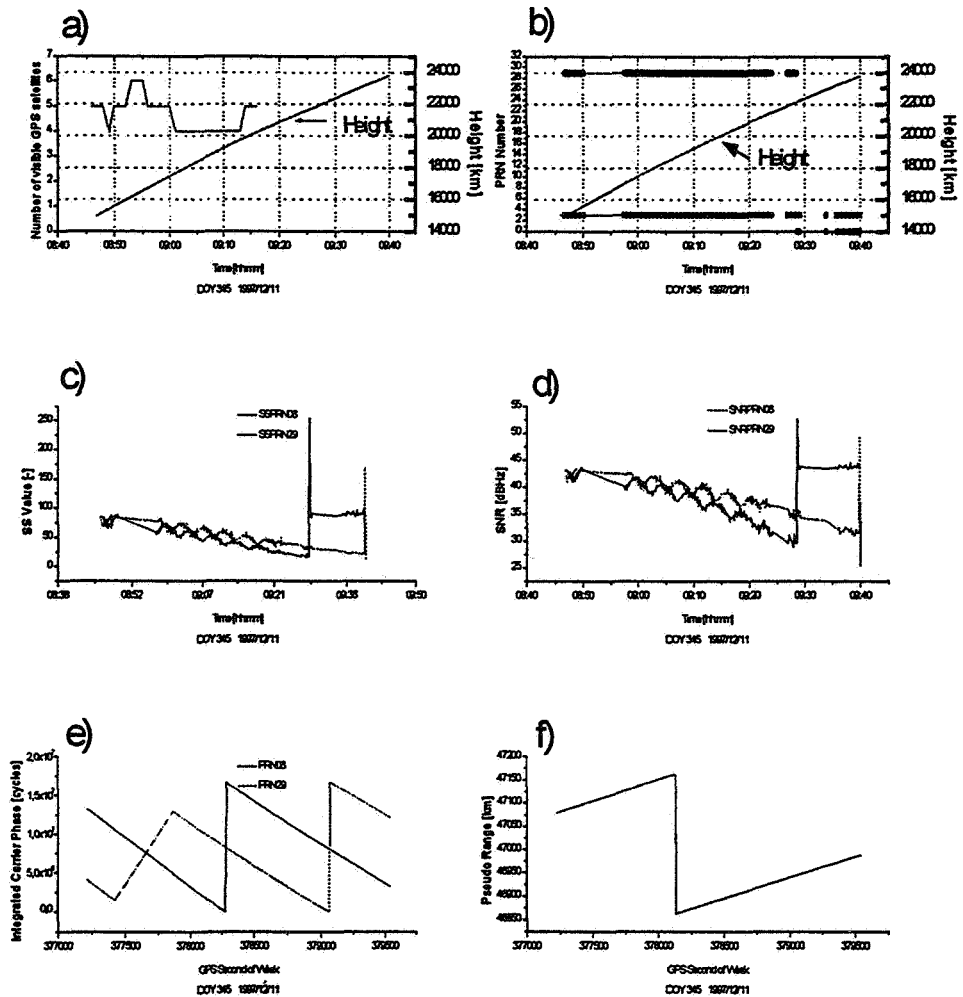


Figure 15: Tracking of PRN29, longest tracking period

## CONCLUSION

The results presented in this paper shows, that it is generally possible to acquire and track GPS signals in near GEO altitudes. The GPS experiment on-board EQUATOR-S gives first answers about the SNR values in altitudes near GEO. It also could be proved, that it is possible to track GPS satellites in the first side lobe. The fact of GPS signal reception from the side lobe increases the number of visible GPS satellites in high altitudes significantly. In spite of all constrains concerning the operations, it could be shown that it was possible to operate the GPS receiver under difficult circumstances and receive good measurements. In this context the developed GPS visibility predict SW 'HEOVIS' was important and delivered very good results.

The experiment is still running and we are looking forward to reach the next two goals, 1. tracking of four or more GPS satellites at the same time and 2. tracking of GPS satellites above the GEO altitude.

## REFERENCES

1. W. Enderle, Lagebestimmung von Satelliten in hochexzentrischen Orbits, basierend auf GPS Messungen, Ph.D. Thesis, Technical University of Berlin, will be published.
2. U. Feucht, W. Enderle, D. Moormann, EQUATOR-S Attitude Dynamics Simulation, 12<sup>th</sup> International Symposium on Space Flight Dynamics, Darmstadt 1997.
3. Motorola: Data Sheets for Viceroy GPS Receiver and Antenna
4. F.M. Czopek, S. Shollenberger, Description and performance of the GPS Block I and II L-Band Antenna and Link-Budget. ION GPS-93



## **Data Analysis of Space Based Relative GPS Experiments**

**T.J. Martín Mur, C. García Martínez**

**ESA/European Space Operations Centre  
Darmstadt, Germany  
GMV at ESOC**

526-17  
169308

337566  
14.

Three ground-breaking experiments involving simultaneous collection of GPS data by spacecraft took place between November 1996 and October 1997. These experiments had the goal of demonstrating the feasibility of using GPS for relative navigation of spacecraft. The experiments took place within ESA's ATV (Automated Transfer Vehicle) Rendezvous Pre-development (ARP) program. This program aims to validate rendezvous technologies that will be used in ATV for its proximity operations around the International Space Station.

The spacecraft involved were NASA's Shuttle and the US/German retrievable Astropas satellite for the first flight demonstration that took place during the STS-80 flight at the end of 1996 and the Shuttle and the Russian MIR space station during the STS84 and 86 flights. GPS receivers were installed in the spacecraft involved and GPS data were collected for several intervals during the rendezvous and separation phases.

ESOC Flight Dynamics was entrusted with the challenge of providing the most accurate trajectories that could be computed using the on-board collected GPS data in combination with ground collected data. These precise trajectories were required in order to validate the algorithms to be used in the ATV for relative navigation. The baseline for ATV is that the GPS data collected on-board the ATV and the ISS will be processed in real time on-board the ATV to obtain a relative navigation solution.

ESOC routinely produces precise orbits and clocks for the GPS satellites as part of its involvement as Analysis Centre in the International GPS Service for Geodynamics. With those precise products it is possible to correct in post-processing for the errors introduced by Selective Availability. For these experiments the GPS measurements are corrected and then used to calculate the absolute position of each of the two spacecraft. The biggest sources of error that have to be dealt with are the ionospheric delay, because only L1 frequency data are being collected, the pseudo range noise and the cycle slips in the carrier phase.

So far the data for the first Flight Demonstration have been processed, with results that compare well with those derived from the Shuttle TCS laser ranging system and we are currently waiting for the availability of the data for Flight Demos 2 and 3. For these last two Flight Demos there is a delay in the retrieval of data because some of them have to be down-linked from the MIR space station, but they should be available soon and it is expected that data processing will be completed before the end of the year.

This paper will present the strategy used to obtain the best estimated trajectories, the problems found during the analysis of the data and the results obtained, including comparisons with trajectories obtained using other tracking systems or algorithms.



527-13

169309

337567  
10f.

## AN EFFICIENT ON-BOARD ORBIT PROPAGATOR/ESTIMATOR FOR LEO MISSIONS

Karl Hans Neumayer and Rolf König\*

In the context of scientific investigations related to the CHAMP project and other upcoming LEO missions, the GeoForschungsZentrum Potsdam (GFZ) initiated the development of an efficient real-time on-board orbit estimation and propagation software called POPE. The methods specific to POPE are in fact adaptations of orbit prediction algorithms that are being in operational use for the PRARE system on-board METEOR 3/7 and ERS-2 for several years. Simulation studies show that orbit elements generated by POPE from on-board GPS measurements suffice to bridge a gap of up to one week without GPS data with position errors of 10 to 20 km on the average for LEO orbits at 300 km altitude.

### INTRODUCTION

CHAMP<sup>1</sup> is a mini-satellite mission for geopotential and atmospheric research that will be launched by the end of 1999 into a near-circular, near-polar orbit. It will cover 5 years, with the orbital altitude decaying from initial 450 km to 300 km towards the end of the mission. The payload instruments include a TurboRogue space receiver providing GPS navigation solutions at 0.1 Hz frequency with an accuracy of approximately 55 m standard deviation in position.

The attitude and orbit control system has to keep CHAMP earth-oriented within 2 degrees during normal mode operations. For this task, orbital position is needed at 1 Hz frequency with errors not exceeding 240 km in along-track direction. From the GPS navigation solutions, accurate positions can easily be interpolated. In case of GPS navigation downtimes, an orbit propagator shall extrapolate positions and velocities for the missing time intervals.

Within this context, we present the newly developed propagation software POPE (PRARE elements on-board Orbit Propagator/Estimator).

---

\*GeoForschungsZentrum Potsdam (GFZ), Div.I: Kinematics and Dynamics of the Earth, c/o DLR, D-82230 Oberpfaffenhofen, Germany. Contact: Dr. Karl Hans Neumayer, Phone (+49) 8153 28-1330, FAX (+49) 8153 28-1585, e-mail hans.neumayer@dlr.de

The orbit parametrization in POPE is based on the ephemeris initially designed for the PRARE system on-board ERS-1<sup>3</sup>. PRARE was successfully tested on-board the METEOR-3/7 satellite during the years 1992 until 1995. In 1995 ERS-2 overtook the space segment function<sup>4</sup>. The PRARE orbital elements are generated on ground from laser tracking data and uploaded once a week during nominal operation.

Upcoming LEO missions like CHAMP that carry on-board GPS receivers have on-board data processing capabilities. For the orbit prediction chain, off-line processing is no longer necessary. Orbit parameters can be generated from GPS data on-board and on-line on the side in order to be utilized when the GPS receiver is down.

The above-mentioned PRARE orbit parametrization is based on a series expansion of *regularized Kepler elements*

$$a, \xi, \eta, i, \Omega, u. \quad (1)$$

that are used instead of the common Kepler elements

$$a, e, i, \omega, \Omega, M \quad (2)$$

for near-circular orbits in order to avoid singularities. Here  $a$  is the semimajor axis,  $e$  the eccentricity,  $i$  the inclination,  $\omega$  argument of perigee,  $\Omega$  longitude of ascending node,  $M$  the mean anomaly and  $u$  the argument of latitude. Both sets of elements are connected by the equations

$$\xi = e \cdot \cos \nu ; \eta = e \cdot \sin \nu ; u = \omega + \nu, \quad (3)$$

where  $\nu$  is the true anomaly.

The series expansion is a result given by classical perturbation theory<sup>2</sup>. The overall perturbations of the elements are composed of periodic effects with frequencies that are multiples of the Earth rotation, mean motion of the satellite, and secular rates of longitude of node and argument of perigee. Thus for the PRARE system, orbital elements are represented by linear combinations of common time-dependent and trigonometric polynoms. A core coefficient set of the polynomial expansion has been chosen for the CHAMP mission enabling the design of safe algorithms and providing fast computing performance at the same time. The selection is the result of a significance analysis; it is not specific to CHAMP, indeed all LEO orbits can be approximated in the same way.

For the update of the expansion coefficients, the GPS coordinates and velocities provided by the on-board GPS receiver in the terrestrial reference frame WGS84 are not used directly. In a first step, they are transported into the pseudo-inertial true-of-date system by a removal of the Earth rotation. They are then transformed into osculating regularized Kepler elements (1) that, instead of the original positions and velocities, are considered as the raw measurements.

As the above-mentioned series expansion in fact establishes a linear model for the orbit elements in (1), the whole update can be taken care of within the framework of

linear estimation theory. That would not be possible if the the GPS coordinates and velocities were used as raw measurements, as the elements in (1) depend on the state vector in cartesian coordinates in a complicated non-linear manner.

In order to further facilitate the procedures involved we assume that the six measured Kepler elements are mutually uncorrelated a-priori. Thus we have to deal only with six independent noisy measurement channels instead of a fully occupied measurement noise matrix, and we need not establish relative weights between the different observed orbit elements.

## REVOLUTION-DEPENDENT PERTURBATIONS

From the different kinds of perturbations given by analytic orbit theory<sup>2</sup>, the following ones have been considered important for the orbit propagator POPE: All the elements have perturbations that are periodic with the orbit frequency of the spacecraft. The sixth element, the argument of latitude  $u$ , exhibits a linear drift with revolution-dependent components superimposed. The length of the ascending node  $\Omega$  has an additional small drift due to the influence of the oblateness of the earth.

If these periodic terms are removed, among the resulting smoothed elements

$$\bar{a}, \bar{\xi}, \bar{\eta}, \bar{i}, \bar{\Omega}, \bar{u}, \quad (4)$$

the first four are constants and the last two are linear functions of the elapsed time. Those constants and the slopes of the linearly varying terms can be conveniently estimated from the smoothed measurements (4).

The indicated smoothing operation is performed by subtracting a trigonometric polynomial from each one of the elements listed in (1). The polynomial coefficients  $A_m$ ,  $B_m$  are given by a numerical approximation of the integrals

$$A_m = \frac{1}{\pi m} \int_{u=0}^{2\pi} f(u) d \sin(mu) \quad (5)$$

$$B_m = \frac{-1}{\pi m} \int_{u=0}^{2\pi} f(u) d \cos(mu) \quad (6)$$

where  $f(u)$  symbolically stands for the periodic part of one of the elements in (1). For the argument of latitude  $u(t)$  e.g. we have

$$f(u) = u_p(t) \quad (7)$$

with

$$u(t) = \bar{u}(t) + u_p(t); \quad (8)$$

i.e.  $u(t)$  is composed of a purely linear varying part  $\bar{u}(t)$  and a purely periodic part  $u_p(t)$ .

The smoothed signal which is taken care of by the rest of the filter is

$$\bar{u} = u - \sum_{m=1}^M \{A_m \cos(mu) + B_m \sin(mu)\}. \quad (9)$$

In order to facilitate the book-keeping inside the orbit propagator algorithm, the coefficients  $A_m$ ,  $B_m$  are re-computed during every revolution. However, as revolution-dependent gravity perturbations of orbit elements are known to be extremely stable phenomena, in theory the trigonometric coefficients could be refreshed only sporadically, say once a week.

At this point, some remarks are in order. From the purely logical viewpoint, the argument of latitude  $u$  should be represented by an expression of the form

$$u = \bar{u} + \sum_{m=1}^M \{A_m \cos(m\bar{u}) + B_m \sin(m\bar{u})\}, \quad (10)$$

i.e. in (9) the trigonometric quantities  $\cos(mu)$ ,  $\sin(mu)$  should be replaced by  $\cos(m\bar{u})$ ,  $\sin(m\bar{u})$ . The formula (10) is indeed the one which is used in the prediction part of the orbit propagator: First, the smoothed argument of latitude  $\bar{u}(t)$  is predicted, then the result is inserted in (10) in order to predict  $u(t)$ . But apart from the fact that, from the numerical viewpoint,  $\cos(m\bar{u})$ ,  $\sin(m\bar{u})$  are not perceptibly different from  $\cos(mu)$ ,  $\sin(mu)$  needed in (5), (6) and (9), they have a big advantage at the same time: They can be derived from  $\cos(u)$ ,  $\sin(u)$  by well-known trigonometric formulas, and the latter quantities are computed on the side if an update is due by the transform of the state of the spacecraft in cartesian coordinates into osculating Kepler elements without the necessity of actually invoking trigonometric functions.

It is also clear that the filter algorithm has to work in a revolution-wise interleaving manner: For the removal of the periodic part  $u_p(t)$ , we need at least an approximative value of the linear part  $\bar{u}(t)$ , and for the subsequent filtering of the linear part, the periodic terms have to be removed. This leads to a dedicated startup procedure, for during the first revolution, there is no preceding revolution interval. Here the drift term of the argument of latitude is set equal to the orbit frequency  $\sqrt{GM/r^3}$  of a circular orbit, only the second revolution uses the correct drift term, and consequently only during the second revolution the Fourier expansion coefficients of the periodic part are computed correctly. As these coefficients can be used only from the third revolution onwards, and allowing for a stabilizing period for the filter of the smoothed Kepler elements, it is clear that the whole algorithm needs at least three revolutions of the spacecraft to attain its maximal accuracy.

Figure 1 illustrates the transient part for an example LEO: After some five hours, the along-track error has shrunk from the order of several kilometres to several hundred metres. The above-mentioned startup procedure covers the first five instead of the first three revolutions in order to stay on the safe side.

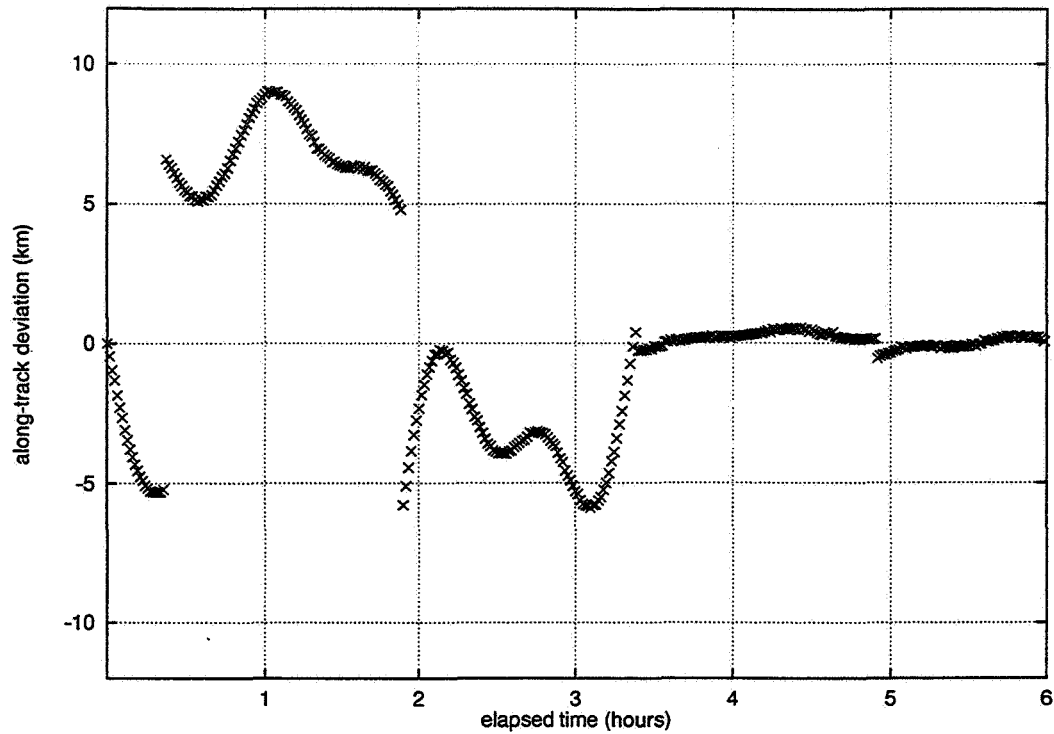


Figure 1 Example for the transient phase of the filter.

## FILTERING THE SMOOTHED ELEMENTS

The smoothed elements of equation (4) in theory are either constants, or they have a linear trend. They are separately modelled by linear stochastic systems whose state dimensions are either one or two.

Without going into details, we wish to make only two remarks:

Due to the small state dimension of the models for the individual elements of equation (4), and as the individual observation noise channels have been assumed to be mutually uncorrelated, the update equations of the filters are extremely simple; in case of the nominal constants  $\bar{a}$ ,  $\bar{\xi}$ ,  $\bar{\eta}$ ,  $\bar{i}$  they can be represented by trivial convex combinations of predicted and measured value.

The method of filtering chosen is described in the literature as *exponential age weighting*, also: *fading memory filter*<sup>5</sup> without system noise. Due to the stationary character of the filter involved however, only the constant filter feedback matrices explicitly appear in the update part of the filter algorithm, and these matrices have been designed as telecommand parameters. Thus the overall concept (classical Kalman, Kalman without system noise, fading memory filter etc.) the filtering equations are derived from has no effect on the explicit coding, as long as the filters are considered

stationary. After some real-world experience with the satellite in orbit, the filtering algorithm could be redesigned and the filter feedback matrices could be overloaded remotely by the ground segment.

## DIURNAL EFFECTS

It has already been mentioned in the introduction that linear drift terms and revolution-dependent perturbations do not explain all deviations from an ideal Kepler orbit. There are still the effects to consider that are periodic with the frequency of the Earth rotation. Figure 2 shows the along-track error between a simulated LEO satellite trajectory that is the output of a high-precision orbit integrator and its representation by our on-line estimator after the transient phase of Figure 1 with regular updates every 60 seconds between hours 12 through 48. Apart from residual contamination of orbit frequency we see an offset of some 400 m and a superimposed diurnal oscillation of some 600 m amplitude.

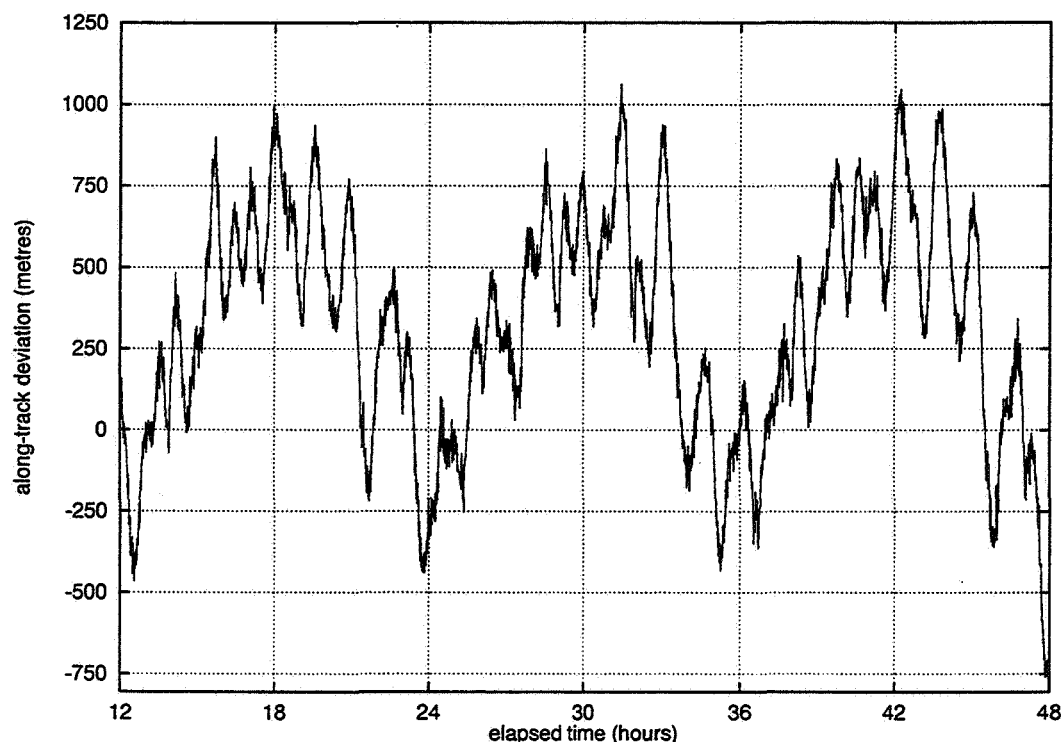


**Figure 2 Diurnal along-track deviations in steady-state.**

However, as those daily perturbations do mainly concern the along-track error and therefore, among all the elements of eq. (1), the argument of latitude  $u(t)$ , and as the revolution-dependent perturbations are known to have an amplitude of 20-30 km



at orbit altitudes between 350-450 km and thus surpass the observed diurnal effect by far, we choose to neglect it.

## AIRDRAG EFFECTS

Up to now, we have a kind of cascaded filter: First, the revolution-dependent terms are removed by Fourier techniques, then the remaining smoothed elements are treated with a steady-state Kalman filter. Diurnal effects are neglected.

If trial runs are conducted with simulated orbits that are the output of a high precision orbit integrator, then mainly the argument of latitude  $u(t)$  exhibits a runaway phenomenon if a data gap occurs and the orbit propagator is not updated: The difference between the true and the predicted value increases in a roughly quadratic manner, and the corresponding along-track error in a LEO environment may surpass 200 km within two to three days. The reason for this effect is the air drag which has not been accounted for.

Also affected is the semimajor axis  $a(t)$  of the spacecraft orbit, but not in such a pronounced manner, and the deviation is more like a linear shrinking.

A first and straightforward attempt to replace the linear model

$$\bar{u}(t) = \bar{u}_0 + \bar{u}_1 (t - t_0) \quad (11)$$

for the smoothed argument of latitude in the Kalman filter with a quadratic model

$$\bar{u}(t) = \bar{u}_0 + \bar{u}_1 (t - t_0) + \frac{1}{2} \bar{u}_2 (t - t_0)^2 \quad (12)$$

fails due to numerical reasons: Whereas  $\bar{u}_1$  is fairly large - in fact, it is roughly given by  $2\pi/90\text{min}^{-1} \approx 10^{-3}\text{s}^{-1}$  - it can be seen by a rule-of-thumb estimation from the perceived runaway phenomenon that  $\bar{u}_2$  is of a magnitude of  $10^{-12}\text{s}^{-1}$ . As the input  $\bar{u}$  of (9) into the Kalman filter is still contaminated with a residuum of imperfect removal of revolution-dependent terms and neglected daily effects,  $\bar{u}_2$  cannot be estimated in a reliable manner, with catastrophic consequences for an attempted prediction.

Thus, for the estimation of the airdrag correction, a brute-force method was chosen: Parallel with the actual filter for (11) which is updated with every incoming measurement (9), a second identical dummy filter runs whose state is periodically (e.g. once a week, this time parameter can be adjusted) reset to the state of the first filter, and which receives no update from measurements at all. From the difference between the actual filter and the dummy, the coefficient  $\bar{u}_2$  of (12) is estimated over the time span between two adjacent resets with a recursive least-squares procedure. Basically, the dummy filter conducts an attempted prediction over the latter time span neglecting the airdrag, and we simply look up the error we commit and count on it that this error varies only slightly over a few days.

With respect to the airdrag our method of parametrizing the orbit with regularized Kepler elements has one big advantage over other orbit propagation schemes that are

based on integrating the dynamic equations of the spacecraft in cartesian coordinates directly. Those dynamic equations are

$$\ddot{\mathbf{r}} = -\text{grad } U(t, \mathbf{r}) \quad (13)$$

where  $\mathbf{r}$  and  $\mathbf{v} = \dot{\mathbf{r}}$  are the three-dimensional vectors of position and velocity and  $U(t, \mathbf{r})$  is a model function for the gravity potential of the Earth. At a first glance, the latter treatment of (13) saves computer time, as no trigonometric functions have to be evaluated, contrary to our method. But, as the air drag mainly causes an along-track error that, roughly spoken, appears in the argument of latitude  $u$  alone, we have to correct only  $\bar{u}(t)$  in the simple manner indicated by eqs. (11), (12) without caring for the underlying physics. In (13) however, the neglect of air friction in cartesian coordinates does not affect only one, but all entries of the vectors  $\mathbf{r}$  and  $\mathbf{v}$  in a non-separable manner. Accounting for the airdrag in this framework furthermore means a tricky non-linear on-line estimation of a non-negative scaling parameter  $\gamma$  in the extended dynamical model

$$\ddot{\mathbf{r}} = -\text{grad } U(t, \mathbf{r}) - \gamma \|\mathbf{v}\| \mathbf{v} \quad (14)$$

whereas we can rely on linear theory alone as can be seen from eqs. (11), (12).

## SIMULATION STUDIES

Tests with simulated orbits generated by a high-precision orbit integrator indicate that a prediction accuracy of 10 to 20 km on the average over a dataless gap of one week at an orbit altitude between 300 to 460 km can be expected from an airdrag correction estimated from the data of the preceeding week. In one case, an along-track error of 80 km occurred. The outcome depends on the actual variability of the atmosphere—mainly influenced by solar and geomagnetic activity—during the time when no measurements are available.

Figure 3 shows the error for a 300 km altitude orbit produced by the filter for a slightly different setting where the air drag effect was estimated from data over two days rather than from a whole week. The coordinate system is the earth-fixed cartesian reference frame WGS84. During the first two days, the filter received a regular update of vehicle position and velocity at sampling intervals of 60 seconds. The following data gap of five days (i.e. no update at all) leads to a position error in every coordinate of 12 km at most for all three coordinate directions.

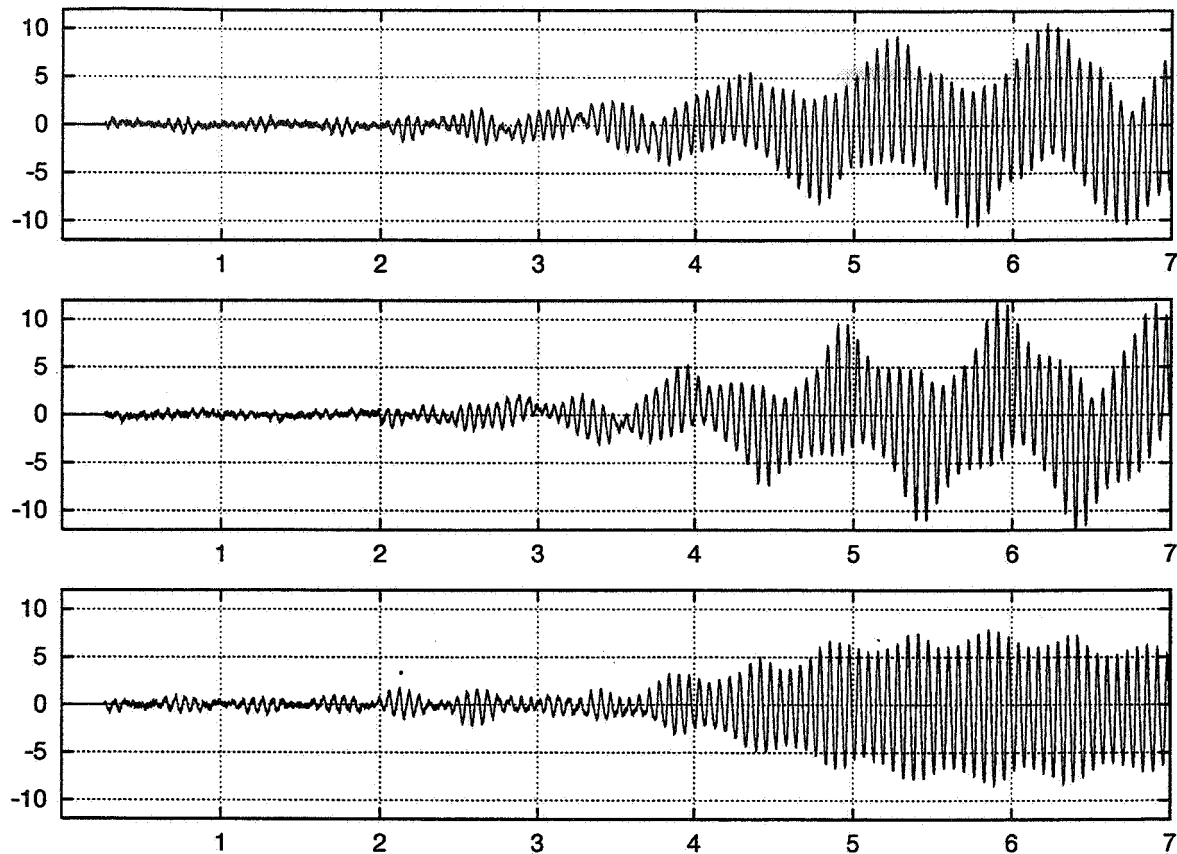


**Figure 3** Example orbit error for the three coordinate directions;  
abscissa: elapsed time in days, ordinate: deviation in km.

## CONCLUSION

The method for the off-line estimation of PRARE orbit elements on ground that has proved its reliability by being operational on two LEO satellites for years has been successfully transformed into an on-line on-board orbit propagator. The techniques employed as e.g. numerical Fourier expansion and Kalman filtering of constants and drift terms, are conservative, straightforward and robust. The use of regularized Kepler elements in the framework of semi-analytic orbit theory guarantees that the air drag effect is mainly restricted to the quadratic runoff of one orbit element alone. It can be taken care of by an extremely simple estimation procedure. The quality of orbit parameters obtained from a few (2 to 7) days with complete data coverage suffices to restrict the orbit error over a data gap of 5 to 7 days to some 10 to 20 km.

## REFERENCES

- 1 Reigber, Ch., Bock, R., Förste, Ch., Grunwaldt, L., Jakowski, N., Lühr, H., Schwintzer, P., Tilgner, C.: *CHAMP Phase B, Executive Summary*, Scientific Technical Report STR96/13, GeoForschungsZentrum Potsdam, 1996
- 2 W. M. Kaula *Theory of Satellite Geodesy*, Blaisdell Publishing Company, 1966
- 3 R. König, *Predictions for ERS-1*, in: Veillet, C., 7th International Workshop on Laser Ranging Instrumentation, Matera 1989, pp.385-392, proceedings, Grasse 1989
- 4 F. Flechtner, S. Bedrich, F. H. Massmann, *PRARE/ERS-2: System Status and Results*, CSTG Bulletin 13, 1997, pp. 67-71
- 5 Peter S. Maybeck, *Stochastic Models, Estimation and Control*, Volume 2, Academic Press, 1982

528-13

169310

# ATTITUDE/ATTITUDE-RATE ESTIMATION FROM GPS DIFFERENTIAL PHASE MEASUREMENTS USING INTEGRATED-RATE PARAMETERS

Yaakov Oshman\* and F. Landis Markley†

337569  
16P.

A sequential filtering algorithm is presented for attitude and attitude-rate estimation from Global Positioning System (GPS) differential carrier phase measurements. A third-order, minimal-parameter method for solving the attitude matrix kinematic equation is used to parameterize the filter's state, which renders the resulting estimator computationally efficient. Borrowing from tracking theory concepts, the angular acceleration is modeled as an exponentially autocorrelated stochastic process, thus avoiding the use of the uncertain spacecraft dynamic model. The new formulation facilitates the use of aiding vector observations in a unified filtering algorithm, which can enhance the method's robustness and accuracy. Numerical examples are used to demonstrate the performance of the method.

## INTRODUCTION

Attitude determination methods using Global Positioning System (GPS) signals have been intensively investigated in recent years. In general, these methods can be classified into two main classes. Point estimation algorithms (also called "deterministic" algorithms), in which the GPS measurements at each time point are utilized to obtain an attitude solution independently of the solutions at other time points, were introduced, among others, in Refs. 1, 2 and 3. Stochastic filtering algorithms, which process the measurements sequentially and retain the information content of past measurements, can produce better attitude solutions by more effectively filtering the noisy measurements. Such algorithms were recently introduced in Refs. 4 and 5, both of which utilized extended Kalman filtering to sequentially estimate the attitude from GPS carrier phase difference measurements. Both attitude and attitude-rate were estimated, and the filters used the nonlinear Euler equations of motion for attitude propagation. While avoiding the traditional usage of the costly and unreliable gyro package, this approach rendered the resulting filters computationally burdensome and sensitive to inevitable modeling errors.<sup>6</sup> In Ref. 4 an attempt was made to robustify the dynamics-based filter by estimating the unknown disturbance torques, modeled as unknown constants.

Although GPS-based attitude estimation methods should enjoy, in principle, the low price and low power consumption of state-of-the-art GPS receivers, and the general availability and robustness of the global positioning system, these methods are very sensitive to multipath effects and to the geometry of the antennae baseline configuration, and they inherently rely on precise knowledge of the antennae baselines in the spacecraft body frame. On the other hand, methods based on

\*National Research Council Research Associate, NASA/Goddard Space Flight Center, Guidance, Navigation and Control Center/Code 571, Greenbelt, MD 20771; currently on sabbatical from Department of Aerospace Engineering, Technion - Israel Institute of Technology, Haifa 32000, Israel. Email: [oshman@tx.technion.ac.il](mailto:oshman@tx.technion.ac.il).

†Staff Engineer, NASA/Goddard Space Flight Center, Guidance, Navigation and Control Center/Code 571, Greenbelt, MD 20771. Email: [landis.markley@gsfc.nasa.gov](mailto:landis.markley@gsfc.nasa.gov).

vector observations have reached maturity and popularity in the last three decades. However, as is well known, they too suffer from disadvantages, that can be attributed to the particular attitude sensors on which they are based. Thus, while their readings are relatively noiseless, Sun sensors are very sensitive to Earth radiation effects, and are rendered completely useless during Eclipse. Star trackers can provide accuracy on the order of a few arc-sec, but are usually extremely expensive. Magnetometers always provide measurements of the Earth magnetic field in spacecraft flying in low Earth orbits, but they are sensitive to unmodeled residual magnetic fields in the spacecraft and to magnetic field model imperfections and variations.

The method presented herein is a sequential estimator for both the spacecraft attitude matrix and attitude-rate, which mainly uses differential GPS carrier phase measurements, but can also process aiding vector observations (such as low accuracy coarse Sun sensor measurements, or magnetic field measurements). Conceptually similar to the principle of complementary filtering, the idea underlying this estimator is that, due to the different nature of these signals, the combination of both in a unified data processing algorithm can benefit from the relative advantages of both sensor systems, while alleviating the disadvantages of both.

The new estimator is based on a third-order minimal-parameter method for solving the attitude matrix evolution equation using integrated-rate parameters (IRP).<sup>7</sup> Similarly to Refs. 5 and 4, the new estimator is a sequential filtering algorithm and not a deterministic (point estimation) algorithm. However, the new algorithm differs from other works addressing the same problem in two main respects. First, the estimator's propagation model does not utilize the nonlinear Euler equations. Instead, employing an approach borrowed from linear tracking theory,<sup>8</sup> the uncertain dynamic model of the spacecraft is abandoned, and the angular acceleration is modeled as a zero-mean stochastic process with exponential autocorrelation. Combined with the extremely simple evolution equation of the integrated-rate parameters, this results in a simple, linear propagation model. Second, in contrast with other methods relying mainly on the attitude quaternion, the algorithm presented herein directly estimates the attitude matrix, a natural, nonsingular attitude representation. Building upon the minimal, third-order integrated-rate parametrization, the new estimator assigns just three state variables for the parametrization of the nine-parameter attitude matrix, which is at the heart of its computational efficiency.

## INTEGRATED-RATE PARAMETERS

Consider the matrix differential equation

$$\dot{V}(t) = W(t)V(t), \quad V(t_0) = V_0 \quad (1)$$

where  $V(t) \in \mathbb{R}^{n,n}$ ,  $W(t) = -W^T(t)$  for all  $t \geq t_0$ ,  $V_0 V_0^T = I$  and the overdot indicates the temporal derivative. Defining

$$A(t, t_0) \triangleq \int_{t_0}^t W(\tau) d\tau \quad (2)$$

$$\bar{W}_0(t) \triangleq W(t) - (t - t_0)\dot{W}(t) \quad (3)$$

it can be shown that the following matrix-valued function is a third-order approximation of  $V(t)$ :

$$\tilde{V}(t, t_0) \triangleq \left\{ I + A(t, t_0) + \frac{A^2(t, t_0)}{2!} + \frac{A^3(t, t_0)}{3!} + \frac{t - t_0}{3!} [A(t, t_0)\bar{W}_0(t) - \bar{W}_0(t)A(t, t_0)] \right\} V_0 \quad (4)$$

Moreover,  $\tilde{V}$  is a third-order approximation of an orthogonal matrix, i.e.,  $\tilde{V}(t, t_0)\tilde{V}^T(t, t_0) = I + \mathcal{O}((t - t_0)^4)$  where  $\mathcal{O}(x)$  denotes a function of  $x$  that has the property that  $\mathcal{O}(x)/x$  is bounded as  $x \rightarrow 0$ .

In the 3-D case, the off-diagonal entries of  $A(t, t_0)$ , termed integrated-rate parameters, have a simple geometric interpretation: they are the angles resulting from a temporal-integration of the

three components of the angular velocity vector  $\omega(t) \triangleq [\omega_1(t) \ \omega_2(t) \ \omega_3(t)]^T$ , where  $\omega_i$  is the angular velocity component along the  $i$ -axis of the initial coordinate system, and  $i = 1, 2, 3$  for  $x, y, z$ , respectively. The orthogonal matrix differential equation (1) is rewritten, in this case, as

$$\dot{D}(t) = \Omega(t)D(t), \quad D(t_0) = D_0 \quad (5)$$

where  $D(t)$  is the attitude matrix, or the direction cosine matrix (DCM),  $\Omega(t) = -[\omega(t) \times]$ , and  $[\omega(t) \times]$  is the usual *cross product matrix* corresponding to  $\omega(t)$ . In this case, the matrix  $A(t, t_0)$  takes the form

$$A(t, t_0) \triangleq -[\theta(t) \times] \quad (6)$$

where the parameter vector  $\theta(t)$  is defined as

$$\theta(t) \triangleq [\theta_1(t) \ \theta_2(t) \ \theta_3(t)]^T \quad (7)$$

and

$$\theta_i(t) \triangleq \int_{t_0}^t \omega_i(\tau) d\tau, \quad i = 1, 2, 3 \quad (8)$$

Let the sampling period be denoted by  $T \triangleq t_{k+1} - t_k$ . Using the notation  $\theta(k) \triangleq \theta(t_k)$ , the parameter vector at time  $t_k$  is  $\theta(k) = [\theta_1(k) \ \theta_2(k) \ \theta_3(k)]^T$  and Eq. (8) implies

$$\theta_i(k) = \int_{t_0}^{t_k} \omega_i(\tau) d\tau, \quad i = 1, 2, 3 \quad (9)$$

From Eq. (9) we have

$$\theta(k+1) = \theta(k) + \int_{t_k}^{t_{k+1}} \omega(\tau) d\tau \quad (10)$$

Define  $A(k+1, k)$  to be the discrete-time analog of  $A(t, t_0)$ , i.e.,

$$A(k+1, k) \triangleq -[(\theta(k+1) - \theta(k)) \times] \quad (11)$$

Also, let  $\Psi(k+1) \triangleq -[\psi(k+1) \times]$ , where

$$\psi(k+1) \triangleq \omega(k+1) - \dot{\omega}(k+1)T \quad (12)$$

Then, the corresponding discrete-time equivalent of Eq. (4) is

$$\begin{aligned} D(k+1) = & \left\{ I + A(k+1, k) + \frac{1}{2}A^2(k+1, k) + \frac{1}{6}A^3(k+1, k) \right. \\ & \left. + \frac{1}{6}T[A(k+1, k)\Psi(k+1) - \Psi(k+1)A(k+1, k)] \right\} D(k) \end{aligned} \quad (13)$$

which, using Eqs. (11) and (12), can be written as

$$D(k+1) = D[\theta(k+1) - \theta(k), \omega(k+1), \dot{\omega}(k+1), D(k)] \quad (14)$$

## KINEMATIC MOTION MODEL

To avoid using the uncertain spacecraft dynamic model, the spacecraft angular acceleration is modeled as a zero-mean stochastic process with exponential autocorrelation function. The acceleration dynamic model is, therefore, the following first-order Markov process,

$$\ddot{\omega}(t) = -\Lambda\dot{\omega}(t) + \tilde{v}(t) \quad (15)$$

For simplicity, a decoupled kinematic model is chosen for the three angular rate components, i.e.,  $\Lambda \triangleq \text{diag}\{\tau_1^{-1}, \tau_2^{-1}, \tau_3^{-1}\}$ , where  $\{\tau_i\}_{i=1}^3$  are the acceleration decorrelation times associated with the corresponding body axes. The driving noise is a zero-mean white process, with power spectral density (PSD) matrix

$$\tilde{Q}(t) = 2\Lambda\Sigma^2, \quad \Sigma \triangleq \text{diag}\{\sigma_1, \sigma_2, \sigma_3\} \quad (16)$$

The noise variances in Eq. (16) were chosen according to the Singer angular acceleration probabilistic model,<sup>8</sup> in which the angular acceleration components,  $\{\dot{\omega}_i\}_{i=1}^3$ , can be 1) equal to  $\dot{\omega}_{Mi}$  with probability  $p_{Mi}$ , 2) equal to  $-\dot{\omega}_{Mi}$  with probability  $p_{Mi}$ , 3) equal to zero with probability  $p_{0i}$ , or 4) uniformly distributed over the interval  $[-\dot{\omega}_{Mi}, \dot{\omega}_{Mi}]$  with the remaining probability mass. Using this model, it follows that

$$\sigma_i^2 = \frac{\dot{\omega}_{Mi}^2}{3}(1 + 4p_{Mi} - p_{0i}) \quad (17)$$

The parameters  $\dot{\omega}_{Mi}$ ,  $p_{Mi}$  and  $p_{0i}$  are considered as filter tuning parameters. As customarily done, they are selected by experience with real and simulated data, so as to optimally adapt the filter to the characteristics of the problem at hand.

Now let the system's state vector be defined as  $x(t) \triangleq [\theta^T(t) \ \omega^T(t) \ \dot{\omega}^T(t)]^T$ , then the state equation is

$$\dot{x}(t) = Fx(t) + \tilde{v}(t) \equiv \begin{bmatrix} 0 & I & 0 \\ 0 & 0 & I \\ 0 & 0 & -\Lambda \end{bmatrix} x(t) + \begin{bmatrix} 0 \\ 0 \\ \tilde{v}(t) \end{bmatrix} \quad (18)$$

with obvious definitions of  $F$  and  $\tilde{v}(t)$ . Corresponding to the sampling interval  $T$ , the discrete-time state equation is

$$x(k+1) = \Phi(T)x(k) + v(k) \quad (19)$$

where the transition matrix is

$$\Phi(T) \equiv e^{FT} = \begin{bmatrix} I & TI & \Lambda^{-2}(e^{-\Lambda T} - I + T\Lambda) \\ 0 & I & \Lambda^{-1}(I - e^{-\Lambda T}) \\ 0 & 0 & e^{-\Lambda T} \end{bmatrix} \quad (20)$$

and  $v(k)$  is a zero-mean, white noise sequence, with covariance matrix

$$Q(k) \triangleq E\{v(k)v^T(k)\} = \int_0^T e^{F(T-t)} \text{diag}\{0, 0, \tilde{Q}(t)\} e^{F^T(T-t)} dt \quad (21)$$

## MEASUREMENT PROCESSING

### GPS Differential Phase Measurements

Consider the basic GPS antenna array, depicted in Fig. 1. The array consists of the master antenna,



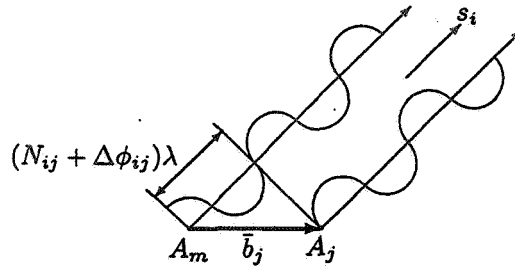


Figure 1. GPS Phase Difference Measurement Geometry

$A_m$ , and the slave antenna,  $A_j$ . These antennas are located on the satellite's surface, such that the baseline vector between them, resolved in a body-fixed coordinate system, is  $\bar{b}_j$ . It is assumed that the entire system consists of  $m_b$  antennas, in addition to the master antenna, so that there exist  $m_b$  independent baselines. It is also assumed that at time  $t_{k+1}$ ,  $m_s$  GPS satellites are in view.

Consider the  $i$ th satellite, and denote the sightline (unit) direction vector to that satellite, resolved in an inertial coordinate system, by  $s_i$ . Let  $D(k+1)$  be the attitude matrix transforming vectors in the inertial coordinate system to their body-fixed system representations at time  $t_{k+1}$ . Let  $N_{ij}(k+1)$  and  $\Delta\phi_{ij}(k+1)$  denote the integer and fractional parts, respectively, of the phase difference between the two carrier signals, corresponding to the  $i$ th satellite, as acquired by the antennas  $A_m$  and  $A_j$ . Denoting by  $\lambda$  the GPS carrier wavelength, the true (noiseless) signals satisfy

$$[\Delta\phi_{ij}(k+1) + N_{ij}(k+1)]\lambda = \bar{b}_j^T D(k+1)s_i \quad (22)$$

The standard GPS carrier wavelength is 19.03 cm. In this work, it is assumed that the integer part of the phase difference between the two receivers is known from a previous solution.<sup>1,9</sup>

In practice, the phase measurements will be contaminated by noise, the primary source of which is due to the multipath effect.<sup>1</sup> Denoting the noise corresponding to the baseline  $\bar{b}_j$  and the sightline  $s_i$  by  $\tilde{n}_{ij}(k+1)$ , the real measurement equation is

$$[\Delta\phi_{ij}(k+1) + N_{ij}(k+1)]\lambda = \bar{b}_j^T D(k+1)s_i + \tilde{n}_{ij}(k+1) \quad (23)$$

where it is assumed that  $\tilde{n}_{ij}(k+1) \sim \mathcal{N}(0, \tilde{\sigma}_{ij}^2(k+1))$ . Typically it can be assumed that the noise standard deviation is on the order of 5 mm.<sup>1</sup> From Eq. (23) we obtain the normalized measurement equation

$$\Delta\phi_{ij}(k+1) + N_{ij}(k+1) = b_j^T D(k+1)s_i + n_{ij}(k+1) \quad (24)$$

where we have defined  $b_j \triangleq \bar{b}_j/\lambda$  and  $n_{ij}(k+1) \triangleq \tilde{n}_{ij}(k+1)/\lambda$ . The normalized measurement noise satisfies  $n_{ij}(k+1) \sim \mathcal{N}(0, \sigma_{ij}^2(k+1))$ , where  $\sigma_{ij}(k+1) = \tilde{\sigma}_{ij}(k+1)/\lambda$ .

### GPS Measurement Linearization

At  $t_{k+1}$  the minimum mean square error (MMSE) predicted vector is  $\hat{x}(k+1|k)$ , and its corresponding prediction error covariance matrix is  $P(k+1|k) \triangleq E\{\tilde{x}(k+1|k)\tilde{x}^T(k+1|k)\}$ , where the estimation error is  $\tilde{x}(j|k) \triangleq x(j) - \hat{x}(j|k)$ . Using Eq. (14), Eq. (24) is rewritten as

$$N_{ij}(k+1) + \Delta\phi_{ij}(k+1) = b_j^T D[\theta(k+1) - \theta(k), \omega(k+1), \dot{\omega}(k+1), D(k)]s_i + n_{ij}(k+1) \quad (25)$$

Next, we linearize the nonlinear measurement equation (25) about the most recent estimate at  $t_{k+1}$ , i.e.,

$$x(k+1) = \hat{x}(k+1|k) + \delta x(k+1) \equiv \begin{bmatrix} \hat{\theta}(k+1|k) \\ \hat{\omega}(k+1|k) \\ \hat{\dot{\omega}}(k+1|k) \end{bmatrix} + \begin{bmatrix} \delta\theta(k+1) \\ \delta\omega(k+1) \\ \delta\dot{\omega}(k+1) \end{bmatrix} \quad (26)$$

where  $\delta\theta(k+1)$ ,  $\delta\omega(k+1)$  and  $\delta\dot{\omega}(k+1)$  are the perturbations of the state components about the nominal (i.e., predicted) state. Let  $\hat{D}^*(k|k)$  denote the a posteriori, *orthogonalized* estimate of the attitude matrix at time  $t_k$ , to be discussed in the next section. Using now the most recent estimates for  $D(k)$  and  $x(k)$ , namely  $\hat{D}^*(k|k)$  and  $\hat{x}(k|k)$ , respectively, in Eq. (25), it follows that

$$\Delta\phi_{ij}(k+1) + N_{ij}(k+1) = b_j^T D[\hat{\theta}(k+1|k) + \delta\theta(k+1) - \hat{\theta}(k|k), \hat{\omega}(k+1|k) + \delta\omega(k+1), \hat{\dot{\omega}}(k+1|k) + \delta\dot{\omega}(k+1), \hat{D}^*(k|k)] s_i + n_{ij}(k+1) \quad (27)$$

As discussed in the sequel, the a posteriori IRP estimate is zeroed after each measurement update (due to full reset control of the IRP state). We will, therefore, use the reset value of the IRP estimate,  $\hat{\theta}^c(k|k) = 0$ , in Eq. (27). Now expand  $D$  about the nominal state using a first-order Taylor series expansion, i.e.,

$$\begin{aligned} & D[\hat{\theta}(k+1|k) + \delta\theta(k+1), \hat{\omega}(k+1|k) + \delta\omega(k+1), \hat{\dot{\omega}}(k+1|k) + \delta\dot{\omega}(k+1), \hat{D}^*(k|k)] \\ &= \hat{D}(k+1|k) + \sum_{i=1}^3 \frac{\partial D[\hat{\theta}(k+1|k), \hat{\omega}(k+1|k), \hat{\dot{\omega}}(k+1|k), \hat{D}^*(k|k)]}{\partial \theta_i} \Big|_{\hat{\theta}(k+1|k)} \delta\theta_i(k+1) \\ &+ \sum_{i=1}^3 \frac{\partial D[\hat{\theta}(k+1|k), \omega(k+1), \hat{\dot{\omega}}(k+1|k), \hat{D}^*(k|k)]}{\partial \omega_i} \Big|_{\hat{\omega}(k+1|k)} \delta\omega_i(k+1) \\ &+ \sum_{i=1}^3 \frac{\partial D[\hat{\theta}(k+1|k), \hat{\omega}(k+1|k), \dot{\omega}(k+1), \hat{D}^*(k|k)]}{\partial \dot{\omega}_i} \Big|_{\hat{\dot{\omega}}(k+1|k)} \delta\dot{\omega}_i(k+1) \end{aligned} \quad (28)$$

where  $(\bullet) \Big|_{\zeta}$  denotes ‘evaluated at  $\zeta$ ’ and  $\hat{D}(k+1|k) \triangleq D[\hat{\theta}(k+1|k), \hat{\omega}(k+1|k), \hat{\dot{\omega}}(k+1|k), \hat{D}^*(k|k)]$ . Differentiating Eq. (13), the sensitivity matrices appearing in Eq. (28) are computed as

$$\frac{\partial}{\partial \theta_i} D[\theta(k+1), \hat{\omega}(k+1|k), \hat{\dot{\omega}}(k+1|k), \hat{D}^*(k|k)] = G_i[\theta(k+1), \hat{\psi}(k+1|k)] \hat{D}^*(k|k) \quad (29a)$$

$$\frac{\partial}{\partial \omega_i} D[\hat{\theta}(k+1|k), \omega(k+1), \hat{\dot{\omega}}(k+1|k), \hat{D}^*(k|k)] = \frac{1}{6} T F_i[\hat{\theta}(k+1|k)] \hat{D}^*(k|k) \quad (29b)$$

$$\frac{\partial}{\partial \dot{\omega}_i} D[\hat{\theta}(k+1|k), \hat{\omega}(k+1|k), \dot{\omega}(k+1), \hat{D}^*(k|k)] = -\frac{1}{6} T^2 F_i[\hat{\theta}(k+1|k)] \hat{D}^*(k|k) \quad (29c)$$

for  $i = 1, 2, 3$ , where  $\hat{\psi}(k+1|k) \triangleq \hat{\omega}(k+1|k) - T\hat{\dot{\omega}}(k+1|k)$ , and

$$G_i(\theta, \psi) = \frac{1}{2}(\theta e_i^T + e_i \theta^T) - \theta_i I - (1 - \frac{1}{6} \|\theta\|^2)[e_i \times] + \frac{1}{6} T(\psi e_i^T - e_i \psi^T) + \frac{1}{3} \theta_i [\theta \times] \quad (30a)$$

$$F_i(\theta) = e_i \theta^T - \theta e_i^T \quad (30b)$$

where  $e_i$  is the unit vector on the  $i$ th axis,  $i = 1, 2, 3$ .

Using Eqs. (28), (29) and (30) in Eq. (27) yields

$$\Delta\phi_{ij}(k+1) + N_{ij}(k+1) - b_j^T \hat{D}(k+1|k) s_i = h_{ij}^T(k+1) \delta x(k+1) + n_{ij}(k+1) \quad (31)$$

where the observation vector  $h_{ij}(k+1) \in \mathbb{R}^9$  is defined as

$$h_{ij}(k+1) \equiv \begin{bmatrix} h_{\theta_{ij}}^T(k+1) & h_{\omega_{ij}}^T(k+1) & h_{\dot{\omega}_{ij}}^T(k+1) \end{bmatrix}^T \quad (32)$$

and the elements of the vectors  $h_{\theta_{ij}}(k+1) \in \mathbb{R}^3$ ,  $h_{\omega_{ij}}(k+1) \in \mathbb{R}^3$  and  $h_{\dot{\omega}_{ij}}(k+1) \in \mathbb{R}^3$  are

$$h_{\theta_{ij}p}(k+1) = b_j^T G_p [\hat{\theta}(k+1|k), \hat{\psi}(k+1|k)] \hat{D}^*(k|k) s_i, \quad p = 1, 2, 3 \quad (33a)$$

$$h_{\omega_{ij}p}(k+1) = \frac{1}{6} T b_j^T F_p [\hat{\theta}(k+1|k)] \hat{D}^*(k|k) s_i, \quad p = 1, 2, 3 \quad (33b)$$

$$h_{\dot{\omega}_{ij}p}(k+1) = -T h_{\omega_{ij}p}(k+1), \quad p = 1, 2, 3 \quad (33c)$$

Define now the *effective* GPS measurement to be

$$y_{ij}^\phi(k+1) \triangleq \Delta \phi_{ij}(k+1) + N_{ij} - b_j^T \hat{D}(k+1|k) s_i \quad (34)$$

Then, using this definition in Eq. (31) yields the following scalar measurement equation:

$$y_{ij}^\phi(k+1) = h_{ij}^T(k+1) \delta x(k+1) + n_{ij}(k+1) \quad (35)$$

For the  $m_b$  baselines and  $m_s$  sightlines, there exist  $m_s \times m_b$  scalar measurements like Eq. (35). We next aggregate all of these equations into a single vector equation, such that the measurement associated with the baseline  $b_j$  and sightline  $s_i$  corresponds to the  $p$ th component of the vector measurement equation, where  $p = (j-1)m_s + i$ . This yields

$$y^\phi(k+1) = H^\phi(k+1) \delta x(k+1) + n^\phi(k+1) \quad (36)$$

where the  $p$ th row of the matrix  $H^\phi(k+1)$  is  $h_{ij}^T(k+1)$ ,  $n^\phi(k+1) \sim \mathcal{N}(0, R^\phi(k+1))$ , and  $R^\phi(k+1)$  is a diagonal matrix whose diagonal elements are  $R_{pp}^\phi(k+1) = \sigma_{ij}^2$ .

## Vector Observation Aiding

If the sole source of attitude information is the GPS carrier phase signals, then Eq. (36) should serve as the basis for the development of the measurement update algorithm (in the next section). In the case that vector observations are available, this information structure needs to be augmented.

Assume that a new pair of corresponding noisy vector measurements is acquired at  $t_{k+1}$ . This pair consists of the *unit* vectors  $u(k+1)$  and  $v(k+1)$ , which represent the values of the same vector  $r(k+1)$ , as modeled in the reference coordinate system and measured in the body coordinate system, respectively. The direction-cosine matrix  $D(k+1)$  transforms the *true* vector representation  $u_0$  into its corresponding *true* representation  $v_0$  according to

$$v_0(k+1) = D(k+1) u_0(k+1) \quad (37)$$

Assuming no constraint on the measurement noise direction, the body-frame measured unit vector,  $v(k+1)$ , is related to the true vector according to

$$v(k+1) = \frac{v_0(k+1) + n'_v(k+1)}{\|v_0(k+1) + n'_v(k+1)\|} \quad (38)$$

where the white sensor measurement noise is  $n'_v(k+1) \sim \mathcal{N}(0, R'_v(k+1))$ . Since both  $v_0(k+1)$  and  $v(k+1)$  are unit vectors, it follows from Eq. (38) that

$$v(k+1) = v_0(k+1) + n_v(k+1) \quad (39)$$

where  $n_v(k+1) \triangleq \mathcal{P}_{v_0}^\perp(k+1)n'_v(k+1)$  and  $\mathcal{P}_{v_0}^\perp(k+1) \triangleq I - v_0(k+1)v_0^T(k+1)$ . To a good approximation, the effective measurement noise is a zero mean, white Gaussian sequence with covariance

$$R_v(k+1) = \mathcal{P}_{v_0}^\perp(k+1)R'_v(k+1)\mathcal{P}_{v_0}^\perp(k+1) \quad (40)$$

To account for non-ideal effects (e.g., star catalog errors), it is assumed that the modeled reference vector is related to the true vector according to

$$u(k+1) = u_0(k+1) + n_u(k+1) \quad (41)$$

where  $n_u \perp u_0$  is a zero mean, white Gaussian noise, that is uncorrelated with  $n_v$  and has a known covariance matrix  $R_u(k)$ .

### Vector Measurement Linearization

Using Eqs. (11), (12) and (13), Eq. (37) can be rewritten as

$$v_0(k+1) = D[\theta(k+1) - \theta(k), \omega(k+1), \dot{\omega}(k+1), D(k)]u_0(k+1) \quad (42)$$

Linearizing about the predicted estimates and using Eqs. (26), (39) and (41), it follows that

$$\begin{aligned} v(k+1) - n_v(k+1) &= D[\hat{\theta}(k+1|k) + \delta\theta(k+1), \hat{\omega}(k+1|k) + \delta\omega(k+1), \\ &\quad \hat{\dot{\omega}}(k+1|k) + \delta\dot{\omega}(k+1), \hat{D}^*(k|k)] [u(k+1) - n_u(k+1)] \end{aligned} \quad (43)$$

where the reset value of the IRP estimate,  $\hat{\theta}^c(k|k) = 0$ , has been used. Expanding  $D$  about the nominal state using the first-order Taylor series (28) yields

$$\begin{aligned} v(k+1) - \hat{D}(k+1|k)u(k+1) &= \sum_{i=1}^3 [G_i[\hat{\theta}(k+1|k), \hat{\psi}(k+1|k)]\delta\theta_i(k+1) \\ &\quad + \frac{1}{6}TF_i[\hat{\theta}(k+1|k)]\delta\omega_i(k+1) - \frac{1}{6}T^2F_i[\hat{\theta}(k+1|k)]\delta\dot{\omega}_i(k+1)]\hat{D}^*(k|k)u(k+1) \\ &\quad - \hat{D}(k+1|k)n_u(k+1) + n_v(k+1) = H^\nu(k+1)\delta x(k+1) - \hat{D}(k+1|k)n_u(k+1) + n_v(k+1) \end{aligned} \quad (44)$$

where the observation matrix  $H^\nu(k+1)$  is written in block matrix form as

$$H^\nu(k+1) \equiv \begin{bmatrix} H_1(k+1) & H_2(k+1) & H_3(k+1) \end{bmatrix} \in \mathbb{R}^{3,9} \quad (45)$$

and the columns of the submatrices  $H_i(k+1) \in \mathbb{R}^{3,3}$ ,  $i = 1, 2, 3$  are

$$H_{1j}(k+1) = G_j[\hat{\theta}(k+1|k), \hat{\psi}(k+1|k)]\hat{D}^*(k|k)u(k+1) \quad (46a)$$

$$H_{2j}(k+1) = \frac{1}{6}TF_j[\hat{\theta}(k+1|k)]\hat{D}^*(k|k)u(k+1) \quad (46b)$$

$$H_{3j}(k+1) = -TH_{2j}(k+1) \quad (46c)$$

for  $j = 1, 2, 3$ . Define now the *effective* measurement and measurement noise to be, respectively,

$$y^\nu(k+1) \triangleq v(k+1) - \hat{D}(k+1|k)u(k+1) \quad (47)$$

$$n^\nu(k+1) \triangleq n_v(k+1) - \hat{D}(k+1|k)n_u(k+1) \quad (48)$$

Then, using these definitions in Eq. (44) yields the following measurement equation:

$$y^\nu(k+1) = H^\nu(k+1)\delta x(k+1) + n^\nu(k+1) \quad (49)$$

where  $n^\nu(k+1) \sim \mathcal{N}(0, R^\nu(k+1))$  is the white measurement noise, and

$$R^\nu(k+1) \triangleq R_\nu(k+1) + \hat{D}(k+1|k)R_u(k+1)\hat{D}^T(k+1|k) \quad (50)$$

## Measurement Update

To process the measurements, define now

$$y \triangleq \begin{bmatrix} y^\phi \\ y^\nu \end{bmatrix}, \quad n \triangleq \begin{bmatrix} n^\phi \\ n^\nu \end{bmatrix} \quad (51)$$

where  $n \sim \mathcal{N}(0, R)$  and  $R \triangleq \text{diag}\{R^\phi, R^\nu\}$ . Since  $\delta x(k+1) = x(k+1) - \hat{x}(k+1|k) = \tilde{x}(k+1|k)$  and  $\hat{x}(k+1|k)$  is an unbiased, MMSE predictor, we have  $E\{\delta x(k+1)\} = E\{\tilde{x}(k+1|k)\} = 0$  and  $\text{cov}\{\delta x(k+1)\} = \text{cov}\{\tilde{x}(k+1|k)\} = P(k+1|k)$ , thus  $\delta x(k+1) \sim \mathcal{N}(0, P(k+1|k))$ . Using the linearized measurement equation and the statistical properties of the measurement and prediction errors, the MMSE estimator of  $\delta x(k+1)$  is

$$\widehat{\delta x}(k+1|k+1) = K(k+1)y(k+1) \quad (52)$$

where  $K(k+1)$ , the estimator gain matrix, is computed as

$$K(k+1) = P(k+1|k)H^T(k+1)[H(k+1)P(k+1|k)H^T(k+1) + R(k+1)]^{-1} \quad (53)$$

Also,  $\widehat{\delta x}(k+1|k+1) = \hat{x}(k+1|k+1) - \hat{x}(k+1|k)$  which, used in Eq. (52), yields the state measurement update equation

$$\hat{x}(k+1|k+1) = \hat{x}(k+1|k) + K(k+1)y(k+1) \quad (54)$$

Subtracting  $x(k+1)$  from both sides of the last equation yields

$$\tilde{x}(k+1|k+1) = [I - K(k+1)H(k+1)]\tilde{x}(k+1|k) - K(k+1)n(k+1) \quad (55)$$

from which the resulting covariance update equation is

$$P(k+1|k+1) = [I - K(k+1)H(k+1)]P(k+1|k)[I - K(k+1)H(k+1)]^T + K(k+1)R(k+1)K^T(k+1) \quad (56)$$

where the filtering error covariance is  $P(k+1|k+1) \triangleq E\{\tilde{x}(k+1|k+1)\tilde{x}^T(k+1|k+1)\}$ .

To compute the measurement-updated attitude matrix at time  $t_{k+1}$ , we use the most recent estimate  $\hat{x}(k+1|k+1)$  and the estimated attitude matrix corresponding to time  $t_k$  in Eq. (13). This yields

$$\begin{aligned} \hat{D}(k+1|k+1) = & \left\{ I + \hat{A}(k+1, k) + \frac{1}{2}\hat{A}^2(k+1, k) + \frac{1}{6}\hat{A}^3(k+1, k) \right. \\ & \left. + \frac{1}{6}T[\hat{A}(k+1, k)\hat{\Psi}(k+1|k+1) - \hat{\Psi}(k+1|k+1)\hat{A}(k+1, k)] \right\} \hat{D}^*(k|k) \end{aligned} \quad (57)$$

where the *a posteriori* estimates of  $A(k+1, k)$  and  $\Psi(k+1)$  are defined, respectively, as

$$\hat{A}(k+1, k) \triangleq -[\hat{\theta}(k+1|k+1) \times], \quad \hat{\Psi}(k+1|k+1) \triangleq -[\hat{\psi}(k+1|k+1) \times] \quad (58)$$

where  $\hat{\psi}(k+1|k+1) \triangleq \hat{\omega}(k+1|k+1) - T\hat{\omega}(k+1|k+1)$ , and  $\hat{D}^*(k|k)$  is the *a posteriori*, *orthogonalized* estimate of the attitude matrix at time  $t_k$ , to be discussed in the next section.

Finally, since the *a posteriori* attitude matrix,  $\hat{D}(k+1|k+1)$ , is computed based on the *a posteriori* estimate,  $\hat{\theta}(k+1|k+1)$ , this implies a full *reset control* of the parameter vector, i.e.,  $\theta^c(k+1) = \theta(k+1) - \hat{\theta}(k+1|k+1)$ , where  $\theta^c(k+1)$  is the *reset state vector* at  $t_{k+1}$ , and a corresponding reset of the state estimate,  $\hat{\theta}^c(k+1|k+1) = 0$ , which is then used in the ensuing time propagation step. Since the reset control is applied to *both* the state vector and its estimate, no changes are necessary in the estimation error covariance matrix.

## ATTITUDE MATRIX ORTHOGONALIZATION

To improve the algorithm's accuracy and enhance its stability, an additional orthogonalization procedure is introduced into the estimator, following the measurement update stage. In this procedure, the orthogonal matrix closest to the filtered attitude matrix is computed.

Given the filtered attitude matrix  $\hat{D}(k+1|k+1)$ , the matrix orthogonalization problem is to find the matrix

$$\hat{D}^*(k+1|k+1) \triangleq \arg \min_{D \in \mathbb{R}^{3,3}} \left\| \hat{D}(k+1|k+1) - D \right\|, \quad \text{subject to} \quad D^T D = I \quad (59)$$

Being a special case of the orthogonal Procrustes problem, the matrix orthogonalization problem can be easily solved using the singular value decomposition (SVD). In cases where the excessive computational burden associated with the SVD might render its use prohibitive, e.g., in *real-time* attitude determination and control, the following approximate orthogonalization method, based on the iterative method introduced in Ref. 10, can be utilized:

$$\hat{D}^*(k+1|k+1) = N(k+1) \hat{D}(k+1|k+1) \quad (60)$$

where

$$N(k+1) \triangleq \frac{3}{2}I - \frac{1}{2}\hat{D}(k+1|k+1)\hat{D}^T(k+1|k+1) \quad (61)$$

*Remark 1.* Using an approach similar to that used in Ref. 11, it can be shown that, to first-order accuracy, the orthogonalization procedure does not affect the statistical properties of the estimator and, therefore, does not necessitate any adjustments in the algorithm.

## PREDICTION

In the prediction step at  $t_k$ , the reset *a posteriori* estimate at time  $t_k$ ,  $\hat{x}^c(k|k)$  (computed with the reset IRP estimate) and its corresponding error covariance matrix,  $P(k|k)$ , are propagated to time  $t_{k+1}$ .

Using Eq. (19), we have

$$\hat{x}(k+1|k) = \Phi(T)\hat{x}^c(k|k) \quad (62)$$

Using this result with Eq. (19) yields the covariance propagation equation

$$P(k+1|k) = \Phi(T)P(k|k)\Phi^T(T) + \Gamma(T)Q_f(k)\Gamma^T(T) \quad (63)$$

To propagate the attitude matrix to  $t_{k+1}$  we use the most recent IRP, attitude-rate and angular acceleration estimates, and the orthogonalized DCM estimate corresponding to  $t_k$ , in Eq. (13). This yields

$$\begin{aligned} \hat{D}(k+1|k) = & \left\{ I + \bar{A}(k+1, k) + \frac{1}{2}\bar{A}^2(k+1, k) + \frac{1}{6}\bar{A}^3(k+1, k) \right. \\ & \left. + \frac{1}{6}T \left[ \bar{A}(k+1, k)\hat{\Psi}(k+1|k) - \hat{\Psi}(k+1|k)\bar{A}(k+1, k) \right] \right\} \hat{D}^*(k|k) \end{aligned} \quad (64)$$

where the *a priori* estimates of  $A(k+1, k)$  and  $\Psi(k+1)$  are defined, respectively, as

$$\bar{A}(k+1, k) \triangleq -[\hat{\theta}(k+1|k) \times], \quad \hat{\Psi}(k+1|k) \triangleq -[\hat{\psi}(k+1|k) \times] \quad (65)$$

## NUMERICAL STUDY

### Example I

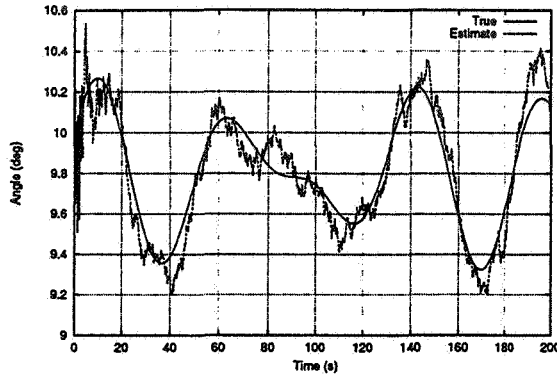
In this example, three non-orthogonal baselines were used:  $\bar{b}_1 = [1.0, 1.0, 0.0]^T$ ,  $\bar{b}_2 = [0.0, 1.0, 0.0]^T$ ,  $\bar{b}_3 = [0.0, 0.0, 1.0]^T$ . Two fixed sightlines were observed at all times,  $s_1 = \frac{1}{\sqrt{3}}[1.0, 1.0, 1.0]^T$  and  $s_2 = \frac{1}{\sqrt{2}}[0.0, 1.0, 1.0]^T$ . The non-normalized GPS signal noise standard deviation was 5.0 mm. When vector measurements were used, the noise equivalent angle of the inertially-referenced observations was set to 5.0 arc-s, while the body-referenced vector measurements were simulated to be acquired by a low accuracy attitude sensor with a noise equivalent angle of 0.1 deg. These measurements corresponded to a randomly selected vector, which was kept constant throughout the run.

The angular rates of the satellite satisfied  $\omega_i(t) = A_i \sin(\frac{2\pi}{T_i}t + \phi_i)$ , where  $A_i = 0.02, 0.05, 0.03$  deg/s,  $\phi_i = \pi/4, \pi/2, 3\pi/4$  rad, and  $T_i = 85, 45, 65$  s for  $i = 1, 2, 3$ , respectively. The initial angular rate estimates were all set to zero. The true initial attitude corresponded to Euler angles of 30 deg, 20 deg and 10 deg in roll, pitch and yaw, respectively, while the filter's initial state corresponded to Euler angles of 25 deg, 15 deg and 5 deg, respectively. The filter was run at a rate of 20 Hz, and the measurement processing rate was 10 Hz. The Singer angular acceleration model was used with parameters set to  $\tau = 10$  s,  $\dot{\omega}_M = 10^{-4}$  rad/s<sup>2</sup>,  $p_M = p_0 = .001$  for all three axes.

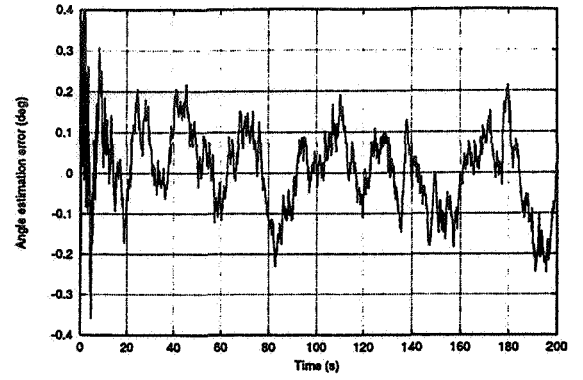
In Fig. 2, the true and estimated yaw angle time histories, and their corresponding estimation errors, are shown for a typical run, with and without vector measurement aiding. (The estimated yaw angle was computed using the estimated attitude matrix, assuming a 3-2-1 Euler angle sequence). Using only GPS measurements, the average yaw estimation error was  $7.15 \times 10^{-3}$  deg, with a standard deviation of 0.095 deg. When vector measurements were used in combination with the GPS signals, the average estimation error was  $9.87 \times 10^{-4}$  deg, and the estimation error standard deviation reduced to 0.022 deg. In Fig. 3, the third component of the angular velocity vector, its estimates and corresponding estimation errors are shown for the same run. Using GPS only measurements, the steady state estimation error standard deviation was 0.015 deg/s. When vector measurements were used in combination with the GPS signals, the estimation error standard deviation reduced to 0.0065 deg/s (the average rate estimation errors were on the order of  $10^{-4}$  deg/s in both cases).

### Example II

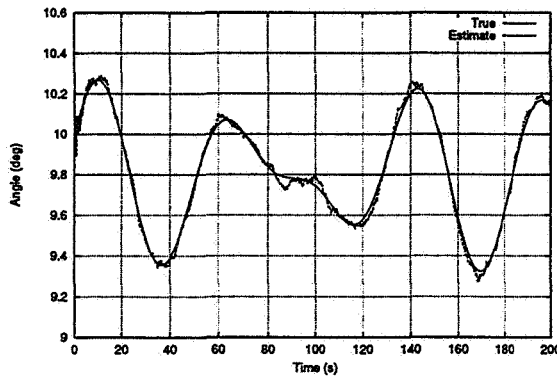
In this example, the same parameters were used as in Example I, except for the following. The three baselines used were now  $\bar{b}_1 = [0.1, 1.0, 0.1]^T$ ,  $\bar{b}_2 = [0.0, 1.0, 0.0]^T$ ,  $\bar{b}_3 = [0.0, 0.0, 1.0]^T$ . As can be observed, the first two baselines are almost colinear. The angular rates of the satellite were  $\omega = [0, 236, 0]^T$  deg/hr. The Singer angular acceleration model parameters were set to  $\tau = 10$  s,  $\dot{\omega}_M = 10^{-5}$  rad/s<sup>2</sup>,  $p_M = p_0 = .001$  for all three axes. As in the first example, vector measurements, when available, corresponded to a randomly selected, constant vector.



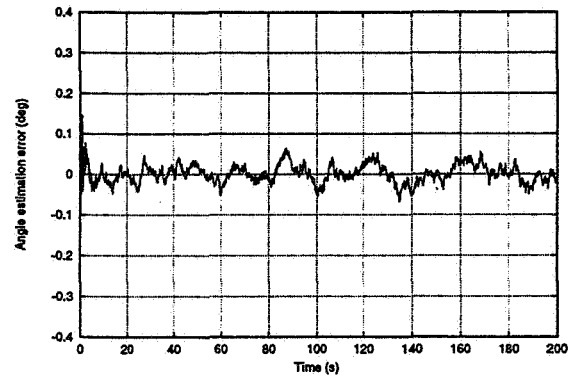
(a) Yaw angle



(b) Yaw angle estimation error



(c) Yaw angle

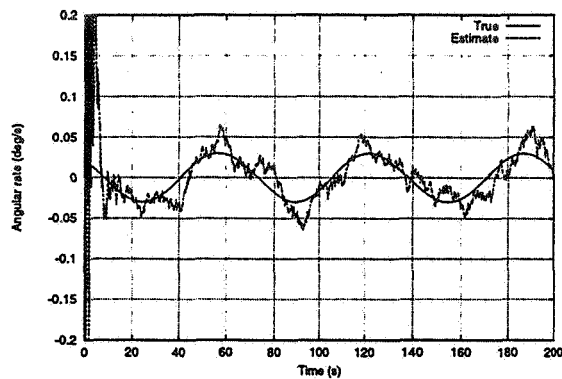


(d) Yaw angle estimation error

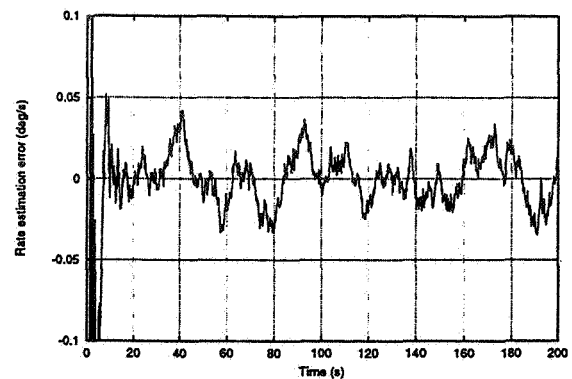
**Figure 2. Yaw Angle Estimation: (a) and (b) GPS Only Measurements, (c) and (d) With Vector Measurement Aiding.**

In Fig. 4, the true yaw angle time history is shown, along with the estimation error time histories corresponding to the cases where only GPS measurements were used and where vector observations were used along with the GPS measurements. (The estimated yaw angle was computed using the estimated attitude matrix, assuming a 3-2-1 Euler angle sequence). As can be observed from Fig. 4, the effect of aiding the GPS measurements with vector observations is very substantial in this ill-conditioned case. Using only GPS measurements, the average yaw angle steady-state estimation error in this run was  $7.72 \times 10^{-3}$  deg, with an estimation error standard deviation of 0.087 deg. When the GPS measurements were aided by vector measurements, the average Euler angle steady-state estimation error reduced to  $4.6 \times 10^{-3}$  deg, with an estimation error standard deviation of 0.022 deg. In Fig. 5, the estimation error of the third rate component is shown, with and without vector observation aiding. Using GPS only measurements, the steady-state rate estimation error standard deviation was  $9.34 \times 10^{-4}$  deg/s. When vector measurements were used in combination with the GPS signals, the standard deviation reduced to  $3.51 \times 10^{-4}$  deg/s (the average rate estimation error was on the order of  $10^{-5}$  deg/s in both cases).

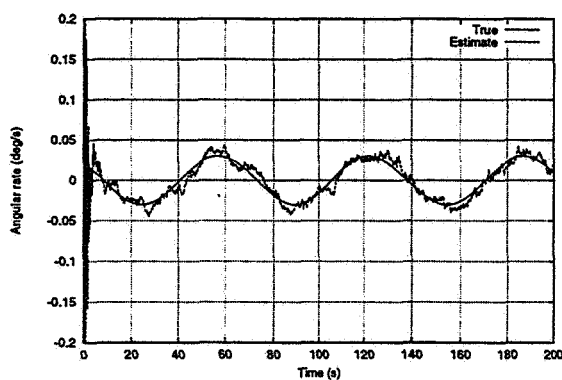




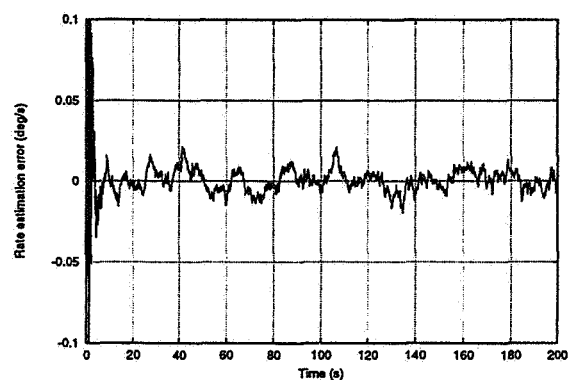
(a)  $\omega_3$



(b)  $\omega_3$  estimation error



(c)  $\omega_3$

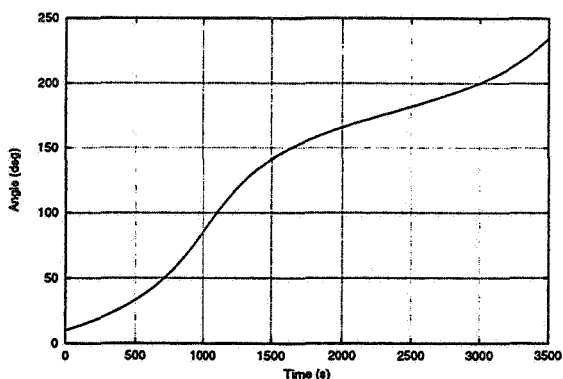


(d)  $\omega_3$  estimation error

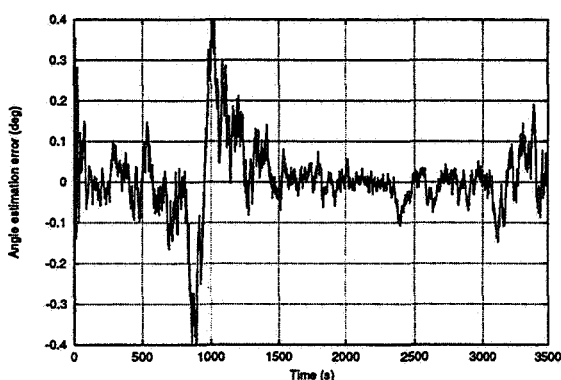
**Figure 3.  $\omega_3$  Estimation: (a) and (b) GPS Only Measurements, (c) and (d) With Vector Measurement Aiding.**

## CONCLUSIONS

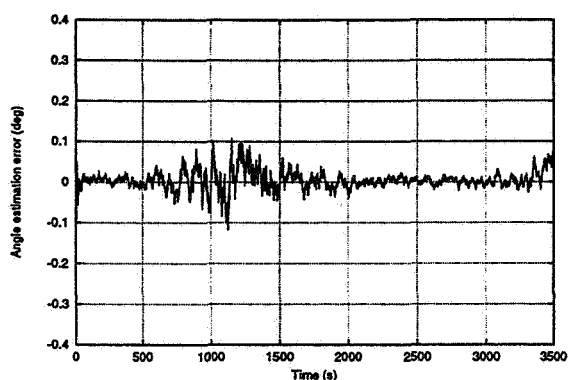
A nonlinear sequential estimator has been presented, that uses differential GPS carrier phase measurements to estimate both the attitude matrix and the angular velocity of a spacecraft. The algorithm is based on the IRP third-order minimal parametrization of the attitude matrix, which is at the heart of its computational efficiency. Avoiding the use of the typically uncertain (and frequently unknown) spacecraft dynamic model, the filter uses a polynomial state space model, in which the spacecraft angular acceleration is modeled as an exponentially autocorrelated stochastic process. When vector observations are available (e.g., from low accuracy Sun sensors or magnetometers), the estimator's structure can be easily modified to exploit this additional information and, thereby, significantly enhance the algorithm's robustness and accuracy. Numerical examples have been presented, that demonstrate the performance of the proposed algorithm and the advantages of aiding the GPS carrier phase signals with vector observations, even when the vector measurements are of relatively low accuracy.



(a) Yaw angle



(b) Yaw angle estimation error



(c) Yaw angle estimation error

**Figure 4. Yaw Angle Estimation: (a) True Angle, (b) GPS Only Measurements, (c) With Vector Measurement Aiding.**

## ACKNOWLEDGEMENT

This work was performed while the first author held a National Research Council—NASA Goddard Space Flight Center Research Associateship.

## REFERENCES

1. Cohen, C. E., "Attitude Determination," *Global Positioning System: Theory and Applications, Vol. II*, edited by B. W. Parkinson and J. J. Spilker, Progress in Astronautics and Aeronautics, AIAA, Washington, D.C., 1996.
2. Crassidis, J. L. and Markley, F. L., "Attitude Determination Using Global Positioning System Signals," *Proceedings of the AIAA Guidance, Navigation and Control Conference*, New Orleans, LA, Aug. 1997, pp. 23–31.

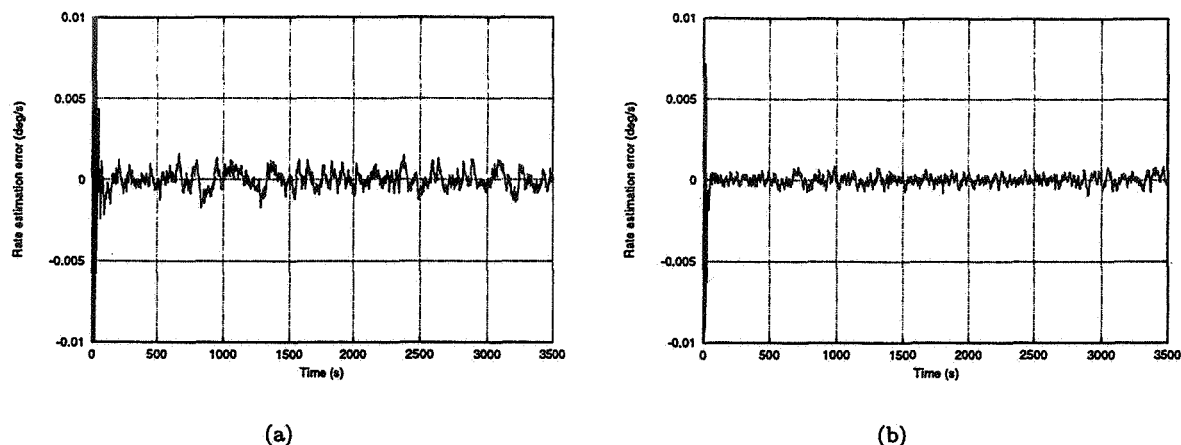


**Figure 5.  $\omega_3$  Estimation Error: (a) GPS Only Measurements, (b) With Vector Measurement Aiding.**

3. Bar-Itzhack, I. Y., Montgomery, P. Y., and Garrick, J. C., "Algorithms for Attitude Determination Using GPS," *Proceedings of the AIAA Guidance, Navigation and Control Conference*, New Orleans, LA, Aug. 1997, pp. 841-851.
4. Fujikawa, S. J. and Zimbelman, D. F., "Spacecraft Attitude Determination by Kalman Filtering of Global Positioning System Signals," *Journal of Guidance, Control, and Dynamics*, Vol. 18, No. 6, Nov.-Dec. 1995, pp. 1365-1371.
5. Axelrad, P. and Ward, L. M., "Spacecraft Attitude Estimation Using the Global Positioning System: Methodology and Results for RADCAL," *Journal of Guidance, Control, and Dynamics*, Vol. 19, No. 6, Nov.-Dec. 1996, pp. 1201-1209.
6. Lefferts, E. J. and Markley, F. L., "Dynamic Modeling for Attitude Determination," *Proceedings of the AIAA Guidance and Control Conference*, San Diego, California, Aug. 1976, Paper No. 76-1910.
7. Ronen, M. and Oshman, Y., "A Third-Order, Minimal-Parameter Solution of the Orthogonal Matrix Differential Equation," *Journal of Guidance, Control, and Dynamics*, Vol. 20, No. 3, May-June 1997, pp. 516-521.
8. Singer, R. A., "Estimating Optimal Tracking Filter Performance for Manned Maneuvering Targets," *IEEE Transactions on Aerospace and Electronic Systems*, Vol. AES-6, No. 4, Jul. 1970, pp. 473-483.
9. Crassidis, J. L., Markley, F. L., and Lightsey, E. G., "Optimal Integer Resolution for Attitude Determination Using Global Positioning System Signals," *Proceedings of the AAS/GSFC 13th International Symposium on Space Flight Dynamics*, NASA Goddard Space Flight Center, Greenbelt, MD, May 1998.
10. Bar-Itzhack, I. Y. and Meyer, J., "On the Convergence of Iterative Orthogonalization Processes," *IEEE Transactions on Aerospace and Electronic Systems*, Vol. AES-12, No. 2, Mar. 1976, pp. 146-151.
11. Oshman, Y. and Markley, F. L., "Minimal-Parameter Attitude Matrix Estimation from Vector Observations," *Proceedings of the AIAA Guidance, Navigation and Control Conference*, New Orleans, LA, Aug. 1997, pp. 12-22, AIAA Paper 97-3451.



## Improvements in Precise GPS Attitude Determination using Predetect Data, Gyro Data, and Redundant Antennas

Mark S. Asher  
 The Johns Hopkins University  
 Applied Physics Laboratory  
 Johns Hopkins Road  
 Laurel, MD 20723-6099  
 (410) 792-5327  
 asherms1@aplcomm.jhuapl.edu

529-13

AOS 0147

169311

337570

JP.

### ABSTRACT

The existing paradigm for GPS attitude determination is to track the signals in a conventional tracking loop and use the phase observables as input to the attitude determination process. The dominant error sources limiting the accuracy of this process are the differential phase pattern of the antennas and multipath. These error sources are essentially indistinguishable and currently limit the accuracy of the GPS attitude determination process to about 0.1 degree for a 1 m baseline. For higher accuracies one needs to include a high quality Inertial Measurement Unit for accelerating platforms or a star camera for space platforms. This paper describes improvements to GPS attitude determination which may make it competitive with star cameras down to the 0.01 degree level.

The essential elements of the technique are:

1. Use predetect GPS data to do the attitude estimation, instead of the output of a phase tracker.
2. Use redundant antennas to reject signals inconsistent with a plane wave arriving from infinity.
3. Take advantage of gyro data to reject the multipath signal on the basis of its temporal signature.

The main advantages of the approach are:

1. It tends to reject signals that are not plane waves and that do not have temporal signatures consistent with the direct path signal. Self-multipath signals are re-radiated from reflecting surfaces a few meters away and have significant curvature to their wave fronts. They also do not evolve in time the same way that the direct-path signal does.
2. It is robust since it does not depend on knowledge of the specific form of the multipath.

3. It is not restricted to space platforms, where the multipath is very repeatable and where vehicle motion is low. In fact, the relatively high angular motion of aircraft and terrestrial vehicles would tend to assist in rejection of multipath by the difference in temporal signature.

A practical for processing the predetect data which does not require the accumulation of large amounts of data is presented. The key to this technique is that the GPS spectrum is despread by using the local code and message data bits generated by an auxiliary conventional tracking loop tracking the same GPS satellite. The resultant (narrow band) signal is sampled at a low rate buffered and optimally combined with similar signals from the other antennas as well as the gyro data.

We present computer simulations of the new techniques in a scenario containing extremely strong multipath and examine the parameter sensitivities. It is shown that the use of predetect data can attenuate the multipath error by a factor of three or more. The total improvement from all of the techniques, redundant antennas and gyros, can be a factor of 10.

536-13  
169319

## OPTIMAL INTEGER RESOLUTION FOR ATTITUDE DETERMINATION USING GLOBAL POSITIONING SYSTEM SIGNALS

337571  
161

John L. Crassidis,\* F. Landis Markley,<sup>†</sup> E. Glenn Lightsey<sup>†</sup>

In this paper, a new motion-based algorithm for GPS integer ambiguity resolution is derived. The first step of this algorithm converts the reference sightline vectors into body frame vectors. This is accomplished by an optimal vectorized transformation of the phase difference measurements. The result of this transformation leads to the conversion of the integer ambiguities to vectorized biases. This essentially converts the problem to the familiar magnetometer-bias determination problem, for which an optimal and efficient solution exists. Also, the formulation in this paper is re-derived to provide a sequential estimate, so that a suitable stopping condition can be found during the vehicle motion. The advantages of the new algorithm include: it does not require an a-priori estimate of the vehicle's attitude; it provides an inherent integrity check using a covariance-type expression; and it can sequentially estimate the ambiguities during the vehicle motion. The only disadvantage of the new algorithm is that it requires at least three non-coplanar baselines. The performance of the new algorithm is tested on a dynamic hardware simulator.

### INTRODUCTION

The utilization of phase difference measurements from Global Positioning System (GPS) receivers provides a novel approach for three-axis attitude determination and/or estimation. These measurements have been successfully used to determine the attitude of air-based,<sup>1</sup> space-based,<sup>2-3</sup> and sea-based<sup>4</sup> vehicles. Since phase differences are used, the correct number of integer wavelengths between a given pair of antennas must be found. The determination of the integer ambiguities can either be accomplished by using "static" (motionless) or "dynamic" (motion-based) techniques. The ambiguities essentially act as integer biases to the phase difference measurements. Once the integer ambiguities are resolved, then the attitude determination problem can be solved.<sup>5</sup>

The static method finds a solution that minimizes the error residual at a specific time by searching through an exhaustive list of all possible integers and rejecting classes of

\* Assistant Professor. The Catholic University of America, Department of Mechanical Engineering, Washington, DC 20064.

<sup>†</sup> Engineer. NASA-Goddard Space Flight Center, Guidance, Navigation, and Control Center, Greenbelt, MD 20771.

solutions when the residual becomes too large.<sup>6</sup> Refinements can be made to the solution by restricting the search space with knowledge of a-priori information, such as the maximum tilt the baseline should encounter.<sup>7</sup> Static methods generally rely on solving a set of Diophantine equations.<sup>8</sup> The appeal of these methods is that they provide an “instantaneous” attitude solution, limited only by computation time, and are well suited for the short baselines. However, the minimum residual does not guarantee a correct solution in the presence of noise.<sup>1</sup> In fact, it is possible that static methods can report a wrong solution as valid, especially when some of the calibration information, such as line bias, is incorrect. This lack of integrity can cause significant problems if the sensor output is used to control a high bandwidth actuator, such as gas jets on a spacecraft. Another consideration is that static methods sometime require that the antenna array must be within a defined angle (typically 30 degrees) of a reference attitude, which is often true for ground-based applications, but is less likely for space-based applications. Also, structural flexibility in the baselines may lead to erroneous solutions. All of the aforementioned limitations imply that static methods, while attractive because of their fast solutions, are not totally acceptable for general purpose applications.

The other technique for resolving integer ambiguities involves collecting data for a given period of time and performing a batch solution, in which the integer terms remain constant over the collection period. This technique relies on the fact that a certain amount of motion has occurred during the data collection, either from vehicle body rotation or GPS line of sight motion. The main disadvantage of this technique, compared to static approaches, is that it takes time for the motion to occur, which may be on the order of several minutes. Another consideration is that a potentially significant amount of memory is required for the storage of the batch data collection. But, motion-based techniques also have significant advantages over static methods. Most importantly, motion-based techniques are inherently high integrity methods because there are numerous checks that can be implemented into the solution before it is accepted. These include using statistical checks applied to error residuals, matrix condition number checks, and using the closeness of the computed floating-point “integers” to actual integers as a check. The probability of an erroneous solution being reported as valid can be made as small as desired by appropriately setting the thresholds on these integrity checks. For these reasons, motion-based techniques have been more widely used for on-board applications.

Traditional motion-based techniques of integer ambiguity resolution rely on the fact that either GPS line of sight motion or vehicle motion dominates the changes in differential carrier phase measurements. Cohen<sup>9</sup> developed an algorithm, known as “quasi-static” integer resolution, that can be used when the GPS line of sight motion and the vehicle rotation both account approximately evenly for the differential carrier phase measurement changes. This algorithm can be adapted to almost any vehicle motion, slow or fast, simply by varying the sample rate and the data collection time. The quasi-static method solves a collection of differential phase measurements for a single attitude estimate and then considers perturbations to the initial estimate at each measurement epoch to produce a time varying batch solution to the data. Although this is a widely used algorithm, there are certain disadvantages. First, an a-priori attitude estimate must be



given. Second, the algorithm is an iterative batch estimator that may produce erroneous estimates, depending on the accuracy of the a-priori attitude estimate. Finally, if a large number of samples in the data collection are required to observe the motion, large-order matrix inversions may be required. Another method (Ref. 10) performs a minimization on three Euler-angle attitude parameters independent of each other, followed by determining the integers. This approach has been shown to provide better convergence than Cohen's method and works well for non-coplanar baselines; however, singular conditions can exist at various attitude rotations and a significant amount of vehicle motion may be necessary for a solution.

In this paper, a new motion-based algorithm is derived. The main advantages of the new algorithm over the prior methods include: (i) it resolves the integer ambiguities without any a-priori attitude knowledge, (ii) it requires less computational effort, since large matrix inverses are not needed, and (iii) it is non-iterative. The only disadvantage of the new algorithm is that it requires at least three non-coplanar baselines. The algorithm is first shown as a batch solution, and then shown as a sequential solution. A covariance expression is also derived which can be used to bound the integer solution so that a sufficient integrity check for convergence can be developed. This is extremely useful in the sequential formulation, since the solution can be found as the motion occurs, rather than taking a batch solution at a specific data collection interval. For these reasons, the new algorithm provides an attractive method for real-time ambiguity resolution.

The organization of this paper proceeds as follows. First, the concept of the GPS phase difference measurement is introduced. Then, a brief review of Cohen's quasi-static method is shown, and limitations and computational aspects of this algorithm are discussed. Next, the new motion-based algorithm is derived. The conversion of the GPS sightline vector into the body frame is first reviewed. Then, the batch solution used to resolve the integer ambiguities is derived, followed by the sequential solution. Finally, the new algorithm is validated by using an actual GPS receiver with a hybrid dynamic simulator to simulate the vehicle motions of a low-altitude Earth-orbiting spacecraft.

## GPS SENSOR MODEL

In this section, a brief background of the GPS phase difference measurement is shown. The main measurement used for attitude determination is the phase difference of the GPS signal received from two antennas separated by a baseline. The wavefront angle and wavelength are used to develop a phase difference, as shown in Figure 1. The phase difference measurement is obtained by

$$b_l \cos \theta = \lambda(\Delta\phi - n) \quad (1)$$

where  $b_l$  is the baseline length (in cm),  $\theta$  is the angle between the baseline and the line of sight to the GPS spacecraft,  $n$  is the number of integer wavelengths between two receivers,  $\Delta\phi$  is the phase difference (in cycles), and  $\lambda$  is the wavelength (in cm) of the GPS signal. The two GPS frequency carriers are L1 at 1575.42 MHz and L2 at 1227.6 MHz. As of this writing, non-military applications generally use the L1 frequency. The phase difference can be expressed by

$$\Delta\phi = \underline{b}^T \underline{A} \underline{s} + n \quad (2)$$

where  $\underline{s} \in R^3$  is the normalized line of sight vector to the GPS spacecraft in a reference frame,  $\underline{b} \in R^3$  is the baseline vector (in wavelengths), which is the relative position vector from one receiver to another, and  $A \in R^{3 \times 3}$  is the attitude matrix, which is an orthogonal matrix with determinant 1 (i.e.,  $A^T A = I_{3 \times 3}$ ). The measurement model is given by

$$\Delta\tilde{\phi}_{ij} = \underline{b}_i^T A \underline{s}_j + n_{ij} + w_{ij} \quad (3)$$

where  $\Delta\tilde{\phi}_{ij}$  denotes the phase difference measurement for the  $i^{\text{th}}$  baseline and  $j^{\text{th}}$  sightline, and  $w_{ij}$  represents a zero-mean Gaussian measurement error with standard deviation  $\sigma_{ij}$  which is  $0.5 \text{ cm}/\lambda = 0.026$  wavelengths for typical phase noise.<sup>9</sup>

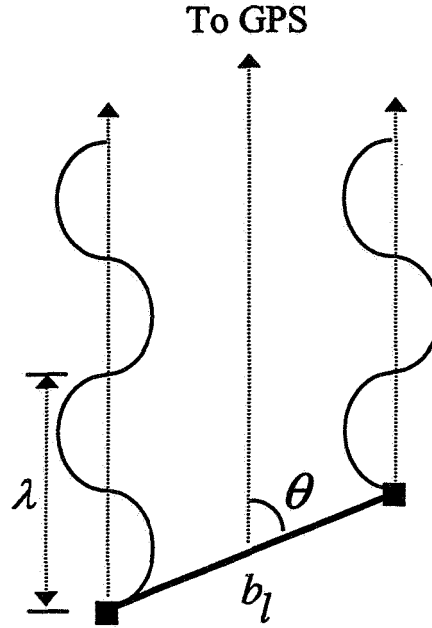


Figure 1 GPS Wavelength and Wavefront Angle

## QUASI-STATIC APPROACH

Cohen's quasi-static method<sup>9</sup> is a motion-based technique that begins by taking measurements for  $k = 1$  to  $L$  ("measurement epochs") to which a single attitude solution will be determined. At each epoch it is assumed that  $M$  baselines exist and  $N$  sightlines. The measurement model is linearized by assuming a small perturbation about a nominal attitude  $A_0$  and an assumed set of integer phases  $(n_0)_{ij}$ , so that

$$A = A_0(I_{3 \times 3} + [\underline{\delta\theta} \times]) \quad (4)$$

where  $I_{3 \times 3}$  is a  $3 \times 3$  identity matrix,  $\underline{\delta\theta}$  is assumed to be a small angle rotation, and  $[\underline{\delta\theta} \times]$  is a cross product matrix with

$$[\underline{a} \times] \equiv \begin{bmatrix} 0 & -a_3 & a_2 \\ a_3 & 0 & -a_1 \\ -a_2 & a_1 & 0 \end{bmatrix} \quad (5)$$

Substituting Equation (4) into Equation (3) for all available measurements yields

$$\begin{aligned} \underline{\delta\phi} = [\underline{\Delta\phi} - \underline{\Delta\phi}_0] &= \begin{bmatrix} \underline{s}_1^T A_0^T [\underline{b}_1 \times] \\ \vdots \\ \underline{s}_N^T A_0^T [\underline{b}_M \times] \end{bmatrix} \bar{I} \begin{bmatrix} \underline{\delta\theta} \\ \underline{\delta n} \end{bmatrix} \\ &\equiv [H \quad \bar{I}] \begin{bmatrix} \underline{\delta\theta} \\ \underline{\delta n} \end{bmatrix} \end{aligned} \quad (6)$$

where  $\bar{I}$  is a quasi-identity matrix with possible zeros along the diagonal where states have been removed at various measurement epochs, and

$$\underline{\Delta\phi} \equiv \begin{bmatrix} \Delta\phi_{11} \\ \vdots \\ \Delta\phi_{MN} \end{bmatrix}, \quad \underline{\delta n} \equiv \begin{bmatrix} (n-n_0)_{11} \\ \vdots \\ (n-n_0)_{MN} \end{bmatrix}, \quad (\Delta\phi_0)_{ij} = \underline{b}_i^T A_0 \underline{s}_j + (n_0)_{ij} \quad (7)$$

Equation (6) is a set of  $MN$  equations for  $(3+MN)$  states. Allowing perturbations at all epochs leads to

$$\begin{bmatrix} \underline{\delta\phi}(1) \\ \underline{\delta\phi}(2) \\ \vdots \\ \underline{\delta\phi}(L) \end{bmatrix} = \begin{bmatrix} H(1) & 0 & \dots & 0 & \bar{I}(1) \\ 0 & H(2) & \ddots & \vdots & \bar{I}(2) \\ \vdots & \ddots & \ddots & 0 & \vdots \\ 0 & \dots & 0 & H(L) & \bar{I}(L) \end{bmatrix} \begin{bmatrix} \underline{\delta\theta}(1) \\ \vdots \\ \underline{\delta\theta}(L) \\ \underline{\delta n} \end{bmatrix} \quad (8)$$

This compact representation has  $LMN$  rows and  $(3L+MN)$  states. In principle, the integers and the attitude of the vehicle at each measurement epoch may be found by applying an iterative linearized least-squares approach using Equation (8) and updating the nominal attitude using Equation (4).

The quasi-static method has been successfully implemented to resolve the integer ambiguities on an actual system (Ref. 1), and works extremely well when a fairly accurate a-priori attitude is known, and significant vehicle motion is present. However, this approach has a number of disadvantages. First, if the a-priori attitude estimate is poorly known, then the solution may never converge (even if the integers are known exactly). Second, not only does this algorithm require a good a-priori guess, but requires fairly accurate attitude estimates at all measurement times. The reason for this is that as time increases, the perturbations to the a-priori attitude guess may become too large for the solution to converge. This may be overcome by augmenting the state equations to include a constant, but unknown, body rate that is also estimated. Finally, a  $(3L+MN)$  matrix inverse is required, which may cause computational problems. Many of these

problems may be overcome by developing an algorithm that is independent of any attitude information.

## NEW ALGORITHM

In this section a new algorithm to resolve the integer ambiguities is shown. The main advantage of this algorithm is that it is attitude independent. First, a conversion of the sightline vectors into the body frame is shown. This converts the problem into the familiar magnetometer-bias problem. Then, a batch solution for this problem is shown, followed by a sequential approach.

The new algorithm begins by determining the sightline vector in the body frame, denoted by  $\tilde{\underline{s}} = A\underline{s}$ . This is accomplished by minimizing the following loss function<sup>11</sup>

$$J(\tilde{\underline{s}}_j) = \frac{1}{2} \sum_{i=1}^M \frac{1}{\omega_{ij}^2} (\Delta\tilde{\phi}_{ij} - n_{ij} - \underline{b}_i^T \tilde{\underline{s}}_j)^2 \quad \text{for } j = 1, 2, \dots, N \quad (9)$$

If at least three non-coplanar baselines exist, the minimization of Equation (9) is straightforward and leads to

$$\tilde{\underline{s}}_j = \hat{\underline{s}}_j - \underline{c}_j \quad (10a)$$

$$\hat{\underline{s}}_j = B_j^{-1} \left[ \sum_{i=1}^M \frac{1}{\omega_{ij}^2} \Delta\tilde{\phi}_{ij} \underline{b}_i \right] \quad (10b)$$

$$\underline{c}_j = B_j^{-1} \left[ \sum_{i=1}^M \frac{1}{\omega_{ij}^2} n_{ij} \underline{b}_i \right] \quad (10c)$$

$$B_j = \sum_{i=1}^M \frac{1}{\omega_{ij}^2} \underline{b}_i \underline{b}_i^T \quad (10d)$$

The computed sightline in the body frame is related to the sightline vector in the reference frame by

$$\hat{\underline{s}}_j = A\underline{s}_j + \underline{c}_j + \underline{\varepsilon}_j \quad (11)$$

where  $\underline{c}_j$  is a constant bias since the baselines are assumed constant, and  $\underline{\varepsilon}_j$  is a zero-mean Gaussian process with covariance  $R_j = B_j^{-1}$ . Again, the inverse in Equation (10) exists only if three non-coplanar baseline vectors exist.

The next step is to use an attitude-independent method to find the phase-bias vector  $\underline{c}_j$ . Doing this for each sightline gives us all the sightlines in both the body frame and the reference frame. The explicit integer phases are not needed for this solution, but it is important to check that they are close to integer values, as mentioned in the Introduction. In the general case, the explicit integer phases can be found from the attitude solution.

The three-baseline case ( $M = 3$ ) is simpler, for in this case Equation (10c) can be inverted to give

$$n_{ij} = \underline{b}_i^T \underline{c}_j \quad (12)$$

With more than three baselines, however, Equation (10c) does not have a unique solution for  $\underline{c}_j$ , so the  $M$  integer phases for sightline  $\underline{s}_j$  cannot be found from  $\underline{c}_j$  alone. We will consider the three-baseline case, which is the most common in practice. If more baselines are available, we are always free to select a three-baseline subset. Then, after the integer phases have been determined, a refined attitude estimate can be computed using all baselines (i.e., three baselines are sufficient to determine an attitude, which may then be used to resolve the integers corresponding to the other baselines).

To eliminate the dependence on the attitude, the square of Equation (11) is computed, so that

$$\begin{aligned} \|\underline{s}_j\|^2 &= \|A \underline{s}_j\|^2 = \|\hat{\underline{s}}_j - \underline{c}_j - \underline{\varepsilon}_j\|^2 \\ &= \|\hat{\underline{s}}_j\|^2 - 2\hat{\underline{s}}_j \cdot \underline{c}_j + \|\underline{c}_j\|^2 - 2(\hat{\underline{s}}_j - \underline{c}_j) \cdot \underline{\varepsilon}_j + \|\underline{\varepsilon}_j\|^2 \end{aligned} \quad (13)$$

Next, the following effective measurement and noise are defined

$$z_j \equiv \|\hat{\underline{s}}_j\|^2 - \|\underline{s}_j\|^2 \quad (14a)$$

$$v_j \equiv 2(\hat{\underline{s}}_j - \underline{c}_j) \cdot \underline{\varepsilon}_j - \|\underline{\varepsilon}_j\|^2 \quad (14b)$$

Then, the effective measurement can be written as

$$z_j = 2\hat{\underline{s}}_j \cdot \underline{c}_j - \|\underline{c}_j\|^2 + v_j \quad (15)$$

Alonso and Shuster (Ref. 12) showed that  $v_j$  is approximately Gaussian for small  $\underline{\varepsilon}_j$  with mean given by

$$\mu_j \equiv E\{v_j\} = -\text{trace}\{R_j\} \quad (16)$$

and variance given by

$$\sigma_j^2 \equiv E\{v_j^2\} - \mu_j^2 = 4(\hat{\underline{s}}_j - \underline{c}_j)^T R_j (\hat{\underline{s}}_j - \underline{c}_j) \quad (17)$$

The negative-log-likelihood function for the bias is given by

$$J(\underline{c}_j) = \frac{1}{2} \sum_{k=1}^L \left\{ \frac{1}{\sigma_j^2(k)} \left[ z_j(k) - 2\hat{\underline{s}}_j(k) \cdot \underline{c}_j + \|\underline{c}_j\|^2 - \mu_j(k) \right]^2 + \log \sigma_j^2(k) + \log 2\pi \right\} \quad (18)$$

The symbol  $k$  denotes the variable at time  $t_k$ . The maximum-likelihood estimate for  $\underline{c}_j$ , denoted by  $\underline{c}_j^*$ , minimizes the negative-log-likelihood function, and satisfies

$$\left. \frac{\partial J(\underline{c}_j)}{\partial \underline{c}_j} \right|_{\underline{c}_j^*} = 0 \quad (19)$$

The minimization of Equation (18) is not straightforward since the likelihood function is quartic in  $\underline{c}_j$ . A number of algorithms have been proposed for estimating the bias (see Ref. 12 for a survey). The simplest solution is obtained by scoring, which involves a Newton-Raphson iterative approach. Another approach avoids the minimization of a quartic loss function by using a “centered” estimate. A statistically correct centered estimate is also derived in Ref. 12. Furthermore, Alonso and Shuster show a complete solution of the statistically correct centered estimate that determines the exact maximum likelihood estimate  $\underline{c}_j^*$ . This involves using the statistically correct centered estimate as an initial estimate, and iterating on a correction term using a Gauss-Newton method. Although this extension to the statistically correct centered estimate can provide some improvements, this part is not deemed necessary for the GPS problem since the estimated quantity for  $n_{ij}$  is rounded to the nearest integer.

### Batch Solution

In this section the statistically correct centered estimate algorithm (see Ref. 12 for details) and its application to the integer ambiguity problem are shown. First, the following weighted averages are defined

$$\begin{aligned} \bar{z}_j &\equiv \bar{\sigma}_j^2 \sum_{k=1}^L \frac{1}{\sigma_j^2(k)} z_j(k), & \bar{s}_j &\equiv \bar{\sigma}_j^2 \sum_{k=1}^L \frac{1}{\sigma_j^2(k)} \hat{s}_j(k), \\ \bar{v}_j &\equiv \bar{\sigma}_j^2 \sum_{k=1}^L \frac{1}{\sigma_j^2(k)} v_j(k), & \bar{\mu}_j &\equiv \bar{\sigma}_j^2 \sum_{k=1}^L \frac{1}{\sigma_j^2(k)} \mu_j(k) \end{aligned} \quad (20)$$

where

$$\frac{1}{\bar{\sigma}_j^2} \equiv \sum_{k=1}^L \frac{1}{\sigma_j^2(k)} \quad (21)$$

Next, the following variables are defined

$$\tilde{z}_j(k) \equiv z_j(k) - \bar{z}_j, \quad \tilde{s}_j(k) \equiv \hat{s}_j(k) - \bar{s}_j, \quad \tilde{v}_j(k) \equiv v_j(k) - \bar{v}_j, \quad \tilde{\mu}_j(k) \equiv \mu_j(k) - \bar{\mu}_j \quad (22)$$

The statistically correct centered estimate now minimizes the following loss function

$$\tilde{J}(\underline{c}_j) = \frac{1}{2} \sum_{k=1}^L \frac{1}{\sigma_j^2(k)} [\tilde{z}_j(k) - 2\tilde{s}_j(k) \cdot \underline{c}_j - \mu_j(k)]^2 \quad (23)$$

which is now a quadratic function in  $\underline{c}_j$ . The minimization leads directly to

$$\underline{c}_j^* = P_j \sum_{k=1}^L \frac{1}{\sigma_j^2(k)} [\tilde{z}_j(k) - \tilde{\mu}_j(k)] 2 \tilde{\underline{z}}_j(k) \quad (24)$$

where the estimate error covariance is given by

$$P_j = \left[ \sum_{k=1}^L \frac{1}{\sigma_j^2(k)} 4 \tilde{\underline{z}}_j(k) \tilde{\underline{z}}_j^T(k) \right]^{-1} \quad (25)$$

The ambiguity for the  $i^{\text{th}}$  baseline and  $j^{\text{th}}$  sightline can be resolved by rounding the following to the nearest integer

$$n_{ij} = \underline{b}_i^T \underline{c}_j^* \quad (26)$$

The integer error covariance, denoted by  $Q_{ij}$ , can be shown to be given by

$$Q_{ij} = \underline{b}_i^T P_j \underline{b}_i \quad (27)$$

Equation (27) can be used to develop an integrity check for the algorithm. For example, a suitable criterion can be developed from a three-sigma bound using  $3\sqrt{Q_{ij}}$ .

### Sequential Formulation

This section expands upon the batch solution so that a sequential estimate of the integers can be found. The main advantage of a sequential formulation is that the convergence (integrity) check can be made on-the-fly (i.e., in real-time). The covariance in Equation (25) to be expanded to the  $L+1$  time point, so that

$$\begin{aligned} P_j^{-1}(L+1) &= \sum_{k=1}^L \frac{1}{\sigma_j^2(k)} 4 \tilde{\underline{z}}_j(k) \tilde{\underline{z}}_j^T(k) + \frac{1}{\sigma_j^2(L+1)} 4 \tilde{\underline{z}}_j(L+1) \tilde{\underline{z}}_j^T(L+1) \\ &= P_j^{-1}(L) + \frac{1}{\sigma_j^2(L+1)} 4 \tilde{\underline{z}}_j(L+1) \tilde{\underline{z}}_j^T(L+1) \end{aligned} \quad (28)$$

From the matrix inversion lemma,<sup>13</sup> the following sequential formation for the covariance is developed

$$P_j(k+1) = K_j(k) P_j(k) \quad (29)$$

where

$$K_j(k) \equiv I - P_j(k) \tilde{\underline{z}}_j(k+1) \left[ \tilde{\underline{z}}_j^T(k+1) P_j(k) \tilde{\underline{z}}_j(k+1) + \frac{1}{4} \sigma_j^2(k+1) \right]^{-1} \tilde{\underline{z}}_j^T(k+1) \quad (30)$$

In order to derive sequential formulas for the quantities in Equation (20), first consider the following identity

$$\sum_{k=1}^L \frac{1}{\sigma_j^2(k)} z_j(k) = \frac{1}{\bar{\sigma}_j^2(L)} \bar{z}_j(L) = \left[ \sum_{k=1}^L \frac{1}{\sigma_j^2(k)} \right] \bar{z}_j(L) \quad (31)$$

Expanding out this expression using  $L-1$  points in the summation yields

$$\frac{1}{\bar{\sigma}_j^2(L-1)}\bar{z}_j(L-1) + \frac{1}{\sigma_j^2(L)}z_j(L) = \left[ \frac{1}{\bar{\sigma}_j^2(L-1)} + \frac{1}{\sigma_j^2(L)} \right] \bar{z}_j(L) \quad (32)$$

and so

$$\bar{z}_j(L) = \frac{\sigma_j^2(L)\bar{z}_j(L-1) + \bar{\sigma}_j^2(L-1)z_j(L)}{\sigma_j^2(L) + \bar{\sigma}_j^2(L-1)} \quad (33)$$

Therefore, the following sequential expressions for the quantities in Equation (20) are given

$$\bar{z}_j(k+1) = \frac{1}{\sigma_j^2(k+1) + \bar{\sigma}_j^2(k)} \left[ \sigma_j^2(k+1)\bar{z}_j(k) + \bar{\sigma}_j^2(k)z_j(k+1) \right] \quad (34a)$$

$$\bar{\underline{z}}_j(k+1) = \frac{1}{\sigma_j^2(k+1) + \bar{\sigma}_j^2(k)} \left[ \sigma_j^2(k+1)\bar{\underline{z}}_j(k) + \bar{\sigma}_j^2(k)\hat{\underline{z}}_j(k+1) \right] \quad (34b)$$

$$\bar{\mu}_j(k+1) = \frac{1}{\sigma_j^2(k+1) + \bar{\sigma}_j^2(k)} \left[ \sigma_j^2(k+1)\bar{\mu}_j(k) + \bar{\sigma}_j^2(k)\mu_j(k+1) \right] \quad (34c)$$

where

$$\frac{1}{\bar{\sigma}_j^2(k+1)} = \frac{1}{\bar{\sigma}_j^2(k)} + \frac{1}{\sigma_j^2(k+1)} \quad (35)$$

The estimated bias in Equation (24) can also be found in a similar manner, so that

$$\underline{c}_j^*(k+1) = K_j(k)\underline{c}_j^*(k) + \frac{1}{\sigma_j^2(k+1)} \left[ \bar{z}_j(k+1) - \bar{\mu}_j(k+1) \right] 2P_j(k+1)\bar{\underline{z}}_j(k+1) \quad (36)$$

Since the baselines are constant, Equations (26) and (27) can be used directly to determine the sequential integer value and error covariance, given by

$$n_{ij}(k) = \underline{b}_i^T \underline{c}_j^*(k) \quad (37a)$$

$$Q_{ij}(k) = \underline{b}_i^T P_j(k) \underline{b}_i \quad (37b)$$

The complete solution proceeds as follows. First, use Equations (10b) and (10d) to convert the sightline vectors into the body frame. Then, perform an initial batch solution using Equations (20)-(25) in order to initialize the sequential routine (an accurate initial estimate is not required as will be seen in the results section). Then, perform a sequential estimate for the integers using Equations (29), (30), and (34)-(37). Finally, continue until the covariance in Equation (37b) is below a pre-specified value.

There are many advantages of the new algorithm. First, the algorithm is fully autonomous (i.e., it requires no a-priori information such as an a-priori attitude guess). Second, the largest matrix inverse is of a  $3 \times 3$  matrix, which makes the algorithm



computationally efficient and stable. Third, it is non-iterative, which makes it suitable for a sequential formulation. This has a significant advantage since the convergence can be checked during the actual motion in the vehicle. Finally, the integers for other sightlines can be easily resolved by calling the same subroutine. Therefore, the algorithm can easily be implemented using all available sightlines, and attitude determination can begin once the integers corresponding to two sightlines have been resolved. For these reasons, the new algorithm provides an attractive approach to resolve the integers.

## HARDWARE SIMULATION AND RESULTS

A hardware simulation of a typical spacecraft attitude determination application was undertaken to demonstrate the performance of the new algorithm. For this simulation, a Northern Telecom 40 channel, 4 RF output STR 2760 unit was used to generate the GPS signals that would be received at a user specified location and velocity. The signals are then provided directly (i.e., they are not actually radiated) to a GPS receiver that has been equipped with software tracking algorithms that allow it operate in space (see Figure 2).

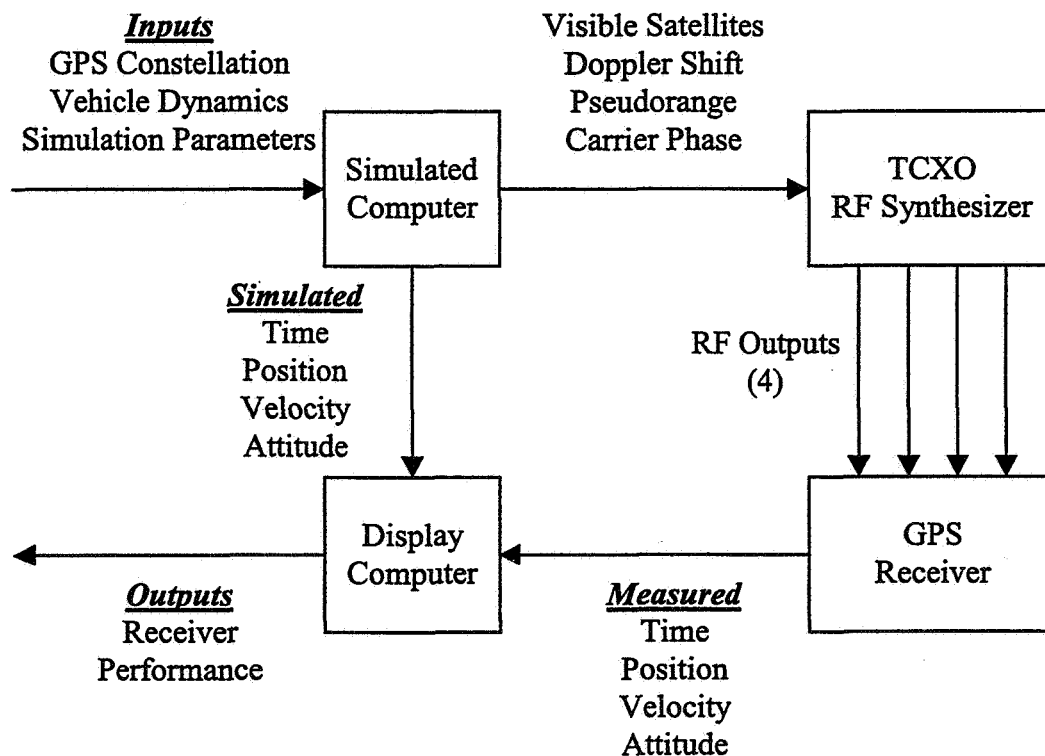


**Figure 2 Hardware Simulation Block Diagram**

The receiver that was used was a Trimble TANS Vector; which is a 6 channel, 4 RF input multiplexing receiver that performs 3-axis attitude determination using GPS carrier phase and line of sight measurements. This receiver software was modified at Stanford University and NASA-Goddard to allow it to operate in space. This receiver model has been flown and operated successfully on several spacecraft, including: REX-II, OAST-Flyer, GANE, Orbcomm, Microlab, and others.

The simulated motion profile was for an actual spacecraft, the Small Satellite Technology Initiative (SSTI) Lewis satellite, which carried an experiment to assess the performance of GPS attitude determination on-orbit. Although the spacecraft was lost due to a malfunction not related to the GPS experiment shortly after launch, this motion profile is nonetheless very representative of the types of attitude determination applications. The orbit parameters and pointing profile used for the simulation are given in Table 1.

**Table 1 SSTI Lewis Orbit parameters**

Semimajor axis (a)	6901.137 km
Inclination (i)	97.45 deg
Right Ascension of Ascending Node (RAAN)	-157.1 deg
Eccentricity (e)	0.0001
Pointing profile	Earth pointed
Launch date	August 22, 1997

The simulated SSTI Lewis spacecraft has four GPS antennas that form three baselines. The antenna separation distances are 0.61 m, 1.12 m, and 1.07 m, respectively. One antenna (in baseline 3) is located 0.23 m out of plane (below) the other three antennas. On the spacecraft, the antennas are mounted on pedestals with ground planes to minimize signal reflections and multipath. For the simulation, the signal was provided to the GPS receiver without multipath noise. The baseline vectors in wavelengths are given by

$$\underline{b}_1 = \begin{bmatrix} 2.75 \\ 1.64 \\ -0.12 \end{bmatrix}, \quad \underline{b}_2 = \begin{bmatrix} 0.00 \\ 6.28 \\ -0.17 \end{bmatrix}, \quad \underline{b}_3 = \begin{bmatrix} -3.93 \\ 3.93 \\ -1.23 \end{bmatrix} \quad (38)$$

Line biases are first determined before the new algorithm is tested to resolve the integer ambiguities. The GPS raw measurements are processed at 1 Hz over a forty minute simulation. During the simulated run, a minimum of three visible GPS are given at all times. Also, there are a number of eight minute spans when two of the same (in time) sightlines are available for the ambiguity resolution algorithm. Again, in practice, all available sightlines should be processed simultaneously, but with three baseline vectors only two simultaneously available sightlines are required to determine the attitude of the vehicle.

As mentioned previously, the first step in the algorithm involves using the baselines and phase difference measurements to convert the sightline vector into the body-frame, using Equations (10b) and (10d). Then, a small batch run is used to initialize the sequential routine. For this case, only 5 seconds of data was required to perform the initialization. Again, only two sightlines are required to determine the attitude. Sequential error results (i.e., actual integer minus the computed values without rounding) for the first sightline are shown in Figure 3. The integer error can be found by rounding

the values in Figure 3 to the nearest integer. Clearly, for this case, the integer ambiguities have been resolved even before the sequential process begins (i.e., within 5 seconds). A plot of the  $3\sqrt{Q_{ij}}$  values is shown in Figure 4 for the first sightline (a suitable integrity check is given when  $3\sqrt{Q_{ij}}$  is below 0.5). Clearly, the integrity check shows that the ambiguities are resolved within 5 minutes. Note, that this is a sufficiency test (i.e., the integers may be resolved well before 5 minutes, which is seen in this case). A plot of the errors for the second sightline is shown in Figure 5. For this case, all of the ambiguities have been resolved within 30 seconds (the error value corresponding to the second baseline goes below -0.5 before 30 seconds). A plot of integrity check for the second sightline is shown in Figure 6. The integrity check shows that the ambiguities are resolved within 7 minutes. This hardware simulation of a spacecraft clearly demonstrates that the new algorithm presented in this paper provides an accurate method to resolve the integer ambiguities with even slight vehicle motion.

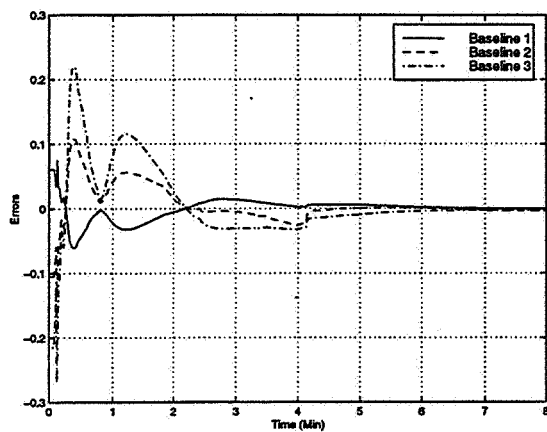


Figure 3 Errors for First Sightline

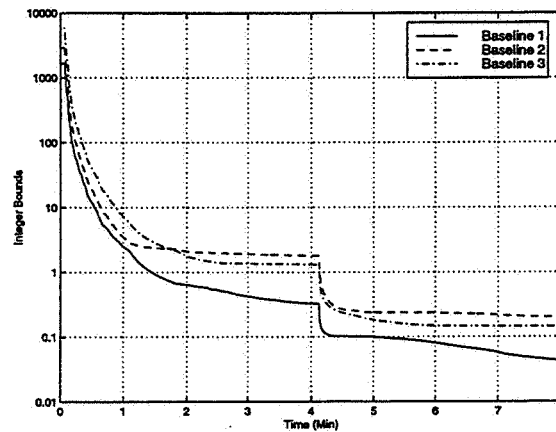


Figure 4 Integrity Check for First Sightline

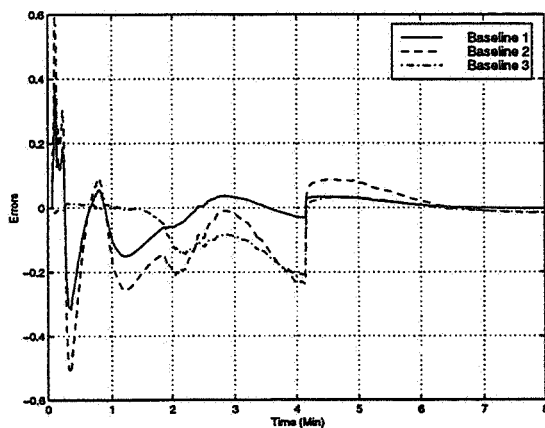


Figure 5 Errors for Second Sightline

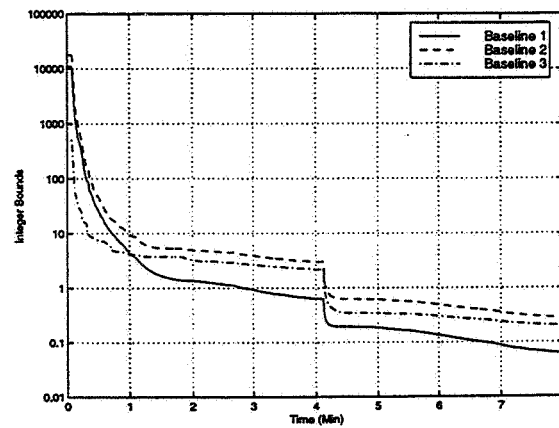


Figure 6 Integrity Check for Second Sightline

## CONCLUSIONS

In this paper, a new algorithm was developed for GPS integer ambiguity resolution. The new algorithm has several advantages over previously existing algorithms. First, the algorithm is attitude independent so that no a-priori attitude estimate (or assumed vehicle motion) is required. Second, the algorithm is sequential so that it may be implemented in real-time. Also, a suitable integrity check can be used to determine when the determined values have converged to the correct values. Finally, the algorithm is computationally efficient since only a  $3 \times 3$  matrix inverse is required, and the same subroutine can be used on different sightlines. The only disadvantage of the new algorithm is that it requires at least three non-coplanar baselines. The algorithm was tested using a GPS hardware simulator to simulate the motions of a typical low-altitude Earth-orbiting spacecraft. Results indicated that the new algorithm provides a viable and attractive means to effectively resolve the integer ambiguities.

## ACKNOWLEDGMENT

The first author's work was partially supported by a NASA/ASEE Summer Faculty Fellowship, under the supervision of Mr. Frank Bauer at NASA-Goddard Space Flight Center. The author greatly appreciates this support. Also, this author wishes to thank Dr. Malcolm Shuster of the University of Florida for introducing him to the concept of magnetometer-bias estimation.

## REFERENCES

1. C.E. Cohen, "Attitude Determination Using GPS," Ph.D. Dissertation, Stanford University, Dec. 1992.
2. E.G. Lightsey, E. Ketchum, T.W. Flatley, J.L. Crassidis, D. Freesland, K. Reiss, and D. Young, "Flight Results of GPS-Based Attitude Control on the REX-II Spacecraft," *Proceedings of the 1996 ION-GPS*, Kansas City, MO, Sept. 1996.
3. P.J. Melvin, L.M. Ward, and P. Axelrad, "The Analysis of GPS Attitude Data from a Slowly Rotating, Symmetrical Gravity Gradient Satellite," *Advances in the Astronautical Sciences*, Vol. 89, Part 1, AAS Paper #95-113, pp. 539-558.
4. G. Lachapelle, M.E. Cannon, and B. Loncarevic, "Shipborne GPS Attitude Determination During MMST-93," *IEEE Journal of Oceanic Engineering*, Vol. 21, No. 1, Jan. 1996, pp. 100-105.
5. J.L. Crassidis, E.G. Lightsey, and F.L. Markley, "Efficient and Optimal Attitude Determination Using Recursive Global Positioning System Signal Operations," to appear in the *Proceedings of the Guidance, Navigation, and Control Conference*, Boston, MA, Aug. 1998, AIAA Paper #98-4496.
6. P.G. Quinn, "Instantaneous GPS Attitude Determination," *Proceedings of the 1993 ION-GPS*, Salt Lake City, UT, Sept. 1993, pp. 603-615.
7. C.D. Hill and L. AG, "An Optimal Ambiguity Resolution Technique for Attitude Determination," *Proceedings of the IEEE Position, Location, and Navigation Symposium*, Atlanta, GA, April 1996, pp. 262-269.

8. W.E. Deskins, *Abstract Algebra*, Dover Publications, New York, 1995, Chapter 4.
9. C.E. Cohen, "Attitude Determination," *Global Positioning System: Theory and Applications, Volume 2*, edited by B.W. Parkinson and J.J. Spilker, Progress in Astronautics and Aeronautics, Vol. 164, AIAA, Washington, DC, 1996, Chapter 19.
10. A. Conway, P. Montgomery, S. Rock, R. Cannon, and B. Parkinson, "A New Motion-Based Algorithm for GPS Attitude Integer Resolution," *Navigation*, Vol. 43, No. 2, Summer 1996, pp. 179-190.
11. J.L. Crassidis and F.L. Markley, "New Algorithm for Attitude Determination Using Global Positioning System Signals," *Journal of Guidance, Control and Dynamics*, Vol. 20, No. 5, Sept.-Oct. 1997, pp. 891-896.
12. R. Alonso and M.D. Shuster, "A New Algorithm for Attitude-Independent Magnetometer Calibration," *Proceedings of the Flight Mechanics/Estimation Theory Symposium*, NASA-Goddard Space Flight Center, Greenbelt, MD, 1994, pp. 513-527.
13. R.F. Stengle, *Optimal Control and Estimation*, Dover Publications, New York, 1994, pg. 62.



## INITIAL FLIGHT RESULTS OF THE TRMM KALMAN FILTER

Stephen F. Andrews\*  
Wendy M. Morgenstern\*

The Tropical Rainfall Measuring Mission (TRMM) spacecraft is a nadir pointing spacecraft that nominally controls attitude based on the Earth Sensor Assembly (ESA) output. After a potential single point failure in the ESA was identified, the contingency attitude determination method chosen to backup the ESA-based system was a sixth-order extended Kalman filter that uses magnetometer and digital sun sensor measurements. A brief description of the TRMM Kalman filter will be given, including some implementation issues and algorithm heritage. Operational aspects of the Kalman filter and some failure detection and correction will be described. The Kalman filter was tested in a sun pointing attitude and in a nadir pointing attitude during the in-orbit checkout period, and results from those tests will be presented. This paper will describe some lessons learned from the experience of the TRMM team.

### INTRODUCTION

#### TRMM Spacecraft

The Tropical Rainfall Measuring Mission (TRMM) spacecraft, seen in Figure 1, is a joint NASA/NASDA mission that was launched on November 27, 1997 from Tanegashima Space Center, Japan. The spacecraft is three-axis stabilized, in a near circular 350 km orbit at a 35 degree inclination. The Mission Mode is nadir pointing, and due to Sun constraints, the spacecraft must be rotated 180 degree about nadir (yaw) every few weeks. The sensor complement includes a static Earth Sensor Assembly (ESA), two two-axis Digital Sun Sensors (DSS), a redundant three-axis Inertial Rate Unit (IRU), eight Coarse Sun Sensors (CSS), and two Three-Axis Magnetometers (TAM). The spacecraft is controlled with four Reaction Wheels (RW), twelve thrusters (Reaction Engine Modules, REM), and momentum is unloaded with three Magnetic Torquer Bars (MTB). In Mission Mode, which is the nominal science configuration, attitude determination is done with the ESA for roll and pitch, and integrated IRU rate for yaw.

#### Problem Description

A potential single point failure of the ESA was first identified at Goddard Space Flight Center (GSFC) in 1992, with the discovery of a "fogging" effect of the ESA lenses<sup>1</sup>. This problem could cause the ESA to fail the Mission Mode attitude determination requirement. A backup attitude determination method was needed to satisfy the system redundancy requirements. Buying another ESA or a star tracker (ST) was not a realistic option, given the TRMM budget and schedule. A software backup using the available sensor measurements added redundancy without requiring additional hardware or affecting other subsystems such as power or structures.

---

\*Aerospace Engineer, Guidance, Navigation, and Control Center, NASA's GSFC

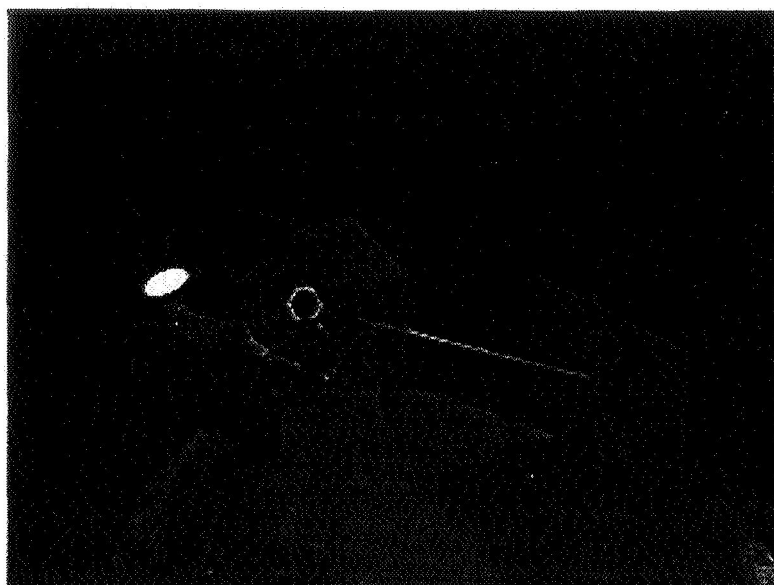


Figure 1 TRMM Spacecraft

## ALGORITHM HERITAGE

A six state extended Kalman filter was chosen to backup the ESA based on the results of a trade study of several attitude determination algorithms<sup>2</sup>. The TRMM Kalman filter was adapted from the Rossi X-ray Timing Explorer (RXTE) Kalman filter, which was based on the Kalman filter developed for the Multimission Modular Spacecraft (MMS) by Murrell<sup>3</sup>, and described in Lefferts, Markley, and Shuster<sup>4</sup>. The major changes to the RXTE algorithm were the replacement of the ST processing with TAM processing, the addition of a second DSS, and the coding of new initialization functions, associated subroutines, and new interfaces to fit the algorithm into the existing flight code<sup>5</sup>. The mathematical checks in the RXTE code were reused for TRMM, with modified limits. Since the core part of the Kalman filter code was already tested and working in flight on RXTE, there was a high degree of confidence in it which allowed a 'black box' testing approach to the new algorithm.

Typical spacecraft applications of a Kalman filter, such as on the Extreme Ultraviolet Explorer (EUVE) and RXTE, use a DSS and a ST to update the IRU propagated attitude. A DSS and a TAM were used in a TRIAD algorithm<sup>6</sup> for a deterministic attitude on the SAMPEX satellite. The TRMM Kalman filter updates the IRU propagated attitude and the IRU drift rate biases with TAM and DSS measurements. It is the first onboard attitude estimation algorithm at GSFC to use a DSS and a TAM to estimate spacecraft attitude to better than  $0.25^\circ$ .

## ALGORITHM

The main portion of the TRMM algorithm is a discrete, extended Kalman filter.<sup>7</sup> For brevity's sake, only a few relevant points will be mentioned here.

The term residual as used in this paper refers to the difference between the vector measured by the sensor and the vector predicted by the model. The scalar implementation used in the flight software introduces another term that is called the adjusted residual. As each measurement component is processed, the vector predicted by the model is updated.



As a result, subsequent residual components have to be corrected for that update. These corrected residuals are referred to as adjusted residuals. The corrections are usually so small that the values of the residual and the adjusted residual are almost identical.

The algorithm also includes checks on the data in the filter. The first check is made on the availability and quality of the sensor data. For example, if the sun is in the DSS field of view but the measurement is not valid, the filter will not use that DSS measurement. In addition, there is a residual tolerance test that rejects any measurements that create residuals larger than a set tolerance. These checks prevent the estimation from using bad sensor data. This is not an algorithm failure, so no corrective action is taken.

There are three Failure Detection and Correction (FDC) checks designed specifically to monitor the Kalman filter algorithm. Two checks monitor the covariance matrix for divergence and positive semidefiniteness. The third test ensures that the adjusted residual remains within  $3\sigma$  of the expected value of the residual. For all three tests, the ACS software autonomously performs the same actions. First, the software stops updating the attitude quaternion and the gyro drift with the failed sensor, and then it commands the spacecraft to a power and thermal safe attitude after a specified amount of time.

## GROUND TESTING

Using software to add redundancy is not a trivial task. For TRMM, the most difficult issue was adding the new Kalman filter code into tested flight software without altering the existing ESA-based controllers. In addition, there were concerns about processor speed. Since it was unclear if the hardware could run fast enough to simultaneously process the ESA information and run the Kalman filter algorithm, the attitude control system (ACS) team decided to run one algorithm at a time.

A more detailed description of the software implementation and testing can be found in Andrews and D'Agostino<sup>5</sup>. Tests were run to verify the nominal performance of the Kalman filter, and to ensure that the existing control modes were not affected by the addition of the new algorithm. All test results were nominal, except one. In that test, the filter rejected DSS measurements after an eclipse. The DSS residuals passed the initial tolerance test, but failed the adjusted residual test, causing the filter to reject the DSS data. This indicates that either the DSS tolerance was set too tight or that the covariance did not grow large enough during eclipse, leaving the filter knowledge of the TAM noise smaller than it should have been. At the time, the ACS team believed the failure was the result of a mismatch between the 'true' ephemeris and the 'modeled' ephemeris in the test setup.

## FLIGHT RESULTS

### Sun Acquisition Mode Test

On the second day of the mission, TRMM was still in Sun Acquisition Mode holding the spacecraft x-axis 16.5 degrees from the sunline. In this mode, the spacecraft is controlled directly off the CSSs and the IRUs; the Kalman filter output is not used in the control loop. The Kalman filter was run for a total of 13000 seconds. After converging for 9640 seconds, the filter was reinitialized during eclipse to study the TAM-only filter performance. The TAM residuals for the entire test are shown in Figure 2. The flat line portions in this figure are periods of loss of signal (LOS), when TRMM was not in contact with the ground. It is obvious that the TAM residuals are not the zero mean, white noise processes modeled by the filter equations. The magnitude of this modeling error has

implications for setting the proper sensor noise parameters in the filter that will be discussed later.

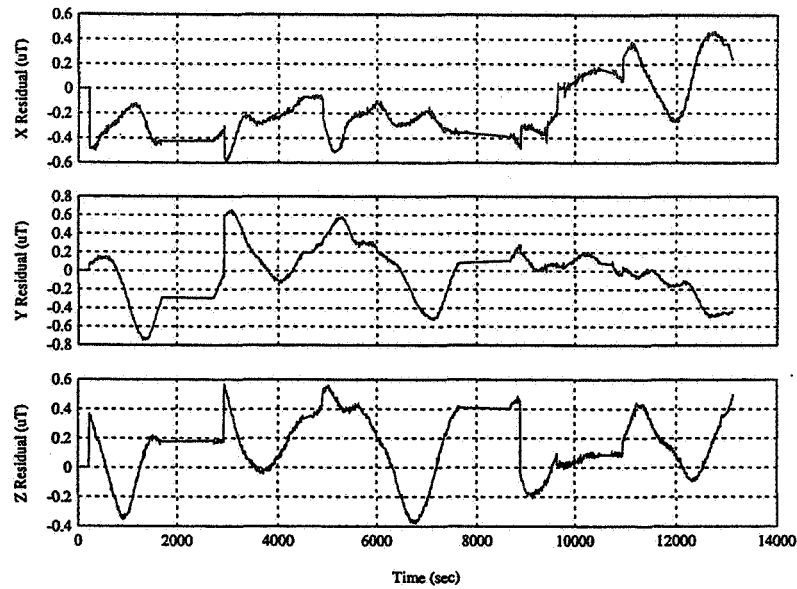


Figure 2 Sun Acquisition Mode Test: TAM Residuals

The standard deviations of the attitude estimate, shown in Figure 3, converged to  $[0.02, 0.006, 0.002]$  degrees within 8000 seconds. In Sun Acquisition Mode, the sun is held in the same location in the body frame, perpendicular to the z axis and primarily along the x axis. This reduces observability in the x axis, a phenomenon that is reflected in the relative size of the attitude standard deviations.

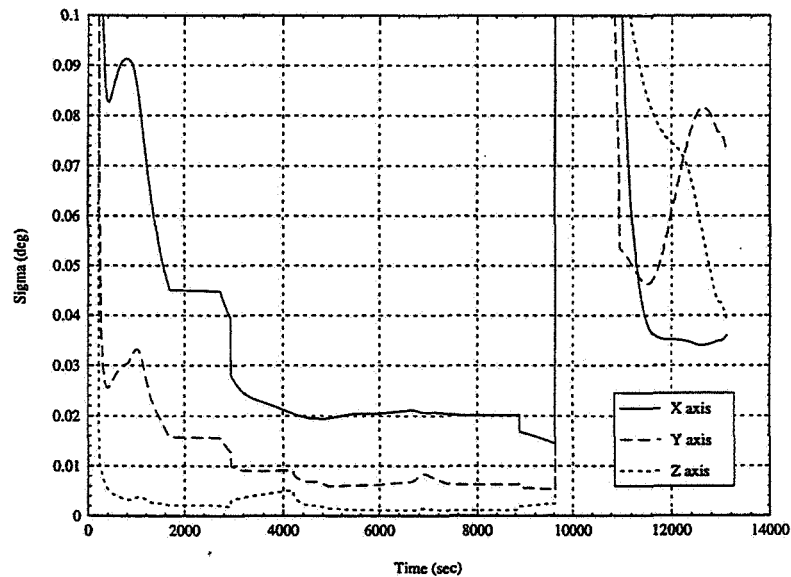


Figure 3 Sun Acquisition Mode Test: Standard Deviation of the Attitude Estimate

The standard deviations of the gyro bias estimates are shown in Figure 4. As with the attitude standard deviations, the relative sizes of the bias standard deviations indicate the measurement geometry. The value of the gyro bias estimate shown in Figure 5 reached steady state before the filter was reinitialized. The impact of the reset can be seen clearly, and the bias estimate was still reconverging when the test ended.

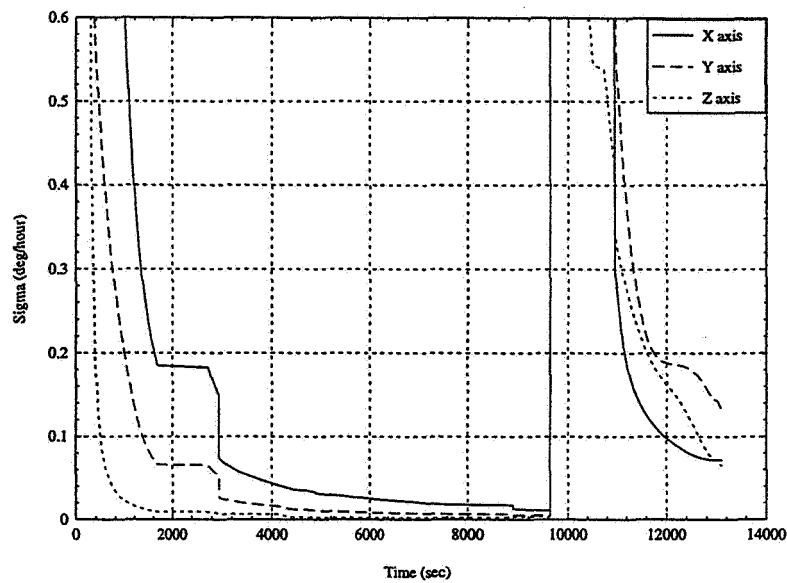


Figure 4 Sun Acquisition Mode Test: Standard Deviation of the Gyro Bias Estimate

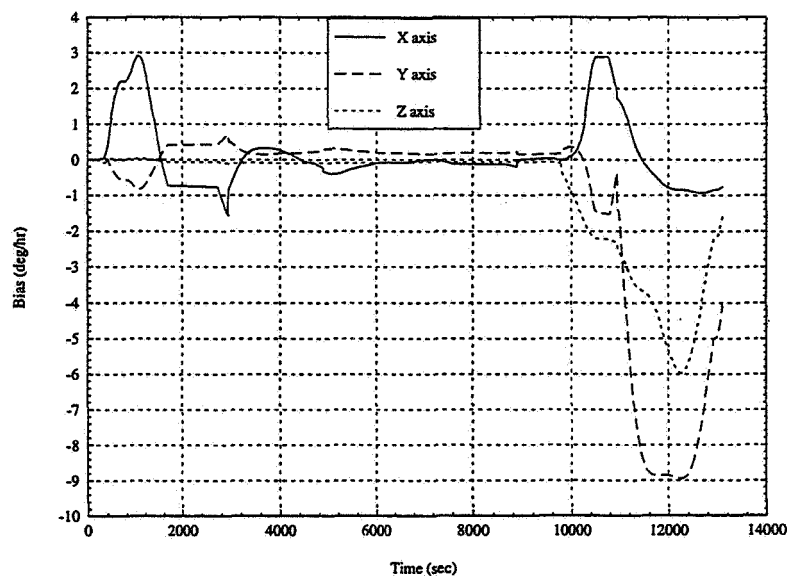


Figure 5 Sun Acquisition Mode Test: Estimated Biases

The DSS residuals are shown in Figure 6. When the Kalman filter is first enabled during sunlight, the DSS residuals were well within acceptable limits. When TRMM entered sunlight about 300 seconds after the filter was reinitialized, the DSS adjusted residual failed the  $3\sigma$  tolerance check ( $\sim 0.15$  degrees) after less than 700 seconds in daylight. The adjusted residual continued to fail its tolerance check for the entire daylight portion of the orbit. TRMM went into eclipse before the DSS measurement was accepted again, and the test was ended.

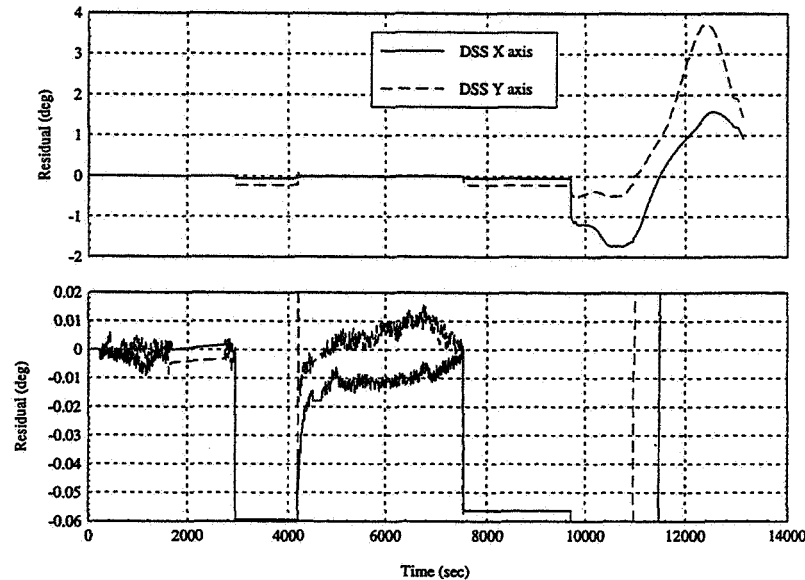


Figure 6 Sun Acquisition Mode Test: DSS1 Residuals

This adjusted residual test failed because the actual DSS adjusted residual was larger than the expected adjusted residual that is calculated from the  $3\sigma$  tolerance, the state covariance, and the sensor noise. Review of the data showed that the state covariance was too small and the  $3\sigma$  tolerance was too tight. The state covariance was too small because the Kalman filter was overweighing the TAM measurement, and converging too quickly. This weighting factor is a function of the TAM measurement noise covariance matrix that was set to model sensor noise on a zero mean process. The actual TAM measurement residual has a nonzero mean due to modeling errors. The  $3\sigma$  tolerance was set too tight because the filter should be allowed to accept  $5\sigma$  DSS data since the DSS was performing better than expected.

Other problems were identified later, after GSFC's Flight Dynamics Facility had time to analyze several days of flight data. It was found that the DSS heads were misaligned by as much as 0.3 degrees, which caused biased DSS residuals, leading to biased estimates. Also, the influence of the MTBs on the TAM measurements had not been accurately compensated for, and that increased the TAM residuals. In addition, the IRU calibration maneuvers had not been done yet, and the alignment matrices on-board did not properly account for the true IRU alignments. Finally, it was found that the magnetic field model on board was not internally consistent. The coefficients were from a 1995 model, but the epoch time for computation of the secular variations was set to 1990. This means that the residuals between the magnetic field model and the TAM measurements had a much larger bias and variance than expected.

## Mission Mode Test

Before the next Kalman filter test, the filter parameters were retuned by modifying the on-board tables. First, the TAM measurement noise covariance matrix was increased from  $0.25 \mu\text{T}^2$  to  $1.0 \mu\text{T}^2$  to try to account for the model errors. Second, the DSS adjusted residual tolerance was increased from  $3\sigma$  to  $5\sigma$ . Third, the magnetic field model coefficients were set to the 1990 values to match the epoch time. Fourth, the DSS parameters were updated to account for some of the misalignment errors. The on-board software precluded compensating for the DSS misalignments completely, so there were still unmodeled DSS misalignments of up to 0.08 degrees. Once the changes were made, the Mission Mode test began.

The TAM residuals are shown in Figure 7, and, as in the Sun Acquisition Mode test, they are neither zero mean nor Gaussian distributed. The high frequency component of the signal is due to the unmodeled 0.5 Hz rotation of one of the payload instruments, and the low frequency variation may be due to the effects of the MTBs on the TAM measurements. The sharp spikes on the plot are caused by the on-board magnetic field model.

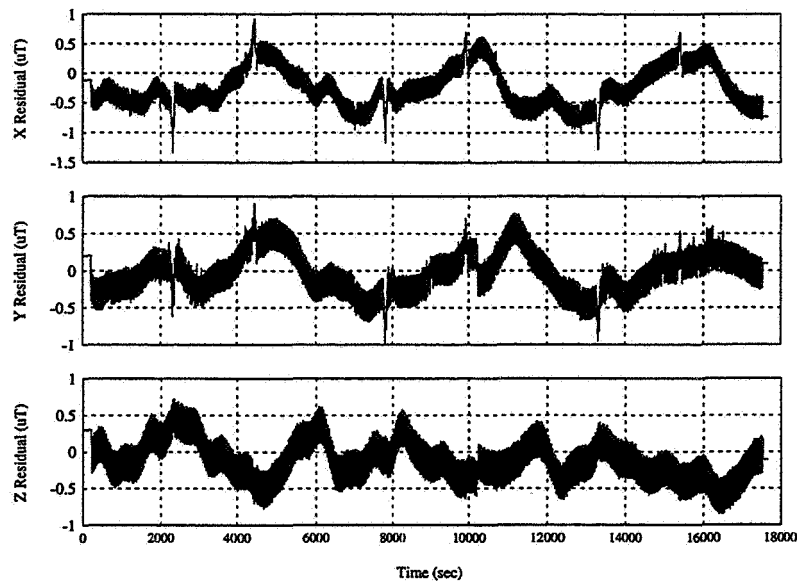


Figure 7 Mission Mode Test: TAM Residuals

The standard deviation of the attitude estimate is shown in Figure 8. The x/z (roll/yaw) quarter-orbit coupling is due to the one revolution per orbit rotation of the spacecraft about the y (pitch) axis. The spacecraft y axis is generally perpendicular to the sunline, and thus shows the greatest estimated accuracy. During eclipse, the covariance increases because the less accurate TAM is the only update sensor available. Figure 9 shows that the gyro bias estimate is also affected by the availability of the DSS measurement. The periods when the bias covariance is increasing or holding steady are periods of eclipse.

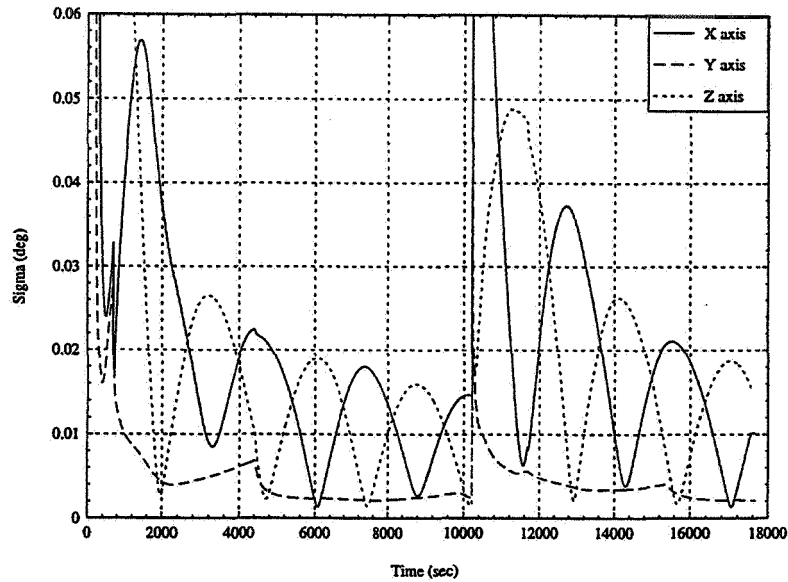


Figure 8 Mission Mode Test: Standard Deviation of the Attitude Estimate

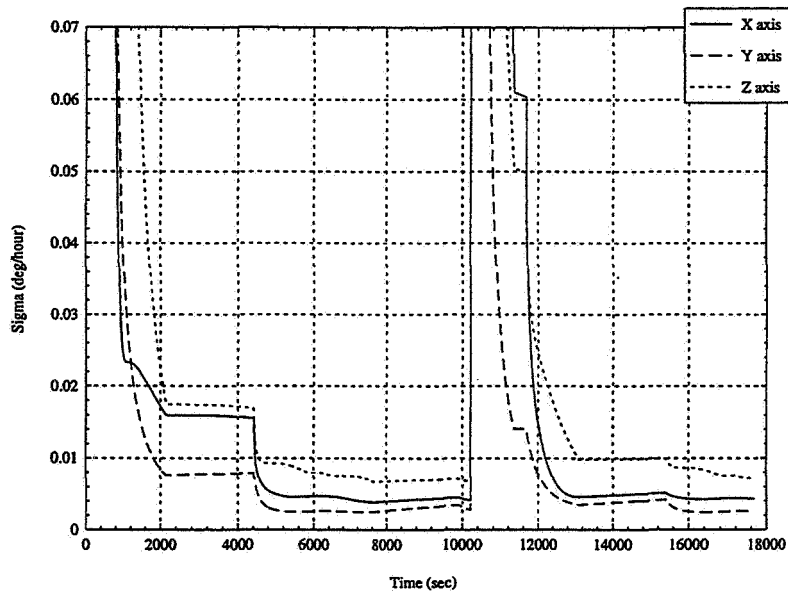


Figure 9 Mission Mode Test: Standard Deviation of the Gyro Bias Estimate

The Kalman filter estimated gyro biases are shown in Figure 10. Upon initialization and reinitialization, the initial attitude transient lasts about 2000 seconds. The filter bias estimate settles to the same values before and after the reinitialization; this shows that the gyro drift rate is steady on a time scale of hours. This result is expected because of the high quality and drift stability of the TRMM IRUs.

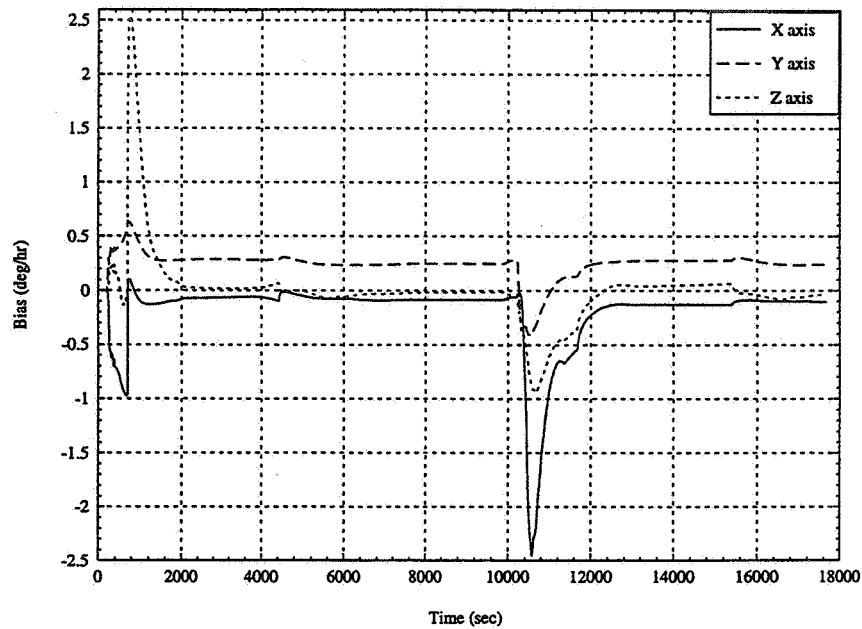


Figure 10 Mission Mode Test: Estimated Biases

The DSS residuals are plotted in Figures 11 and 12. Between measurements, the filter simply stores the last value of the residual, and the data goes static. The effect of the DSS misalignments can be seen in the large initial values of the residuals when the sun first enters the DSS field of view.

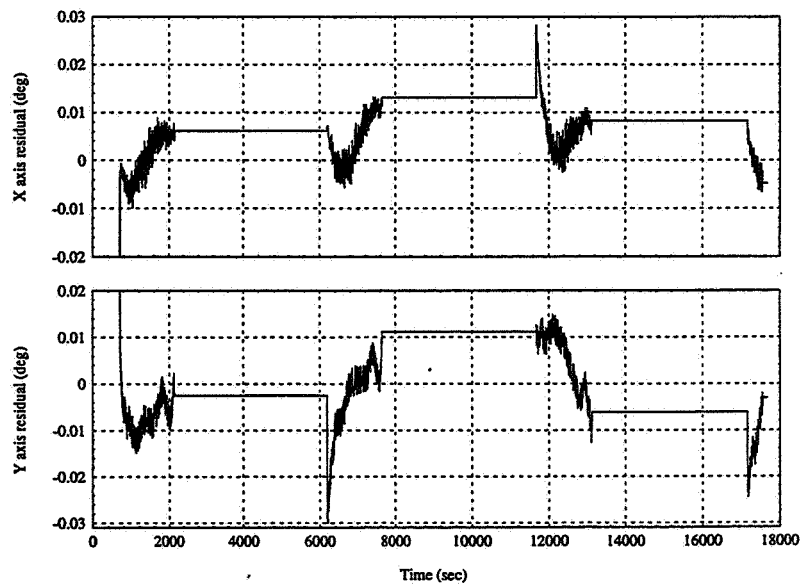


Figure 11 Mission Mode Test: DSS1 Residuals

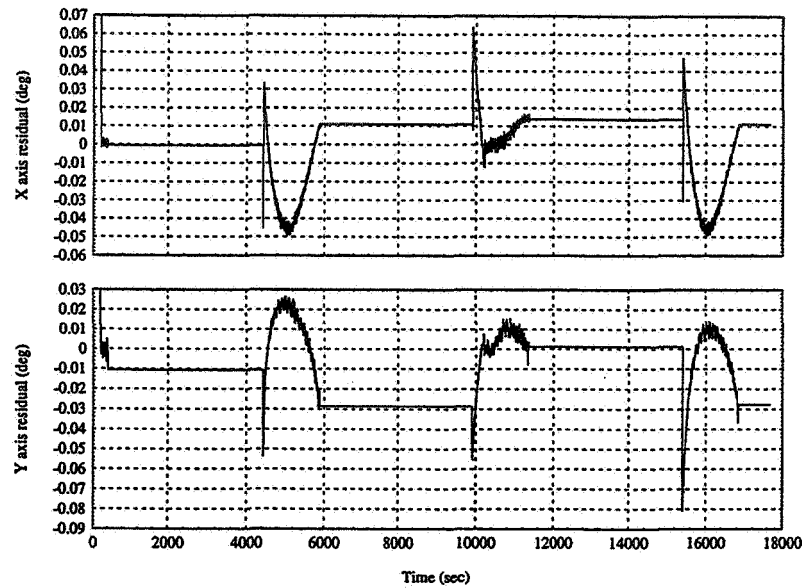


Figure 12 Mission Mode Test: DSS2 Residuals

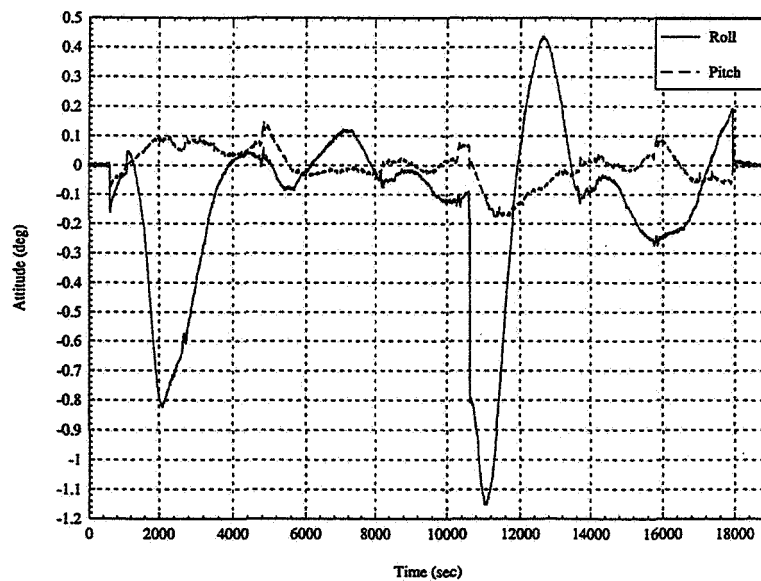


Figure 13 Mission Mode Test: ESA Attitude

The best measure of the performance of the Kalman filter is the attitude derived from the ESA. Although the ESA data is not processed on board when the Kalman filter is running, the unprocessed data is available in telemetry. With this information, the ESA attitude was calculated on the ground and is shown in Figure 13. The initial attitude



transients are on the order of  $1^\circ$  in roll, and  $0.2^\circ$  in pitch. The best performance of the filter is the period from 5000 to 10000 seconds, when the largest attitude error is about  $0.12^\circ$ .

## LESSONS LEARNED

The possible improvements in the TRMM Kalman filter fall into two basic categories: operational issues and performance issues. Operational issues include transitions to the backup mode, testing, software design, and data flow. Performance issues pertain mostly to properly tuning a Kalman filter so that it functions effectively with real sensors.

### Operations issues

Since the TRMM Kalman filter was added late in the testing cycle, the concern about onboard processing power forced the software design to an either/or mindset. Either the ESA processing could be run or the Kalman filter could be run, but not both. The filter was designed under the assumptions that the ESA had failed and that once the Kalman filter was turned on, it would never be turned off. It was also assumed that the Kalman filter would have to replace only the ESA functions, such as the earth acquisition maneuvers, maintaining nadir pointing, and inertial slews and holds.

Assuming the filter only had to replace the ESA functions meant that the filter's performance during other cases, such as thruster maneuvers, was not thoroughly considered. This led to several oversights in the filter design. First, in all of the ACS control modes, except during thruster maneuvers, the ACS software runs at a 2 Hz cycle. During thruster maneuvers, the controller runs at 8 Hz. However, since the Kalman filter was only coded as a replacement for ESA functions, the 2 Hz duty cycle was hardcoded into the Kalman filter algorithm, and the filter cannot run during the thruster maneuvers. Second, the software propagates the attitude estimate during thruster maneuvers, but it does not propagate the filter covariance. Thus, after completing the thruster burn, the covariance gives an incorrect indication of the accuracy of the attitude estimate. A solution is to reinitialize the filter and allow it to reconverge, a process the flight tests show takes several hours, which reduces the quality of the science data for that period of time. Finally, since normal operations, such as the Delta-V maneuver, require the filter to be reinitialized periodically, testing all possible reset conditions should be included in both ground and flight testing, a luxury the TRMM schedule did not allow. More thorough testing might have revealed more of these problems in time for the development team to modify the design, rather than forcing the operations team to resort to work-arounds.

Since it was assumed the Kalman filter would never be turned off, the ground verification did not test the transition between the filter and ESA processing. Again, this led to several oversights. The first problem concerns the gyro biases. The filter is continually estimating the gyro biases for all three axes. When the filter stops running, these bias estimates are stored in memory. As the spacecraft's orientation changes during nadir pointing, misalignment errors map differently into the gyro drift bias error. If the filter is running, these changes will be compensated for on board. If the filter is not running, the estimate that is in memory may actually introduce a small error in the drift biases. Thus, it is necessary to reset the gyro drift biases after exiting the filter. However, the initial estimated bias is set in the gyro initialization subroutine, not in the Kalman filter initialization/reset subroutine. Commanding a filter reset only reruns the filter initialization. To zero the estimated bias, the gyro initialization subroutine must be rerun. This can only be accomplished by rebooting the ACS software, which is extremely risky to do in flight.

To eliminate this risk, a separate gyro reset command had to be incorporated into the ACS software a few months prior to launch. Including the zeroing of this initial biases in the filter initialization subroutine would have been a much cleaner solution.

These issues make the transition between ESA attitude determination and Kalman filter attitude determination unnecessarily awkward, and complicated the on-orbit testing. The availability of the Kalman filter data is another operational problem that resulted from adding a backup algorithm to a mature software design.

Currently, there are problems getting flight data from the Kalman filter because the telemetry packet is available only by special request, or asynchronously. This means that the operations team must send a new command to the spacecraft every nine hours to keep the Kalman filter data in the telemetry stream. In addition, the filter packet is only issued every eight samples, which is insufficient for a thorough performance evaluation if the filter ever becomes the primary attitude determination method. Since it is in an asynchronous packet, the flight recorder does not store the filter data, so real-time playbacks must be used to regenerate the data on the ground. This is inefficient, and requires a large effort from the Flight Operations team. The resulting data is full of gaps, since the Flight Operations team only records the telemetry stream during real time passes. Fortunately, the flight software allows the team to modify the data storage operations, so it is possible to record a continuous data stream for the filter information. Unfortunately, the data rate is still one sample in every eight, and it involves yet another operational workaround. Many of these data problems could have been avoided if the asynchronous packet had been redefined as a synchronous packet that is always available in the telemetry stream and is always sent to the flight recorder, and issued at a higher data rate.

## **Performance issues**

The Kalman filter models assume zero-mean white noise measurement residuals, which is mostly true of the DSS residuals but is not true of the TAM residuals. The filter has no knowledge of biased sensor readings unless they are included in the state equations, so the DSS misalignment has a large impact on the accuracy of the filter. To characterize the estimation errors caused by instruments, the sensors and relevant instruments must be accurately modeled in the simulation including biases, scale factor errors, and misalignments. In particular, an accurate gyro model is essential if gyro biases are included in the filter states. Also, the full effects of the Earth's magnetic field on the Kalman filter cannot be properly seen in simulation because the low frequency variations of the Earth's magnetic field are hard to model accurately. Ideally, the simulation should model all of the errors that will be seen on orbit, but that is not always easy to achieve.

The on-orbit test needs to be run for many hours to adequately test the backup algorithm. Ideally, the filter should be tested under all the conditions where it is expected to be used. As with all on-orbit tests however, this requirement has to be balanced with other subsystem tests and the science schedule.

As mentioned previously, FDC is designed to capture certain problems, and to keep the spacecraft safe. The three FDC tests discussed will not indicate if the filter is trying to estimate an attitude error or a gyro bias error larger than it was told to expect. If the true error is larger than the error indicated by state covariance, the filter may converge to an incorrect attitude. This type of error is indicated when the filter's estimates do not match the true attitude. Outside of computer simulation, however, there is no truth model to use for comparison. If this type of problem is suspected, the best option is to compare the

estimates from the filter to ground estimates and adjust, or tune, the filter based on the comparison, a luxury that is not always available to the operations team. To properly tune a filter, the designers must be aware of the largest possible state error, and choose initial state covariance values larger than expected. Even though this greatly increases the filter's convergence time, it will allow the filter to converge from larger, more uncertain initial estimation errors. This is obviously a filter design tradeoff.

### **Implementation features**

The flight software developers should rarely hardcode a number; a table design that allows parameters to be changed with a simple uplink rather than a software patch should be used instead. Software patches require a significant development and testing effort from the software maintenance team, and risk the safety of the spacecraft. For example, some of the DSS misalignment error was calibrated out of the data by changing some table values, but updating the magnetic field model to a 1995 epoch will require a software change.

One good feature of the flight software design is that it allowed the flight operations team to safely verify the filter's performance. There should be a control mode available to check out the Kalman filter performance before controlling with the filter's attitude estimates. On TRMM, the Sun Acquisition control mode uses the CSSs and IRUs for attitude determination, which allowed the filter to be tested in-flight without affecting the safety of the spacecraft. If the processing power had been sufficient to run both the Kalman filter and the ESA processing, much of the awkward testing done on TRMM would have been unnecessary. Running both algorithms simultaneously would provide two attitude estimates at all times, allowing ground personnel the luxury of evaluating the long term performance of the filter without affecting nominal mission operations.

A vital safety feature of the TRMM design is the FDC logic. The three FDC tests pertaining to the Kalman filter allow the on-board algorithm to determine when it is inappropriate to use the filter results. The TRMM design stops updating the filter and autonomously places the spacecraft in a power safe mode if a bad attitude estimate is computed.

With approximately six months to go from a trade study to completely tested flight software, time constraints made it impossible to test the Kalman filter under every possible flight condition. Better system engineering should be able to identify possible failures and available backups early in the design phase. Flight results and trend data from each component should be reviewed early in the design to identify potential failures. Decisions to incorporate backups for hardware failures, whether using redundant hardware or implemented software backups, should be made early in the program. For TRMM it would have been best if the backup mode had been included in the earlier design, so that the additional processing needs would be reflected in the processor requirements and design. Once backups algorithms are selected, good subsystem engineering should help identify all possible uses of these algorithms so those conditions can be tested. 'Expected' usage tests do not cover all reasonable situations. The fundamental lesson learned is that software designed for one spacecraft can be reused on a different spacecraft if the software design is modular enough and the reused software is well tested, even though it is easy to underestimate the difficulty of the conversion.

### **CONCLUSION**

In the unlikely event of a complete ESA failure, TRMM can meet pointing

requirements by using TAM and DSS data. The additional software in the form of an extended Kalman filter saved the expense of providing a star tracker for backup. It was not easy to convert existing software, but the software modifications were completed quickly, largely due to the modular design of the RXTE and TRMM software. Pre-flight testing of the software was extensive, but it did not find all the problems, both because there was not enough time to modify the simulation system to include all known error sources, and because some unexpected errors showed up in flight tests. However, flight testing showed pointing performance better than the required  $0.7^\circ$  and approaching the  $0.2^\circ$  performance of the primary attitude control system.

## REFERENCES

- 1 D. K. Ward, internal memo, "TRMM ACS Peer Review Action Items Regarding Earth Sensor Assembly Concerns", August 18, 1992.
- 2 J. L. Crassidis, S. F. Andrews, F. L. Markley, K. Ha, "Contingency Designs for Attitude Determination of TRMM", *Flight Mechanics/Estimation Theory Symposium*, 1995 pp. 419-433.
- 3 J. W. Murrell, "Precision Attitude Determination for Multimission Spacecraft, "AIAA Paper 78-1248, Aug. 1978.
- 4 E. J. Lefferts, F. L. Markley, and M. D. Shuster, "Kalman Filtering for Spacecraft Attitude Estimation," *Journal of Guidance, Control and Dynamics*, Vol. 5, No. 5, Sept-Oct. 1982, pp 417-429.
- 5 S. F. Andrews, J. M. D'Agostino, "Development, Implementation, and Testing of the TRMM Kalman Filter," *Flight Mechanics Symposium 1997*, pp. 457-471.
- 6 J. S. Wertz, (ed.), *Spacecraft Attitude Determination and Control*, D. Reidel Publishing Co., Dordrecht, The Netherlands, 1984.
- 7 A. Gelb (ed), *Applied Optimal Estimation*, The M.I.T. Press, Cambridge, Massachusetts, 1974.

148

532-13

169330

# AN EFFICIENT ALGORITHM FOR SPACECRAFT ATTITUDE DETERMINATION WITH OPTICAL SENSORS

Malcolm D. Shuster\*

339578

An earlier algorithm for multiple sensors is extended to provide three-axis attitude from multiple line-of-sight observations with a single optical sensor. The algorithm, called SCAD, is simpler computationally than either the QUEST or FOAM algorithms and, although suboptimal, suffers only imperceptible loss of accuracy for typical star cameras with limited fields of view. An approximate covariance analysis of the algorithm is presented.

## INTRODUCTION

A central problem in Spacecraft Attitude Determination has been that of determining the three-axis attitude which minimizes the cost function

$$L(A) = \frac{1}{2} \sum_{k=1}^N a_k \left| \hat{\mathbf{W}}_k - A \hat{\mathbf{V}}_k \right|^2, \quad (1)$$

where  $A$  is the direction-cosine matrix<sup>1</sup>,  $\hat{\mathbf{W}}_k$ ,  $k = 1, \dots, N$ , are directions (lines of sight, observation vectors) observed in the spacecraft body frame,  $\hat{\mathbf{V}}_k$ ,  $k = 1, \dots, N$ , are the corresponding directions known in an inertial frame (the reference vectors) and  $a_k$ ,  $k = 1, \dots, N$ , are a set of positive weights. A caret in this work will be used to denote a unit vector. This cost function was first proposed by G. Wahba<sup>2</sup> in 1965 and has been the starting point of many algorithms, of which the most popular has been the QUEST algorithm<sup>3</sup>, although other attractive algorithms exist<sup>4-8</sup>.

Of particular importance is the fact that the Wahba cost function can be derived from maximum-likelihood estimation<sup>9</sup> provided one assumes the following measurement model<sup>10</sup>, which has been called the QUEST model, because it was used in an early accuracy study of the QUEST algorithm<sup>3</sup>,

$$\hat{\mathbf{W}}_k = A \hat{\mathbf{V}}_k + \Delta \hat{\mathbf{W}}_k, \quad (2)$$

with the measurement error  $\Delta \hat{\mathbf{W}}_k$  having first and second moments<sup>†</sup>

$$E\{\Delta \hat{\mathbf{W}}_k\} = 0, \quad (3)$$

$$E\{\Delta \hat{\mathbf{W}}_k \Delta \hat{\mathbf{W}}_k^T\} = \sigma_k^2 [I - (A \hat{\mathbf{V}}_k)(A \hat{\mathbf{V}}_k)^T], \quad (4)$$

\*Professor, Department of Aerospace Engineering, Mechanics and Engineering Science, University of Florida, Gainesville, Florida 32611-6250. Phone: (352) 392-7164, FAX (352) 392-7303, email: m.shuster@ieee.org

†In fact, because of the unity constraint on the norm of  $\hat{\mathbf{W}}_k$ , the mean of  $\Delta \hat{\mathbf{W}}_k$  will have a small non-vanishing part<sup>10</sup> equal to  $-\sigma_k^2 \hat{\mathbf{W}}_k$ . This may be safely neglected in our discussion.

where  $E\{\cdot\}$  denotes the expectation,  $I$  is the  $3 \times 3$  identity matrix, and one chooses the weights to be

$$a_k = \frac{\sigma_{\text{tot}}^2}{\sigma_k^2}, \quad (5)$$

with

$$\frac{1}{\sigma_{\text{tot}}^2} \equiv \sum_{k=1}^N \frac{1}{\sigma_k^2}. \quad (6)$$

The common constant in the numerators of Eq. (5) is arbitrary, of course, but the choice of Eq. (6) makes

$$\sum_{k=1}^N a_k = 1. \quad (7)$$

One defines the attitude covariance matrix  $P_{\theta\theta}$  (Refs. 3, 10) as the covariance of the attitude error vector, which is the rotation vector<sup>1</sup> of the small rotation carrying the true attitude into the estimated attitude. Assuming the QUEST model for the measurements, this leads to the following expression for the attitude covariance matrix

$$P_{\theta\theta}^{-1} = \sum_{k=1}^N \frac{1}{\sigma_k^2} \left( I - \hat{\mathbf{W}}_k^{\text{true}} \hat{\mathbf{W}}_k^{\text{true}T} \right), \quad (8)$$

and

$$\hat{\mathbf{W}}_k^{\text{true}} \equiv A \hat{\mathbf{V}}_k, \quad (9)$$

In actual computations we must replace  $\hat{\mathbf{W}}_k^{\text{true}}$  by  $\hat{\mathbf{W}}_k$ , because the former is not known in general. Since we will be interested in calculating quantities only to lowest nonvanishing order in  $\Delta \hat{\mathbf{W}}_k$  this replacement will not lead to important errors in general.

In a previous work<sup>11</sup> a method was presented which simplified the attitude estimation process using data from an Earth albedo sensor. In that work, an approximate measurement for the direction of the Earth albedo centroid was determined by taking an average of the centroid of the directions of individual elements of the Earth albedo sensor weighted by the measured intensity, which was compared with a simulated model centroid. The effective vector measurement was combined with a measurement of the Sun direction and used as input to the TRIAD algorithm<sup>3</sup>. It could equally well have been used as input to the QUEST algorithm, but the minuscule improvement in accuracy was not justified by the additional computational burden. Brozenec and Bender<sup>12</sup> used a similar averaging of multiple star directions in a star camera to generate a reduced set of measurements for the QUEST algorithm. In the present work we present a method for retaining full three-axis attitude information from multiple data from a single optical sensor, typically a star camera. In addition, rather than relying on heuristic arguments, we will develop the algorithm in a rigorous manner. We call the algorithm SCAD (Star Camera Attitude Determination).

## CONSTRUCTION OF A SUBOPTIMAL COST FUNCTION

Let us reexamine the Wahba cost function, which we write in the form of the data-dependent part of the negative-log-likelihood function<sup>9, 10</sup>, assuming that the measurement model of Eqs. (2) through (4) is valid, namely,

$$L(A) = \frac{1}{2} \sum_{k=1}^N \frac{1}{\sigma_k^2} \left| \hat{\mathbf{W}}_k - A \hat{\mathbf{V}}_k \right|^2, \quad (10)$$

Let us now introduce vectors  $\overline{\mathbf{W}}$  and  $\overline{\mathbf{V}}$  into the cost function as

$$L(A) = \frac{1}{2} \sum_{k=1}^N \frac{1}{\sigma_k^2} \left| [\overline{\mathbf{W}} - A\overline{\mathbf{V}}] + [(\hat{\mathbf{W}}_k - \overline{\mathbf{W}}) - A(\hat{\mathbf{V}}_k - \overline{\mathbf{V}})] \right|^2, \quad (11)$$

and expand the cost function to obtain

$$\begin{aligned} L(A) = & \frac{1}{2} \frac{1}{\sigma_{\text{tot}}^2} |\overline{\mathbf{W}} - A\overline{\mathbf{V}}|^2 \\ & + (\overline{\mathbf{W}} - A\overline{\mathbf{V}})^T \sum_{k=1}^N \frac{1}{\sigma_k^2} \left( (\hat{\mathbf{W}}_k - \overline{\mathbf{W}}) - A(\hat{\mathbf{V}}_k - \overline{\mathbf{V}}) \right) \\ & + \frac{1}{2} \sum_{k=1}^N \frac{1}{\sigma_k^2} \left| (\hat{\mathbf{W}}_k - \overline{\mathbf{W}}) - A(\hat{\mathbf{V}}_k - \overline{\mathbf{V}}) \right|^2. \end{aligned} \quad (12)$$

If now  $\overline{\mathbf{W}}$  and  $\overline{\mathbf{V}}$  are chosen to have the values

$$\overline{\mathbf{W}} = \sum_{k=1}^N a_k \hat{\mathbf{W}}_k, \quad \text{and} \quad \overline{\mathbf{V}} = \sum_{k=1}^N a_k \hat{\mathbf{V}}_k, \quad (13)$$

with  $a_k$  given by Eq. (5), then the second line of Eq. (12) will vanish identically, and the third line will be a minimum (for given  $A$ ) leaving

$$L(A) = \frac{1}{2} \frac{1}{\sigma_{\text{tot}}^2} |\overline{\mathbf{W}} - A\overline{\mathbf{V}}|^2 + \frac{1}{2} \sum_{k=1}^N \frac{1}{\sigma_k^2} \left| (\hat{\mathbf{W}}_k - \overline{\mathbf{W}}) - A(\hat{\mathbf{V}}_k - \overline{\mathbf{V}}) \right|^2. \quad (14)$$

For a focal-plane sensor with a field of view of  $\pm 0.1$  rad per axis (roughly  $\pm 6$  deg per axis), we anticipate that the effective contribution of the second summation in Eq. (14) will be roughly  $(0.1)^2$  or one per cent of the first. Thus, the estimation of the spacecraft attitude will be “dominated” by the first term. The second term, which could be discarded if another vector sensor were present<sup>11,12</sup>, is not unimportant, however, if data from this sensor alone must be used to construct the three-axis attitude\*. Minimizing only the first term is not sufficient to determine the spacecraft attitude. If  $A_o$  minimizes the first term, then so does  $R(\widehat{\mathbf{W}}, \psi) A_o$ , where  $R(\widehat{\mathbf{W}}, \psi)$  denotes the direction-cosine matrix for a rotation through an arbitrary angle  $\psi$  about the direction  $\widehat{\mathbf{W}}$ ,

$$\widehat{\mathbf{W}} = \frac{\overline{\mathbf{W}}}{|\overline{\mathbf{W}}|}. \quad (15)$$

It is the second term of Eq. (14) which provides the information on  $\psi$ .

Since the overall weight of the first summation in Eq. (14) will be so much greater than that of the second term, we can determine an approximate value for the optimal attitude by writing

$$A = R(\widehat{\mathbf{W}}, \psi) A_o, \quad (16)$$

\*In fact, in the illustrative example of (Ref. 12), the second sensor is an Earth horizon scanner, whose data is sufficiently poor that attitude accuracy about the star camera boresight is worsened by an order of magnitude by the averaging procedure. The algorithm of (Ref. 12) will not lead to a loss of attitude estimation accuracy, however, if applied to the case of two noncollinear star cameras, or if the second sensor is a precise Sun sensor.

and seeking first the value  $A_o^*$  which minimizes

$$L'(A_o) \equiv \frac{1}{2} \frac{1}{\sigma_{\text{tot}}^2} |\overline{\mathbf{W}} - A_o \overline{\mathbf{V}}|^2 \quad (17)$$

and then the value  $\psi^*$  which minimizes

$$L''(\psi) \equiv \frac{1}{2} \sum_{k=1}^N \frac{1}{\sigma_k^2} \left| (\hat{\mathbf{W}}_k - \overline{\mathbf{W}}) - R(\widehat{\overline{\mathbf{W}}}, \psi) A_o^* (\hat{\mathbf{V}}_k - \overline{\mathbf{V}}) \right|^2. \quad (18)$$

Given these  $A_o^*$  and  $\psi^*$ , we anticipate that

$$A^* \equiv R(\widehat{\overline{\mathbf{W}}}, \psi^*) A_o^*, \quad (19)$$

will be a good approximation for the optimal direction-cosine matrix which minimizes the cost function of Eq. (10).

## SIMPLIFICATION OF THE COST FUNCTIONS

We can simplify the two cost functions,  $L'(A_o)$  and  $L''(\psi)$ , without loss of accuracy. Examine first  $L'(A_o)$ . Defining

$$\epsilon \equiv \frac{|\overline{\mathbf{W}}| - |\overline{\mathbf{V}}|}{|\overline{\mathbf{W}}|}, \quad (20)$$

we write

$$|\overline{\mathbf{V}}| = (1 - \epsilon) |\overline{\mathbf{W}}|, \quad (21)$$

and we can recast  $L'(A_o)$  accordingly in the form

$$L'(A_o) = \frac{1}{2} \frac{|\overline{\mathbf{W}}|^2}{\sigma_{\text{tot}}^2} \left| \widehat{\overline{\mathbf{W}}} - (1 - \epsilon) A_o \widehat{\overline{\mathbf{V}}} \right|^2. \quad (22)$$

The optimizing value of  $A_o$  will cause  $A_o \widehat{\overline{\mathbf{V}}}$  to be parallel to  $\widehat{\overline{\mathbf{W}}}$  independently of the value of  $\epsilon$ . Thus, we will achieve the identical value of  $A_o^*$  if we discard  $\epsilon$  in Eq. (22).

Likewise, substituting Eq. (21) into Eq. (18) leads to

$$L''(\psi) = \frac{1}{2} \sum_{k=1}^N \frac{1}{\sigma_k^2} \left| \left( \hat{\mathbf{W}}_k - R(\widehat{\overline{\mathbf{W}}}, \psi) A_o^* \hat{\mathbf{V}}_k \right) - \left( \overline{\mathbf{W}} - R(\widehat{\overline{\mathbf{W}}}, \psi) A_o^* \overline{\mathbf{V}} \right) \right|^2 \quad (23a)$$

$$= \frac{1}{2} \sum_{k=1}^N \frac{1}{\sigma_k^2} \left| \left( \hat{\mathbf{W}}_k - R(\widehat{\overline{\mathbf{W}}}, \psi) A_o^* \hat{\mathbf{V}}_k \right) - \epsilon \overline{\mathbf{W}} \right|^2. \quad (23b)$$

Separating the terms in the argument of the vector norm which are parallel and perpendicular to  $\widehat{\overline{\mathbf{W}}}$  leads further to

$$L''(\psi) = \frac{1}{2} \sum_{k=1}^N \frac{1}{\sigma_k^2} \left\{ \left| \left( I - \widehat{\overline{\mathbf{W}}} \widehat{\overline{\mathbf{W}}}^T \right) \left( \hat{\mathbf{W}}_k - R(\widehat{\overline{\mathbf{W}}}, \psi) A_o^* \hat{\mathbf{V}}_k \right) \right|^2 + \left| \widehat{\overline{\mathbf{W}}}^T \left( \hat{\mathbf{W}}_k - A_o^* \hat{\mathbf{V}}_k \right) - \epsilon |\overline{\mathbf{W}}| \right|^2 \right\} \quad (24a)$$

$$= \frac{1}{2} \sum_{k=1}^N \frac{1}{\sigma_k^2} \left\{ \left| \hat{\mathbf{W}}_k - R(\widehat{\overline{\mathbf{W}}}, \psi) A_o^* \hat{\mathbf{V}}_k \right|^2 - \left| \widehat{\overline{\mathbf{W}}}^T \left( \hat{\mathbf{W}}_k - A_o^* \hat{\mathbf{V}}_k \right) \right|^2 + \left| \widehat{\overline{\mathbf{W}}}^T \left( \hat{\mathbf{W}}_k - A_o^* \hat{\mathbf{V}}_k \right) - \epsilon |\overline{\mathbf{W}}| \right|^2 \right\}. \quad (24b)$$



The last two terms of Eq. (24b) are independent of  $\psi$  and may be discarded, therefore, from the cost function. Thus, we may write, finally,

$$L'(A_o) = \frac{1}{2} \left| \widehat{\mathbf{W}} - A_o \widehat{\mathbf{V}} \right|^2, \quad (25a)$$

$$L''(\psi) = \frac{1}{2} \sum_{k=1}^N \frac{1}{\sigma_k^2} \left| \widehat{\mathbf{W}}_k - R(\widehat{\mathbf{W}}, \psi) A_o^* \widehat{\mathbf{V}}_k \right|^2. \quad (25b)$$

Note that the simplification of Eqs. (17) and (18) to obtain Eqs. (25) did not rely on any approximation for the value of  $\epsilon$ . Note also that we have discarded an uninteresting factor in Eq. (25a).

We determine the suboptimal attitude by minimizing the two cost functions of Eq. (25),  $L'(A_o)$  and  $L''(\psi)$ , in sequence.

## CONSTRUCTION OF THE SUBOPTIMAL ATTITUDE

The cost function of Eq. (25a) can be made to vanish exactly for a continuum of solutions  $A_o^*$ . Except for the special case  $\widehat{\mathbf{W}} = -\widehat{\mathbf{V}}$ , for which an  $A_o^*$  may be found trivially, a suitable  $A_o^*$  is given by (Ref. 13)

$$A_o^* = (\widehat{\mathbf{W}} \cdot \widehat{\mathbf{V}}) I + \frac{(\widehat{\mathbf{W}} \times \widehat{\mathbf{V}})(\widehat{\mathbf{W}} \times \widehat{\mathbf{V}})^T}{1 + \widehat{\mathbf{W}} \cdot \widehat{\mathbf{V}}} + [[\widehat{\mathbf{W}} \times \widehat{\mathbf{V}}]]. \quad (26a)$$

$$= I + [[\widehat{\mathbf{W}} \times \widehat{\mathbf{V}}]] + \frac{1}{1 + \widehat{\mathbf{W}} \cdot \widehat{\mathbf{V}}} [[\widehat{\mathbf{W}} \times \widehat{\mathbf{V}}]]^2. \quad (26b)$$

corresponding to the quaternion<sup>1</sup>

$$\bar{q}_o^* = \sqrt{\frac{1 + \widehat{\mathbf{W}} \cdot \widehat{\mathbf{V}}}{2}} \begin{bmatrix} \frac{\widehat{\mathbf{W}} \times \widehat{\mathbf{V}}}{1 + \widehat{\mathbf{W}} \cdot \widehat{\mathbf{V}}} \\ 1 \end{bmatrix}, \quad (27)$$

and Rodrigues vector<sup>1</sup>

$$\rho_o^* = \frac{\widehat{\mathbf{W}} \times \widehat{\mathbf{V}}}{1 + \widehat{\mathbf{W}} \cdot \widehat{\mathbf{V}}}. \quad (28)$$

The particular  $A_o^*$  that we chose is of no consequence, provided that it satisfy

$$A_o^* \widehat{\mathbf{V}} = \widehat{\mathbf{W}}. \quad (29)$$

It remains only to find the angle  $\psi^*$  which minimizes the cost function of Eq. (25b).

To determine  $\psi^*$  we rewrite  $L''(\psi)$ , using techniques developed by Davenport<sup>14</sup> which have become part of the development of the QUEST algorithm<sup>3</sup>, as

$$L''(\psi) = \frac{1}{\sigma_{\text{tot}}^2} - \sum_{k=1}^N \frac{1}{\sigma_k^2} \widehat{\mathbf{W}}_k^T R(\widehat{\mathbf{W}}, \psi) A_o^* \widehat{\mathbf{V}}_k \quad (30a)$$

$$= \frac{1}{\sigma_{\text{tot}}^2} - \text{tr} \left[ B^T R(\widehat{\mathbf{W}}, \psi) \right], \quad (30b)$$

where  $\text{tr}(\cdot)$  denotes the trace operation, and

$$B = \left( \sum_{k=1}^N \frac{1}{\sigma_k^2} \hat{\mathbf{W}}_k \hat{\mathbf{V}}_k^T \right) A_o^* T \equiv C A_o^* T. \quad (31)$$

Writing Euler's formula<sup>1</sup> in the form

$$R(\hat{\mathbf{W}}, \psi) = \hat{\mathbf{W}} \hat{\mathbf{W}}^T + \sin \psi [[\hat{\mathbf{W}}]] + \cos \psi \left( I - \hat{\mathbf{W}} \hat{\mathbf{W}}^T \right), \quad (32)$$

where

$$[[\mathbf{v}]] \equiv \begin{bmatrix} 0 & v_3 & -v_2 \\ -v_3 & 0 & v_1 \\ v_2 & -v_1 & 0 \end{bmatrix}, \quad (33)$$

we have

$$L''(\psi) = \frac{1}{\sigma_{\text{tot}}^2} - \text{tr}[B] - \sin \psi \text{tr} \left[ B^T [[\hat{\mathbf{W}}]] \right] - \cos \psi \text{tr} \left[ B^T \left( I - \hat{\mathbf{W}} \hat{\mathbf{W}}^T \right) \right] \quad (34a)$$

$$\equiv \frac{1}{\sigma_{\text{tot}}^2} - \text{tr}[B] - s \sin \psi - c \cos \psi, \quad (34b)$$

with

$$\mathbf{Z} \equiv \begin{bmatrix} B_{23} - B_{32} \\ B_{31} - B_{13} \\ B_{12} - B_{21} \end{bmatrix}, \quad s \equiv \left( \mathbf{Z}^T \hat{\mathbf{W}} \right), \quad \text{and} \quad c \equiv \left( \text{tr}[B] - \hat{\mathbf{W}}^T B \hat{\mathbf{W}} \right). \quad (35)$$

Minimization of  $L''(\psi)$  leads straightforwardly to

$$-s \cos \psi^* + c \sin \psi^* = 0, \quad (36)$$

or

$$\psi^* = \arctan_2(s, c). \quad (37)$$

Here  $\arctan_2(s, c)$  is the function which returns the arc tangent of  $s/c$  in the correct quadrant. In the FORTRAN language this function is called ATAN2. The angle  $\psi^*$  will be indeterminate if both  $s$  and  $c$  vanish. This is possible, however, only if all of the  $\hat{\mathbf{W}}_k$  are identical.

The parallelism of the calculation of  $\psi^*$  in the present algorithm with that of  $\bar{q}^*$  in the QUEST algorithm is apparent. However, these methods are applied to a single angle variable and not to the four components of the quaternion of rotation. The computational burden is therefore much smaller, particularly since the need to compute the overlap eigenvalue has been eliminated.

## COVARIANCE ANALYSIS OF THE ALGORITHM

A simple approximate expression for the covariance matrix of the SCAD algorithm can be obtained if we neglect correlations between the two steps. In that case, we effectively treat the estimation of  $A_o$  and  $\psi$  as separate maximum likelihood estimation problems and can obtain an approximate estimate error covariance matrix from the Fisher information matrix associated with each of the estimation steps. Clearly, the direction-cosine matrix of Eqs. (26) causes the cost function  $L'(A_o^*)$  to vanish identically. Therefore, the coefficient in Eq. (25a) has no direct connection to the covariance matrix of the suboptimal attitude estimate, once we have embarked on our two-step optimization sequence. To compute

the attitude covariance matrix,  $P_{\theta\theta}$ , we must begin with the correct measurement model characterizing  $\widehat{\mathbf{W}}$ .

From the definition of  $\overline{\mathbf{W}}$  and  $\overline{\mathbf{V}}$  we may write

$$\overline{\mathbf{W}} = A_o \overline{\mathbf{V}} + \Delta \overline{\mathbf{W}}, \quad (38)$$

where

$$\Delta \overline{\mathbf{W}} = \sum_{k=1}^N a_k \Delta \hat{\mathbf{W}}_k. \quad (39)$$

$\Delta \overline{\mathbf{W}}$  will have vanishing expectation (to order  $\sigma_{\text{tot}}$ ) and covariance matrix

$$R_{\overline{\mathbf{W}}} = \sigma_{\text{tot}}^2 \sum_{k=1}^N a_k \left( I - \hat{\mathbf{W}}_k \hat{\mathbf{W}}_k^T \right). \quad (40)$$

From Eq. (38) it follows that

$$\widehat{\mathbf{W}} = A \widehat{\mathbf{V}} + \Delta \widehat{\mathbf{W}}, \quad (41)$$

with

$$\Delta \widehat{\mathbf{W}} = \frac{1}{|\overline{\mathbf{W}}|} \left( I - \overline{\mathbf{W}} \overline{\mathbf{W}}^T \right) \Delta \overline{\mathbf{W}}. \quad (42)$$

Thus,  $\Delta \widehat{\mathbf{W}}$  also has vanishing expectation and covariance matrix

$$R_{\widehat{\mathbf{W}}} = \frac{1}{|\overline{\mathbf{W}}|^2} \left( I - \overline{\mathbf{W}} \overline{\mathbf{W}}^T \right) R_{\overline{\mathbf{W}}} \left( I - \overline{\mathbf{W}} \overline{\mathbf{W}}^T \right), \quad (43)$$

The data-dependent part of the negative-log-likelihood<sup>9</sup> corresponding to the measurement model of Eq. (41) is, therefore, (Refs. 9, 10)

$$J(A) = \frac{1}{2} \left( \widehat{\mathbf{W}} - A \widehat{\mathbf{V}} \right)^T R_{\widehat{\mathbf{W}}}^{\#} \left( \widehat{\mathbf{W}} - A \widehat{\mathbf{V}} \right), \quad (44a)$$

$$= \frac{1}{2} \left( \widehat{\mathbf{W}} - (I + [\Delta \theta]) \widehat{\mathbf{W}}^{\text{true}} \right)^T R_{\widehat{\mathbf{W}}}^{\#} \left( \widehat{\mathbf{W}} - (I + [\Delta \theta]) \widehat{\mathbf{W}}^{\text{true}} \right), \quad (44b)$$

$$= \frac{1}{2} \left( \widehat{\mathbf{W}} - \widehat{\mathbf{W}}^{\text{true}} + [\widehat{\mathbf{W}}^{\text{true}}] \Delta \theta \right)^T R_{\widehat{\mathbf{W}}}^{\#} \left( \widehat{\mathbf{W}} - \widehat{\mathbf{W}}^{\text{true}} + [\widehat{\mathbf{W}}^{\text{true}}] \Delta \theta \right), \quad (44c)$$

where

$$\widehat{\mathbf{W}}^{\text{true}} \equiv A \widehat{\mathbf{V}}, \quad (45)$$

and  $\Delta \theta$  is the attitude error vector. The Hessian matrix (i.e., the matrix of second-order partial derivatives) of the negative-log-likelihood function of Eq. (44) with respect to  $\Delta \theta$  is then the contribution of the effective measurement  $\widehat{\mathbf{W}}$  to  $P_{\theta\theta}^{-1}$ . Thus

$$(P_{\theta\theta}^{-1})' = [[\widehat{\mathbf{W}}^{\text{true}}]] R_{\widehat{\mathbf{W}}}^{\#} [[\widehat{\mathbf{W}}^{\text{true}}]]^T \quad (46)$$

and the single prime denotes that this is the contribution to the attitude covariance arising from  $\widehat{\mathbf{W}}$ .

To determine the information matrix associated with the degree of freedom expressed by  $\psi$  let us write

$$\hat{\mathbf{U}}_k \equiv R(\widehat{\mathbf{W}}, \psi_{\text{true}}) A_o^* \hat{\mathbf{V}}_k, \quad (47)$$

where  $\psi_{\text{true}}$  is the true value of  $\psi$ . (Since the errors associated with  $A_o^*$  are expected to be very small compared to the errors associated with  $\psi^*$ , because of the geometric dilution of precision associated with the limited field of view of the star tracker, we expect  $\hat{\mathbf{U}}_k$  to be very close to  $\hat{\mathbf{W}}_k^{\text{true}}$ . Thus, we now seek the value of the infinitesimal  $\Delta\psi$  which minimizes

$$L''(\Delta\psi) \equiv \frac{1}{2} \sum_{k=1}^N \frac{1}{\sigma_k^2} |\hat{\mathbf{W}}_k - R(\widehat{\mathbf{W}}, \Delta\psi) \hat{\mathbf{U}}_k|^2 \quad (48a)$$

$$= \frac{1}{2} \sum_{k=1}^N \frac{1}{\sigma_k^2} |\hat{\mathbf{W}}_k - \hat{\mathbf{U}}_k - [[\Delta\psi \widehat{\mathbf{W}}]] \hat{\mathbf{U}}_k|^2 \quad (48b)$$

$$= \frac{1}{2} \sum_{k=1}^N \frac{1}{\sigma_k^2} |\hat{\mathbf{W}}_k - \hat{\mathbf{U}}_k + \Delta\psi \widehat{\mathbf{W}} \times \hat{\mathbf{U}}_k|^2 \quad (48c)$$

$$= \frac{1}{2} \sum_{k=1}^N \frac{1}{\sigma_k^2} \left[ |\hat{\mathbf{W}}_k - \hat{\mathbf{U}}_k|^2 + 2(\hat{\mathbf{W}}_k - \hat{\mathbf{U}}_k)^T (\widehat{\mathbf{W}} \times \hat{\mathbf{U}}_k) \Delta\psi + |\widehat{\mathbf{W}} \times \hat{\mathbf{U}}_k|^2 |\Delta\psi|^2 \right]. \quad (48d)$$

The information for  $\Delta\psi$  is just the second derivative of this quantity with respect to  $\Delta\psi$ , and since this angle is about the direction  $\widehat{\mathbf{W}}$  its contribution to the attitude information is just

$$(P_{\theta\theta}^{-1})'' = \sum_{k=1}^N \frac{1}{\sigma_k^2} |\widehat{\mathbf{W}} \times \hat{\mathbf{U}}_k|^2 \widehat{\mathbf{W}} \widehat{\mathbf{W}}^T.$$

Thus, the inverse of the covariance matrix of our new algorithm is

$$(P_{\theta\theta}^{\text{SCAD}})^{-1} = [[\widehat{\mathbf{W}}]] R_{\widehat{\mathbf{W}}}^{\#} [[\widehat{\mathbf{W}}]]^T + \left( \sum_{k=1}^N \frac{1}{\sigma_k^2} |\widehat{\mathbf{W}} \times \hat{\mathbf{W}}_k|^2 \right) \widehat{\mathbf{W}} \widehat{\mathbf{W}}^T. \quad (49)$$

In anticipation of practical application we have made the replacements

$$\widehat{\mathbf{W}}^{\text{true}} \rightarrow \widehat{\mathbf{W}}, \quad \text{and} \quad \hat{\mathbf{U}}_k^* \rightarrow \hat{\mathbf{W}}_k. \quad (50)$$

The geometric dilution of precision is manifest in the factors  $|\widehat{\mathbf{W}} \times \hat{\mathbf{W}}_k|^2$ .

The computation of the pseudo-inverse is easily accomplished. Let  $\hat{\mathbf{u}}$  and  $\hat{\mathbf{v}}$  be any two unit vectors such that  $\{\hat{\mathbf{u}}, \hat{\mathbf{v}}, \widehat{\mathbf{W}}\}$  form a right-handed orthonormal set. Since the singularity of  $R_{\widehat{\mathbf{W}}}$  is solely the manifestation that  $\widehat{\mathbf{W}}$  is a null vector of the covariance matrix, it follows that

$$R_{\widehat{\mathbf{W}}} = F F^T R_{\widehat{\mathbf{W}}} F F^T, \quad (51)$$

where

$$F \equiv [\hat{\mathbf{u}} : \hat{\mathbf{v}}] \quad (52)$$

is a  $3 \times 2$  matrix labeled by its columns. Note that

$$F F^T = I - \widehat{\mathbf{W}} \widehat{\mathbf{W}}^T. \quad (53)$$

The  $2 \times 2$  matrix  $R'$ ,

$$R' \equiv F^T R_{\widehat{\mathbf{W}}} F, \quad (54)$$

will be nonsingular if the attitude is observable. Hence, in the only cases of interest

$$R_{\widehat{\mathbf{W}}}^\# = F \left( F^T R_{\widehat{\mathbf{W}}} F \right)^{-1} F^T. \quad (55)$$

The verification that  $R'$  is nonsingular would be a routine step in the computation of the attitude to verify observability. A similar step occurs in implementation the QUEST algorithm in which the rank of the QUEST information matrix is tested<sup>15</sup>.

We may simplify the expression for the SCAD inverse covariance matrix further by noting that

$$[[\widehat{\mathbf{W}}]] F \equiv G = [-\hat{\mathbf{v}} : \hat{\mathbf{u}}]. \quad (56)$$

Hence, we have finally

$$(P_{\theta\theta}^{\text{SCAD}})^{-1} = G \left( F^T R_{\widehat{\mathbf{W}}} F \right)^{-1} G^T + \left( \sum_{k=1}^N \frac{1}{\sigma_k^2} |\widehat{\mathbf{W}} \times \hat{\mathbf{W}}_k|^2 \right) \widehat{\mathbf{W}} \widehat{\mathbf{W}}^T. \quad (57)$$

Note that the second term in Eq. (57) may be written as

$$\widehat{\mathbf{W}} \widehat{\mathbf{W}}^T \left( P_{\theta\theta}^{\text{QUEST}} \right)^{-1} \widehat{\mathbf{W}} \widehat{\mathbf{W}}^T.$$

Note that the QUEST covariance matrix will be a good approximation for the SCAD covariance matrix when the field of view of the sensor has a small diameter. The comparison of these expressions will be carried out in the next section.

If  $\rho$  is the root-mean-square arc length of the individual star observations from  $\widehat{\mathbf{W}}$ , then we anticipate that the first term in Eq. (57) will differ from the corresponding term of Eq. (49) by fractional errors of order  $\rho^2$ . By this same token, we observe that the contribution of second term in Eq. (49) or (57) to the total inverse covariance matrix will be smaller than that of the first by a factor of  $\rho^2$ .

## MODEL COVARIANCE ANALYSIS

It follows from the Cramér-Rao Theorem<sup>9</sup> that

$$P_{\theta\theta}^{\text{QUEST}} \leq P_{\theta\theta}^{\text{SCAD}}. \quad (58)$$

The important question is how large is the difference between the two attitude covariance matrices. To answer this question, we examine the two covariances (rather the two inverse covariance matrices) in a simple model, in which the star camera is assumed to have a circular field of view of angular radius  $\rho$ , and the stars are assumed to be distributed uniformly over the field of view of the sensor. We will assume for convenience that the star camera has its boresight along the spacecraft  $z$ -axis. We assume in addition that the covariance matrix of every line-of-sight observation is characterized by the same standard deviation  $\sigma^2$ .

In the limit that  $N$  is large we may replace the summation over the observations by an integral. Thus, if  $f(\hat{\mathbf{W}})$  is any function of an observed direction, we may write

$$\sum_{k=1}^N f(\hat{\mathbf{W}}_k) \rightarrow \frac{N}{\Omega} \int_0^{2\pi} \int_0^\rho f(\hat{\mathbf{W}}(\vartheta, \varphi)) \sin \vartheta d\vartheta d\varphi, \quad (59)$$

with  $\Omega$  the solid angle subtended by the star camera field of view,

$$\Omega = 2\pi(1 - \cos \rho), \quad (60)$$

and

$$\hat{\mathbf{W}}(\vartheta, \varphi) = \begin{bmatrix} \sin \vartheta \cos \varphi \\ \sin \vartheta \sin \varphi \\ \cos \vartheta \end{bmatrix}. \quad (61)$$

With these substitutions the inverse covariance matrix for each star camera using the QUEST algorithm for computing the attitude is

$$(P_{\theta\theta}^{\text{QUEST}})^{-1} = \frac{N}{\sigma^2} \text{diag}(a, a, b), \quad (62)$$

where

$$\text{diag}(a, b, c) \equiv \begin{bmatrix} a & 0 & 0 \\ 0 & b & 0 \\ 0 & 0 & c \end{bmatrix}, \quad (63)$$

and

$$a = (4 + \cos \rho + \cos^2 \rho)/6, \quad (64a)$$

$$b = (2 - \cos \rho - \cos^2 \rho)/3. \quad (64b)$$

Note that as  $\rho \rightarrow 0$  we have that  $a \rightarrow 1$  and  $b \rightarrow 0$ .

For the SCAD algorithm, we note first that

$$\overline{\mathbf{W}} = \left( \frac{1 + \cos \rho}{2} \right) \hat{\mathbf{z}}, \quad (85a)$$

$$R_{\overline{\mathbf{W}}} = \frac{\sigma^2}{N} \text{diag}(a, a, b), \quad (65b)$$

$$R_{\widehat{\mathbf{W}}} = \frac{\sigma^2}{N} \left( \frac{2}{1 + \cos \rho} \right)^2 \text{diag}(a, a, 0). \quad (65c)$$

From these results we may compute the inverse covariance matrix for the SCAD algorithm given in Eq. (49) to obtain

$$(P_{\theta\theta}^{\text{SCAD}})^{-1} = \frac{N}{\sigma^2} \left\{ \left( \frac{1 + \cos \rho}{2} \right)^2 \text{diag}(1/a, 1/a, 0) + \text{diag}(0, 0, b) \right\}. \quad (66)$$

The two covariance matrices are both diagonal in the model case examined.

We note first that the variance about the boresight is identical for this example for both the QUEST and the SCAD algorithms

$$\frac{\sigma_b^{\text{SCAD}}}{\sigma_b^{\text{QUEST}}} = 1, \quad (67)$$

**TABLE 1**  
**COMPARISON OF THE SCAD AND QUEST ALGORITHMS**

Field of View	$\sigma_t^{\text{SCAD}} / \sigma_t^{\text{QUEST}}$	$\sigma_b^{\text{SCAD}} / \sigma_b^{\text{QUEST}}$
$\pm 6$ deg	1.000004	1.000000
$\pm 12$ deg	1.000007	1.000000
$\pm 30$ deg	1.003	1.000000
$\pm 60$ deg	1.04	1.000000
$\pm 90$ deg	1.33	1.000000

where the subscript  $b$  stands for "boresight." Thus, not only do we recover the information on the attitude about the boresight, we recover it completely.

The ratio of the standard deviation of the SCAD algorithm to that of the QUEST algorithm for attitude errors about axes normal to  $\widehat{\mathbf{W}}$  is

$$\frac{\sigma_t^{\text{SCAD}}}{\sigma_t^{\text{QUEST}}} = \frac{\alpha}{|\widehat{\mathbf{W}}|} = \frac{2}{1 + \cos \rho} \frac{4 + \cos \rho + \cos^2 \rho}{6}, \quad (68)$$

where  $t$  stands for "transverse." Since we are interested in this algorithm primarily for a sensor of limited field of view, we define

$$\delta \equiv 1 - \cos \rho. \quad (69)$$

Then

$$\frac{\sigma_t^{\text{SCAD}}}{\sigma_t^{\text{QUEST}}} = \frac{2}{2 - \delta} \frac{6 - 3\delta + \delta^2}{6} = 1 + \frac{1}{6} \frac{\delta^2}{1 - \delta/2}. \quad (70)$$

Thus, for this simple example, the standard deviation of attitude errors for axes perpendicular to the bore sight is approximately

$$\frac{\sigma_t^{\text{SCAD}}}{\sigma_t^{\text{QUEST}}} \approx 1 + \rho^4/24 + O(\rho^6/96). \quad (71)$$

For limited fields of view, the relative loss in accuracy compared to the QUEST algorithm is imperceptible. Table 1 gives the relative loss of accuracy for several fields of view. Note that because of the rotation symmetry of our example about the star camera boresight, the cross covariance between  $\Delta\psi$  and  $\Delta\theta$  will vanish. Thus, the errors introduced by our approximate treatment of the attitude estimate covariance are completely suppressed.

## REFERENCES

- 1 SHUSTER, M. D. "A Survey of Attitude Representations," *Journal of the Astronautical Sciences*, Vol. 41, No. 4, Oct.-Dec. 1993, pp. 439-517.
- 2 WAHBA, G., "Problem 65-1: A Least Squares Estimate of Spacecraft Attitude," *Siam Review*, Vol. 7, No. 3, July 1965, p. 409.
- 3 SHUSTER, M. D., and OH, S. D. "Three-Axis Attitude Determination from Vector Observations," *Journal of Guidance and Control*, Vol. 4, No. 1, Jan.-Feb. 1981, pp. 70-77.
- 4 MARKLEY, F. L. "Attitude Determination using Vector Observations and the Singular Value Decomposition," *Journal of the Astronautical Sciences*, Vol. 36, No. 3, July-Sept. 1988, pp. 245-258.

- 5 MARKLEY, F. L., "Attitude Determination Using Vector Observations: A Fast Optimal Matrix Algorithm," *Journal of the Astronautical Sciences*, Vol. 41, No. 2, April–June 1993, pp. 439–517.
- 6 MORTARI, D., "Energy Approach Algorithm for Attitude Determination from Vector Observations," *Journal of the Astronautical Sciences* (to appear).
- 7 MORTARI, D., "Euler-q Algorithm for Attitude Determination from Vector Observations," submitted to the *Journal of Guidance, Control and Dynamics*.
- 8 MORTARI, D., "A Closed-Form Solution to the Wahba Problem," submitted to the *Journal of the Astronautical Sciences*.
- 9 SORENSON, H. W., *Parameter Estimation*, Marcel Dekker, New York, 1980.
- 10 SHUSTER, M. D., "Maximum Likelihood Estimation of Spacecraft Attitude," *Journal of the Astronautical Sciences*, Vol. 37, No. 1, Jan.–March, 1989, pp. 79–88.
- 11 FISHER, H. L., MUSSER, K. L., and SHUSTER, M. D., "Coarse Attitude Determination from Earth Albedo Measurements," *IEEE Transactions on Aerospace and Electronic Systems*, Vol. 29, No. 1, Jan.–Feb. 1993, pp. 22–26.
- 12 BROZENEC, THOMAS F., and BENDER, DOUGLAS J., "A Simple Suboptimal Least-Squares Algorithm for Attitude Determination with Multiple Sensors," *Proceedings, Flight Mechanics/Estimation Theory Symposium*, NASA Goddard Space Flight Center, Greenbelt, Maryland, May 17–19, 1994, pp. 529–743.
- 13 SHUSTER, M. D., "Attitude Estimation from the Measurement of a Direction and an Angle," *Revista Brasileira de Ciências Mecânicas*, Vol. 16, Special Issue, 1994, pp. 19–23.
- 14 DAVENPORT, P. B. (unpublished).
- 15 SHUSTER, M. D., (unpublished).
- 16 SHUSTER, M. D., and NATANSON, G. A., "Quaternion Computation from a Geometric Point of View," *Journal of the Astronautical Sciences*, Vol. 41, No. 4, Oct.–Dec. 1993, pp. 545–556.
- 17 SHUSTER, M. D., "Kalman Filtering of Spacecraft Attitude and the QUEST Model," *Journal of the Astronautical Sciences* Vol. 38, No. 3, July–Sept. 1990, pp. 377–393.

## Appendix: Implementation of SCAD

The following are the steps for computing the optimal attitude using the SCAD algorithm:

- From the input data,  $\hat{\mathbf{W}}_k$ ,  $k = 1, \dots, N$ , the corresponding reference vectors,  $\hat{\mathbf{V}}_k$ ,  $k = 1, \dots, N$ , and the sensor variances,  $\sigma_k^2$ ,  $k = 1, \dots, N$ , compute: (1)  $\sigma_{\text{tot}}^2$  according to Eq. (6); (2) the weights  $a_k$ ,  $k = 1, \dots, N$ , according to Eq. (5); (3)  $\overline{\mathbf{W}}$  and  $\overline{\mathbf{V}}$  according to Eq. (13); and (4) the matrix  $\mathbf{C}$  according to Eq. (31).
- From these quantities compute the unit vectors  $\widehat{\overline{\mathbf{W}}}$  and  $\widehat{\overline{\mathbf{V}}}$  according to Eq. (15) for  $\widehat{\overline{\mathbf{W}}}$  and similarly for  $\widehat{\overline{\mathbf{V}}}$ .
- Compute  $R_{\widehat{\overline{\mathbf{W}}}}$  according to Eqs. (40) and (43).
- Calculate the matrices  $\mathbf{F}$  and  $\mathbf{G}$  according to Eqs. (54) and (56).



- Compute  $R'$  from Eq. (54) and verify that it is full rank. If  $R'$  is not full rank, the attitude is not observable from the data and the computation is terminated. If  $R'$  is full rank, continue.
- Compute  $A_o^*$  according to the following method:
  - If  $\widehat{\mathbf{W}} \cdot \widehat{\mathbf{V}} > 1 - \varepsilon$  for some predetermined value of  $\varepsilon$ , set  $A_o^* = I$ . (The value of  $\varepsilon$  will be a function of the machine precision and the accuracy of the data.)
  - If  $\widehat{\mathbf{W}} \cdot \widehat{\mathbf{V}} < -1 + \varepsilon$  for some predetermined value of  $\varepsilon$ , set  $A_o^* = R(\hat{\mathbf{n}}, \pi)$ , where  $\hat{\mathbf{n}}$  is the representation of the sensor coordinate axis for which  $|\hat{\mathbf{n}} \times \widehat{\mathbf{W}}|$  is largest.
  - Otherwise, use any of Eqs. (26a) through (28) to generate  $A_o^*$  either directly or via the quaternion or Rodrigues vector.
- Compute  $B$  according to Eq. (31), and  $Z$ ,  $s$ , and  $c$  according to Eq. (35).
- Compute  $\theta^*$  according to Eq. (37) and  $A^*$  according to Eq. (19).
- Compute  $P_{\theta\theta}^{\text{SCAD}}$  according to Eq. (57).

This completes the SCAD algorithm.

The above implementation was given with a mind to generating the direction-cosine matrix as final output. If it is desired to generate instead either the quaternion or the Rodrigues vector as final output, one requires the formulae:

$$\cos(\theta^*/2) = \sqrt{\frac{1+c}{2}}, \quad \text{and} \quad \sin(\theta^*/2) = \frac{s}{2 \cos(\theta^*/2)}, \quad (\text{A1})$$

whence

$$\bar{q}(\widehat{\mathbf{W}}, \theta^*) = \begin{bmatrix} \sin(\theta^*/2) \widehat{\mathbf{W}} \\ \cos(\theta^*/2) \end{bmatrix}, \quad \text{and} \quad \rho(\widehat{\mathbf{W}}, \theta^*) = \frac{\sin(\theta^*/2)}{\cos(\theta^*/2)} \widehat{\mathbf{W}}, \quad (\text{A2})$$

and combining these directly with  $\bar{q}_0^*$  and  $\rho_o^*$  according to the prescriptions in (Ref. 1).



533-35

16933/

## A TRANSITION MATRIX APPROACH TO THE DAVENPORT GYRO CALIBRATION SCHEME\*

337587

16A

G. A. Natanson†

The in-flight gyro calibration scheme commonly used by NASA Goddard Space Flight Center (GSFC) attitude ground support teams closely follows an original version of the Davenport algorithm developed in the late seventies. Its basic idea is to minimize the least-squares differences between attitudes gyro-propagated over the course of a maneuver and those determined using post-maneuver sensor measurements. The paper represents the scheme in a recursive form by combining necessary partials into a rectangular matrix, which is propagated in exactly the same way as a Kalman filter's square transition matrix. The nontrivial structure of the propagation matrix arises from the fact that attitude errors are not included in the state vector, and therefore their derivatives with respect to estimated gyro parameters do not appear in the transition matrix defined in the conventional way.

In cases when the required accuracy can be achieved by a single iteration, representation of the Davenport gyro calibration scheme in a recursive form allows one to discard each gyro measurement immediately after it was used to propagate the attitude and state transition matrix. Another advantage of the new approach is that it utilizes the same expression for the error sensitivity matrix as that used by the Kalman filter. As a result the suggested modification of the Davenport algorithm made it possible to reuse software modules implemented in the Kalman filter estimator, where both attitude errors and gyro calibration parameters are included in the state vector.

The new approach has been implemented in the ground calibration utilities used to support the Tropical Rainfall Measuring Mission (TRMM). The paper analyzes some preliminary results of gyro calibration performed by the TRMM ground attitude support team. It is demonstrated that an effect of the second iteration on estimated values of calibration parameters is negligibly small, and therefore there is no need to store processed gyro data. This opens a promising opportunity for onboard implementation of the suggested recursive procedure by combining it with the Kalman filter used to obtain necessary attitude solutions at the beginning and end of each maneuver.

---

\* This work was supported by the National Aeronautics and Space Administration (NASA) / Goddard Space Flight Center (GSFC), Greenbelt, Maryland, Contract GS-35F-4381G, Task Order No. S-03365-Y.

† Computer Sciences Corporation (CSC), 10110 Aerospace Rd., Seabrook, MD, USA 20706

## I. INTRODUCTION

Propagation of a state vector from one measurement time to another is usually done<sup>1</sup> by introducing a transition matrix formed by partial derivatives of the current state with respect to the state at an epoch time. A well-known technique<sup>2,3</sup> has been developed to propagate the transition matrix between sequential measurements using gyro data. The paper extends this propagation technique to the Davenport gyro calibration scheme.<sup>4,7</sup> The main obstacle to such an extension comes from the fact that the cited gyro calibration scheme treats an a priori given change in the spacecraft attitude within a specified time interval as a pseudo-measurement, and therefore attitude errors are not included in the state vector anymore; as a result, their derivatives with respect to estimated gyro parameters (such as misalignments, biases, and scale factors) do not appear in the transition matrix defined in the conventional way. To overcome this complication, the new approach combines necessary partials into a *rectangular* matrix, which can be propagated in exactly the same way as the conventional (*square* by definition) transition matrix.<sup>2,3</sup>

Assuming that the first iteration eliminates bulk errors, representation of the least-squares gyro calibration scheme in a recursive form allows one to discard each gyro measurement immediately after it is used to propagate the attitude and state transition matrix. Due to a significant decrease in required storage size, this feature of the new approach seems especially promising for onboard applications.

The next Section presents a simplified derivation of the original version of the Davenport algorithm.<sup>4,5</sup> Its final result is an explicit expression of the vector attitude residual in terms of the error sensitivity matrices  $\psi_k$  utilized by Kalman filter estimator.<sup>3</sup> It is shown that the derived expression turns into the conventional one<sup>7</sup> if only linear terms are kept in the expansion of each matrix  $\psi_k$  as a Taylor series in the duration  $\Delta t_k$  of the  $k^{\text{th}}$  propagation interval.

Section III introduces a *rectangular* matrix which gyro-governed evolution is performed via the same recurrence relations as those used for gyro propagation of the conventional state transition matrix. The derivation is accomplished in Section IV, which outlines main steps of the suggested recursive procedure.

The new algorithm has been implemented<sup>8</sup> and successfully used to calibrate gyros<sup>9</sup> for the Tropical Rainfall Measuring Mission (TRMM). One of the advantages of the suggested modification of the Davenport algorithm is that it allowed a reuse of software modules implemented in the Kalman filter estimator,<sup>3</sup> where both attitude errors and gyro calibration parameters are included in the solve-for state vector. Section V discusses some preliminary results of the TRMM gyro calibration. It is shown that the required accuracy of gyro calibration can be indeed achieved by a single iteration, and therefore each gyro measurement can be indeed discarded immediately after it was used. The paper also studies a possibility to reduce a volume of processed gyro data without jeopardizing the accuracy of calibration.

## II. MATHEMATICAL GROUNDS OF DAVENPORT ALGORITHM

The Davenport method<sup>4</sup> is a two-step procedure. The first step is to determine attitudes at the ends of specially selected calibration intervals. For successful calibration, the selected time intervals usually cover a series of maneuvers associated with significant changes in body rates. It is essential that, regardless of maneuver specifics, each calibration interval must both start and end in a constant-rate mode. To determine the spacecraft attitude at the ends of each interval, sensor measurements are then collected only during time periods within constant-rate modes, when unknown errors in gyro misalignments and scale factors are compensated by additional gyro biases estimated simultaneously with the spacecraft attitude. As a result, one can assume that gyro propagation from one sensor measurement time to another is done accurately enough, despite the fact that gyros have not been properly calibrated yet.

The second step is quaternion propagation starting from the predetermined attitude quaternion at the beginning of each calibration interval and stopping at its end. The resultant propagated quaternion is then compared with the second of two attitude quaternions predetermined for this calibration interval. The comparison is done by multiplying one of the two quaternions at the ending time by the inverse of other. The vector part of the product is then treated as a vector residual, with the total number of these attitude quaternion vector residuals (AQVRs) always equal to the number of the calibration intervals.

Davenport's principal result is an approximate expression for the AQVRs in terms of vector deviations of the observed angular velocity vectors from the true rates. The outline of the Davenport method presented here mainly follows Keat's<sup>5</sup> interpretation of Davenport's original work.<sup>4</sup> To simplify the notation, the discussion will be limited only to a single maneuver so that the index labeling different maneuvers can be omitted. An extension of the final expression for an AQVR to a series of sequential maneuvers is performed in a trivial way by attaching an additional index to both residual and all angular velocity vectors.

Let  $\vec{\omega}_k^{\text{adj}}$  be an observed angular velocity vector obtained by adjusting measured rates with some estimated parameters, where subscript  $k$  refers to the  $k$ -th available gyro measurement within the maneuver in question. The observed vector differs from a true vector  $\vec{\omega}_k$  by a rate error  $\delta\vec{\omega}_k$ , that is,

$$\vec{\omega}_k = \vec{\omega}_k^{\text{adj}} - \delta\vec{\omega}_k. \quad (1)$$

Both vectors  $\vec{\omega}_k^{\text{adj}}$  and  $\vec{\omega}_k$  are assumed to remain constant during a time interval  $\Delta t_k$  so that the quaternion propagated over  $n$  intervals (starting from the known quaternion  $\vec{q}_{\text{init}}$ ) can be represented as

$$\vec{q}_{\text{prop}} = \vec{q}_{\text{init}} \prod_{k=1}^n \vec{q}(\vec{\omega}_k^{\text{adj}} \Delta t_k), \quad (2)$$

where<sup>10</sup>  $\bar{q}(\bar{\omega} \Delta t) = [\hat{\omega} \sin(\phi/2), \cos(\phi/2)]$ , with  $\hat{\omega} \equiv \bar{\omega}/|\bar{\omega}|$  and  $\phi \equiv |\bar{\omega}| \Delta t$ . The AQVR  $\bar{Z}$  is defined via the relation:\*

$$[\bar{Z}, \sqrt{1-|\bar{Z}|^2}] = \delta\bar{Q} \equiv \bar{q}_{\text{fin}}^{-1} \bar{q}_{\text{prop}}, \quad (3)$$

where  $\bar{q}_{\text{fin}}$  is the given attitude quaternion in the end of the maneuver.

It is assumed that the attitude quaternion  $\bar{q}_{\text{fin}}$  can be obtained from  $\bar{q}_{\text{init}}$  by propagating the latter with the true constant angular velocity vectors  $\bar{\omega}_k$  over the time intervals  $\Delta t_k$ , so that

$$\bar{q}_{\text{fin}} = \bar{q}_{\text{init}} \prod_{k=1}^n \bar{q}(\bar{\omega}_k \Delta t_k). \quad (4)$$

To express the AQVR  $\bar{Z}$  in terms of errors in gyro parameters, one first needs to linearize the quaternion product  $\bar{q}_{\text{fin}}^{-1} \bar{q}_{\text{prop}}$  in  $\delta\bar{\omega}_k$ . At this point one has to deal with unnormalized quaternions, which form the so-called 'associative algebra'. Note that both attitude and propagation quaternions discussed above are normalized quaternions, which cannot be either summed up or multiplied by a scalar, in contrast with unnormalized quaternions. On the other hand, the inverse operation  $\bar{q}^{-1}$  is well defined just for normalized quaternions. Only the multiplication law given by Eq. (D-8) in Ref. 10 is common for both normalized and unnormalized quaternions. It is essential that, by analogy with orthogonal matrices, the multiplication law is associative, i. e.,  $\bar{q}(\bar{q}'\bar{q}'') = (\bar{q}\bar{q}')\bar{q}''$  for any three unnormalized quaternions,  $\bar{q}$ ,  $\bar{q}'$ , and  $\bar{q}''$ . Another important features of the multiplication law are that  $\bar{q}(\bar{q}' + \bar{q}'') = \bar{q}\bar{q}' + \bar{q}\bar{q}''$  and that  $\bar{q}(k\bar{q}') = (k\bar{q})\bar{q}'$  for a scalar multiplication. After the mentioned features of the multiplication law are established, unnormalized quaternions can be formally treated in the same way as square matrices, with the norm of quaternion given by Eq. (D-9) in Ref. 10 used instead of the matrix determinant. In particular, all Taylor expansions look very similarly, except that each product should be computed based on the quaternion multiplication law.

Substituting Eqs. (2) and (4) into Eq. (3) and keeping only terms linear in  $\delta\bar{\omega}_k$ , one can represent the latter expression as

$$\delta\bar{Q} \approx (1-n)[\bar{0}, 1] + \sum_{k=1}^n \bar{q}_{k \rightarrow n}^{-1} \delta\bar{q}_k \bar{q}_{k \rightarrow n}, \quad (5)$$

where

$$\bar{q}_{k \rightarrow k+\Delta k} \equiv \prod_{k'=k+1}^{k+\Delta k} \bar{q}(\bar{\omega}_{k'}^{\text{adj}} \Delta t_{k'}) \quad \text{for } \Delta k = 1, \dots, n-k > 0, \quad (6a)$$

---

\* Note that our definition of the AQVR differs by the factor (-1) from that used by Keat.<sup>5</sup>

$$\bar{q}_{n \rightarrow n} \equiv [\bar{0}, 1], \quad (6b)$$

and

$$\left[ \bar{z}_k, \sqrt{1 - |\bar{z}_k|^2} \right] = \delta \bar{q}_k \equiv \bar{q}(-\bar{\omega}_k \Delta t_k) \bar{q}(\bar{\omega}_k^{\text{adj}} \Delta t_k). \quad (7)$$

Note that the sum in the right-hand side of Eq. (5) is formed by the products of normalized quaternions, and hence, to simplify each product, one can take advantage of the existent isomorphism between normalized quaternions and  $3 \times 3$  orthogonal matrices. Making use of Eq. (12-7b) in Ref. 10, one can easily verify that

$$\mathbf{R} \mathbf{A}(\bar{\mathbf{g}}) \mathbf{R}^T = \mathbf{A}(\mathbf{R}\bar{\mathbf{g}}), \quad (8)$$

where  $\mathbf{R}$  is an arbitrary  $3 \times 3$  orthogonal matrix, whereas the rotation matrix  $\mathbf{A}(\bar{\mathbf{g}})$  associated with the Gibbs vector  $\bar{\mathbf{g}}$  is given by Eq. (12-7b) in Ref. 10, with  $\bar{\mathbf{g}} \equiv \hat{\mathbf{e}} \tan(\Phi/2)$ . Representing Eq. (8) in the quaternion form and substituting the resultant expression in the sum in the right-hand side of Eq. (5), one can finally represent the AQVR  $\bar{\mathbf{Z}}$  as

$$\bar{\mathbf{Z}} = \sum_{k=1}^n \left[ \mathbf{R}_{k \rightarrow n} \bar{\mathbf{z}}_k + O(|\delta \bar{\omega}_k|^2) \right], \quad (9)$$

where  $\mathbf{R}_{k \rightarrow k'}$  is the rotation matrix associated with the propagation quaternion  $\bar{q}_{k \rightarrow k'}$ .

As discussed in detail in Ref. 11, an explicitly expression of the vector  $\bar{\mathbf{z}}_k$  in terms of the rate error  $\delta \bar{\omega}_k$  has the form:

$$\bar{\mathbf{z}}_k = \frac{1}{2} \psi_k \delta \bar{\omega}_k + O(|\delta \bar{\omega}_k|^2), \quad (10)$$

where  $\psi_k$  is the error sensitivity matrix used by the Kalman filter estimator,<sup>3</sup> that is,

$$\psi_k \equiv \mathbf{I}_3 \Delta t_k - \frac{1}{2} [\bar{\omega}_k^{\text{adj}} \times] \Delta t_k^2 v^2(\phi_k^{\text{adj}}/2) + 2 [\bar{\omega}_k^{\text{adj}} \times]^2 \eta(\phi_k^{\text{adj}}) \Delta t_k^3, \quad (11)$$

with  $v(\phi) \equiv \sin \phi / \phi$ ,  $\eta(\phi) \equiv 0.5 (1 - \sin \phi) / \phi^2$ , and  $\phi_k^{\text{adj}} \equiv |\bar{\omega}_k^{\text{adj}}| \Delta t_k$ . Note that a slightly different representation for error sensitivity matrix (11), compared with Ref. 3, makes it possible to compute this matrix using expansions explicitly stable at the limit  $|\bar{\omega}_k^{\text{adj}}| \rightarrow 0$ .

Finally, AQVRs (9) are represented as linear combinations of errors  $\Delta x_i$  ( $i=1, \dots, p$ ) in gyro parameters:

$$\bar{\mathbf{Z}} \approx \frac{1}{2} \sum_{i=1}^p \Delta x_i \sum_{k=1}^n \mathbf{R}_{k \rightarrow n} \psi_k \bar{\mathbf{f}}_i(\bar{\omega}_k^{\text{adj}}). \quad (12)$$

by substituting the rate errors

$$\delta \bar{\omega}_k = \sum_{i=1}^p \bar{f}_i(\bar{\omega}_k^{\text{adj}}) \Delta x_i. \quad (13)$$

into Eq. (10). Computation of necessary partials is then performed in a trivial way.

Note that Keat's formula<sup>5</sup> for the AQVR (utilized in the conventional version<sup>7</sup> of the Davenport algorithm<sup>4</sup>) is obtained from Eq. (13) by keeping only the first term in the right-hand side of Eq. (11), which seems to be a sufficiently accurate approximation in most cases (see comments made in the end of Section V). Another minor modification comes from a slightly different choice of the state vector  $\Delta \bar{x}$ , which is formed by three bias errors  $\Delta b_i$  ( $i=1,2,3$ ), three scale factor errors  $\Delta k_i$  ( $i=1,2,3$ ), and two misalignment angle errors  $\varepsilon_{k,i}$  ( $k=1,2$ ) for each of three gyros ( $i=1,2,3$ ). Such a choice of gyro calibration parameters<sup>8</sup> makes it possible to calibrate each gyro separately, which is convenient in case of a spacecraft having only one gyro, such as Solar and Heliospheric Observatory (SOHO).<sup>12</sup>

### III. PROPAGATION OF ATTITUDE MATRIX VECTOR RESIDUALS

The main purpose of this Section is to show that an attitude residual can be represented in the general form:

$$\bar{\theta} = \tilde{H} \tilde{\Phi}_{\text{state}} \Delta \bar{x}, \quad (14)$$

where  $\bar{\theta}$ ,  $\Delta \bar{x}$ ,  $\tilde{H}$ , and  $\tilde{\Phi}_{\text{state}}$  are usually referred to as a measurement residual, a state error vector, a sensitivity matrix, and a state transition matrix, respectively. The crucial point is that the transition matrix  $\tilde{\Phi}_{\text{state}}$  can be computed as the last term  $\tilde{\Phi}_{\text{state}} = \tilde{\Phi}_n$  in a sequence of recurrence relations:

$$\tilde{\Phi}_k = \Phi_{k-1 \rightarrow k} \tilde{\Phi}_{k-1}, \quad (15)$$

where the  $(p+3) \times (p+3)$  matrix  $\Phi_{k-1 \rightarrow k}$  is an incremental transition matrix conventionally used in Kalman filter applications to propagate the attitude state vector (see, for example, Eq. (F8-26) in Ref. 3). A certain complication, however, comes from the fact that the calibration scheme in question estimates only gyro calibration parameters, and therefore attitude errors are not included into the state vector  $\Delta \bar{x}$ . As a result  $\tilde{\Phi}_k$  turn out to be rectangular matrices having  $p+3$  rows but only  $p$  columns.

As mentioned above, the initial and final attitudes in the Davenport method are determined using sensor measurements in constant-rate modes, when solved-for biases compensate for errors in gyro misalignments and scale factors. The attitude matrix vector residual (AMVR),  $\bar{\theta}$ , is then defined via the relation:



$$\exp[\bar{\theta} \times] \equiv \mathbf{A}_{\text{obs}} \mathbf{A}_{\text{prop}}^T, \quad (16)$$

where  $\mathbf{A}_{\text{obs}}$  and  $\mathbf{A}_{\text{prop}}$  are the attitude matrices associated with the attitude quaternions  $\bar{\mathbf{q}}_{\text{fin}}$  and  $\bar{\mathbf{q}}_{\text{prop}}$  in the previous Section.\* One thus finds

$$\bar{\theta} \sin(|\bar{\theta}|/2)/|\bar{\theta}| = \bar{\mathbf{Z}}. \quad (17)$$

Since we are interested only in terms linear in gyro errors, one can simply put

$$\bar{\theta} \approx 2\bar{\mathbf{Z}} \quad (18)$$

and make use of Eq. (12) to represent the AMVR  $\bar{\theta}$  as the last term  $\bar{\theta} \approx \bar{\theta}_n$  in the sequence

$$\bar{\theta}_k = \sum_{i=1}^p \Delta x_i \psi_k \bar{\mathbf{f}}_i(\bar{\omega}_k^{\text{adj}}) + \mathbf{R}_{k-1 \rightarrow k} \bar{\theta}_{k-1}, \quad (19)$$

with  $\bar{\theta}_0 = \bar{\mathbf{0}}$ .

Eq. (19) immediately leads to the conventional Kalman filter expression<sup>3</sup> for propagation of the combined attitude error / gyro calibration parameter state vector:

$$\begin{bmatrix} \bar{\theta}_k \\ \Delta \bar{\mathbf{x}} \end{bmatrix} = \Phi_{k-1 \rightarrow k} \begin{bmatrix} \bar{\theta}_{k-1} \\ \Delta \bar{\mathbf{x}} \end{bmatrix}, \quad (20)$$

where

$$\Phi_{k-1 \rightarrow k} \equiv \begin{bmatrix} \mathbf{R}_{k-1 \rightarrow k} & \psi_k \mathbf{F}_k \\ \mathbf{0}_{p \times 3} & \mathbf{I}_p \end{bmatrix}, \quad (21)$$

with

$$\mathbf{F}_k \equiv [\bar{\mathbf{f}}_1(\bar{\omega}_k^{\text{adj}}), \dots, \bar{\mathbf{f}}_p(\bar{\omega}_k^{\text{adj}})]. \quad (22)$$

By initializing sequence (15) via the relation

---

\* The author is thankful to J. Sedlak for pointing to a misprint in the definition of the AMVR  $\bar{\theta}$  in Ref. 11 leading to a sign error in Eqs. (III-5), (III-6), (III-8), (III-14), and (III-17) there.

$$\tilde{\Phi}_0 \equiv \begin{bmatrix} \mathbf{0}_{3 \times p} \\ \mathbf{I}_p \end{bmatrix} \quad (23)$$

one finds that

$$\tilde{\Phi}_1 \equiv \begin{bmatrix} \psi_1 \mathbf{F}_1 \\ \mathbf{I}_p \end{bmatrix} \quad (24)$$

and hence, making use of Eq. (20) at  $k=1$ ,

$$\bar{\theta}_1 = \tilde{\mathbf{H}} \tilde{\Phi}_1 \Delta \bar{\mathbf{x}}, \quad (25)$$

with

$$\tilde{\mathbf{H}} \equiv \begin{bmatrix} \mathbf{I}_3 & \mathbf{0}_{3 \times p} \end{bmatrix}. \quad (26)$$

By applying mathematical induction to Eq. (20) and making use of the fact that the first three rows of the matrix  $\tilde{\mathbf{H}} \tilde{\Phi}_k$  coincide with the first three rows of the transition matrix  $\tilde{\Phi}_k$  for any  $k$ , one can easily verify that

$$\bar{\theta}_k = \tilde{\mathbf{H}} \tilde{\Phi}_k \Delta \bar{\mathbf{x}}. \quad (27)$$

Substituting the state transition matrix  $\tilde{\Phi}_{\text{state}}$  for  $\tilde{\Phi}_n$  then immediately leads to Eq. (14), which constitutes the main result of this work.

#### IV. REPRESENTATION OF THE DAVENPORT GYRO CALIBRATION SCHEME IN A RECURSIVE FORM

The suggested recursive procedure has been implemented in the following way.<sup>8</sup>

Estimation starts by setting elements of the so-called ‘measurement accumulation’ vector  $\Delta \bar{\mathbf{u}}$  to zero. One also initializes elements of the covariance matrix  $\mathbf{P}$  with some a priori values. The attitude matrix is then propagated from one gyro measurement to another:

$$\mathbf{A}_k = \mathbf{R}_{k-1 \rightarrow k} \mathbf{A}_{k-1} \quad (28)$$

starting from the given observed attitude  $\mathbf{A}_0$  associated with the quaternion  $\bar{\mathbf{q}}_{\text{init}}$  at the beginning of the first maneuver. At the same step one also computes error sensitivity matrix (11) and rate-dependent partials in the right-hand side of Eq. (22) which are then substituted,

together with the rotation matrix  $\mathbf{R}_{k-1 \rightarrow k}$ , into Eq. (21) for the matrix  $\Phi_{k-1 \rightarrow k}$  used to propagate the state transition matrix via recurrence sequence (15). At the end of the maneuver the AMVR  $\bar{\theta}$  is computed by linearizing Eqs. (16):

$$\bar{\theta} \approx \frac{1}{2} [\delta A_{23} - \delta A_{32}, \delta A_{31} - \delta A_{13}, \delta A_{12} - \delta A_{21}]^T \quad (29)$$

where  $\delta A_{ij}$  are elements of the orthogonal matrix

$$\delta \mathbf{A} \equiv \mathbf{A}_{\text{obs}} \mathbf{A}_{\text{prop}}^T \quad (30)$$

After the AMVR  $\bar{\theta}$  is computed, one updates the measurement accumulation vector and the inverse covariance matrix  $\mathbf{W} \equiv \mathbf{P}^{-1}$  according to the standard equations:

$$\Delta \bar{\mathbf{u}} \leftarrow \Delta \bar{\mathbf{u}} + \tilde{\Phi}_{\text{state}}^T \tilde{\mathbf{H}}^T \mathbf{C}^{-1} \bar{\theta} \quad (31)$$

and

$$\mathbf{W} \leftarrow \mathbf{W} + \tilde{\Phi}_{\text{state}}^T \tilde{\mathbf{H}}^T \mathbf{C}^{-1} \tilde{\mathbf{H}} \tilde{\Phi}_{\text{state}} \quad (32)$$

where  $\mathbf{C}$  is a 3×3 measurement covariance matrix. The state transition matrix is then reset to  $\tilde{\Phi}_0$  and the processing continues starting from the beginning of the next maneuver.

After the last maneuver is processed, one obtains the covariance matrix  $\mathbf{P}$  by inverting the resultant  $\mathbf{W}$  matrix and computing the state error vector  $\Delta \bar{\mathbf{x}}$  from the measurement accumulation vector  $\Delta \bar{\mathbf{u}}$ :

$$\Delta \bar{\mathbf{x}} = \mathbf{P} \Delta \bar{\mathbf{u}} \quad (33)$$

The magnitude of the state error vector  $\Delta \bar{\mathbf{x}}$  is then compared with the given tolerance to proceed with iterations if necessary.

## V. TRMM IN-FLIGHT GYRO CALIBRATION

The TRMM is an Earth-pointing three-axis stabilized spacecraft. Its body z-axis is nominally pointed along the geodetic nadir.<sup>13</sup> It can be in '+x forward' or '-x forward' nominal mode, with its body x-axis being approximately either parallel or anti-parallel to the spacecraft velocity. For power and thermal protection of science instruments from direct exposure to the Sun, yaw maneuvers from one nominal mode to another (similar to those depicted in Figs. 1a and 1b) are periodically performed. Since the body y-axis is parallel (anti-parallel) to the orbit normal in the '-x forward' ('+x forward') mode, the only nonzero component of the spacecraft angular velocity vector is the pitch rate, nominally equal to +1 revolution per orbit (RPO) in the '-x forward'

mode and -1 RPO in '+x forward' mode. This is illustrated by the flat portions of the dashed curves in Figures 1a and 1b. It is essential that rates remain nearly constant in both nominal modes, and therefore the spacecraft attitude can be determined with a sufficient accuracy without a complete gyro calibration, provided that gyro biases are included in the state vector to be solved for. (Unknown errors in scale factors and gyro misalignments manifest themselves as some additional biases, which differ for different modes.)

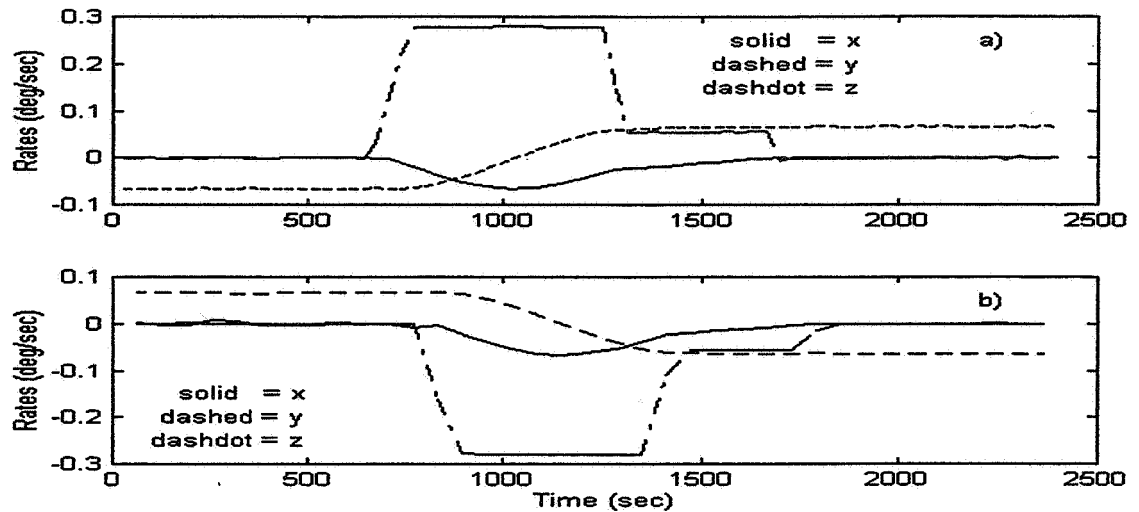


Figure 1. TRMM body rates during +X to -X (upper) and -X to +X (lower) yaw maneuvers.

On December 14, 1997 the TRMM was also placed in the '-y forward' mode to calibrate scientific instruments, with the y body axis being anti-parallel to the spacecraft velocity vector. As seen from gyro rate profiles depicted in Fig. 2, the spacecraft was rotating for about one hour around its body x-axis with the rate of +1 RPO, before coming back to the '-x forward' mode.

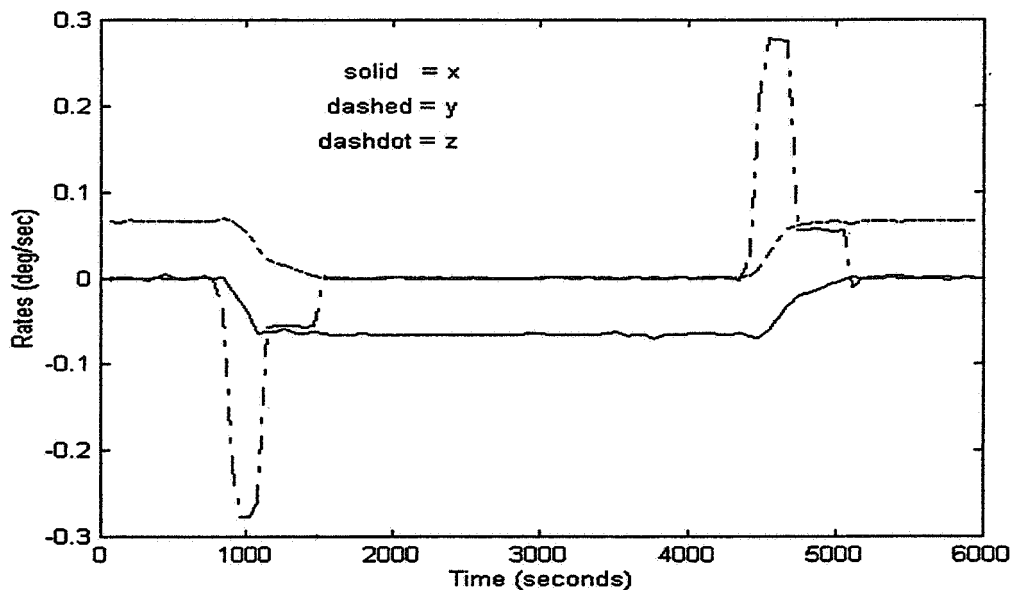


Figure 2. TRMM body rates in the -Y forward mode.

In addition to maneuvers between the three Earth-pointing modes mentioned above, the TRMM was commanded on January 7, 1998 to stay for one orbit in the inertial hold mode used to calibrate a science instrument by pointing it toward cold space. Fig. 3 presents the corresponding x and y body rates. (The z body rate is omitted since its deviations from zero would be practically invisible at the figure scale.)

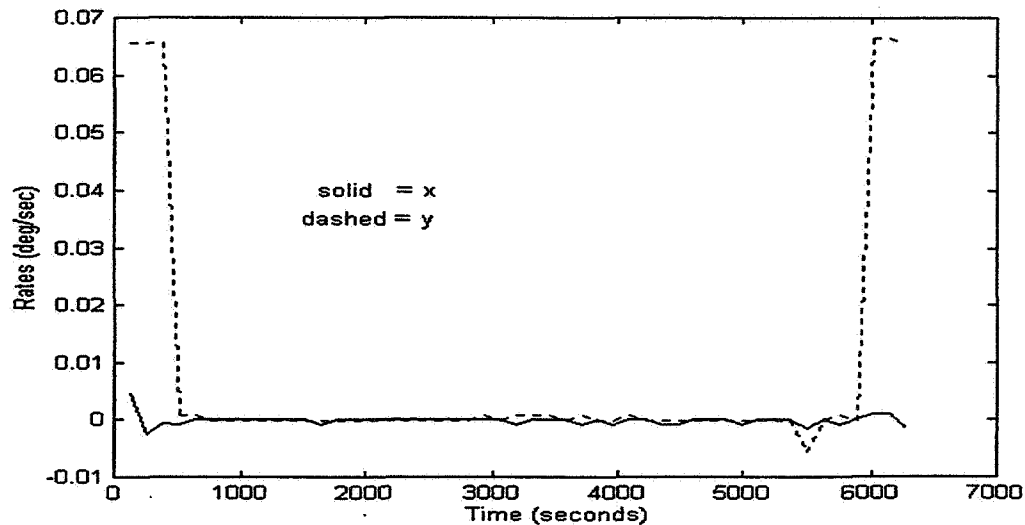


Figure 3. TRMM body rates during inertial hold.

Table 1 lists time intervals selected for calibration of the TRMM inertial reference unit (IRU).<sup>9</sup> The reference attitudes were determined at the beginning and at the end of each maneuver using Digital Sun Sensor (DSS) and Barnes Static Earth Sensor Assembly (SESA) measurements.<sup>13</sup>

Table 1 - Intervals of Gyro Data Used for IRU Calibration

Maneuvers	Time Interval	Spacecraft Activity
1	9:45:00 – 11:25:00, Dec. 13, 1997	+x forward
2	13:11:00 – 13:29:00, Dec. 13, 1997	+x to –x yaw maneuver
3	15:05:00 – 16:40:00, Dec. 13, 1997	–x forward
4	11:43:30 – 12:58:00, Dec. 14, 1997	–y forward mode
5	13:07:00 – 14:39:15, Jan. 7, 1998	Inertial hold
6	20:47:30 – 21:06:00, Jan. 14, 1998	–x to +x yaw maneuver

Three residuals per maneuver were then obtained by propagating the spacecraft attitude with gyro rates from the beginning of each maneuver and comparing the result with the predetermined reference attitude at the end of the maneuver. Table 2 presents roll, pitch, and yaw attitude residuals obtained by gyro propagation with pre-launch and calibrated gyro biases, scale factors, and misalignment matrix. The corresponding values of calibration parameters for each gyro (i. e., a bias, a scale factor, and misalignment angles\* relative to body axes) are listed in Table 3.

\* A deviation of the gyro axis from its nominal direction can be derived from two other misalignments; however, it is included in Table 2 just to simplify the notation, with zeros standing for some rather small numbers completely irrelevant to our discussion.

**Table 2- Roll, Pitch, and Yaw Attitude Residuals (deg) Before and After Calibration**

Maneuvers	Pre-launch			1st iteration		
	$\Delta t = 0.5 \text{ s}$	$\Delta t = 1 \text{ s}$	$\Delta t = 2 \text{ s}$	$\Delta t = 0.5 \text{ s}$	$\Delta t = 1 \text{ s}$	$\Delta t = 2 \text{ s}$
1	0.012	0.022	-0.008	0.005	0.024	0.001
	-0.044	-0.072	-0.105	-0.015	-0.004	-0.008
	0.045	0.030	0.053	0.002	0.002	0.012
2	0.195	0.212	0.202	-0.006	0.009	-0.009
	0.002	-0.001	-0.003	-0.004	-0.003	-0.001
	0.024	0.031	0.031	0.003	-0.004	0.002
3	0.018	0.015	-0.021	0.006	0.001	-0.040
	-0.433	-0.412	-0.441	-0.007	-0.002	-0.003
	-0.011	0.003	0.034	0.003	0.008	-0.042
4	0.235	0.233	0.265	-0.0002	0.001	-0.001
	-0.243	-0.233	-0.243	-0.0001	-0.001	-0.001
	-0.108	-0.116	-0.131	0.003	-0.006	0.007
5	0.073	0.094	0.099	-0.003	-0.001	-0.001
	-0.194	-0.223	-0.248	0.028	0.008	0.011
	0.066	0.071	0.075	0.024	0.008	0.006
6	0.273	0.266	0.271	0.002	-0.004	0.006
	0.105	0.086	0.078	0.010	0.005	0.003
	0.047	0.045	0.074	0.006	-0.005	0.004

**Table 3 - Calibration parameters**

	Pre-launch	1st iteration		
		$\Delta t = 0.5 \text{ s}$	$\Delta t = 1 \text{ s}$	$\Delta t = 2 \text{ s}$
Biases (deg/sec)	$-1.41 \times 10^{-4}$	$-1.55 \times 10^{-4}$	$-1.58 \times 10^{-4}$	$-1.59 \times 10^{-4}$
	$1.58 \times 10^{-4}$	$1.98 \times 10^{-4}$	$2.00 \times 10^{-4}$	$2.04 \times 10^{-4}$
	$0.86 \times 10^{-4}$	$0.78 \times 10^{-4}$	$0.75 \times 10^{-4}$	$0.73 \times 10^{-4}$
Scale factors	1.00000	1.00044	1.00035	1.00031
	1.00000	1.00053	1.00046	1.00046
	1.00000	1.00088	1.00092	1.00096
Misalignment angles (deg) relative body axis x	0.000	0.000	0.000	0.000
	0.059	0.044	0.051	0.044
	0.005	0.054	0.067	0.071
Misalignment angles (deg) relative body axis y	-0.036	-0.058	-0.068	-0.086
	0.000	0.000	0.000	0.000
	0.030	0.096	0.063	0.079
Misalignment angles (deg) relative body axis z	0.006	0.039	0.034	0.033
	-0.033	-0.124	-0.119	-0.118
	0.000	0.000	0.000	0.000

To investigate the possibility of reducing the amount of processed gyro data (about 60 000 points for all six maneuvers), propagation was performed using several time steps:  $\Delta t = 0.5$  s, 1 s, 2s. Inspection of Table 2 and Table 4 shows that every other gyro measurement can be successfully skipped without any noticeable effect on the accuracy of estimation. Skipping three of every four gyro measurements still gives reasonably good results, though some degradation in the accuracy can be clearly seen.

**Table 4 - Mean and RMS Residuals (deg)**

	Pre-launch			1st iteration		
	$\Delta t = 0.5$ s	$\Delta t = 1$ s	$\Delta t = 2$ s	$\Delta t = 0.5$ s	$\Delta t = 1$ s	$\Delta t = 2$ s
Mean	0.1343	0.1404	0.1343	0.0008	0.0050	-0.0073
Residuals	-0.1343	-0.1426	-0.1603	0.0016	0.0004	0.0001
	0.0103	0.0105	0.0226	0.0068	0.0004	0.0123
RMS	0.0694	0.0707	0.0738	0.0015	0.0043	0.0070
Residuals	0.0908	0.0892	0.0960	0.0058	0.0019	0.0024
	0.0242	0.0249	0.0303	0.0043	0.0024	0.0075

It is essential that the calibration be accomplished by a single iteration. This can be easily seen by comparing corrections to gyro biases and elements of the G-matrix due to the first and second iterations, presented in Table 5. Contributions to attitude residuals from the second iteration are so small that they would have no effect on the values  $t$  in Tables 2 and 4 (to the precision shown).

**Table 5- Bias and G-Matrix Corrections**

	1st iteration			2nd iteration		
	x-gyro	y-gyro	z-gyro	x-gyro	y-gyro	z-gyro
Bias corrections (deg/sec)	$-1.74 \times 10^{-5}$	$4.15 \times 10^{-5}$	$-1.15 \times 10^{-5}$	$-3.89 \times 10^{-8}$	$4.18 \times 10^{-8}$	$0.11 \times 10^{-8}$
Corrections to G-matrix elements	$-0.44 \times 10^{-3}$	$0.39 \times 10^{-3}$	$-0.57 \times 10^{-3}$	$-2.69 \times 10^{-6}$	$-1.90 \times 10^{-6}$	$-0.72 \times 10^{-6}$
	$0.27 \times 10^{-3}$	$-0.54 \times 10^{-3}$	$1.59 \times 10^{-3}$	$-2.86 \times 10^{-6}$	$-0.58 \times 10^{-6}$	$0.81 \times 10^{-6}$
	$-0.86 \times 10^{-3}$	$-1.16 \times 10^{-3}$	$-0.88 \times 10^{-3}$	$-0.85 \times 10^{-6}$	$-4.08 \times 10^{-6}$	$-1.43 \times 10^{-6}$

To study the significance of higher-order powers of  $\Delta t_k$  in the error sensitivity, calibration was repeated using only the linear terms in Eq. (11), which is equivalent to the use of the Davenport method in its conventional implementation.<sup>7</sup> It was found that neglecting higher-order terms does not practically affect the calibration results, so that the linear approximation seems to be sufficiently accurate for calibration purposes.

## VI. CONCLUSIONS

A new approach has been implemented in the ground calibration utilities<sup>8</sup> and successfully used for the TRMM IRU calibration. It has been shown that the required accuracy can be achieved by a single iteration. As a result the new approach seems to be especially useful for onboard applications by allowing one to discard each gyro measurement immediately after it is used to update the state vector and covariance matrix.

Recently the *Rossi X-Ray Timing Explorer (RXTE)* ground launch support team has reported<sup>14</sup> some problems in Kalman filter estimation of gyro scale factors and gyro misalignments, and the new least-squares approach to gyro calibration makes it possible to extend advantages of the Davenport algorithm to onboard applications. To avoid memory-consuming batch attitude determination, one can use the Kalman filter to determine the spacecraft attitudes before and after each of the selected maneuvers. The Kalman filter state vector is composed only of attitude and gyro bias errors, so that gyro biases will change with each new gyro measurement, in contrast with those used in the Davenport method. For this reason one has to propagate in parallel two separate transition matrices, namely, propagation rates for the spacecraft attitude and the transition matrix used by the suggested recursive algorithm are obtained by adjusting raw measurements with a priori biases which remain the same for all the selected maneuvers. On the other hand, propagation rates for attitude errors and the transition matrix utilized by the Kalman filter are obtained by adjusting raw measurements with the solved-for biases (and the same scale factors and misalignments as in the former case). Feasibility of this approach is currently investigated using Submillimeter Wave Astronomy Satellite (SWAS) simulated data.

## ACKNOWLEDGEMENTS

The author would like to thank J. Sedlak for very thorough editing of the manuscript and numerous critical remarks, J. Hashmall for providing preliminary calibration results, as well as the necessary attitude history file and gyro measurements, and J. Glickman for a comprehensive overview of TRMM mission requirements and some useful comments on the paper.

## References

1. L. Fallon, III, and P. V. Rigterink, "Introduction to Estimation Theory" in *Spacecraft Attitude Determination and Control*, J. Wertz, editor, D. Reidel, Dordrecht, Holland, 1978
2. M. Nicholson, F. Markley, and E. Seidewitz, "Attitude Determination Error Analysis System (ADEAS) Mathematical Specifications Document," CSC/TM-88/6001, prepared by Computer Sciences Corporation, October 1988
3. J. Landis et al, "Multimission Three-Axis Stabilized Spacecraft (MTASS) Flight Dynamics Support System," Section 2.4, CSC/TR-91/6071R1UD0, prepared by Computer Sciences Corporation, Sept. 1995
4. P. Davenport, "In-flight Calibration of Gyros," Goddard Space Flight Center, Spring 1976



5. J. Keat, "Gyro Calibration Analysis for the High Energy Astronomy observatory-A (HEAO-A)," CSC/TM-77/6082, prepared by Computer Sciences Corporation, June 1977
6. P. Davenport and G. Welter, "Algorithm for In-flight Gyroscope Calibration," Flight Mechanics/Estimation Theory Symposium, May 10-11, 1988
7. J. Landis et al, "Multimission Three-Axis Stabilized Spacecraft (MTASS) Flight Dynamics Support System," Section 4.2, CSC/TR-91/6071R1UD0, prepared by Computer Sciences Corporation, Sept. 1995
8. G. Klitsch, M. Lambertson, G. Natanson, R. Strang, et al., "Flight Dynamics Distributed Systems (FDDS) Generalized Support Software (GSS) Functional Specification," Revision 1, Update 4, CSC/TR-92/6023R1UD4, prepared by Computer Sciences Corporation, September 1996
9. J. Hashmall, "TRMM Inertial Reference Unit Calibration," unpublished memo, Febr. 1998.
10. F. Markley, "Three-Axis Attitude Determination Methods" in *Spacecraft Attitude Determination and Control*, J. Wertz, editor, D. Reidel, Dordrecht, Holland, 1978
11. G. Natanson, "A Transition Matrix Approach to the Davenport Gyro Calibration Scheme ", Memo CSC-27434-62, Nov. 1997.
12. T. Becher et al., "International Solar-Terrestrial Physics (ISTP) / Collaborative Solar-Terrestrial Research (COSTR) Initiative: Solar and Heliospheric Observatory (SOHO) Mission, Flight Dynamics Support System (FDSS) Functional Specifications," CSC/TR-92/6102R0UD0, prepared by Computer Sciences Corporation, February 1993
13. J. Glickman et al., "Tropical Rainfall Measuring Mission (TRMM) Flight Dynamics Support System (FDSS) Functional Specifications," CSC/TR-94/6045R0UD0, prepared by Computer Sciences Corporation, October 1994
14. D. Fink, W. Davis et al., "Rossi X-Ray Timing Explorer (RXTE) Postlaunch Report," CSC 10032526, prepared by Computer Sciences Corporation, June 1996



# EFFECTS OF MAGNETOMETER CALIBRATION AND MANEUVERS ON ACCURACIES OF MAGNETOMETER-ONLY ATTITUDE-AND-RATE DETERMINATION\*

M. Challa<sup>†</sup> and G. Natanson<sup>†</sup>

## ABSTRACT

Two different algorithms—a deterministic magnetic-field-only algorithm and a Kalman filter for gyroless spacecraft—are used to estimate the attitude and rates of the Rossi X-Ray Timing Explorer (RXTE) using only measurements from a three-axis magnetometer. The performance of these algorithms is examined using in-flight data from various scenarios. In particular, significant enhancements in accuracies are observed when the telemetered magnetometer data are accurately calibrated using a recently developed calibration algorithm. Interesting features observed in these studies of the inertial-pointing RXTE include a remarkable sensitivity of the filter to the numerical values of the noise parameters and relatively long convergence time spans. By analogy, the accuracy of the deterministic scheme is noticeably lower as a result of reduced rates of change of the body-fixed geomagnetic field. Preliminary results show the filter-per-axis attitude accuracies ranging between 0.1 and 0.5 deg and rate accuracies between 0.001 deg/sec and 0.005 deg./sec, whereas the deterministic method needs a more sophisticated techniques for smoothing time derivatives of the measured geomagnetic field to clearly distinguish both attitude and rate solutions from the numerical noise. Also included is a new theoretical development in the deterministic algorithm: the transformation of a transcendental equation in the original theory into an 8<sup>th</sup>-order polynomial equation. It is shown that this 8<sup>th</sup>-order polynomial reduces to quadratic equations in the two limiting cases—infinitely high wheel momentum, and constant rates—discussed in previous publications.

## INTRODUCTION

It has been demonstrated<sup>1-10</sup> that the attitude and rates of low-Earth orbiting spacecraft can be simultaneously estimated using measurements of the Earth's magnetic field,  $\vec{B}$ , using only a three-axis magnetometer (TAM) and *no a priori* information. The feasibility of this "TAM-Only" scheme essentially

---

\* This work was supported by the National Aeronautics and Space Administration (NASA) / Goddard Space Flight Center (GSFC), Greenbelt, Maryland, Contract GS -35F-4381G, Task Order No. S-03365-Y.

<sup>†</sup> Computer Sciences Corporation, 10110 Aerospace Road, Lanham-Seabrook, MD 20706

relies upon  $\vec{B}$  changing direction rapidly enough in the spacecraft body frame to make computation of its time derivative possible, and these changes during the course of an orbit are sufficiently large to enable determination of all three Euler angles using only TAM data.

Our approach consists of using two independent algorithms—deterministic attitude determination from magnetometer-only data (DADMOD) and the Real Time Sequential Filter (RTSF). The DADMOD<sup>1-3</sup> is a TAM-only algorithm that relates the time derivatives of  $\vec{B}$  in inertial and spacecraft body coordinates to determine the attitude and the body rates. The RTSF<sup>4-5</sup> is a robust Kalman filter that estimates, in addition to the attitude, errors in rates propagated via Euler's equation. Note that the RTSF is a general algorithm for gyroless spacecraft; however, its sensitivity to rate errors as small as 0.0003 deg/sec makes it a robust and accurate real-time algorithm even in TAM-only situations with no *a priori* spacecraft information.

The highlights of our past applications to in-flight data from the Solar, Anomalous, and Magnetospheric Explorer (SAMPEX) and the Earth Radiation Budget Satellite (ERBS) have shown that with a TAM-Only approach: (1) SAMPEX attitude and rate requirements can be met even when the on-board Sun sensor fails<sup>4,6</sup>, (2) using partially calibrated magnetometer data from ERBS nominal mission mode the RTSF yields<sup>8</sup> accuracies within 0.4 deg and rate accuracies within 0.005 deg/sec, and (3) ERBS attitude and rates could be reliably determined<sup>10</sup> during its 1987 control anomaly<sup>11</sup> when the spacecraft tumbled at approximately 2 deg/sec. Another useful aspect of the past work is the combination of the strengths of these algorithms in an automated scheme<sup>7</sup> wherein the deterministic algorithm is used to initialize the more accurate Kalman filter to within a few degrees of the correct spacecraft attitude.

In the present work, we examine the performances of these algorithms during some important scenarios of the RXTE: (1) calibrated and uncalibrated TAMs and (2) during maneuvers. While the first scenario does not require further explanation, the motivation for the second is the possible application of the RTSF to extend aging missions. For example, ERBS (launch: 1984) needs monthly thruster-based maneuvers for solar-power purposes, and these are currently conducted using rate information from the one remaining gyro channel. This paper demonstrates that, by providing magnetometer-only rate solutions, the filter can be a useful tool during such maneuvers, especially when the last gyro channel also fails.

The present work concentrates on results for RXTE that are interesting in their own right, because, in contrast to SAMPEX and ERBS:

- RXTE is inertial pointing so that  $\vec{B}$  changes very slowly in the body frame, and this leads to observability and convergence issues when only short data spans are used (as is the case here).
- RXTE is a zero-momentum spacecraft, whereas SAMPEX and ERBS are momentum-biased about the pitch axis. We believe this leads to the RTSF results being very sensitive to the numerical values of its propagation noise parameters and their relationship to the weightage of the TAM data. For a similar reason, the accuracy of the deterministic scheme becomes noticeably lower.

The rest of the paper is organized as follows. Section 2 briefly describes the algorithms; included here are recent developments in DADMOD and a novel TAM calibration algorithm<sup>12</sup> that is used to calibrate the RXTE TAM data. Sections 3 and 4 analyze the performances for RXTE and ERBS respectively, and Section 5 summarizes the conclusions.

## ALGORITHMS

### Deterministic Attitude and Rate Determination Using Magnetometer-Only Data (DADMOD)

As discussed in detail in previous publications, determination of the spacecraft attitude and rates based on magnetometer measurements and their first and second time derivatives can be cast in the form of the following vector equation:

$$\vec{\Lambda}_0(\Phi) + \vec{\Lambda}_1(\Phi) \omega_1 + \vec{\Lambda}_2 \omega_1^2 = \vec{0} \quad (1)$$

where the angle  $\Phi$  and the body rate  $\omega_1$  around the body-fixed geomagnetic field vector  $\vec{B}^A$  are two unknown variables. It is essential that

$$\vec{\Lambda}_1(\Phi) \equiv \hat{B}^A \times \vec{H}_1(\Phi), \quad \vec{\Lambda}_2 \equiv \vec{\Omega}_2 \times \vec{B}^A, \quad (2)$$

where the vectors  $\vec{H}_1(\Phi)$  and  $\vec{\Omega}_2$  are given by Eqs. (5) and (6) in Ref. 10, and  $\hat{B}^A \equiv \vec{B}^A / |\vec{B}^A|$ .

The third vector  $\vec{\Lambda}_0(\Phi)$  is also perpendicular to  $\vec{B}^A$  at any value of the angle  $\Phi$  so that two nontrivial equations to determine both  $\Phi$  and  $\omega_1$  are obtained by projecting vector equation (1) on two directions perpendicular to the geomagnetic field. As a new development, we show that these two directions can be chosen in such a way that  $\zeta(\Phi) = \tan(\Phi/2)$  becomes one of roots of an 8<sup>th</sup>-order polynomial  $P_8[\zeta]$ .

In fact, by projecting Eq. (1) onto the vector  $\vec{B}^A \times \vec{\Lambda}_2$  one finds

$$\omega_1(\Phi) = - |\vec{B}^A| (\vec{\Lambda}_0(\Phi) \cdot \vec{\Omega}_2) / (\vec{H}_1(\Phi) \cdot \vec{\Lambda}_2) \quad (3)$$

Substituting the latter expression into the projection of Eq. (1) onto the vector  $\vec{H}_1(\Phi)$  then gives

$$(\vec{H}_1(\Phi) \cdot \vec{\Lambda}_2) (\vec{\Lambda}_0(\Phi) \cdot \vec{H}_1(\Phi)) + |\vec{B}^A|^2 (\vec{\Lambda}_0(\Phi) \cdot \vec{\Omega}_2)^2 = 0 \quad (4)$$

It can be shown that the vectors  $\vec{\Lambda}_0(\Phi)$  and  $\vec{H}_1(\Phi)$  have the form:

$$\vec{\Lambda}_0(\Phi) = c^4(\Phi) \vec{Q}_4[\zeta(\Phi)], \quad \vec{H}_1(\Phi) = c^2(\Phi) \vec{Q}_2[\zeta(\Phi)] \quad (5)$$

where the vectors  $\vec{Q}_n[\zeta]$  are formed by polynomials of the  $n^{\text{th}}$  order in  $\zeta$  and  $c(\Phi) \equiv \cos(\Phi/2)$ , and therefore the solution sought for is given by one of roots of the 8<sup>th</sup>-order polynomial:

$$P_8[\zeta] \equiv P_2[\zeta] P_6[\zeta] + (P_4[\zeta])^2 \quad (6)$$

where

$$P_2[\zeta] \equiv (\vec{Q}_2[\zeta] \cdot \vec{\Lambda}_2), \quad P_4[\zeta] \equiv |\vec{B}^A| (\vec{Q}_4[\zeta] \cdot \vec{\Omega}_2), \quad P_6[\zeta] \equiv (\vec{Q}_2[\zeta] \cdot \vec{Q}_4[\zeta])$$

Note that all coefficients of polynomial (6) are equal to zero when the geomagnetic field is directed along one of the spacecraft principal axes of inertia since both vectors  $\vec{\Omega}_2$  and  $\vec{\Lambda}_2$  vanish. By analogy these coefficients are nullified if the vector  $\vec{\Lambda}_2$  becomes perpendicular to the vector  $\vec{H}_1(\Phi_1)$  for the sought-for root  $\zeta(\Phi_1)$ . However, it can be shown that the ratio  $(P_4[\zeta])^2 / P_2[\zeta]$  tends to zero in both cases so that the solution sought for can be found among real roots of the polynomial  $P_6[\zeta]$ . Because Eq. (3) is no longer applicable, one has to solve a quadratic equation to find  $\omega_1$ . To avoid instabilities, a special algorithm was developed to select the direction associated with the maximum of the discriminant. As a result, the resultant solution remains stable as the coefficient of the quadratic term tends to zero.

The ratio  $(P_4[\zeta])^2 / P_2[\zeta]$  also vanishes as the wheel momentum  $\bar{h}$  tends to  $\infty$ , while the polynomial  $P_6[\zeta]$  takes the form:

$$P_6[\zeta] \approx (1 + \zeta^2)^2 \Pi_2[\zeta] \quad (7)$$

As a result, we come to the quadratic equation  $\Pi_2[\zeta] = 0$  discussed in Ref. 6. A similar decomposition of the polynomial  $P_6[\zeta]$  takes place in case of constant body rates after one drops all terms associated with the time derivative of the angular velocity vector  $\bar{\omega}$ . The solution solved for can be found from the requirement for the vectors  $\bar{H}_1(\Phi)$  and  $\bar{A}_0(\Phi)$  to be perpendicular to each other, which is equivalent to the condition  $P_6[\zeta(\Phi)] = 0$ . The resultant quadratic equation  $\Pi_2^0[\zeta] = 0$  has been studied in detail in Refs. 1 and 2.

### Real Time Sequential Filter (RTSF)

In view of space considerations, only details relevant to the tuning of the RTSF are presented here. A full mathematical description of the RTSF has been provided elsewhere (References 4 and 5). The RTSF's state vector  $\bar{X}$  is comprised of the four components of the attitude quaternion,  $\bar{q}$ , and the corrections,  $\bar{b}$ , to the spacecraft's rates,  $\bar{\omega}$ :

$$\bar{X} = [\bar{q}^T \bar{b}^T]^T \quad (8)$$

(Note that the components of  $\bar{b}$  and  $\bar{\omega}$  are resolved along the spacecraft's x, y, z axes.)

The RTSF uses sensor data to estimate  $\bar{q}$  as well as  $\bar{b}$ , with  $\bar{b}$  being estimated kinematically in the same manner as gyro biases for a gyro-based spacecraft; i.e., by attributing differences between the measured and propagated attitudes to errors in  $\bar{\omega}$ . The  $\bar{b}$  estimates are then used to correct  $\bar{\omega}$ , and these corrected rates are used as initial conditions to propagate Euler's equation to the next measurement time. The propagation of  $\bar{b}$  is modeled via a first-order Markov model:

$$\frac{d\bar{b}}{dt} = -\frac{\bar{b}}{\tau} + \bar{\eta}_b \quad (9)$$

where  $\bar{\eta}_b$  is a white noise term, and  $\tau$  is a finite time constant. A suitable value for  $\tau$  is the time between measurements.

The rates are assumed to contain a white noise component,  $\bar{\eta}_a$  and are propagated using Euler's equation after accounting for the angular momentum contributed by the wheels, and for the total external torques acting on the spacecraft. TAMONLY currently models the gravity-gradient torque and the magnetic control torque acting on the spacecraft. (The aerodynamic drag torque and the radiation pressure torque have been intentionally omitted to reduce the amount of spacecraft modeling required. The RTSF relies on the rate-corrections,  $\bar{b}$ , to compensate for the small effects of these torques.)

The covariance matrix,  $P$ , is propagated by numerically integrating the following equation:

$$\frac{dP}{dt} = F(\bar{\omega})P + P F^T(\bar{\omega}) + Q \quad (10)$$

Here  $F(\bar{\omega})$  is described in Reference 5; the quantity of interest is the  $6 \times 6$  matrix  $Q$  that quantifies the propagation noise and is of the following diagonal form:

$$Q = \text{diag} [ Q_a, Q_a, Q_a, Q_b, Q_b, Q_b ] \quad (11)$$

Here  $Q_a$  is related to the noise term  $\bar{\eta}_a$  and contributes to the growth of the attitude error covariances about the body X-, Y-, and Z-axes during propagation. Similarly,  $Q_b$  is related to noise term  $\bar{\eta}_b$ , and contributes to the growth of the error covariances of  $\bar{b}$  during propagation. Another quantity that we must consider during tuning is  $\sigma$ , the strength of the white noise in the TAM measurements.

The filter can be initialized in one of the following two ways before processing a span of telemetry data.

- Inertial initial conditions (IIC), where the spacecraft is assumed at rest in the Geocentric Inertial Coordinates (GCI) with its axes coinciding with the GCI axes; this results in large initial errors.
- Deterministic initial conditions (DIC) where the filter makes short (2 to 5 min) runs and determines which of the DADMOD solutions is a good *a priori* solution. This results in small initial errors.

### The TAM Calibration Algorithm

The effects of TAM calibration were determined using a recently-developed algorithm<sup>12</sup> where the following set of 21 time-independent parameters are used to "adjust" the magnetic field vector measured by the TAM whose axes nominally coincide with the spacecraft body axes.

- $E$  ..... 3x3 scale factor/misalignment matrix nominally equal to the identity matrix,  $I_{3 \times 3}$
- $G$  ..... 3x3 TAM-torquer coupling matrix nominally equal to the null matrix,  $O_{3 \times 3}$
- $\bar{f}$  ..... 3x1 bias vector nominally equal to the null vector,  $O_{3 \times 1}$

If at any instant  $\bar{B}$  is the magnetic field vector measured by the TAM,  $\bar{D}$  is the 3x1 dipole moment vector of the magnetic torquer bars,  $A$  is the *known* GCI -to-spacecraft body frame attitude matrix, and  $\bar{B}_I^R$  is the corresponding International Geomagnetic Reference Field (IGRF)<sup>13</sup> vector in the inertial frame, the calibration model assumes

$$B_i = \sum_{j=1}^3 (E_{ij} B_j^R - G_{ij} D_j) - f_i + v_i, \quad i = 1, 2, 3 \quad (12)$$

where  $\bar{B}^R = A\bar{B}_I^R$  is the predicted field in the spacecraft body frame, and  $\bar{v}$  is a white-noise term of root-mean-square (r-m-s) value  $\sigma$ . The goal of the calibration then is to estimate  $E$ ,  $G$ , and  $\bar{f}$ , by applying statistical methods to a span of TAM measurements,  $\{\bar{B}_1, \dots, \bar{B}_N\}$  and the corresponding predictions  $\{\bar{B}_1^R, \dots, \bar{B}_N^R\}$ .

Resolving  $E$  and  $G$  into the vectors  $\bar{E}_1, \bar{E}_2, \bar{E}_3, \bar{G}_1, \bar{G}_2$ , and  $\bar{G}_3$  as follows,

$$E = \begin{bmatrix} \bar{E}_1^T \\ \bar{E}_2^T \\ \bar{E}_3^T \end{bmatrix}, \quad G = \begin{bmatrix} \bar{G}_1^T \\ \bar{G}_2^T \\ \bar{G}_3^T \end{bmatrix}, \quad (13)$$

three independent loss functions are now formulated as:

$$L_i = \frac{1}{\sigma_{T,i}^2} \sum_{n=1}^N a_{n,i} \left[ \bar{E}_i^T \bar{B}_n^R - \bar{G}_i^T \bar{D}_n - f_i - B_{n,i} \right]^2, \quad i = 1, 2, 3 \quad (14)$$

where the subscript  $n$  denotes the measurement time,

$$\frac{1}{\sigma_{T,i}^2} = \sum_{n=1}^N \frac{1}{\sigma_{n,i}^2} , \quad (15)$$

and

$$a_{n,i} = \frac{\sigma_{T,i}^2}{\sigma_{n,i}^2} . \quad (16)$$

The following notation for the statistical quantities formed from vectors is followed here.

$$\text{Means:} \quad \langle \bar{X} \rangle = \sum_{i=1}^N a_i \bar{X}_i \quad (17)$$

$$\text{Covariances:} \quad \langle \bar{X} \bar{Y} \rangle = \langle \bar{X} \bar{Y}^T \rangle - \langle \bar{X} \rangle \langle \bar{Y}^T \rangle \quad (18)$$

where the superscript  $T$  denotes matrix transpose.

Minimizing  $L_i(\bar{E}_i, \bar{G}_i, f_i)$  yields

$$\bar{E}_i^T \langle \bar{B}^R | \bar{B}^R \rangle_i - \bar{G}_i^T \langle \bar{D} | \bar{B}^R \rangle_i = \langle B_i | \bar{B}^R \rangle_i \quad (19a)$$

$$\bar{E}_i^T \langle \bar{B}^R | \bar{D} \rangle_i - \bar{G}_i^T \langle \bar{D} | \bar{D} \rangle_i = \langle B_i | \bar{D} \rangle_i \quad (19b)$$

$$f_i = \bar{E}_i^T \langle \bar{B}^R \rangle_i - \bar{G}_i^T \langle \bar{D} \rangle_i - \langle B_i \rangle_i \quad (19c)$$

where subscript  $i$  indicates that the averages are only over the  $i$ -th set. Equations (19a) and (19b) can be readily solved yielding:

$$\bar{E}_i^T = \left[ \langle B_i | \bar{B}^R \rangle_i \langle \bar{D} | \bar{B}^R \rangle_i^{-1} - \langle B_i | \bar{D} \rangle_i \langle \bar{D} | \bar{D} \rangle_i^{-1} \right] \left[ \langle \bar{B}^R | \bar{B}^R \rangle_i \langle \bar{D} | \bar{B}^R \rangle_i^{-1} - \langle \bar{B}^R | \bar{D} \rangle_i \langle \bar{D} | \bar{D} \rangle_i^{-1} \right]^{-1} \quad (20a)$$

$$\bar{G}_i^T = \left[ \langle B_i | \bar{B}^R \rangle_i \langle \bar{B}^R | \bar{B}^R \rangle_i^{-1} - \langle B_i | \bar{D} \rangle_i \langle \bar{B}^R | \bar{D} \rangle_i^{-1} \right] \left[ \langle \bar{D} | \bar{D} \rangle_i \langle \bar{B}^R | \bar{D} \rangle_i^{-1} - \langle \bar{D} | \bar{B}^R \rangle_i \langle \bar{B}^R | \bar{B}^R \rangle_i^{-1} \right]^{-1} \quad (20b)$$

$f_i$  is then obtained by using Equations (20) in (19c).

## RESULTS USING THE ROSSI X-RAY TIMING EXPLORER IN-FLIGHT DATA

### Overview of the Mission and Data

The RXTE is an inertial-pointing spacecraft and was launched in December 1995 into a near-circular orbit of altitude 580 km and inclination 23 deg. The primary attitude sensors on board are charge-coupled device star trackers that provide accurate sensor-determined attitudes during inertial periods. The attitude during maneuvers (as many as eight each day) is obtained from accurately calibrated gyros. The predicted field values  $\bar{B}$  were generated using a 10<sup>th</sup> order IGRF model for the reference field values. Three sets of data from 1/4/96, 7/4/96, and 11/6/97 were used in the present study. Of these, the first two contain spacecraft slews (primarily about the  $z$  axis), while the last is wholly inertial. The telemetry data received at the FDF are nominally 2 sec apart, but various samples at a slower rate were generated to increase observability of the magnetic field variations. Thus, data were generated with pseudo-periods ranging from 4 sec to 40 sec, and several different telemetry periods were used for each set of data. However, the results presented here used 40 sec sampling for the 7/4/96 data and 8 sec sampling for the other two sets.

### Terminology

Some notes about the figures and tables presented here are in order. The "truth" models used to evaluate the attitude and rate accuracies of the algorithms are the on-board computer (OBC) determined



attitudes and rates computed from their time derivatives. GCI-to-Body attitude results are presented in the form of 1-2-3 Euler angles, and these angles are respectively referred to as "Angle-1", "Angle-2", and "Angle-3". The body-frame components of the spacecraft rates are depicted in the figures as "wx", "wy", and "wz". "Raw" and "adjusted" refer to the quality of the TAM data, and denote pre- and post-calibration values for the TAM measurements. "Residuals" are the differences between TAM measurements and fields predicted using the RTSF attitude estimates. "TAM angle" is the angle between the measured and predicted fields. It is a convenient scalar parametrization of the separate TAM residuals along the three body axes and, as will be seen, is useful when evaluating the filter in the absence of truth models. Only TAM-1 measurements have been used throughout the paper although TAM-2 measurements are also available for the RXTE. The TAM-2 measurements and the residual statistics are not very different from the TAM-1 measurements, although significant differences do exist in the calibration parameters. "RTSF rate-errors" are the corrections,  $\bar{b}$ , estimated by the RTSF (see Equation (9)) as part of its state vector and are different from a term such as "error in wz" that refers to the differences between the RTSF rates and gyro rates. Thus  $\bar{b}$  may be viewed as "rate residuals" since convergence of the RTSF implies small  $\bar{b}$ .

### TAM-1 Calibration Results

Excellent residual statistics were obtained after calibration of the data and the results are shown in Table 1 for each axis separately. For example, the root-mean-square residuals are of the order of 0.5 mG. The mean residuals are most impressive: of the order of  $10^{-14}$  (i. e. of the order of "e-14" in the notation of the Table).

**Table 1**  
**RXTE RESIDUAL STATISTICS FOR TAM-1**

Dataset	Pre-Calibration (Raw) Data (mG)		Post-Calibration (Adjusted) Data (mG)	
	Mean Residuals (X,Y,Z)	R-M-S Residuals (X,Y,Z)	Mean Residuals (X,Y,Z)	R-M-S Residuals (X,Y,Z)
1/4/96	4.105, -0.481, -1.792 Max: 9.290 Min: -6.949	4.720, 1.563, 3.191	-2e-14, -9e-15, -6e-14 Max: 3.019 Min: -1.296	0.519, 0.335, 0.272
7/4/96	3.055, -4.510, 3.413 Max: 7.984 Min: -3.196	3.162, 4.54, 4.114	2e-14, 2e-14, 4e-14 Max: 0.712 Min: -0.923	0.139, 0.216, 0.203
11/06/97	-1.561, -0.579, 8.221 Max: 15.670 Min: -6.635	2.778, 2.160, 9.085	7e-14, 7e-14, 2e-13 Max: 2.799 Min: -1.544	0.601, 0.312, 0.494

### RTSF Tuning

The RTSF was tuned as follows. The largest of the r-m-s residuals results for a given dataset of Table 1 was used as the RTSF tuning parameter  $\sigma$  during the TAM-only runs; for example, this value would be 4.72 mG for the raw data of 1/4/96. At the outset of the TAM-only runs approximate numerical values for the filter propagation noise parameters,  $Q_a$  and  $Q_b$  of Equation (11), were obtained by analyzing the errors in the angular momentum of the spacecraft and wheels and the effects these errors would have on the RTSF rate and attitude while propagating between measurements. The uncertainties in the system net wheel

angular momentum was determined to be about 0.025 N-m, which resulted in rate uncertainties of  $9.4 \times 10^{-6}$  rad/sec. This implied  $Q_a$  was of the order of  $10^{-10} \Delta t$  rad<sup>2</sup>/sec where  $\Delta t$  is the telemetry period. A related analysis using the convergence properties of the Markov model resulted in  $Q_b$  of the order of  $2 \times 10^{-10} \Delta t$  rad<sup>2</sup>/sec<sup>3</sup>. Tuning was then accomplished by: (1) choosing a constant  $\sigma$  from Table 1 as stated above, (2) setting  $Q_a$  equal to  $Q_b$  during all of the runs, and (3) varying this adjustable single adjustable parameter  $Q_{a,b}$  about the numerical value of  $10^{-10} \Delta t$  until the attitude errors were minimized. The accuracy of the tuning parameters was verified later by studying the performance of the filter over several orders of magnitude of  $Q_{a,b}$ . For each dataset a few runs were also made using different  $\sigma$  but none yielded better performance. Each dataset was also studied using different telemetry periods. All in all a few *hundred* runs were made for each dataset, and only a small portion of the results are shown below.

A striking difference between the RTSF performance for RXTE and past experience with SAMPEX and ERBS data is the sensitivity to the numerical values of the numerical parameters, which in turn were somewhat dependent on the telemetry period. Thus, whereas it was sufficient for  $Q_{a,b}$  to be accurate to one significant figure for SAMPEX and ERBS, it turns out that the tuning parameters have to be accurate to *three to four significant figures* for RXTE. As an example, for the 11/6/97 data with 8 sec telemetry period, the total RTSF attitude error was 15.6 deg when  $Q_{a,b} = 1.1 \times 10^{-10}$  whereas this error dropped to 5.1 deg when  $Q_{a,b} = 1.01 \times 10^{-10}$ .

### TAM-Only Results

DADMOD and RTSF (using IIC) attitude results for the 7/4/96 RXTE data with a telemetry period of 40 sec are presented in Fig. 1, which shows a spacecraft maneuver about the z-axis between 1500 sec and

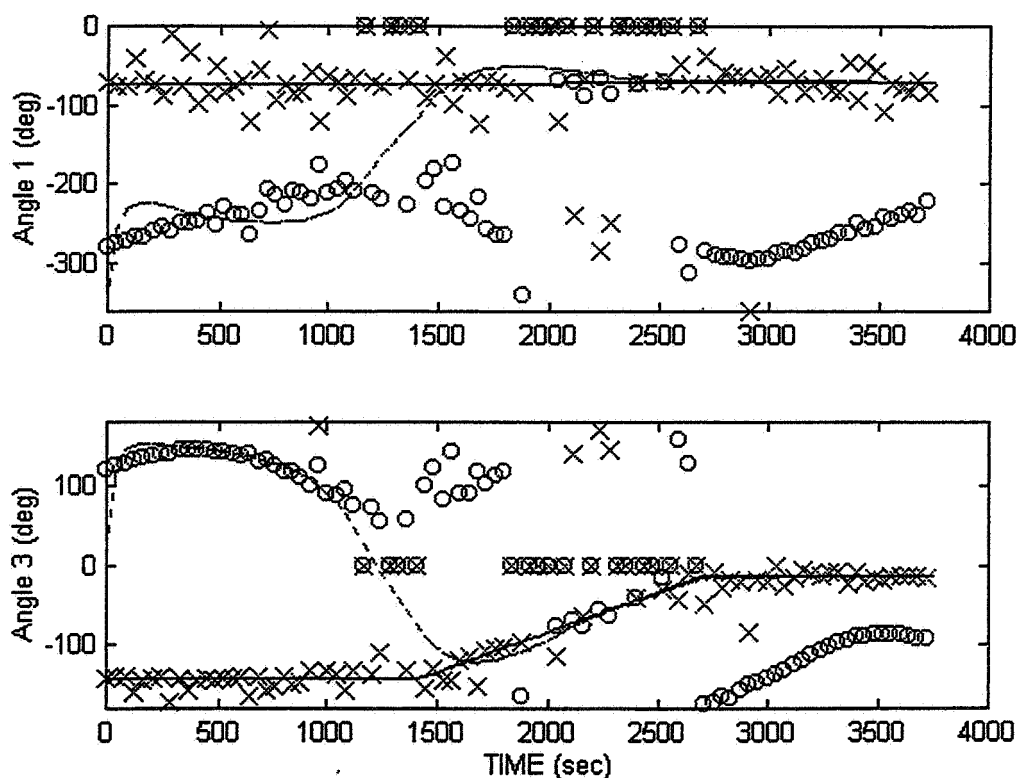


**Figure 1. GCI-to-Body 1-2-3 Attitude Euler Angle Results for Adjusted 7/4/96 Data (solid = true, dashed = RTSF, crosses = DADMOD 1st root, circles = DADMOD 2nd root)**

2500 sec. In this figure the lines represent the truth and the RTSF solutions (solid and dashed respectively) while the symbols represent the DADMOD correct and spurious solutions (crosses and circles respectively). The filter was started with IIC (large initial errors) and converged within 100 sec to a *metastable spurious* state that also shows up in the DADMOD solutions. The RTSF converges to the correct solution only about 1000 sec later—towards the start of the maneuver. This slow convergence of the filter is a direct result of the inertial-pointing nature of the spacecraft, which results in the orbital motion being the sole cause for changes in  $\bar{B}$ . (In fact,  $\bar{B}_i^R$  is approximately constant over the maneuver period.) *Note that: (1) this is the first independent confirmation of the DADMOD spurious solutions, and (2) such ambiguities will not arise if gyros provided the rate information and a TAM is used solely for attitude information. Note also a relatively large spread of the physical deterministic solution as a result of relatively low rate of change of  $\bar{B}$ .*

The slow convergence severely limits any rating of the accuracy of the filter: statistics for the last 15 points in Fig. 1 reveal r-m-s attitude errors of (0.43, 0.39, 0.17) deg about the three body axes. For more reliability, the filter was studied using data from the 1/4/96 dataset where an inertial span of nearly 4500 sec duration precedes the maneuver. The results are shown in Figs. 2 and 3.

Fig. 2 presents sample attitude and rate results for the 1/4/96 data of 8 sec telemetry period with the RTSF using IIC. These results were obtained with the numerical values of  $Q_a = Q_b = 2.23 \times 10^{-11}$  and were deemed the optimal parameters after examining the error statistics. (See Table 2 below). We see that the filter converges by about 4000 sec even though the initial errors ranged from about 65 deg in Angle-3 to about 113 in Angle-1. Additional residual results from the same run are presented in Fig. 3. The RTSF state vector evolves so as to minimize all these quantities, and we see that all are small only after 4000 sec.

The convergence is slow here also, and it is instructive to examine the RTSF errors after 3200 sec separated into before, during, and after the maneuver. These are presented in the first and second columns of Table 2. Table 2 also compares these error statistics with the ones obtained using raw TAM data and a different set of tuning parameters ( $Q_a = Q_b = 1.12 \times 10^{-9}$ ) separately determined to be optimal for the raw data. Some clear inferences can be drawn from examining Table 2.

- The attitude errors are significant before the maneuver but noticeably decrease during the maneuver, which we attribute to the increased observability of changes in  $\bar{B}$ .
- In contrast to the attitude errors, the errors in the rates *increase* during the maneuver, which we attribute to (small) dynamical modeling errors of the spacecraft.
- TAM calibration significantly improves TAM-only accuracies.

The above information is also seen qualitatively in the bottom plot of Fig. 2 and the middle and bottom plots of Fig. 3. Thus, Fig. 3 clearly shows us that the rates have converged well before the attitude; this is in accord with past experiences with the RTSF. It should be noted, though, that there will always be differences in the convergence times of the RTSF attitude and rate estimates because the rates are corrected based on the TAM residuals. Nevertheless, it would be interesting to examine in the future if better accuracies result from tuning  $Q_a$  and  $Q_b$  to yield the same convergence times for both attitude and rates.

The RTSF performance using IIC was further examined using the wholly inertial span of 11/6/97, IIC, and some of the results are shown in Fig. 4. It is clear (especially from the TAM angle plot) that the convergence time is of the order of 4400 sec. The error statistics from 4400 sec to the end of the data span are as follows:

r-m-s attitude errors = (0.54, 0.13, 0.33) deg

r-m-s errors in rates = (0.0049, 0.0010, 0.0024) deg/sec

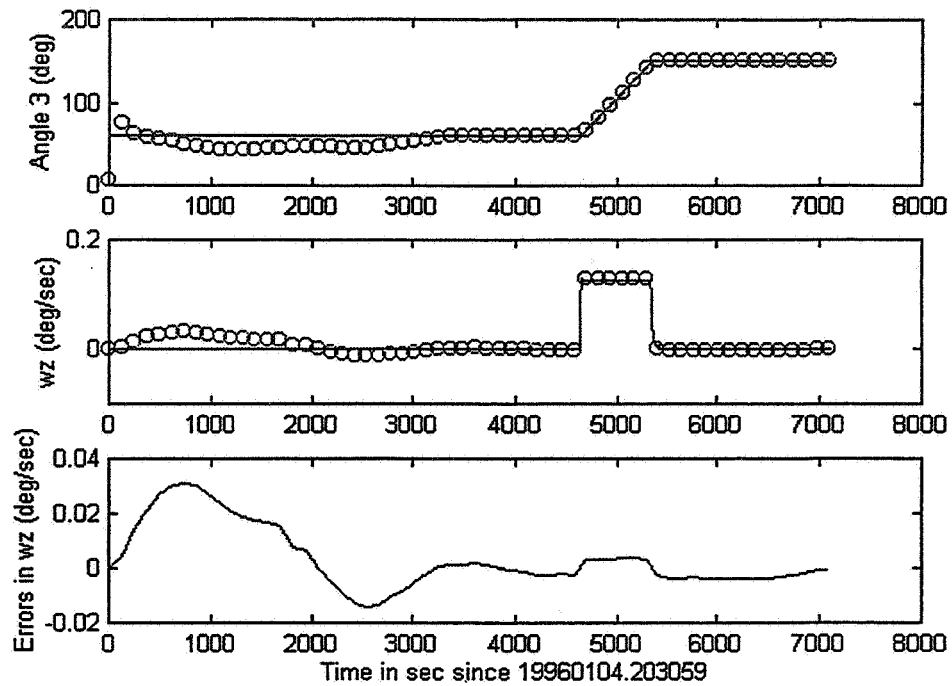


**Figure 2. RTSF Attitude and Rate Results for Adjusted 1/4/96 Data (circles = RTSF and solid = truth in top two plots)**

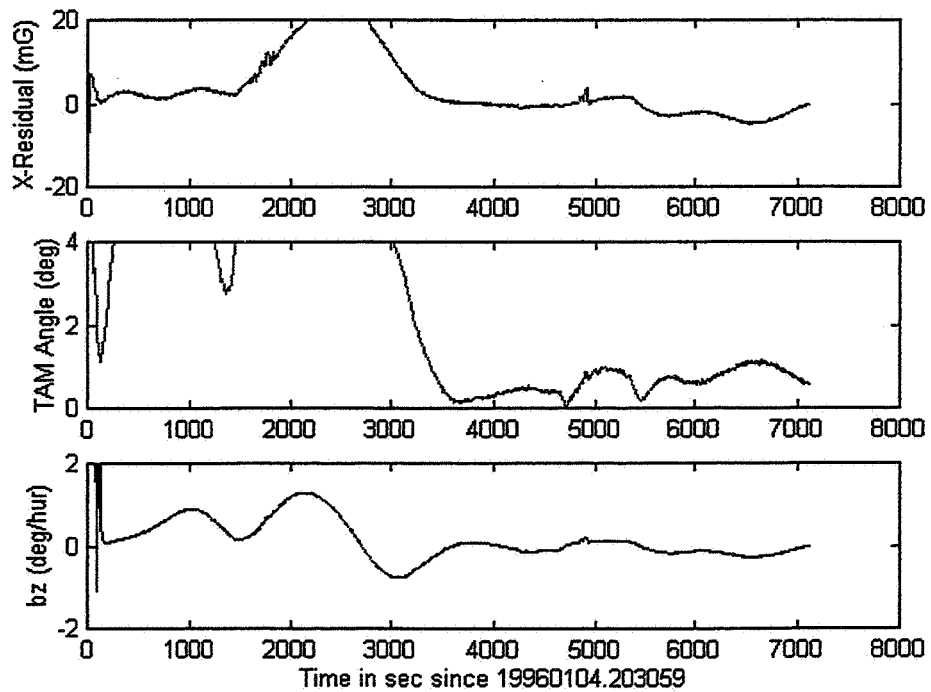


**Figure 3. Additional RTSF Results for Adjusted 1/4/96 Data Showing TAM-1 Residuals (top two plots) and RTSF Rate-Error Estimates (bottom plot)**

**Table 2**  
**RTSF ACCURACIES FOR 1/4/96 DATA SHOWING STATISTICS AFTER 3200 SEC**

	Adjusted Data		Raw Data	
	R-M-S Attitude Errors (x, y, z) deg	R-M-S Errors in Rates (x, y, z) deg/sec	R-M-S Attitude Errors (x, y, z) deg	R-M-S Errors in Rates (x, y, z) deg/sec
<b>Before</b>	(1.15, 0.51, 0.68)	(0.0025, 0.0015, 0.0019)	(8.56, 2.37, 3.12)	(0.0099, 0.0035, 0.0075)
<b>During</b>	(0.70, 0.31, 0.36)	(0.0026, 0.0041, 0.0037)	(0.74, 1.09, 0.92)	(0.0023, 0.0073, 0.0030)
<b>After</b>	(0.38, 1.33, 0.65)	(0.0015, 0.0038, 0.0034)	(0.68, 2.06, 0.57)	(0.0017, 0.0043, 0.0033)

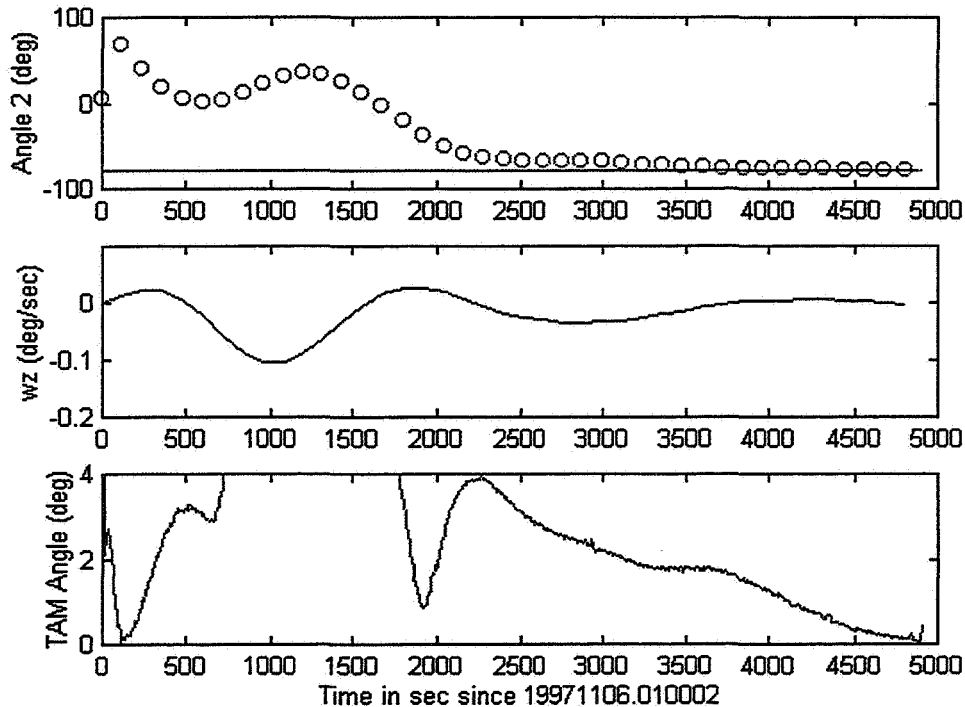


**Figure 4. RTSF Results for Adjusted 11/6/97 Data (circles = filter in top plot)**

## CONCLUSIONS

In contrast to our past experiences with SAMPEX and ERBS, which were momentum-biased spacecraft spinning at the orbit rate, the RTSF performance for the zero-momentum, inertial-pointing RXTE is characterized by extreme sensitivity to filter tuning and long convergence times (about 4000 sec). Thus, while past SAMPEX and ERBS results demanded accuracies of only 1 significant figure in the tuning parameters, it was clear that accuracies of three to four significant figures were needed for success application to RXTE. The performance of both DADMOT and RTSF improved significantly once the

telemetry period was increased from the nominal value of 2 sec to between 8 and 40 sec. Presently we attribute this sensitivity to a combination of telemetry period and the zero-momentum nature of RXTE.

Careful tuning of the RTSF demonstrated per-axis attitude accuracies between 0.13 and 0.54 deg and rate accuracies between 0.0010 deg/sec and 0.0049 deg/sec when adjusted data were used. The corresponding values during the maneuver of 1/4/96 were 0.31 - 0.70 deg and 0.0026 - 0.0041 deg/sec. These results are similar to our past results for ERBS<sup>8</sup>: attitude accuracies within 0.4 deg and rate accuracies within 0.005 deg/sec. We consider these accuracies preliminary in view of the long convergence times and the limited number of post-convergence results. More definitive accuracy studies are needed using long spans of inertial data. It would also be useful to study the relationship between the performance, the tuning, and the telemetry period.

Accurate TAM calibration was performed using a recently developed algorithm, and the subsequent RTSF TAM-only results show a significant improvement in the attitude accuracies upon using calibrated TAM data. This conclusion is in general agreement with studies using a TAM-gyro combination<sup>14</sup>.

An important theoretical development presented here is the transformation of a DADMOD transcendental equation into an 8th order polynomial. The first independent evidence of the accuracy of the DADMOD *spurious* solutions was obtained in the form of initial convergence of the RTSF to the metastable solution using the 4/7/96 data. To improve the DADMOD performance for inertial-pointing modes, a more sophisticated technique for smoothing time derivatives of the measured geomagnetic field should be applied to separate the physical root from the numerical noise.

## REFERENCES

1. G. Natanson, S. McLaughlin, and R. Nicklas, "A Method of Determining Attitude From Magnetometer Data Only," *Proceedings of the Flight Mechanics/Estimation Theory Symposium 1990*, NASA Conference Publication 3102, Goddard Space Flight Center, Greenbelt, MD, May 1990
2. G. Natanson, J. Keat, and S. McLaughlin, *Sensor and Advanced Attitude Studies: Deterministic Attitude Computation Using Only Magnetometer Data*, Goddard Space Flight Center, Flight Dynamics Division, 554-FDD-91/010, prepared by Computer Sciences Corporation, March 1991
3. G. Natanson, "A Deterministic Method for Estimating Attitude From Magnetometer Data Only," Paper No. IAF-92-0036, *Proceedings of the World Space Congress*, Washington, DC, September 1992
4. M. Challa, *Solar, Anomalous, and Magnetospheric Particle Explorer (SAMPEX) Real Time Sequential Filter (RTSF): Evaluation Report*, Goddard Space Flight Center, Flight Dynamics Division, 553-FDD-93/024R0UD0, prepared by Computer Sciences Corporation, April 1993
5. M. Challa, G. Natanson, D. Baker, and J. Deutschmann, "Advantages of Estimating Rate Corrections During Dynamic Propagation of Spacecraft Rates—Applications to Real-Time Attitude Determination of SAMPEX," *Proceedings of the Flight Mechanics/Estimation Theory Symposium 1994*, NASA Conference Publication No. 3265, Goddard Space Flight Center, Greenbelt, MD, May 1994
6. G. Natanson, M. Challa, J. Deutschmann, and D. Baker, "Magnetometer-Only Attitude and Rate Determination for a Gyroless Spacecraft," *Proceedings of the Third International Symposium on Space Mission Operations and Ground Data Systems*, NASA Conference Publication 3281, Greenbelt, MD, November 1994, pp. 791–798.
7. M. Challa and G. Natanson, "A PC-Based Magnetometer-Only Attitude-and-Rate Determination System for Gyroless Spacecraft," *Proceedings of the Flight Mechanics and Estimation Theory Symposium*, NASA Conference Publication No. 3299, Goddard Space Flight Center, Greenbelt, MD, May 1995
8. M. Challa and C. Wheeler, "Accuracy Studies of a Magnetometer-Only Attitude-and-Rate Determination System," *Proceedings of the Flight Mechanics and Estimation Theory Symposium*, NASA Conference Publication No. 3333, Goddard Space Flight Center, Greenbelt, MD, May 1996

9. M. Challa, G. Natanson, and C. Wheeler, "Simultaneous Determination of Spacecraft Attitude and Rates Using Only a Magnetometer," *Proceedings of the American Institute of Aeronautics and Astronautics (AIAA)/American Astronautical Society (AAS) Astrodynamics Specialist Conference*, San Diego, CA, July 1996
10. M. Challa, S. Kotaru, and G. Natanson, "Magnetometer-Only Attitude and Rate Estimates During the Earth Radiation Budget Satellite 1987 Control Anomaly," AIAA Guidance, Navigation and Control Conference, New Orleans, August 11-13, 1997
11. J. Kronenwetter, M. Phenneger, and W. Weaver, "Attitude Analysis of the Earth Radiation Budget Satellite (ERBS) Yaw Turn Anomaly", *Proceedings of the Flight Mechanics/Estimation Theory Symposium*, NASA Conference Publication No. 3011, Goddard Space Flight Center, Greenbelt, MD, May 1988
12. M. Challa and R. Harman, "A New Magnetometer Calibration Algorithm and Application to the X-Ray Timing Explorer", *Proceedings of the AIAA Guidance, Navigation and Control Conference*, Boston, August 10-12, 1998 (to be published)
13. See, for example, the IGRF World Wide Web page at:  
[http://ftp.ngdc.noaa.gov/Solid\\_Earth/Mainfld\\_Mag/Models/](http://ftp.ngdc.noaa.gov/Solid_Earth/Mainfld_Mag/Models/)
14. J. Hashmall and J. Deutschmann, "An Evaluation of Attitude-Independent Magnetometer-Bias Determination Methods", *Proceedings of the Flight Mechanics/Estimation Theory Symposium 1996*, NASA Conference Publication 3333, Goddard Space Flight Center, Greenbelt, MD, May 1996





## EMPIRICAL CORRECTION FOR EARTH SENSOR HORIZON RADIANCE VARIATION

Joseph A. Hashmall,<sup>\*†</sup> Joseph Sedlak,<sup>\*</sup> Daniel Andrews,<sup>\*</sup>  
and Richard Luquette<sup>\*</sup>

A major limitation on the use of infrared horizon sensors for attitude determination is the variability of the height of the infrared Earth horizon. This variation includes a climatological component and a stochastic component of approximately equal importance. The climatological component shows regular variation with season and latitude. Models based on historical measurements have been used to compensate for these systematic changes. The stochastic component is analogous to tropospheric weather. It can cause extreme, localized changes that for a period of days, overwhelm the climatological variation.

An algorithm has been developed to compensate partially for the climatological variation of horizon height and at least to mitigate the stochastic variation. This method uses attitude and horizon sensor data from spacecraft to update a horizon height history as a function of latitude. For spacecraft that depend on horizon sensors for their attitudes (such as the Total Ozone Mapping Spectrometer-Earth Probe—TOMS-EP) a batch least squares attitude determination system is used. It is assumed that minimizing the average sensor residual throughout a full orbit of data results in attitudes that are nearly independent of local horizon height variations. The method depends on the additional assumption that the mean horizon height over all latitudes is approximately independent of season. Using these assumptions, the method yields the latitude dependent portion of local horizon height variations.

This paper describes the algorithm used to generate an empirical horizon height. Ideally, an international horizon height database could be established that would rapidly merge data from various spacecraft to provide timely corrections that could be used by all.

---

\* Computer Sciences Corporation, 10110 Aerospace Rd. Lanham/Seabrook, MD 20706, USA

† Phone (301)-794-1279, e-mail joseph.hashmall@gsfc.nasa.gov

✱ NASA Goddard Space Flight Center, Greenbelt MD, 20771, USA

## INTRODUCTION

Earth horizon sensors have recently regained some of their early popularity as attitude sensors. Although they have the advantage of reliability and relatively low cost, their accuracy for near-Earth orbit missions is limited by the variability in the height of the layer of the stratosphere that they detect as the surface of the Earth's infrared spheroid. Most modern horizon sensors limit their sensitivity to radiation in the 14-16 $\mu$  band to eliminate diurnal effects and because at these wavelengths the Earth spheroid is most stable and homogeneous.

Scanning horizon sensors rotate the field-of-view (FOV) of an infrared telescope around a circular path. The sensor FOV points towards space over part of the circle and points towards Earth during the rest. The angle at which a sudden change between the low radiance of space and the high radiance of the Earth occurs is interpreted as the horizon-crossing angle. Differences and mean values of Earth-in and Earth-out horizon crossing angles can be used to provide estimates of the spacecraft pitch and roll.

Static horizon sensors have detectors that point towards the Earth horizon when the spacecraft is near its nominal attitude. The level of output from these detectors represents the portion of their FOVs that contains the Earth. Differences and means of the output from detectors viewing different portions of the horizon can be used to provide estimates of the spacecraft pitch and roll.

For both types of sensor, several effects can alter the detector output and result in attitude errors. These effects include the variation of the atmosphere's radiance in the wavelength range (roughly 14-16 $\mu$ ) in which the detectors are sensitive. This paper analyzes those horizon height variations caused by those changes in radiance that result from stratospheric temperature variation. Other phenomena can also cause significant horizon sensor errors. These include the effects Earth's oblateness, of high, cold clouds, and of the proximity of the Sun or Moon image to the horizon crossing point. Some of these can easily be compensated (e.g. Earth oblateness) while others must be predicted or detected and the contaminated data removed from the processing stream. None of these other effects will be extensively discussed in this paper.

Changes in stratospheric temperatures can be interpreted as changes in the height of the infrared Earth horizon and often are the single largest uncompensated contributor to horizon sensor attitude error. These temperature changes can be classified as climatic or stochastic. In this paper the term "climatic" will be used to designate those effects that depend on latitude and season and which are repeatable from year to year. Similarly, "stochastic" will be used to designate those effects that change rapidly (over a period of days), are usually localized (over a range of a few thousand km), and are correlated in time. Stochastic effects are similar to weather and cannot be accurately predicted long in advance. For attitude determination they can best be modeled as colored noise.

Attempts have been made to analyze and mitigate the effect of the climatic variations of horizon radiance on horizon sensor attitude estimates. Extensive historical measurements of stratospheric temperatures from balloon and rocket probes have been combined with atmospheric models and electronic models of sensor triggering to produce horizon radiance models.<sup>1</sup> These models have been incorporated in software to compensate for the climatic variation of the infrared horizon height.<sup>2,3,4</sup>

Studies of the stochastic variations of horizon radiance have shown that errors due to these variations can be as large as those due to uncompensated climatic horizon radiance

variations. Sudden stratospheric warming events<sup>5</sup> can overwhelm the climatic effects in large regions of the winter hemisphere making the horizon height over a large portion of the winter hemisphere higher than that over the summer hemisphere.<sup>6</sup> These events can last for as little as a few days to as much as a few weeks. Observations of the Earth infrared brightness by the GOES-8 and -9 sounders have been correlated with errors in Earth sensor based attitude control. Results show that stratospheric radiance changes can arise suddenly and can result in significant attitude errors.<sup>7</sup>

In preparation for the launch of the Total Ozone Mapping Spectrometer-Earth Probe (TOMS-EP), an empirical radiance modeling utility<sup>8</sup> (ERMU) was developed by NASA's Goddard Space Flight Center (GSFC). This utility was to be used in an attempt to minimize the effects of horizon radiance variation on TOMS-EP attitude. This paper is a description of the results of measurements made by the TOMS-EP horizon sensors and their interpretation as changes in the Earth's infrared horizon height.

TOMS-EP was launched in July 1996 into a Sun synchronous orbit at an altitude of approximately 500 km and an inclination of 97.4 deg. After 16 months of data collection, in December 1997 it was boosted to an altitude of about 740 km and the inclination adjusted to 98.4 deg to maintain Sun synchrony. The nominal TOMS-EP attitude is Earth pointing with the Z-axis (yaw) pointing towards the Earth, the Y-axis (pitch) along the negative orbit normal, and the X-axis (roll) pointing in the general direction of the spacecraft velocity vector.

The principal attitude sensors used by TOMS-EP are two Ithaco T-scanwheel horizon sensors (HS), two fine Sun sensors (FSS), and a set of accurate rate determining gyros. The two horizon sensors are mounted with their scan axes in the Y-Z plane, canted 20 deg towards nadir from the +Y and -Y-axes respectively. Their half cone angles are 46 deg. The HSs are insensitive to Yaw so the primary Yaw information is obtained from the two Sun sensors. The Sun sensors' FOVs are directed in the +X and -X directions allowing these sensors to measure the Sun direction while the satellite is near the polar regions.

## METHOD

The TOMS-EP ERMU was developed to reduce the effect of horizon radiance variation on horizon sensor performance. It was to do this by using horizon sensor data to determine horizon height variations weekly and apply the corrections needed to compensate for these variations in the following week. Although the ERMU was tested in the early phases of the TOMS-EP mission, it was never used in normal operations because its use was found to be unnecessary to meet mission requirements (0.25 deg per axis,  $3\sigma$ ). The approximately one year span during which horizon height variations were measured serves as an excellent reference for horizon height behavior and mitigation studies.

The basis of the ERMU horizon height measurements is the determination of the spacecraft attitude using a batch least-squares algorithm. This algorithm is implemented in GSFC's multimission three-axis stabilized spacecraft (MTASS) coarse and fine-attitude determination system (CFADS). CFADS has been used with data from many missions and has been shown to be flexible, reliable, and accurate.

The CFADS algorithm minimizes the loss function for the Wahba<sup>9</sup> problem given by:

$$L = \sum_t W_s [(P_{t_0} A_{t_0}) \hat{R}_t - \hat{S}_t]^2 \quad (1)$$

with respect to a state vector including the attitude at an epoch time and gyro biases. In Eq. (1),  $W_s$  is the relative weight of the sensor with a measurement at some time  $t$ ,  $t_0$  is the reference time,  $A_{t_0}$  is the attitude at the reference time,  $P_{t_0}$  is the transition matrix transforming the attitude at epoch to the attitude at time  $t$  (obtained by integration of gyro observations with added biases from  $t_0$  to  $t$ ), and  $\hat{R}_t$  and  $\hat{S}_t$  are reference and observed sensor measurements at time  $t$ . The sum is performed over all valid sensor measurements in a batch, including both Sun sensor and horizon sensor measurements. The primary CFADS output is the attitude of the spacecraft at times throughout the batch obtained by propagating the epoch attitude solution using gyro data modified by the determined gyro biases.

As long as the gyro biases are nearly constant (as assumed in Eq. (1) and as expected from mission experience), the attitudes obtained from CFADS will be far more accurate than single frame attitudes, and in cases with correlated errors in sensor measurements or correlated errors in reference vectors, more accurate than ordinary Kalman filters. Note that errors in horizon sensor measurements due to horizon height variations are highly correlated in time. This is because horizon height changes occur over finite areas of the Earth surface (they are correlated in space) and, therefore, measurement deviations persist while the spacecraft traverses the affected region. These correlations strongly affect the accuracy of Kalman filter derived attitudes but have little effect on the batch least-squares attitudes used in this study.

The accuracy of CFADS attitudes arises from the use of all of the sensor data in the batch. Errors arising from sensor deviations at one time can be compensated by opposing errors at other times because of gyro propagation. This compensation does not require uncorrelated errors, but increases accuracy as mean errors over the batch approach zero. In this study, an integral number of orbits were used in all CFADS batches, minimizing (due to North-South mirror symmetry) the effect of climatic horizon radiance variation.

TOMS-EP Earth sensor data is preprocessed onboard the spacecraft and reported as pitch and roll estimates for each of the two horizon sensors. They are reported every 32 seconds.

Once CFADS attitudes have been computed, sensor residuals are obtained by first computing reference roll and pitch angles. These reference angles are computed by converting the negative spacecraft position vectors to body coordinates using the corresponding calculated attitudes. The converted vectors are expressed in terms of roll and pitch angles in an nadir referenced coordinate system. Differences between these reference pitch and roll angles and the observed angles, compensated for sensor misalignment, constitute the sensor residuals.

The spacecraft orbit was divided into equal bins of orbit phase and the roll and pitch errors within each bin were averaged to give mean residuals:  $\Delta \bar{r}_n$  and  $\Delta \bar{p}_n$  for bin  $n$ . These are converted into mean horizon height deviations by the following steps:<sup>8</sup>

1. Compute a mean angular radius of the subtended Earth,  $\rho$ , from the nominal semimajor axis,  $E$ , the equatorial Earth radius,  $R_e$ , and the nominal horizon height,  $h_{nom}$  ( $h_{nom} = 37.9$  km), by:

$$\rho = \sin^{-1} \left( \frac{R_e + h_{nom}}{E} \right) \quad (2)$$

2. Compute the nominal Earth chord width,  $\Omega$ , as:

$$\Omega = \cos^{-1} \left( \frac{\cos \rho - \cos \eta \cos \psi}{\sin \eta \sin \psi} \right) \quad (3)$$

where  $\eta$  is the complement of the cant angle and  $\psi$  is the half cone angle.

3. Geometry coefficients for roll,  $K_r$ , and pitch,  $K_p$ , are computed from:

$$K_r = \frac{\tan \rho}{2E(\sin \eta \cos \psi - \cos \eta \sin \psi \cos \Omega)} \quad (4)$$

and

$$K_p = \frac{\tan \rho}{2E(\sin \Omega \sin \psi)} \quad (5)$$

4. Finally, the horizon height deviations for the Earth-in and Earth-out transitions are found from:

$$\Delta h_n^{in} = \frac{1}{2} \left[ \frac{\Delta \bar{r}_n}{K_r} + \frac{\Delta \bar{p}_n}{K_p} \right] \quad (6)$$

and

$$\Delta h_n^{out} = \frac{1}{2} \left[ \frac{\Delta \bar{r}_n}{K_r} - \frac{\Delta \bar{p}_n}{K_p} \right] \quad (7)$$

where  $\Delta \bar{r}_n$  is the mean roll residual and  $\Delta \bar{p}_n$  the mean pitch residual in bin  $n$ .

A minimum of four orbits of data (approximately 200 Earth observations per sensor per orbit) in each of four days were used to produce weekly averages of Earth-in and Earth-out horizon height deviations for each sensor and for each orbit phase measured from the ascending node. Horizon heights that fell within orbit phase bins having a width of 2 deg were averaged. This empirical horizon height database was produced for approximately 1 year of TOMS-EP data.

The tables of horizon heights stored by TOMS-EP orbit phase angle and week of year were designed for this single mission. Corrections to the nominal height of any of the horizon crossings were to be obtained by interpolation of phase angle using the previous weeks results. Once on orbit, it was found that this correction was not needed to attain the mission's modest attitude accuracy requirements. If one of the TOMS-EP Earth sensors fails it may be necessary to use of the ERMU to improve attitude accuracy.

To make tables of horizon heights more generally useable, and to allow compatible input from spacecraft other than the one making horizon height measurements, it is convenient to express the results in terms of the latitude of the horizon crossing rather than the phase of the spacecraft orbit. This transformation is accomplished by determining the declination angle,  $\rho$ , as:

$$\rho_n = \sin^{-1} \left( \frac{R_s + h_{nom} + \Delta h_n}{E_n} \right) \quad (8)$$

Equation (8) is virtually identical to Eq. (2) except that the oblate Earth radius beneath the (-in or -out) horizon crossing,  $R_s$ , and the true Earth to spacecraft distance,  $E_n$ , are used in place of nominal values, and the horizon height is corrected by values from the ERMU table. The geometry defining  $\rho$  is shown in Fig. 1. The location of the tangent point is obtained by finding the intersection of the nadir pointing cone with a half-cone angle of  $\rho$  and the scan cone. This

intersection consists of two possible scan vectors,  $\hat{S}$ . After selecting the correct scan vector, the vector from Earth center to this point is simply the sum of the spacecraft position vector,  $\vec{E}_n$ , and the scan vector adjusted to the correct length:

$$\vec{R}_n = \vec{E}_n + \vec{S}_n \quad (9)$$

where

$$\vec{S}_n = \hat{S}_n \sqrt{\vec{E}_n^2 - (|\vec{R}_n| + h_{nom} + \Delta h_n)^2} \quad (10)$$

The latitude,  $\lambda_n$ , of the tangent point can then be computed as:

$$\lambda_n = \tan^{-1} \left( \frac{\vec{R}_3}{\sqrt{\vec{R}_1^2 + \vec{R}_2^2}} \right) \quad (11)$$

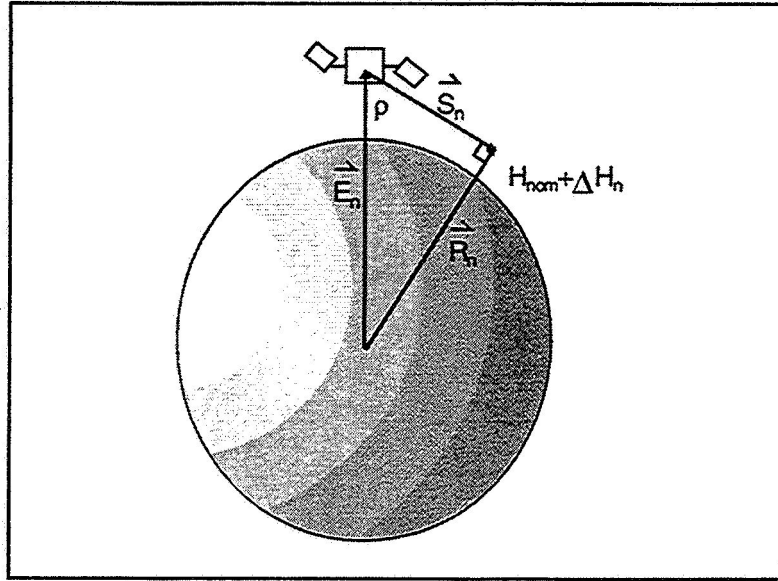


Figure 1. Geometry of Horizon Sensor Tangent Height

Strictly speaking, because of oblateness, the Earth radius is a function of the latitude of the horizon crossing, but an iterative algorithm compensating for oblateness changes latitude from the values calculated using Eq. (11) only by a negligible amount.

## RESULTS AND DISCUSSION

For a period of approximately 1 year (from Summer 1996 to Summer 1997) TOMS-EP horizon sensor measurements were used to determine weekly horizon height variation tables. For each week's entries at least one orbit of data per day for at least 4 days in the week were processed. In each batch of data, observations at 32-second intervals from each of the Earth sensors were processed. A total of about 190 observations per orbit or at least 760 observations each week were used to determine Earth-in and Earth-out horizon heights for each sensor using Eqs (6) and (7). Horizon heights were collected in bins of 2 deg phase angle and averaged for each sensor and each horizon crossing (-in or -out).

The latitude corresponding to the Earth-in and Earth-out horizon crossing for the center of each phase angle bin was computed. For each week of data, horizon heights falling in the same 2-deg latitude bin were averaged even if they arose from different horizon crossings or different sensors. A contour plot showing these mean horizon heights as a function of season and latitude is presented in Fig. 2.

Individual horizon heights range from a minimum of 24.6 km to a maximum of 56.8 km. The horizon height variations with latitude and season clearly show both regular, climatic trends as well as more chaotic, stochastic effects.

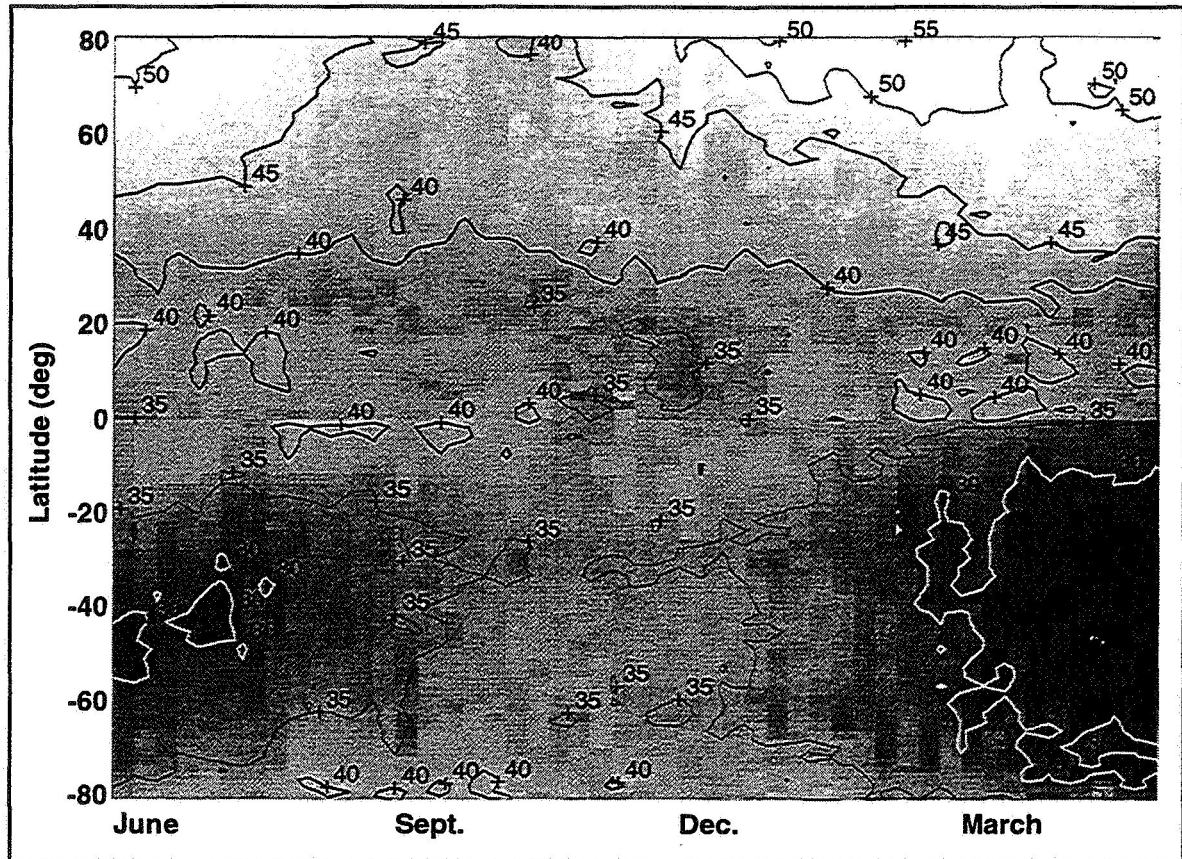


**Figure 2. Measured Average Earth Sensor Horizon Heights (km) From TOMS-EP Data**

The climatic effects for the study year show expected features as well as some surprising ones:

- Near the equator, the horizon height varied least throughout the year.
- In each hemisphere, there was a regular change of horizon height with season.
- Near the North Pole, the minimum horizon heights occurred in the northern autumn.
- Near the South Pole, the minimum horizon heights occurred in late in the northern spring.
- At about 50-deg south latitude, a local minimum horizon height was found in all seasons.

The stochastic effects are best demonstrated by the occurrence of numerous regions of a few weeks duration and 10 or less deg of latitude extent with average horizon heights 5 or more kilometers different from the surrounding regions.

To better describe the variation of horizon heights with time and position, weekly mean values were converted to tangent angles,  $\rho$  in Eq. (8) and Fig. 1, and the differences in these values were computed as a function of latitude for different weeks. These plots of  $\Delta\rho$  against latitude for adjacent weeks, for a separation of half a year, and for a separation of approximately 1 year are presented in Fig. 3. Again, each set of weekly mean values were obtained by computed average heights (eqs. 6 and 7) using data collected during several arbitrary orbits on each of at least 4 days in each week and converting the average heights to average scanner rotation angles. The plots in Fig. 3. show differences between average scanner angles for typical weeks separated by 1 week, 26 weeks, and 1 year.

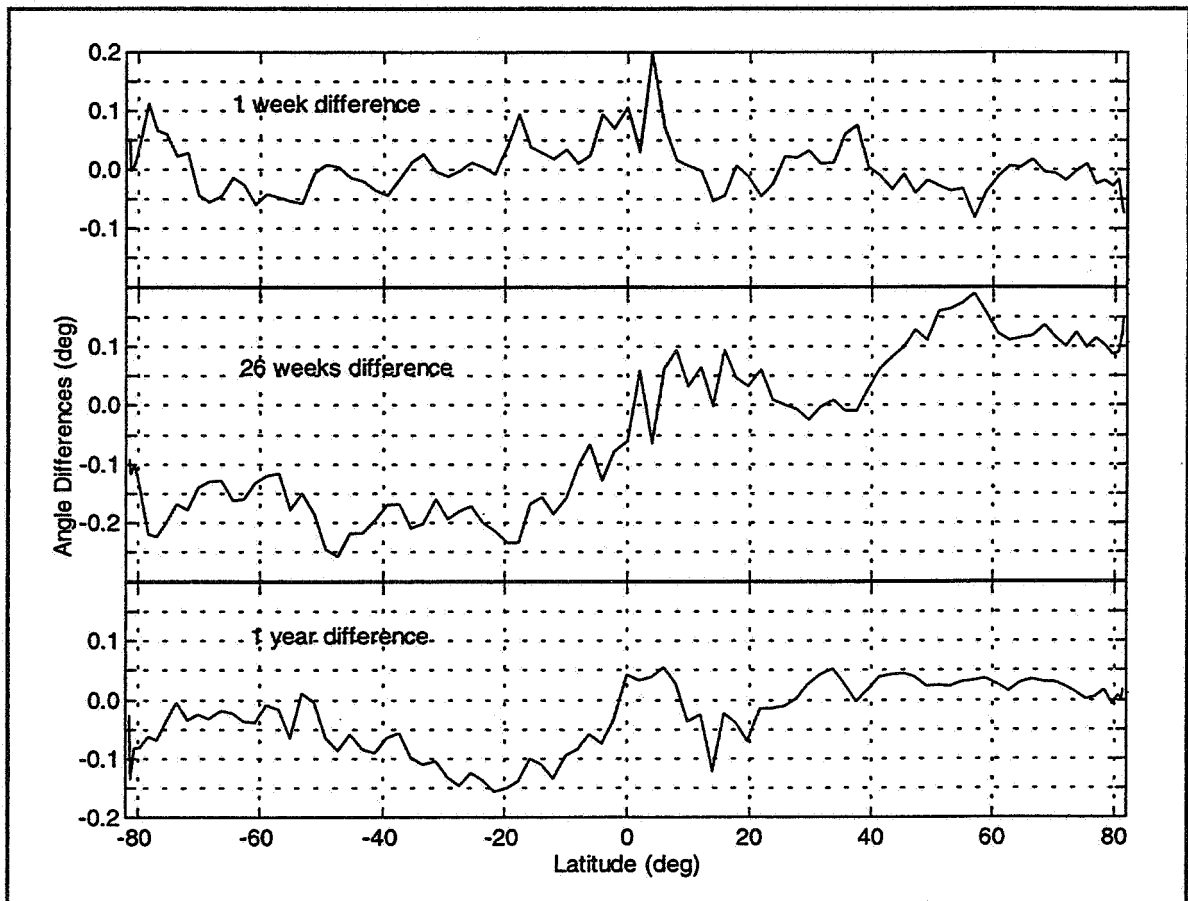


**Figure 3. Tangent Angle Differences for 1 Week, 26 Weeks, and 1 Year Time Difference**

In these plots, several important features of the mean tangent angles are clear:

- Values separated by either 1 week or 1 year have smaller differences than those separated by half a year.
- Values separated by half a year show the largest differences indicating clear seasonal changes.
- Values near the equator are similar, regardless of time difference.



- Values separated by 1 week are similar but large differences ( $\approx 0.2$  deg) occur in some regions.

In order to evaluate the effect of the horizon radiance variance on attitude, TOMS-EP data for early in 1998 were examined. During this period, the spacecraft altitude had been increased to 740 km. At this altitude, horizon height variations subtend a smaller angle at the spacecraft, so the resulting measurement errors are somewhat smaller than they were earlier in the mission.

For each of 3 weeks (Feb 1-7, Feb 8-14, and March 1-7, 1998), data were processed using CFADS for 3 orbits per day on 4 or 5 days in each week. The pitch and roll residuals of each HS were accumulated and averaged in bins of 5 deg of phase angle. Data from any single day contributed an average of 8 values to each bin average. These average residuals for one day (Feb 4, 1998) are plotted against orbit phase in Fig. 4. Error bars for each bin, corresponding to  $\pm 1\sigma$  deviations from the mean, are also included in this figure.

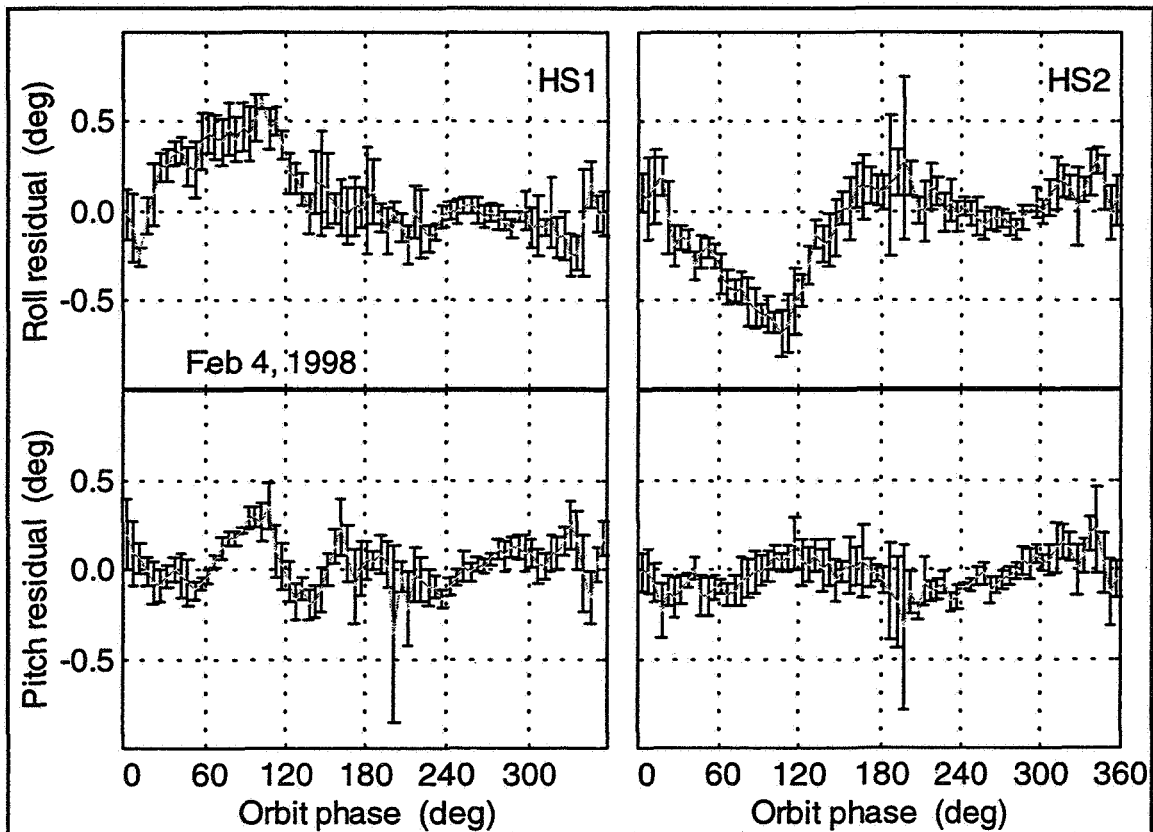


Figure 4. Mean TOMS-EP Roll and Pitch Errors for Feb 4, 1998

Several interesting features are apparent in these plots:

- Single sensor roll and pitch errors can have residuals that are as large as 0.5 deg.
- Residuals show systematic variations with orbit phase.
- The standard deviations of the residuals in any orbit phase bin may differ by large amounts from those in other bins.

- Noisy bins (those with large standard deviations) seem to be clustered near each other, as are bins with small standard deviations.
- The noisiest bins are clustered in the same general region of the orbit (phase near 200 deg) for both of the sensors.

These observations can be explained by the existence of regions of unusual horizon height. At phase angles in an orbit where one or the other of the horizon crossings for a HS passes through such a region large residuals are produced. If the region is localized in longitude, the horizon crossing on subsequent orbits will not be affected, producing large standard variations of the mean. At other phase angles, where no anomalous horizon height regions are observed, the standard deviations will be smaller.

Were this explanation true, the plots in Fig. 4 would change in an unusual manner as more data from other days is added. In cases with normal distributions of measurements, adding data should systematically reduce the standard deviations. Assuming normal distribution, adding 4 additional days of data to the one day shown in Fig. 4 should decrease the standard deviations to less than half their previous values. The actual changes are shown in Fig. 5. In the plots shown in this figure, each bin represents an average of about 40 observations.

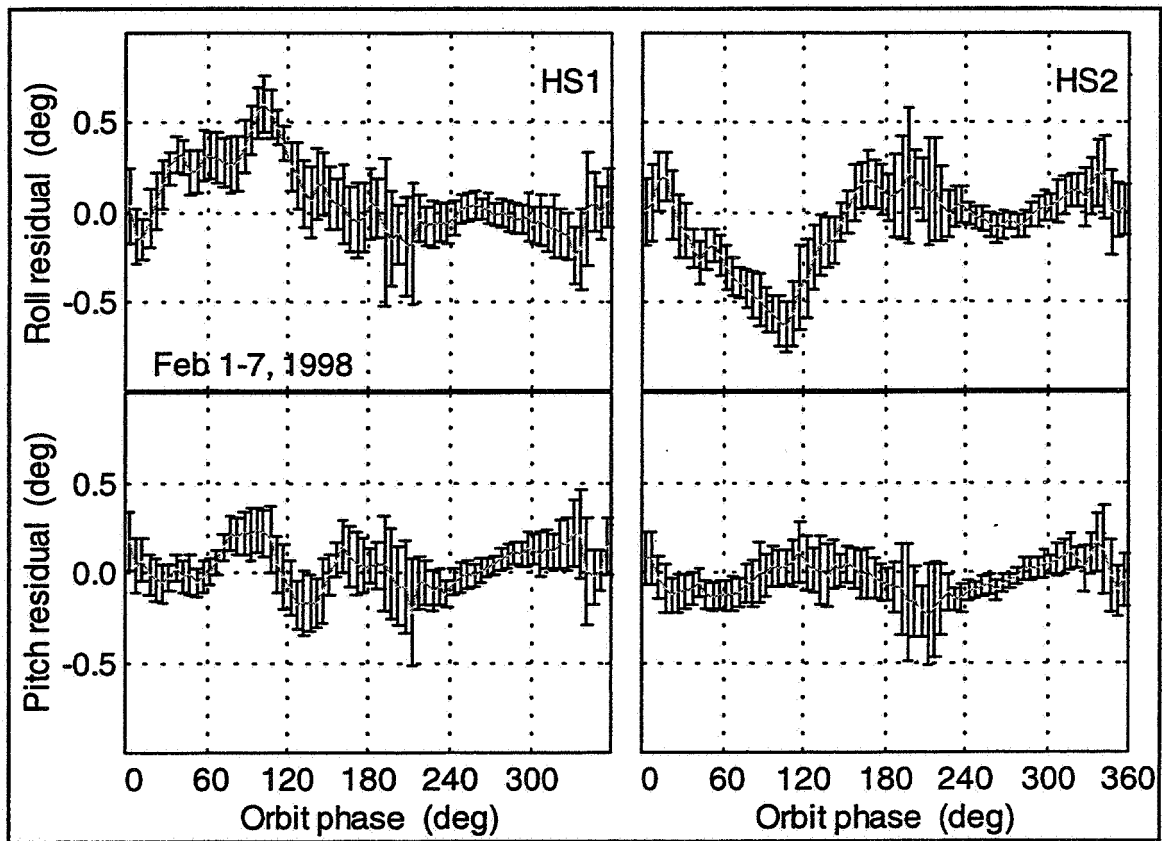


Figure 5. Mean TOMS-EP Roll and Pitch Errors for Feb. 1-7, 1998

It is clear from this figure that adding more data increases the standard deviations at most orbit phases. This result is consistent with the growth and decay of anomaly regions within the week period covered by each plot. As a new anomaly region grows it changes the residuals

during the portion of some orbits. This increases the standard deviations and shifts the mean. The same effect occurs as the region disappears.

Also for most values of phase angle, adding data from different days reduces the differences in standard deviations among adjacent bins. Even with this smoothing, for some regions (e.g. near 200-deg phase angle in the week of Feb. 1) the standard deviations are consistently large, while for others (e.g. between 240 and 300 deg phase) the standard deviations are consistently low.

Figures 6 and 7 show similar averages obtained from data in the following week (Feb. 8-14, 1998) and three weeks after that (March 1-7, 1998), respectively.

In the plots representing HS1 residuals in the week of Feb. 8-15, there are exceptionally large values of the mean residual as well as standard deviations near 200 deg phase angles. Most of these large values can be traced to short periods (1-2 minutes in duration) during which HS1 measured anomalous values. These roll and pitch values were more than 1 deg from nominal, lasted for several measurement periods, and occurred on at least 2 days. They were not observed in every orbit and, although their approximate position remained the same, moved by several deg of orbit phase from day to day.

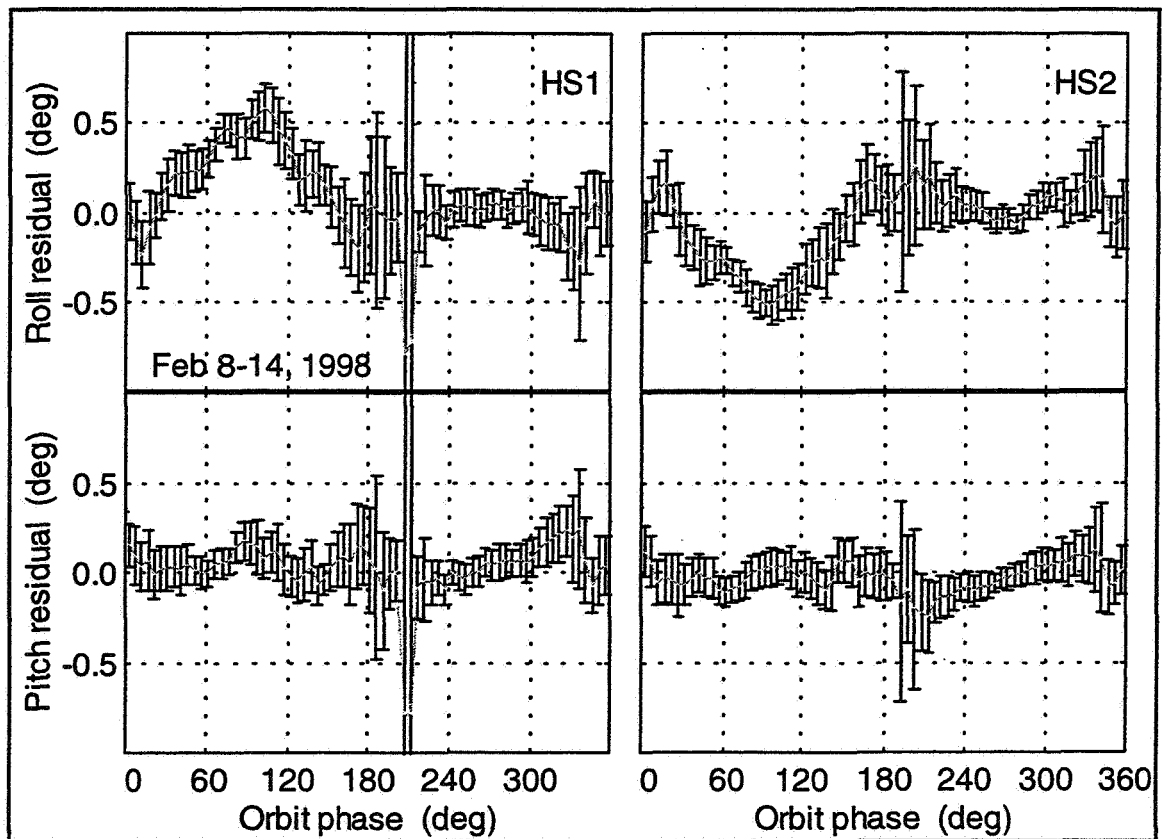


Figure 6. Mean TOMS-EP Roll and Pitch Errors for Feb. 8-14, 1998

There are many possible causes for the anomalous behavior near 200 deg phase angle. It is well known that the presence of the Sun or Moon near the position where a HS detects the horizon can cause large errors in attitude measurements.<sup>10</sup> Although Sun and Moon interference

can cause pitch and roll errors of this size, examination of standard TOMS-EP HS interference utility results show no Sun or Moon interference for at least 24 hours before and after these anomalies. High, cold clouds can also cause HS errors,<sup>11</sup> but the size of these errors is usually limited to a 0.1-0.2 deg. Other possible causes for this anomaly, including Sun glint, shading, etc. were not investigated.

These anomalies probably are not an artifact of telemetry processing because the moderately large standard deviations in HS2 for the same period and phase angle are probably due to a response to HS1 anomalies by the OBC attitude control system. The facts that they recur at approximately the same phase angle on adjacent days, and that they contain more than a single observation each, makes it likely that these anomalies are caused by a physical phenomenon.

Except for the anomalous portions of the data in the week of Feb. 8-14, the mean values of horizon sensor residuals are quite similar from week to week. Differences of about 0.1 deg can be seen (for example near 125 to 175 deg of phase angle in the plot of pitch residuals). The size of these differences is consistent with the results shown in Fig. 3.

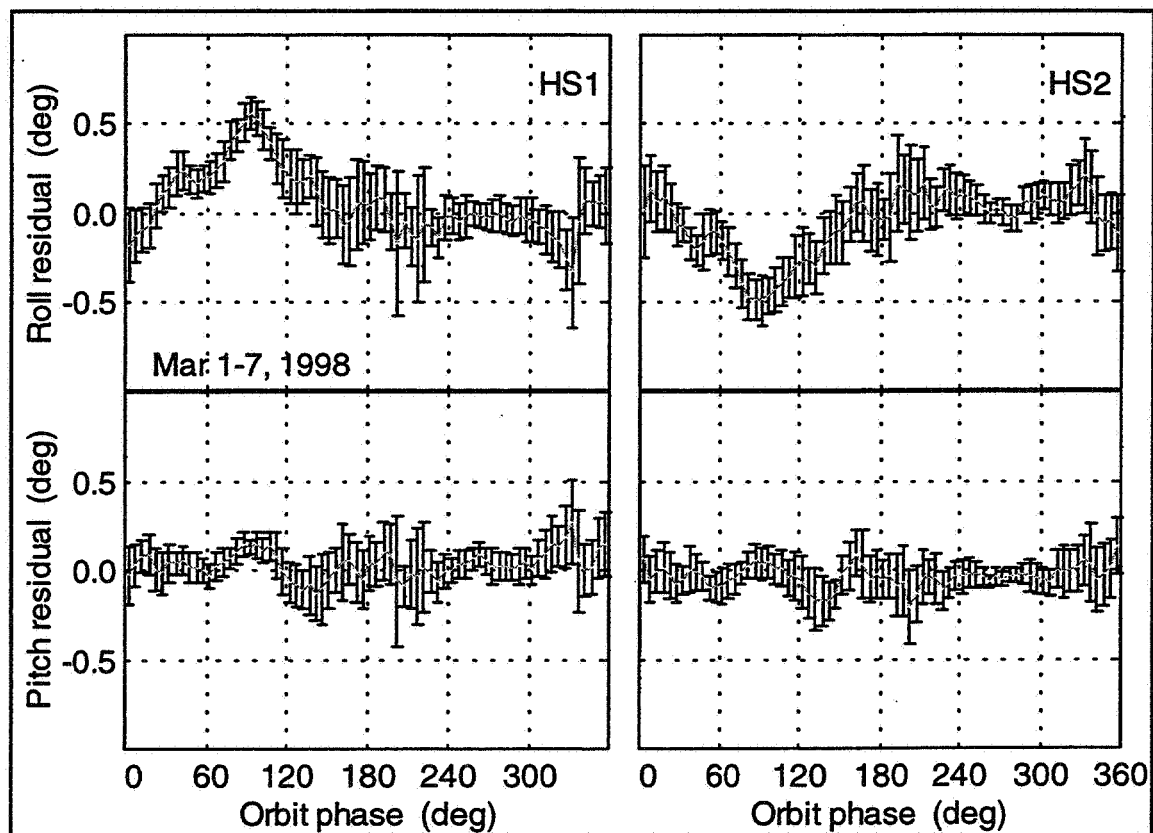


Figure 7. Mean TOMS-EP Roll and Pitch Errors for March 1-7, 1998

The standard deviations are consistently larger in some portions of the orbit and smaller in others. The mean of the standard deviations over all of the phase angle bins, both of the sensors, and both attitude directions is about 0.15 deg. This value reveals more about the fraction of the time during which a HS will have relatively large errors than it does about either the random noise the sensor will experience or the reliability of a horizon height model.

The relative size of the residuals throughout any orbit also shows a consistent pattern. Much of this pattern can be explained by the positions of the HS horizon crossing points as a function of orbit phase. The latitudes of these positions (using a nominal orbit and nominal horizon heights) are shown in Fig. 8

When the -in and -out horizon crossings for both HSs fall at nearly the same latitude (e.g. near orbit phases of 90- and 270-deg), the standard deviations are smaller than in regions where the horizon crossings fall at different latitudes. The largest standard deviations in all of the weeks occur between orbit phases of 180 and 240 deg. where one of the horizon crossings in each sensor is approaching the summer pole and the other remains at much lower latitudes.

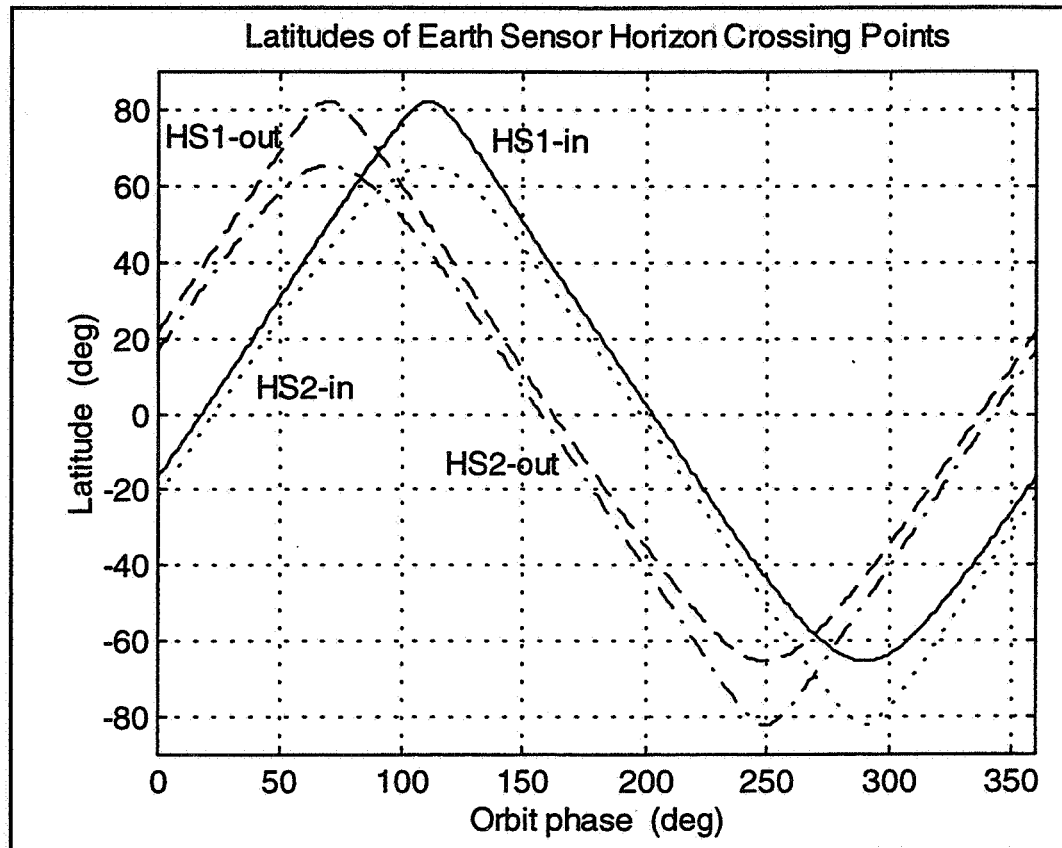


Figure 8. Horizon Crossing Latitudes vs. Phase Angles for a Nominal TOMS-EP Orbit

## CONCLUSIONS

The data presented here as well as that cited from earlier studies is consistent with a horizon height model that includes climatic and stochastic effects of approximately the same importance. The climatic effects are, by definition, predictable and can therefore be reduced through the proper use of models. The stochastic effects can not be predicted and their effects can not therefore be completely removed.

Stochastic effects are localized in both time and space and introduce colored noise into the horizon radiance. Treating these effects as uncorrelated noise with normal distribution

produces sensor error models that, although convenient to use, are not optimal since they do not accurately reflect the system's statistics.

When evaluating the accuracy of a sensor in the design phase of a mission, that sensor's measurement error statistics should be used explicitly to evaluate the probability that a certain level of attitude error will occur. Because the horizon height variation contains a significant contribution from sequentially correlated errors, the assumption of white noise and use of the corresponding simple standard deviation as a measure of sensor error yields a misleading description of attitude errors.

Given the observed error distribution on TOMS-EP, it is probable that in any orbit there will be regions in which the sensor error will be much higher than the standard deviation obtained from statistics on measurements over many orbits, many days, and even many years. Using more observations to determine the standard deviation may refine this value but will not help to determine the fraction of each orbit that the sensor (and the spacecraft attitude) can be expected to have large errors.

The effect of correlated sensor errors cannot easily be removed by the typical Kalman filters used for spacecraft attitude determination. These filters give optimal results assuming uncorrelated, gaussian-distributed noise. Although the inherent sensor noise may indeed be random and white, the sensor and attitude residuals contain contributions from the colored errors in the Earth horizon height model. In a similar case, that of correlated errors in magnetic field models, a filter that explicitly accounts for correlated noise has been developed and has improved attitude determination markedly.<sup>12</sup>

Several approaches are currently being pursued to evaluate and mitigate horizon radiance errors on Earth sensor derived attitudes. These include:

- development and testing of a correlated noise filter
- evaluation of the attitude accuracy improvements that can be expected in Kalman filters and through use of a system similar to the ERMU
- evaluation of the attitude accuracy improvements that can be expected in batch-least squares methods using a system similar to the ERMU
- evaluation of the attitude accuracy improvements that can be expected in Kalman filters by ignoring HS measurements with high latitude horizon crossing.

Many factors not discussed here affect the height at which a horizon sensor detects the Earth. These include the trigger logic and rotation rate for scanning HSs as well as the size and shape of the instantaneous FOV and the sensor mounting geometry. Differences from nominal triggering height at a particular location on the Earth's surface should be more nearly equivalent for different missions than are the heights themselves.

If a system like the ERMU proves to be successful in reducing attitude errors to a level lower than attainable with climate models, input to horizon height correction tables from many spacecraft might be desirable. In this case, weekly horizon radiance correction tables might be generated and used by each contributing spacecraft to correct its horizon height model and improve its attitude accuracy.

## ACKNOWLEDGMENTS

This work was supported by the National Aeronautics and Space Administration (NASA)/ Goddard Space Flight Center (GSFC) under contracts NAS 5-31000 and GS-35F-4381G, task order No. S-03365-Y.

## REFERENCES

1. M. C. Phenneger, S. P. Singhal, T. H. Lee, and T. H. Stengle, "Infrared Horizon Sensor Modeling for Attitude Determination and Control: Analysis and Mission Experience," NASA, TM 86181, March 1985.
2. W. Nutt and M. C. Phenneger, "Horizon Radiance Modeling Utility System Description and User's Guide," *Computer Sciences Corporation*, CSC/SD-78/6032, March 1978.
3. E. J. Burgess, "Earth Radiation Budget Satellite (ERBS) Horizon Radiance Modeling Utility (HRMU) User's Guide and System Description," *Computer Sciences Corporation*, CSC/SD-84/6007, June 1984.
4. R. Shendock, "DE-B Horizon Radiance Modeling Utility (HRMU) System Description and User's Guide," *Computer Sciences Corporation*, CSC/SD-80/6096, 1980.
5. S. Fritz and S. D. Soules, "Planetary Variations of Stratospheric Temperatures," *Monthly Weather Reviews*, Vol. 110, no. 7, July 1972.
6. E. Harvie, O. Filla, and D. Baker, "In-Flight Measurement of the National Oceanic and Atmospheric Administration (NOAA)-10 Static Earth Sensor Error," *AAS/AIAA Spaceflight Mechanics Meeting*, Pasadena, CA. AAS 93-101, Feb. 1993.
7. M. C. Phenneger, W. C. Bryant, J. Baucom, and K. Woodham, "Evaluating the Goes-8 & -9 Earth IR Horizon Sensor Error Response Using the Goes-9 Sounder IR Channel 1 thru 4 Data," *Proc. SPIE*, Vol. 2812, Oct. 1996.
8. S. Shulman, *et al.*, "Total Ozone Mapping Spectrometer-Earth Probe (TOMS-EP), Flight Dynamics Support System (FDSS), Functional Specifications," (revised version) *Computer Sciences Corporation*, CSC/TR-92/6008R1UD0, Nov. 1993.
9. G. Wahba, "A Least-Squares Estimate of Spacecraft Attitude," *SIAM Rev.* Vol. 7, No. 3, July 1965.
10. M. C. Phenneger, S. P. Singhal, T. H. Lee, and T. H. Stengle, *op. cit.*, Sec. 4.
11. *ibid.*
12. J. Sedlak, "Improved Spacecraft Attitude Filter Using a Sequentially Correlated Magnetometer Noise Model," *Proceedings of the 16<sup>th</sup> Digital Avionics Subsystems Conference*, Irvine CA, October 1997.





# NEW ACCURATE INFRARED EARTH RADIANCE MODEL FOR POINTING ACCURACY IMPROVEMENT OF LEO PLATFORMS.

161  
337595

169334

S. Sallard\*, G. Samson\*, J.P Krebs\*  
P. Faucher-Lagracie†, P. Prieur†, M. Burello†

The accurate orientation of a spacecraft with respect to the Earth is generally achieved through a passive infrared electro-optical sensor as a part of attitude control subsystem : an Earth sensor. The spatial and temporal Earth radiance non-uniformities make up the main limitation of LEO Earth sensor accuracy. Then recent investigations have been performed with CNES (the French National Space Agency) collaboration on a better understanding and on a characterization of Earth radiance fluctuations, in order to update compensation laws used to improve the satellite pointing accuracy.

In fact several analyses have been engaged on in-flight Earth sensor radiance telemetry data from French LEO satellites (SPOT 1, 2, 3) oriented by Earth sensors and rate gyro systems. From these in-flight data a first step has consisted of a radiance variations modelling versus Earth coordinates and seasons, and has led to separate deterministic variations from random fluctuations and attitude measurements. However without absolute measurement reference the software modelling accuracy is limited by the gyro one. Now, thanks to the presence of both accurate SED 12 star-trackers and scanning infrared Earth sensors STD 16 on the French satellite HELIOS 1, it is possible to compare the Earth sensor in-flight output data to almost absolute angular references. It is then possible, by analysing these data over a long period of time, to deduce the Earth sensor error and how this error changes versus the satellite motion and the season.

The purpose of this paper is to present the analyses performed with CNES specialists from the STD16 sensor transitions and radiance telemetries on board HELIOS 1 in order to improve the knowledge of the infrared Earth radiance mapping and consequently to significantly decrease the radiance error terms of infrared earth sensors. The opportunity to work on one and a half year period telemetry data has allowed at one hand to optimize the deterministic radiance fluctuations modelling and at the other hand to update our software model of Earth sensor radiance errors. After a brief recall of the sensor operating principle and telemetry characteristics, radiance variations according to spatial and temporal references are analyzed on about 8000 observations.

Existing seasonal compensations laws have been updated from Earth radiance errors modelling and results in terms of performances are discussed. So with these new compensation laws the radiance error can be largely decreased by a factor 50 up to 100 % (mainly depending on the season) compared to the previous laws by which the error was only reduced by a maximum factor of 50%. This new model should improve the prediction of the infrared sensor radiance error and could be used by the AOCS of LEO satellites to compensate the in-flight radiance error whatever the altitude and the orbit parameters.

---

\* Société Anonyme d'Etudes et Réalisations Nucléaires (Sodern), 20 Avenue Descartes,  
F-99451 Limeil-Brevannes Cedex, France.

† Centre National d'Etudes Spatiales (CNES), 18 avenue Edouard Belin,  
F- 31055 Toulouse Cedex, France.

## INTRODUCTION

Attitude determination from InfraRed Earth Sensors (IRES) is based on radiometric Earth observations : the useful information delivered by the sensor is the measurement of the thermal discontinuity between the Earth and the Space radiances.

STD16 (fig.1) is an Earth Horizon crossing sensor designed for 'Low Earth Orbiting' (LEO) missions. It delivers 4 transitions between Earth and Space from which roll and pitch attitude angles are determined. To achieve good accuracy performances Earth sensors generally need to operate in the infrared spectral band of 14-16.5  $\mu\text{m}$  corresponding to the  $\text{CO}_2$  absorption band which provides the more uniform and stable Earth radiance distribution than other bands. However they present non negligible seasonal and spatial variations creating transition shifts.

Today, to withstand the on-market accuracy requirements, it has become necessary to compensate attitude errors due to the non uniformity of Earth radiance.

In fact a long term study based on telemetry data from French remote sensing satellites has been engaged with the CNES (French Space Agency) for few years (Ref.1) to progress in the knowledge of Earth radiance fluctuations in the 15  $\mu\text{m}$  spectral band. The analysis of telemetry data from SPOT satellites, oriented by SODERN Earth sensors (Ref.2) and rate gyro systems, has allowed to separate the deterministic radiance variations from the random ones for finally deducing a simple Earth mapping model. However without absolute measurement reference the accuracy of this software modelling was limited by the gyro's one.

Then this paper, for the first time, presents analysis results from Earth sensor outputs compared to absolute angular references given by star-tracker systems (Ref.3). This new data bank from HELIOS 1 satellite has allowed, with CNES collaboration, on the one hand to update existing infrared Earth radiance model and on the other hand to develop compensation laws of LEO Earth sensors errors due to Earth radiance fluctuations.

This study is aimed at the improvement of LEO platforms pointing accuracy.

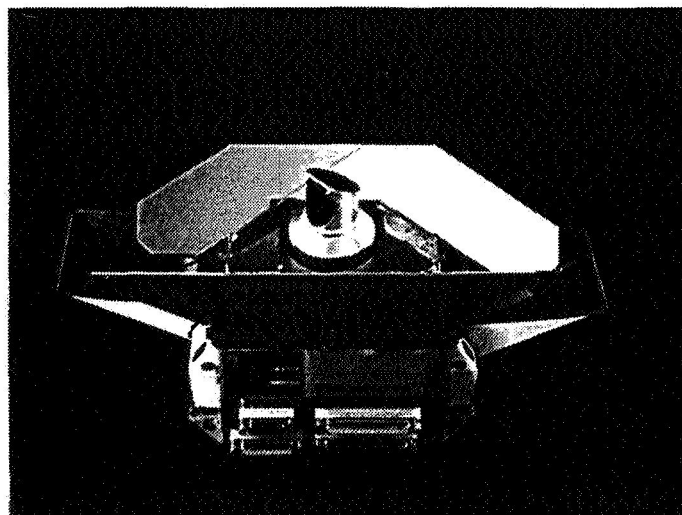


Figure 1 : The STD16 Earth sensor

## SENSOR OPERATING PRINCIPLE

The STD16 infrared Earth sensor is designed for 3 axis stabilized spacecrafts orbiting at low altitudes. A full description of STD16 is given in reference (Ref.2). Briefly, STD16 sensor is an Earth infrared Horizon scanner. Its function is to provide the angular position, with respect to some reference, of transitions which occur on the scanned traces between Space and Earth : the knowledge of these transitions enables the AOCS to compute the angular position of the satellite, with respect to the Earth, in terms of pitch and roll.

The main feature of STD16 is that two opposite scan cones are generated by scanning a single bolometer image thanks to a 1 rps rotating head and two fixed mirrors then inducing 4 transitions between Earth and Space (fig.2). Bolometer signal is then fed through an electronic unit which processes it and drives the scanning mechanism. The processing circuit consists in a band pass filter coupled to sign discriminators and proportional threshold detectors. The two Space to Earth transition signals are stored in analog memories. The peak values of the four transitions are directly proportional to the magnitude of the radiance peak values.

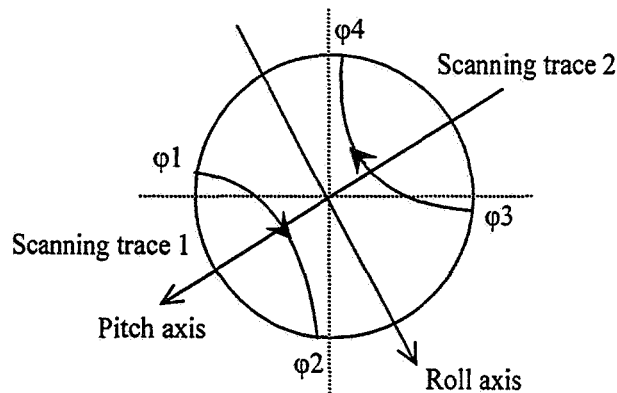


Figure 2 : Sensor operating principle

## DATA CHARACTERISTICS

### Telemetry data description

HELIOS 1 satellite, in a circular sun synchronous high inclination ( $98^\circ$ ), orbits at an altitude of 700 km which results in an orbit period of approximately 90 minutes. Therefore, the satellite orbits around the Earth about 14 times each day. It is oriented thanks to 5 SODERN equipments : 3 SED12 star-trackers and 2 STD16 Earth sensors.

HELIOS 1 has been launched in July 1995 and STD16 telemetry data have been analysed over 1.5 years period (1995-1997). Two kinds of telemetry data have been provided by the CNES :

- the  $L_1$ ,  $L_2$ ,  $L_3$ ,  $L_4$  Earth radiance telemetries measured at each transition between Earth and Space, according to  $\alpha$  parameter, ( $\alpha$  = satellite position on orbit,  $\alpha = 0$  at the ascending node) (fig.3).

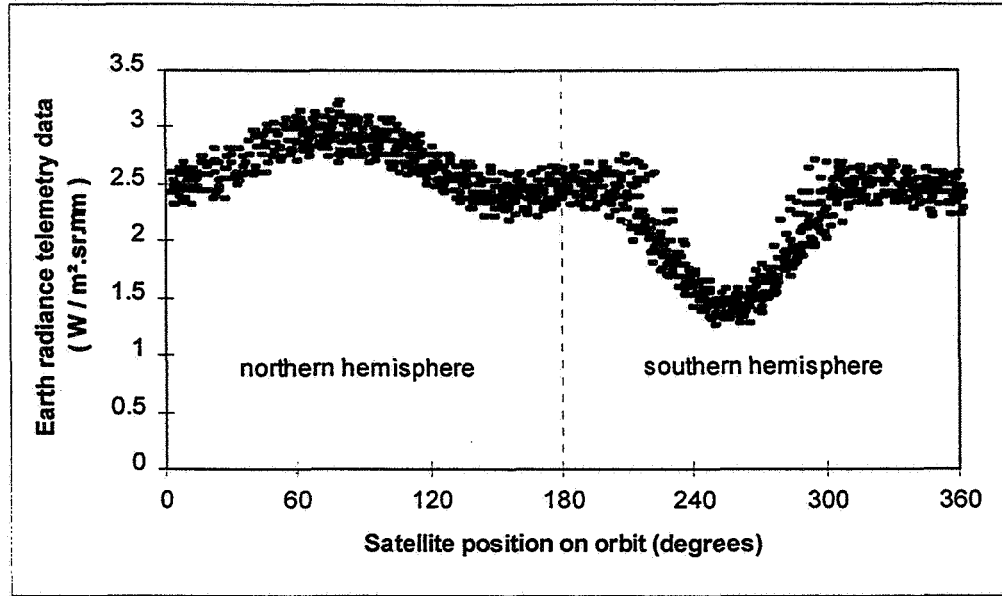


Figure 3 : Earth radiance telemetry data ( $L_1$ ) : August 1995.

- the Earth radiance error, deduced from attitude telemetry data, according to  $\alpha$  parameter, (fig.4).

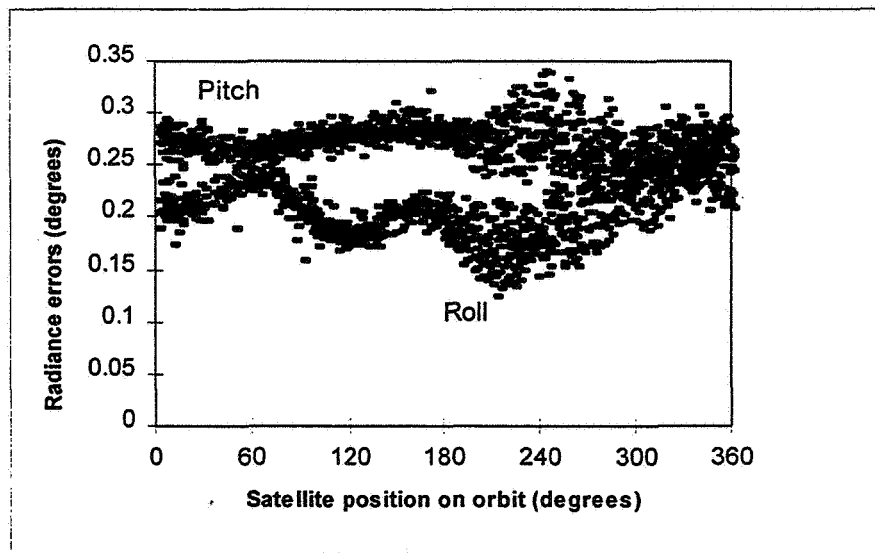


Figure 4 : STD16 Pitch and Roll errors due to Earth radiance fluctuations (August 95).

The Earth radiance error is defined by the difference between attitude angles directly deduced from Earth sensor outputs and attitude reference angles delivered by the star-tracker system :

$$\text{Earth radiance error (Roll, Pitch)} = (\text{Roll, Pitch})_{\text{STD16}} - (\text{Roll, Pitch})_{\text{STAR TRACKER}} - \text{constants}$$

where : constants = mechanical bias and mission characteristics constants.

With a rate of one day per fifteen days, with 10 to 14 orbits per day, each orbit was containing about from 20 to 50 measurement points (sensor telemetries sampled at 1/80 Hz). The day of the fortnight, for which telemetries are available, has been assumed as pretty representative for the all over fifteen days. However, for confidentiality reasons, March, April and September telemetry data have not been available.

With this data bank, study investigations about Earth radiance characterization have been engaged to improve STD16 accuracy.

### **Data accuracy**

- Earth radiance telemetries :

The relationship between Earth radiance in the 15  $\mu\text{m}$  band and the STD16 telemetry data was calibrated with on-ground Earth simulator. The accuracy of measured values are estimated to be about  $\pm 4 \%$  taking into account thermal effects, quantization noise and memory variations.

- Earth radiance errors :

Because of the very high measurement accuracy of the star-tracker (a few  $10^{-3}$  degrees), we can assume in this way that we have a very representative Earth radiance error.

### **EARTH RADIANCE FLUCTUATIONS CHARACTERIZATION**

As it has been previously observed with SPOT 1,2,3 data bank (Ref.1), Earth radiance fluctuations present a deterministic part and a random one.

Deterministic fluctuations correspond to seasonal variations and random fluctuations are revealed by irregular and unexpected variations.

The seasonal variations correspond to two deterministic phenomena :

- a seasonal radiance gradient on Earth surface, with an important latitude dependence,
- a fluctuation of the infrared horizon depth.

These deterministic fluctuations have been modelled by analytical functions giving Earth radiance variations versus latitude and seasonal parameters.

## **EARTH RADIANCE MODEL**

With the aim of estimating attitude errors due to Earth radiance fluctuations before spacecraft launch rather than trying to compensate them in flight, a software errors model has been developed by SODERN.

### **Description**

A software simulation model has been developed to simulate the Earth sensor operation in front of a thermal scene. This software delivers the Earth sensor output data for all possible input parameters of the modelled radiance configurations. It allows then to estimate STD16 attitude errors due to Earth radiance fluctuations according to mission characteristics.

The modelled scene, deduced from previous analyses (Ref.1), represents an infrared Earth radiance mapping according to latitude and seasonal parameters.

In fact seasonal radiance gradients on Earth surface are expressed by monthly function versus latitude and time parameters and the fluctuations of the infrared horizon depth are represented by analytical functions deduced from NASA studies according to altitude, latitude and season parameters (Ref.5 and Ref.6).

This software developed from STD16 radiance telemetry data ( $L_1$ ,  $L_2$ ,  $L_3$ ,  $L_4$ ) has been validated and improved using HELIOS 1 very accurate and representative telemetry data.

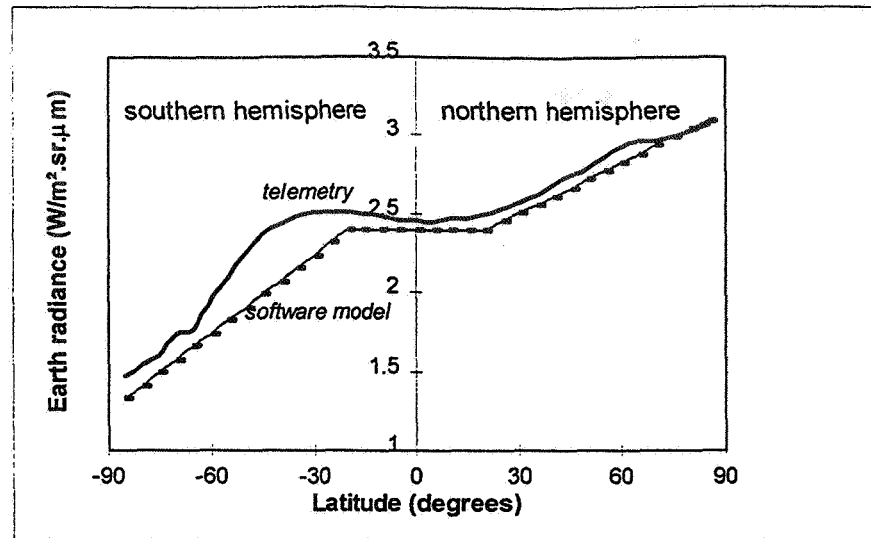
### **Validation**

The software has been validated in two steps. The comparison between software model and telemetry data has concerned, at first, the thermal scene observed by the sensor (Earth radiance fluctuations) and secondly the Earth sensor errors (errors induced by the Earth radiance).

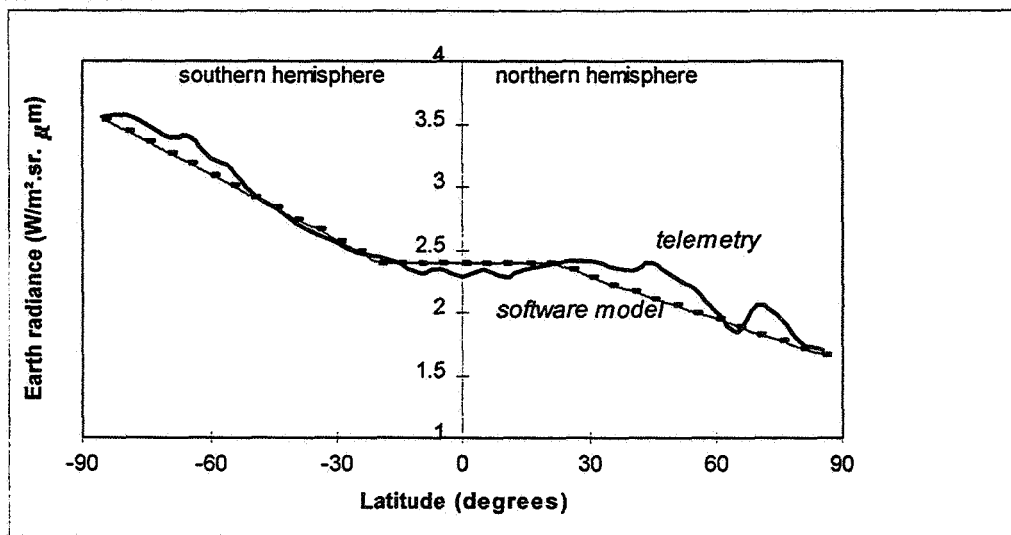
For available periods, the mean fluctuations of Earth radiance and standard deviations have been compared to the modeled functions. It appears that for the whole year analytical functions give a first order quite good estimation of Earth radiance fluctuations. However the comparison gave also prominence to differences particularly in southern hemisphere for winter periods and less differences in the both hemisphere for spring summer and autumn periods (fig.5).

For attitude errors induced by deterministic radiance fluctuations, the main conclusions of comparison are on the one hand a rather good synchronization of phases according to  $\alpha$  parameter but a larger error amplitude from telemetry data and on the other hand a pretty good estimation for pitch angle (fig. 6).

- August 1995 :



- December 1996 :



- May 1996 :

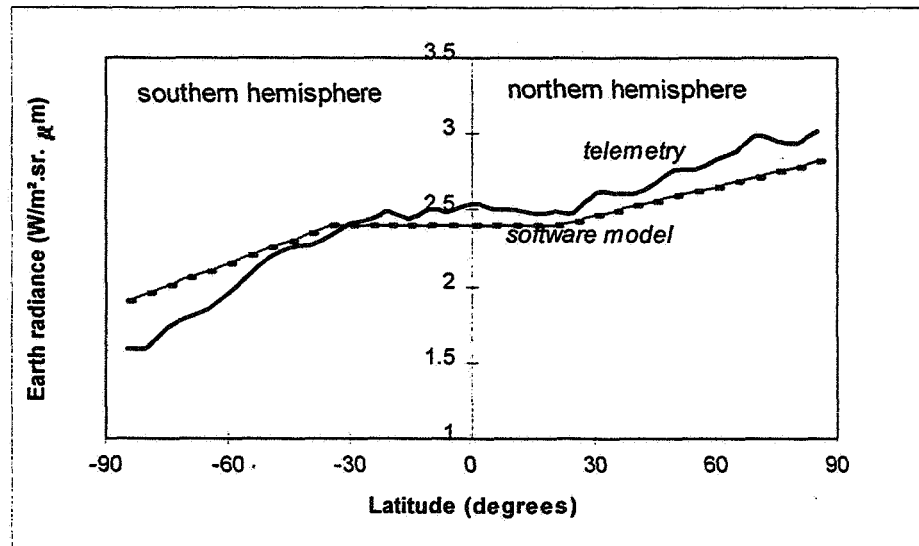


Figure 5 : Earth radiance profiles versus latitude parameter.

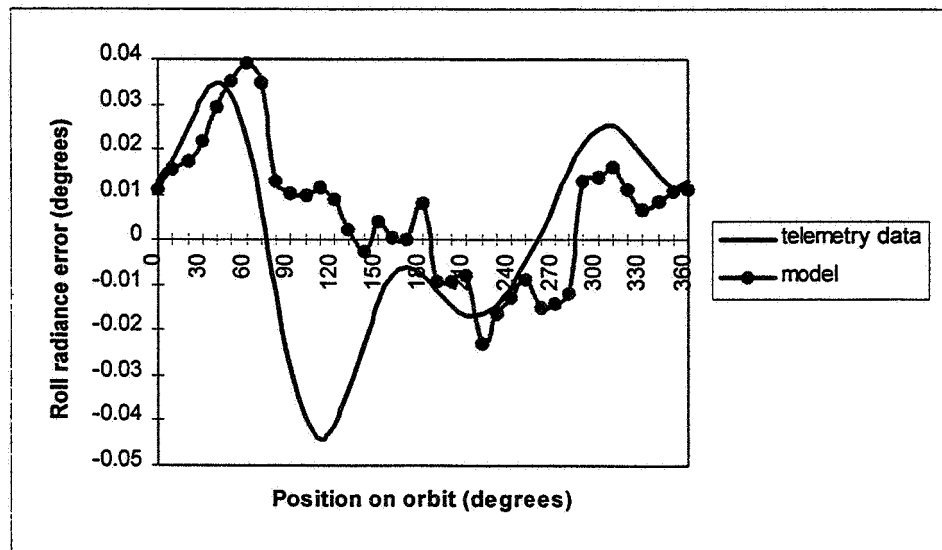
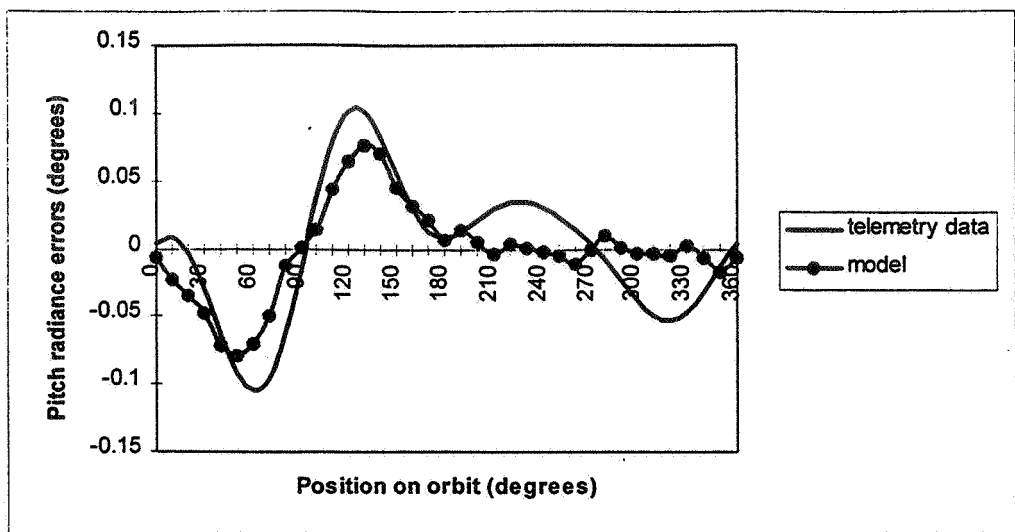


Figure 6 : Radiance errors profiles versus satellite position on orbit  
(end of December 1996)

### Updating of software model

The software model improvement has concerned the Earth radiance mapping according to HELIOS available telemetry data.

The approximate and simple formulas for radiance variations, versus latitude and time, deduced from SPOT telemetry data analysis have been modified in the way of a better fitting of radiance variations including a seasonal dependence.



- Spring :

$$\text{for latitude} < 20^\circ \text{ S : } L = 2.4 + 1.28 * \sin\left(\frac{2 \pi (t - t_0)}{T}\right) \left(\frac{\text{latitude} + 20}{70}\right) \text{ in } [\text{W} / \text{m}^2.\text{sr}.\mu\text{m}]$$

$$\text{for } 20^\circ \text{ S} < \text{latitude} < 35^\circ \text{ N : } L = 2.4 \text{ in } [\text{W} / \text{m}^2.\text{sr}.\mu\text{m}]$$

$$\text{for latitude} > 35^\circ \text{ N : } L = 2.4 + 1.0 * \sin\left(\frac{2 \pi (t - t_0)}{T}\right) \left(\frac{\text{latitude} - 35}{55}\right) \text{ in } [\text{W} / \text{m}^2.\text{sr}.\mu\text{m}]$$

- Summer :

$$\text{for latitude} < 20^\circ \text{ S : } L = 2.4 + 1.28 * \sin\left(\frac{2 \pi (t - t_0)}{T}\right) \left(\frac{\text{latitude} + 20}{70}\right) \text{ in } [\text{W} / \text{m}^2.\text{sr}.\mu\text{m}]$$

$$\text{for } 20^\circ \text{ S} < \text{latitude} < 20^\circ \text{ N : } L = 2.4 \text{ in } [\text{W} / \text{m}^2.\text{sr}.\mu\text{m}]$$

$$\text{for latitude} > 20^\circ \text{ N : } L = 2.4 + 0.83 * \sin\left(\frac{2 \pi (t - t_0)}{T}\right) \left(\frac{\text{latitude} - 20}{70}\right) \text{ in } [\text{W} / \text{m}^2.\text{sr}.\mu\text{m}]$$

- Autumn :

$$\text{for latitude} < 35^\circ \text{ S : } L = 2.4 + 1.32 * \sin\left(\frac{2 \pi (t - t_0)}{T}\right) \left(\frac{\text{latitude} + 35}{55}\right) \text{ in } [\text{W} / \text{m}^2.\text{sr}.\mu\text{m}]$$

$$\text{for } 35^\circ \text{ S} < \text{latitude} < 20^\circ \text{ N : } L = 2.4 \text{ in } [\text{W} / \text{m}^2.\text{sr}.\mu\text{m}]$$

$$\text{for latitude} > 20^\circ \text{ N : } L = 2.4 + 0.83 * \sin\left(\frac{2 \pi (t - t_0)}{T}\right) \left(\frac{\text{latitude} - 20}{70}\right) \text{ in } [\text{W} / \text{m}^2.\text{sr}.\mu\text{m}]$$

- Winter :

$$\text{for latitude} < 35^\circ \text{ S : } L = 2.4 + 1.2 * \sin\left(\frac{2 \pi (t - t_0)}{T}\right) \left(\frac{\text{latitude} + 35}{55}\right) \text{ in } [\text{W} / \text{m}^2.\text{sr}.\mu\text{m}]$$

$$\text{for } 35^\circ \text{ S} < \text{latitude} < 20^\circ \text{ N : } L = 2.4 \text{ in } [\text{W} / \text{m}^2.\text{sr}.\mu\text{m}]$$

$$\text{for latitude} > 20^\circ \text{ N : } L = 2.4 + 0.85 * \sin\left(\frac{2 \pi (t - t_0)}{T}\right) \left(\frac{\text{latitude} - 20}{70}\right) \text{ in } [\text{W} / \text{m}^2.\text{sr}.\mu\text{m}]$$

With :  $t - t_0$  : day of the year dated from April 10<sup>th</sup>

$T = 365.25$  days

latitude : in degrees.

N : northern hemisphere

S : southern hemisphere

## Performances

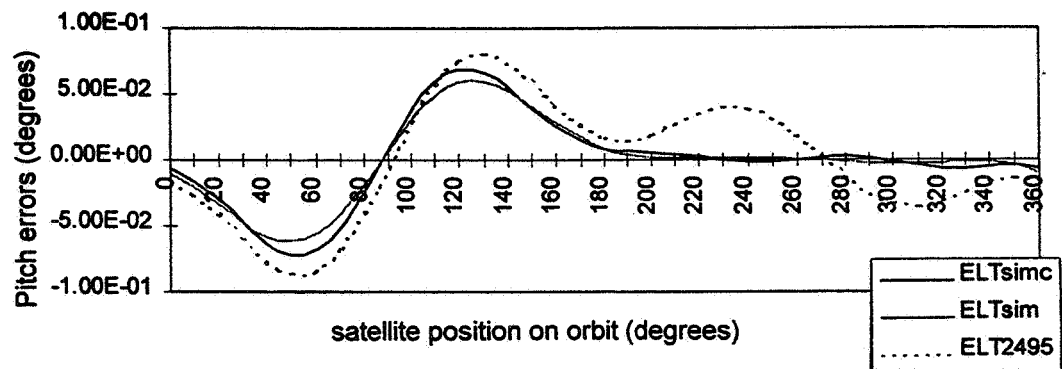
Although more complex functions could have resulted in a better approximation, these simple laws give satisfactory results : the residual errors compared to the measured values are always less than the standard deviation.

The software optimization has been evaluated with respect to the computed attitude radiance errors. In fact software modifications have influenced the error amplitude leading to a significant improvement in the attitude error estimation. Maximum amplitude error differences between software results and telemetry data are given hereafter (illustration on table1 and figure 8):

**Table 1**  
**MAXIMUM AMPLITUDE ERRORS DIFFERENCES BETWEEN UPDATED SOFTWARE AND TELEMETRY DATA**

<u>Attitude angles</u>	<u>Spring</u> (degrees)	<u>Summer</u> (degrees)	<u>Autumn</u> (degrees)	<u>Winter</u> (degrees)
Pitch	0.015°	0.025°	0.010°	0.020°
Roll	0.010°	0.020°	0.020°	0.015°

- Pitch



- Roll

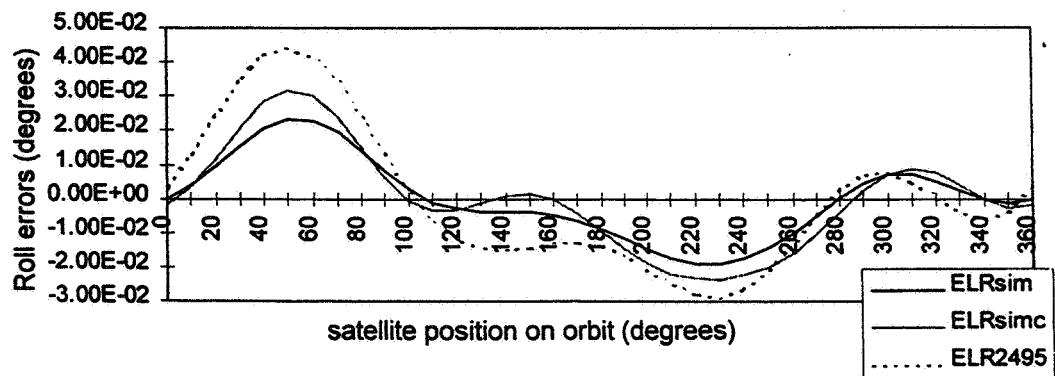


Figure 8 : Radiance errors profiles (beginning of December 1996)  
telemetry data (EL2495), software model (ELsim), software model updated (ELsimc).

These results, given for a maximum pitch radiance error of about  $0.080^\circ$  and a maximum roll radiance error of about  $0.050^\circ$ , show that a better model of Earth radiance gradient mapping allows a better estimation of STD16 errors but that some residual errors are still remaining. This is mainly due to the Earth horizon depth rough model and to the fact that longitude effects on Earth radiance are not taken into account. In fact HELIOS telemetry analysis showed a daily longitude influence on attitude errors (particularly for roll errors) ; works are still carried out on this point.

## **Conclusion**

After updating Earth radiance mapping model, the SODERN software model allows to evaluate 75% of pitch radiance errors and 40% of roll radiance errors due to deterministic Earth radiance fluctuations. These performances could be yet improved on the one hand with more telemetry data (yearly repeatability) and on the other hand with the updating of Earth horizon depth model and an analysis of longitude influence on seasonal Earth radiance fluctuations. Therefore, for LEO missions, SODERN software model allows a first order pretty good estimation of STD16 in-flight errors, according to geographical and time parameters, thanks to a simple and representative Earth radiance mapping model. Then consequently this model allows to determine compensation laws to improve the Earth sensor accuracy budget.

## **CORRECTION LAWS OF ATTITUDE ERRORS DEDUCED FROM TELEMETRY DATA**

With the aim of improving significantly STD16 accuracy for LEO platforms orbiting at 800 km, compensation laws of radiance errors have been directly deduced from HELIOS telemetry data. This study has been performed in collaboration with the CNES.

Compensation laws of attitude radiance errors are analytical functions depending on  $\alpha$  parameter (satellite position on orbit) and on seasonal coefficients.

### **Correction laws evaluation method**

The first step was to deduce deterministic error laws from a large dispersion of Earth radiance telemetry data. The best fittings of radiance error variations in time have been obtained by using analytical and statistical methods, such as the least square algorithms method according to polynomial sinus and cosine formulas. This method allows to set free from sensor noise and telemetry accuracy. Nevertheless, for a few periods, telemetry data were not available and error functions have then been extrapolated for these periods.

With this data processing, random errors have also been reducing by an averaging process and statistical analysis.

The deduced laws are then representative of seasonal radiance variations.

$$P = P' - (A_{p1} \cdot \cos \alpha + A_{p3} \cdot \cos 3\alpha + B_{p2} \cdot \sin 2\alpha + B_{p4} \cdot \sin 4\alpha)$$

$$R = R' - (A_{R0} + A_{R1} \cdot \cos \alpha + A_{R2} \cdot \cos 2\alpha + A_{R3} \cdot \cos 3\alpha + B_{R1} \cdot \sin \alpha + B_{R2} \cdot \sin 2\alpha)$$

with : R, P : corrected roll and pitch values,  
R', P' : measured roll and pitch values,  
 $\alpha$  : angle from the spacecraft ascending node,  
 $A_{Ri}, B_{Ri}, A_{Pi}, B_{Pi}$  : seasonal coefficients (to be changed every 15 days).

## Validation on SPOT

The compensation laws for STD16 system are deduced from very representative Earth radiance errors data, thanks to star-tracker systems giving absolute references in term of roll and pitch angles. These compensation laws have been validated by CNES on SPOT telemetry measurements.

Telemetry data collected over 5 years from satellites SPOT 1, 2, 3 represent a large data bank which has been used to deduce compensation laws of attitude radiance errors. In fact with the knowledge of « measurement / radiance errors » transfer function, attitude radiance errors have been reconstituted orbit by orbit.

HELIOS 1 compensation laws have then been statistically validated by applying them on the SPOT 1, 2, 3 radiance error profiles giving very satisfying results. In fact, in comparison with previous compensation laws (deduced from SPOT data bank telemetries) the HELIOS compensation laws improve with an average of 50% the on-board compensation level. The performance in terms of platform pointing accuracy is confidential but HELIOS compensation laws will be used on SPOT 4 satellite.

## Performances

With HELIOS compensation laws the roll and pitch radiance errors can be largely decreased by a factor 50 up to 100 % (mainly depending on the season) compared to the previous laws by which errors were only reduced by a maximum factor of 50%.

Then it has allowed to determine the following realistic Earth radiance residual error budget (see table 2):

**Table 2**  
**RESIDUAL EARTH RADIANCE ERRORS**

<u>Attitude angles</u>	<u>Compensation levels</u> worst to best (%)	<u>Residual error after compensation</u> min to max (degrees)
Roll	50 to 100	0.003 to 0.035
Pitch	70 to 100	0.002 to 0.035

The maximum value of residual error takes into account a  $\pm 0.015^\circ$  term due to the correction periodicity (every 15 days).

Figures 9 and 10 allow to compare roll and pitch radiance errors deduced from telemetry data ('telemetries' curves) with radiance errors compensated by HELIOS updated laws ('new law' curves).

'Previous law' curves correspond to the compensation laws deduced from SPOT 1, 2, 3 data bank : so the compensation level did not exceed 50% for pitch and 20% for roll with sometimes some error increase.

It shows that roll compensation is not as good as pitch compensation, but absolute error is smallest. These uncompensated residual errors are mainly due to longitude influence and software extrapolation accuracy.

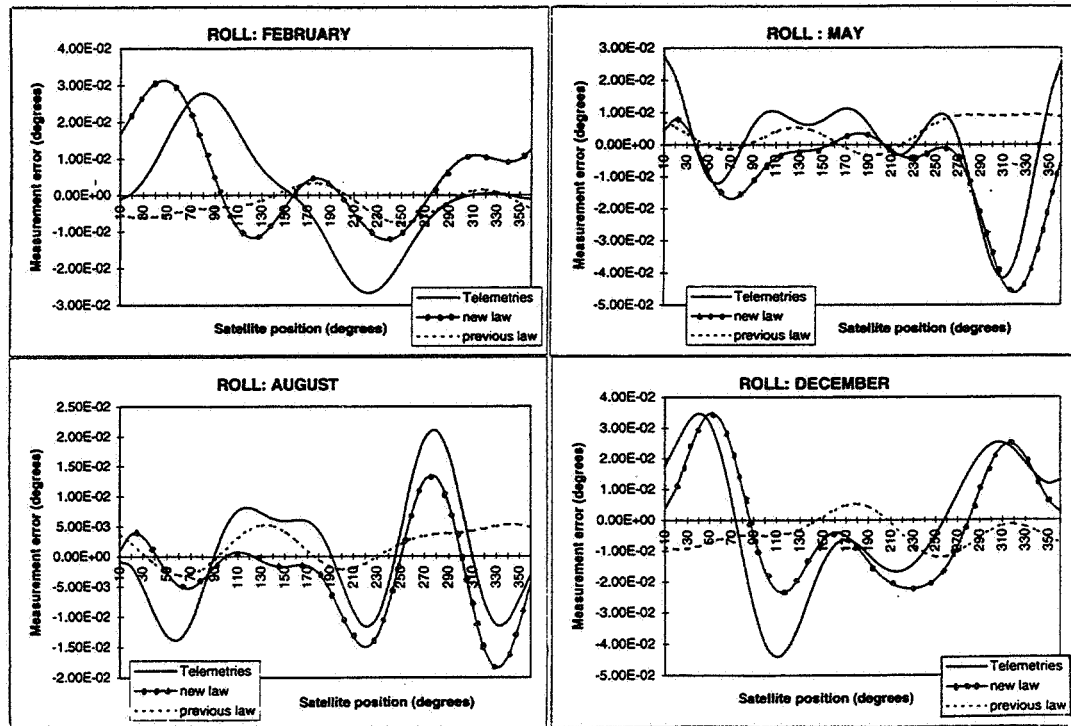


Figure 9 : Roll radiance error profiles

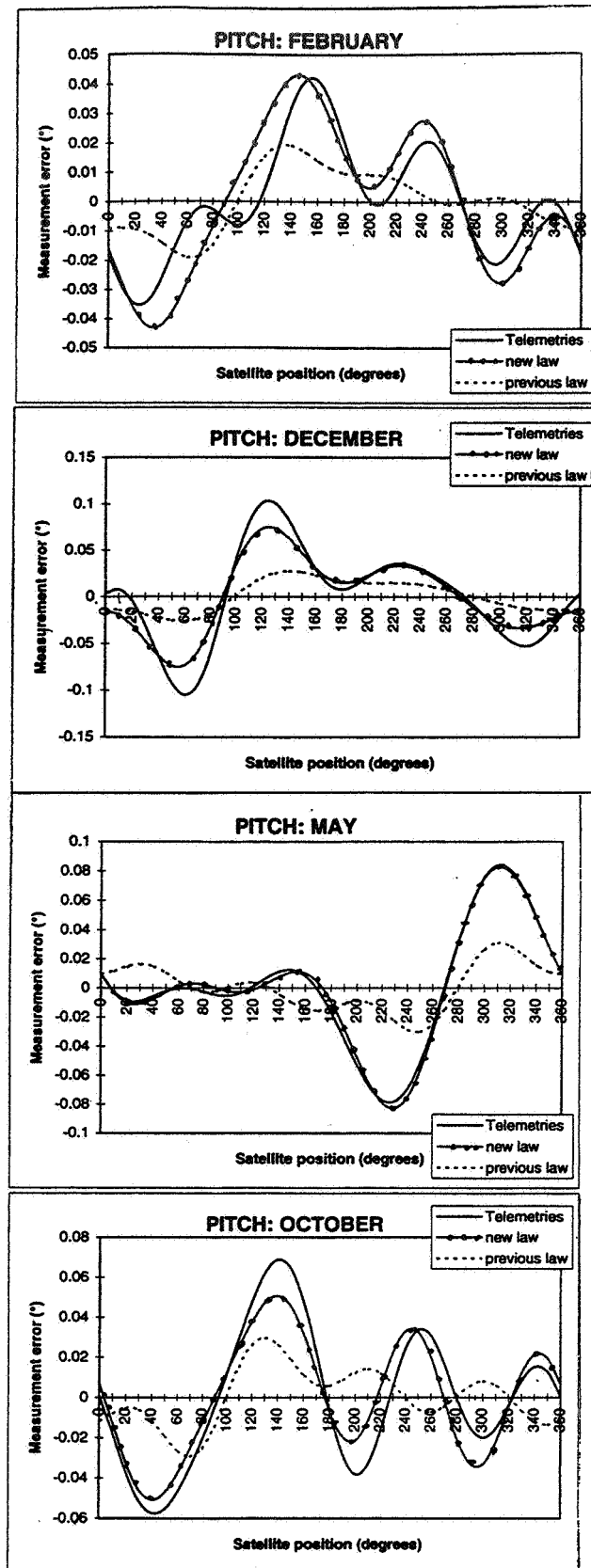


Figure 10 : Pitch radiance error profiles

## CONCLUSION

A new data bank of very accurate telemetry data from HELIOS satellite has allowed to progress in the knowledge of Earth radiance.

In fact for the first time Earth sensor telemetry data have been compared to an absolute attitude reference given by a star-trackers system on the same spacecraft. The opportunity to work on 1.5 years period telemetry data has allowed on the one hand to update the SODERN software model of Earth radiance mapping and on the other hand to improve sensor accuracy by computing new errors compensation laws. The estimation level of SODERN software to evaluate attitude errors due to radiance fluctuations is 2 times better and is now used for in-flight errors estimation and compensation. And thanks to new compensation laws the correction percentage of the total deterministic Earth radiance error varies from 50 to 100 % with a residual error after compensation not exceeding 0.035°.

From this data bank, the longitude influence on seasonal radiance errors and the random radiance fluctuations could be analysed to still improve the accuracy of LEO platforms.

## REFERENCES

1. O. Brunel, F. Haignere, JP. Krebs, JC. Peltier and M. Burello, A 15  $\mu\text{m}$  Infrared Earth mapping through the STD12 sensor telemetries on board SPOT satellites, Ref. AAS 93-322.
2. O. Brunel, J. Jamet, JP. Krebs, A versatile Earth Sensor for LEO Satellites, 20<sup>th</sup> ISTS Japan, Ref.96-c-72 p. 1996.
3. O. Brunel, P. Dureux, Y. Kocher, JP. Krebs, Les capteurs d'attitude des plates-formes Envisat et Helios, International Symposium Optronics and Defense, Nato Confidential, Montigny le Bretonneux, France, 3-5 December 1996.
4. P. Faucher, Calcul de compensations d'erreurs de luminance pour SPOT 4, CNES report 1997.
5. Whitman, Ruth I., Thomas B. Mc Kee, and Richard E. Davis, Infrared Horizon Profiles for Winter Conditions from Project scanner, NASA TN D-49.5, Dec.1968.
6. Thomas, John R., Erniss E. Jones, Robert O'B. Carpenter, and George Ohring, The Analysis of 15 $\mu\text{m}$  Infrared Horizon Radiance Variations Over a Range of Meteorological, Geographical, and Seasonal conditions, NASA CR-725, April 1967.





## ANALYSIS OF EARTH ALBEDO EFFECT ON SUN SENSOR MEASUREMENTS BASED ON THEORETICAL MODEL AND MISSION EXPERIENCE\*

Dan Brasoveanu<sup>†</sup> and Joseph Sedlak<sup>†</sup>

Analysis of flight data from previous missions indicates that anomalous Sun sensor readings could be caused by Earth albedo interference. A previous Sun sensor study presented a detailed mathematical model of this effect. The model can be used to study the effect of both diffusive and specular reflections and to improve Sun angle determination based on perturbed Sun sensor measurements, satellite position, and an approximate knowledge of attitude. The model predicts that diffuse reflected light can cause errors of up to 10 degrees in Coarse Sun Sensor (CSS) measurements and 5 to 10 arc sec in Fine Sun Sensor (FSS) measurements, depending on spacecraft orbit and attitude. The accuracy of these sensors is affected as long as part of the illuminated Earth surface is present in the sensor field of view. Digital Sun Sensors (DSS) respond in a different manner to the Earth albedo interference. Most of the time DSS measurements are not affected, but for brief periods of time the Earth albedo can cause errors which are a multiple of the sensor least significant bit and may exceed one degree.

This paper compares model predictions with Tropical Rainfall Measuring Mission (TRMM) CSS measurements in order to validate and refine the model. Methods of reducing and mitigating the impact of Earth albedo are discussed. The CSS sensor errors are roughly proportional to the Earth albedo coefficient. Photocells that are sensitive only to ultraviolet emissions would reduce the effective Earth albedo by up to a thousand times, virtually eliminating all errors caused by Earth albedo interference.

---

\* This work was supported by the National Aeronautics and Space Administration (NASA) / Goddard Space Flight Center (GSFC), Greenbelt, MD, USA under Contract GS-35F-4381G, Task Order No. S-03365-Y.

<sup>†</sup> Computer Sciences Corporation (CSC), 10110 Aerospace Rd., Seabrook, MD, USA 20706.

## INTRODUCTION

All Sun sensors are designed based on the assumption that only one bright object, i.e., the Sun, is present within the sensor field of view (FOV). Current Sun sensors cannot distinguish the effect of a single light source if several bright objects are simultaneously visible (discounting pattern recognition schemes that would not be practical for a relatively simple sensor). Therefore, it is expected that Earth albedo interference will degrade the accuracy of Sun Sensors. An analysis of Solar Maximum Mission flight data<sup>1</sup> provided indications that Fine Sun Sensor (FSS) measurements were affected by Earth albedo, but not a definite proof. Many other questions were also left unanswered. Is the accuracy of all Sun Sensors reduced by the Earth albedo interference? Is it possible to model and accurately quantify the effect of illuminated Earth on Sun Sensor measurements? A subsequent study by one of the authors<sup>2</sup> attempted to answer these questions by providing a detailed theoretical model of the Earth albedo effect on Coarse Sun Sensors (CSS), Digital Sun Sensors (DSS), and FSS. That study shows that all types of Sun sensors are adversely affected by the Earth albedo interference and predicts the accuracy degradation based on spacecraft, Earth and Sun positions, sensor boresight orientation, and sensor design data. For Coarse Sun Sensors (CSS), which are affected most, the theoretical model predicts measurement errors of up to 10 degrees.

The model has been tested before only for a few Sun, Earth, and spacecraft geometries. The goals of this study are to thoroughly test the model using Tropical Rainfall Measuring Mission (TRMM) flight data and then to determine whether the model could be used to increase the accuracy of CSS measurements. Coarse Sun Sensors were chosen as a benchmark due to their simplicity (their behavior can be predicted without a detailed knowledge of proprietary sensor design data) and significant response to Earth albedo interference. These CSS characteristics facilitate the testing of the model and the establishing of a procedure for improving the accuracy of CSS measurements. After being validated by application to the CSS, the procedure can be modified to include other Sun sensor types.

## MODELING THE EARTH ALBEDO EFFECT

The theoretical model of Earth albedo effect on CSS is discussed briefly here. For more details and for modeling other Sun sensors see Reference 2. The Earth albedo effect has to be determined numerically for each individual CSS eye. The Earth surface is divided into a set of area elements using a map-like grid (see Figure 1). An Earth surface element increases the intensity of the electric current produced by a CSS eye whenever the element is located on the illuminated side of the Earth, within the sensor FOV, and not beyond the spacecraft horizon. Surface elements with these characteristics will be called *active* (see Figure 2).

Define the model frame of reference as the Earth centered frame with axes parallel to the CSS eye axes. Mathematically, the three conditions that define an active element (the  $j^{th}$  element) can be expressed as follows:

$$X_j \cdot X_{Sun} + Y_j \cdot Y_{Sun} + Z_j \cdot Z_{Sun} \geq 0 \quad (\text{surface element is illuminated})$$

$$(X_j - X_c)^2 + (Y_j - Y_c)^2 - (Z_j - Z_c)^2 \tan^2 \left( \frac{FOV}{2} \right) < 0 \quad (\text{surface element within the FOV})$$

$$X_j \cdot X_c + Y_j \cdot Y_c + Z_j \cdot Z_c \geq R_{Earth}^2 \quad (\text{surface element is not beyond horizon})$$

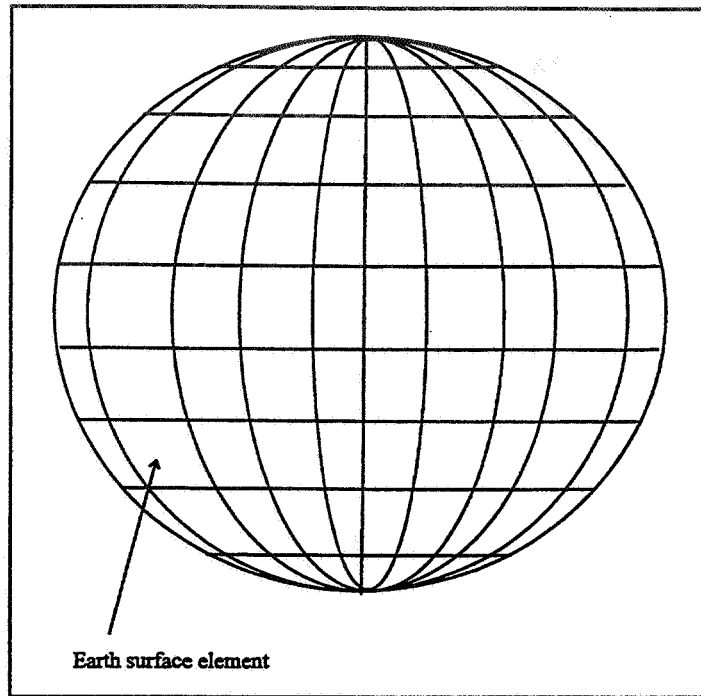


**Figure 1. Surface Grid**

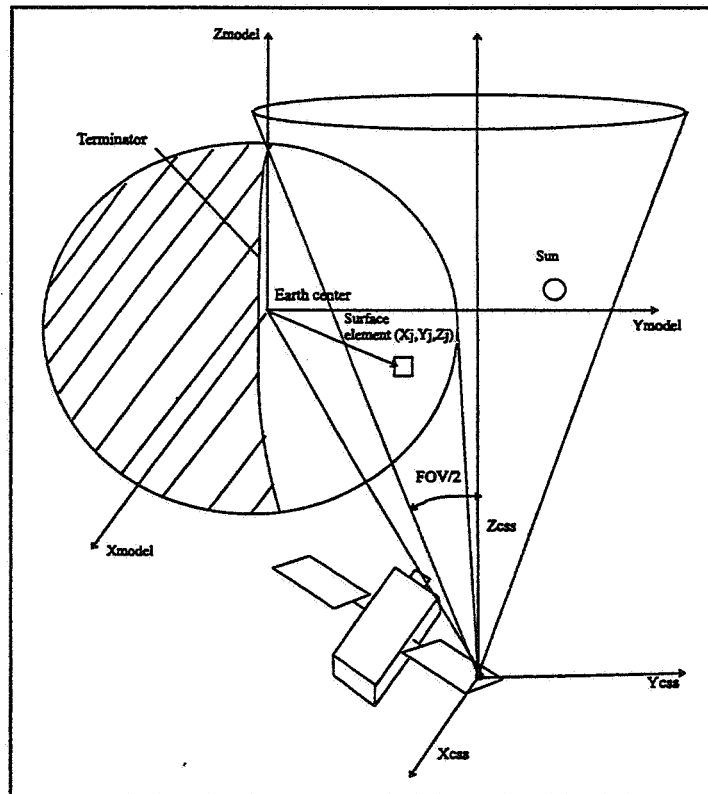


**Figure 2. Spacecraft, Earth, and Sun geometry**

where  $(X_c, Y_c, Z_c)$  is the CSS eye position,  $(X_{Sun}, Y_{Sun}, Z_{Sun})$  is the Sun vector, and  $(X_j, Y_j, Z_j)$  is the position of the  $j^{th}$  element, all in the model frame. The CSS FOV is a 160 deg cone.

Neglecting specular reflections, the light flux reflected by the  $j^{th}$  active element,  $\delta\phi_j^{(r)}$ , is given by

$$\delta\phi_j^{(r)} = A_j \phi_s S_j \cos u_j \quad (1)$$

where  $A_j$  and  $S_j$  are the albedo coefficient and surface area of the active element, respectively,  $\phi_s$  is the incident solar flux, and  $u$  is the angle between the normal to the surface element and the Sun direction. This light is reflected within a solid angle of  $2\pi$  steradians (half-sphere). The perturbation flux due to the  $j^{th}$  active element,  $\delta\phi_j$ , is given by

$$\delta\phi_j = \frac{\delta\phi_j^{(r)}}{2\pi[(X_c - X_j)^2 + (Y_c - Y_j)^2 + (Z_c - Z_j)^2]} \quad (2)$$

In general, the electric current,  $I$ , produced by a bright object in the sensor FOV is

$$I = K\phi \cos \alpha \quad (3)$$

where  $K$  is a sensor constant,  $\phi$ , is the light flux detected by the solar sensor and  $\alpha$  is the angle between the sensor boresight and the bright object direction. So, the perturbation flux produces a perturbation current,  $I_j$ , given by

$$I_j = K\delta\phi_j \cos \alpha_j \quad (4)$$

where,  $\alpha_j$  is the angle between the eye boresight and the area element direction. Therefore, the maximum current expected from the CSS eye photocell,  $I_0$ , is

$$I_0 = K\phi_s \quad (5)$$

Based on Eq. (3), the current due to the Sun can be expressed as

$$I_s = K\phi_s \cos \alpha_s \quad (6)$$

where  $\alpha_s$  is the Sun angle (i.e., the angle of interest between the boresight and Sun direction).

Due to the Earth albedo effect, the total current provided by the CSS eye photocell,  $I_{total}$ , is

$$I_{total} = I_s + \sum_{j=1}^n I_j \quad (7)$$

where  $n$  is the total number of active elements. Equations (4), (6), and (7) show that

$$I_{total} = K \left( \phi_s \cos \alpha_s + \sum_{j=1}^n \delta\phi_j \cos \alpha_j \right) \quad (8)$$

Assuming the only bright object present within the sensor FOV is the Sun, Eqs. (5) and (6) show that the Sun angle is given by

$$\alpha_s = \text{acos}\left(\frac{I_s}{I_0}\right) \quad (9)$$

Unfortunately, Eq. (9) is always used to calculate the Sun angle, even when other bright objects are present within the field of view. Therefore, the angle  $\alpha'_s$  calculated using  $I_{total}$  is not the true Sun angle but a perturbed value:

$$\begin{aligned} \alpha'_s &= \text{acos}\left(\frac{I_{total}}{I_0}\right) = \text{acos}\left(\frac{K\left(\phi_s \cos \alpha_s + \sum_{j=1}^n \delta \phi_j \cos \alpha_j\right)}{K \phi_s}\right) \\ &= \text{acos}\left(\cos \alpha_s + \sum_{j=1}^n \frac{A_j S_j \cos u_j \cos \alpha_j}{2\pi[(X_j - X_c)^2 + (Y_j - Y_c)^2 + (Z_j - Z_c)^2]}\right) \end{aligned} \quad (10)$$

The difference,  $\delta\alpha_s$ , between the true Sun angle and the CSS eye measurement thus is given by

$$\delta\alpha_s = \alpha_s - \alpha'_s = \alpha_s - \text{acos}\left(\cos \alpha_s + \sum_{j=1}^n \frac{A_j S_j \cos u_j \cos \alpha_j}{2\pi[(X_j - X_c)^2 + (Y_j - Y_c)^2 + (Z_j - Z_c)^2]}\right) \quad (11)$$

According to the above theoretical model, Eq. (10) should accurately predict the Earth-induced current whenever the albedo coefficient of each active element is known. However, the local albedo coefficients are strongly dependent on weather conditions over large regions (but not so large that a global average is sufficient). Even using advanced weather monitoring and prediction systems, creating and maintaining a database of local albedo coefficients would be a formidable undertaking. The simplest approach is to replace the local albedo coefficient everywhere with a constant value,  $a$ , and replace Eq. (10) with

$$\begin{aligned} \alpha'_s &= \text{acos}\left(\frac{I_{total}}{I_0}\right) \\ &\approx \text{acos}\left(\cos \alpha_s + a \cdot \sum_{j=1}^n \frac{S_j \cos u_j \cos \alpha_j}{2\pi[(X_j - X_c)^2 + (Y_j - Y_c)^2 + (Z_j - Z_c)^2]}\right) \end{aligned} \quad (12)$$

Then the Sun angle error is approximately

$$\delta\alpha_s = \alpha_s - \alpha'_s \approx \alpha_s - \text{acos}\left(\cos \alpha_s + a \cdot \sum_{j=1}^n \frac{S_j \cos u_j \cos \alpha_j}{2\pi[(X_j - X_c)^2 + (Y_j - Y_c)^2 + (Z_j - Z_c)^2]}\right) \quad (13)$$

The average albedo coefficient of active areas and the average albedo coefficient of the entire Earth<sup>3</sup> (i.e., 0.30) can be quite different. Therefore, model predictions based on the average Earth albedo can be quite inaccurate. Nonetheless, the model was tested by comparing TRMM flight data with predictions based on Eq. (12) using the average Earth albedo coefficient. The following sections present more detail.

## THE TROPICAL RAINFALL MEASURING MISSION

TRMM is one of a series of National Aeronautics and Space Administration (NASA) missions designed for the study of the Earth as a dynamical system. TRMM is a joint project between NASA and the National Space Development Agency (NASDA) of Japan. The TRMM instruments will determine the rate and total amount of rainfall occurring over the tropics and subtropics (from latitude 35 S to 35 N).

The TRMM spacecraft was launched on November 27, 1997 onboard a NASDA H-II launch vehicle. The nominal orbit is circular with an altitude of 350 km and an inclination of 35 deg. The attitude is three-axis stabilized and Earth-pointing. Primary attitude sensors include a Barnes static Earth sensor, a Kearfott inertial reference unit, two Adcole digital Sun sensors, and two three-axis magnetometers. The nominal attitude determination accuracy is 0.2 deg per axis ( $3\sigma$ ). The required control accuracy is 0.4 deg ( $3\sigma$ ) with stability of 0.1 deg/sec.

TRMM is equipped with eight CSS eyes.<sup>4</sup> Two eyes (numbers 1 and 2) are located on solar panel 1; another two (numbers 5 and 6) are on solar panel 2. The boresight directions of eyes 1, 2, 5, and 6 in the solar panel frame of reference are given in Table 1. The other eyes are located on the body and their boresights in the body frame are given in Table 2.

**Table 1. Boresight directions of CSS eyes located on solar panels**

CSS eye number	1	2	5	6
Boresight unit vector	0.773372 -0.168597 -0.6111227	-0.2820903 -0.6468678 -0.7085105	-0.2796423 0.8598846 -0.42708166	0.7697018 0.3757137 -0.5161380

**Table 2. Boresight directions of CSS eyes located on the satellite body**

CSS eye number	3	4	7	8
Boresight unit vector	0.7625562 0.5507738 -0.3393467	-0.96013227 0.27954134 -0.00163112	0.3369986 -0.8775453 -0.3410957	-0.96013227 0.27954134 -0.00163112

## BIAS ESTIMATION

Before comparing measured and predicted CSS output currents, some account must be made for sensor calibration errors. In particular, separate biases need to be determined for each CSS eye. Systematic sensor errors can arise from a number of physical causes. A bias in the measured current shifts the cosine of all angles by the same amount; whereas, an error in the maximum current,  $I_0$ , is a scale error that changes the cosines all by the same fraction. A misalignment will show up as a shift in the angles that depends on the location of the Sun in the field of view.

A simplification occurs for the CSS eyes that are mounted on the solar array panels. For these eyes, the Sun remains at nearly a constant angle throughout the sunlit part of the orbit. In this case, all the calibration parameters can be absorbed into a single bias; separate bias, scale factor, and misalignment parameters cannot be distinguished without observing the Sun over a range of angles in the CSS frame. This study analyzes these solar panel mounted eyes only.

For each eye, a bias was determined using only data from that part of the orbit where the predicted Earth albedo interference was less than 0.02 deg. These measurements have essentially no Earth interference so the difference between the measured and the expected CSS current can be attributed to sensor bias. Table 3 shows the biases obtained by averaging this difference over all points where the Earth interference is negligible. The fourth column in Table 3 indicates the scatter of observations. This scatter contributes an angular uncertainty proportional to the bias standard deviation divided by  $\sin \theta$ . (Angular sensitivity is worst when observing near the boresight.) At  $\theta = 45$  deg, an error of 0.006 corresponds to an angular uncertainty of about 0.5 deg.

Table 3 shows bias values obtained using a data set consisting of one orbit from Feb. 22, 1998. Biases recalculated using another data set from Mar. 10, 1998 differ by less than 0.02  $I_0$ .

**Table 3. TRMM CSS Biases for Selected Solar Array Mounted Eyes**

CSS Eye	Number of Points	Bias ( $\Delta I / I_0$ )	Std. Dev. of Bias
1	245	-0.0743	0.00662
5	77	-0.0895	0.0230
6	355	-0.0707	0.00643

## EVALUATION OF ERRORS

Tests with different grid sizes (see Figure 1) were performed. The total number of grid cells ranged from 7200 to 7,372,800 in these tests. The grid selected for the TRMM analyses had 115,200 cells. This discretization leads to numerical errors of no more than 0.00004  $I_0$ .

The measurement residual,  $r$ , which is the sensor error after compensating for bias and predicted Earth albedo effect, is

$$r = \alpha'_s - \alpha_{m,c} \quad (14)$$

where  $\alpha_{m,c}$  is the measured sensor output corrected only for bias, and  $\alpha'_s$  is the predicted CSS output corrected for albedo interference.

Uncompensated for Earth albedo, the sensor error is

$$e = \alpha_{m,c} - \alpha_{ref} \quad (15)$$

where  $\alpha_{ref}$  is the reference Sun angle, uncorrected for bias or Earth interference. The residual  $r$  and error  $e$  are displayed in the plots presented below as sensor errors either corrected or uncorrected for Earth albedo interference; the measured angle in both cases is  $\alpha_{m,c}$  so both  $r$  and  $e$  are corrected for sensor bias.

## NUMERICAL APPROACH

Based on TRMM telemetry, Sun and spacecraft position vectors in the geocentric inertial reference frame (GCI) were calculated every other second using a set of MATLAB 4.2 scripts. These vectors were rotated from GCI into the model frame using another MATLAB script. A FORTRAN code was then used to determine the reference Sun angle and predicted CSS output every other second. CSS biases and resulting statistics were calculated using MathCAD 6.0.

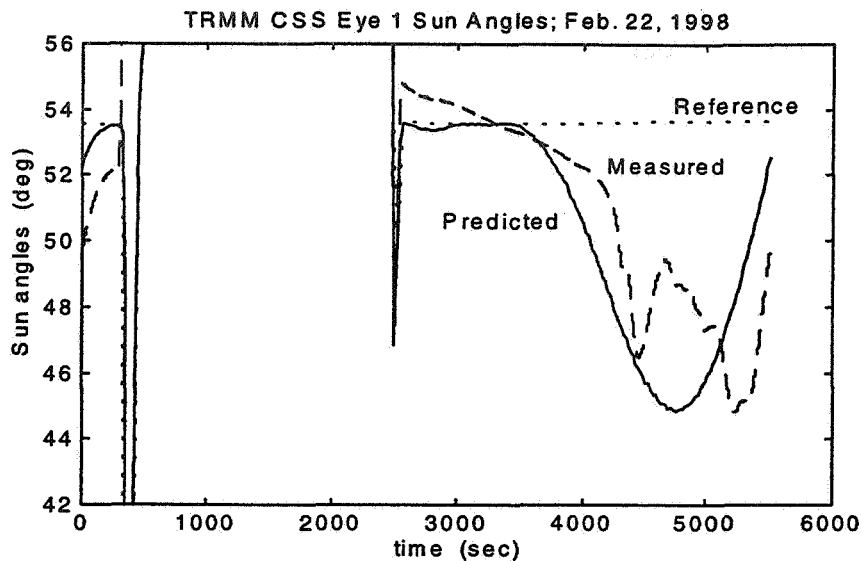
## RESULTS AND DISCUSSION

The CSS eyes that were analyzed are those subject to Earth interference for extended periods of time. These were eyes 1, 5, and 6. Figure 3 shows the reference  $\alpha_{ref}$  (dotted line), predicted  $\alpha'_s$  (solid line), and measured sensor output  $\alpha_{m,c}$  (dashed line) for eye 1 based on the Feb. 22, 1998 data set. The predicted sensor output was calculated using the average Earth albedo coefficient. The value of  $\alpha_{ref}$  is nearly constant since the CSS eye is mounted on the solar array which follows the Sun.

A large discrepancy between the measured and predicted angles is apparent in Figure 3 from  $t = 300$  to 600 seconds. This occurs because the model in this prototype version of the code does not take into account Sun occultations by the Earth.

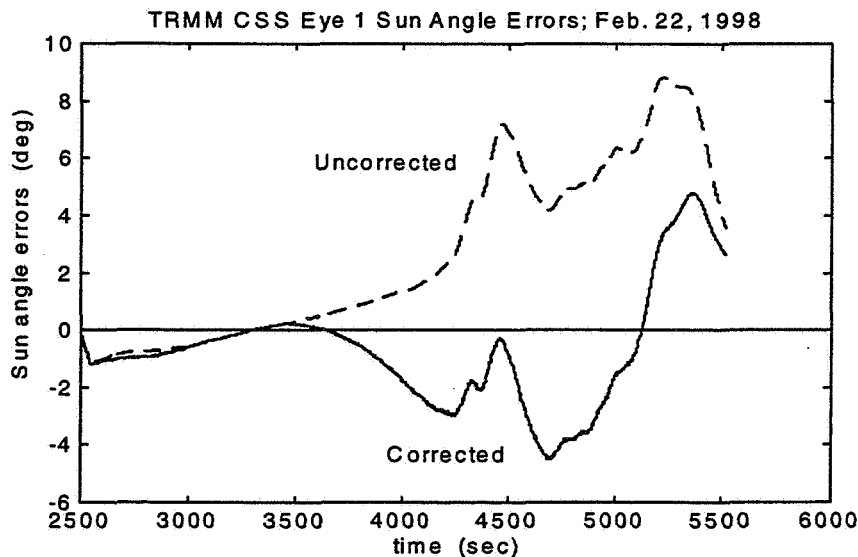
Differences between the reference Sun angle and the measured sensor output seen in Figure 3 are due to Earth albedo interference. The sensor output and the reference angle agree within the measurement uncertainty due to bias scatter (roughly 1 deg) except from 0 to 250 sec and from 3500 to 5500 sec. These are the time intervals when the Earth interference is significant and are accurately predicted by the model. For these intervals, the predicted curve is smooth while the measured curve shows abrupt changes. This qualitative difference is due to using Eq. (12) instead of (10), i.e., assuming a constant albedo coefficient. In reality this coefficient varies from one Earth area to another; the local albedo coefficient can vary from 0.05 to 0.6.<sup>3</sup> As a consequence, the predicted and measured output differ by up to 5 deg (at  $t = 4700$  sec). Nevertheless, the predicted and measured angles show similar overall trends. According to both measured and predicted CSS output, Earth albedo interference causes errors of up to 10 deg (from 4500 to 5500 sec).





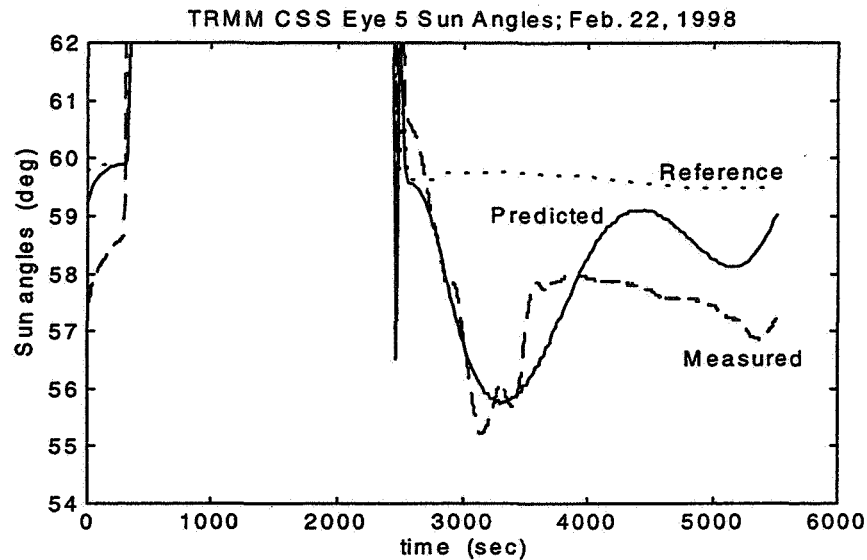
**Figure 3. Reference, predicted, and measured Sun angles for CSS eye 1; Feb. 22, 1998 (albedo coefficient = 0.30)**

The eye 1 errors before and after compensating for predicted Earth albedo effect are shown in Figure 4. For this orbit, model predictions based on the average Earth albedo coefficient provide a significantly better CSS accuracy. After compensating for the Earth albedo effect, the average CSS error is 0.5 deg with a RMS of 2.1 deg. Without compensation, the average error is 2.6 deg with a RMS of 3.9 deg. The maximum error is reduced from 9 deg to 5 deg.



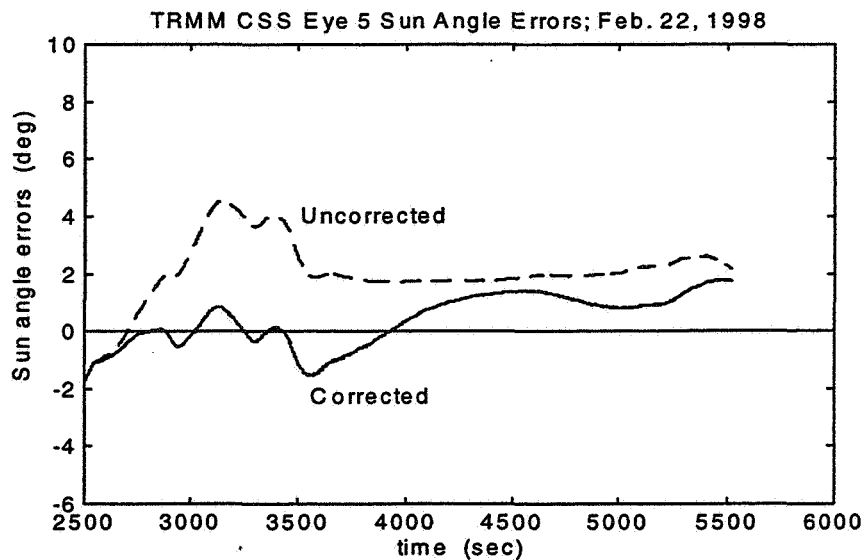
**Figure 4. CSS eye 1 errors for Feb. 22, 1998, corrected and uncorrected for Earth interference (albedo coefficient = 0.30)**

Figure 5 shows the reference, predicted, and measured Sun angles for eye 5. The same February 22 data set was used here as for Figures 3 and 4. Again, the model accurately predicts the time intervals when the CSS eye is exposed to Earth albedo interference (i.e., roughly from 0 to 100 seconds and from 2600 to 5500 seconds); the overall shape of the predicted sensor output also is approximately correct. The predicted and measured outputs differ by up to 2 deg.



**Figure 5. Reference, predicted, and measured Sun angles for CSS eye 5; Feb. 22, 1998 (albedo coefficient = 0.30)**

The eye 5 errors before and after applying the model corrections are shown in Figure 6. Using the average Earth albedo, the model reduces the CSS average error from 2.0 deg to 0.49 deg and the RMS error from 2.3 to 1.0 deg. The maximum error is reduced from 5 to 2 deg.



**Figure 6. CSS eye 5 errors for Feb. 22, 1998, corrected and uncorrected for Earth interference (albedo coefficient = 0.30)**

For eye 6, the reference, predicted, and measured Sun angles are shown in Figure 7. As before, the model and reference angles differ at the start of the Sun occultation period. Eye 6 is affected by the Earth albedo from 0 to about 100 seconds and from 3800 to 5500 seconds. The Earth interference periods are accurately predicted. The predicted sensor response again is only qualitatively correct because the average Earth albedo coefficient is used. The eye 6 errors before and after accounting for the Earth albedo interference are shown in Figure 8. The model reduces the maximum error from 7 to 4.0 deg. The average error decreases from 1.7 deg to 0.67, and the RMS decreases from 3.0 to 1.8 deg.

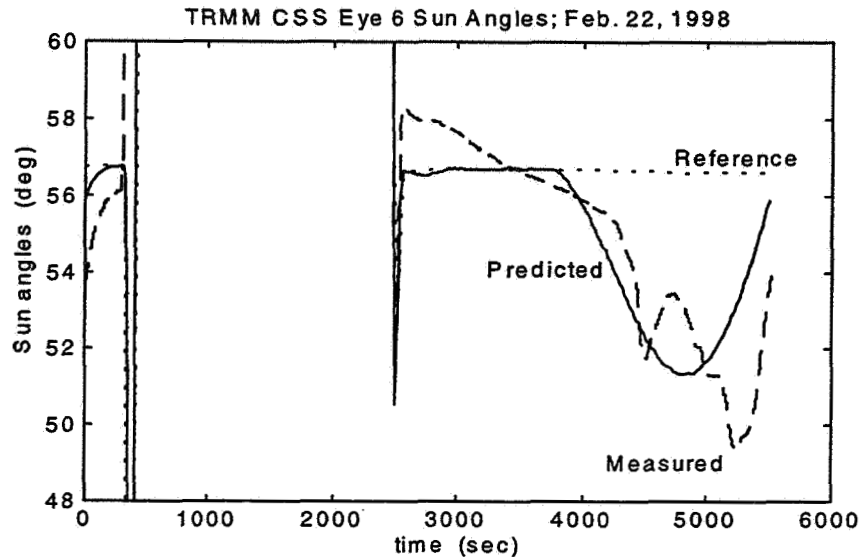


**Figure 7. Reference, predicted, and measured Sun angles for CSS eye 6; Feb. 22, 1998 (albedo coefficient = 0.30)**

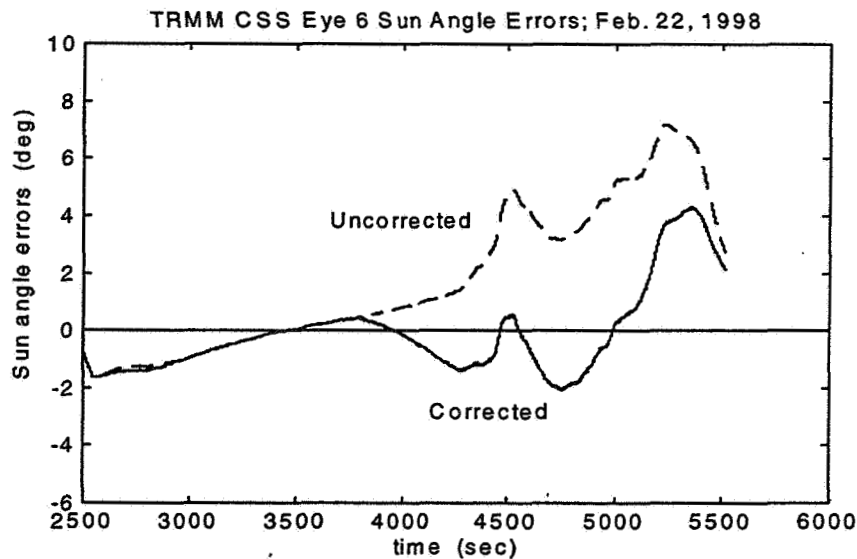


**Figure 8. CSS eye 6 errors for Feb. 22, 1998, corrected and uncorrected for Earth interference (albedo coefficient = 0.30)**

At other times, as shown by analyzing a March 10, 1998 data set, model predictions based on the average Earth albedo coefficient may over-correct the CSS, actually increasing the sensor error. Figure 9 shows reference, predicted, and measured angles for eye 1. The interference time spans are accurately predicted, as usual. Nevertheless, between 0 and 1000 seconds the predicted and measured sensor output differ by more than 7 deg, while the average uncorrected sensor error is less than 4 deg. Overall, the model correction based on the average Earth albedo coefficient increases the average eye 1 error from 1.0 to 2.0 deg and the RMS from 1.8 to 3.0 deg.

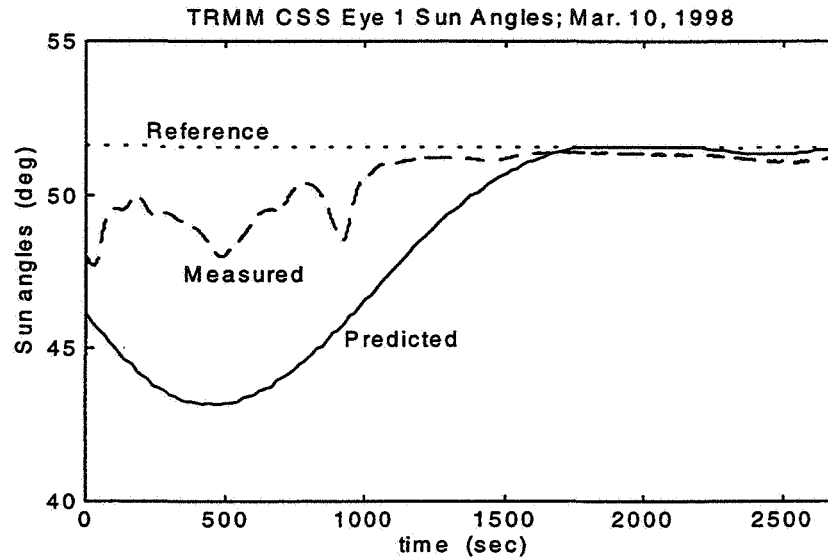


**Figure 9. Reference, predicted, and measured Sun angles for CSS eye 1; Mar. 10, 1998 (albedo coefficient = 0.30)**

This increased error is not due to an error in the model itself. Rather, the adverse effect is due the assumption that the average albedo of active areas and the average Earth albedo are equal. The altitude of TRMM is about 350 km, which means that during an entire orbit, a swath of about 16% of the entire Earth area is visible. This is a large area and therefore great albedo variations should be expected. The average error can be reduced to 0 by taking the average albedo for the active areas to be 0.105 instead of 0.30 (see Figure 10). The maximum error then is 1.5 deg and the RMS is 0.94 deg. Finding the optimum coefficient, i.e., the albedo coefficient that provides an average corrected error of 0, improves the maximum error and the RMS as compared to the correction based on a global average value of 0.30. This optimum value improves the CSS measurements at all times that were analyzed. The optimum albedo coefficient can be easily determined a posteriori. Unfortunately, a cost-effective and general method of determining it a priori, i.e., before the CSS measurements are made, is not available. For the most accurate results, Eq. (10) should be used. This method requires a detailed database containing the albedo coefficients of thousands of Earth surface elements that is frequently updated using accurate weather input. Such an approach would be difficult and expensive.

## CONCLUSIONS

The model presented here accurately predicts the time intervals when Earth albedo affects Sun sensor measurements. Regardless of the Earth albedo coefficient that is used, the model

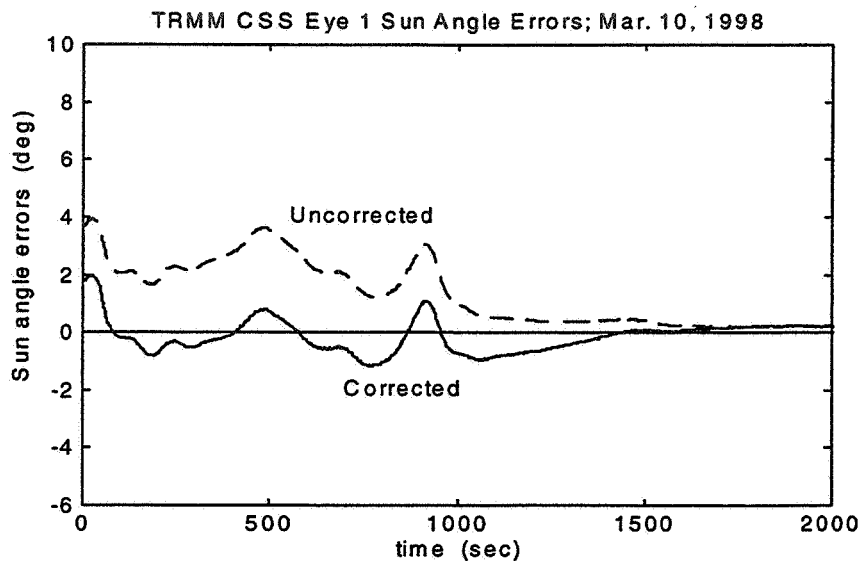


**Figure 10. CSS eye 1 errors for March 10, 1998, corrected and uncorrected for Earth interference (albedo coefficient = 0.105)**

provides a good qualitative prediction of Earth interference. In general, the model predictions based on the average Earth albedo coefficient increase the CSS accuracy. Nevertheless, there are times when this method severely over-corrects the sensor and reduces accuracy. The optimum albedo coefficient improves the accuracy of CSS measurements at all times, but it is not clear how to determine it a priori. The best Earth interference predictions could be made by maintaining a detailed database of local albedo values.

This study shows that the straightforward method of predicting Earth interference using a global mean albedo coefficient is insufficiently accurate. An albedo database adequate to improve matters is not readily available. A far more reasonable approach, as mentioned in previous studies,<sup>1</sup> is to reduce the effect of Earth interference in the first place by using a filter. Earth albedo is very low for several ranges of ultraviolet and infrared radiation. If the filter restricts the sensor sensitivity to such a range, the Earth albedo becomes negligible relative to the Sun. All types of Sun sensors could benefit from such a design modification.

## REFERENCES

1. D. Kulp, *Solar Maximum Mission Fine Pointing Sun Sensor Dawn and Dusk Errors, Flight Data and Model Analysis*, Computer Sciences Corporation, CSC/TM-87/6700, January 1987.
2. D. Brasoveanu, H. Arabshahi, and M. Phenneger, *Study of Earth Albedo Interference on Sun Sensors*, Computer Sciences Corporation, CSC/TM-90/6103, September 1990.
3. J. R. Wertz, ed., *Spacecraft Attitude Determination and Control*, D. Reidel Publishing Co., Dordrecht, The Netherlands, 1978.
4. M. Lambertson and J. Glickman, *Flight Dynamics Distributed Systems, Generalized Support Software, Tropical Rainfall Measuring Mission Application Program Specifications, Vol. 3: Measurement Processing System*, Computer Sciences Corporation, November 1997.



337599 538-19  
121. 169336

## MOMS-2P EQUIPMENT ADJUSTMENT BY ANGULAR VELOCITY MEASUREMENT DATA AND OPTICAL STAR SENSOR READINGS

M.Yu.Beliaev, V.M.Stazhkov, N.I.Efimov\*, V.V.Sazonov†,  
H.Frank, M.Schneller‡

The adjustment procedure of the MOMS-2P German hardware accommodated on the Priroda module integrated with the Mir orbital station is described. This hardware consists of three separate cameras installed in a special manner for surveying the Earth's surface, and angular velocity sensors for attitude determination. The proper interpretation of the observation results requires precise reference of the MOMS-2P coordinate system with respect to the Astro-1 optical star sensor coordinate system. Adjustment is made as a result of the joint processing of measurements of the star sensor and angular velocity sensors. Measurements are made while maintaining the fixed attitude of the station in the orbital coordinate system. Measurements made when maintaining only one attitude state are not sufficient for the adjustment as by these measurements one can determine only two of three angles characterizing mutual arrangement of the MOMS-2P and star sensor coordinate systems. The joint processing of the measurement data obtained when maintaining two and more different attitudes of the station allows to solve this problem. Examples of actual data processing and results of mathematical modeling are given.

### INTRODUCTION

The MOMS-2P German equipment has been installed on board the Priroda module of the Mir orbital station. This equipment has special cameras envisaged for the Earth surface observation while maintaining the fixed attitude of the station relative to the orbital coordinate system. For the proper interpretation of the observation results precise reference of the MOMS-2P coordinate system with respect to the Earth-fixed coordinate system is required. Reference is provided by knowledge of the station center of mass position in the Greenwich coordinate system and knowledge of the station attitude in the absolute space. The Greenwich coordinates of the station are determined by a GPS-receiver being a part of the MOMS-2P equipment; the station attitude is defined by readings of the Astro-1 optical star sensor. The latter is not related to MOMS-2P. In order to obtain precise attitude information of the MOMS-2P equipment in the Earth-fixed coordinate system it is necessary to know the MOMS-2P coordinate system relative to the coordinate system of the star sensor. As a result of this preceding adjustment the following is known: orientation of the coordinate systems with reference to each of the three optical units of the star sensor in the coordinate system of the MIR station (Ref.1). Therefore, it is convenient to define the MOMS-2P coordinate system orientation in relation to the construction system indicated. The adjustment of this orientation is

---

\* Korolev Rocket-Cosmic Corporation Energia, Russia. Phone 007 (095) 513-51-37, Fax 007 (095) 513-61-38, E-mail DNR@MCC.R.SA.RU.

† Keldysh Institute of Applied Mathematics, Russia.

‡ DLR, GSOC, Munich, Germany.

provided as a result of the joint processing of the measurement data of the optical star sensor and angular velocity sensors being a part of MOMS-2P equipment. Measurements for the adjustment are made in nominal operation mode of MOMS-2P when maintaining the fixed attitude of the station in the orbital coordinate system.

## COORDINATE SYSTEMS

During the adjustment three right-handed Cartesian systems are used:

$OX_1X_2X_3$  - inertial coordinate system referenced to mean equator and equinox of epoch 1950.0.

$Ox_1x_2x_3$  - construction coordinate system of the station core module.

$Oy_1y_2y_3$  - coordinate system referenced to MOMPS-2P angular velocity sensors. Positions of the cameras in this system are known accurately enough.

The systems introduced are used only to specify components of free vectors, therefore their origins are taken as coinciding.

Let us designate:

$A = \|a_{ij}\|_{i,j=1}^3$  - transition matrix from coordinate system  $Ox_1x_2x_3$  to system  $OX_1X_2X_3$ ,

$B = \|b_{ij}\|_{i,j=1}^3$  - transition matrix from coordinate system  $Oy_1y_2y_3$  to system  $OX_1X_2X_3$ ,

$U = \|u_{ij}\|_{i,j=1}^3$  - transition matrix from system  $Oy_1y_2y_3$  to system  $Ox_1x_2x_3$  with  $a_{ij}$  - cosine of the angle between axes  $OX_i$  and  $Ox_j$ ,  $b_{ij}$  - cosine of the angle between axes  $OX_i$  and  $Oy_j$ ,  $u_{ij}$  is cosine of the angle between axes  $Ox_i$  and  $Oy_j$ . The matrices introduced are related as  $B = AU$ . Matrix  $U$  is constant and in general, matrices  $A$  and  $B$  are time-dependent.

Below we will express matrix  $U$  elements by Krylov angles  $\psi$ ,  $\theta$  and  $\varphi$ . These angles are defined in the following way. System  $Ox_1x_2x_3$  can be converted into system  $Oy_1y_2y_3$  by three successive rotations: 1) through angle  $\psi$  around axis  $Ox_2$ , 2) through angle  $\theta$  around new axis  $Ox_1$ , 3) through angle  $\varphi$  around new axis  $Ox_3$  coinciding with axis  $Oy_3$ . The elements of the transition matrix in terms of Krylov angles are:

$$\begin{aligned} u_{11} &= \cos \psi \cos \varphi + \sin \psi \sin \theta \sin \varphi, & u_{21} &= \cos \theta \sin \varphi, \\ u_{12} &= -\cos \psi \sin \varphi + \sin \psi \sin \theta \cos \varphi, & u_{22} &= \cos \theta \cos \varphi, \\ u_{13} &= \sin \psi \cos \theta, & u_{23} &= -\sin \theta, \\ u_{31} &= -\sin \psi \cos \varphi + \cos \psi \sin \theta \sin \varphi, \\ u_{32} &= \sin \psi \sin \varphi + \cos \psi \sin \theta \cos \varphi, \\ u_{33} &= \cos \psi \cos \theta. \end{aligned}$$

In an analogous way we will present matrix  $B$  elements. Let us designate Krylov angles  $\theta$ ,  $\psi$  and  $\varphi$  used to prescribe  $U$   $p_1$ ,  $p_2$  and  $p_3$ , respectively; analogous let us designate the Krylov angles used to prescribe  $B$  at some fixed instant of time as  $q_1$ ,  $q_2$  and  $q_3$ .

Angles  $p_1$ ,  $p_2$  and  $p_3$  are known only approximately. Description of the refinement procedure of their values is the aim of this paper.



## MEASUREMENT DATA

The Astro-1 optical star sensor is installed on board the Kvant-2 module and allows to define the station attitude-coordinate system  $Ox_1x_2x_3$  orientation relative to system  $OX_1X_2X_3$  at some discrete instants of time. The measurement data of this sensor and methods of its processing are given in (Ref.1). Based on the star sensor measurement data processing one can define values of matrix  $A$  at some instants of time at intervals of several seconds.

The angular velocity sensors being a part of the MOMS-2P equipment allow to measure components  $\omega_\alpha$  ( $\alpha = 1, 2, 3$ ) of the absolute angular velocity of the station in coordinate system  $Oy_1y_2y_3$ . There are two sensor packages and each package measures four velocity components. For component  $\omega_2$  there are two sets of measurements (redundancy), components  $\omega_1$  and  $\omega_3$  are measured once in each package. Measurements of all the components are made at discrete time steps  $h = 8.30078$  ms. The certificate accuracy of measurements is 0.0001 deg/s. Examples of the station angular rate measurements made by the sensors are given in Figure. 1. In this Figure points conforming to measurements neighbouring in time are connected with straight lines. The broken lines characterize the angular velocity components behavior in time.

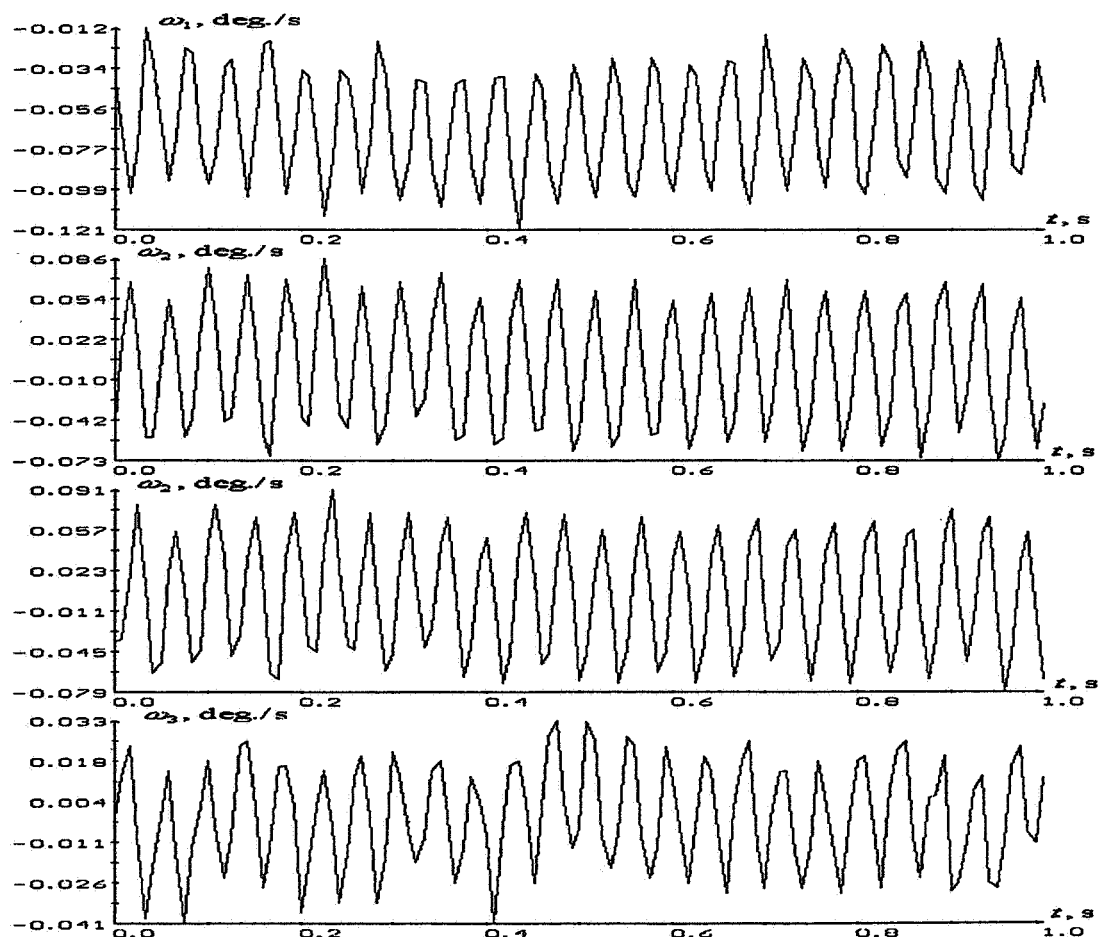


Figure 1 Examples of the station angular velocity measurements

As shown in the Figure, the angular velocity components demonstrate cyclical trend. The measurement data spectral analysis allowed to find a frequency of this trend. It is 24 Hz. If such variations took place in reality, then due to the large moments of inertia of the station they would require a very large torque. Rough estimates show that the moment required cannot be provided with any onboard devices. Therefore, the variations indicated are caused by properties of the angular velocity sensors. Using the measurement data of these sensors, the variations indicated must be eliminated - suppressed using low-frequency filtering.

Such filtering is provided in the following way. Assume that measurements of any component of the angular velocity are given. Let us designate these measurements as  $x_i$  ( $i = 0, 1, \dots, mn$ ), where  $m$  and  $n$  are natural numbers. Measurement  $x_i$  is made at the instant of time  $t_i = ih$ ,  $h > 0$ . A low-frequency component contained in this data will be taken as

$$\hat{x}(t) = \alpha + \beta t + \sum_{k=1}^{n-1} a_k \sin(\pi k t / mn h). \quad (1)$$

Here  $\alpha$ ,  $\beta$  and  $a_k$  are coefficients. We will select values of these coefficients from the functional minimum condition.

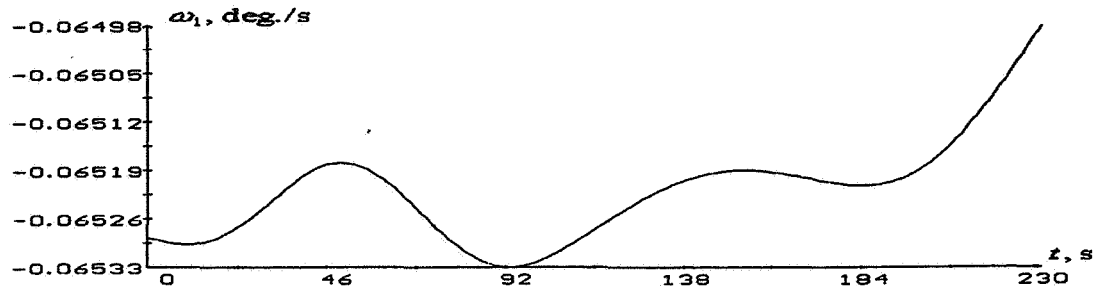
$$\Phi = \sum_{i=0}^{mn} [\hat{x}(ih) - x_i]^2.$$

This approximation method is a slight modification of one of the methods considered in (Ref.2). To calculate coefficients there are simple design formulae. The function prescribed by Eq. (1) often experiences noticeable comparatively high-frequency oscillations. In order to get rid of them this expression is corrected using Lanczos  $\sigma$ -factors (Ref.2):

$$\hat{x}(t) = \alpha + \beta t + \sum_{k=1}^{n-1} a_k \frac{\sin(\pi k / n)}{\pi k / n} \sin(\pi k t / mn h)$$

One can use other analogous factors as well.

Examples of the low-frequency component extraction from the measurement data of angular velocity components  $\omega_\alpha$  ( $\alpha = 1, 2, 3$ ) are given in Figure 2. Filtering is provided with  $m = 3000$ . Instant of time  $t = 0$  in this Figure corresponds to instant of time



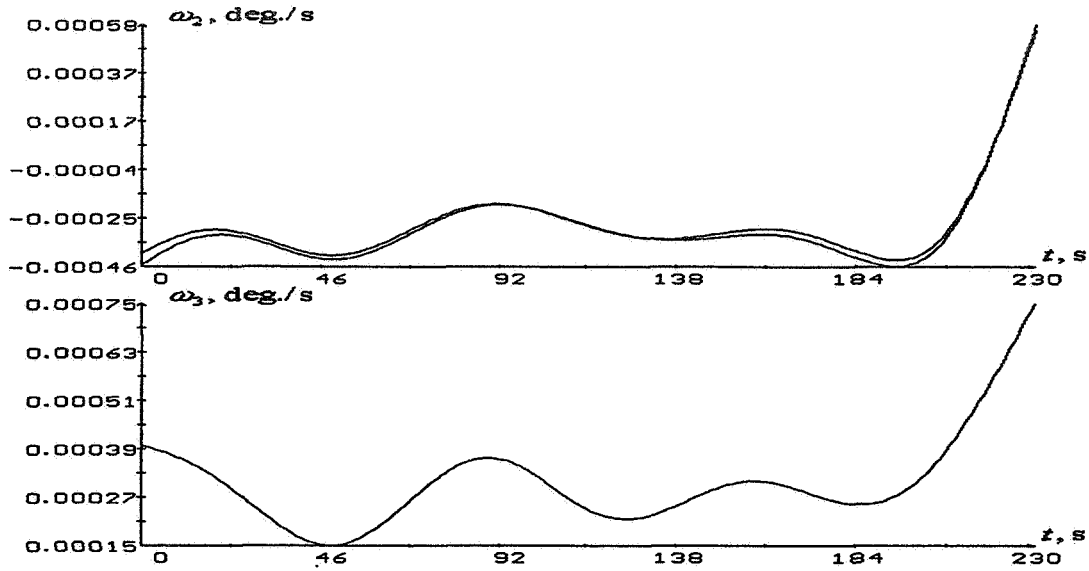


Figure 2 Examples of the low-frequency component extraction from the measurement data

$t = 0$  in Figure 1. Two plots obtained by measurements of redundant sensors are given for component  $\omega_2$ . These plots almost coincide. For the adjustment the approximation of a low-frequency component in  $\omega_2$  obtained by readings of only one sensor was used.

### ADJUSTMENT PROBLEM ANALYSIS

Assume that values of matrix  $A$  at instants of time  $t_1 < t_2 < \dots < t_n$  are got as a result of the star sensor measurement data processing. Let us denote a value relating to instant  $t_i$  as  $A_i$ .

Matrix  $B$  satisfies the following relation:

$$\dot{B} = B\Omega, \quad (2)$$

where the time differentiation is designated by a point.

$$\Omega = \begin{bmatrix} 0 & -\omega_3 & \omega_2 \\ \omega_3 & 0 & -\omega_1 \\ -\omega_2 & \omega_1 & 0 \end{bmatrix}$$

Let us specify angular velocity components  $\omega_\alpha$  ( $\alpha = 1, 2, 3$ ) with functions constructed by the measurement data of the angular velocity sensors using the previous section method and now consider relation (2) in which  $\Omega = \Omega(t)$  as a differential equation defining matrix  $B$ . Interval  $t_1 \leq t \leq t_n$  must lie deeply enough within the interval defining matrix function  $\Omega(t)$  to exclude the boundary effects related to its construction.

We will represent the solution of Eq. (2) as  $B(t) = B_0 X(t)$ , where  $B_0 = B(t_0)$ ,

$$\dot{X}(t) = X\Omega(t), \quad (3)$$

$X(t_0)$  is a unit matrix, instant  $t_0$  is selected near interval  $t_1 \leq t \leq t_n$ . By definition of matrices  $A$ ,  $B$  and  $U$  they are linked with relation  $AU = B$ . However, for matrices  $A_i$  only relations  $A_i U \approx B_0 X_i$ , where  $X_i = X(t_i)$  ( $i = 1, \dots, n$ ) are valid.

Matrices  $U$  and  $B_0$  are known beforehand only approximately but they can be refined as a result of statistical processing of the measurement data. Following the least-squares method we will take values of these matrices from the functional minimum condition

$$S = \frac{1}{2} \sum_{i=1}^n \text{tr}(A_i U - B_0 X_i)^T (A_i U - B_0 X_i).$$

In minimization we will use explicit expressions for  $U$  and  $B_0$  using two sets of Krylov angles  $p_\alpha$  and  $q_\lambda$  ( $\alpha, \lambda = 1, 2, 3$ ), respectively. In this case the problem consists in minimizing  $S$  by  $p_\alpha$  and  $q_\lambda$  and is reduced to the solution of the following equations:

$$\partial S / \partial p_\alpha = 0, \partial S / \partial q_\lambda = 0 \quad (4)$$

Eqs. (4) are solved numerically by Gauss-Newton iteration method (Ref.3). This method is a version of the Newton method with simplified calculation of the matrix of the linearized system occurring during each iteration. Let us cite the basic formulae used.

First, we will give formulae for partial derivatives of matrices  $U$  and  $B_0$  by angles  $p_\alpha$  and  $q_\lambda$ . We have the following:

$$\frac{\partial U}{\partial p_\alpha} = U \Phi_\alpha, \quad \Phi_\alpha = \begin{vmatrix} 0 & -\varphi_{\alpha 5} & \varphi_{\alpha 2} \\ \varphi_{\alpha 5} & 0 & -\varphi_{\alpha 1} \\ -\varphi_{\alpha 2} & \varphi_{\alpha 1} & 0 \end{vmatrix},$$

$$\frac{\partial B_0}{\partial q_\lambda} = B_0 \Psi_\lambda, \quad \Psi_\lambda = \begin{vmatrix} 0 & -\psi_{\lambda 5} & \psi_{\lambda 2} \\ \psi_{\lambda 5} & 0 & -\psi_{\lambda 1} \\ -\psi_{\lambda 2} & \psi_{\lambda 1} & 0 \end{vmatrix}$$

Values  $\phi_{\alpha 1}$ ,  $\phi_{\alpha 2}$  and  $\phi_{\alpha 3}$  are determined by differential identities.

$$\begin{aligned} \phi_{\alpha 1} \delta p_\alpha &= \cos \theta \sin \varphi \delta \psi + \cos \varphi \delta \theta, \\ \phi_{\alpha 2} \delta p_\alpha &= \cos \theta \cos \varphi \delta \psi - \sin \varphi \delta \theta, \\ \phi_{\alpha 3} \delta p_\alpha &= -\sin \theta \delta \psi + \delta \varphi, \end{aligned}$$

where  $\theta, \psi, \varphi$  are ordinary designations for Krylov angles  $p_\alpha$ . Doubly recurring of Greek indices means the summation from 1 to 3. Values  $\psi_{\lambda 1}$ ,  $\psi_{\lambda 2}$  and  $\psi_{\lambda 3}$  are determined in an analogous way. It is convenient to introduce vectors

$$\varphi_\alpha = (\varphi_{\alpha 1}, \varphi_{\alpha 2}, \varphi_{\alpha 3})^T, \quad \psi_\lambda = (\psi_{\lambda 1}, \psi_{\lambda 2}, \psi_{\lambda 3})^T,$$

corresponding to matrices  $\Phi_\alpha$  and  $\Psi_\lambda$ .

The following formula is true:

$$\frac{\partial S}{\partial \varphi_\alpha} = \text{tr} \sum_{i=1}^n (A_i U - B_0 X_i)^T A_i \frac{\partial U}{\partial \varphi_\alpha} = -\text{tr} \left( \sum_{i=1}^n X_i^T B_0^T A_i U \right) \Phi_\alpha.$$

is the derivation which is based on the relation  $\text{tr} \Phi_\alpha = 0$  and the condition of orthogonality of matrices  $A_i$  and  $U$ . Let us introduce matrix

$$Z = \sum_{i=1}^n X_i^T B_0^T A_i U = \|z_{ij}\|_{i,j=1}^3$$

and using its elements, specify row vector  $f = (z_{23} - z_{32}, z_{31} - z_{13}, z_{12} - z_{21})$ .

Then  $\partial S / \partial \varphi_\alpha = -f \varphi_\alpha$ .

In a similar way we will get

$$\begin{aligned} \partial S / \partial q_\lambda &= -\text{tr} W \Psi_\lambda = -g \psi_\lambda, \quad W = \sum_{i=1}^n X_i U^T A_i^T B_0 = \|w_{ij}\|_{i,j=1}^3, \\ g &= (w_{23} - w_{32}, w_{31} - w_{13}, w_{12} - w_{21}). \end{aligned}$$

Now let us go to the second derivatives of  $S$ . Using orthogonality properties of matrices  $A_i$ ,  $X_i$ ,  $U$ ,  $B_0$  and usual simplifications of Gauss-Newton method, i.e. assuming that  $A_i U = B_0 X_i$  ( $i = 1, \dots, n$ ) we will get

$$\begin{aligned} \frac{\partial^2 S}{\partial \varphi_\alpha \partial \varphi_\beta} &\approx 2n \varphi_\beta^T \varphi_\alpha, \quad \frac{\partial^2 S}{\partial q_\lambda \partial q_\mu} \approx 2n \psi_\mu^T \psi_\lambda, \\ \frac{\partial^2 S}{\partial \varphi_\alpha \partial q_\lambda} &\approx -2\psi_\lambda^T M \varphi_\alpha, \quad M = \sum_{i=1}^n X_i. \end{aligned}$$

The system of the linearized equations solved during each iteration of Gauss-Newton method and defining corrections  $\Delta p_\beta$  and  $\Delta q_\mu$  to available estimates of unknowns  $p_\beta$  and  $q_\mu$  is the following

$$\begin{aligned} 2n \varphi_\alpha^T \varphi_\beta \Delta p_\beta - 2\varphi_\alpha^T M^T \psi_\mu \Delta q_\mu &= f \varphi_\alpha, \\ -2\psi_\lambda^T M \varphi_\beta \Delta p_\beta + 2n \psi_\lambda^T \psi_\mu \Delta q_\mu &= g \psi_\lambda \end{aligned} \tag{5}$$

This system is named normal. Its matrix is symmetrical and positive semi definite. If this matrix has non zero eigenvalue then this normal system has a unique solution and Gauss-Newton method converges with sufficiently exact initial estimates of the unknowns. However, unfortunately, this zero eigenvalue exists.

The proof will be given assuming that the station orbit is Keplerian and the station maintains a fixed attitude in the orbital coordinate system. It is an idealized case. Obviously, the degeneration will not take place for the actual orbit, however, the problem of the concurrent refinement of  $U$  and  $B_0$  will be ill-conditioned. With assumptions made matrix  $X(t)$  is defined by Eq. (3) in which  $\Omega(t)$  is specified by the orbital coordinate system angular velocity. In this system we will direct axis 3 along the radius vector of the station and axis 2 along the normal to the orbital plane. Then the angular velocity of this system in its proper basis will be  $(0, \dot{\nu}, 0)$ , where  $\nu$  is the station true anomaly. Denote by  $D$  the transition matrix from coordinate system  $Oy_1y_2y_3$  to the orbital system. Then

$$X(t) = D^T \Pi_2 [\nu(t) - \nu(t_0)] D, \quad \Pi_2(\varphi) = \begin{vmatrix} \cos \varphi & 0 & \sin \varphi \\ 0 & 1 & 0 \\ -\sin \varphi & 0 & \cos \varphi \end{vmatrix}$$

Assume that  $e_2 = (0, 1, 0)^T$ ,  $a = D^T e_2$ . As  $\Pi_2(\varphi) e_2 = e_2$  and  $e_2^T \Pi_2(\varphi) = e_2^T$ , we have  $X(t) a = a$  and  $a^T X(t) = a^T$ . Hence,  $M a = M^T a = n a$ .

Let us consider normal Eqs. (5) with zero right-hand sides

$$\begin{aligned} n \varphi_\alpha^T \varphi_\beta \Delta p_\beta - \varphi_\alpha^T M^T \psi_\mu \Delta q_\mu &= 0, \\ -\psi_\lambda^T M \varphi_\beta \Delta p_\beta + n \psi_\lambda^T \psi_\mu \Delta q_\mu &= 0. \end{aligned}$$

Here  $\Delta p_\beta$  and  $\Delta q_\mu$  are unknown values. Let us show that this system has a nontrivial solution. It is this solution that will be an eigenvector conforming to the zero eigenvalue of the matrix of system (5). Rewrite the latter equations as

$$\begin{aligned} \varphi_\alpha^T (n \varphi_\beta \Delta p_\beta - M^T \psi_\mu \Delta q_\mu) &= 0, \\ \psi_\lambda^T (-M \varphi_\beta \Delta p_\beta + n \psi_\mu \Delta q_\mu) &= 0. \end{aligned}$$

Let us determine  $\Delta p_\beta$  and  $\Delta q_\mu$  from the following systems of equations  $\varphi_\beta \Delta p_\beta = a$  and  $\psi_\mu \Delta q_\mu = a$ . These systems have unique solutions if both sets of Krylov angles are non-degenerate. Having substituted such solutions in normal equations we will get obvious identities:

$$\varphi_\alpha^T (n a - M^T a) = 0, \quad \psi_\lambda^T (-M a + n a) = 0.$$

Thus, the matrix of normal equations has a zero eigenvalue. The problem of this zero eigenvalue of the matrix of system (5) is related to non-uniqueness of matrices  $U$  and  $B_0$

providing minimum of  $S$ . In order to state this fact it will suffice to prove non-uniqueness of these matrices in relation  $A(t) = B_0 X(t) U^T$ . Using the expression above for  $X(t)$  one can prove that  $A(t) = \tilde{B}_0 X(t) \tilde{U}^T$ , where  $\tilde{B}_0 = B_0 D^T \Pi_2(s) D$ ,  $\tilde{U} = U D^T \Pi_2(s) D$ ,  $s$  is any number.

## COMPUTATIONAL ALGORITHMS

Due to system (5) degeneracy one interval with the angular velocity sensors and optical star sensor measurements is not enough to provide the adjustment. However, by measurements on one interval one can refine two of three angles  $p_\alpha$ . The case of one interval can be considered more generally. One can specify values of all three angles but in this case it will be required to provide an additional scalar relationship between them. Let us take such an additional relationship as linear

$$a_\alpha p_\alpha = a_0. \quad (6)$$

We will add this relationship as an additional equation to system (4). With the appropriate selection of coefficients  $a_1, a_2, a_3$  system (4), (6) will have the unique solution.

The numerical search for this solution is performed using the obvious modification of Gauss-Newton method. To the system of normal Eqs. (5) occurring during each iteration of this method we add linearized Eq. (6)

$$a_\alpha \Delta p_\alpha = 0. \quad (7)$$

and get a system of 7 linear equations relative to 6 unknowns. However, the rank of this new system does not exceed 6; it will equal to 6 with an apt choice of coefficients in Eq. (6). The solution of this system is found using the singular decomposition of its matrix (Ref.4). We consider the Gauss-Newton iteration process to be convergent when norm of the correction vector with components  $\Delta p_\alpha, \Delta q_\lambda$  is less than the given positive number.

The calculation of the matrix singular decomposition of system (5), (7) allows to find out if the selection of coefficients  $a_\alpha$  in Eq. (6) was suitable. This matrix must be well-posed enough, i.e. the ratio between its maximum and minimum singular values must be not very high.

In order to specify values of all angles  $p_\alpha$  it is necessary to provide simultaneous processing of two and more intervals with measurements for different attitudes of the station. In this case the following will be specified: matrix  $U$  the same for all intervals and matrices  $B_0$  for each interval. If these matrices are given parametrically then during the simultaneous processing of  $l$  intervals the parameter  $3(l+1)$  values will be specified. The refinement can be provided by Gauss-Newton method. The calculation of the matrix and right-hand side of the corresponding system of normal equations is made in the following way. First the matrix and vector of the right-hand side of system (5) are calculated for each interval, then all these matrices and vectors are divided into blocks of the following sizes:  $3 \times 3$  and  $3 \times 1$ , respectively and the required matrix and vector of the right-hand

side of this new system of normal equations of the order of  $3(l+1)$  are formed of the blocks obtained.

As an example we will consider generation of a system of normal equations during the joint processing of two intervals which will be numbered as 1 and 2. Let us specify matrix  $U$  by angles  $p_\alpha$ ; matrix  $B_0^{(j)}$ , presented as matrix  $B_0$  for the  $j$ -th interval, is specified by angles  $q_\lambda^{(j)}$ . Write system (5) for the  $j$ -th interval as

$$\begin{aligned} C_{11}^{(j)} \Delta p + C_{12}^{(j)} \Delta q^{(j)} &= d_1^{(j)}, \\ C_{21}^{(j)} \Delta p + C_{22}^{(j)} \Delta q^{(j)} &= d_2^{(j)}. \end{aligned}$$

Here  $\Delta p = (\Delta p_1, \Delta p_2, \Delta p_3)^T$ ,  $\Delta q^{(j)} = (\Delta q_1^{(j)}, \Delta q_2^{(j)}, \Delta q_3^{(j)})^T$ ,  $[C_{21}^{(j)}]^T = C_{12}^{(j)}$ . Then the system of normal equations occurring during the joint processing of two intervals will be:

$$\begin{aligned} [C_{11}^{(1)} + C_{11}^{(2)}] \Delta p + C_{12}^{(1)} \Delta q^{(1)} + C_{12}^{(2)} \Delta q^{(2)} &= d_1^{(1)} + d_1^{(2)}, \\ C_{21}^{(1)} \Delta p + C_{22}^{(1)} \Delta q^{(1)} &= d_2^{(1)}, \\ C_{21}^{(2)} \Delta p + C_{22}^{(2)} \Delta q^{(2)} &= d_2^{(2)}. \end{aligned}$$

The covariance estimate matrix of parameters  $p_\alpha$  and  $q_\lambda^{(j)}$  obtained as a result of the adjustment is calculated within usual assumptions of the least - squares method (Ref.4). In this case it is considered (comp. Ref.1) that mismatches of matrices  $A_i$  and  $B_0 X_i U^T$  ( $i = 1, \dots, n$ ) can be described by infinitesimal rotation vectors which components in any Cartesian system are independent random variables with zero mean value and identical variance.

## ADJUSTMENT RESULTS

Presently there is data of the angular velocity sensors and Astro-1 only for one time interval adequate for adjustment. This interval falls on 9<sup>h</sup> 00<sup>m</sup> – 9<sup>h</sup> 12<sup>m</sup>, March 14, 1997. It contains 148 points with the station attitude measurements. As indicated above, one interval is not enough to provide adjustment. However, if an additional scalar constraint is imposed upon angles  $p_\alpha$  then some refinement of these angles is feasible. For example, one can fix a value of one angle and find values of two other angles. Assume that in Eq. (6)  $a_1 = a_3 = 0$ ,  $a_2 = 1$ ,  $a_0 = \pi/2$ . Such coefficient selection means fixing of angle  $p_2 = \pi/2$ . The adjustment result is the following:  $p_1 = 0.062^\circ$ ,  $p_3 = 90.105^\circ$ . Standard deviations of the given estimates are:  $\sigma_{p_1} = 0.013^\circ$ ,  $\sigma_{p_3} = 0.013^\circ$ .

Let us give some characteristics of the system of normal equations at the minimum point of  $S$ . The standardized eigenvector conforming to a zero eigenvalue of the matrix of system (5) is: (0.004, -0.639, -0.004, 0.354, 0.612, 0.302). Nonzero eigenvalues of this matrix are: 1.037, 1.381, 324.3, 431.1, 538.2. The matrix singular values of system (5), (7) are: 0.6295, 1.050, 1.384, 324.3, 431.1, 538.2.



To check the adjustment methods described above two time intervals with the artificial measurement data were used. These intervals were obtained in the following way. The actual measurement data of all sensors was taken and artificially combined with each other. The first artificial interval was of the length of 9 min and there were 275 instants of time with the star sensor measurements on it. The second artificial interval was of the length of 4 min and there were 121 instants of time with this sensor measurements on it. The joint processing results of the actual interval considered above and the first artificial interval allowed to get the following results:  $p_1 = 0.061^\circ$ ,  $p_2 = 90.299^\circ$ ,  $p_3 = 90.057^\circ$ ,  $\sigma_{p_1} = 0.013^\circ$ ,  $\sigma_{p_2} = 0.0066^\circ$ ,  $\sigma_{p_3} = 0.0059^\circ$ . The maximum and minimum eigenvalues of the matrix of the system of normal equations in the case given are 0.5888 and 1045.

Now let us give the joint processing results of the actual interval and two artificial intervals:  $p_1 = 0.099^\circ$ ,  $p_2 = 90.175^\circ$ ,  $p_3 = 90.062^\circ$ ,  $\sigma_{p_1} = 0.013^\circ$ ,  $\sigma_{p_2} = 0.0070^\circ$ ,  $\sigma_{p_3} = 0.0062^\circ$ . In the case given the maximum and minimum proper values of the matrix of the system of normal equations are 0.4908 and 1355.

Of the results given the eigenvalues and singular values of matrices of the system of linear equations solved are of the most interest. These values show a capability of using the proposed adjustment method. Note that the use of the artificial measurement data in calculations has no effect on the conclusion drawn. This conclusion is based only on the selection of the station positions during the adjustment and on the selection of instants of time with measurements. The accuracy rating of specified angles  $p_\alpha$  that are obtained during the adjustment is also of interest. Though this accuracy rating depends on the artificial data selection the data origin allows to hope for impartiality of the rating indicated. One will not attach great significance to the estimated discrepancy of angles  $p_\alpha$  and standard deviations  $\sigma_{p_\alpha}$  in case of adjustments provided in two and three intervals. This discrepancy can be explained by the artificial data preparation method.

## CONCLUSION

It is shown that the optical star sensor and angular velocity sensors measurements made when maintaining only one fixed attitude of the station are not sufficient for the adjustment; by these measurements one can determine only two of three angles characterizing the mutual arrangement of the MOMS-2P coordinate system and construction coordinate system of the station. The joint processing of the measurement data obtained when maintaining two and more different attitudes of the station allows to solve this problem. These conclusions are validated by examples of the actual data processing and mathematical modeling results.

## REFERENCES

1. M.Yu. Beliaev, N.I.Efimov, V.V.Sazonov. Determination of the attitude of the Mir orbital complex from indications of an optical star sensor. Cosmic Research, 1995, v. 33, N 4, p.357-364.
2. C. Lanczos. Applied analysis. M., Prentice Hall, Inc.,1956.

3. Y. Bard. Nonlinear parameter estimation. Academic Press, New York, San Francisco, London, 1974.
4. G.H.Golub, C.Reinsch. Singular values decomposition and least-squares solution. Num. Math. 1970, v. 14, N. 5, p. 403-420.

337600-539-14  
148  
AAS 98-340  
169337

## TEST OF A FLEXIBLE SPACECRAFT DYNAMICS SIMULATOR

Donald Dichmann\* and Joseph Sedlak†

There are a number of approaches one can take to modeling the dynamics of a flexible body. While one can attempt to capture the full dynamical behavior subject to disturbances from actuators and environmental torques, such a detailed description often is unnecessary. Simplification is possible either by limiting the amplitude of motion to permit linearization of the dynamics equations or by restricting the types of allowed motion. In this work, we study the nonlinear dynamics of bending deformations of wire booms on spinning spacecraft. The theory allows for large amplitude excursions from equilibrium while enforcing constraints on the dynamics to prohibit those modes that are physically less relevant or are expected to damp out fast. These constraints explicitly remove the acoustic modes (i.e., longitudinal sound waves and shear waves) while allowing for arbitrary bending and twisting motions which typically are of lower frequency.

As a test case, a spin axis reorientation maneuver by the Polar Plasma Laboratory (POLAR) spacecraft has been simulated. POLAR was chosen as a representative spacecraft because it has flexible wire antennas that extend to a length of 65 meters. Bending deformations in these antennas could be quite large and have a significant effect on the attitude dynamics of the spacecraft body. Summary results from the simulation are presented along with a comparison with POLAR flight data.

### INTRODUCTION

This work describes the design and application of a flexible spacecraft dynamics simulator, named Cartwheel, to model a spin axis reorientation maneuver by the Polar Plasma Laboratory (POLAR) spacecraft. It presents a summary of the simulation results and a comparison with flight data. Overviews of the theory and the software are also given.

The general purpose of this research was to study the applicability of a particular flexible dynamics method to spacecraft attitude dynamics. As described below, the Cartwheel simulator captures the most important parts of the nonlinear dynamics but leaves out a number of smaller effects. As a prototype analysis tool, Cartwheel has been used for basic theoretical tests but is not intended for operations support.

---

\* The Aerospace Corporation, 2350 El Segundo Blvd., El Segundo, CA, USA 90245.

† Computer Sciences Corporation (CSC), 10110 Aerospace Rd., Seabrook, MD, USA 20706.

We chose POLAR as a representative spacecraft because it has flexible wire antennas that extend up to 65 m in length, so the wire antennas contribute a large fraction of the total moment of inertia. Due to the great length of these thin wire booms, bending deformations can have a significant effect on the attitude dynamics of the hub of the spacecraft body. Flexure of the antennas can cause large changes in the total moment of inertia, which, in turn, can affect the spacecraft rotation rate. The motions of the antennas couple through the rigid hub. In addition, the antennas have some intrinsic stiffness, that is, a tendency to spring back to their default orientation (normally straight). The resulting highly nonlinear dynamics leads to complex perturbations to the attitude.

The POLAR spacecraft periodically executes a 180 degree spin reorientation maneuver to prevent the Sun from coming into view of certain instruments. We anticipated that this type of maneuver would induce vibration in the wire booms that could measurably influence the attitude dynamics of the hub. This paper describes the application of the Cartwheel simulator to such a maneuver.

The next sections contain overviews of the dynamics theory and the Cartwheel software. This is followed by a description of the POLAR spacecraft, orbit, attitude, and the spin axis reorientation maneuver. Finally, a summary of the simulation results and comparison with POLAR flight data is given.

## THEORY

The flexible spacecraft dynamics simulation program, Cartwheel, was designed to model the nonlinear dynamics of large bending deformations of wire booms on spacecraft. In these simulations, we enforce constraints on the dynamics to prohibit the generally lower amplitude, higher frequency acoustic modes (i.e., longitudinal sound waves and shear waves) but to allow the larger, lower frequency bending and twisting motions. While it is possible to model the full dynamical problem, this is made difficult by the presence of both very slow and very fast characteristic appendage motions. Describing all the characteristic frequencies accurately leads to difficulties and inefficiencies when integrating the governing equations. Dynamical systems with this problem are called *stiff*. There are two broad kinds of simplifications that make solution of the governing equations more tractable. One can assume the deviations of the appendages from their equilibrium positions are of low amplitude and then discard all terms in the equations that are of second or higher order in this amplitude. The resulting linear system of equations can be analyzed in terms of its normal modes of vibration. Alternatively, one can disallow types of motion that are physically less important for the system under consideration. The approach taken in this work is to discard the generally high frequency motions associated with stretching and shearing of the appendages (acoustic modes) while keeping the full nonlinear description of the rest of the motion (flexing and twisting).

Constraining the dynamics to disallow acoustic modes makes numerical solutions easier to obtain without appreciably limiting their validity. The only motions of interest here are those that affect the spacecraft attitude; these are likely to be combinations of simple oscillations and possibly “whiplash” motions of the booms. These motions are not

likely to excite or couple strongly to the acoustic modes. In addition, acoustic modes are likely to damp out fast in the multi-stranded boom material. Eliminating these modes from the start is very nearly the same as describing the full dynamics of a system with highly damped acoustic modes.

The method chosen for enforcing the dynamical constraints is called the *impetus-striction* method (Ref. 1). The method has proven valuable in theoretical analyses of stability conditions (Ref. 2) as well as in numerical simulations to rod dynamics (Ref. 3). The key features of the impetus-striction method are as follows:

- The method applies to systems having a Lagrangian formulation subject to holonomic constraints. It transforms constrained Lagrangian dynamics into an unconstrained Hamiltonian formulation where constraints appear as constants of the motion.
- Each constraint equation is replaced by its time-derivative; the Lagrange multipliers associated with these time-differentiated constraints are called the *strictions* and have dimensions of momentum.
- One derives the conjugate variables to be used in the Hamiltonian formulation from the constrained Lagrangian (the classical Lagrangian plus constraint terms). Thus, the conjugate variables are not quite the same as the usual momentum variables that arise from the classical Lagrangian alone; these new variables are the *impetuses*.
  - Roughly speaking, the striction describes that part of the momentum arising from the constraint forces, and the impetus describes that part due to the remaining forces. Note that if there are no external forces, it is still the total momentum that is conserved, not the impetus.
- One constructs a “pre-Hamiltonian” from the constrained Lagrangian; this differs from the usual Hamiltonian only in that it still depends on the as yet undetermined strictions.
- The Hamiltonian is obtained by minimizing the pre-Hamiltonian with respect to the strictions for fixed values of the state variables. This minimization determines the strictions and can usually be reduced to the solution of a system of linear algebraic equations.
- The resulting unconstrained Hamiltonian system is integrated in time, solving for the strictions at each time step.

## OVERVIEW OF CARTWHEEL

The physical model of the boom dynamics yields a system of nonlinear partial differential equations in which the independent variables are time and arc length along each boom, both of which must be discretized for the numerical implementation.

For the discretization in arc length (often called the semi-discretization), we model each boom as a sequence of  $N_n$  elastically connected rigid segments. As implemented, the

integration errors are of order  $h^2$  as the segment length,  $h$ , goes to zero, and the errors vanish for any segment length when the spacecraft rotates uniformly with zero deflection in the wires.

There is a position and orientation associated with each boom segment. Orientations are represented by quaternions, so there are seven configuration variables for each segment, along with their conjugates (the impetuses). Note that the quaternion normalizations are not imposed by brute force but are maintained by the integration method. There are  $N_a$  antennas ( $N_n$  can be different for each antenna). There also is a position and orientation for the spacecraft hub and a position for the center of mass of the entire system.

For each time step, the strictions are calculated as the solution of a linear system of equations; the number of strictions is  $3N_nN_a$  representing the stretch and shear constraints for each segment, plus  $3N_a$  to constrain the position of the antenna attachments to the hub, plus 3 more to separate relative position coordinates from the system center of mass. (The striction equations decouple into  $N_a$  banded, linear systems, each with  $3N_n$  unknowns, together with the solution of one system with  $3N_a$  unknowns, and one with 3 unknowns for the center of mass.)

For the discretization in time, the Hamiltonian system, consisting of  $(14N_nN_a + 20)$  first-order ordinary differential equations for the coordinates and conjugate impetuses, is stepped forward using a midpoint method. That is, if  $z^k$  is the state at time  $t_k$  and  $F(z)$  is its time derivative, then

$$z^{k+1} = z^k + \Delta t F\left(\frac{z^{k+1} + z^k}{2}\right) \quad (1)$$

This is an implicit integration scheme wherein the time derivative evaluation requires knowledge of the new state. Implicit methods are numerically more stable than explicit methods but require solution of a possibly nonlinear system of equations for  $z^{k+1}$  at each time step. Equation (1) is solved by a fixed-point iteration method but a Newton method could also be used.

The integrator was chosen not only for its inherent stability but because it is one of the simplest of the symplectic integration methods. One consequence of this is that it preserves quadratic invariants (see, for example, Ref. 4). This means that any theoretical constant of the motion that is quadratic in the state variables will not be subject to any numerical error beyond machine roundoff. In practice, the error level is determined by the tolerance allowed when iterating for a solution to Eq. (1).

Some examples of quadratic invariants are the quaternion norms and the amount of stretch and shear between segments of the appendages. Other invariants may depend on the boundary conditions of a particular example. For this problem, total linear momentum and total angular momentum are quadratic invariants. On the other hand, although the total energy is a conserved quantity (there is no damping in the model), the Hamiltonian is not quadratic in the state variables. Consequently, the code is not expected to conserve the energy as well as the quadratic invariants.

Note that this formalism enforces the constraints by solving for and imposing the requisite forces, and the resulting *augmented* Hamiltonian system is unconstrained. Thus, while the stretch and shear are constrained to vanish, they are not set to zero *ad hoc*. They are free to take on any value but remain small only because of the imposed forces (the strictions). The point here is that the finite step size in the time-integration scheme could conceivably cause growing errors in the constraints. The use of a symplectic integrator guarantees that this will not happen.

The first test of the code was to examine the invariants. The errors in the quadratic invariants should remain small (close to the tolerance of the solution of Eq. (1)), and the error in the total energy should grow with a slope proportional to the time step squared. This has been demonstrated remarkably well for both single rod and closed ring simulations (Ref. 3). (Interest in these early rod and ring tests goes beyond just verifying the impetus-striction method. They are well suited for modeling some aspects of biomolecules such as bacterial DNA (Ref. 5).)

Later tests verified that the invariants are properly conserved also for the full spacecraft model (multiple booms coupled through a rigid hub) and that accurate results are obtained for small perturbations with the booms discretized into relatively few segments.

## THE POLAR SPACECRAFT

The mission of the POLAR spacecraft is to observe the electromagnetic field of the Earth's polar regions. The hub of the spacecraft is about 1.58 m in radius. The mass is roughly 1000 kg. Nominally, the spacecraft spins at a rate of 10 revolutions per minute (rpm) with the spin axis oriented near the orbit normal vector. Spin axis direction is determined using a Sun sensor and an Earth sensor. The spacecraft has two axial booms extending along the positive and negative spin axes. The axial booms are effectively rigid and are rigidly attached to the spacecraft hub. The spacecraft also has two radial booms, holding magnetometers, that are effectively rigid and rigidly attached to the spacecraft hub.

The spacecraft has four flexible wire booms extending radially from the hub and arranged symmetrically. Each wire boom can be deployed to a maximum length of 65 m. Each wire has a radius of 1 mm. The wire booms serve as antennas to observe the ambient electromagnetic field and also to help stabilize the spacecraft rotation. During the phase of the mission treated in this study, one pair of wire booms was deployed to 50 m while the other was deployed to 65 m.

The POLAR spacecraft orbits the Earth in a near polar, elliptical orbit (roughly  $2 \times 9$  Earth radii). The pre-maneuver orbit had semimajor axis equal to 34251 km, the eccentricity was 0.662, the inclination was 86.01 deg, and the right ascension of the ascending node was 26.809 deg. The orbital period is approximately 12 hours.

During most of the mission, the spacecraft spin axis is maintained along the positive or negative orbit normal. As the Sun-orbit plane geometry changes, it is necessary about every 6 months to reorient the spin axis for solar thermal constraints and to keep the Sun out of the field of view of sensitive instruments. At those times, the spin axis is reoriented

by 180 deg from positive to negative orbit normal, or vice versa. This is done while keeping the Sun vector nearly perpendicular to the spin axis. Due to current thruster limitations, this maneuver is performed in two separate 90 degree slews, each lasting roughly 3.5 hours.

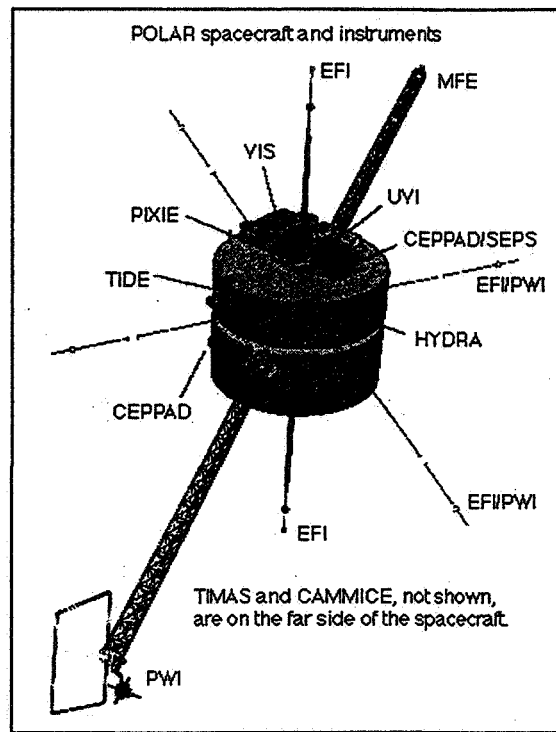


Figure 1. The POLAR spacecraft and instruments.

This study discusses one such maneuver that was performed on April 16-17, 1996. We anticipated that the maneuver, although performed slowly, would induce small vibrations in the flexible wire booms. There are no instruments onboard the spacecraft to measure directly the deformations of the booms. However, due to their length during this phase of the mission, the booms contribute about 50% of the total moment of inertia about the spacecraft's spin axis. It was therefore expected that if there were any flexure of the booms, this would have a measurable effect on the attitude of the spacecraft hub.

## SIMULATION RESULTS

In this section, we describe the results of numerical simulations of the POLAR spin reorientation maneuver and compare results from flexible and rigid body models. Our simulations focused upon the effects of boom flexibility on the attitude dynamics of the spacecraft hub. Because of their length, the booms could exhibit large bending motions under the appropriate circumstances. However, because the spacecraft spins at 10 rpm, each boom experiences a stiffening centrifugal force that tends to inhibit deformations. In addition, the rate of the spin reorientation maneuver is small (90 degrees in 3.5 hours), so



the perturbing forces and torques acting on the booms are small. For these reasons, only small deformations of the wire booms were found.

To display the deformations, the position of the end of each segment is represented in a rotating body coordinate system attached to the spacecraft hub. If a boom continued to point radially outward from the hub, as it does during a steady spin, then the boom would exhibit no motion in this body frame. During the simulation of the spin reorientation maneuver, each boom oscillated primarily out of the spin plane and parallel to the hub's spin axis, designated as the z-axis. This motion is shown in Figure 2, where the tip's displacement is plotted as a function of time each 0.5 second. The spacecraft rotates 200 times during the 20 minute period shown. In Figure 2, the displacement is displayed as a fraction of the boom length, which is 50 meters. The amplitude of the oscillation is about 0.014 of the total length, or about 0.7 m.

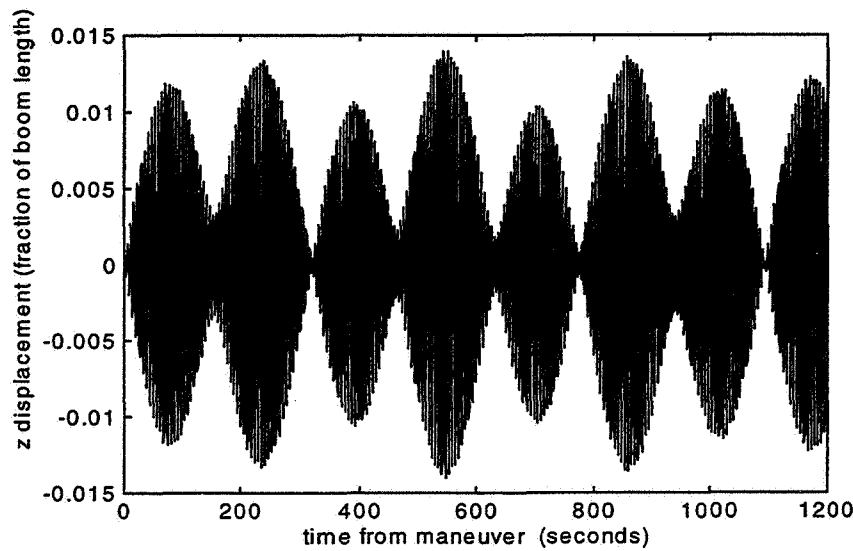


**Figure 2. Out-of-plane displacement of boom tip for model with two unequal length pairs of wire booms (peak amplitude corresponds to 0.7 m).**

The complex motion in Figure 2 can be approximated well by a superposition of three distinct oscillations:

$$z(t) = \sum_{j=1}^3 A_j \cos(2\pi t / T_j) + B_j \sin(2\pi t / T_j) \quad (2)$$

where the periods are  $T_1 = 6.0$  sec,  $T_2 = 5.778$  sec, and  $T_3 = 5.872$  sec. The amplitudes are  $A_1 = -5.25 \times 10^{-3}$ ,  $B_1 = 2.8 \times 10^{-6}$ ,  $A_2 = 6.91 \times 10^{-3}$ ,  $B_2 = -3.6 \times 10^{-5}$ ,  $A_3 = -1.85 \times 10^{-3}$ , and  $B_3 = 1.3 \times 10^{-6}$ .

The oscillation with 6 sec period is associated with the spin rate of the spacecraft. The other two frequencies appear to be associated with driven oscillations of the two pairs of booms of length 50 m and 65 m, respectively. To test this, we ran a simulation

with equal length booms and all other parameters the same. The resulting motion of the tip of each boom was less complex and decomposed into the sum of oscillations with only two distinct periods of 6.00 sec and 5.79 sec as shown in Figure 3.

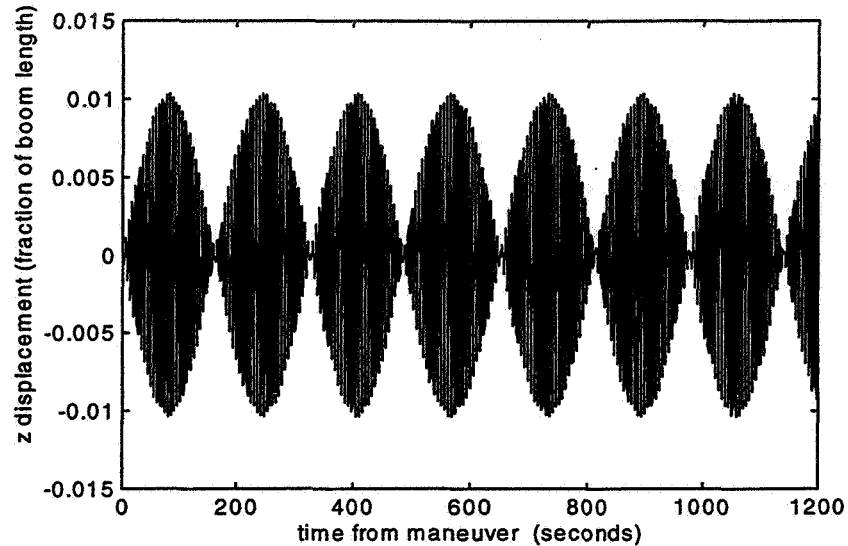


**Figure 3. Out-of-plane displacement of boom tip for model with four equal length booms (peak amplitude corresponds to 0.5 m).**

Although the motion of the tip of each boom is fairly complex, each boom moves nearly as a rigid rod. To demonstrate this, Figure 4 shows the maximum deviation of a boom from the straight line between its base and its tip. Thus, the oscillations shown in Figure 2 are subtracted out, leaving only the deviation caused by any curvature of the

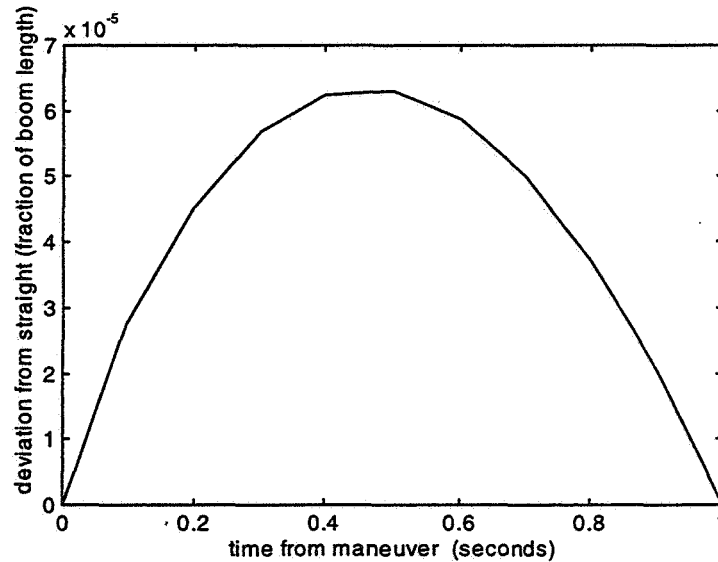


**Figure 4. Maximum deviation of boom from straight line (peak amplitude corresponds to 3 mm).**

boom. Again, the displacement is measured as a fraction of the boom length. The maximum displacement from the straight configuration is seen to be only about  $6 \times 10^{-5}$  times the 50 m length, or 3 mm.

Because each boom behaves essentially as a rigid body, the most significant flexibility effects can be captured by representing each boom as a rigid rod attached to the hub by a flexible hinge. Simulations with various, reasonable amounts of spring force in the hinge at the base show that even this elasticity has only a small effect. Thus, one can set the deformation restoring force to zero at the base.

In this simulation, the initial conditions were taken from the April 1996 reorientation maneuver. The spin axis was initially pointing toward right ascension 116.3 deg and declination -7.7 deg. The final attitude following the first 90 deg maneuver segment was estimated to be right ascension 27.2 deg and declination -80.0 deg (Ref. 6). Figure 5 shows the right ascension and declination of the hub for the simulated maneuver. For comparison, the simulation for a totally rigid spacecraft with the same mass properties is also shown. (Note that the initial attitude differs somewhat from values given in Ref. 6. This small offset is caused by a different choice of sensor biases solved for together with the attitude and does not affect the analysis.)

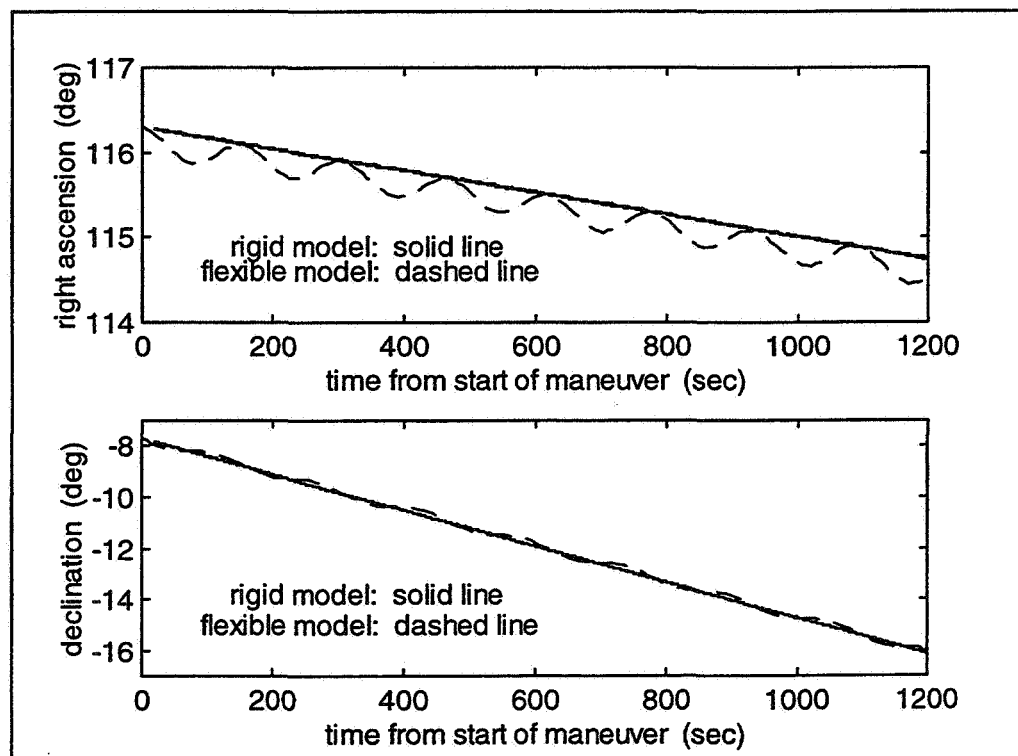


**Figure 5. Rigid body and flexible model simulations showing right ascension and declination of spin axis for the first 1200 seconds of spin reorientation maneuver.**

Comparison of the two simulations (flexible and rigid body) allows the effects of flexibility to be seen clearly. The flexible body simulation shows sinusoidal oscillations absent from the rigid body simulation. The period of the oscillation is about 2.6 minutes. The maximum difference in right ascension between rigid and flexible model is about 0.3 degrees. The maximum difference in declination is about 0.15 degrees. (There also are higher frequency oscillations in the rigid body attitude due to nutation that are too low in amplitude to show clearly on these plots.)

It should be noted that the flexible dynamics simulator neglects several perturbing forces that could influence the spacecraft motion. It is expected that most of these disturbances are negligible for the case under consideration. For example, gravity-gradient torques are not included. The spacecraft is near apogee during the maneuver, so the large distance from the Earth (9 Earth radii) greatly reduces the influence of gravity-gradient torque.

Internal dissipation within the wire booms could have a more significant effect on the dynamics. In particular, internal dissipation tends to damp out oscillations in the wires. Thus the current model would not yield physically correct results over long periods of time, but should be accurate for times shorter than the decay time. This is observed to be on the order of tens of minutes (see results below). An accurate model of internal dissipation could be difficult, due to the complex composite structure of the wire, and would require a more detailed knowledge of the material parameters.

The driving torque was modeled as continuous and constant. In reality, thrusters are used to supply the torque. They are fired in pulses, timed with the spin period, to perform the maneuver. The periodic pulsing of the control torque is expected to excite higher frequency vibrations of the wires that are not excited in the model.

Thermal effects are known to influence the dynamics on other spacecraft. However, these tend to be small and brief disturbances. Furthermore, for the orbital geometry during this reorientation maneuver, the POLAR spacecraft does not enter the Earth's shadow so the wire temperature is not expected to vary significantly.

Some other effects one might consider are perturbations due to atmospheric drag and fuel slosh. However, the spacecraft is at a sufficiently high altitude that torques from atmospheric drag are negligible, and fuel slosh is not a factor because the maneuver is performed sufficiently slowly compared to the spin rate.

## **COMPARISON OF SIMULATION WITH FLIGHT DATA**

To estimate the true attitude of the POLAR spacecraft during the maneuver, the spacecraft telemetry was processed using an Attitude Ground Support System (Ref. 7) designed for spinning spacecraft. Attitude estimation was based upon Earth horizon sensor and spinning Sun sensor readings. The Earth and Sun angle measurements later were reprocessed using MATLAB where it was possible to insert sensor biases overlooked in the initial processing. In particular, this reprocessing corrected timing errors and rejected spurious solutions.

Knowing the Sun and Earth reference vectors, the measured Earth midscan angle yields the angle from the spin axis to the nadir vector with twofold ambiguity. (As the spacecraft spins, the Earth is measured as a time offset from the Sun pulse. This is converted into an angle using the spin period determined from the time between Sun pulses.) The spin axis then is found at the intersection of the two cones defined by the nadir and Sun angles (another twofold ambiguity). Knowing the path of the planned maneuver made it simple to select the correct solution. (The initial spin direction is unambiguously estimated from a large batch of data obtained before the slew.) Reference 8 gives details on methods for spacecraft attitude determination.

Figure 6 shows the estimated spin axis right ascension and declination angles for POLAR during the interval 03:16:46 GMT to 03:40:06 GMT, on April 16, 1996. The spin reorientation maneuver begins at time 03:20:06 GMT. The results of the flexible dynamics simulation from Figure 5 are also overlaid on Figure 6.

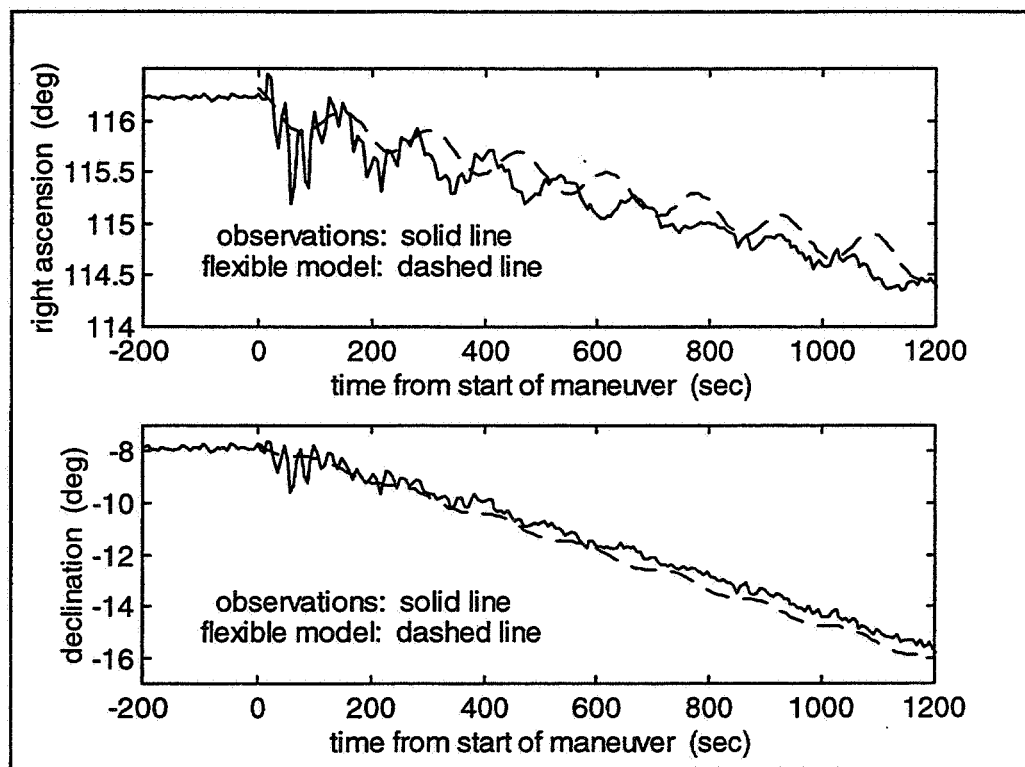


**Figure 6. Observed and simulated spin axis attitude for the first 1200 seconds of spin reorientation maneuver (observations are from POLAR spacecraft maneuver on April 16, 1996).**

As the maneuver progresses, the Earth horizon sensor scans across the Earth along various chords. The scan cone moves off the Earth at 03:42:58 GMT (time = 1372 sec, off scale on Figure 6). After that time, only Sun data is available and there is insufficient information to compute an attitude until the Earth again comes into view near the end of the maneuver. The estimated attitude also is less reliable due to larger Earth sensor uncertainty during the minutes immediately before the Earth horizon signal is lost. Thus,

although this 90 deg segment of the maneuver takes 3.5 hrs, the attitude is observable only for the first 23 min while both the Sun and Earth are detectable, and the final 3 min are discarded.

As seen in Figure 6, the flexible body model exhibits oscillations that are qualitatively similar to the oscillations in the observed flight data. These slow oscillations are not present in the rigid body model in Figure 5. The flexible model oscillations match up exactly with the envelope of the boom tip displacements shown in Figure 2 and probably correspond to a beat frequency between two out-of-plane modes.

The quantitative features of the slow oscillations depend primarily on the material parameters of the wire booms, in particular the mass density and the bending stiffnesses. The periods are approximately 2.6 min for the flexible simulation and 2.2 min for the observed attitude. This 15% difference might be attributed to uncertainties in the material parameters available to us.

There also is fairly good agreement between the simulated and observed amplitudes, however the observed oscillation decays with time while the amplitude of the simulation does not. This reflects the absence of dissipative terms in the dynamics model. As expected, there also are higher frequency oscillations (dominated by a mode with a 30 sec period) that are not found in the simulation results. The simulation would likely have shown a much richer spectrum if the model had included more realistic pulsed thrusters rather than a continuous control torque.

## CONCLUSIONS

In this study we have examined the attitude of the POLAR spacecraft during a reorientation maneuver of the spin axis. The attitude computed using flight telemetry was compared with simulated data obtained by modeling the spacecraft as a rigid hub with four flexible wire booms. A comparison with a totally rigid body model also was given. The flexible model simulation captures the most important qualitative features of the flight data and is in reasonable quantitative agreement, as well.

The Cartwheel simulator employs an implicit midpoint time-stepping scheme to perform the numerical time integration and to preserve the dynamics constraints to a high accuracy. If high numerical accuracy is not maintained, the simulation will diverge after only a few minutes of simulated dynamics. The price for high accuracy is relatively slow computational speed. For example, with each boom represented as a single rigid rod, twenty minutes of simulated data required about ten minutes of CPU time on a DEC Alpha workstation. When each boom was subdivided into five-meter segments, yielding 46 segments in all, then twenty minutes of simulated data required about ten hours of CPU time.

A number of features could be added to Cartwheel to improve its accuracy. The most important additional feature would be a more complete actuator model, particularly pulsed thrusters. Following this, one could improve the modeled material properties of the wire booms, including dissipation and more accurate mass and stiffness parameter

values. Environmental perturbations could contribute small corrections, and sophisticated control laws would allow testing a wider variety of scenarios. These improvements could be implemented without making major changes to the underlying flexible dynamics model. With these additions, Cartwheel would be useful as an analysis tool to study the nonlinear dynamics of extended systems such as long-boom spinners or tethered satellites. Its strength would be most apparent for applications to systems under contingency conditions where the deformations are too extreme to be described using linearized or modal dynamics.

## ACKNOWLEDGMENTS

This work was performed under a cooperative agreement among the National Science Foundation (Industrial Postdoctoral Fellowship award number 9505450), the National Aeronautics and Space Administration/Goddard Space Flight Center (contracts GS-35F-4381G and NAS 5-31000), Computer Sciences Corporation, and the University of Maryland Institute for Physical Science and Technology. Additional support came from the Air Force Office of Scientific Research. The authors would particularly like to thank Professor John Maddocks, currently at the Swiss Federal Institute of Technology, who provided guidance for much of the theoretical work that preceded the simulator development.

## REFERENCES

1. D. J. Dichmann, *Hamiltonian Dynamics of a Spatial Elastica and the Stability of Solitary Waves*, Ph. D. thesis, University of Maryland, 1994.
2. D. J. Dichmann, J. H. Maddocks, and R. L. Pego, "Hamiltonian Dynamics of an Elastica and the Stability of Solitary Waves," *Arch. of Rational Mech.*, to appear.
3. D. J. Dichmann and J. H. Maddocks, "An Impetus-Striction Simulation of the Dynamics of an Elastica," *J. Nonlinear Sci.*, Vol. 6, 1996, pp. 271-292.
4. J. M. Sanz-Serna and M. P. Calvo, *Numerical Hamiltonian Problems*, Chapman and Hall, 1994.
5. M. Tabor and I. Klapper, "Dynamics of Twist and Writhe and the Modeling of Bacterial Fibers," in *Mathematical Approaches to Biomolecular Structure and Its Applications*, 82, Springer, New York, 1996, pp. 139-160.
6. J. Dibble and S. Good, "Interplanetary Physics Laboratory (WIND) and Polar Plasma Laboratory (POLAR) Postlaunch Report," Goddard Space Flight Center, Flight Dynamics Division, 553-FDD-96/006R0UD0, July 1994.
7. A. Calder, "Multimission Spin-Axis Stabilized Spacecraft (MSASS) Flight Dynamics Support System User's Guide, Update 1," Goddard Space Flight Center, Flight Dynamics Division, 552-FDD-91/019R0UD1, March 1993.
8. J. S. Wertz, ed., *Spacecraft Attitude Determination and Control*, D. Reidel Publishing Co., Dordrecht, The Netherlands, 1978.





# XMM: SLEW PERFORMANCE CALIBRATION AND ASSESSMENT

M. J. Tuttlebee<sup>†</sup>

540-18

169338

339601  
12P.

During slew manoeuvres between scientific observations, the XMM Inertial Pointing and Slew (IPS) mode control laws compute profiled momentum demands to the reaction wheels in order to achieve the desired change in three-axis attitude. These momentum profiles are computed on-board, together with the demanded Sun position in the Fine Sun Sensor (FSS) field-of-view, such that the change in attitude is about the eigenaxis. The outputs of the FSS along with the demanded sun position are used to provide closed-loop attitude control about the roll and pitch axes during the slew, with the yaw axis being open-loop.

This implies that a number or a combination of system model parameters must be calibrated, in order to limit the size of the attitude error with respect to the planned target attitude due to the lack of yaw control.

A description of the IPS mode control law and the principal contributors to slew errors is presented and an algorithm based on an Extended Kalman Filter is used to estimate 15 states (3 spacecraft rates, 3 external torques, and 9 components of the 'effective' normalised inertia matrix), during a series of small offset manoeuvres separated by stable pointing phases used to estimate the environmental disturbance torques.

The performance of the algorithm has been assessed by a complete simulation of the XMM dynamics, kinematics, sensors (Star Tracker and Fine Sun Sensor), control laws and actuators (Reaction Wheel Unit) and the results are presented.

Finally, a series of tests on ISO, which uses the same Star Tracker (STR) and FSS, are planned at the end of its operational life. This data will be processed on-ground using the proposed algorithm.

## INTRODUCTION

ESA's X-ray Multi Mirror observatory, XMM, is planned for launch on August 2nd 1999 by an Ariane 5 launch vehicle.

During the Launch and Early Orbit Phase, (LEOP), about seven hours after separation from the launcher, an initial calibration of the yaw principal inertia will be performed to remove the largest source of attitude error for open-loop slews. The LEOP will last up until 10 days after launch whereby it will be followed by a commissioning phase.

During the commissioning phase, a complete calibration of the spacecraft moments and products of inertia, Reaction Wheel Unit (RWU) alignments and reaction wheel moments of inertia will be performed. These uncertainties in the RWU model parameters being the second most important source of attitude errors for open-loop slews.

The Flight Dynamics mission planning functions, during the XMM<sup>1</sup> routine scientific phase, should benefit from these improved open-loop slew accuracies.

---

<sup>†</sup> Science Systems Space Ltd., 23 Clothier Rd., Brislington, Bristol, BS4 5PS, England. Currently based at the European Space Operations Centre, Robert Bosch Str. 5, 64293 Darmstadt, Germany.

# THE IPS MODE CONTROL LAWS

The IPS mode<sup>2,3</sup> provides two distinct functions which are described as follows.

## Fine Pointing Phase

This is used to maintain a stable fine pointing inertial attitude throughout the mission, including scientific observation phases. During nominal sunlit operations, the Fine Sun Sensor (FSS) is used to control the roll axis. The pitch and yaw axes are controlled using the Star Tracker (STR).

In order to maintain a true inertial attitude, a sun steering law is implemented on-board. This is used to adapt the roll reference demand input to the control law, in order to take into account the motion of the Sun in the FSS field-of-view.

During the stable pointing phase, the yaw control law computes a filtered estimate of the yaw disturbance, which the on-board software uses to initialise the controller as soon as the slew phase has been commanded. This is necessary to compensate for the yaw disturbance torque throughout the slew phase. Any changes of the disturbance torque throughout the slew will not be compensated. At the same time, the proposed calibration algorithm estimates the disturbance torques prior to executing the calibration slews.

In addition, it is also possible to make small adjustments to the spacecraft attitude by redefining the demanded position of the guide star and the sun. These changes can be commanded using references generated by a profiled offset steering law (small offset manoeuvre) or in the case of attitude changes less than 1 arcmin, a step change to the demanded positions can be commanded. In both cases, the attitude control references are exactly the same as for the stable pointing phases with three-axis attitude control.

The profiled offset steering law (small offset manoeuvre) is used to execute the slew performance calibration manoeuvres.

## Slew Phase

Slew manoeuvres are performed open-loop about the yaw axis and closed-loop about the roll and pitch axes, using FSS outputs. The control law inputs are the predicted sun positions and wheel momenta as a function of time, to give the required slew about the eigenaxis.

The computation of the wheel momentum profiles assumes a knowledge of the following system model parameters:-

- The spacecraft moments and products of inertia
- The moments of inertia of the reaction wheels
- The alignments of the reaction wheels with respect to the spacecraft functional coordinate system

It is for this reason and the fact that the yaw axis is open-loop, that the accuracy of slew manoeuvres is significantly more dependant upon the accuracy of these on-board parameters, in comparison to attitude control systems where gyroscopes are employed. The build up of attitude error is shown to be about the instantaneous sun-line<sup>3,4</sup>.

It is possible to update these on-board parameters by ground command once they have been calibrated in-orbit.

# SLEW PERFORMANCE CALIBRATION ALGORITHM

The calibration algorithm is used to estimate nine parameters that can be expressed as a function of the following unknown system model parameters:-

- Spacecraft Inertia matrix (rigid body)
- Reaction wheel moment of inertia uncertainties
- Reaction wheel unit alignment uncertainties

Then by selecting the unknown system model parameters such that the estimation results are preserved, then in the case of perfect estimates, the effects due to the above uncertainties can be compensated and will therefore not introduce errors during open-loop slew manoeuvres.

The system dynamic model used to propagate the system state vector between measurement updates and the associated measurement equation as required in the formulation of the estimation algorithms, are presented as follows. These algorithms are based on a 15 state Extended Kalman Filter, which is used to estimate 3 spacecraft body rates, 3 external environmental disturbance torques and 9 parameters that are a function of the unknown system model parameters described above.

## System Dynamic Model

We assume that the spacecraft is a rigid body with a reaction wheel unit. The model of the system dynamics is therefore given by:-

$$\dot{\omega} = J^{-1}(\tau_{ext} - \omega \wedge (J\omega + h) - \dot{h}) \quad (1)$$

where

- $\omega$  is the spacecraft body rate vector at time  $t$
- $J$  is the spacecraft inertia matrix (rigid body)
- $\tau_{ext}$  are the externally applied torques (environmental disturbance torques)
- $h$  is the wheel momentum vector in spacecraft axes at time  $t$

Then the derivative of the wheel momentum vector is given by the equation:-

$$\dot{h} = \frac{d}{dt}(A_{bw}J_w\omega_w) \quad (2)$$

where

- $A_{bw}$  is the transformation from wheel axes to the spacecraft functional frame,
- $J_w$  is a diagonal matrix of wheel moments of inertia, and
- $\omega_w$  are the reaction wheel speeds which are available in telemetry.

The reaction wheel unit alignment matrix and moments of inertia are in general known only to within specified uncertainties:-

$$\begin{aligned} A_{bw} &= \hat{A}_{bw} + \Delta A_{bw} \\ J_w &= \hat{J}_w + \Delta J_w \end{aligned} \quad (3)$$

where

- $\Delta A_{bw}$  is a 3x3 matrix of the reaction wheel unit alignment uncertainties, and
- $\Delta J_w$  is a diagonal 3x3 matrix of reaction wheel moment of inertia uncertainties.

Substituting Eq(3) into Eq(2) yields:-

$$\begin{aligned}\dot{\hat{h}} &= (\hat{A}_{bw} + \Delta A_{bw} + \hat{A}_{bw} \Delta J_w \hat{J}_w^{-1} + \Delta A_{bw} \Delta J_w \hat{J}_w^{-1}) \hat{J}_w \dot{\omega}_w \\ \dot{\hat{h}} &= (\hat{A}_{bw} + \Delta A_{bw} + \hat{A}_{bw} \Delta J_w \hat{J}_w^{-1} + \Delta A_{bw} \Delta J_w \hat{J}_w^{-1}) \hat{A}_{wb} \frac{d}{dt}(\hat{h})\end{aligned}\quad (4)$$

where

$\Delta A_{bw}$  is a 3x3 matrix of the reaction wheel unit alignment uncertainties,

$\Delta J_w$  is a diagonal 3x3 matrix of reaction wheel moment of inertia uncertainties,

$A_{bw}$  is the transformation from wheel axes to the spacecraft functional frame,

$A_{wb}$  is the inverse of  $A_{bw}$ , and

$\hat{h}$  is the wheel momentum vector in the spacecraft functional frame.

$\wedge$  denotes the nominal value of the quantity. In the case of the wheel alignments and moments of inertia, this data is based on pre-flight measurements.

Then substituting Eq(4) into Eq(1) yields:-

$$\dot{\omega} = J^{-1}(\tau_{ext} - \omega \wedge (J\omega + D\hat{h})) - J^{-1}D \frac{d}{dt}(\hat{h})\quad (5)$$

where on neglecting 2nd order error terms:-

$$D = \begin{bmatrix} d_1^T \\ d_2^T \\ d_3^T \end{bmatrix} \approx I_3 + \Delta A_{bw} \hat{A}_{wb} + \hat{A}_{bw} \Delta J_w \hat{J}_w^{-1} \hat{A}_{wb}\quad (6)$$

The state vector chosen for estimation is then given by:-

$$x = \begin{bmatrix} \omega \\ \tau \\ d \end{bmatrix}\quad (7)$$

where the 9-vector,  $d$ , is made up of the rows of the matrix  $D$ ,  $(d_1, d_2, d_3)$ .

Eq(5) forms the basis for propagation of the system state vector between measurement updates.

Linearisation of this equation will be required to propagate between measurement updates: the system state transition matrix, using Eq (8), and the error state covariance matrix, using Eq(9). This linearisation is done numerically using the current estimate of the system state vector.

$$\dot{\Phi}(t, t_{k-1}) = F(t)\Phi(t, t_{k-1})\quad (8)$$

$$P^-(t_k) = \Phi(t_k, t_{k-1})P^+(t_{k-1})\Phi^T(t_k, t_{k-1}) + U(t_k, t_{k-1})\quad (9)$$

where

$F(t)$  is the linearised system dynamics matrix,

$\Phi$  is the system state transition matrix,

$P$  is the error state covariance matrix, and

$U$  is the state noise covariance matrix.

## Measurement Equations

The measurements available during the short calibration slews, performed using the IPS small offset manoeuvre law, are the sun vector constructed from the fine sun sensor outputs and the star vector constructed from the star tracker outputs. For the estimation algorithm, equations are required to be a function of the system state vector, which was previously defined by Eq (7). During slew manoeuvres the observation vectors,  $(S_{k-1}, S_k)$ , constructed from two successive samples of the sensor measurements, are perpendicular to the instantaneous spacecraft body rate vector. The rate vector can therefore be written as:-

$$\omega_{orthog} = \frac{S_k \wedge S_{k-1}}{\Delta T} \quad (10)$$

where  $\Delta T$  is the sampling period, and it follows that:-

$$\dot{S}_k = S_k \wedge \omega_k = S_k \wedge (S_k \wedge S_{k-1}) \frac{1}{\Delta T} \quad (11)$$

Applying the vector triple product identity yields:-

$$z_k = S_k \wedge \omega_k = [S_k S_k^T - I_3] \frac{S_{k-1}}{\Delta T} \quad (12)$$

The measurement equation is then a time-varying linear function of the system state vector and can be expressed as a function of the current estimate of the state vector as:-

$$z_k = H_k x_k \quad (13)$$

where it follows from Eq(12) that:-

$$H_k = \begin{bmatrix} H_{\omega, k} & 0_{3 \times 3} & 0_{3 \times 9} \end{bmatrix}$$

$$H_{\omega, k} = \begin{bmatrix} 0 & -S_{z, k} & S_{y, k} \\ S_{z, k} & 0 & -S_{x, k} \\ -S_{y, k} & S_{x, k} & 0 \end{bmatrix} \quad (14)$$

The measurements provided by Eq(12) will be used to derive state corrections, using Eq(15), in order to refine the current estimates of the state vector. Also, the measurement geometry matrix given by Eq(14) will be used to compute the update gains, using Eq(16) and to perform measurement updates to the error state covariance matrix, using a numerically stable version of Eq(17).

$$\hat{x}_k^+ = \hat{x}_k^- + K_k (z_k - H_k \hat{x}_k^-) \quad (15)$$

$$K_k = P^-(t_k) H_k^T [H_k P^-(t_k) H_k^T + R]^{-1} \quad (16)$$

$$P^+(t_k) = (I_3 - K_k H_k) P^-(t_k) \quad (17)$$

where

$K$  is the update gain matrix,

$P$  is the error state covariance matrix, and

$R$  is the measurement noise covariance matrix.

## Solution for Unknown System Model Parameters

The estimation algorithm provides an accurate estimate of the following matrix

$$\hat{D} = \hat{J}J^{-1}(\hat{A}_{bw} + \Delta A_{bw} + \hat{A}_{bw}\Delta J_w\hat{J}_w^{-1})\hat{A}_{wb} \quad (18)$$

Rearranging, we have

$$J = (\hat{A}_{bw} + \Delta A_{bw} + \hat{A}_{bw}\Delta J_w\hat{J}_w^{-1})\hat{A}_{wb}\hat{D}^{-1}\hat{J} \quad (19)$$

Now for the operational wheelset, the transformation from wheel reference axes to the spacecraft functional coordinate system is given by

$$A_{bw} = [B_1 | B_2 | B_3] = \hat{A}_{bw} + \Delta A_{bw} \quad (20)$$

where the alignment for the  $i^{\text{th}}$  wheel in the spacecraft functional coordinate system is given by

$$B_i = \begin{bmatrix} \sin \theta_i \\ -\cos \theta_i \sin \phi_i \\ \cos \theta_i \cos \phi_i \end{bmatrix} = \begin{bmatrix} \sin(\hat{\theta}_i + \Delta \theta_i) \\ -\cos(\hat{\theta}_i + \Delta \theta_i) \sin(\hat{\phi}_i + \Delta \phi_i) \\ \cos(\hat{\theta}_i + \Delta \theta_i) \cos(\hat{\phi}_i + \Delta \phi_i) \end{bmatrix} \quad (21)$$

which, after neglecting 2nd order terms, becomes

$$B_i = \hat{B}_i + \Delta B_i \quad (22)$$

$$B_i = \begin{bmatrix} \sin \hat{\theta}_i \\ -\cos \hat{\theta}_i \sin \hat{\phi}_i \\ \cos \hat{\theta}_i \cos \hat{\phi}_i \end{bmatrix} + \begin{bmatrix} \cos \hat{\theta}_i & 0 \\ \sin \hat{\theta}_i \sin \hat{\phi}_i & -\cos \hat{\theta}_i \cos \hat{\phi}_i \\ -\sin \hat{\theta}_i \cos \hat{\phi}_i & -\cos \hat{\theta}_i \sin \hat{\phi}_i \end{bmatrix} \begin{bmatrix} \Delta \theta_i \\ \Delta \phi_i \end{bmatrix}$$

Using Eq(22), the  $i^{\text{th}}$  column of the following matrix

$$\hat{A}_{bw} + \Delta A_{bw} + \hat{A}_{bw}\Delta J_w\hat{J}_w^{-1} \quad (23)$$

is given as follows

$$c_i = \begin{bmatrix} \cos \hat{\theta}_i & 0 & \sin \hat{\theta}_i \\ \sin \hat{\theta}_i \sin \hat{\phi}_i & -\cos \hat{\theta}_i \cos \hat{\phi}_i & -\cos \hat{\theta}_i \sin \hat{\phi}_i \\ -\sin \hat{\theta}_i \cos \hat{\phi}_i & -\cos \hat{\theta}_i \sin \hat{\phi}_i & \cos \hat{\theta}_i \cos \hat{\phi}_i \end{bmatrix} \begin{bmatrix} \Delta \theta_i \\ \Delta \phi_i \\ \Delta R_i \end{bmatrix} + \hat{B}_i \quad (24)$$

$$c_i = D_i v_i + \hat{B}_i$$

where the quantity,  $\Delta R_i$ , is defined as follows

$$\Delta R_i = \frac{J_{w_i} - \hat{J}_{w_i}}{\hat{J}_{w_i}} = \frac{\Delta J_{w_i}}{\hat{J}_{w_i}} \quad (25)$$

Then, the spacecraft inertia matrix given by Eq(19) can be written as

$$J = \begin{bmatrix} c_1 & c_2 & c_3 \end{bmatrix} \hat{A}_{wb} \hat{D}^{-1} \hat{J} \quad (26)$$

Defining the error in the spacecraft inertia matrix as

$$\Delta J = J - \hat{J} \quad (27)$$

Then, Eq(26) can be re-written as

$$\Delta J E = \begin{bmatrix} D_1 v_1 & D_2 v_2 & D_3 v_3 \end{bmatrix} + F \quad (28)$$

where

$$E = \hat{J}^{-1} \hat{D} \hat{A}_{bw} = \begin{bmatrix} e_1 & e_2 & e_3 \end{bmatrix} \quad (29)$$

$$F = (I_3 - \hat{D}) \hat{A}_{bw} = \begin{bmatrix} f_1 & f_2 & f_3 \end{bmatrix}$$

From Eq(28) above and using the fact that  $\Delta J$  is a symmetric matrix, then

$$\Delta J e_i = \begin{bmatrix} e_{1i} & e_{2i} & e_{3i} & 0 & 0 & 0 \\ 0 & e_{1i} & 0 & e_{2i} & e_{3i} & 0 \\ 0 & 0 & e_{1i} & 0 & e_{2i} & e_{3i} \end{bmatrix} \begin{bmatrix} \Delta J_{11} \\ \Delta J_{12} \\ \Delta J_{13} \\ \Delta J_{22} \\ \Delta J_{23} \\ \Delta J_{33} \end{bmatrix} = G_i \Delta \vec{J} \quad (30)$$

Then from Eqs (28), (29), and (30), we can express these equations as a system of linear equations of the form

$$\begin{bmatrix} G_1 & -D_1 & 0 & 0 \\ G_2 & 0 & -D_2 & 0 \\ G_3 & 0 & 0 & -D_3 \end{bmatrix} \begin{bmatrix} \Delta \vec{J} \\ v_1 \\ v_2 \\ v_3 \end{bmatrix} = \begin{bmatrix} f_1 \\ f_2 \\ f_3 \end{bmatrix} \quad (31)$$

where the coefficient matrix is rank-deficient and the 15 unknowns are the errors in the system model parameters.

This problem possesses an infinite number of solutions, but exactly one with a minimal 2-norm. A minimisation of the estimation errors is the desired solution. Weights which are a function of the worst case uncertainties in the system model parameters are applied to the state vector, such that the errors are equally weighted.

# SLEW PERFORMANCE CALIBRATION PROCEDURES

The procedures consist of executing 3 independent yaw, pitch and roll slews using the profiled offset steering law. The procedures for each calibration slew are essentially the same for each axis but with different initial conditions. In all cases, a guide star must remain tracked continuously throughout the slew manoeuvre.

Due to the operational time constraints (1 hour) during the LEOP, only the calibration of the yaw principal inertia will be performed.

During the subsequent commissioning phase, after the perigee raising burns and the opening of the mirror doors, the full calibration sequence will be performed.

The following data are read at regular intervals from the local flight dynamics telemetry history files and are converted, as specified earlier, into a suitable format as required by the algorithms:

- STR position coordinates, magnitude and star data status.
- Raw FSS roll and pitch angle data.
- Raw wheel speed data.

## Calibration Procedure

The following describes the operational procedures required to execute the yaw axis calibration small offset manoeuvre:-

- (a) Within the Inertial Pointing and Slew (IPS) Mode, slew the spacecraft to boresight the Sun on the +Z-axis (FSS axis) such that measured FSS  $\alpha = \beta = 0$  (to within 1 FSS output quantum) and the  $\pm X$  axes are in the ecliptic plane\*. This will be done using the open-loop slew mode so that a star map can be processed at the end of the slew. Select a high quality† guide star from one of the stars in the map near the centre of the STR FOV. If necessary, perform a small offset manoeuvre to place the guide star close to the centre of the STR field-of-view.
- (b) Transition to Thruster Control Mode (TCM). Command the desired wheel speeds in order to avoid operating the wheels in low speed regions ( $\omega_w > 300$  RPM) and overspeed regions ( $\omega_w < 3000$  RPM). These constraints should be taken into account during the planning of the small offset manoeuvre as well as the start and end points.
- (c) Transition back to IPS Mode. Slew back to a Sun boresighted attitude with the guide star near the edge of the STR field-of-view, so that the whole yaw width of the STR field-of-view can be used for the calibration small offset manoeuvre (~ 4 degrees).
- (d) After 1800 seconds without any motion in IPS‡, command the calibration small offset manoeuvre to execute a pure yaw slew. The maximum yaw rate during the slew is limited by the on-board control laws to about 32 arcsec/sec.
- (e) After completion of the calibration slew, and 1800 seconds without any motion in IPS, command another small offset manoeuvre back to the initial attitude. The maximum yaw rate during the slew is limited by the on-board control laws to about 32 arcsec/sec.

The pitch and roll axis calibration slews are very similar to the yaw procedure described previously and are described in<sup>4</sup>.

---

\*. This ensures that there is no attitude drift due to the motion of the Sun during the stable pointing phase and the small offset manoeuvre phase, when the sun steering law is not active

†. This star should be a bright star, ( $8.5 < m < 2$ ), to reduce the effects of STR noise and biases.

‡. This time is allocated for the on-board control law and the on-ground disturbance torque estimation processes to converge.



# SLEW PERFORMANCE CALIBRATION ASSESSMENT

The algorithm has been validated using a complete simulation of the dynamics, sensors, XMM IPS mode control laws, and actuators. These cases have been selected to demonstrate the correct performance of the estimation algorithm and its sensitivity to various conditions. The algorithm performance and sensitivity has been assessed<sup>4</sup> with respect to the following conditions:

1. Sensitivity to extreme variations of the spacecraft moments and products of inertia.
2. Sensitivity to extreme variations in reaction wheel moment of inertia and alignment uncertainties.
3. Sensitivity to FSS misalignment and biases.
4. Sensitivity to environmental disturbance torques.

In all cases, the worst case sensor and actuator noise and quantisations are used<sup>4</sup>. Also, the reaction wheels were biased to the desired values prior to the calibration small offset manoeuvre.

These simulations consist of independently executed yaw, pitch and roll slews carried out using the small offset manoeuvre law required to estimate all parameters, (i.e. the column vectors of the matrix in Eq(6)). From these column vectors, the components of the spacecraft inertia matrix, ( $J_{11}$ ,  $J_{12}$ ,  $J_{13}$ ,  $J_{22}$ ,  $J_{23}$ ,  $J_{33}$ ), three reaction wheel unit alignment angles, ( $\Delta\theta_1$ ,  $\Delta\theta_2$ ,  $\Delta\theta_3$ ), and wheel moments of inertia, ( $J_{w1}$ ,  $J_{w2}$ ,  $J_{w3}$ ) are computed by solving Eq(31). The estimation results for two examples are presented in Tables 1 and 2 below.

Spacecraft Inertias (kgm <sup>2</sup> )	Actual	Initial Predicted	Estimated
$J_{11}$	5928	6587	5926.377
$J_{12}$	73	23	72.102
$J_{13}$	260	160	241.016
$J_{22}$	24545	27273	24549.277
$J_{23}$	24	4	22.444
$J_{33}$	27821	30913	27847.007
Wheel Inertia Errors (%)	Actual	Initial Predicted	Estimated
$\Delta J_{w1}$	-0.5	0.0	-0.3542
$\Delta J_{w2}$	0.0	0.0	0.0024
$\Delta J_{w3}$	0.5	0.0	0.421
Wheel Alignment Errors (deg)	Actual	Initial Predicted	Estimated
$\Delta\theta_1$	-0.0667	0.0	-0.0771
$\Delta\theta_2$	0.0	0.0	0.0029
$\Delta\theta_3$	-0.0667	0.0	-0.0778

Table 1 : Uncertainties in wheel moments of inertia and RWU alignments (Case 1)

Spacecraft Inertias (kgm <sup>2</sup> )	Actual	Initial Predicted	Estimated
$J_{11}$	5928	6587	5929.022
$J_{12}$	73	23	75.440
$J_{13}$	260	160	246.676
$J_{22}$	24545	27273	24539.060
$J_{23}$	24	4	18.839
$J_{33}$	27821	30913	27836.088
Wheel Inertia Errors (%)	Actual	Initial Predicted	Estimated
$\Delta J_{w1}$	0.5	0.0	0.5702
$\Delta J_{w2}$	0.0	0.0	-0.0326
$\Delta J_{w3}$	-0.5	0.0	-0.4704
Wheel Alignment Errors (deg)	Actual	Initial Predicted	Estimated
$\Delta\theta_1$	-0.0667	0.0	-0.0709
$\Delta\theta_2$	0.0	0.0	0.0067
$\Delta\theta_3$	-0.0667	0.0	-0.0781

Table 2 : Uncertainties in wheel moments of inertia and RWU alignments (Case 2)

In order to show clearly the accuracy of open-loop slews, before and after the slew performance calibrations have been performed, three separate simulation cases are presented. The open-loop slew is about the yaw axis with an amplitude of  $20^\circ$  and a slew rate of  $20^\circ/\text{hour}$ . These are listed as follows:-

- Without any compensation applied.
- Compensation only for the yaw principal inertia applied.
- Complete compensation of the spacecraft inertia matrix, reaction wheel moments of inertia and RWU alignments applied.

The simulation results are presented in the same order as the slew calibration results are presented in Tables 1 and 2, thereby showing the effects of the above three scenarios for each example.

The main conclusion that can be drawn from these simulation results, is the justification of the statement made earlier about selecting the unknown system model parameters in order to preserve the estimation results of the matrix given in Eq(6). This is clearly seen by the low slew errors shown in the last of the three plots in Figures 1 and 2, where the complete compensation is applied.

It is also interesting to note that with the introduction of constant FSS misalignments and biases, that the estimated parameters from the slew calibrations are referred to the optical references and not the spacecraft functional reference frame. This has the effect of taking into account the alignments of the reaction wheels relative to the optical references. This is necessary so that FSS misalignments and biases do not contribute to slew errors<sup>3</sup>. Simulation results for this case are given in<sup>4</sup>.

Finally, several other simulations have been performed the results of which have not been included in this paper, and consist of the following:

- Increased slew rates ( $20^\circ/\text{hour}$  up to  $90^\circ/\text{hour}$ ).
- More general slews where the Sun is not boresighted and the eigenaxis is in different directions.

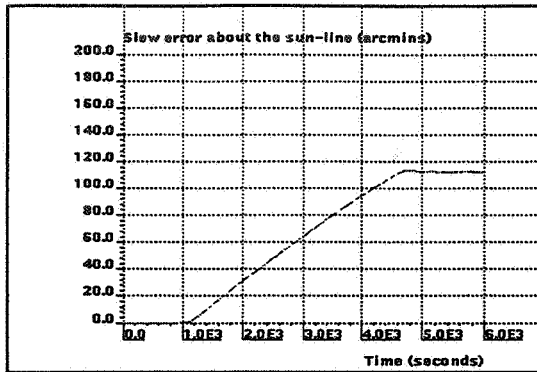
It is confirmed that by commanding higher slew rates, the slew accuracy is improved even more, due to the fact that errors are inversely proportional to the slew rate.

Also, more general slews can be worse in terms of accuracy than the pure yaw slew results that are presented in Figures 1 and 2. However, it is assumed in general that they are still significantly more accurate than the corresponding cases where only the yaw principal inertia has been calibrated.

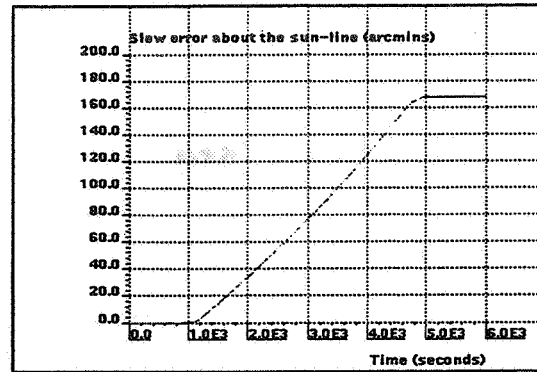
## IN-FLIGHT TESTING USING ISO

The aim of these tests is to have an apriori in-orbit evaluation of the following points:-

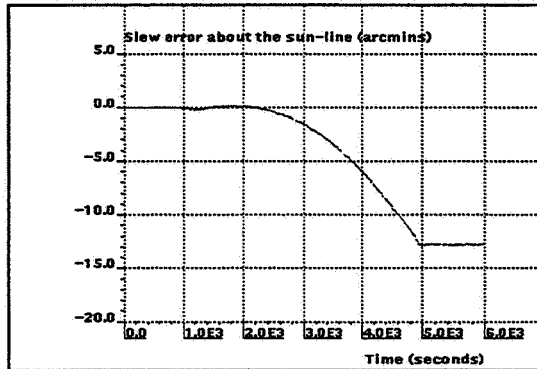
- Rate estimation accuracy from FSS and STR outputs throughout the short calibration slews<sup>5</sup>. Derived rates<sup>6</sup> will be compared with accurate rate signals from the gyropackage to determine the effects of slew rates on the quality of the STR outputs.
- Partial validation of the estimation algorithms. Only a partial verification of the algorithms to estimate the unknown system parameters can be performed due to the fact that the ISO AOCS multiple gyro failure on-board software does not have a completely gyroless slew mode. The design of this new on-board software assumes that there is at least one gyro left out of the four for use during slew manoeuvres. Although it is possible to load on-board, different values of the spacecraft inertia matrix, it is unlikely that these effects would produce slew errors as large as those experienced during the XMM slew phase, where no gyros are used.



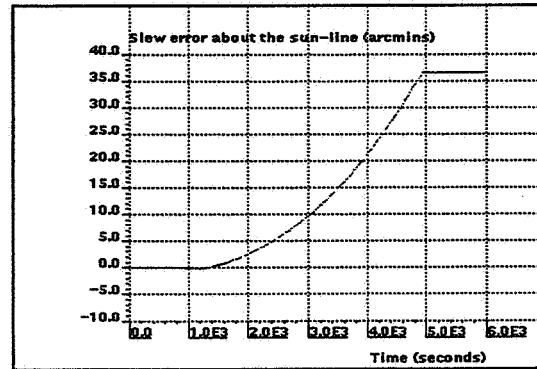
No compensation applied



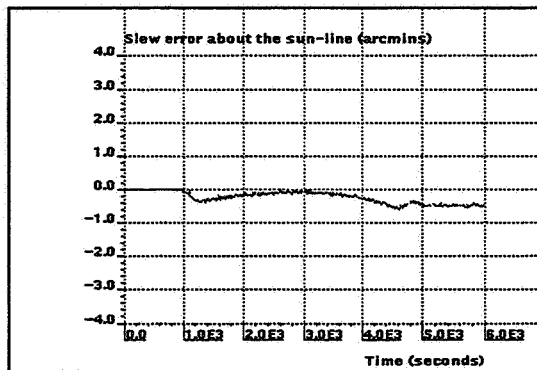
No compensation applied



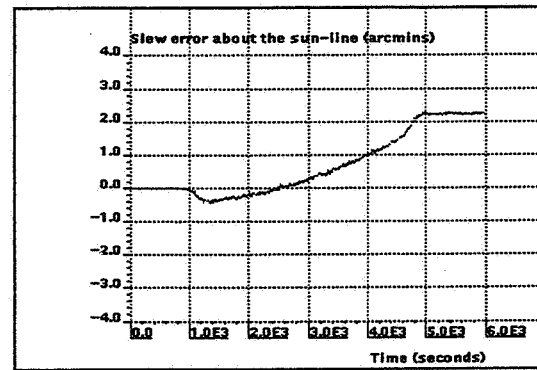
Compensation for error in spacecraft  
yaw principal inertia



Compensation for error in spacecraft  
yaw principal inertia



Complete compensation applied



Complete compensation applied

Figure 1 : Uncertainties in wheel moments of  
inertia and RWU alignments (Case 1)

Figure 2 : Uncertainties in wheel moments of  
inertia and RWU alignments (Case 2)

## CONCLUSIONS

A method to calibrate the spacecraft moments and products of inertia, reaction wheel moments of inertia and alignments for the XMM Inertial Pointing and Slew mode attitude control system has been proposed. Simulation results show that an order of magnitude improvement in the accuracy of open-loop slews is achieved, when these parameters have been loaded on-board in the AOCS flight software, compared with the same slews where only the yaw principal inertia has been calibrated. This should be enough to ensure that for most observational slews that the guide star intended for use at the final target attitude, will lie within the  $3^{\circ} \times 4^{\circ}$  field-of-view of the STR. A small offset manoeuvre can then be used to reposition the guide star to the desired location following every open-loop slew.

## ACKNOWLEDGEMENTS

The author would like to acknowledge various members of the ISO and XMM flight dynamics teams for their contributions. In particular, Mr C. Stephenson for setting up the IPS mode calibration tests on ISO and providing the flight data for these tests and to Mr G. Gienger for his help and suggestions.

## REFERENCES

1. G. Gienger, A. McDonald, and J. Palmer, "Flight Dynamics Support for the Gyroless Operations of XMM," Proceedings of the International Symposium on Space Flight Dynamics, Darmstadt, June 1997.
2. Harris R. S. (Matra Marconi Space), "XMM AOCS Design Report, " XM-RP-MMB-0018, Issue 3, September 1997.
3. Chapman P. D. (Matra Marconi Space), "XMM AOCS Performance Review Document Volume 5, Inertial Pointing and Slew (IPS) Mode" XM-RP-MMB-0026, Issue 2.
4. M. J. Tuttlebee, "Calibration of the Inertial Pointing and Slew Mode for XMM and INTEGRAL, " XMM-MOC-TN-0114-OAD, Issue 1, December 1997.
5. ISO Flight Control Team, "Infrared Space Observatory (ISO) Technology Test Plan, " TOS-OFC-ISO-TTP/JF, Issue 1 Rev 0, January 1998.
6. M. J. Tuttlebee, F. Dreger, "Feasibility of FSS?STR based slew attitude determination, " INT-MOC-TN-0002-OAD, Issue 1, March 1997.

# DEEP SPACE PASSIVE SUN TRACKING

David Sonnabend<sup>1</sup>

## Abstract

For the Rosetta mission to orbit a comet, due to launch in 2003, and spend about a decade en route, the European Space Agency contemplates the use of a series of "hibernation" periods. This is both to conserve resources, and to reduce expensive ground operations. The general idea is to point the solar arrays at the sun, spin the spacecraft at a low rate about the sun line, suspend communications with the ground, and turn off most spacecraft equipment. A factor tending to limit the value of this idea is that, as Rosetta moves in its orbit, the direction to the sun changes, reducing the available power from the array. The worst case from this standpoint is a final hibernation period between a 2nd asteroid flyby and the comet approach phase; because the spacecraft is then most distant from the sun. This hibernation could be as long as 3 years, and the sun direction (true anomaly) could change as much as 70 deg. Even biasing the initial direction of the spin axis to favor the later, more distant part of the orbit, would still lead to a maximum array offset of around 30 deg, when the loss of power would be about 13%, worse if various asymmetries and external disturbances are taken into account. This paper advances a passive technique for using radiation pressure to cause the spin axis to track the sun. A fairly complete analysis is presented, along with calculations of the performance.

## 1 DISCUSSION

To discuss the main idea, and various possibilities for disturbance, the spacecraft and the body axes need to be defined. When this study was done by the DASA - Aerospatiale proposal team, the spacecraft had a pair of solar wings, on separate array drives. The design details are given below. In spin mode, the direction to the sun is close to the spacecraft  $x$  axis, the axis of maximum moment of inertia. The  $y$  axis is the solar array shaft axis, the axis of minimum moment of inertia; and  $z$  completes a right handed system.

1st, suppose the center of pressure doesn't coincide with the center of mass. If there is an  $x$  displacement, there is clearly no effect. A  $y$  displacement causes a torque along  $z$ ; but this rotates with spin, and averages out. Similarly, a  $z$  displacement leads to a  $y$  torque, which also averages out. Clearly, we are not concerned with center of pressure migration. Another possibility is a shape or reflective properties variation between wings. In either case, we again have a rotating disturbance, which averages out. Finally, if the array shaft axis is rotated, either from bias or deliberate control, there will be a force component along  $z$ . Either an asymmetry between the wings, or a differential control of the 2 array shaft angles, yields a torque along  $x$ . This torque is unaffected by rotation, and thus tends to change the magnitude of the angular momentum. A formula for this "propeller" torque is derived in Section 5, followed by a discussion of possible methods for controlling spin rate.

There is one other substantial source of solar torque. If both wings are bent back, away from the sun, we have what aircraft designers call "positive dihedral". If the  $x$  axis is pointed at the sun, as desired, the effect is balanced, and there is no torque. However, if  $x$  is offset from the sun by some angle, then one wing receives greater illumination than the other, yielding a  $z$  torque. This torque varies during spin; but, after a half rotation, it's the other wing that is more favorably placed.

<sup>1</sup>President, Analytical Engineering, 303-530-9641, E-mail: dsennabend@worldnet.att.net

Moreover, the torque has the same direction in space; so, the torque history looks more or less like a rectified sine wave; and on average, there is a torque along  $z$ , tending to cause the spin axis to precess about the sun line. It will be shown below that the precession cone naturally tracks the sun direction. A similar idea was analyzed in the Reference, and put forward as a method of passive control of spin axis direction. A simplified analysis of the dihedral effect is presented in Section 3, and then applied to the present design.

The configuration explored in the Reference kept the solar panels parallel, but added fixed dihedral vanes at the ends of the panels. Relative to the design proposed here, vanes pose some disadvantages. 1) the vanes add some mass; 2) there are 2 extra deployment joints, with their associated mass and deployment commands; and 3) the most natural accordion folding would cause the vanes to cover the outer array panels, thus eliminating any solar power before deployment. The disadvantage of the proposed design is that dihedral causes some loss of power; however, even with 3 deg of dihedral, the loss is only 0.137%. A few years earlier, a Russian proposal for a series of satellites called Regatta employed essentially this same idea for passive attitude control; but the program died for lack of support; and I haven't seen their analysis.

## 2 FLAT PANEL ANALYSIS

The forces and torques discussed in this paper all depend on the force on a flat panel at some angle to the sun. If an object absorbs sunlight, and reemits this energy isotropically, then the pressure is given by  $I_s/c$ , where  $I_s$  is the solar irradiance, and  $c = 2.99776 \times 10^8$  m/s = the speed of light. Applying this to a flat panel of area  $A$ , whose normal is pointed toward the sun, the force is:

$$F_0 = I_{se}A/(r^2c) \quad (1)$$

where  $I_{se} = 1367.5$  w/m<sup>2</sup>, the mean solar irradiance at 1 AU; and  $r$  is the solar distance, expressed in AU. In the current design, each wing is 14.142 m long and 2.216 m wide, from which  $A = 31.339$  m<sup>2</sup>. Thus, at 1 AU,  $F_0 = 1.4296 \times 10^{-4}$  N on each wing. To stray a bit, counting both wings, plus something for the antenna and spacecraft body, the total solar force would be about  $3 \times 10^{-4}$  N at 1 AU; so with a nearly dry spacecraft at 1200 kg, the solar acceleration would be about  $2.5 \times 10^{-7}$  m/s<sup>2</sup>. This would not be directly detectable by any accelerometer Rosetta would likely carry, but possibly would show up in a long term average.

Now suppose the spacecraft remains correctly pointed, but the panel is somehow tipped about the  $y$  axis through an angle  $0 \leq \phi < \pi/2$ . Further, suppose that the incoming photons are divided into a fraction  $\sigma_r$  that's specularly reflected, a fraction  $\sigma_d$  that's diffusely reflected, and a remaining fraction  $\sigma_a$  that's absorbed and isotropically reradiated. Then these fractions obey

$$\sigma_r + \sigma_d + \sigma_a = 1 \quad (2)$$

For the absorbed fraction, the force is along the sun line, and is  $F_0$ , reduced by  $c\phi$  ( $c$  and  $s$  stand for the cosine and sine respectively). The specularly reflected fraction gives twice the force, similarly reduced, whose resultant is along the panel normal. Finally, for the diffusely reflected fraction, the incoming part behaves like the absorbed rays; but the reflected photons are spread into a cosine distribution, whose resultant is along the panel normal. These features are shown in Fig. 1. A well known result is that the average of the cosine over a hemisphere is  $2/3$ . From this, the normal and transverse force components are readily shown to be:

$$F_N = -F_0 \left[ (1 + \sigma_r)c^2\phi + \frac{2}{3}\sigma_dc\phi \right] \quad (3)$$

$$F_T = -F_0(1 - \sigma_r)s\phi c\phi \quad (4)$$

In the latter formula, the transverse direction is taken as in the panel, and closest to the sun line. These formulas will be applied below to obtain particular torque components. As an aside, the Reference assumed that  $\sigma_r = 1$ , when these equations reduce to

$$F_N = -2F_0 c^2 \phi \quad ; \quad F_T = 0$$

However, solar cells are dark blue to the eye in sunlight, so we must have  $\sigma_a > \sigma_r$ .

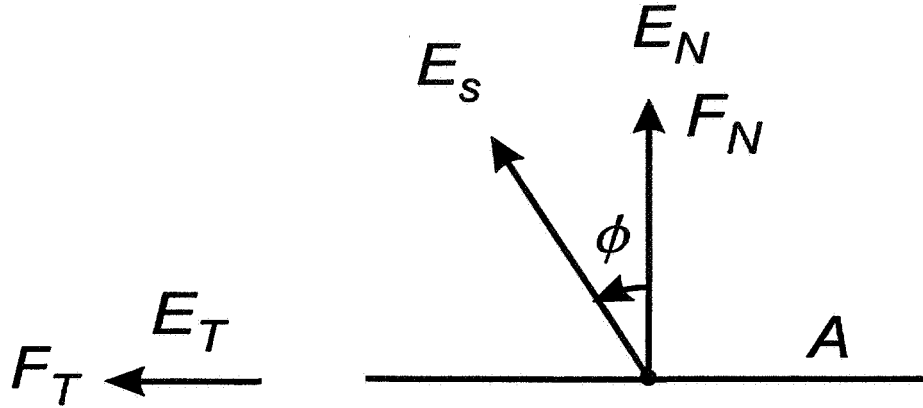


Figure 1 – Flat panel

### 3 DIHEDRAL TORQUES

To analyze this 3 dimensional problem, it's helpful to introduce some coordinate systems. 1st, a more or less inertial system is defined by choosing a unit vector  $E_1$  along the spacecraft spin axis, followed by an orthogonal unit vector  $E_2$  in the plane containing the sun, and a 3rd unit vector  $E_3$ , completing an orthonormal system. If the sun is an angle  $\theta$  forward from  $E_1$ , then its direction is

$$E_s = [c\theta, s\theta, 0]^T \quad (5)$$

where the subscript indicates that the resolution is in the inertial system, and the superscript signifies transpose.

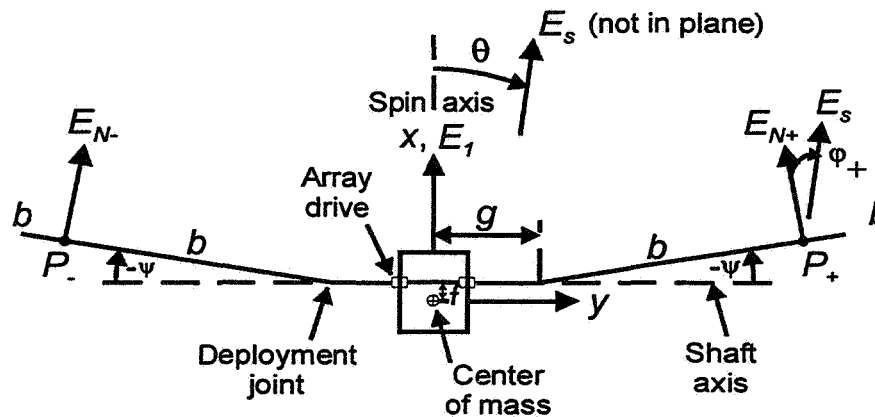


Figure 2 – Dihedral forces

The spacecraft system; with base vectors  $E_x$ ,  $E_y$ , and  $E_z$ ; is obtained by rotating the inertial coordinates about  $E_1$  through the angle  $\alpha$ , which advances at spin rate. To analyze dihedral solar

panels, we need some definitions. Referring to Fig. 2, shown with negative dihedral, suppose the solar array shaft axes are aligned with  $E_y$ , and that these axes are forward along  $E_x$  by a distance  $f$ . Also suppose the joint connecting the mounting yoke to the beginning of the array is a distance  $g$  from the center line. We then assume that the arrays are each bent back by a dihedral angle  $\psi$ . If the array length is  $2b$ , and if the shafts are displaced by a distance  $h$  along  $z$ , the locations of the centers of pressure of the 2 wings are

$$P_{+/-} = [f - bs\psi, \pm(g + bc\psi), h]_B^T \equiv [P_1, \pm P_2, h]_B^T \quad (6)$$

where this time the resolution is in body coordinates. We also need the directions of the outward normals at these points. These are readily worked out from Fig. 2. In body and inertial coordinates we have

$$E_{N+/-} = [c\psi, \pm s\psi, 0]_B^T = [c\psi, \pm s\psi\cos\alpha, \pm s\psi\sin\alpha]_I^T \quad (7)$$

These relations are sufficient to compute the solar offsets used in Section 2, for each wing:

$$c\phi_{+/-} = E_s \cdot E_{N+/-} = c\theta c\psi \pm s\theta s\psi\cos\alpha \quad (8)$$

It remains to determine the direction of the transverse component of the solar force. This lies along the panel surface, and in the plane defined by the panel normal and the sun direction. It's not hard to show that this obeys:

$$E_s = E_{N+}c\phi_+ + E_{T+}s\phi_+ = E_{N-}c\phi_- + E_{T-}s\phi_- \quad (9)$$

These last relations are only useful if the sun illuminates the front of both wings, a condition met if  $|\theta| < (\pi/2) - \psi$ .

We're now ready to compute the combined torque. Since torque is the cross product of the center of pressure vector by the applied force, we have here:

$$\tau = P_+ \times F_+ + P_- \times F_- \quad (10)$$

where the total force on each wing is given by

$$F_{+/-} = F_{N+/-}E_{N+/-} + F_{T+/-}E_{T+/-} \quad (11)$$

From (3) and (4), the + wing is

$$F_+ = -F_0 \left\{ \left[ (1 + \sigma_r)c^2\phi_+ + \frac{2}{3}\sigma_d c\phi_+ \right] E_{N+} + (1 - \sigma_r)E_{T+}s\phi_+ c\phi_+ \right\} \quad (12)$$

and using (9) to eliminate  $E_{T+}$ , this reduces to

$$F_+ = -F_0 \left[ 2 \left( \sigma_r c\phi_+ + \frac{1}{3}\sigma_d \right) E_{N+} + (1 - \sigma_r)E_s \right] c\phi_+ \quad (13)$$

and similarly for  $F_-$ . Next, we construct the cross products:

$$P_{+/-} \times E_{N+/-} = [\mp h s\psi, h c\psi, \mp P_3]_B^T = [\mp h s\psi, h c\psi\cos\alpha \pm P_3\sin\alpha, h c\psi\sin\alpha \mp P_3\cos\alpha]_I^T \quad (14)$$

where

$$P_3 \equiv P_2 c\psi - P_1 s\psi = b + g c\psi - f s\psi \quad (15)$$

On substituting these into (13), and the corresponding  $F_-$  relation, and averaging over  $\alpha$  for one spin cycle, we find

$$\bar{\tau}_{N+/-} = F_0 \sigma_r \begin{bmatrix} \pm h(2c^2\psi c^2\theta + s^2\psi s^2\theta) \\ \mp 2h c^2\psi s\theta c\theta \\ 2P_3 c\psi s\theta c\theta \end{bmatrix} s\psi + \frac{1}{3} F_0 \sigma_d \begin{bmatrix} \pm 2h c\psi c\theta \\ \mp h c\psi s\theta \\ P_3 s\theta \end{bmatrix} s\psi \quad (16)$$



and on combining the 2 wings:

$$\bar{\tau}_N = F_0 P_3 \left( 4\sigma_r c\psi c\theta + \frac{2}{3}\sigma_d \right) E_3 s\psi s\theta \quad (17)$$

So the normal components lead only to a torque along  $E_3$ , vanishing if either  $\theta$  or  $\psi$  is zero.

A somewhat different procedure is needed for the  $E_s$  terms. This time, the total torque is:

$$\tau_s = -F_0(1 - \sigma_r)(P_+ c\phi_+ + P_- c\phi_-) \times E_s \quad (18)$$

The 1st vector is easily found in body axes, transformed to inertial axes, and averaged, when

$$(P_+ c\phi_+ + P_- c\phi_-)_{av} = [2P_1 c\theta c\psi, P_2 s\theta s\psi, 0]_I^T \quad (19)$$

so that

$$\bar{\tau}_s = -F_0(1 - \sigma_r)P_4 E_3 s\theta c\theta \quad (20)$$

where

$$P_4 \equiv 2P_1 c\psi - P_2 s\psi = 2fc\psi - gs\psi - 3bs\psi c\psi \quad (21)$$

Note that if  $\psi = 0$ , i.e. there is no dihedral, this reduces to

$$\bar{\tau}_s = -2F_0 f(1 - \sigma_r)E_3 s\theta c\theta \quad (\psi = 0) \quad (22)$$

So there is a torque along  $E_3$  even without dihedral. It may be seen that it arises from the transverse components of the force, caused by the absorbed and diffusely reflected fractions of the incident sunlight. Moreover, it's proportional to the distance  $f$ , the forward displacement of the solar array drive axis along  $x$ . Finally, we may combine these components and get:

$$\bar{\tau} = F_0 \left[ 2P_3 \left( 2\sigma_r c\theta c\psi + \frac{1}{3}\sigma_d \right) s\psi - P_4(1 - \sigma_r)c\theta \right] E_3 s\theta \quad (23)$$

For small  $\theta$ , this last expression reduces to

$$\bar{\tau} = F_0 \left[ P_3 \left( 4\sigma_r c\psi + \frac{2}{3}\sigma_d \right) s\psi - P_4(1 - \sigma_r) \right] E_3 \theta \equiv \tau' E_3 \theta \quad (24)$$

The scalar  $\tau'$  introduced here is a measure of the control authority available from the dihedral idea; i.e., it's the precession torque per unit solar offset. It will be computed for the proposal design parameters in the next section, and used to determine the dynamics of solar tracking.

In passing, it's been suggested that another source of control torque might come from solar pressure on the high gain antenna, especially as the antenna drive angles could be fixed in any desired positions during hibernation. The calculation of the effect closely follows that of the dihedral arrangement. To use the same nomenclature, suppose an az-el configuration is adopted, and the azimuth axis is fixed in the position where the elevation axis is normal to the spin axis. Then, if we approximate the antenna reflector as a flat circular plate of radius  $b = 1.1$  m, we have an area of  $3.8$  m<sup>2</sup>; when from (1),  $\tau^2 F_0 = 1.734 \times 10^{-5}$  N. Now, suppose the elevation axis grips the plate on an edge at the body coordinates  $[f, g, 0]$ , and the plate is bent back through an angle  $\psi$ . Here,  $g$  is actually the radial coordinate from the spin axis; so the  $h$  coordinate used in the dihedral analysis is here unnecessary. With these definitions, the center of pressure is at

$$P = [f - bs\psi, g + bc\psi, 0]_B^T \equiv [P_1, P_2, 0]_B^T \quad (25)$$

corresponding to  $P_+$  in (6). The analysis proceeds in the same way, and the spin averaged torque can be read off from (16):

$$\bar{\tau}_N = F_0 P_3 \left( 2\sigma_r c\psi c\theta + \frac{1}{3}\sigma_d \right) E_3 s\psi s\theta \quad (26)$$

Now in body axes:

$$P = [P_1, P_2 c\alpha, P_2 s\alpha]_B^T \quad (27)$$

so that

$$(Pc\phi)_{av} = \left[ P_1 c\psi c\theta, \frac{1}{2}P_2 s\psi s\theta, 0 \right]_I^T \quad (28)$$

and, similar to (20):

$$\bar{\tau}_s = -\frac{1}{2}F_0(1 - \sigma_r)P_4 E_3 s\theta c\theta \quad (29)$$

Thus, if  $\theta$  is small,  $\tau'$  becomes independent of  $\theta$ :

$$\tau' = F_0 \left[ P_3 \left( 2\sigma_r c\psi + \frac{1}{3}\sigma_d \right) s\psi - \frac{1}{2}P_4(1 - \sigma_r) \right] \quad (30)$$

This expression closely resembles (24); it will also be computed in the next section.

## 4 CONTROLLING SPIN DIRECTION

We may now consider what happens when the sun is in motion, as seen from the spacecraft. For coordinates, take a system whose origin is at the spacecraft, and whose orientation is fixed relative to J2000 (i.e., the stars). Then arrange things such that  $E_3$  is the spacecraft orbit normal, and that the sun is initially in the direction  $E_1$ . These axes aren't the same as in the last section. Then the sun will appear to move forward toward  $E_2$  at a rate  $n$ , the current rate of change of the spacecraft true anomaly. Assuming  $n$  to be fairly constant (to be refined below), we may express this as

$$E_s = [c(nt), s(nt), 0]^T \quad (31)$$

We also need to express the spacecraft angular momentum  $L$  in this system. Choosing spin axis latitude  $\beta$  and longitude  $\lambda$  as the descriptive variables, we have:

$$L = I_x \omega_s [c\beta c\lambda, c\beta s\lambda, s\beta]^T \equiv I_x \omega_s E_L \quad (32)$$

where  $I_x$  is the spin moment of inertia of the spacecraft, and  $\omega_s$  is the spin angular velocity. In these terms, the angle  $\theta$  between  $E_L$  and  $E_s$ , as used in the last section is

$$c\theta = E_L \cdot E_s = c(\lambda - nt)c\beta \equiv c\gamma c\beta \quad (33)$$

Clearly, for  $\theta$  to be small, both  $\beta$  and the differential longitude  $\gamma$  must be small.

Now, in the last section, the solar torque due to dihedral wings was found to have the form

$$\bar{\tau} = \tau' E_\tau s\theta = \tau' E_L \times E_s = \tau' [-s(nt)s\beta, c(nt)s\beta, -s\gamma c\beta]^T \quad (34)$$

where from (24) and small  $\theta$ ,  $\tau'$  has the constant value

$$\tau' = F_0 \left[ (1 - \sigma_r)P_4 + \left( 4\sigma_r c\psi + \frac{2}{3}\sigma_d \right) P_3 s\psi \right] \quad (35)$$

The stage is now set for the dynamics. From  $\dot{L} = \bar{\tau}$ , and the above expressions, we find

$$\dot{\lambda}c\beta s\lambda + \dot{\beta}s\beta c\lambda = \omega_p s(nt)s\beta \quad (36)$$

$$\dot{\lambda}c\beta c\lambda - \dot{\beta}s\beta s\lambda = \omega_p c(nt)s\beta \quad (37)$$

$$\dot{\beta}c\beta = -\omega_p s\gamma c\beta \quad (38)$$

where

$$\omega_p \equiv \tau'/(I_x \omega_s) \quad (39)$$

Strictly speaking, this assumes that the spacecraft is spinning on a principal axis, not necessarily the case. However, with good design, and some form of passive damping, the assumption should be good enough. There are actually only 2 independent relations here — the 3rd relation, and from a combination of the 1st 2:

$$(\dot{\gamma} + n)c\beta = \omega_p c\gamma s\beta \quad (40)$$

Now, the small angle hypothesis may be applied to  $\beta$  and  $\gamma$ , when

$$\dot{\beta} = -\omega_p \gamma \quad ; \quad \dot{\gamma} + n = \omega_p \beta \quad (41)$$

That this linear system has a sinusoidal solution is immediately apparent:

$$\beta = A c(\omega_p t + \rho) + \frac{n}{\omega_p} \quad ; \quad \gamma = A s(\omega_p t + \rho) \quad (42)$$

as is readily verified by differentiation. Thus, the angular momentum  $L$  precesses circularly, but displaced in latitude from the sun by an angle  $n/\omega_p$ . Moreover,  $\omega_p$  is the precession frequency given in (39). The precession is in the opposite direction from the spin. By summing the squares, we obtain a constant of the motion, revealing further insight:

$$\left(\beta - \frac{n}{\omega_p}\right)^2 + \gamma^2 = A^2 \quad (43)$$

Some reflection shows that, to keep  $\theta$  as small as possible, we should point the spin axis initially to the coordinates

$$\beta = n/\omega_p \quad ; \quad \gamma = 0 \quad (44)$$

when  $A = 0$ , and the spin axis follows the sun at a fixed separation  $\theta = n/|\omega_p|$ . On the other hand, if we initially pointed at the sun ( $\beta = \gamma = 0$ ), the later maximum deviation of  $\theta$  would be twice this. This behavior is illustrated in Fig. 3.

A physical argument may help to make this precession behavior more understandable. Suppose we initially point the spin axis to the optimal offset position. Then, from the analysis of the last section, the resulting torque will be orthogonal to both the spin axis, and the projected direction of the sun. In the coordinate system used here, this torque is in the longitude direction, which is just what is needed to follow the sun. As for the magnitude, the required torque is given by  $\tau/L = n$ . But we also have  $\tau = \tau'\theta$ , so

$$\theta = \tau/\tau' = nL/\tau' = n/\omega_p \quad (45)$$

and we may conclude that just this offset is required to produce the torque needed to cause  $L$  to precess at the desired rate  $n$ .

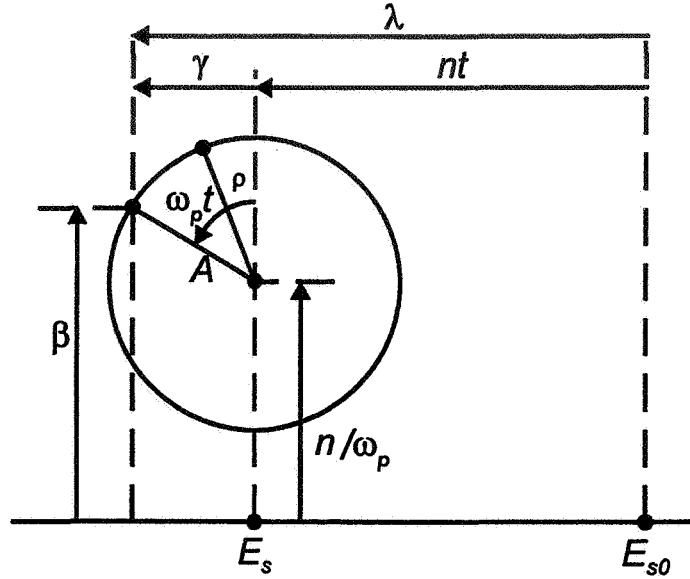


Figure 3 – Apparent solar precession

In following this strategy, there are 2 requirements that limit the choice of  $\omega_s$ . One of these arises in the control of spin, and will be discussed in Section 6. The other is because we need to make  $|\omega_p| \gg n$  in order to keep the offset within reason, say  $\Delta\theta = .01$  or  $.02$  rad. This may be stated as

$$\omega_p > n/\Delta\theta \quad (46)$$

From (39), the corresponding limitation on  $\omega_s$  is

$$\omega_s < \tau' \Delta\theta / (nI_x) \quad (47)$$

It's useful to see some numbers. In the design examined here, we have  $f = .024$  m,  $g = 2.82$  m, and  $b = 7.071$  m. Also, the reflection coefficients are  $\sigma_a = 0.69$ ,  $\sigma_r = 0.31$ , and  $\sigma_d = 0$ . Now from (23), for small  $\theta$  and  $\psi$ , we have

$$\tau' = F_0 \left[ (1 - \sigma_r)(2b + g) + (4\sigma_r + \frac{2}{3}\sigma_d)(b + g) \right] \psi - 2F_0(1 - \sigma_r)f \quad (48)$$

$$= F_0(39.072\psi - .03312) \quad (49)$$

For a few values of  $\psi$  and  $r$  this is

$\psi$ - rad	0	.01	.02	.05	0.1
$\tau'$ at 1 AU - $\mu\text{N-m/rad}$	-4.73	51.1	107	275	554
$\tau'$ at 5 AU - $\mu\text{N-m/rad}$	-0.189	2.04	4.28	11	22.2

Note that the contribution of the constant term is small; but, in a different design, the distance  $f$ , from the center of mass forward to the solar array drive axis, could be a good deal larger. When this analysis was 1st undertaken, it was believed that positive dihedral was necessary for stability. However, it's now clear that a negative dihedral would merely reverse the direction of precession and the latitude of the offset. Moreover, from (49), it's clear that the sign of  $\psi$  should be opposite from  $f$ ; so it would be better to make  $\psi < 0$  here. In this case,  $f$  is so small that this change would improve  $\tau'$  by only about 2%.

To compute  $\omega_p$ , an average value of  $I_x$  is about  $2 \times 10^4$  kg/m<sup>2</sup>. Thus, at 1 AU, for say  $\omega_s = 1$  deg/s, and  $\psi = .05$  rad, we get  $\omega_p = 7.88 \times 10^{-7}$  rad/s, yielding a precession period of  $7.98 \times 10^6$  s or 92.3 days. Alternatively, for 5 AU, we might lower  $\omega_s$  to 0.1 deg/s, when  $\omega_p = 3.15 \times 10^{-7}$  rad/s, for a period of 231 days. As for the precession, if we take  $\Delta\theta = .02$  rad, and consider the final hibernation period, about 1 rad is traversed in 3 years, giving  $n \approx 10^{-8}$  rad/s, so we require  $\omega_s < .0011$  rad/s = .063 deg/s.

This whole behavior may become clearer by considering what happens with increasing  $\omega_s$ . This causes  $L$  to increase, increasing the "resistance" to the torque  $\bar{\tau}$ , when the tendency to follow  $E_s$  weakens. Geometrically,  $\omega_p$  is decreasing, which increases the latitude offset of the precession circle from the sun. If the spin axis is initially pointed at the sun, the precession circle is tangent to the  $\gamma$  axis, and  $L$  heads backward. If  $\omega_s \rightarrow \infty$ ,  $L$  merely moves backward at the rate  $-n$ ; i.e., it is inertially fixed.

A similar calculation may be made for the high gain antenna. As the position, and elevation drive details weren't settled at the time of the study, we took  $f = g = 1.5$  m as representative nominal dimensions, along with the established  $b = 1.1$  m.  $f$  and  $g$  were varied, to see if  $\tau'$  could be substantially changed. Also, except for the last case, suppose the antenna is painted with thermal white, for which  $\sigma_r = 0$  and  $\sigma_d = 0.8$ . This time we're free to choose  $\psi$  to be anywhere in the range  $|\psi| \leq \pi/2$ . So, for each choice of the parameters,  $\psi$  was varied to find the maximum  $|\tau'|$ . The results are in the table below.

Case	f m	g m	$\sigma_r$	$\sigma_d$	$\psi_{\text{opt}}$ rad	$\tau'^2$ $\mu\text{N-m/rad}$
1	1.5	1.5	0	0.8	-0.79838	-52.435
2	-1.5	1.5	0	0.8	0.79845	-52.435
3	0	1.5	0	0.8	$\pm 0.93823$	$\pm 31.541$
4	3	1.5	0	0.8	-0.70032	-74.714
5	1.5	3	0	0.8	-0.86885	-65.530
6	1.5	1.5	1	0	-0.78540	-55.858

Case 1 is the nominal case cited above. For comparison the previous table shows that similar performance is available from the solar arrays with a dihedral bend of about .01 rad; and for 0.1 rad, the arrays yield an order of magnitude greater authority. Also note that  $\psi_{\text{opt}} < 0$ , so that bending the array forward is preferable. This preference is much stronger than for the array, as the value of  $f$  is much larger here.

Case 2 differs from Case 1 in that the sign of  $f$  has been reversed. While such a change would be impractical in the above design, it shows the expected behavior — that only the signs of  $\psi_{\text{opt}}$  and  $\tau'$  have reversed. Case 3 supports this conclusion by examining  $f = 0$ . As expected, the variation with respect to  $\psi$  is antisymmetric; and equal performance may be achieved by bending the antenna either forward or backward.

Cases 4 and 5 inquire into what happens if the elevation joint can be pushed further out, either forward of the center of mass, or radially from the spin axis. There are improvements in  $\tau'$ , but not as large as might be expected, as both  $f$  and  $g$  increase the authority. Finally, Case 6 returns to the nominal dimensions, but replaces the white paint with a purely specular reflector (polished aluminum, say). Since the results vary only slightly, it would appear that the surface properties make little difference.

We're now in a position to bring all this theory together to calculate the optimal  $\psi$ . One design constraint is that  $|\Delta\theta| \leq 20$  deg during hibernation, to avoid excessive heating of the side panels. If no stronger constraint is active, and  $\psi$  is given, then the maximum  $\omega_s$  during a particular hibernation may be calculated from (49) and (47). However, during the final hibernation, there could be a very tight requirement that the average power loss not exceed 0.5% due to mispointing of the array. This

amounts to a limitation on the average values of  $\phi_+$  and  $\phi_-$ . From (8), this means we must enforce

$$c\theta c\psi \leq c\phi_{+/-} = 0.995 \quad (50)$$

Since all these angles must be small, this may be written as

$$\theta^2 + \psi^2 \leq \phi_M^2 \quad (51)$$

where  $\phi_M = 0.10004$  rad = 5.731 deg. Our optimization of  $\psi$  now comes from the need to relax (47) as much as possible, consistent with the constraint (51). Since we're combining the contributions of the arrays and the antenna, it's best to rewrite (49) as

$$r^2\tau' = -1.4296 \times 10^{-4}(39.072\psi + .03312)$$

while the nominal antenna has  $r^2\tau' = -5.2435 \times 10^{-5}$  N-m/rad; so the combined authority is

$$r^2\tau' = -.0055857\psi - 5.717 \times 10^{-5} = -.0055857(\psi + \xi)$$

where  $\xi = .010235$  rad. To get optimal performance, we must maximize the function

$$J = (\psi + \xi)\theta = (\psi + \xi)\sqrt{\phi_M^2 - \psi^2} \quad (52)$$

The solution is readily shown to be

$$\psi = \frac{1}{4} \left( \sqrt{\xi^2 + 8\phi_M^2} - \xi \right) = .068226 \text{ rad} = 3.9091 \text{ deg} \quad (53)$$

when  $\theta = .073166$  rad = 4.1921 deg, and the combined authority is  $r^2\tau' = -4.3826 \times 10^{-4}$  N-m/rad. For the final hibernation, the average  $r = 3.65$  AU, and the average  $n = 1.4 \times 10^{-8}$  rad/s. Thus, with this design, the upper limit on spin rate is:

$$\omega_s \leq \frac{(4.3826 \times 10^{-4})(4.1921)}{(3.65)^2(1.4 \times 10^{-8})(2 \times 10^4)} = 0.49252 \text{ deg/s}$$

and at this spin rate, the precession rate is

$$\omega_p = 1.4 \times 10^{-8} / .073166 = 1.9135 \times 10^{-7} \text{ rad/s}$$

for a precession period of 380.06 days. Rather long, but with accurate initial pointing, it shouldn't make much difference.

For contrast, we may ask how these results would vary if the average power loss requirement were relaxed. When this study was completed it was believed that a 2% loss could be tolerated, in contrast to the 0.5% used above. In this case we find  $\phi_M = 11.478$  deg,  $\psi = -7.9711$  deg,  $\theta = 8.2588$  deg,  $r^2\tau' = -8.3427 \times 10^{-4}$  N-m/rad, and  $\omega_s \leq 0.9703$  deg/s, at which speed,  $\omega_p = 9.7128 \times 10^{-8}$  rad/s, for a precession period of 748.73 days.

## 5 PROPELLOR TORQUES

Up to this point, it's been assumed that the solar array drive angles have both been set to zero; so that, with no dihedral, both array normals are along the body  $x$  axis; i.e.,  $E_{N+/-} = [1, 0, 0]^T_B$ . More generally, suppose the drives are controlled to the angles  $\eta_+$  and  $\eta_-$  for the 2 wings. A pure propeller setting would nominally have  $\eta_- = -\eta_+$ ; but in order to examine errors, this assumption won't be made for the main derivation.

From the layout of the spacecraft, the array drive angles must be inserted before the dihedral bends. As the drives rotate about spacecraft  $y$ , this causes the normals to shift to

$$E_{N+/-} = [c\eta_{+/-}, 0, -s\eta_{+/-}]_B^T$$

Now putting in the dihedral bend about the rotated  $z$  axis gives

$$E_{N+} = [c\psi c\eta_+, s\psi c\eta_+, -s\eta_+]_B^T \quad (54)$$

$$E_{N-} = [c\psi c\eta_-, -s\psi c\eta_-, -s\eta_-]_B^T \quad (55)$$

The new rotations also modify the locations of the centers of pressure. Some consideration of the diagram shows that (6) is generalized to

$$P_+ = [f - bs\psi c\eta_+, g + bc\psi, h + bs\psi s\eta_+]_B^T \equiv [P_{+1}, P_2, P_{+3}]_B^T \quad (56)$$

$$P_- = [f - bs\psi c\eta_-, -g - bc\psi, h + bs\psi s\eta_-]_B^T \equiv [P_{-1}, -P_2, P_{-3}]_B^T \quad (57)$$

when the essential cross products become (in body axes)

$$P_+ \times E_{N+} = \begin{bmatrix} -b(s^2\psi c\eta_+ + c\psi)s\eta_+ - gs\eta_+ - hs\psi c\eta_+ \\ fs\eta_+ + hc\psi c\eta_+ - b(1 - c\psi)s\psi s\eta_+ c\eta_+ \\ [fs\psi - gc\psi - b(s^2\psi c\eta_+ + c^2\psi)] c\eta_+ \end{bmatrix} \equiv \begin{bmatrix} U_1 \\ U_2 \\ U_3 \end{bmatrix} \quad (58)$$

$$P_- \times E_{N-} = \begin{bmatrix} b(s^2\psi c\eta_- + c\psi)s\eta_- + gs\eta_- + hs\psi c\eta_- \\ fs\eta_- + hc\psi c\eta_- - b(1 - c\psi)s\psi s\eta_- c\eta_- \\ [b(s^2\psi c\eta_- + c^2\psi) - fs\psi + gc\psi] c\eta_- \end{bmatrix} \equiv \begin{bmatrix} V_1 \\ V_2 \\ V_3 \end{bmatrix} \quad (59)$$

To analyze this more general arrangement, we may again make use of the inertial coordinates introduced in Section 3. Thus,  $E_s$  is again given by (5); and again the body axes are rotated forward from inertial axes about  $E_1$  by an angle  $\alpha = \omega_s t$ . Thus, after switching the cross products to inertial coordinates we have:

$$P_+ \times E_{N+} = [U_1, U_2 c\alpha - U_3 s\alpha, U_2 s\alpha + U_3 c\alpha]_I^T \quad (60)$$

$$P_- \times E_{N-} = [V_1, V_2 c\alpha - V_3 s\alpha, V_2 s\alpha + V_3 c\alpha]_I^T \quad (61)$$

The angles between the sun and the array normals are again important; but instead of (8) we now have

$$c\phi_+ = E_s \cdot E_{N+} = c\psi c\eta_+ c\theta + s\eta_+ s\theta s\alpha + s\psi c\eta_+ s\theta c\alpha \quad (62)$$

$$c\phi_- = E_s \cdot E_{N-} = c\psi c\eta_- c\theta + s\eta_- s\theta s\alpha - s\psi c\eta_- s\theta c\alpha \quad (63)$$

The analysis leading to (10) and (13) is unchanged; so, after averaging over a spin cycle, the inertial components from the  $E_N$  terms are:

$$\bar{\tau}_{N+} = -F_0 \begin{bmatrix} U_1 \{ \sigma_r [(2 - 3s^2\theta)c^2\psi c^2\eta_+ + s^2\theta] + \frac{2}{3}\sigma_d c\psi c\eta_+ c\theta \} \\ (U_2 s\psi c\eta_+ - U_3 s\eta_+) (2\sigma_r c\psi c\eta_+ c\theta + \frac{1}{3}\sigma_d) s\theta \\ (U_2 s\eta_+ + U_3 s\psi c\eta_+) (2\sigma_r c\psi c\eta_+ c\theta + \frac{1}{3}\sigma_d) s\theta \end{bmatrix} \quad (64)$$

$$\bar{\tau}_{N-} = -F_0 \begin{bmatrix} V_1 \{ \sigma_r [(2 - 3s^2\theta)c^2\psi c^2\eta_- + s^2\theta] + \frac{2}{3}\sigma_d c\psi c\eta_- c\theta \} \\ -(V_2 s\psi c\eta_- + V_3 s\eta_-) (2\sigma_r c\psi c\eta_- c\theta + \frac{1}{3}\sigma_d) s\theta \\ (V_2 s\eta_- - V_3 s\psi c\eta_-) (2\sigma_r c\psi c\eta_- c\theta + \frac{1}{3}\sigma_d) s\theta \end{bmatrix} \quad (65)$$

We also need the torque due to the  $E_s$  term in the force equations. As in Section 3, these are best worked out directly in the inertial frame. To this end, starting from (56) and (57):

$$P_+ = [P_{+1}, P_2 c\alpha - P_{+3} s\alpha, P_2 s\alpha + P_{+3} c\alpha]^T \quad (66)$$

$$P_- = [P_{-1}, -P_2 c\alpha - P_{-3} s\alpha, P_{-3} c\alpha - P_2 s\alpha]^T \quad (67)$$

On taking the cross products with  $E_s$ , substituting the results into (13) and the similar equation for  $F_-$ , and averaging over  $\alpha$ , we're led to:

$$\bar{\tau}_{s+} = -\frac{1}{2}F_0(1 - \sigma_r) \begin{bmatrix} -(P_2 s\eta_+ + P_{+3} s\psi c\eta_+) s\theta \\ (P_2 s\eta_+ + P_{+3} s\psi c\eta_+) c\theta \\ (2P_{+1} c\psi c\eta_+ - P_2 s\psi c\eta_+ + P_{+3} s\eta_+) c\theta \end{bmatrix} s\theta \quad (68)$$

$$\bar{\tau}_{s-} = -\frac{1}{2}F_0(1 - \sigma_r) \begin{bmatrix} (P_2 s\eta_- + P_{-3} s\psi c\eta_-) s\theta \\ -(P_2 s\eta_- + P_{-3} s\psi c\eta_-) c\theta \\ (2P_{-1} c\psi c\eta_- - P_2 s\psi c\eta_- + P_{-3} s\eta_-) c\theta \end{bmatrix} s\theta \quad (69)$$

The complete torques are found by adding these to (64) and (65) respectively. As a check, we may put  $\eta_+ = \eta_- = 0$  in all these relations, when they reduce to (16) in Section 3.

There are some important special cases. 1st, suppose  $\eta = \eta_+ = -\eta_-$ . This corresponds to pure roll control on an aircraft by ailerons. Then:

$$\bar{\tau}_N = 2F_0 \begin{bmatrix} (P_2 + bs^2\psi c\eta) \{ \sigma_r [(2 - 3s^2\theta)c^2\psi c^2\eta + s^2\theta] + \frac{2}{3}\sigma_d c\psi c\eta c\theta \} s\eta \\ -(P_2 + bs^2\psi c\eta) (2\sigma_r c\psi c\eta c\theta + \frac{1}{3}\sigma_d) c\psi s\eta c\eta s\theta \\ [P_2 s\psi c\psi c^2\eta - P_1(1 - c^2\psi c^2\eta) - bs\psi c\psi s^2\eta c\eta] (2\sigma_r c\psi c\eta c\theta + \frac{1}{3}\sigma_d) s\theta \end{bmatrix} \quad (70)$$

$$\bar{\tau}_s = F_0(1 - \sigma_r) \begin{bmatrix} P_2 s\eta s\theta \\ -P_2 s\eta c\theta \\ -P_4 c\eta c\theta \end{bmatrix} s\theta \quad (71)$$

and these again reduce to (23) for  $\eta = 0$ . Note that, as in Section 3, the symmetry has led to the disappearance of  $h$ ; i.e., a displacement of the shaft axis along  $z$  has no effect.

Another special case is if  $\psi = 0$ , i.e., no dihedral. Then:

$$\bar{\tau}_N = 2F_0 \begin{bmatrix} (b + g) \{ \sigma_r [(2 - 3s^2\theta)c^2\eta + s^2\theta] + \frac{2}{3}\sigma_d c\eta c\theta \} \\ -(b + g) (2\sigma_r c\eta c\theta + \frac{1}{3}\sigma_d) c\eta s\theta \\ -f (2\sigma_r s\eta c\theta + \frac{1}{3}\sigma_d) s\eta s\theta \end{bmatrix} s\eta \quad (72)$$

$$\bar{\tau}_s = F_0(1 - \sigma_r) \begin{bmatrix} (b + g) s\eta s\theta \\ -(b + g) s\eta c\theta \\ -2f c\eta c\theta \end{bmatrix} s\theta \quad (73)$$

This has some interesting features. 1st, the expected propeller (or aileron like) torque shows up, as  $\bar{\tau}_{N1}$  is proportional to  $(b + g)s\eta$ , and depending only weakly on  $\theta$ . 2nd, there is a weak precession torque, mostly from  $\bar{\tau}_{s3}$ , proportional to  $fs\theta$ . The weakness is because  $f$  is very small in the above design. Note that the dependence on  $\eta$  is very weak — corresponding to the finding in Section 3 that there is a torque along  $E_3$ , even in the absence of dihedral.

Finally, the  $\bar{\tau}_2$  components are proportional to  $(b + g)s\eta s\theta$ , showing that propeller twist gives rise to a torque that moves  $L$  directly toward or away from the sun. The implications of this for the control of the spin direction, relative to the sun, will be taken up in the next section.



## 6 CONTROLLING SPIN RATE

This section presents the results of several calculations made to illuminate the control design issues, when propeller twist is added to the previous dihedral bend. It's a continuation of the work in Section 4. One factor limiting the control capabilities is the loss of power due to tilting the wings away from the sun. For reasonable angles, the loss factor on each wing is essentially  $c\phi_{+/-}$ , as given by (62) and (63). All we have to do is average these formulas over  $\alpha$ , when:

$$c\bar{\phi}_{+/-} = c\psi c\eta_{+/-} c\theta \quad (74)$$

and if all these angles are small:

$$\phi_{+/-}^2 = \psi^2 + \eta_{+/-}^2 + \theta^2 \quad (75)$$

For example, if  $\theta = 5$  deg,  $\psi = 3$  deg, and  $|\eta_{+/-}| = 2$  deg; then  $\phi_{+/-} = 6.16$  deg; and the average power loss is 0.58%.

Another important question is how long does it take to spin up (or down) the spacecraft. To answer this, suppose the twist angles are balanced; and that all the angles  $\psi$ ,  $\eta$ , and  $\theta$  are small. Then from (70) and (71), to 1st order in these angles:

$$\bar{\tau} = F_0 \begin{bmatrix} 4(\sigma_r + \frac{1}{3}\sigma_d)(b+g)\eta \\ 0 \\ -2(1-\sigma_r)f\theta \end{bmatrix} \quad (76)$$

Here, the  $\bar{\tau}_1$  term is the simplified propeller torque; while  $\bar{\tau}_3$  is the  $E_s$  term, previously seen in (23). Thus, a change in the spin rate  $\Delta\omega_s$  due to applying  $\bar{\tau}_1$  for a time  $\Delta t$  is:

$$\Delta\omega_s = \frac{\Delta L}{I_x} = \frac{\bar{\tau}_1 \Delta t}{I_x} = \frac{4}{I_x}(b+g) \left( \sigma_r + \frac{1}{3}\sigma_d \right) F_0 \eta \Delta t \quad (77)$$

and with the numbers in Sections 2 and 4 this is

$$\Delta\omega_s = \frac{4}{2 \times 10^2} (7.071 + 2.82)(0.31)(1.4296 \times 10^{-4}) \frac{\eta \Delta t}{r^2} = 8.767 \times 10^{-8} \frac{\eta \Delta t}{r^2}$$

Now, if we wish to change  $\omega_s$  by, say, 0.1 deg/s, and are at 4 AU, and let  $\eta = 10$  deg, then we'll need

$$\Delta t = \frac{(4)^2(0.1)}{(8.767 \times 10^{-8})(10)} = 1.825 \times 10^6 \text{ s} = 21.12 \text{ days}$$

Clearly, changing  $\omega_s$  by this method requires a lot of patience.

Another calculation examines the possibility of using the torque components  $\bar{\tau}_2$  in the no dihedral case for passive sun tracking. I'll give an approximate analysis. From (72) and (73), for small  $\eta$  and  $\theta$ , we have:

$$\bar{\tau}_2 = -F_0(b+g) \left( 1 + 3\sigma_r + \frac{2}{3}\sigma_d \right) \eta \theta \equiv -q\eta\theta \quad (78)$$

Now suppose this is simple linear motion; i.e., the apparent sun motion is directly away from the spin axis at a rate  $n$ . Then this torque component is normal to  $L$ , and will pull  $L$  toward the sun if  $\eta > 0$ . Then  $\theta$  evolves as

$$\theta(t) = \theta_0 + nt - \frac{L_2}{|L|} \quad (79)$$

where  $|L| = I_x \omega_s$ , a fixed quantity; and the component  $L_2$  evolves as

$$\dot{L}_2 = \bar{\tau}_2 = -q\eta\theta(t) \quad (80)$$

This equation has a simple solution:

$$\theta(t) = (\theta_0 - \theta_F)e^{nt/\theta_F} + \theta_F \quad (81)$$

where  $\theta_F$  is the terminal value of  $\theta(t)$ , given by

$$\theta_F = -Ln/(q\eta) \quad (82)$$

and the system settles to this value with a time constant

$$t_e = -\frac{\theta_F}{n} = \frac{L}{q\eta} \quad (83)$$

For numbers, the above design at 4 AU yields

$$q = 1.4296 \times 10^{-4} (7.071 + 2.82) [1 + (3)(0.31)] / (4)^2 = 1.706 \times 10^{-4} \text{ N-m/rad}^2$$

If we again take  $\omega_s = 0.1 \text{ deg/s}$ , then

$$L = (2 \times 10^4)(0.1)\pi/180 = 34.91 \text{ N-m-s}$$

and with  $\eta = 10 \text{ deg}$  once again, the time constant is

$$t_e = \frac{(34.91)(180)}{(1.706 \times 10^{-4})(10)\pi} = 1.172 \times 10^6 \text{ s} = 13.56 \text{ days}$$

and the offset angle for  $n = 10^{-8} \text{ rad/s}$ , as in Section 4, is

$$\theta_F = -nt_e = -.01172 \text{ rad} = -0.6715 \text{ deg}$$

This looks pretty good; but the problem is that we have just shown that, with these numbers,  $\omega_s$  would double in just 21.12 days. Because of this, I see no way to avoid an active spin control loop complementing this tracking technique; and as reversing the twist to spin down would also destabilize the sun tracking, it would be necessary to dump this unwanted momentum by the thrusters fairly often. In short, I see no way to construct a passive control system based on this technique.

Finally, this is a good place to ask what the possible effects on  $L$  would be from the impact of a meteor. To look at this, suppose a particle of mass  $m$  and speed  $v$  strikes normally near the tip of a wing. Well, the largest possible moment arm is  $l = g + 2bc\psi$ , or about 16 m. The speed of a particle at near solar system escape velocity might be as high as 70 km/s, relative to the spacecraft; so, to confer a momentum comparable to  $L$ , for  $\omega_s = 0.1 \text{ deg/s}$  requires a mass

$$m = \frac{L}{vl} = \frac{35}{(7 \times 10^4)(16)} = 3.2 \times 10^{-5} \text{ kg}$$

For size, a cube of ice of this mass would have an edge of about 3.15 mm. While the probability of such an event should be examined, a full spacecraft upset during hibernation seems quite unlikely.

**Reference:** P Regnier, "Hibernation Dynamics/AOCS Analyses", Matra Marconi Space, WP301T, ROS/TN/PR/162.95, 31/01/96.

## CONTROL SYSTEM AND FLEXIBLE SATELLITE INTERACTION DURING ORBIT TRANSFER MANEUVER.

10P.

Adenilson Roberto da Silva\*  
Luiz Carlos Gadelha de Souza\*\*

337603

In this paper the interaction between the attitude control system and the flexible structure of an artificial satellite during orbit transfer maneuver has been investigated. The satellite was modeled by a rigid central body with one or more flexible appendages. The dynamics equations were obtained by Lagrangean approach. The flexible appendages were treated as clamped-free beam and its displacement was discretized by assumed-mode method. In order to transfer the satellite, a typical Hohmann transfer and a burn-coast-burn strategy were used and the attitude was controlled by an on-off controller. During transfer procedure a global analysis of satellite has been done, such as: performance of control system, influence of elastic response in control system, thruster firing frequency, fuel consumption and variation of orbital elements. In order to avoid the interaction with structure motion, a control system with bandwidth of one decade below the fundamental frequency was used. In the simulations the firing frequency was evaluated in an approximately way but kept below the fundamental frequency of the structure. The control system has kept the attitude below the specifications. As a result, the orbit transfer maneuvering has been done correctly without excessive excitation of flexible appendage.

### INTRODUCTION

Study in dynamics and control of hybrid space structure (rigid body plus flexible appendages), has had a great interest in space engineering in last decades<sup>1,2,3</sup>. Because of diversity application and experiments, the power consumption has become a crucial point. As a result, the flexible structures of satellite tend to be larger and complex reflecting in the size and in the number of solar pannels. On the other hand, the mass in space operation is constrained, so that the solar pannels need to be thin and large, becoming flexible. These components are exposed to structural vibrations that if they are not

---

\* Ph.D. student. National Institute for Space Research - INPE-Space Mechanics & Controls Division, CP 515, S J Campos, S P. 12227-010 Phone (055-012) 345-6240, Fax 345 6226, adenilson@dem.inpe.br.

\*\* Space Engineer. National Institute for Space Research - INPE-Space Mechanics & Controls Division, CP 515, S J Campos, S P. 12227-010 Phone (055-012) 345-6197, Fax 345 6226, gadelha@dem.inpe.br.

damped they can affect the performance of the control system and the attitude determination. So, the missions that need more accuracy of pointing or stability will be damaged.

Orbit transfer maneuver and/or orbit corrections are often necessary due to thruster inaccuracy and/or orbit transfer strategy. In other cases, the orbit transfer maneuver must be performed in order to put the satellite in the desired final orbit. A study in orbit transfer maneuver can be found in (Ref. 4).

In this paper, the problem of transferring a satellite with flexible appendages has been studied. During transfer procedure a global analysis of satellite has been done, such as: performance of control system, influence of elastic response in control system, frequency of firing of thruster, fuel consumption and variation of orbital elements.

## TRANSFER PROCEDURE

During the transfer procedure, three different coordinates system has been used in order to characterize the dynamics, the orientation and the localization of the satellite in orbit.  $OXYZ_b$  is the coordinate system of body; its origin is in the center of mass of the satellite.  $XYZ_{lvh}$  is used to describe the position of satellite in orbit. It is defined as:  $X_{lvh}$  is roll axis,  $Z_{lvh}$  is yaw axis that is pointing to Earth center and  $Y_{lvh}$  is pitch axis, perpendicular to orbit plane, composing a right-handed coordinate system. In order to describe the elastic and rotational motion of the flexible appendages with respect to  $OXYZ_b$ , the  $XYZ_a$  coordinate system was used, which center is the point of join between flexible appendages and rigid body.

The thrusters are denoted by  $J_i$  and their locations are showed in Figure 1. If we supposed that resultant force vector used in transfer maneuver has an offset with respect to  $Z_b$  axis, the firing of thruster can generate yaw motion. Because of the asymmetry pitch and roll motions will occur. As the tolerance of attitude excursion is reduced ( $\pm 3^\circ$ ), the firing frequency can be increased and reach the natural frequency of solar pannels. Any cycle of firing close to this frequency could cause an excessive response of appendages. The thruster used in orbit transfer provides a force of 20 N and the thrusters used in attitude correction provides 1 N each one

In order to transfer the satellite from a circular initial orbit to a final circular orbit, a burn-coast-burn procedure was used. It is assumed that initial and final orbit are maintained in the same orbital plane. The first burn will occur between A and B points as showed in Figure 2 and is long enough to inject the satellite in an elliptical transfer orbit, whose apogee altitude is close to final orbit. Once enough velocity has been obtained, the thruster is stopped and the satellite coasts until reach C point, where the second burn is started. The second burn is applied for a time sufficient to circularize the transfer orbit.

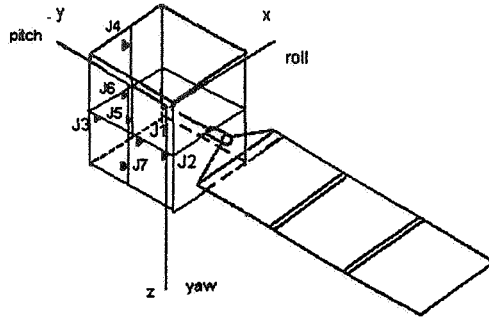


**Figure 1 - Thrusters location**

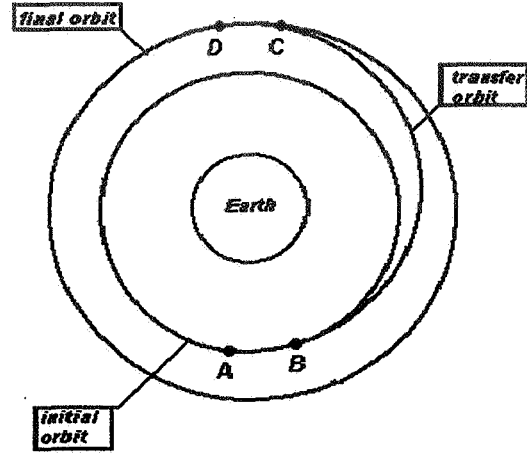


**Figure 2 - Transfer strategy**

From orbital mechanics, we can evaluate the increment in satellite velocity in first and second burn, respectively, by

$$\Delta V_1 = \sqrt{\frac{\mu}{R_1}} * \left( \sqrt{\frac{2 * \left( \frac{R_2}{R_1} \right)}{1 + \left( \frac{R_2}{R_1} \right)}} - 1 \right) \quad (1)$$

$$\Delta V_2 = \sqrt{\frac{\mu}{R_2}} * \left( 1 - \sqrt{\frac{2}{1 + \left( \frac{R_2}{R_1} \right)}} \right) \quad (2)$$

where  $\mu$  is the product of gravitational constant by the mass of Earth;  $R_1$  is the radius of initial orbit;  $R_2$  is the radius of final orbit.

The first and second burn period are given, respectively, by

$$\Delta t_1 = \left( \sqrt{\frac{2 * \left( \frac{R_2}{R_1} \right)}{1 + \left( \frac{R_2}{R_1} \right)}} - 1 \right) * \left( \sqrt{\frac{\mu}{R_1}} * \frac{m_t}{F} \right) \quad (3)$$

$$\Delta t_2 = \left( \sqrt{\frac{\mu}{R_2}} * \left( 1 - \sqrt{\frac{2}{1 + \left( \frac{R_2}{R_1} \right)}} \right) \right) * \frac{m_t}{F} \quad (4)$$

where  $m_t$  is total satellite mass;  $F$  is the thrusters force.

The coast period can be evaluated by

$$t_{\text{coast}} = \pi * \sqrt{\frac{(R_1 + R_2)^3}{8 * \mu}} \quad (5)$$

and the fuel consumption in orbit transfer maneuver and attitude control are given by

$$M_c = \frac{F}{I_{sp} * g} * t \quad (6)$$

where  $I_{sp}$  is specific impulse of fuel;  $g$  is gravitational acceleration;  $t$  is the firing time.

The orbital motion of the center of mass of the satellite is expressed in spherical coordinate system as showed in Figure 3, whose center is located in the center of the Earth. The acceleration of mass center in unit vector  $e_r, e_\theta, e_\phi$  direction can be written as<sup>5</sup>

$$\begin{aligned} a_r &= \ddot{r} - r\dot{\theta}^2 - r\dot{\phi}^2 \sin^2 \theta = F_r / m_t \\ a_\theta &= r\ddot{\theta} + 2\dot{r}\dot{\theta} - r\dot{\phi}^2 \sin \theta \cos \theta = F_\theta / m_t \\ a_\phi &= r\ddot{\phi} \sin \theta + 2\dot{r}\dot{\phi} \sin \theta + 2r\dot{\theta}\dot{\phi} \cos \theta = F_\phi / m_t \end{aligned} \quad (7)$$

The unit vector direction  $e_r$  coincides with  $-Z_{lvh}$  axis and  $F_r, F_\theta, F_\phi$  are the applied forces in  $r, \theta, \phi$  coordinate system.

Considering the thruster directions and the action of gravitational force, the applied forces can be written as<sup>6</sup>

$$\begin{aligned} F_r &= -m_s \frac{\mu}{r^2} \\ F_\theta &= J_1 * \cos(\delta) * \text{sign}(\dot{\theta}) \\ F_\phi &= J_1 * \sin(\delta) \end{aligned} \quad (8)$$

where:

$$\delta = \text{asin}[\cos(\gamma)/\sin(\theta)], \text{ for } 0 < \gamma < \pi/2,$$

$$\delta = \text{asin}[\cos(\pi-\gamma)/\sin(\theta)], \text{ for } \pi/2 < \gamma < \pi, \gamma \text{ is the orbit inclination.}$$

## SATELLITE MODEL

The dynamics characteristics of satellite are represented as combination of rigid body and flexible structures. The environmental torques are supposed negligible if compared with torques due to the thrusters. Since the attitude motion is maintained within  $\pm 3^\circ$ , the satellite orientation can be represented by a time integral of its angular rate.

The equations that describe the rotational dynamics and elastic displacement are obtained by Lagrangean approach<sup>7</sup>. Therefore, the potential and kinetic energy of system must be evaluated. The elastic displacement is discretized by assumed mode<sup>8</sup>.

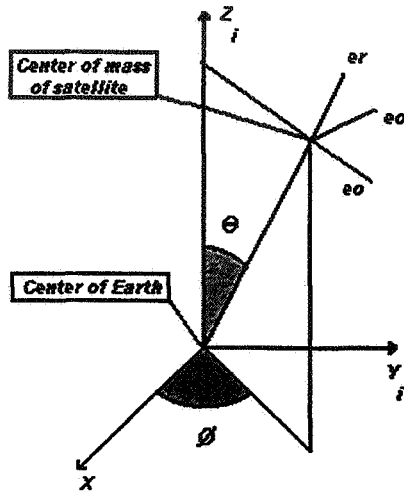


Figure 3 - Spherical coordinate system

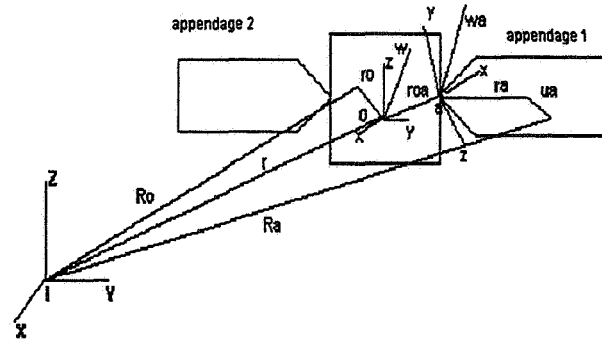


Figure. 4 - Rigid body and flexible appendages

Consider a system formed by a central rigid body and  $n$  flexible appendages fixed to it, as showed in Figure 4. The kinetic energy  $T$  and the potential energy  $V$  of system are given respectively, by<sup>9</sup>

$$T(t) = \frac{1}{2} \int_{m_o} \dot{R}_o \cdot \dot{R}_o dm_o + \frac{1}{2} \int_{m_a} \dot{R}_a \cdot \dot{R}_a dm_a \quad (9)$$

$$V(t) = \frac{1}{2} \sum_a^n \int_{m_a} EI (w'')^2 dx \quad (10)$$

A point in the rigid body and in the panel can be given respectively by

$$R_o = r + r_o \quad (11)$$

$$R_a = r + r_{oa} + r_a + u_a \quad (12)$$

Using vetrix concept<sup>10</sup> and based in Eqs. (11) and (12), the expressions of cinetic energy can be written as<sup>6</sup>

$$T(t) = \left\{ \frac{1}{2} \dot{r}^t m \dot{r} + \frac{1}{2} \dot{\omega}^t I_r \omega + \dot{r}^t C_{xx} \dot{\omega} + \dot{r}^t C_{xx} \sum_a^n C_{ax}^t S_a^t \omega_a + C_{ax}^t S_a^t \dot{\omega}_a + C_{ax}^t \phi_a \dot{q}_a \right\} + \left\{ \dot{\omega}^t \left( \sum_a^n H_a \dot{q}_a \right) + \dot{\omega}^t \sum_a^n N_a \omega_a + \frac{1}{2} \sum_a^n \omega_a^t I_a \omega_a + \frac{1}{2} \sum_a^n \dot{q}_a^t (M_a \dot{q}_a + 2\theta_a^t \omega_a) \right\} \quad (13)$$

where:  $I_o$  = inertia matrix of rigid body;  $I_a$  = inertia matrix of appendage;  $\phi$  = admissible function;  $\omega$  = rigid body rotation;  $\omega_a$  = appendages rotation;  $q_a$  = elastic displacement;  $C_{ij}$  = rotation matrix relating the  $i$  and  $j$  frames.

The terms independent of the time are given by

$$\underline{S}_a = \int_{ma} \underline{r}_a \underline{dm}_a; \quad \underline{\phi}_a = \int_{ma} \underline{\phi}_a \underline{dm}_a; \quad \underline{M}_a = \int_{ma} \underline{\phi}_a^t \underline{\phi}_a \underline{dm}_a; \quad \underline{\theta}_a = \int_{ma} \underline{r}_a^t \underline{\phi}_a \underline{dm}_a;$$

$$\underline{I}_t = \underline{I}_0 + \sum_a^n (\underline{C}_{ax}^t \underline{I}_a \underline{C}_{ax} - \underline{r}_{0a}^2 \underline{m}_a + 2 \underline{r}_{0a} \underline{C}_{ax}^t \underline{S}_a^t \underline{C}_{ax}); \quad \underline{S}_t^t = \sum_a^n (\underline{r}_{0a}^t \underline{m}_a + \underline{C}_{ax}^t \underline{S}_a^t \underline{C}_{ax});$$

$$\underline{N}_a = \underline{r}_{0a} \underline{C}_{ax}^t \underline{S}_a^t + \underline{C}_{ax}^t \underline{I}_a, \quad \underline{H}_a = \underline{r}_{0a} \underline{C}_{ax}^t \underline{\phi}_a + \underline{C}_{ax}^t \underline{\theta}_a$$

the symbol (-) denotes skewsimetric matrix.

The potential energy V can be evaluated by an inner product of energy<sup>8</sup>.

$$V(t) = \frac{1}{2} [\underline{u}_a, \underline{u}_a] = \frac{1}{2} \underline{q}_a^t [\underline{\phi}_a, \underline{\phi}_a] \underline{q}_a = \frac{1}{2} \underline{q}_a^t \underline{K}_a \underline{q}_a \quad (14)$$

where:  $\underline{K}_a = [\underline{\phi}_a, \underline{\phi}_a]$  is the stiffness matrix of system.

The Eqs. (13) and (14) in matrix form can be written as

$$T(t) = \frac{1}{2} \dot{\underline{X}}^t \underline{M} \dot{\underline{X}}, \quad (15)$$

$$V(t) = \frac{1}{2} \underline{X}^t \underline{K} \underline{X} \quad (16)$$

where mass matrix M and stiffness matrix K, are given respectively by

$$\underline{M} = \begin{bmatrix} \underline{n}_t & \underline{C}_{xx} \underline{S}_t^t & \underline{C}_{xx} \sum_a^n \underline{C}_{ax}^t \underline{S}_a^t & \underline{C}_{xx} \sum_a^n \underline{C}_{ax}^t \underline{\phi}_a \\ \underline{C}_{xx}^t \underline{S}_t & \underline{I}_t & \sum_a^n \underline{N}_a & \sum_a^n \underline{H}_a \\ \underline{C}_{xx}^t \sum_a^n \underline{S}_a \underline{C}_{ax} & \sum_a^n \underline{S}_a \underline{C}_{ax} & \underline{I}_a & \sum_a^n \underline{\theta}_a \\ \underline{C}_{xx}^t \sum_a^n \underline{\phi}_a^t \underline{C}_{ax} & \sum_a^n \underline{H}_a^t & \sum_a^n \underline{\theta}_a^t & \underline{M}_a \end{bmatrix}; \quad \underline{K} = \begin{bmatrix} 0 & 0 & 0 & 0 \\ 0 & 0 & 0 & 0 \\ 0 & 0 & 0 & 0 \\ 0 & 0 & 0 & \underline{K}_a \end{bmatrix}$$

The state vector X is defined as

$$\underline{X} = [\underline{r} \quad \underline{\xi} \quad \underline{\alpha} \quad \underline{q}_a]^T \Rightarrow \dot{\underline{X}} = [\dot{\underline{r}} \quad \dot{\underline{\omega}} \quad \dot{\underline{\omega}}_a \quad \dot{\underline{q}}_a]^T$$

where r is linear displacement;  $\underline{\xi}$  is rotational displacement of rigid body;  $\underline{\alpha}$  is rotational displacement of flexible appendage with respect of rigid body;  $\underline{q}_a$  is elastic displacement of appendage.

Using Lagrange's Equation the equations of motion for the system can be written as

$$\underline{M} \ddot{\underline{X}} + \underline{K} \underline{X} = 0 \quad (17)$$

where the force F has been neglected.



Using the properties of spectral decomposition<sup>11</sup>, the Eq. (17) can be written in modal state variable form as:

$$\dot{x} = Ax + Bu, \quad A = \begin{bmatrix} 0 & I_n \\ -\omega_i^2 & -2\zeta\omega_i \end{bmatrix} \quad B = \begin{bmatrix} 0 \\ \psi_i^t b_c \end{bmatrix}$$

$$Y = Cx \quad (18)$$

where  $x$  is modal variables;  $\psi$  is the matrix of eigenvectors of system;  $\omega_i$  ( $i=1..n$ ) are the natural frequencies of vibration,  $B$  represents the actuator locations and  $C$  matrix represents the sensor locations.

An on-off controller<sup>10,11</sup> was used where the feedback are angular position and angular rate. The control laws are given by<sup>6</sup>

$$\begin{aligned} T_x &= -T_i * \text{sign}(\xi_x + k * \omega_x) \\ T_y &= -T_i * \text{sign}(\xi_y + k * \omega_y) \\ T_z &= -T_i * \text{sign}(\xi_z + k * \omega_z) \end{aligned} \quad (19)$$

where  $\xi_i$  and  $\omega_i$  represent respectively position and angular rate,  $T_i$  the control torque and  $k$  the angular rate gain, which was obtained by simulations.

## SIMULATION AND RESULTS

The model of satellite used in simulations has structural characteristic similar of *China – Brazil Earth Research Satellite* [CBERS]<sup>12</sup>. The goal in this study is to analyze the influence of elastic response in control variables when the thruster is firing and the performance of control system. In the orbit transfer maneuver, the satellite has its attitude controlled with respect to  $XYZ_{lvh}$  coordinate system, where the maximum attitude errors must be kept within  $\pm 3^\circ$ . In the simulations, the following data have been used: radius of initial orbit 7118 Km; radius of final orbit: 7156 Km; inclination of orbital plane:  $98.5^\circ$ ; argument of perigee:  $90.0^\circ$ ; longitude of ascendent node:  $60.0^\circ$ ; mean anomaly:  $0.0^\circ$ ;  $m_t$ : 1400 Kg; mass of appendage: 49 Kg; length of appendage: 6.135 m; the inertia moment of satellite and appendages can be found in (Ref. 12).

Initially, the satellite was in circular orbit, when the transfer thrust was fired, the eccentricity increase during the first burn, remain constant in coast period. When the satellite reaches C point the transfer thrust is fired again and the eccentricity decrease and the orbit is circularized (Figure 5). Figure 6, shows that the semi-major axis of orbit is increase during the first and second burn, remain constant during coast period. In the end of second burn, the semi-major axis reaches the specified final value. The other orbital elements remain constant during all transfer period.

As showed in Figure 7, the errors in roll and pitch axes occurred by the influence of flexibility in the control system, because there is no torques applied in this axis; this fact can be observed in Figure 11, which shows that the tolerance is not reach.

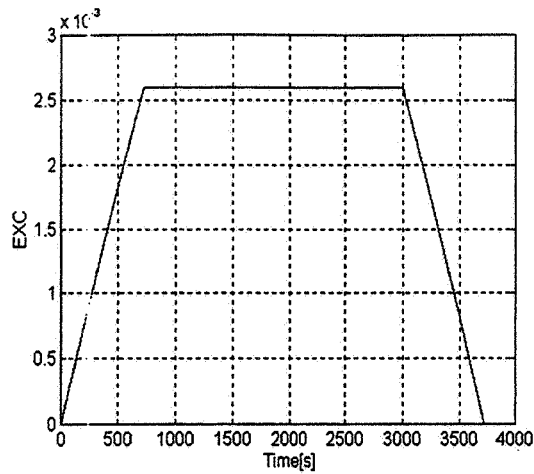


**Figure 5 - Eccentricity change due to maneuver**

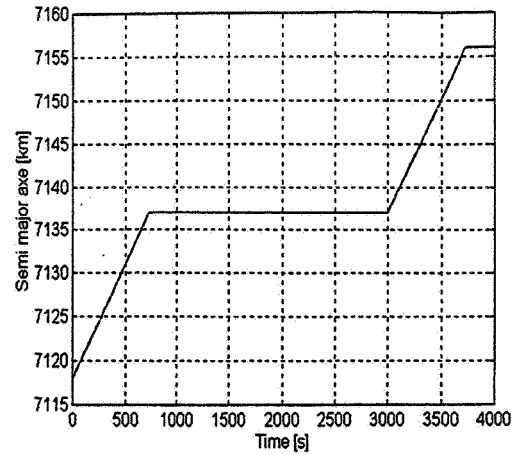


**Figure 6 - Semi-major change due to maneuver**

Because of the offset, the error in yaw axis quickly reaches the tolerance, as showed in Figure 8, then the firing sequence was started by the control system. The angular rates are showed in Figure 9. Finally in Figure 10 the fuel consumption in orbit transfer maneuver and in the attitude control thrusters were showed. The elastic displacement of appendages is showed in Fig. 12, which shows that when transfer thruster is fired in  $X_b$  direction, the appendage initially considered motionless is moved in opposite direction. It is important to note that this force has an offset of 1 cm with respect to yaw axis; which creates a torque around  $Z_b$  axis. Due to this, an oscillation is decreased and stabilized around  $-0.035$  m, keeping in this position during the burn period. The small oscillations during burn period are due to the firing of control system thrusters. In  $Y_b$  direction it was not observe displacement, this is justified by the fact that the model does not have applied force in  $Y_b$  direction. In  $Z_b$  direction have been observed that the appendage initially oscillated and stabilized around  $-0.02$ m.

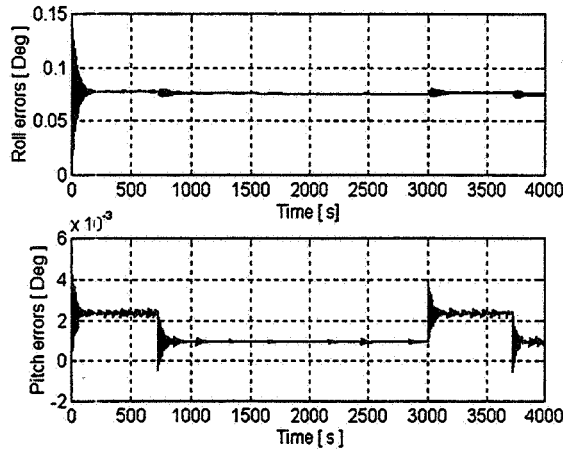


**Figure 7 – Errors in pitch and roll axis**

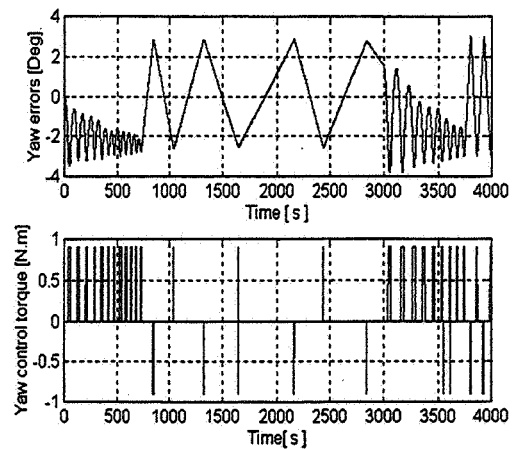


**Figure 8 – Error and firing sequence in yaw axis**

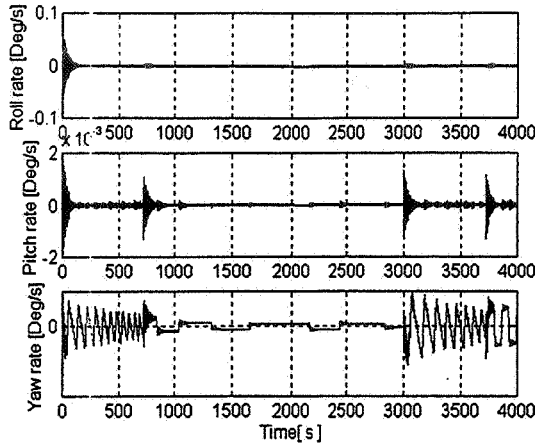


**Figure 9 - Angular rates**

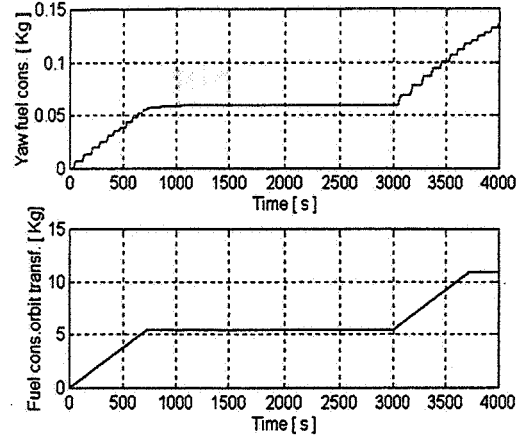


**Figure 10 - Fuel consumption**

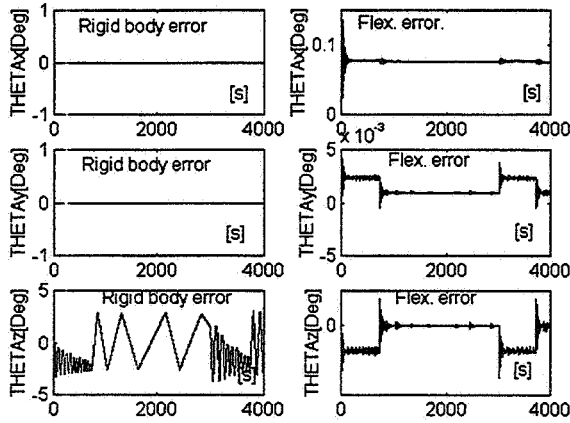


**Figure 11 – Influence of flexibility in control system.**

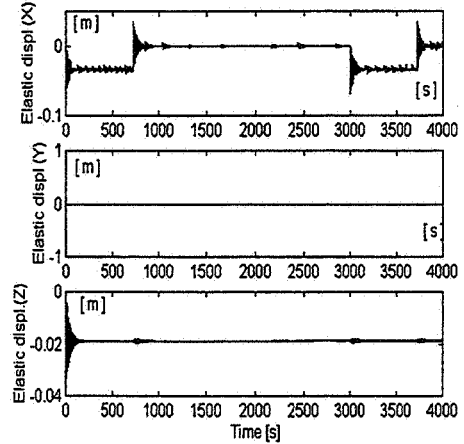


**Figure 12 – Elastic displacement.**

## CONCLUSIONS

In this paper, a generic model of satellite composed by a central rigid body and flexible appendages was developed and a Hohmann transfer maneuvering based in burn-coast-burn strategy was designed. As a result, it was verified that if there is a jet fire cycling close to the fundamental frequency of appendage, a potential possibility of interaction between control system and flexible structure exist. This fact can damages the performance of control system and structural problems can be occur. In order to avoid the interaction with structure motion, a control system with bandwidth of one decade bellow the fundamental frequency was used. In simulations the firing frequency (0.015 Hz) was evaluated in approximately way<sup>6</sup> but kept below the fundamental frequency (0.13 Hz) of the structure. The control system used was able to keep the attitude below specifications, therefore, the orbit transfer maneuvering has been done correctly, without excessive excitation of flexible appendage and with low fuel consumption.

## ACKNOWLEDGEMENTS

This work was funded by Conselho Nacional de Desenvolvimento Científico e Tecnológico – CNPq – Brazil under grant N° 520182/93-6.

## REFERENCES

1. SOUZA, L. C. G, "Robust Controller Design for a Flexible Space System with Mixed Uncertainty Model.", International Symposium on Spacecraft Ground Control and Flight Dynamics SCD1. 7-11 Feb, São José dos Campos - SP, Brasil. Special Issue of Revista Brasileira de Ciências Mecânicas, 1994, pp. 116-123.
2. SOUZA, L. C. G, "Robust Controller Design for Flexible Space System using a combination of LQG/LTR and PRLQG Methods", Dynamics and Control of Structure in Space III, Comp. Mech. Publ., Southampton, U. K., 1996. ISBN 1 85312 415, pp.151-166.
3. SOUZA, L. C. G, "Dynamic Model for a Flexible Space System Aiming at a Robust Control Design", in Mecânica Computacional, Bariloche, Argentina, 1997, pp. 367-376.
4. LIM, T. and COOPER, P., "Control/Structure Interaction Study of the Space Station Freedom First Flight Concept During Reboost", AIAA Paper 90-0747, AIAA 28Th Aerospace Sciences Meeting, Reno, Nevada, 1990.
5. GREENWOOD, D.T., Principles of Dynamics, Prentice Hall, N.J., 1965.
6. SILVA, A., R., Study of control system of an artificial satellite during orbit transfer maneuver and normal operationing mode (Msc thesis). INPE - National Institute for Space Research- São José dos Campos-1997.
7. MEIROVITCH, L., Methods of analytical dynamics, New York, USA, McGraw-Hill Book Company, 1970.
8. MEIROVITCH, L., and KWAK, M.K. "Dynamics and control of spacecraft with retargeting flexible antennas". Journal of Guidance, Control and Dynamics, March-April 1990, pp. 241-248.
9. FLORA, A.L., Design of attitude control system of satellite with flexible appendages by LQG/LTR methods and  $H_\infty$  (Msc thesis). INPE - National Institute for Space Research, São José dos Campos - 1995.
10. SHAHIAN, B. e HASSUL, M., Control System Design Using Matlab, New Jersey, USA, Prentice Hall, 1993.
11. PHILLIPS, C.L. and HARBOR, R. D., Feedback control systems. Prentice Hall International Editions, 1991.
12. NUNES, D., CBERS - Preliminary Design of Attitude and Orbit Control System - INPE - National Institute for Space Research, São José dos Campos - 1988.

543-13

169341

141

# ATTITUDE PROPAGATION USING NON-SINGULAR CANONICAL VARIABLES

Maria Cecília Zanardi\*

331604

Three sets of non-singular canonical variables for the rotational motion are analyzed. These sets are useful when the angle between z-axis of a coordinate system fixed in artificial satellite ( here defined by the directions of principal moments of inertia of the satellite) and the rotational angular momentum vector is zero or when the angle between Z-inertial axis and rotational angular momentum vector is zero. The goal of this paper is to compare all these sets and to determine the benefits of their uses. With this objective, the dynamical equations of each set were derived, when mean hamiltonian associate with the gravity gradient torque is included. For the torque-free rotational motion, analytical solutions are computed for symmetrical satellite for each set of variables. When the gravity gradient torque is included, an analytical solution is shown for one of the sets and a numerical solution is obtained for one of the other sets. By this analysis we can conclude that: the dynamical equation for the first set is simple but it has neither clear geometrical nor physical meaning; the other sets have geometrical and physical meaning but their dynamical equations are more complex.

## INTRODUCTION

Andoyer's variables<sup>1,2,3</sup> are canonical variables and they can describe the rotational motion of an artificial satellite. These variables ( $l_1, l_2, l_3, L_1, L_2, L_3$ ) are shown in the Figure 1, where O is the center of mass of the satellite, Oxyz is the principal moment of inertia axes of the satellite, OXYZ is the inertial axes and OX'Y'Z' is the rotational angular momentum axes, with OZ' onto the rotational angular momentum vector ( $\vec{L}_2$ ).

The Andoyer's variables are defined as:  $L_2$  is the magnitude of the rotational angular momentum vector  $\vec{L}_2$ ;  $L_1$  is projection of  $\vec{L}_2$  onto the z-axis of a coordinate system fixed to the artificial satellite and defined by the direction of principal moment of inertia  $I_{zz}$  ( $L_1 = L_2 \cos J$ , where J is the angle between z-axis and vector  $\vec{L}_2$ );  $L_3$  is the projection of  $\vec{L}_2$  onto the Z-inertial axis ( $L_3 = L_2 \cos I$ , where I is the angle between Z-axis and vector  $\vec{L}_2$ );  $l_3$  is the angle measured from X-inertial axis along the XY-inertial plane up to a node N, defined by the intersection of the XY-plane and a plane perpendicular to  $\vec{L}_2$ ;  $l_2$  is the angle measured from the node N along the plane perpendicular to  $\vec{L}_2$  up to another node  $\bar{N}$ , defined by the intersection of the plane perpendicular to  $\vec{L}_2$  with the xy-plane, defined by the directions of moments of inertia  $I_{xx}$  and  $I_{yy}$ ; and  $l_1$  is the angle measured from the node  $\bar{N}$  along xy-plane up to the x-axis.

\* Grupo de Dinâmica Orbital e Planetologia da UNESP - Department of Mathematics - UNESP - Campus de Guaratinguetá - 12500-000 - Guaratinguetá (SP) - Brazil - phone: (55)-012-525-2800, ext. 105 - fax: (55)12-522-3590 - email: cecilia@feg.unesp.br

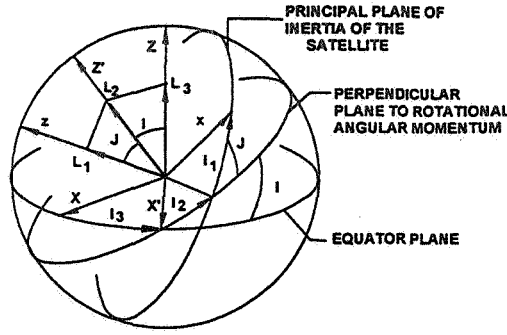


Figure 1 - Andoyer's variables ( $l_1, l_2, l_3, L_1, L_2, L_3$ )

The largest advantage of canonical variables is that the dynamical equation of motion is written in the canonical form

$$\frac{dl_i}{dt} = \frac{\partial F}{\partial L_i} \quad \frac{dL_i}{dt} = -\frac{\partial F}{\partial l_i} \quad i=1,2,3$$

where  $F$  is the Hamiltonian for a conservative problem, given by the sum of the kinetic energy and the potential energy.

In the case of the torque-free rotational motion, the solution of the dynamical equations is given by elliptic functions<sup>2</sup>. This solution is simplified for a symmetrical satellite with  $I_{xx} = I_{yy}$ . When the gravity gradient torque is included in the Hamiltonian  $F$  for the rotational motion and  $I_{xx} \cong I_{yy}$ , an analytical solution of the dynamical equations was computed by Zanardi<sup>4</sup>, using Hori's method.

Although the Andoyer's canonical variables are suitable for theoretical studies of rotational motion, there are difficulties when the angles  $J$  and  $I$  are small, i.e., when  $L_1 \cong L_2$  or  $L_3 \cong L_2$ . Actually, in the limit  $L_1 \rightarrow L_2$  the angles  $l_1$  and  $l_2$  are indefinite while their additional combination such as  $l_1 + l_2$  remains determined. Similarly, when  $L_3 \rightarrow L_2$  the amount  $l_3 + l_2$  is well defined but the separation between  $l_3$  and  $l_2$  become impractical. Because of these singularities, new sets of canonical variables were introduced by Giacaglia and Jefferys<sup>5</sup> in 1971 and Fukushima<sup>6,7</sup> in 1993, using canonical transformations. All these sets of non-singular variables are defined from Andoyer's variables and the dynamical equations of the rotational motion can be gotten using Hamiltonian formalism.

The objective of this paper is to compare all these three sets of non-singular variables for the rotational motion and to determine the benefits of their uses. The dynamical equations of each set are derived, when the mean Hamiltonian associated with the gravity gradient torque was included.

As the Hamiltonian  $F$  of the problem in terms of Andoyer's variables ( $l_i, L_i, i=1,2,3$ ) is given in Zanardi<sup>4</sup>, it's easier to use the partial derivatives of each set of variables ( $x_1, x_2, x_3, y_1, y_2, y_3$ ) with relation to each of Andoyer's variables in order to compute the dynamical equations, i. e.,

$$\begin{aligned} \frac{dx_i}{dt} &= -\frac{\partial F}{\partial y_i} = -\sum_{j=1}^3 \left( \frac{\partial F}{\partial l_j} \frac{\partial l_j}{\partial y_i} + \frac{\partial F}{\partial L_j} \frac{\partial L_j}{\partial y_i} \right) \\ \frac{dy_i}{dt} &= \frac{\partial F}{\partial x_i} = \sum_{j=1}^3 \left( \frac{\partial F}{\partial l_j} \frac{\partial l_j}{\partial x_i} + \frac{\partial F}{\partial L_j} \frac{\partial L_j}{\partial x_i} \right) \end{aligned} \quad (1)$$

$i = 1, 2, 3$

In this paper, for the torque-free rotational motion and a symmetrical satellite, an analytical solution will be gotten for the dynamical equation for each set of variables. When the gravity gradient torque is included in the dynamical equations, an analytical solution is obtained only for the first set of non-singular canonical variables and numerical solutions are obtained for the second set.

### FIRST SET OF VARIABLES

The first set of variables introduced by Giacaglia and Jefferys<sup>5</sup> is valid when the inclinations  $I$  and  $J$  are small. These variables are defined by the following transformation:

$$\begin{aligned} x_1 &= L_2 & y_1 &= l_1 + l_2 + l_3 \\ x_2 &= \sqrt{2(L_2 - L_1)} \cos l_1 & y_2 &= -\sqrt{2(L_2 - L_1)} \sin l_1 \\ x_3 &= \sqrt{2(L_2 - L_3)} \cos l_3 & y_3 &= -\sqrt{2(L_2 - L_3)} \sin l_3 \end{aligned} \quad (2)$$

Introducing  $\varepsilon = \sin(J/2)$  and  $\gamma = \sin(I/2)$ , the Eqs (2) can be written as:

$$\begin{aligned} x_1 &= L_2 & y_1 &= l_1 + l_2 + l_3 \\ x_2 &= 2\sqrt{L_2} \varepsilon \cos l_1 & y_2 &= -2\sqrt{L_2} \varepsilon \sin l_1 \\ x_3 &= 2\sqrt{L_2} \gamma \cos l_3 & y_3 &= -2\sqrt{L_2} \gamma \sin l_3 \end{aligned} \quad (3)$$

We can obtain the inverse form of Eq.(3):

$$\begin{aligned} l_1 &= \tan^{-1}(-y_2 / x_2) & \varepsilon &= \sqrt{(x_2^2 + y_2^2) / 4x_1} \\ l_2 &= y_1 + \tan^{-1}(y_2 / x_2) + \tan^{-1}(y_3 / x_3) & L_2 &= x_1 \\ l_3 &= \tan^{-1}(-y_3 / x_3) & \gamma &= \sqrt{(x_3^2 + y_3^2) / 4x_1} \end{aligned} \quad (4)$$

The dynamical equation for this set can be gotten using Eq.(1) and Eq.(4), with the Hamiltonian  $F = F_0 + F_1$ , given in Zanardi<sup>4</sup>, where  $F_0$  is hamiltonian associate with the torque-free rotational motion and  $F_1$  is the mean Hamiltonian ( terms of  $F_1$  depend only  $l_3, L_1, L_2, L_3$ ) associated with the gravity gradient torque.

For a symmetrical satellite (principal moments of inertia  $I_{xx} = I_{yy}$ ) and for torque-free rotational motion ( $F = F_0$ ), the system of equations are:

$$\begin{aligned} \dot{x}_1 &= 0 & \dot{x}_3 &= 0 & \dot{y}_3 &= 0 \\ \dot{x}_2 &= \left[ \frac{1}{I_{zz}} - \frac{1}{I_{xx}} \right] (2x_1 - x_2^2 - y_2^2) \frac{y_2}{2} \\ \dot{y}_1 &= \frac{1}{I_{xx}} x_1 + \left[ \frac{1}{I_{zz}} - \frac{1}{I_{xx}} \right] \left\{ \left( \frac{2x_1 - x_2^2 - y_2^2}{2x_1} \right)^2 x_1 + \left( \frac{x_2^2 + y_2^2}{4x_1} \right) (2x_1 - x_2^2 - y_2^2) \right\} \\ \dot{y}_2 &= -\left[ \frac{1}{I_{zz}} - \frac{1}{I_{xx}} \right] (2x_1 - x_2^2 - y_2^2) \frac{x_2}{2} \end{aligned} \quad (5)$$

We can note in this case that the magnitude of rotational angular momentum  $x_1$ , the variables  $x_3$  and  $y_3$  are constant. The analytical solutions for the other variations are:

$$x_2 = w \cos(At + \phi) \quad y_2 = -w \sin(At + \phi) \quad y_1 = Bt + y_{10} \quad (6)$$

where

$$\begin{aligned} \phi &= \tan^{-1}\left(\frac{-y_{20}}{x_{20}}\right) \\ w &= \sqrt{x_{20}^2 + y_{20}^2} = 2\varepsilon_0 \sqrt{x_{10}} \\ A &= \left[\frac{1}{I_{zz}} - \frac{1}{I_{xx}}\right](1 - 2\varepsilon_0^2)x_{10} \\ B &= \frac{1}{I_{xx}}x_{10} + \left[\frac{1}{I_{zz}} - \frac{1}{I_{xx}}\right]\left\{(1 - 2\varepsilon_0^2)^2 x_{10} + 2x_{10}\varepsilon_0^2(1 - 2\varepsilon_0^2)\right\} \end{aligned} \quad (7)$$

and the index "0" means the initial conditions.

In the case where the gravity gradient torque is included, the dynamical equations are more complex and we present here the analytical solution for two particular cases:

1 - When the orbital inclination ( $I'$ ) is zero, we have the following solutions:

$$\begin{aligned} x_1 &= x_{10} & y_1 &= Et + y_{10} \\ x_2 &= w \cos(Ct + \phi) & x_3 &= \bar{w} \cos(Dt + \phi) \\ y_2 &= -w \sin(Ct + \phi) & y_3 &= -\bar{w} \sin(Dt + \phi) \end{aligned} \quad (8)$$

where

$$\begin{aligned} C &= A + C_g & E &= B + E_g \\ C_g &= \frac{3k}{2x_{10}}(1 - 2\varepsilon_0^2)\left\{1 + \frac{3}{2}\left[1 - (1 - 2\gamma_0^2)^2\right]\right\} \\ D &= \frac{3k}{4x_{10}}(1 - 2\gamma_0^2)\left[3(1 - 2\varepsilon_0^2)^2 - 1\right] \\ E_g &= \frac{3k\varepsilon_0^2}{x_{10}}(1 - 2\varepsilon_0^2)\left[-1 + \frac{3}{2}\left(1 - (1 - 2\gamma_0^2)^2\right)\right] - \frac{3k\gamma_0^2}{2x_{10}}(1 - 2\gamma_0^2)\left[3(1 - 2\varepsilon_0^2)^2 - 1\right] \\ \bar{w} &= \sqrt{x_3^2 + y_3^2} = 2\sqrt{x_{10}} \gamma_0 \\ k &= \frac{\mu^4 M^6}{L^6}(I_{zz} - I_{xx})\left[1 + \frac{3}{2}e^2\right] \end{aligned} \quad (9)$$

with  $\phi$ ,  $w$ ,  $A$  and  $B$ , given in Eq.(7) and  $\mu$  is the Earth gravitational constant,  $L = M\sqrt{\mu a}$ ,  $M$  is the satellite's mass,  $a$  and  $e$  are the semi-axis and excentricity of the orbit respectively.

We can note that the variables  $x_3$  and  $y_3$  have a small periodic variations due to the gravity gradient torque and it also causes a small periodic variation in the variables  $x_2$  and  $y_2$  and small linear variation on  $y_1$ , given by  $C_g$  and  $E_g$  respectively.

2 - When the inclination  $I = 0$  ( angle between rotational angular momentum vector and Z-inertial axis):



In this case the variables  $x_1$  is constant and  $x_3$  and  $y_3$  are zero . For the other variables we have:

$$x_2 = w \cos(Ft + \phi) \quad y_2 = -w \sin(Ft + \phi) \quad y_1 = Gt + y_{10} \quad (10)$$

where:

$$\begin{aligned} F &= A + F_g & G &= B + G_g \\ F_g &= \frac{3k}{2x_{10}}(1 - 2\varepsilon_0^2) \left[ -1 + \frac{3}{2} \sin^2 \Gamma \right] \\ G_g &= \frac{3k\varepsilon_0^2}{x_{10}}(1 - 2\varepsilon_0^2) \left[ -1 + \frac{3}{2} \sin^2 \Gamma \right] \end{aligned} \quad (11)$$

with  $\phi, w, A$  and  $B$ , given in Eq. (7) and  $k$  in Eq.(9).

We can observe that the gravity gradient torque introduces periodic variations in  $x_2$  and  $y_2$  and linear variations in  $y_1$ , given by  $F_g$  and  $G_g$  respectively, while the variables  $x_3$  and  $y_3$  are zero (because  $I=0$ ).

If other terms associated with the gravity gradient torque were included only periodic variations would appear in the solutions given by Eq. (8) and Eq. (10). In the case where  $I_{xx} < I_{yy} < I_{zz}$  the analytical solution is shown in Giacaglia and Jefferys<sup>5</sup>, in terms of elliptic functions.

## SECOND SET OF VARIABLES

After applying the canonical transformation of freedom two, presented by Fukushima<sup>6,7</sup>, to the subset of Andoyer's variables ( $l_1, l_2, L_1, L_2$ ) we can get the second set of non-singular variables ( $X_1, X_2, X_3, Y_1, Y_2, Y_3$ ), which is useful in the case when the angle  $J$  is zero. They are defined by:

$$\begin{aligned} X_1 &= L_2 & Y_1 &= l_2 + \tan^{-1}(\cos J \tan l_1) \\ X_2 &= L_2 \sin J \sin l_1 & Y_2 &= \tan^{-1}(\tan J \cos l_1) \\ X_3 &= L_3 & Y_3 &= l_3 \end{aligned} \quad (12)$$

Using the angle  $J$ , the Eq. (12) can be rewritten as

$$\begin{aligned} X_1 &= L_2 & Y_1 &= l_2 + l_1 - \tan^{-1} \left[ \frac{\sin 2l_1 \sin^2(J/2)}{1 - 2 \sin^2(J/2) \sin^2 l_1} \right] \\ X_2 &= L_2 \sin J \sin l_1 & Y_2 &= J - \tan^{-1} \left[ \frac{\sin 2J \sin^2(l_1/2)}{1 - 2 \sin^2(l_1/2) \sin^2 J} \right] \\ X_3 &= L_3 & Y_3 &= l_3 \end{aligned} \quad (13)$$

Then, for small values of  $J$  we have  $X_2 \approx L_2 J \sin l_1$ ,  $Y_1 \approx l_1 + l_2$  and  $Y_2 \approx L_2 J \cos l_1$  and these variables ( $X_i, Y_i$ ) are well-defined for all values of  $L_1$  including  $L_1 \approx L_2$ .

This set of variables is shown in Figure 2 and they have clean physical meaning:

- 1-  $X_1$  is the magnitude of the rotational angular momentum ( $\bar{L}_2$ );
- 2 -  $X_2$  is the x-axis components of the  $\bar{L}_2$ ;
- 3 -  $X_3$  is the z-axis component of  $\bar{L}_2$ ;

- 4 -  $Y_1$  is the angle between the projection of x-axis on the plane normal to  $\bar{L}_2$  and the node N (given by the intersection of XY-plane and the plane normal to  $\bar{L}_2$ );
- 5 -  $Y_2$  is the angle between xz-plane and the great circle connecting x-axis and  $\bar{L}_2$  and
- 6 -  $Y_3$  is the angle between N and X-axis.

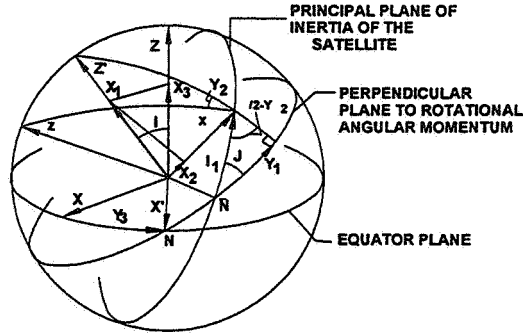


Figure 2 - Second set of non-singular variables ( $X_1, X_2, X_3, Y_1, Y_2, Y_3$ )

The inverse forms the Eq.(12) are given by the canonical transformation of freedom two<sup>6,7</sup>:

$$\begin{aligned} L_2 &= X_1 & L_1 &= \sqrt{X_1^2 - X_2^2} \cos Y_2 \\ l_2 &= Y_1 - \tan^{-1} \left[ \frac{X_2}{X_1} \cot Y_2 \right] & l_1 &= \cot^{-1} \left[ \frac{\sqrt{X_1^2 - X_2^2}}{X_2} \right] \sin Y_2 \end{aligned} \quad (14)$$

The dynamical equations of rotational motion can be derived from the equation Eq.(1), with  $x_i = X_i$  and  $y_i = Y_i$ , and using the Eq.(14) to compute the partial derivatives  $\frac{\partial l_i}{\partial Y_j}, \frac{\partial l_i}{\partial X_j}, \frac{\partial L_i}{\partial Y_j}$  and  $\frac{\partial L_i}{\partial X_j}$ , for  $i=1,2,3$  and  $j=1,2,3$ .

For a symmetric satellite and torque-free motion, the dynamical equations are:

$$\begin{aligned} \dot{X}_1 &= 0 & \dot{X}_3 &= 0 & \dot{Y}_3 &= 0 \\ \dot{X}_2 &= -\frac{1}{2} \left[ \frac{1}{I_{xx}} - \frac{1}{I_{zz}} \right] (X_1^2 - X_2^2) \sin 2Y_2 \\ \dot{Y}_1 &= \frac{X_1}{I_{xx}} \sin^2 Y_2 + \frac{X_1}{I_{zz}} \cos^2 Y_2 \\ \dot{Y}_2 &= \left[ \frac{1}{I_{xx}} - \frac{1}{I_{zz}} \right] X_2 \cos^2 Y_2 \end{aligned} \quad (15)$$

Although we have assumed symmetrical satellite, the Eqs.(15) can be integrate only using elliptic integration and were presented by Fukushima<sup>6,7</sup>. Here we will analyze these equations for  $J = 0$  and  $J \approx 0$ :

- 1- When  $J = 0$ , we have  $X_2 = Y_2 = 0$ . Then the analytic solution for the system given by Eqs.(15) is:

$$Y_1 = \frac{X_1}{I_{zz}}t + Y_{10} \quad (16)$$

$X_1, X_2, X_3, Y_2$  and  $Y_3$  are constant and  $Y_{10}$  is the initial condition.

2- When  $J \approx 0$ , we have  $X_2 \approx 0$  and  $Y_2 \approx 0$  and if the second order terms in  $X_2$  and  $Y_2$  are not considered, the solution of system given by Eqs.(15) is given by:

$$X_2 = W \sin(\bar{A}t + \alpha) \quad Y_2 = \frac{W}{X_{10}} \cos(\bar{A}t + \alpha) \quad Y_1 = \frac{X_{10}}{I_{zz}}t + Y_{10} \quad (17)$$

where

$$W = \sqrt{X_{20}^2 + X_{10}^2 Y_{10}} \quad \alpha = \tan^{-1} \left[ \frac{X_{20}}{Y_{20} X_{10}} \right] \quad \bar{A} = \left[ \frac{1}{I_{zz}} - \frac{1}{I_{xx}} \right] X_{10} \quad (18)$$

In this case the  $X_2$  and  $Y_2$  have periodic variations and the subscript "0" means initial conditions.

In order to compare these analytical solutions with a numerical solution, let us consider an hypothetical satellite with

$$I_{xx} = I_{yy} = 3.9499 \times 10^5 \text{ kg m}^2 \quad \text{and} \quad I_{zz} = 1.0307 \times 10^5 \text{ kg m}^2$$

and the following initial conditions:

$$\begin{aligned} X_{10} &= 9.7307 \times 10^{-3} \text{ kg km}^2/\text{s} & X_{30} &= -2.9956 \times 10^{-3} \text{ kg km}^2/\text{s} \\ Y_{10} &= 0 \text{ rad} & Y_{30} &= 4.8244 \text{ rad} \end{aligned}$$

For the other variables, we will consider two cases:

$$\begin{aligned} \text{a) for } J = 0 \text{ rad :} & \quad Y_{20} = 0 \text{ rad} & X_{20} &= 0 \text{ kg km}^2/\text{s} \\ \text{b) for } J = 0.0873 \text{ rad :} & \quad Y_{20} = 0.0873 \text{ rad} & X_{20} &= 0 \text{ kg km}^2/\text{s} \end{aligned}$$

The numerical solutions for the Eqs. (15) are performed by using a 8<sup>th</sup> order Runge-Kutta method. The analytical and numerical solutions agree for all considered time and are shown in the Figure 3 ( for  $J=0$ ) and Figure 4 ( for  $J=0.08725$  rad). When  $J = 0$  all the variables are constant except  $X_2$  and for  $J \neq 0$   $X_1, X_3$  and  $Y_3$  are constant.

Including the gravity gradient torque in the dynamical equations for this set of variables, the numerical results are presented in the Figure 5 and Figure 6. By these results we can note that the gravity gradient torque causes only periodic variations in variables  $X_2$  and  $Y_2$  for  $J = 0.08725$  rad. The apparent secular variation of  $X_3$ , as shown in these figures, actually is a long term variation produced by terms of  $F_1$  independent of  $l_1$  and  $l_2$ .

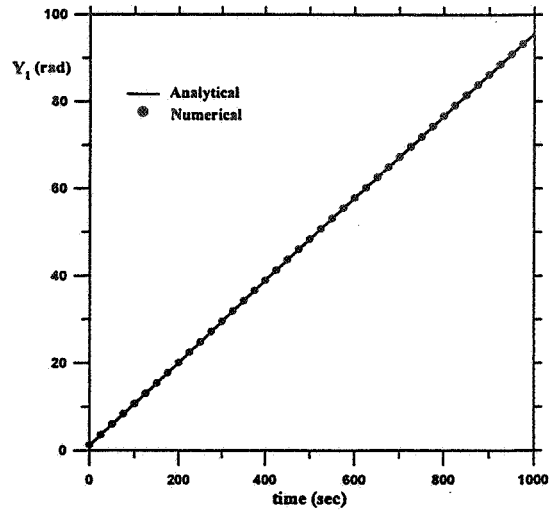


**Figure 3 - Analytical and Numerical results for the torque-free motion using the second set of non-singular canonical variables ( $X_1, X_2, X_3, Y_1, Y_2, Y_3$ ), when  $J = 0$  (rad)**

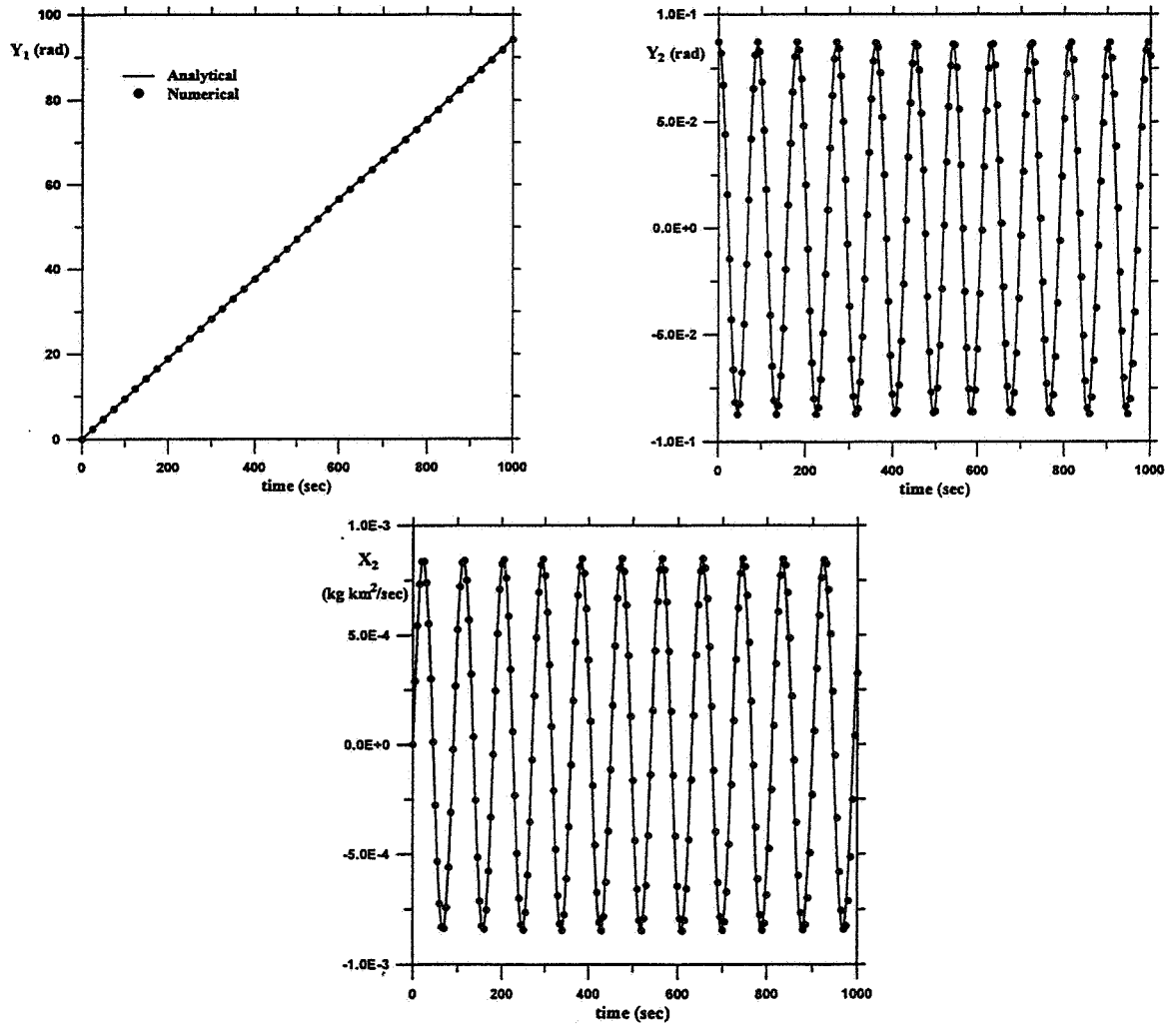


**Figure 4 - Analytical and Numerical results for the torque-free motion using the second set of non-singular canonical variables ( $X_1, X_2, X_3, Y_1, Y_2, Y_3$ ), when  $J = 0.0873$  rad**

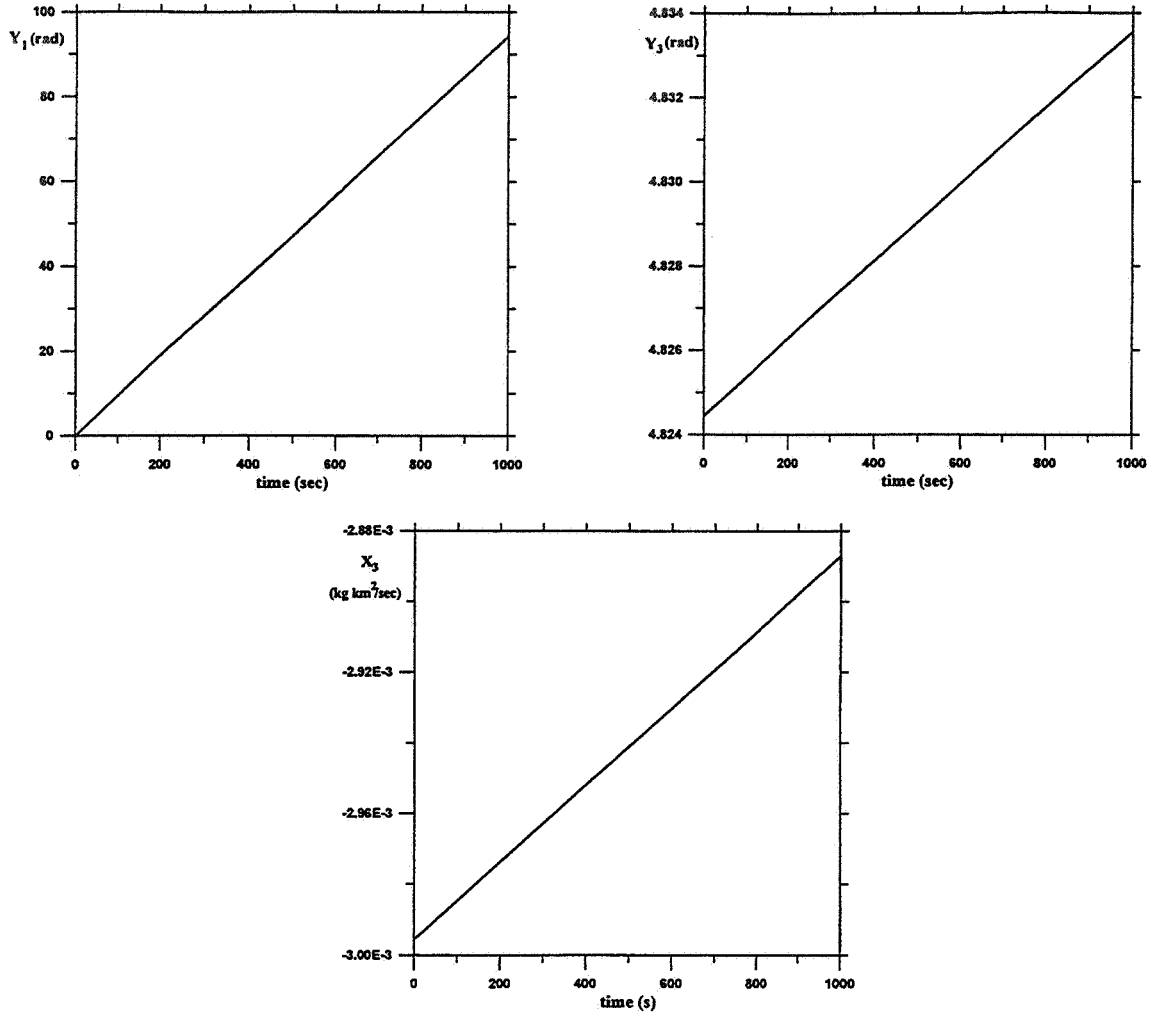


Figure 5 - Numerical results for rotational motion with gravity-gradient torque using the second set of non-angular canonical variables ( $X_1, X_2, X_3, Y_1, Y_2, Y_3$ ), when  $J = 0$  rad

### THIRD SET OF VARIABLES

Applying again the canonical transformation of freedom two<sup>6,7</sup> to the subset ( $X_1, X_3, Y_1, Y_3$ ), introduced in the previous section, we can obtain another set of non-singular variables ( $\bar{X}_1, \bar{X}_2, \bar{X}_3, \bar{Y}_1, \bar{Y}_2, \bar{Y}_3$ ). These variables are useful when the inclinations  $I$  and  $J$  are small and are defined by:

$$\begin{aligned}
 \bar{X}_1 &= L_2 & \bar{Y}_1 &= l_2 + \tan^{-1}(\cos J \tan l_1) + \tan^{-1}(\cos I \tan l_3) \\
 \bar{X}_2 &= L_2 \sin J \sin l_1 & \bar{Y}_2 &= \tan^{-1}(\tan J \cos l_1) \\
 \bar{X}_3 &= L_2 \sin I \sin l_3 & \bar{Y}_3 &= \tan^{-1}(\tan I \cos l_3)
 \end{aligned} \tag{19}$$

Using the inclinations  $I$  and  $J$ , the variables  $\bar{Y}_1$  and  $\bar{Y}_3$  can be rewritten as:

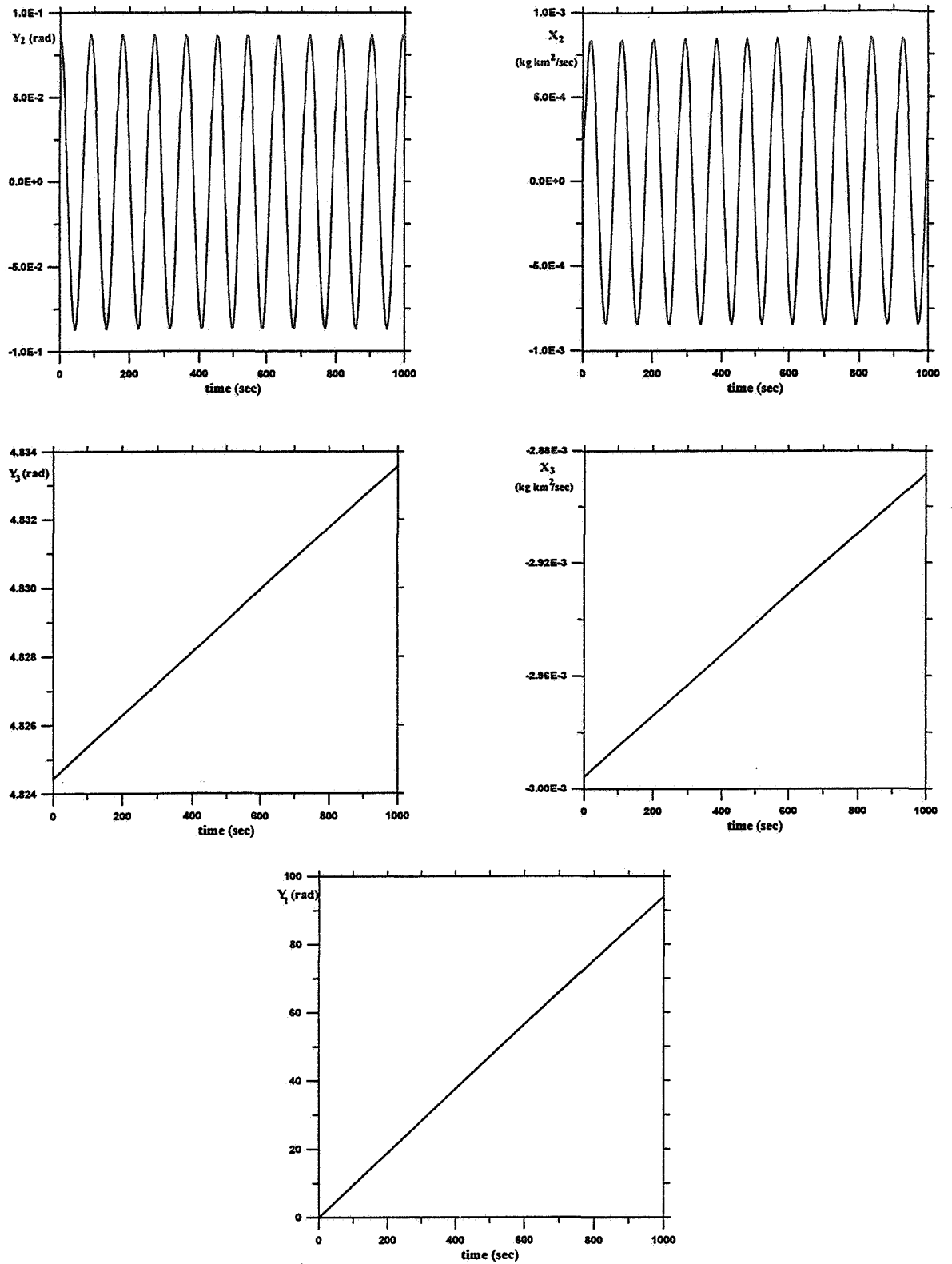


Figure 6 - Numerical results for rotational motion with gravity-gradient torque using the second set of non-singular canonical variables ( $X_1, X_2, X_3, Y_1, Y_2, Y_3$ ), when  $J = 0.0873$  rad

$$\begin{aligned}\bar{Y}_1 &= l_1 + l_2 + l_3 - \tan^{-1} \left[ \frac{\sin 2l_1 \sin^2(J/2)}{1 - 2\sin^2(J/2)\sin^2 l_1} \right] - \tan^{-1} \left[ \frac{\sin 2l_3 \sin^2(I/2)}{1 - 2\sin^2(I/2)\sin^2 l_3} \right] \\ \bar{Y}_3 &= I - \tan^{-1} \left[ \frac{\sin 2I \sin^2(l_3/2)}{1 - 2\sin^2(l_3/2)\sin^2 I} \right]\end{aligned}\quad (20)$$

We can observe that if  $I$  and  $J$  are small we have  $\bar{Y}_1 = l_1 + l_2 + l_3$ ,  $\bar{Y}_3 = L_2 I \cos l_3$  and  $\bar{X}_3 = L_2 I \sin l_3$  and these variables  $(\bar{X}_i, \bar{Y}_i)$  are also well-defined for all values for  $I$  and  $J$ .

The variables  $(\bar{X}_i, \bar{Y}_i)$  are shown in the Figure 7 and they also have clear physical meanings:

- 1)  $\bar{X}_1, \bar{X}_2$  and  $\bar{Y}_2$  are similar  $X_1, X_2$  and  $Y_2$ ;
- 2)  $\bar{X}_3$  is the X-components of  $\bar{L}_2$ ;
- 3)  $\bar{Y}_1$  is the angle between the projection of x-axis onto plane normal  $\bar{L}_2$  and the projection of X-axis onto plane normal to  $\bar{L}_2$  and
- 4)  $\bar{Y}_3$  is the angle between the XZ-plane and a great circle connecting X-axis and  $\bar{L}_2$ .

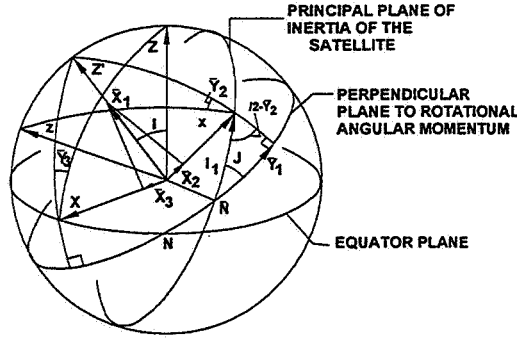


Figure 7 - Third set of non-singular variables  $(\bar{X}_1, \bar{X}_2, \bar{X}_3, \bar{Y}_1, \bar{Y}_2, \bar{Y}_3)$

The inverse forms of Eq.(19) are obtained by the application of inverse transformation given by Fukushima<sup>6,7</sup> and they have the following expressions:

$$\begin{aligned}L_2 &= \bar{X}_1 & L_1 &= \sqrt{\bar{X}_1^2 - \bar{X}_2^2} \cos \bar{Y}_2 & L_1 &= \sqrt{\bar{X}_3^2 - \bar{X}_2^2} \cos \bar{Y}_3 \\ l_2 &= \bar{Y}_1 - \tan^{-1} \left[ \frac{\bar{X}_2}{\bar{X}_1} \cot \bar{Y}_2 \right] - \tan^{-1} \left[ \frac{\bar{X}_3}{\bar{X}_1} \cot \bar{Y}_3 \right] \\ l_1 &= \cot^{-1} \left[ \frac{\sqrt{\bar{X}_1^2 - \bar{X}_2^2} \sin \bar{Y}_1}{\bar{X}_2} \right] & l_3 &= \cot^{-1} \left[ \frac{\sqrt{\bar{X}_3^2 - \bar{X}_2^2} \sin \bar{Y}_3}{\bar{X}_2} \right]\end{aligned}\quad (21)$$

Similar to the previous section, the dynamical equation are computed by using Eqs. (1) and (21), considering  $x_i = \bar{X}_i$  and  $y_i = \bar{Y}_i$ ,  $i=1,2,3$ .

The dynamical equations for symmetrical satellite and torque-free motion ( $F = F_0$ ) are similar to the second set and given by:

$$\begin{aligned}
\dot{\bar{X}}_1 &= 0 & \dot{\bar{X}}_3 &= 0 & \dot{\bar{Y}}_3 &= 0 \\
\dot{\bar{X}}_2 &= -\frac{1}{2} \left[ \frac{1}{I_{xx}} - \frac{1}{I_{zz}} \right] (\bar{X}_1^2 - \bar{X}_2^2) \sin 2\bar{Y}_2 \\
\dot{\bar{Y}}_1 &= \frac{\bar{X}_1}{I_{xx}} \sin^2 \bar{Y}_2 + \frac{\bar{X}_1}{I_{zz}} \cos^2 \bar{Y}_2 \\
\dot{\bar{Y}}_2 &= \left[ \frac{1}{I_{xx}} - \frac{1}{I_{zz}} \right] \bar{X}_2 \cos^2 \bar{Y}_2
\end{aligned} \tag{22}$$

The analytical solution for Eqs.(22) is given only in elliptic function and for two particular case ( $J=0$  and  $J \approx 0$ ) the solution given in Eqs.(16) and (17) are valid for Eqs.(22), doing  $X_i = \bar{X}_i$  and  $Y_i = \bar{Y}_i$ .

Numerical applications are shown in the Figure 8 and Figure 9 for the same hypothetical satellite of previous section. Here, two cases for initial conditions are considered:

1 - For  $J = 0$  and  $I = 0$ :

$$\begin{aligned}
\bar{X}_{10} &= 9.7303 \times 10^{-3} \text{ (kg km}^2 \text{ / sec)} & \bar{Y}_{10} &= 4.8244 \text{ (rad)} \\
\bar{X}_{20} &= 0 \text{ (kg km}^2 \text{ / sec)} & \bar{Y}_{20} &= 0.0873 \text{ (rad)} \\
\bar{X}_{30} &= 0 \text{ (kg km}^2 \text{ / sec)} & \bar{Y}_{30} &= 0 \text{ (rad)}
\end{aligned}$$

2 - For  $J = 0.0873$  rad and  $I = 0.0873$  rad:

$$\begin{aligned}
\bar{X}_{10} &= 9.7303 \times 10^{-3} \text{ (kg km}^2 \text{ / sec)} & \bar{Y}_{10} &= 4.8248 \text{ (rad)} \\
\bar{X}_{20} &= 0 \text{ (kg km}^2 \text{ / sec)} & \bar{Y}_{20} &= 0.0873 \text{ (rad)} \\
\bar{X}_{30} &= -8.4258 \times 10^{-4} \text{ (kg km}^2 \text{ / sec)} & \bar{Y}_{30} &= 0.0098 \text{ (rad)}
\end{aligned}$$

In these figures, the numerical results for Eqs.(22) is also shown. The analytical and numerical solutions agree for all interval of time. We can note that when  $J=I=0$  rad, only  $\bar{Y}_1$  has a linear variation and when  $J=I=0.0873$  (rad) the variables  $\bar{X}_1, \bar{X}_3$  and  $\bar{Y}_3$  are constant while  $\bar{X}_2$  and  $\bar{Y}_2$  have periodic variations and  $\bar{Y}_1$  has linear variation. If the gravity gradient torque is considered, the dynamical equation are complex and the analytical solution could be obtained by using a small perturbation method.

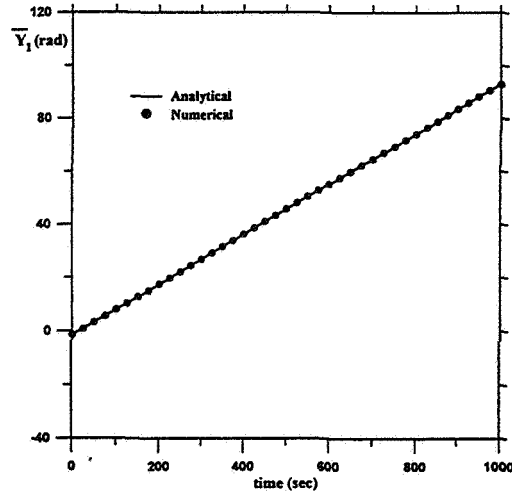
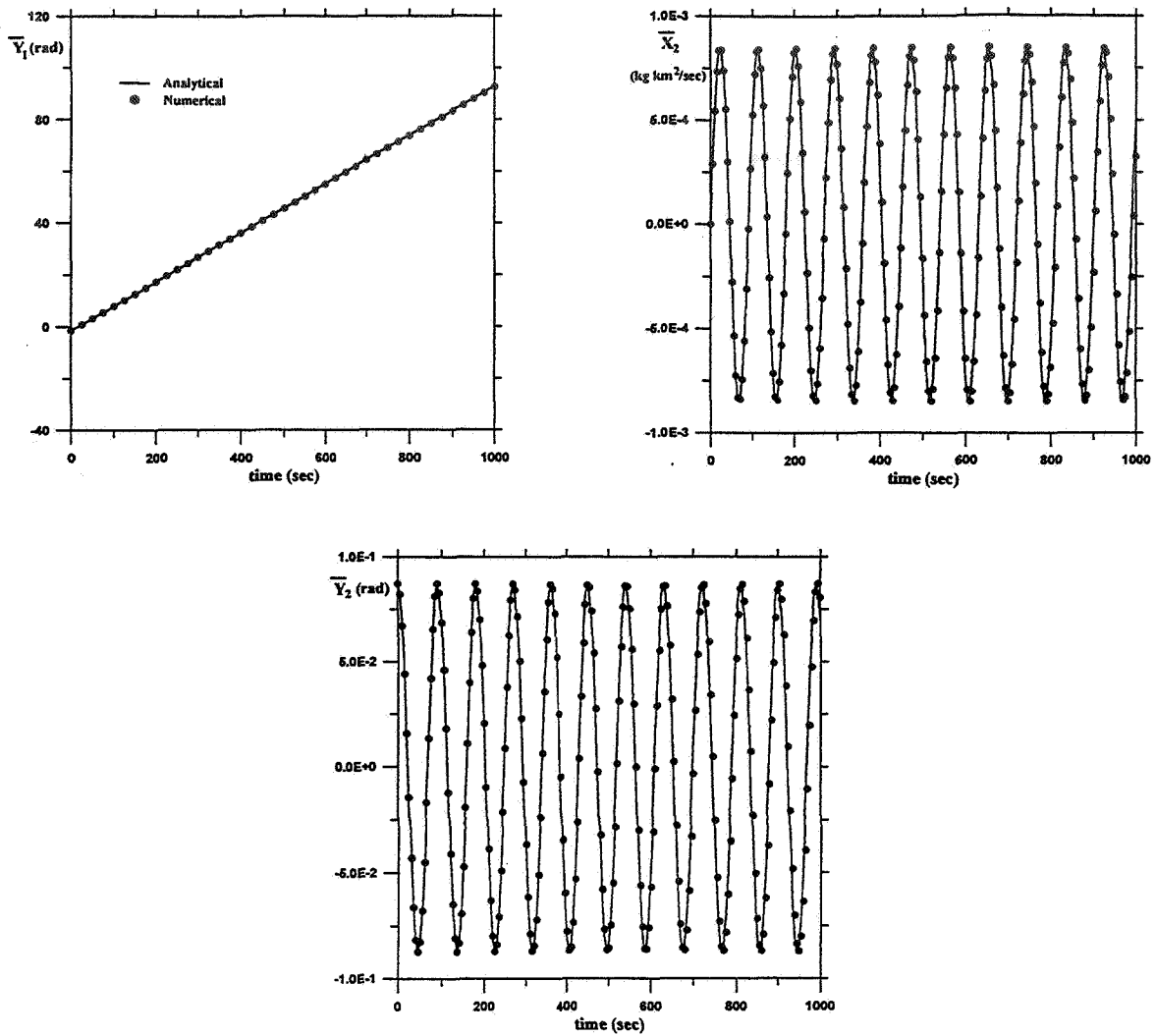


Figure 8 - Analytical and Numerical results for the torque-free motion using the third set of non-singular canonical variables ( $\bar{X}_1, \bar{X}_2, \bar{X}_3, \bar{Y}_1, \bar{Y}_2, \bar{Y}_3$ ), when  $J = I = 0$  rad





**Figure 9 - Analytical and Numerical results for the torque-free motion using the third set of non-singular canonical variables  $(\bar{X}_1, \bar{X}_2, \bar{X}_3, \bar{Y}_1, \bar{Y}_2, \bar{Y}_3)$ , when  $J = I = 0.0873$  rad**

## SUMMARY

In this paper three sets of non-singular variables were analyzed. By these analysis we can conclude:

- 1 - Each set of variables is canonical and all variables are well- defined when the inclination  $I$  or/and  $J$  are small;
- 2 - The dynamical equations for the variables introduced by Giacaglia and Jefferys<sup>5</sup> are simpler than those for Fukushima's variables. The analytical solution for torque-free motion in terms of these variables are computed without elliptic function, assuming symmetrical satellite;
- 3 - The analytical solution for the two sets of Fukushima's variables can be obtained only using elliptic functions and
- 4 - Although the solutions for Giacaglia and Jefferys's set are simpler, this set doesn't have physical meaning. On the other hand, more complex solutions are found with Fukushima's sets but the physical meaning is clear for all the variables.

Then the choice for the canonical variables depends on the space mission. If inclination  $I \gg 0$ , the first Fukushima's set is recommended.

## ACKNOWLEDGMENTS

The present work was partially supported by FAPESP and CNPq. The author thanks Mr Paulo Ricardo de Figueiredo Domingues and Mr Alexandre Pereira Araújo for their help with the algebraic calculations.

## REFERENCES

1. Andoyer, H.: "Cours de Mécanique Céleste", Vol. 1, Gauthier-Villars, Paris, 1923, pp. 54.
2. Deprit, A.: *Amer. J. Phys.*, Vol. 35, 1967, pp. 424-428.
3. Kinoshita, H.: *Publ. Astron. Soc. Jap.*, Vol. 24, 1981, pp. 423-457.
4. Zanardi, M. C.: *Cel. Mech.*, Vol. 39, 1986, pp. 147-158.
5. Giacaglia, G.E.O., Jefferys, W.H.: *Cel. Mech.*, Vol. 4, 1971, pp. 442-467.
6. Fukushima, T.: *Publ. Astron. Soc. Jap.*, 1993, pp. 100-130.
7. Fukushima, T.: *Cel. Mech. and Dyn. Astron.*, Vol. 60, 1994, pp. 51-68.

## SATELLITE ATTITUDE CONTROL USING MULTILAYER PERCEPTRON NEURAL NETWORKS

169342

Valdemir Carrara<sup>+</sup>Sebastião Eduardo Corsatto Varotto<sup>++</sup>Atair Rios Neto<sup>+++</sup>337605  
18p.

This work simulates and tests the use of artificial neural networks for satellite attitude dynamics identification and control. In order to exemplify this application, a satellite with a rigid main body, three reaction wheels and three flexible solar panels was chosen (lay-out similar to Brazilian Remote Sensing Satellite). The main objective is to test the neural control and analyze its interaction with the elastic motion and variable geometry of the satellite. Two control schemes are used, the Internal Model Control (IMC) and the Feedback Learning Control (FLC). The identification of neural nets parameters is performed by a Kalman filtering algorithm with a local parallel processing version in the IMC scheme and by the steepest descent method in the FLC scheme.

### INTRODUCTION

In recent years the neural computing had evolved significantly. Main reason for the coming back of neural nets is, besides the increasing processing power of the new generation of computers, the development of new neural net architectures and training algorithms. The number of applications has also had increased: vehicle guidance, financial analysis, printed circuit layout, voice synthesis and recognition, pattern classification, optical character recognition, exchange rate forecast, manufacturing process control and robotics among others (Ref. 1). Aeronautics also has found use for neural nets, mainly in failure analysis and detection, and automatic guidance and control. Although space applications are still limited, there are several possibilities: subsystem failure detection, isolation and identification, autonomously orbit propagation and control (Ref. 2), attitude determination and control, intelligent task managing, etc.

Attitude control of satellites normally is based on linearization of the dynamical equations of motion and application of an optimization method in order to guarantee the stability and controllability under the environmental conditions. Neural nets can overcome the non-linearities of the attitude behavior. Beyond the non-linearities inherent of the attitude dynamics, the effect of non-rigidity can also be present in the problem, due to flexibility of some structure component and to

---

<sup>+</sup> Instituto Nacional de Pesquisas Espaciais - INPE/MCT  
CEP 12201-970 CP 515 São José dos Campos, SP. E-mail: val@dem.inpe.br

<sup>++</sup> Instituto Nacional de Pesquisas Espaciais - INPE/MCT  
CEP 12201-970 CP 515 São José dos Campos, SP. E-mail: varotto@dem.inpe.br

<sup>+++</sup> Instituto de Pesquisa e Desenvolvimento, Universidade do Vale do Paraíba.  
CEP 12245-720 São José dos Campos, SP. E-mail: atair@univap.br

geometry variation (due to module accretion, mass migration or appendage motion, for instance).

In what follows, two neural control methods are tested for attitude control, by using simulated data a satellite attitude behavior where either flexibles appendages or variable geometry are present. Section 2 presents the general perceptron neural net as well as the training procedures. The equations of motion are presented in Section 3. Simulation, test results and conclusions follow the preceding sections.

## NEURAL NETWORKS

A neural network is a computational structure composed of several basic units called artificial neurons. Each neuron can be understood as an operator that process with a nonlinear activation function  $f$  the weighted sum of its inputs and transfer the output to the next neuron layer. The signal processing performed by the neuron establishes its functionality. The connections between the artificial neurons, on the other hand, define the behavior of the net, identify its applicability and training methods. In a multilayer perceptron network the neurons are grouped in one or more layers, with the output of each layer being the input to the next one.

The training process consists in adjusting the neuron weights based on the expected output and some optimization rules. Normally, the weights are adjusted interactively, by comparing the output of the network with the desired value at each step. This means that the training process teaches the net what should be its output for a given input.

A neural net with linear function in the output and the sigmoid activation function in the hidden layers better represents dynamical systems and limited continuous functions (Ref. 3). The sigmoid function is given by:

$$f(x) = \frac{1 - e^{-x}}{1 + e^x} \quad (1)$$

A feedforward multilayer perceptron network can be seen as a mapping function with  $n_0$  input elements and  $n_l$  output. In other words, a neural network is composed by  $l$  layers with  $n_k$  ( $k = 1, 2, \dots, l$ ) neurons in layer  $k$ . If  $x_i^k$  is the output of the  $i^{\text{th}}$  neuron of layer  $k$ ,  $w_{ij}^k$  is the weight of the  $j^{\text{th}}$  input (coming from the  $j^{\text{th}}$  neuron of the preceding layer) and  $f^k$  is the activation function, then:

$$x_i^k = f^k(\bar{x}_i^k + b_i^k) = f^k\left(\sum_{j=1}^{n_{k-1}} w_{ij}^k x_j^{k-1} + b_i^k\right) \quad (2)$$

where  $b_i^k$  is the bias, introduced to allow the neuron to present a non-null output even in presence of a null input. So, the  $k^{\text{th}}$  layer has  $n_{k-1}$  inputs, and  $n_k$  outputs  $\bar{x}_i^k$  is the weighted input to the  $i^{\text{th}}$  neuron.

The determination process of the neuron bias can be transferred to the determination of the neuron weights if one admits the presence of a new constant input. Eq. (2) can be expressed in vector-matrix form, and if  $W^k$  is the weight matrix, then

$$x^k = f^k(\bar{x}^k) = f^k(W^k x^{k-1}) \quad (3)$$

where  $W^k$  includes the neuron bias:

$$W^k = \begin{bmatrix} w_{11}^k & \cdots & w_{1n_{k-1}}^k & b_1^k \\ w_{21}^k & \cdots & w_{2n_{k-1}}^k & b_2^k \\ \vdots & & \vdots & \vdots \\ w_{n_k 1}^k & \cdots & w_{n_k n_{k-1}}^k & b_{n_k}^k \end{bmatrix}. \quad (4)$$

The dimensions of the output vector  $x^k$  and the weight matrix  $W^k$  are now  $n_k+1$  e  $n_k \times n_{k-1}+1$ , respectively.

The increasing number of hidden layers normally makes the neural net to better represent the dynamical system and to reduce the output error (Ref. 4 and Ref. 5) even when the same number of neurons are taken. Nevertheless, the capacity of generalization, i. e. the ability to interpolate between points where the neural net was not trained, is more accentuated on nets with few or even only one hidden layer (Ref. 6). On the other hand, nets with high number of neurons or layers have small output errors at the trained points. Thus if the dynamics of the system is not complex a neural net with one hidden sigmoid and linear output layers is sufficient for a large number of applications. The number of neurons in the hidden layers is important for the approximation degree: few neurons tend to decrease the stability and result in a bad approximation, too much neurons cause oscillation on the output between the trained points (Ref. 7).

## Backpropagation Algorithm

Training a neural net generally consists in applying methods in order to adjust or estimate the neuron weights. The training process normally minimizes the neural net output error through the application of an optimization method. All methods need to know how the net output varies with respect to the variation of a given neuron weight. This can be achieved with the back propagation algorithm (Ref. 8), which obtains the partial derivative of the output elements in a recursive way. In matrix form the back propagation algorithm gives to the derivative of the output vector with respect to the  $j^{\text{th}}$  weight of the  $i^{\text{th}}$  neuron of the  $k^{\text{th}}$  layer the expression:

$$\frac{\partial x^l}{\partial w_{ij}^k} = \Delta^k \begin{bmatrix} 0 \\ \vdots \\ x_j^{k-1} \\ \vdots \\ 0 \end{bmatrix}, \quad (5)$$

where  $\Delta^k$  is the back propagation matrix, obtained from:

$$\Delta^k = \Delta^{k+1} W^{k+1} F^k \quad (6)$$

with initial condition at output layer  $l$  given by  $\Delta^l = F^l$ , where  $F^k$  is a diagonal matrix with the derivatives of the activation function  $f^k$ :

$$F^k = \frac{df^k(\bar{x}^k)}{d\bar{x}^k} = \begin{bmatrix} f^{k'}(\bar{x}_1^k) & \cdots & 0 \\ \vdots & \ddots & \vdots \\ 0 & \cdots & f^{k'}(\bar{x}_{n_k}^k) \end{bmatrix} \quad (7)$$

It should be noted that, due to the inclusion of the neuron bias on the weight matrix,  $F^k$  should be a  $n_{k-1}+1 \times n_{k-1}+1$  matrix, with the last diagonal element equal to zero. In order to reduce the computational effort both  $F^k$  and  $W^k$  can be resized with elimination of the last row when performing matrix products.

## Steepest Descent Method

The steepest descent method, combined with the backpropagation, exhibits a high degree of parallelism and simplicity. The weights are corrected based on the minimization of the neural net output error. Weight updating starts at the net output layer and then the error is backpropagated to the preceding layer in order to compute its weight corrections. The minimization criterion uses the network output quadratic error as the performance index:

$$J(t) = \frac{1}{2} \varepsilon(t)^T \varepsilon(t) \quad (8)$$

where  $\varepsilon(t)$  is the network output error at time  $t$ , defined by:

$$\varepsilon(t) = y^d(t) - y(t), \quad (9)$$

where  $y^d(t)$  and  $y(t)$  are expected and actual network output. Weight updatings of layer  $k$  are performed using:

$$W^k(t+1) = W^k(t) - \lambda \nabla J^k \quad (10)$$

where the gradient of the square backpropagated error  $\nabla J^k$  comes from the backpropagation matrix:

$$\nabla J^k = -\Delta^{kT} \varepsilon x^{k-1T}. \quad (11)$$

In the above equations, the superscript T means the transpose of the vector or matrix. Convergence of the weights depends on the adjusting of the learning rate coefficient  $\lambda$ , ranging from 0 to 1.

## Stochastic Optimal Parameter Estimation Neural Nets Training

The supervised training of a neural net to learn a nonlinear continuous mapping:

$$f(x): x \in D \subset R^{n_I} \rightarrow y \in R^{n_O} \quad (12)$$

can naturally be treated as a problem of estimating the connection weight parameters  $w$  in the network correspondent mapping:

$$f^e(x, w): x \in D \subset R^{n_I} \rightarrow y^e \in R^{n_O} \quad (13)$$

such as to have  $f^e(x, w)$  as close as possible to  $f(x)$  for  $x \in D$ . A set of pairs  $(x(t), y(t))$ ,  $t=1, 2, \dots, N$ , given by the mapping in Eq.(12) is selected in order to get this approximation, and the parameters are usually determined under the condition of minimizing

$$J(w) = \frac{1}{2} \left[ [w - \bar{w}]^T \bar{P}^{-1} [w - \bar{w}] + \sum_{t=1}^N [y(t) - y^e(t)]^T R^{-1}(t) [y(t) - y^e(t)] \right] \quad (14)$$

where  $\bar{w}$  is given a priori value of  $w$ ;  $y^e(t) = f^e(x(t), w)$ ;  $\bar{P}^{-1}$  and  $\bar{R}^{-1}(t)$  are weight matrices.

To solve problem give by Eq. (14) an iterative scheme based on linear perturbation can to be used (Ref. 9). In a typical iteration, one usually takes:

$$J(w^k) = \frac{1}{2} \left[ [w^k - \bar{w}]^T \bar{P}^{-1} [w^k - \bar{w}] + \sum_{t=1}^N \left[ \alpha^k [y(t) - \bar{y}^k(t)] - f_w^e(x(t), \bar{w}^k) [w^k - \bar{w}^k] \right]^T R^{-1}(t) \left[ \alpha^k [y(t) - \bar{y}^k(t)] - f_w^e(x(t), \bar{w}^k) [w^k - \bar{w}^k] \right] \right] \quad (15)$$

where  $k=1, 2, \dots, k_c$ ;  $\bar{w}^1 = \bar{w}$ ,  $\bar{y}^k(t) = f^e(x(t), \bar{w}^k)$ ,  $f_w^e(x(t), \bar{w}^k)$  is the matrix of first partial derivatives with respect to  $w$ ;  $0 < \alpha^k \leq 1$  is an adjusting parameter to guarantee the hypothesis of linear perturbation. The solution of Eq.(15) is formally equivalent to the following stochastic parameter estimation problem

$$\bar{w} = w^k + \bar{\varepsilon} \quad (16)$$

$$\alpha^k [y(t) - \bar{y}^k(t)] = f_w^e(x(t), \bar{w}^k) [w^k - \bar{w}^k] + v(t) \quad (17)$$

where,  $E[\bar{\varepsilon}] = 0$ ,  $E[\bar{\varepsilon} \bar{\varepsilon}^T] = \bar{P}$ ,  $E[v(t)] = 0$ ,  $E[v(t) v^T(t)] = R(t)$ , usually diagonal;  $E[\cdot]$  is the expectation value operator;  $\bar{\varepsilon}$  e  $v(t)$  are assumed to be gaussian distributed and not correlated; and  $v(t)$  is also assumed not correlated along  $t=1, 2, \dots, N$ .

Thus, the problem of vector weights estimation  $w_{li}$ , it can be solved in a similar way as having placed previously, through an estimator of Gauss Markov, in the Kalman form (Ref. 10); resulting in a typical iteration  $k=1, 2, \dots, k_c$ , the local estimation:

$$w_{li}^k = \bar{w}_{li} + \bar{K}_{li}^k [z_{li}^k - H_{li}^k \bar{w}_{li}^k] \quad (17)$$

$$P_{li}^k = [I - \bar{K}_{li}^k H_{li}^k] \bar{P}_{li} \quad (18)$$

$$\bar{K}_{li}^k = \bar{P}_{li} H_{li}^{k^T} [H_{li}^k \bar{P}_{li} H_{li}^{k^T} + \bar{R}_{li}^k]^{-1} \quad (19)$$

where  $\bar{R}_{li}^k = E[\bar{v}_{li}^k \bar{v}_{li}^{k^T}]$  is the covariance matrix of observation errors and can be evaluate as:

$$\begin{aligned} \bar{R}_{ii}^k = & f_{w_a}(x(t), \bar{w}^k) P_a^k f_{w_a}(x(t), \bar{w}^k)^T + f_{w_s}(x(t), \bar{w}^k) \bar{P}_s^k f_{w_s}(x(t), \bar{w}^k)^T + \\ & f_{w_e}(x(t), \bar{w}^k) \bar{P}_e^k f_{w_e}(x(t), \bar{w}^k)^T + R(t) \end{aligned} \quad (20)$$

## ATTITUDE DYNAMICS

If there is no external torque acting on the satellite, supposed as a rigid body, its angular momentum  $L$  is constant. Therefore, when an external torque is applied to the satellite, the variation rate of the angular momentum, expressed in body coordinates  $x^o$ ,  $y^o$  and  $z^o$ , is equal to the sum of the applied torque (Ref. 11) and (Ref. 12):

$$\dot{L}^o = I_o \dot{\omega}_o^o - \Omega(\omega_o^o) I_o \omega_o^o = N_{cont} + N_{pert} \quad (21)$$

where  $I_o$  is the satellite inertia matrix,  $\omega_o^o$  is its angular velocity, and  $\Omega(\cdot)$  is the vector product matrix, defined by:

$$\Omega(\omega) = \begin{bmatrix} 0 & -\omega_z & \omega_y \\ \omega_z & 0 & -\omega_x \\ -\omega_y & \omega_x & 0 \end{bmatrix} \quad (22)$$

External torque can be separated in environmental or disturbance torque,  $N_{pert}$  and attitude control torque,  $N_{cont}$ . If the satellite is composed of articulated appendages, or if some appendages like the solar arrays are flexible, the above equations shall be modified in order to reflect the effects caused by the non-rigidity.

## Articulated Appendages

An articulated satellite has a variable geometry, due to the relative motion between the appendages. Consider, for instance, a spacecraft pointed to Earth with solar arrays tracking the Sun, or the process of unfolding the solar arrays after orbit injection, a robot space arm or even the docking of a new module in a space station. In all these examples, both the inertia and center of mass position vary in time. Let's suppose that a rigid main body with  $n$  articulated and also rigid appendages composes the satellite. In order to avoid extending the system degrees of freedom, the angular velocities and accelerations of each articulation is supposed known. This is true for a large number of satellites, as for example the Earth pointing satellite which drives the solar arrays to the Sun.

The angular momentum rate of the satellite can now be expressed as a sum of the individual momentum:

$$\dot{L}^o = \int_{V_o} \Omega(r_o^o) \dot{r}_o^o dm_o + \sum_{k=1}^n \int_{V_k} \Omega(r_k^o) \dot{r}_k^o dm_k \quad (23)$$

where  $r_o$  and  $r_k$  are, respectively, the position of the mass elements  $dm_o$  e  $dm_k$ , belonging to the main body and the appendage  $k$  ( $k = 1, \dots, n$ ). The momentum rate with respect to the satellite center of mass and the position vectors are expressed in main body coordinates.  $V_o$  and  $V_k$  are the volumes of the main body and appendage  $k$ . The above integral yields:



$$\dot{L}^o = (I_o + J_n) \dot{\omega}_o^o + \Omega(\omega_o^o) I_o \omega_o^o + H_n. \quad (24)$$

Except by  $J_n$  and  $H_n$ , the angular momentum rate is similar to the Equation 14. So  $J_n$  and  $H_n$  represent the appendage and center of mass motion effects. They are defined by:

$$J_n = \sum_{k=1}^n \left( A_{k,o} I_k A_{k,o}^T - m_k \Omega(a_{ok}^o - a_{ko}^o) \Omega(a_{ok}^o - a_{ko}^o) \right) + \sum_{k=1}^n \left( m_k \Omega(a_{ok}^o - a_{ko}^o) \right) \sum_{k=1}^n \left( \mu_k \Omega(a_{ok}^o - a_{ko}^o) \right) \quad (25)$$

and

$$H_n = \sum_{k=1}^n \left[ \Omega(\omega_o^o + \omega_k^o) A_{k,o} I_k A_{k,o}^T (\omega_o^o + \omega_k^o) + A_{k,o} I_k A_{k,o}^T (\dot{\omega}_k^o + \Omega(\omega_o^o) \omega_k^o) \right] + \sum_{k=1}^n m_k \Omega(a_{ok}^o - a_{ko}^o) \beta_k - \left( \sum_{k=1}^n m_k \Omega(a_{ok}^o - a_{ko}^o) \beta_k \right) \sum_{k=1}^n \mu_k \beta_k, \quad (26)$$

where  $I_k$  is the inertia matrix of appendage  $k$  expressed in the appendage coordinate system.  $A_{k,o}$  is the rotation matrix between the appendage  $k$  and the main body coordinate systems and  $m_k$  is the appendage mass. The position of a fixed point in the articulation  $k$  defines the vector  $a_{ok}$ , with respect to the origin of the main body and  $a_{ko}$ , with respect to the origin of the appendage frames. The mass proportion  $\mu_k$  is defined by:

$$\mu_k = \frac{m_k}{m_o + \sum_{k=1}^n m_k} \quad (27)$$

where  $m_o$  is the main body mass. The angular acceleration  $\beta_k$  is given by:

$$\beta_k = \Omega(\omega_o^o) \Omega(\omega_o^o) (a_{ok}^o - a_{ko}^o) - \Omega(\omega_o^o) \Omega(\omega_k^o) a_{ko}^o - \Omega(\omega_k^o) \Omega(\omega_o^o + \omega_k^o) a_{ko}^o + \Omega(a_{ko}^o) (\Omega(\omega_o^o) \omega_k^o + \dot{\omega}_k^o) \quad (28)$$

Note that the appendage angular velocity  $\omega_k^o$  and acceleration  $\dot{\omega}_k^o$  vectors define both the momentum and the direction of the articulation joint. Eq. 25, together with the cinematic equations of motion can now be integrated in order to simulate the attitude of a satellite with variable geometry.

## Flexible Dynamics

In this case the equations of motion are obtained by the Lagrangian approach for quasi-coordinates (rotational motion) and for generalized coordinates (elastic motion). The development is addressed to a peculiar class of satellites constituted of a rigid central body also containing rigid rotors, and rectangular solar panels which are considered flexible after deployment.

The Lagrangian formulation for quasi-coordinates and for generalized coordinates (Meirovitch, 1970) has been used to derive the equations of motion. A flexible spacecraft represents a distributed-parameter system which in theory has an infinite number of degrees of freedom. In practice, the system must be discretized, to

avoid partial differential equations in the formulation. It can be done by the finite element technique, the lumped parameter method or the assumed modes method. In this work the last one was used and thus, the elastic displacement vector can be written as a linear combination of space-dependent admissible vector functions  $\phi$  multiplied by time-dependent generalized coordinates (Ref. )  $q$  in this form:

$$\{v\} = [\phi]\{q\} \quad (29)$$

where  $[\phi]$  is a rectangular matrix of space-dependent admissible functions and  $\{q\}$  is time-dependent vector of generalized coordinates.

Taking into account this discretization procedure, the kinetic energy can be written as:

$$T = \frac{1}{2}\{\omega\}^T [J]\{\omega\} + \frac{1}{2}\{\Omega\}^T [I]\{\Omega\} + \frac{1}{2}\{\dot{q}\}^T [M]\{\dot{q}\} + \{\omega\}^T [M]\{\Omega\} + \{\omega\}^T [H]\{\dot{q}\} \quad (30)$$

where  $[J]$  e  $[I]$  are the inertia matrices of the satellite in deformed state and of the rotors, respectively;  $\{\omega\}$  e  $\{\Omega\}$  are the angular velocity vectors of the satellite (absolute) and of the rotor (relative to the satellite), respectively;  $\{\dot{q}\}$  is the rate of change in time of the generalized elastic displacement vector, and finally  $[M]$  e  $[H]$  are matrices involving integrals of space-dependent admissible functions.

The elastic potential energy can be written as:

$$V = \frac{1}{2}\{q\}^T [K]\{q\} \quad (31)$$

where  $[K]$  is a symmetric matrix involving spatial derivatives of the admissible functions.

The modified dynamics Euler's Equations were then derived by the Lagrangian Formulation for quasi-coordinates, resulting:

$$[J]\{\dot{\omega}\} + [\dot{J}]\{\omega\} + [\tilde{\omega}][J]\{\omega\} + [\tilde{\omega}][I]\{\Omega\} + [\tilde{\omega}][H]\{\dot{q}\} + [H]\{\ddot{q}\} = \{T_p\} - \{T_c\} \quad (32)$$

The elastic dynamic equations have been derived by the Lagrangian formulation for generalized coordinates and are given by:

$$[M]\{\ddot{q}\} + [H]^T\{\dot{\omega}\} + [K]\{q\} - \{F\} = \{Q_q\} \quad (33)$$

where  $\{F\}$  involves partial derivatives of  $[J]$  relative to generalized elastic coordinates.

The Kinematics Equations were written using the Euler Parameter :

$$\{\dot{q}^*\} = \frac{1}{2}[\tilde{\Omega}^*]\{q^*\} \quad (34)$$

where  $[\tilde{\Omega}^*]$  is a matrix composed by components of the satellite angular velocity and  $\{q^*\}$  is the quaternion of satellite attitude.

In this study only the Gravity Gradient torque as external perturbation (Ref.14) and the first out-of-plane bending mode for each solar arrays were considered. The in-

plane and torsional modes were also no considered. It can be done because the solar arrays are short and somewhat rigid.

## SIMULATION RESULTS

### Satellite with Variable Geometry

The neural network control (NNC) was implemented and simulated using the MECB (Brazilian Complete Space Missions) satellite characteristics. They are small satellites designed to test low Earth orbit communications and to perform Earth observation.

Immediately after orbit injection, the spacecraft shall perform a rate reduction, in order to stop the tumbling and rotation motion imposed by the launcher's last stage and separation torque. The satellite then opens 3 solar panels and enters in attitude acquisition in order to point the panels to Sun. During the deployment, the mass motion of the solar arrays changes the satellite inertia and center of mass position. It was supposed that a neural net controls the attitude of the satellite in this phase. For attitude data acquisition, the satellite uses a magnetometer and an analog sun sensor. Attitude is controlled with hydrazine thrusters, on 3 axes, with a torque generation of 0.19 Nm maximum.

The network training process uses the attitude response to the torque control in order to update the neural weights. A feedback learning control (FLC) algorithm (Ref.15) was employed to train the network. However, FLC showed a strong competition between the neural and the PID controls. If the neural signal  $u^c$  was opposite to the PID output  $u^d$ , then the satellite remained uncontrolled, and the feedback error kept the process in a steady state. Another important drawback of the FLC was the absence of a feedback dynamical signal at the neural network input. If the network is driven only by a reference trajectory, then it can't generate torque when the trajectory reaches the final point and the residual attitude errors is not corrected. A different approach was adopted, as shown in Figure 1. The neural network receives inputs from the trajectory error and the output torque. The learning signal, as in the FLC, comes from the PID controller, but instead of combining both PID and NNC, only the network output torque controls the attitude. The learning process obtains the weights that minimize the PID signal. Due to the delay in the feedback error, some torque oscillations may occur, and the control becomes unstable. In order to avoid this behavior, the network output torque was also added to the learning signal, as shown also in Figure 1. This procedure not only guarantees the control stability, but also tends to minimize the control output and therefore the hydrazine consumption.

Unfortunately, the process of adjusting the PID gains and the network feedback torque gain  $K_c$  was very difficult, as the stability of NNC teaching was assured only within a reduced gain margin. The learning rate coefficient  $\lambda$  had to be small, in order to compensate the deviations of the learning signal from the unknown teaching control  $u^d$ .

Attitude simulations were carried out to teach the neural control. Propagation time was 1000 s duration, with time step of 1 sec. The solar arrays are opened at  $t = 500$  s. Random initial conditions were selected uniformly distributed between  $\pm 45^\circ$  attitude angles and  $\pm 0,5$  rad/s angular velocity. Reference trajectory  $y^d$  was fixed with null angular rate.

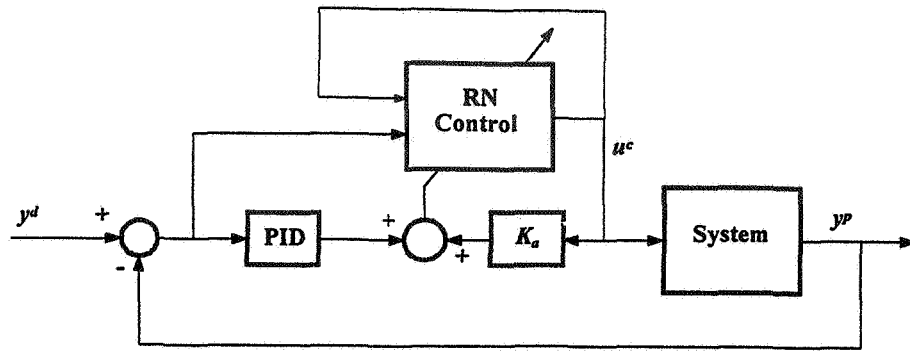


Fig. 1 – Feedback error learning control without PID supervision.

Neural network inputs were composed by the attitude angles  $\phi^p$ ,  $\eta^p$  and  $\psi^p$ , (from a XYZ rotation), the components of the satellite angular velocity,  $\omega_x$ ,  $\omega_y$  and  $\omega_z$  and the solar array deployment sensor angle at time  $t$ . In order to provide information about the attitude dynamics, these values at instant  $t$ ,  $t-1 \dots t-3$  were also given. The input vector contains also the components of the output torque  $\tau_x$ ,  $\tau_y$  and  $\tau_z$  at times  $t-1 \dots t-4$ . The network was composed of 40 neurons in the hidden layer (with sigmoid activation function) and 3 output neurons for torque generation with hard limited linear activation function. The learning rate coefficient,  $\lambda$ , was adopted as 0.001 after several trials with different values. The PID controller gains was 0.08, 0.05 and 20, respectively. These values were obtained by trials, based on learning convergence and stability and do not reflect any optimization criteria.

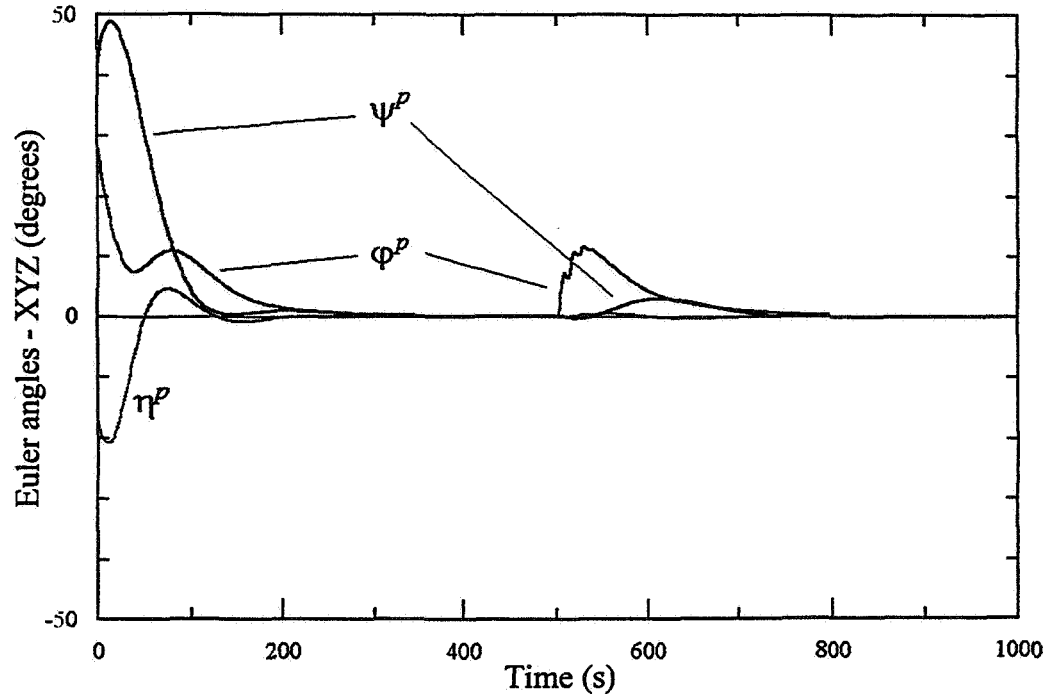


Fig. 2 – Satellite attitude during solar array deployment with a FLC without PID supervising.

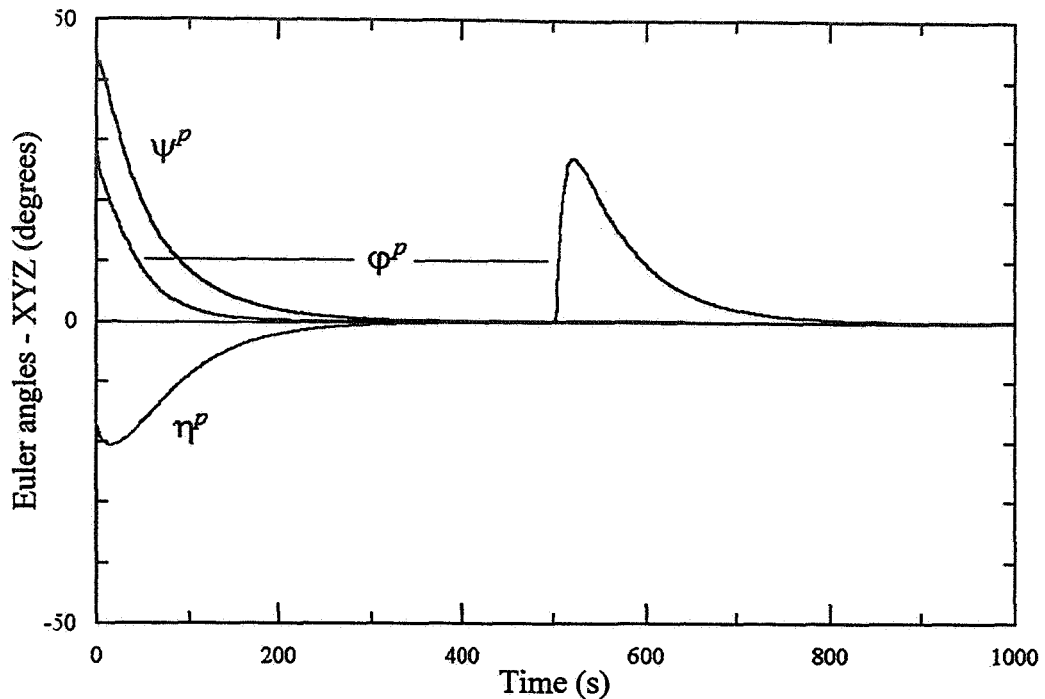


Fig. 3 – Satellite attitude during solar array deployment with PID control.

The same is true for the  $K_c$  gain, adjusted in 0.02. After the training process (6000 interactions), the neural net was used to control the satellite starting with a different attitude, shown in Figure 2. As can be seen, NNC can provide an effective attitude control even without the presence of the PID supervision.

The attitude motion was then compared with that of an exclusive PID controller, with the same gains used to train the neural network. As shown in Figure 3, the PID exerts a control on the satellite similar to that of the NNC when no geometry variation occurs. The main difference, as expected, happens when the solar arrays are opened. In such a situation the NCC performance is better than the PID, mainly due to the adaptation caused by the deployment information.

### Satellite with Flexible Appendages

The control structure used in this implementation is known as Internal Model Control (IMC) (Ref. 16). In this structure an Artificial Neural Network (ANN) is trained to behave as the dynamic system (direct model). Soon after, a second ANN, the control network is trained according to the inverse model, using in the training the retro-propagation of error in the direct model disturbances. The difference among the real trajectory of the plant and the trajectory supplied by the direct model is used then in the form feedback to correct the state and to compensate the effects of the . Due to the fact that the nets are not fed with information that allow the disturbances " d " that affect the behavior of the system, they don't get to eliminate the errors in the trajectory due to the effects of these disturbances (Ref.17).

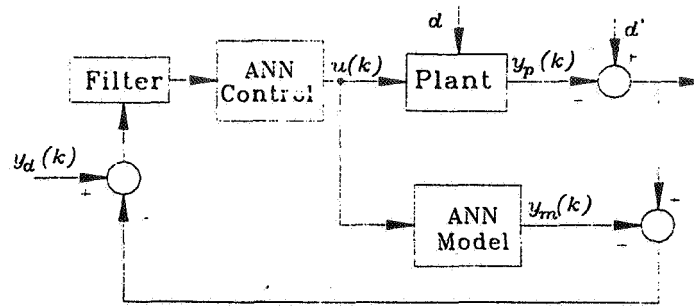


Fig.4 - Internal Model Control (IMC)

The neural network control (IMC) was implemented and simulated using a satellite with configuration similar to MECB satellite characteristics. During the phase of fine pointing, the satellite will have a horizon infra-red and fine solar sensor, positioned in an appropriate way on the main body of the satellite. In this phase of mission the satellite will have three actuators of the type Reaction Wheel with a maximum torque generation of 0,2 Nm, to supply the torque demanded by the control system.

The first step for the implementation of the neural control is to make the identification of an ANN for the direct model, which had as inputs the control torque, the displacements and the angular velocity at instants  $t$ ,  $t-1$  and  $t-2$ . After some tests varying the number of neurons in each layer and being verified the error at the end of the net training, it was adopted a configuration composed by 22 neurons in the input layer (21 elements and one more due to the "bias"), 30 neurons in the first hidden layer, 10 neurons in the second hidden layer and 6 neurons in the exit layer. The hyperbolic tangent activation function was adopted for all the neurons.

After the identification of the direct model, the identification of the control network should be proceeded (identification of the inverse model). This training was also executed in an off-line way using the outline of the specialized inverse model, with an input vector similar to that used previously. The topology of the control network was established taking as a basis the general lines delineated for the identification of the direct model net; tests led to a configuration composed by 25 neurons in the input layer, 30 neurons in the first hidden layer, 10 neurons in the second layer hidden and 3 neurons in the exit layer. The hyperbolic tangent activation function was adopted for all the neurons.

Simulations were made involving several attitude maneuvers with several initial conditions to evaluate the performance of the proposed scheme. A typical maneuver is shown with the objective of illustrating the acting of the control scheme. The Figures 5 and 6 show respectively the answer of the attitude angle and angular velocity in relation to the reference signal. The Figure 7 show the torque demanded to the actuator for the maneuver in the pitch axis. It is observed from these results, that at the end of the pointing maneuver, the attitude angle as well as the angular speed of the satellite are inside the acceptable accuracy. It is also noticed that the torque applied to the rotor stayed limited to the compatible values.

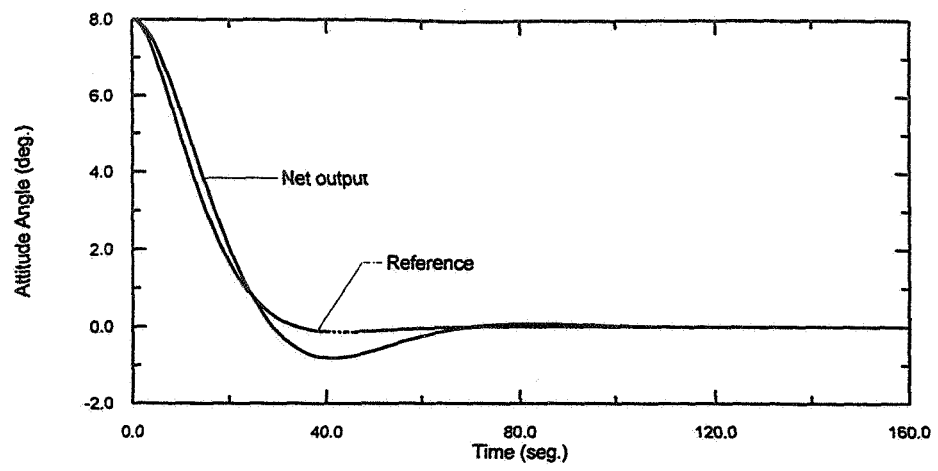


Fig. 5 - Attitude angle.

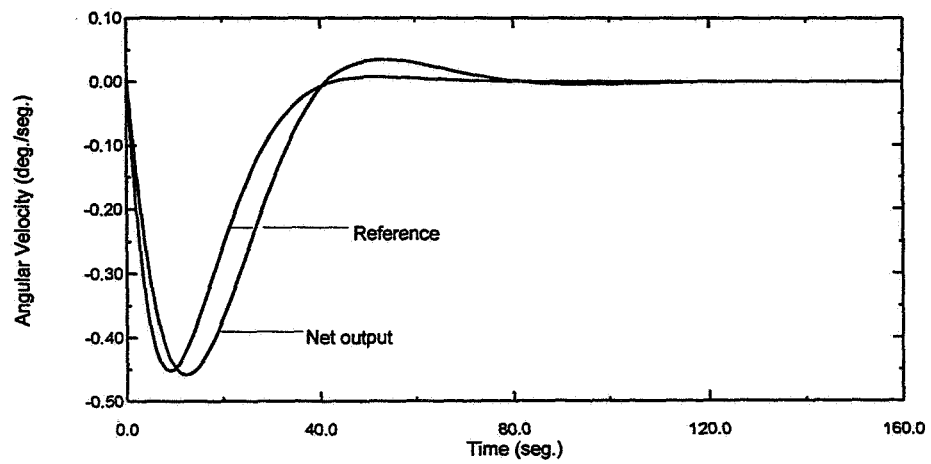


Fig. 6 - Angular velocity.

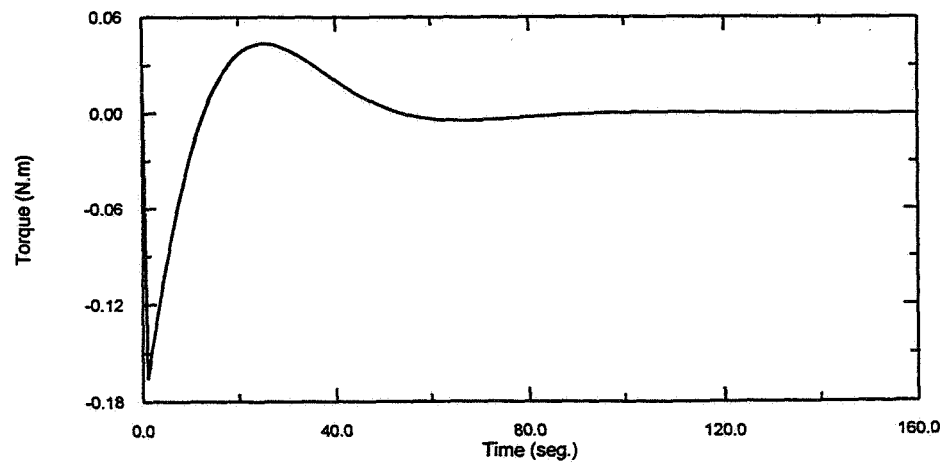


Fig. 7 - Torque demanded to the actuator.

In the tested situations, the neural control procedure was able to execute the satellite pointing maneuver. The free oscillations in the extremity of the panels (not shown in the previous graphs) stayed quite small with values of the order of  $3 \times 10^{-5}$  mm, not introducing any type of sensitive disturbance in the attitude of the vehicle.

## CONCLUSIONS

Two attitude control schemes using multilayer perceptron were developed and tested under simulated conditions of use. The first one was, an attitude controller for a satellite with variable geometry derived from the feedback error learning algorithm, without the PID control supervision. The results indicated that the performance of the NNC can, under certain conditions, be more better than that of a conventional PID controller. The second one was an attitude controller for a satellite with flexible appendages using the IMC control procedure. Results obtained with this scheme are very encouraging. It could be verified that the strong point of ANNs is really their capacity of non linear mapping, mainly in the identification of the System Direct Model. In the Inverse Model identification, special care should taken concerning to the choice of the variables to represent the dynamic system, sence they play a fundamental role in obtaining the correct inverse mapping of the plant.

The control schemes with " off-line " training of the ANNs facilitates a more immediate application, however its reliability and robustness are limited, because such controllers possess a restricted operation and are not capable to compensate eventual disturbances or spurious interactions between the environment and the plant to be controlled. Further studies shall address adaptive schemes using special computational structures and training algorithms for "on-line" retraining of the ANNs.

## BIBLIOGRAPHY

1. Demuth, H; Beale, M. *Neural network toolbox user's guide*. Natick, MA. Math Works, 1992.
2. Rios Neto, A.; Rao, K. R. *A study on the on board artificial satellite orbit propagations using artificial neural networks*. Proceedings of the 11<sup>th</sup> International Astrondynamics Symposium, Gifu, Japan, 1996.
3. Hunt, K. J.; Sbarbaro, D.; Zbikowski, R.; Gawthrop, P. J. Neural networks for control systems - a survey. *Automatica*. 28 (6):1083-1112, 1992.
4. Nguyen, D. H.; Widrow, B. Neural networks for self-learning control systems. *IEEE Control Systems Magazine*, 10 (3), Apr. 1990.
5. Chen, S.; Billings, S. A. Neural networks for nonlinear dynamic system modelling and identification. *International Journal of Control*, 56 (2):319-346, 1992.
6. Baffes, P. T.; Shelton, R. O.; Phillips, T. A. *NETS, a neural network development tool*. Lyndon B. Johnson Space Center, JSC-23366, 1991.
7. Billings, S. A.; Jamaluddin, H. B.; Chen, S. Properties of neural networks with applications to modelling non-linear dynamical systems. *International Journal of Control*. 55 (1):193-224, 1992
8. Zurada, J. M. *Introduction to Artificial Neural Systems*, West Publishing Co. 1992.



9. Rios Neto, A. Stochastic Optimal Linear Parameters Estimation and Neural Nets Training in Systems Modeling. *Journal of the Brazilian Soc. Mechanical Sciences*, Vol. XIX, nº 2, 138-146, 1997.
10. Gelb, A. *Applied Optimal Estimation*. The M.I.T. Press, MA, 1974.
11. Crandall, S. H.; Kornopp, D. C.; Kurtz Jr, E. F.; Pridmore-Brown, D. C.; *Dynamics of mechanical and electromechanical systems*. Mc Graw-Hill, NY, 1968.
12. Wertz, J. R. *Spacecraft attitude determination and control*, London, D. Reidel, 1978 (Astrophysics and Space Science Library).
13. Meirovitch, L. *Method of Analytical Dynamics*, New York, McGraw-Hill, 1970.
14. Kaplan, M. H. *Modern Spacecraft Dynamics*. USA, Jhon Wiley & Sons Inc., 1973.
15. Chen, S.; Billings, S. A.; Grant, P. M. Non-linear system identification using neural networks. *International Journal of Control*, 51 (6):1191-1214, June 1990.
16. Narendra, K. S.; Parthasarathy, K. Identification and control for dynamic systems using neural networks. *IEEE Transactions on Neural Networks*, 1, 1990.
17. Garcia, C. E. ; Morari, M. Internal model control - 1. A Unifying Review and Some New Results, *Ind. Eng. Chem. Process Des. Dev.*, vol. 21, pp. 308-323, 1982.

REPORT DOCUMENTATION PAGE			Form Approved OMB No. 0704-0188	
Public reporting burden for this collection of information is estimated to average 1 hour per response, including the time for reviewing instructions, searching existing data sources, gathering and maintaining the data needed, and completing and reviewing the collection of information. Send comments regarding this burden estimate or any other aspect of this collection of information, including suggestions for reducing this burden, to Washington Headquarters Services, Directorate for Information Operations and Reports, 1215 Jefferson Davis Highway, Suite 1204, Arlington, VA 22202-4302, and to the Office of Management and Budget, Paperwork Reduction Project (0704-0188), Washington, DC 20503.				
1. AGENCY USE ONLY (Leave blank)		2. REPORT DATE May 1998		3. REPORT TYPE AND DATES COVERED Conference Publication
4. TITLE AND SUBTITLE Preprint—AAS/GSFC 13th International Symposium on Space Flight Dynamics, Volume 1			5. FUNDING NUMBERS  572	
6. AUTHOR(S)  Tom Stengle, Editor				
7. PERFORMING ORGANIZATION NAME(S) AND ADDRESS (ES) Guidance, Navigation and Control Center Flight Dynamics Analysis Branch Goddard Space Flight Center Greenbelt, Maryland 20771			8. PERFORMING ORGANIZATION REPORT NUMBER  98B00041	
9. SPONSORING / MONITORING AGENCY NAME(S) AND ADDRESS (ES)  National Aeronautics and Space Administration Washington, DC 20546-0001			10. SPONSORING / MONITORING AGENCY REPORT NUMBER  CP-1998-206858	
11. SUPPLEMENTARY NOTES				
12a. DISTRIBUTION / AVAILABILITY STATEMENT Unclassified—Unlimited Subject Category: 13 Distribution: Nonstandard Availability: NASA CASI (301) 621-0390.			12b. DISTRIBUTION CODE	
13. ABSTRACT (Maximum 200 words) This conference proceedings preprint includes papers and abstracts presented at the 13th International Symposium on Space Flight Dynamics, May 11–15, 1998. Cosponsored by American Astronautical Society and the Guidance, Navigation and Control Center of the Goddard Space Flight Center, this symposium featured technical papers on a wide range of issues related to orbit-attitude prediction, determination, and control; attitude sensor calibration; attitude dynamics; and mission design.				
14. SUBJECT TERMS American Astronautical Society, spaceflight dynamics.			15. NUMBER OF PAGES 545	
			16. PRICE CODE	
17. SECURITY CLASSIFICATION OF REPORT Unclassified	18. SECURITY CLASSIFICATION OF THIS PAGE Unclassified	19. SECURITY CLASSIFICATION OF ABSTRACT Unclassified	20. LIMITATION OF ABSTRACT  UL	